Development and Optimisation of Novel Fibrous Oxygen Carriers for Chemical Looping Reforming Processes

Robert Bloom

Submitted in accordance with the requirements for the degree of

Doctor of Philosophy

University of Leeds

School of Chemical and Process Engineering

October 2018

The candidate confirms that the work submitted is their own and that appropriate credit has been given where reference has been made to the work of others.

This copy has been supplied on the understanding that it is copyright material and that no quotation from the thesis may be published without proper acknowledgement.

The right of Robert Bloom to be identified as Author of this work has been asserted by him in accordance with the Copyright, Designs and Patents Act 1988.

Acknowledgements

First and foremost, I would like to thank my supervisory team Dr Valerie Dupont and Dr Steven J. Milne for their research expertise, guidance and support over the four years of my PhD. Without them both, the quality of my work work and personal wellbeing would undoubtedly have suffered and for this I am truly grateful.

Much of my research would not have been possible without the help of Edmund Woodhouse and the technical staff in SCAPE; their aid in fabrication and construction of the packed bed reactor was essential and they have my sincerest thanks. Moreover, I would like to thank Jenny Forrester for her advice on XRD, Stuart Micklethwaite for his input in SEM analysis, Dr Nicole Hondow for the assistance she gave in TEM analysis and Dr Adrian Cuncliffe, Dr Ben Douglas and Simon Lloyd for their aid in the analytical labs.

I also wish to thank the EPSRC (via the Low Carbon Technologies Doctoral Training Centre) and the UKCCSRC (via the Call 2 Capture Projects) for the financial support without which my research could not have been carried out. Further thanks must be extended to Jonathan Cross (Unifrax Ltd) and Dr Martyn V. Twigg (TST Ltd) for supplying the CG Saffil® material and the conventional catalyst material and for their input into this project.

To all my colleagues and more accurately my friends on the low carbon and bioenergy DTC who are too many to mention in full, my thanks goes out to you. Special mention must be made for Dr Dougie Phillips and Dr Dave Allen with whom I shared so many great times (generally away from research), to Dr Katrina Adam who kept me sane during the final months and to Dr Niamh Ryall and Dr Tom Taynton who kept a roof over my head for my final year.

Of course, I must thank my family especially my parents for their continued belief and support especially at the end.

Finally, to my partner Dr Sally Jennings; your patience, insight, belief, compassion, empathy and advice have not only been a constant crutch throughout my studies but have made made me a far better person – thank you.

Abstract

Aluminosilicate microfibers have been applied as structured catalyst supports for their specific use as oxygen carriers (OC's) in the chemical looping steam reforming (CLSR) of methane for the first time. CLSR is a syngas and hydrogen production technology designed to intensify the traditional catalytic steam methane reforming process by improving the provision of heat to the endothermic steam reforming (SR) reaction whilst producing a non-nitrogen diluted syngas. It does so through the cyclical reduction and oxidation of a solid OC material. Application of fibrous structured OC's to packed bed CLSR can, in principle, offer further intensification through their excellent heat and mass transfer properties and increased process and physical flexibility when compared to conventional OC's.

Nine cobalt doped 18 wt% nickel-based OC's each deposited on a Saffil® (Sf) aluminosilicate fibre support (~ 95 % γ-Al_2O_3, ~5 % SiO_2, fibre width 3 - 4 μm and length ~ 5 mm) were produced using three methodologies; wet impregnation (WI), deposition precipitation (DP) and hydrothermal synthesis (HT). The Sf OC's exhibited a deposited layer consisting of NiO with no evidence of bulk nickel aluminate ($NiAl_2O_4$) spinel phase. These materials were characterised and compared to a granulated 18 wt% NiO/α-Al_2O_3 OC (18NiO GR) prepared from bulk pellets in SR and CLSR experiments using a benchtop packed bed reactor and a N_2 diluted CH_4/H_2O mixture feed (steam to carbon ratio 3:1).

Isothermal CLSR at 700 °C showed that once reduced to Ni by the CH_4/H_2O feed, the Sf OC's increased the average CH_4 conversion during SR when compared on an equal mass basis by up to ~ 10 percentage points (86 % to 96 %) in the 18Ni Sf-HT OC compared to the 18NiO GR OC. When compared to the 18NiO GR OC on an equal volume basis, the Sf OC's produced only a small penalty to these factors above despite operating with 80% less mass of OC. These improvements in catalytic performance of the Sf OC's are likely caused by a reduction in the effective diffusion length required for CH_4 to transfer from the bulk gas to active Ni catalytic sites, and for reaction products to diffuse away from those sites into the bulk gas phase, thereby reducing the effects any diffusion limitation of the SR reaction. The Sf-DP and Sf-HT OC's improved SR performance over the Sf-WI OC's in both the equal volume and equal mass CLSR conditions. These results were similar when tested in SR experiments using an OC pre-reduced by a N_2 diluted H_2 feed.

In a series of kinetic investigations (450 - 700 °C), the reduction reactions of the Sf OC's and the 18NiO GR OC during CLSR of methane were best described by the Avrami-Erofeyev nucleation and nuclei growth model. The Sf OC's exhibited greater reduction reactivity, a higher peak rate of reduction, and a 40% decrease in the activation energy of reduction when compared to the 18NiO GR OC.

Table of Contents

List of Tables

List of Figures

Nomenclature

Symbol	Description	Units
$\bar{W}_i$	Relative molecular mass of component i	g mol^{-1}
$\dot{V}_{i,in}$	Volume flow rate of component i into the reactor	-
$\dot{n}_i$	Molar flow rate of component i	mol s^{-1}
∅	Mol of solid reactant reduced by 1 mol of gaseous reactant	-
∈	Desired molar Ni/Co:urea ratio	-
μ	Viscosity	kg m^{-1} s^{-1}
18NiO GR	Granulated 18 wt% NiO/α-Al_2O_3 catalyst	-
A	Pre-exponential factor	s^{-1}
AAS	Atmoic Adsorption Spectroscopy	-
BET	Brauner-Emmett-Teller model	-
BJH	Barrett-Joyner-Halenda model	-
BSE	Backscattered electrons	-
C:H	Molar carbon to hydrogen ratio	-
CEA	Chemical Equilibrium with Application	-
CG	Catalytic grade	-
C_{ib}	Concentration of component i in the bulk phase	mol m^{-3}
C_{is}	Concentration of component i at the particle surface	mol m^{-3}
CLC	Chemical looping combustion	-
CLG	Chemical looping gasification	-
CLPO	Chemical looping partial oxidation	-
CLR	Chemical looping reforming	-
CLSR	Chemical looping steam reforming	-
CLWS	Chemical looping water splitting	-
C_p	Heat capacity	J kg^{-1} K^{-1}
C_{wp}	Weisz Prater Criterion	-
d	Interplanar distance	nm
$D`_e$	Effective diffusivity	m^2 s^{-1}
$D`_i$	Effective diffusivity of component i in the bulk gas	m^2 s^{-1}
d_f	Fibre diameter	m

DP	Deposition precipitation	-
d_p	Diameter of spherical particle	m
d_s	Sauter diameter	m
d_{str}	Diameter of foam strut	m
E	Electron volts	kV
E_A	Activation energy	kJ mol^{-1}
EM	Equal mass conditions	-
EV	Equal volume conditions	-
f(α)	Solid state kinetic model	-
G	Gibbs free energy	kJ mol^{-1}
g(α)	Integration of solid-state kinetic model	-
GOF	Goodness of fit	-
GHG	Greenhouse gas emissions	-
GWP	Global warming potential	-
H	Enthalpy	kJ mol^{-1}
h	Heat transfer coefficient	W m^{-2}
HAADF	High-angle annualr dark field detector	-
HT	Hydrothermal synthesis	-
HTS	High temperature shift	-
K	Scherrer equation shape factor	-
k	Rate constant	s^{-1}
k_c	Mass transfer coefficient	m s^{-1}
L_f	Length of fibre	m
LPG	Liquified petroleum gas	-
LTS	Low temperature shift	-
m_0,OC	Initial OC mass at time t	g
MEA	Monoethanolamine	-
MFC	Mass flow controller	-
MFEC	Microfibre entrapped catalyst	-
m_i	Mass of component i	g
m_{OC}	Mass of OC	g
$m_{red,max}$,OC	OC wt% loss if complete reduction is achieved	wt%

m_{red},OC	OC wt% loss during TGA reduction	wt%
m_t,OC	OC mass at time t	g
$m_{t=0}$,OC	OC mass at beginning of TGA reduction event	g
m_0,OC	OC mass measured before the TGA experiment	g
n	Diffraction peak order	-
Nu	Nusselt number	-
OC	Oxygen carrier	-
P	pressure	Pa
P_o	Vapour pressure of N_2 adsorbate	Pa
P_c	Critical pressure of component	Pa
Pe	Peclet number	-
PEFB	Palm empty fruit bunch	-
P_{eq}	Equilibrium pressure of N_2 adsorbate	Pa
P_{eq} / P_o	Realtive pressure	-
Pr	Prandtl number	-
PSA	Pressure swing adsorber	-
q	Heat flux	W m^{-2} K^{-1}
R	Universal gas constant	J mol^{-1} K^{-1}
-r`$_{red}$(obs)	Max measured rate of reduction per unit mass	mol kg^{-1} s^{-1}
Re	Reynolds number	-
Re_s	Reynolds number calculated using d_s	-
R_{exp}	Expected residual value	-
r_i	Max rate of reduction by reactant i per unit surface area	mol m^{-2} s^{-1}
RK	Reduction kinetics conditions	-
r_{ox},OC	Rate of OC oxidation	s^{-1} / mol s^{-1}
$r_{red,max}$	Max rate of reduction	mol s^{-1}
r_{red},OC	Rate of OC reduction	s^{-1} / mol s^{-1}
R_{wp}	Weighted residual value	-
S	Entropy	kJ mol^{-1} K^{-1}
S:C	Molar steam to carbon ratio	-
$SA_{p,ext}$	External surface area of the solid particle	m^2 g^{-1}
Sc	Schmidt number	-

SE	Secondary electrons	-
SECLSR	Sorption enhanced chemical looping steam reforming	-
SEM	Scanning electron microscopy	-
Sf	CG Saffil® fibres	-
Sh	Sherwood number	-
Sh_s	Sherwood number calculated using d_s	-
SMR	Steam methane reforming	-
SR	steam reforming (reaction)	-
SS	Stainless steel	-
SSA	Specific surface area	$m^2\ g^{-1}$
STEM	Scanning transmission electron microscopy	-
STP	standard temperature and pressure (20C and 101325 Pa)	-
$S_{v,bed}$	External surface area per foam unit bed volume of spherical pellets	m^{-1}
$S_{v,cell}$	External surface area per foam unit cell volume	m^{-1}
t	time	s
T	Temperature (units always specified)	°C / K
T_o	Bulk fluid temp	K
T_c	Critical temperature of component	K
TEM	Transmission electron microscopy	-
TGA	Thermogravimetric analysis	-
t_m	Temperature (K/1000)	K
TOF	Turnover frequency	-
TPR	Temperature programmed reduction	-
T_r	Ratio of of component temperature to critical temperature	K
T_s	Temperature at the surface	K
UMC	Unmixed combustion	-
U_s	Superficial velocity	$m\ s^{-1}$
USR	Unmixed steam reforming	-
V_{bed}	Volume of OC bed	cm^3
WCO	Waste cooking oil	-
WGS	Water gas shift	-

WI	Wet impregnation	-
W_i	Average molar flux of component i from the bulk gas phase to a solid particle	mol m^{-2} s^{-1}
x_i	Mass fraction of component i	-
XRD	X-ray diffraction	-
y_i	Molar fraction of component i	-
α	Solids conversion	-
α_{red}	Extent of reduction	-
α_t	Thermal diffusivity	m^2 s^{-1}
β	Line broadening	rad
ε	Void fraction	-
η	Effectiveness factor	-
θ	Bragg angle	deg
λ	Wavelength	nm
λ_i	Thermal conductivity of component i	J s^{-1} m^{-1} K^{-1}
ν	Kinematic viscosity	m^2 s^{-1}
ν_i	Special atomic diffusion volume of component i	-
ρ_{bulk}	Bulk density	kg m^{-3}
ρ_i	Density of component i	kg m^{-3}
ρ_p	Density of particle	kg m^{-3}
σ	Mean boundary layer thickness around solid particle	m
σ_p	Constriction factor of pellet	-
τ	Tortuosity of solid particle	-
ϕ_p	Porosity of the solid particle	-
ω	Accentric factor	-

1 Introduction, Background and Context

Hydrogen is a vital component and feedstock in a number of processes and its use has allowed the development of technologies key to population growth, fuel processing and bulk chemical production[1,2]. As a result the world demand for hydrogen is growing[3]. Hydrogen is almost never found in its pure diatomic form; it is almost always bound by other elements, such as oxygen and carbon. Therefore it must be separated from these more complex molecules to be used effectively[1,2].

The means by which hydrogen is produced is therefore important and the development of this field has made great strides in the last 50 years[4]. Despite this, the current methods of hydrogen production are by no means perfect. The vast majority of hydrogen today is produced via steam methane reforming (SMR), a process which was invented in 1868 and first used industrially in the 1930s[1,3,4]. This process is based on the consumption of fossil fuels, produces large amounts of greenhouse gas emissions and is only economic on huge scales due to various inefficiencies in the process[5]. The need for innovation and intensification in hydrogen production is becoming increasingly obvious especially given the widespread awareness of anthropogenic climate change and the detrimental effects human industry is having on the planet's ecosystems.

To understand how these weaknesses in hydrogen production may be remedied, it is important to summarise why hydrogen is used, how it is produced and why the methods of production must change.

1.1 Demand for Hydrogen

Hydrogen is used as a feedstock in several industrial processes, the most important of which are ammonia production for use in fertilisers and the refining of petroleum crudes. These two processes dominate the demand for industrially produced hydrogen accounting 87 % of the hydrogen used worldwide as of 1998, with consumption patterns seeing very little change since the early 2000's[6,7]. Additionally, hydrogen was seen in the early 2000's as a potential energy carrier that could be used as a basis of a "hydrogen economy". In this vision hydrogen would be used in a similar manner to electricity today, powering transport

and used as a means of energy storage. As a result of these three primary uses of hydrogen, demand for the product is increasing[3,8].

1.1.1 Ammonia Production

Arguably the most important use of hydrogen is as a feedstock in the production of ammonia. In the Haber-Bosch process, hydrogen is reacted with nitrogen over an iron catalyst to produce ammonia at high temperature (650 – 750 K) and pressure (50 – 200 bar)[9], Equation 1.1.

$$N_{2(g)} + 3H_{2(g)} \leftrightarrows 2NH_{3(g)} \qquad \Delta H_{298K} = -45.9 \text{ kJ mol}^{-1} \qquad \textbf{Equation 1.1}$$

This process, developed in the early part of the 20th century, finally allowed a method by which a reactive fixed nitrogen compound could be produced synthetically in large amounts[10,11]. The Haber-Bosch process greatly increased the amount of fixed nitrate available on the world market. This allowed the widespread production and use of nitrogen based fertilizers thereby facilitating a significant increase in the mass of food crop that could be grown per unit area of arable land[10,11].

This increase in agricultural efficiency due to the production of ammonia was instrumental in the trebling of the world's population that has been observed during the 20th century. The increase in fixed nitrogen production after 1950 coincides with a much greater rate in population growth, Figure 1.1.

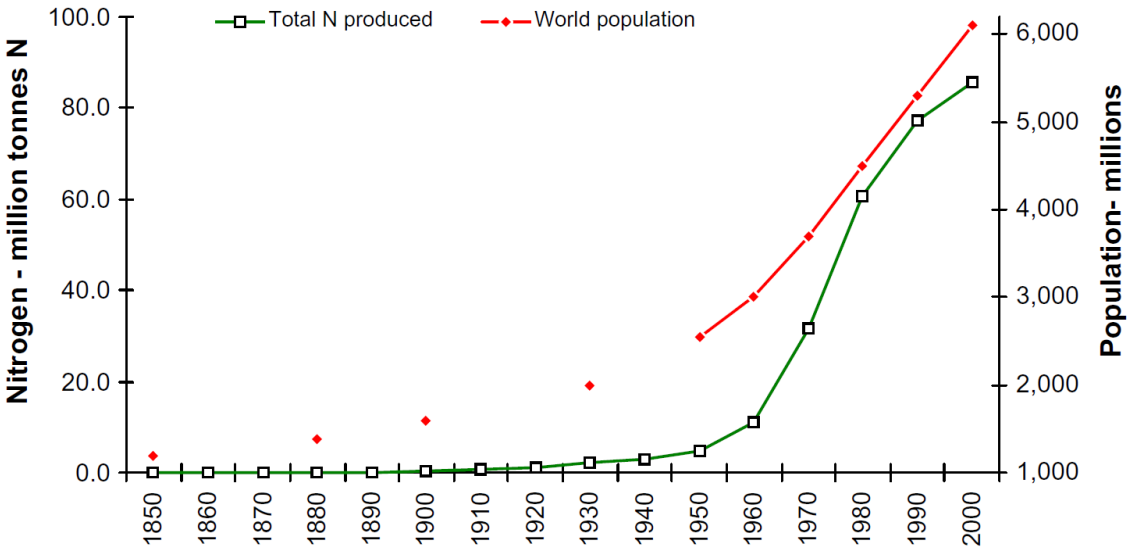

Figure 1.1: Production of nitrogen fertiliser in relation to world population[10]

The world population between 1900 and 2000 in relation to the percentage of the world population fed by Haber-Bosch nitrogen and the predicted world population had Haber-Bosch synthesis not been invented, Figure 1.2. This agrees with the data in Figure 1.1 in

that the advent of Haber-Bosch synthesis has greatly contributed to the increase in world population in the 20th century.

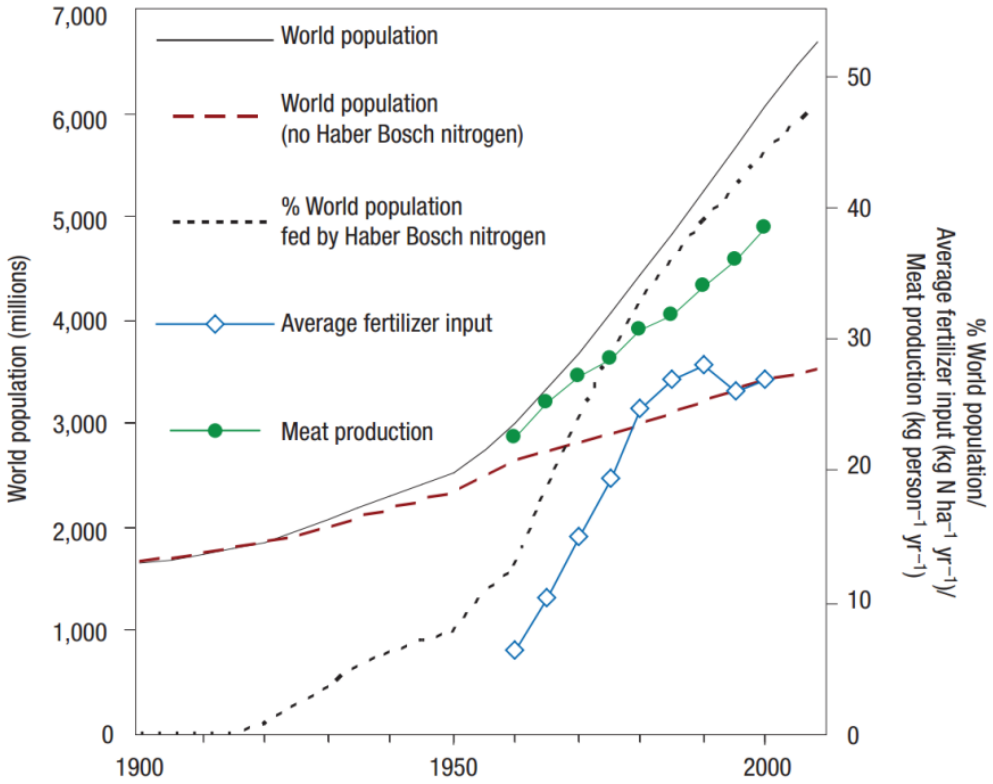

Figure 1.2: Trends in human population and nitrogen use throughout the twentieth century[11]

As a result, a great amount of industrially produced hydrogen is required for the continuation of this process. Over 2.3 million tonnes of hydrogen are produced and used in ammonia production each year in the US alone, demanding 21 % of the industrially produced hydrogen in the country[1,3]. Worldwide this figure increases to 3.6 million tonnes or 50 % of the total industry volume production[6,12].

The demand for hydrogen for the Haber-Bosch process looks set to increase due to the increase in world population over the next 100 years. The UN predicts that the world population will rise from 7.5 billion to anywhere between 9.5 and 13.5 billion in the next 85 years[13]. As the amount of arable land in the world is finite, in order to produce enough food to sustain population growth nitrogen based fertilisers must continue to be used to improve crop yields; without these fertilisers the current population would require 167 % of arable land in the world[10,11]. If the population rises to 9.8 billion (a conservative estimate), 225 % of current arable land would be required[10,11]. It would therefore be surprising if hydrogen demand for the production of ammonia did not also increase due to these factors.

1.1.2 Petroleum Refining

Hydrogen is used as a feedstock for a number of refining processes for the improvement of crude oils. Two key processes are known as hydrocracking and hydroprocessing. Hydrocracking aims to simultaneously crack (i.e. reduce the hydrocarbon chain length) and hydrogenate (i.e lowering the fuel's C:H ratio) the fuel to improve its quality[1,6,7]. Hydroprocessing involves the hydrogenation of sulphurous, nitrogenous and organometallic (V and Ni) compounds in the fuel to remove them from the fuel (S content as H_2S and N content as NH_3), which improves the fuel's quality and allows its use in sensitive applications[6]. These processes are becoming steadily more important to the refining industry due to a shift in end-product demand, more stringent environmental regulations and the need to improve poorer crudes to increase profit[6,14]. Thanks to a decreasing market for heavy fuel oil and the growing scarcity of crude oil, the hydrocracking of heavy oil fractions to produce shorter chain hydrocarbon fractions like kerosene, petrol and diesel is becoming more economically attractive[6,14]. Couple this with greater demand for high quality fuels (such as low sulphur diesel) driven by environmental regulations, an increase in the demand for hydrogen is unsurprising[6,14]. As a direct result of these factors, demand for industrially produced hydrogen for use in petrochemical refining is predicted to increase by 3.5 % annually from 2.1 million tonnes in 2015, through to 2.73 million tonnes in 2025[12].

1.1.3 The Hydrogen Economy

The demand for hydrogen may also increase due to the evolution of the hydrogen economy. This is a term coined in the energy crisis of the 1970's and has come to encompass the use of hydrogen as an alternative to electricity or liquid fossil fuels as an energy carrier[2,15]. The primary advantage of this process is the provision of an energy carrier that can be produced worldwide while producing zero emissions at point of use[16,17]. As a result, this concept is only a logical alternative to more conventional energy solutions when the hydrogen needed is produced from a low or zero emissions process[15–17]. Perhaps the most suitable way to achieve this is through the electrolysis of water. In this process electricity is used to split water into its constituent oxygen and hydrogen elements[15], Figure 1.3 (overleaf).

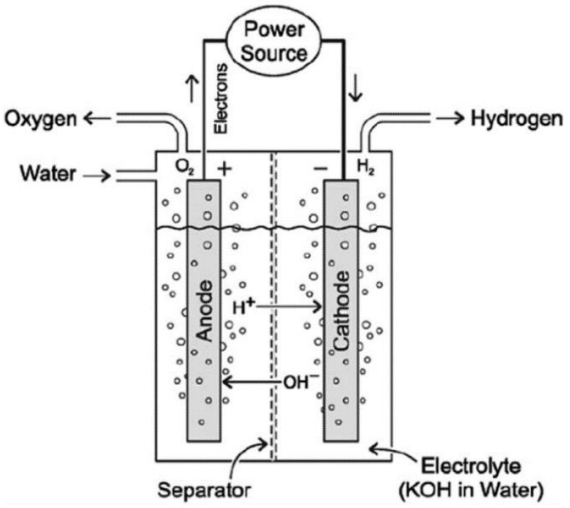

Figure 1.3: Typical alkaline electrolysis cell[18]

With the use of electrolysis, hydrogen can function as a means of energy storage for intermittent and non-demand matching electricity generation[16]. When technologies such as solar, wind and nuclear power generate electricity, their output cannot be manipulated. Therefore, when demand does not match output, excess electricity is generated. Hydrogen functions as an energy carrier when this excess electricity is used to electrolyse water. This process therefore stores the electrical energy as chemical potential energy[16].

Key to the use of hydrogen as an energy carrier is the technology used to harness the chemical energy of the hydrogen. One such technology is the hydrogen fuel cell. This technology functions in a similar manner to an electric cell; however when supplied with a constant feed of hydrogen and oxygen it can generate electricity continuously through the movement of electrons[19], Equation 1.2 and Equation 1.3.

$$2H_2 \rightarrow 4H^+ + 4e^-$$ **Equation 1.2**

$$O_2 + 4H^+ + 4e^- \rightarrow 2H_2O$$ **Equation 1.3**

The two products of this reaction are electricity and water; this makes the fuel cell an emission free technology at point of use[15]. This concept is especially attractive when applied to the transport sector. A distributed hydrogen network could be used to provide hydrogen to fuel cell powered vehicles that would use the electricity generated by the fuel cell to power electric motors[15]. The hydrogen fuel cell can provide a low or zero emissions alternative to the internal combustion vehicle that could potentially offer double the thermal efficiency[15]. However, without a zero/low emissions production method, the emissions associated with the production of the hydrogen will be far too high to provide a viable low emissions alternative to fossil fuels, Figure 1.4 (overleaf).

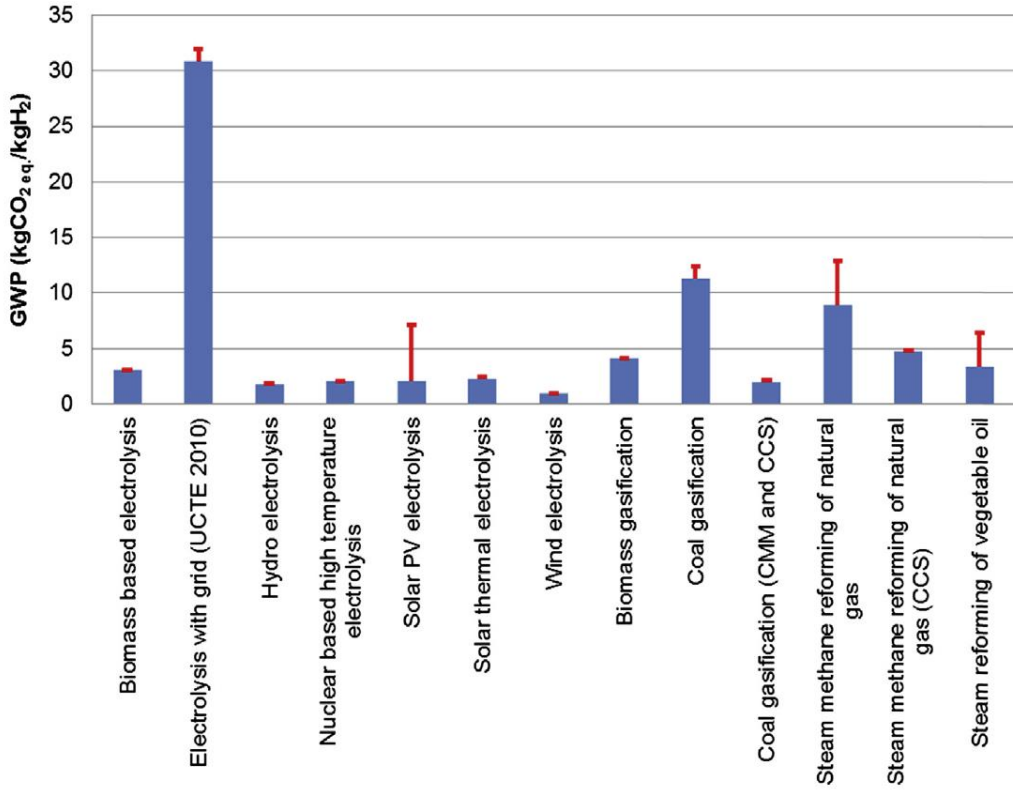

Figure 1.4: Global warming potential of different hydrogen production technologies[16]

There are however, still many issues concerning the development of the hydrogen economy that are yet to be resolved. Issues include low volumetric energy content, energy intense processes for hydrogen storage and the requirement of the provision of a large scale hydrogen supply infrastructure and high transport costs[2,15,17,20]. Nevertheless, perhaps the most pressing issue stopping the rollout of the hydrogen economy is the means of hydrogen production. As stated earlier, the use of electrolysis coupled with renewably generated electricity is crucial to the viability of hydrogen economy. However, electrolysis incurs high production costs due to low conversion efficiency and the current price of electricity[15–17]. Additionally, only 22.3 % of electricity is produced via renewable means worldwide, with 16.4 % being supplied by hydroelectric power (very geographically dependant) and only 6 % from other renewables; as a result the provision of renewable energy for electrolysis would be scarce[21]. Therefore, this scarcity of renewable energy for use in an inefficient production process, coupled with the unsuitability of other fossil fuelled hydrogen production methods provides a significant barrier to the hydrogen economy.

As a result, until electrolytic water splitting becomes more feasible or until fossil fuelled hydrogen production is made less carbon dioxide intense there is little scope for the development of the hydrogen economy.

1.2 Hydrogen Production

Hydrogen can be produced by many methods utilising a variety of different feedstocks or routes, Figure 1.5. The use of renewable and low carbon (i.e. nuclear) energy for the production of hydrogen could potentially offer a means to produce hydrogen without greenhouse gas emissions at point of use. Methods such as biomass gasification, electrolysis (powered by renewable or low carbon energy), thermal decomposition of hydrocarbons and biomass and water splitting via photolysis or thermal decomposition are all in theory either renewable or free of direct carbon emissions[17,22].

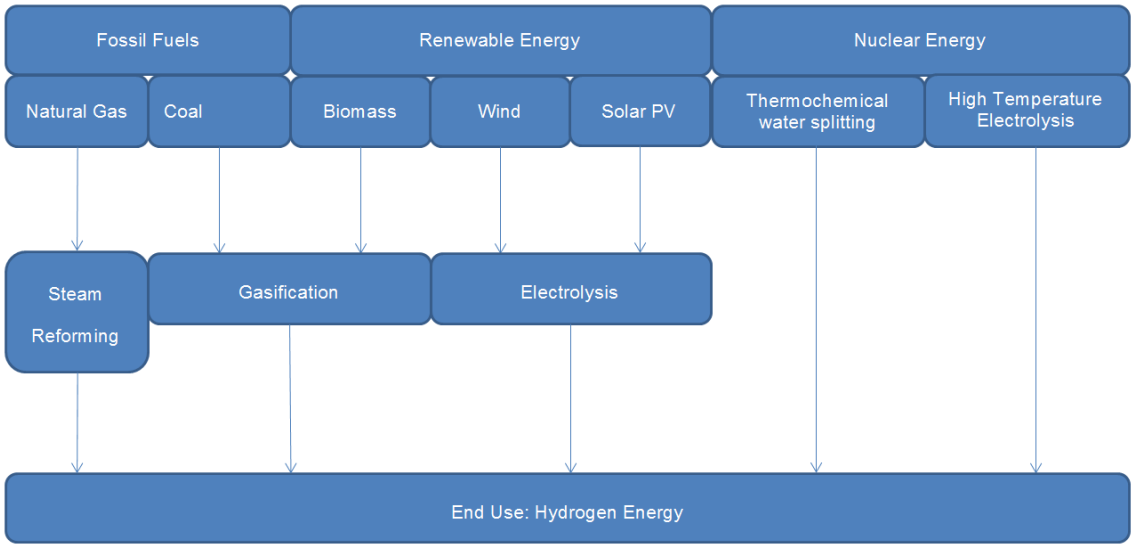

Figure 1.5: Selected hydrogen production methods[22]

However, the technological immaturity of several of the above methods mean that many of these methods exhibit significant barriers to their implementation in commercial hydrogen production. For more information, the excellent review by Acar and Dincer[17] discuss these methods and the barriers to the deployment in detail. As a result, many of these renewable and low carbon methods of hydrogen production methods are not able to produce hydrogen in an energy and cost-efficient manner. Fossil fuel derived technologies SMR and coal gasification are far more energy and cost efficient in comparison with other technologies[17,22], Figure 1.6 (overleaf).

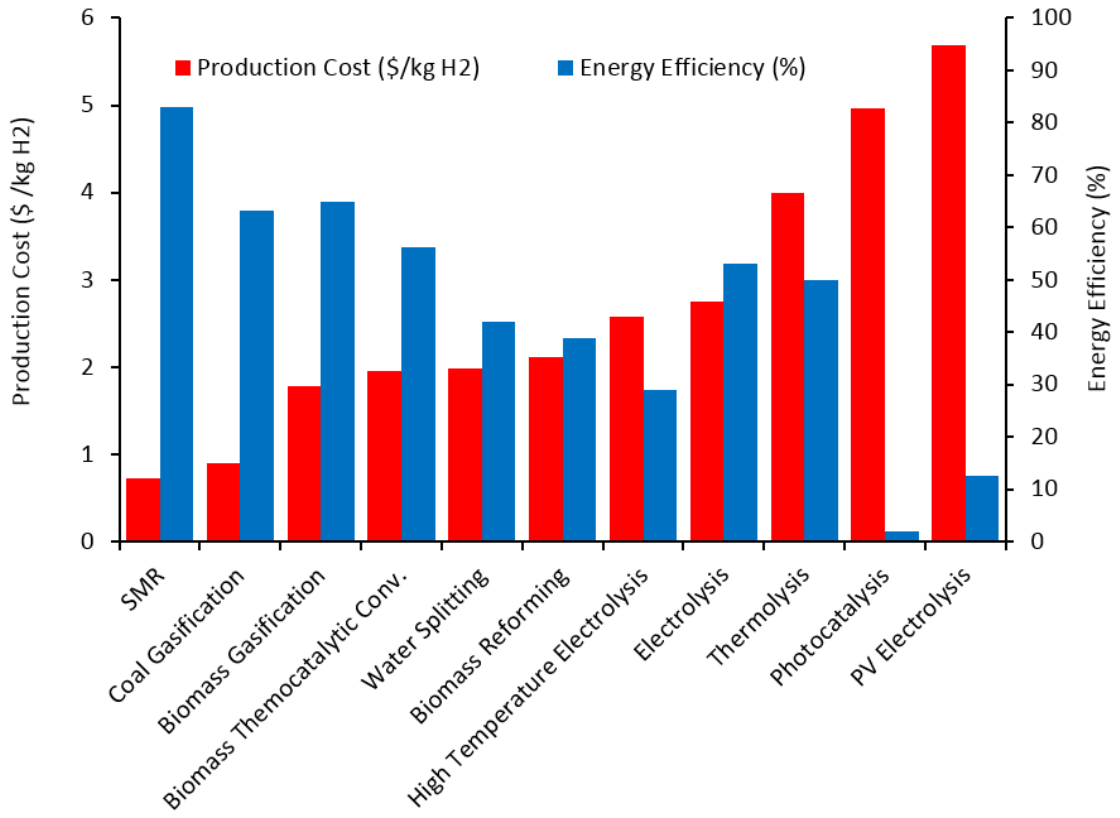

Figure 1.6: Current cost and energy efficiency of hydrogen production technologies, adapted from Dincer et al.[17]

Consequently the vast majority (96 %) of the 65 million tonnes per year of hydrogen produced is produced using fossil fuels; 48 % from natural gas feedstocks principally via SMR; 30 % from oil refinery/chemical off-gases and 18 % by coal gasification[16,23,24]. SMR is the cheapest option currently available for large scale hydrogen production, proving to be over 50 % cheaper per kg of hydrogen produced than any non-fossil fuel or renewable options[17,22]. It therefore dominates the industrial production of hydrogen and as a result, it is useful to analyse this production method in detail.

1.2.1 The Steam Methane Reforming Process

SMR is a technologically mature method of hydrogen production that reacts methane with steam at 800 - 1000 °C and 20 - 35 atm in the presence of a nickel catalyst. The steam reforming (SR, Equation 1.4) and water gas shift (WGS, Equation 1.5) reactions are responsible for the majority of the hydrogen produced via this process[4,25].

$CH_{4(g)} + H_2O_{(g)} \leftrightarrows 3H_{2(g)} + CO_{(g)}$ $\Delta H_{298K} = +206$ kJ mol^{-1} **Equation 1.4**

$CO_{(g)} + H_2O_{(g)} \leftrightarrows CO_{2(g)} + H_{2(g)}$ $\Delta H_{298K} = -41$ kJ mol^{-1} **Equation 1.5**

Both of these reactions are equilibrium limited and in spite of the exothermic nature of the WGS, overall these reactions are endothermic and therefore heat must be supplied to the system to carry out the process[25–27].

In order to extract the greatest hydrogen production efficiency and to provide a pure hydrogen feedstock the SMR process is divided into several unit operations: Desulphurisation, Pre-reforming, Primary Reforming, Water Gas Shift, and Purification. These stages are shown in the plant layout diagrams in Figure 1.7.

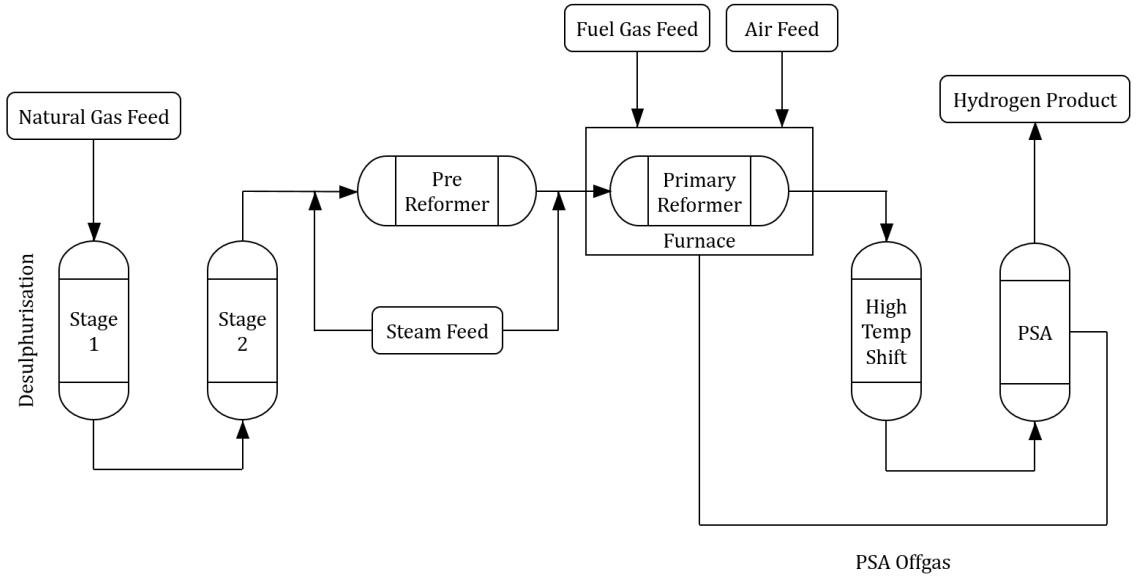

Figure 1.7: Process flow diagram of SMR using pressure swing adsorption (PSA), adapted from Haussinger et al.[27]

1.2.1.1 Desulphurisation and Pre-reforming

The natural gas used in SMR is not pure methane, rather it is a mix of predominantly methane with sulphur impurities and higher hydrocarbons present. Both sulphur and the presence of higher hydrocarbons, through a greater tendency to form carbon than methane, can cause poisoning of the catalyst thereby reducing the effectiveness of the primary reformer. As such desulphurisation and pre-reforming are conducted to reduce the concentrations of these species.

Desulphurisation is achieved through a two-step process at 400 °C that first converts any sulphurous compounds to zinc sulphide over a zinc oxide sorbent (supported by alumina) in an atmosphere of excess hydrogen, Equation 1.6. This reduces the sulphur in the feed natural gas to 0.02ppm[25,27].

$$H_2S_{(g)} + ZnO_{(g)} \rightarrow ZnS_{(s)} + H_2O_{(g)} \qquad \textbf{Equation 1.6}$$

Typically, a steam feed is used to regenerate the zinc sulphide bed when close to saturation thereby releasing SO_2.

The pre-reformer preferentially reforms higher hydrocarbons such as ethane and propane over methane in the natural gas feed by virtue of a lower temperature (500 °C) than the primary reformer, Equation 1.7[28].

$$C_nH_{m(g)} + nH_2O_{(g)} \leftrightarrows nCO_{(g)} + (n+m/2)H_{2(g)} \qquad \textbf{Equation 1.7}$$

The products of this reaction quickly go through the process of methanation (Equation 1.8 and Equation 1.9) which is favoured over the SMR reaction due the comparatively lower temperatures and high pressure, which shift the reaction towards methane production through Le Chatelier's principle[25].

$$3H_{2(g)} + CO_{(g)} \leftrightarrows CH_{4(g)} + H_2O_{(g)} \qquad \Delta H_{298K} = +206 \text{ kJ mol}^{-1} \qquad \textbf{Equation 1.8}$$

$$4H_{2(g)} + CO_{2(g)} \leftrightarrows CO_{(g)} + 2H_2O_{(g)} \qquad \Delta H_{298K} = -165 \text{ kJ mol}^{-1} \qquad \textbf{Equation 1.9}$$

Some SR of methane will occur during this process (reverse of Equation 1.8 and Equation 1.9), however this is not an issue as the duty on the primary reformer is reduced[25,29].

1.2.1.2 The Primary Reformer and Water Gas Shift

The reforming stage is carried out at high temperature (800 – 1000 °C) and high pressure (20 - 35 atm). The high temperatures maximise the conversion of methane as per Le Chatelier's principle. The high pressures, although adverse to CH_4 conversion, permit lower volume throughputs of processing to minimise plant size and therefore reduce and the cost of heat recovery and product compression after the process is complete[25,26,30,31]. According to Equation 1.4, an equimolar steam to carbon ratio (S:C) should be sufficient for steam reforming, however S:C 1.7 or above (typically 3 – 3.5) is used to avoid carbon deposition and accumulation. Carbon accumulation not only poisons the catalyst reducing its effectiveness, but also causes unwanted thermodynamic behaviour[25,27] (see Section 1.2.1.6.1).

The primary reformer consists of a large number of long thin vertical packed bed reactors filled with ceramic supported nickel catalyst (e.g. Ni/α-Al_2O_3) extruded into Raschig rings. These reactors are located within a furnace fuelled by off gases from the downstream purification unit, supplemented if necessary by some of the desulphurised natural gas feedstock. The equilibrium position of the highly endothermic SR reaction is limited by heat provision to the nickel catalyst where the reaction takes place. The long thin geometry and placement of these reactors within the furnace are used to maximise the

heat provision to the catalyst thereby maximising the effectiveness of the reformer[25,26]. The number of tubes varies by output of plant but 650 tubes between 7.5 – 12 m long, with an inside diameter of between 0.07-0.13m is typical. These reactors are fabricated from high strength, corrosion resistant steel alloys to facilitate operation at high enough pressures and temperatures to satisfy the heat demand of the internally occurring endothermic reactions while being exposed from their exterior to a fuel lean, highly radiant combustion environment[25,26].

The WGS, (Equation 1.5) reaction is carried out in two adiabatic fixed bed reactors. The first conducts high temperature shift (HTS) over Fe_2O_3/Cr_2O_3 catalysts at 350 - 400°C and the second conducts low temperature shift (LTS) over CuO/ZnO catalysts at 200 °C[4,25,26,32]. This raises the H_2 and CO_2 content of the gas by overcoming the equilibrium limitations of CO conversion of the exothermic WGS reaction by enforcing external cooling in between the two stages. Alternatively, a single, internally cooled WGS stage at intermediate temperature can achieve a similar degree of CO conversion.

1.2.1.3 Purification

When high purity hydrogen (> 95 %) is desired, any unconverted CH_4, or remaining CO_2, N_2 and CO impurities are typically removed from the syngas using pressure swing adsorption (PSA) although the less effective amine scrubbing process (using monoethanolamine, MEA) has also been used[4,25,26]. Pressure swing adsorption uses multiple packed beds of molecular sieves, silica gel and activated carbon which preferentially adsorb carbon gases from the product stream leaving the hydrogen relatively unchanged[26,33]. The adsorption of these gases is facilitated by high pressure through the beds. This pressure is then lowered to facilitate regeneration of the beds while temperatures remain near ambient throughout due to the small exothermicity of the physical adsorption process and the small endothermicity of physical desorption[26,33]. This process produces a hydrogen stream with a purity of 99.9 %, however approximately 10 % of the H_2 produced is sacrificed in a purge step to complete the desorption process[33].

The process off-gases contain unconverted CH_4 (typically 30 – 40 % of the feed), purge H_2 (10 - 20 % of the CO-shift product), CO, N_2 from the natural gas, and large amounts of CO_2 (60 – 70 % of the carbon feed) produced by regeneration of the beds. This off-gas is recycled as combustion fuel for heat in the large furnace that houses the reformer tubes. Additionally when PSA is used, the low temperature shift stage may not be necessary[26], Figure 1.7.

1.2.1.4 Economic and Thermodynamic Advantages of SMR

As stated earlier SMR is currently both more cost effective and more energy efficient than any renewable or low carbon hydrogen production technology. Moreover the most cost competitive alternative fossil fuel production technology, coal gasification, has been shown to be more expensive than SMR if the natural gas price remains below 8 US$ GJ^{-1} (where typical natural gas prices fluctuate between 6 - 9 US$ GJ^{-1})[34]. It is projected by the IEA that this is unlikely to change between now and 2030 even with the application of carbon dioxide capture and storage to SMR[34], Figure 1.8.

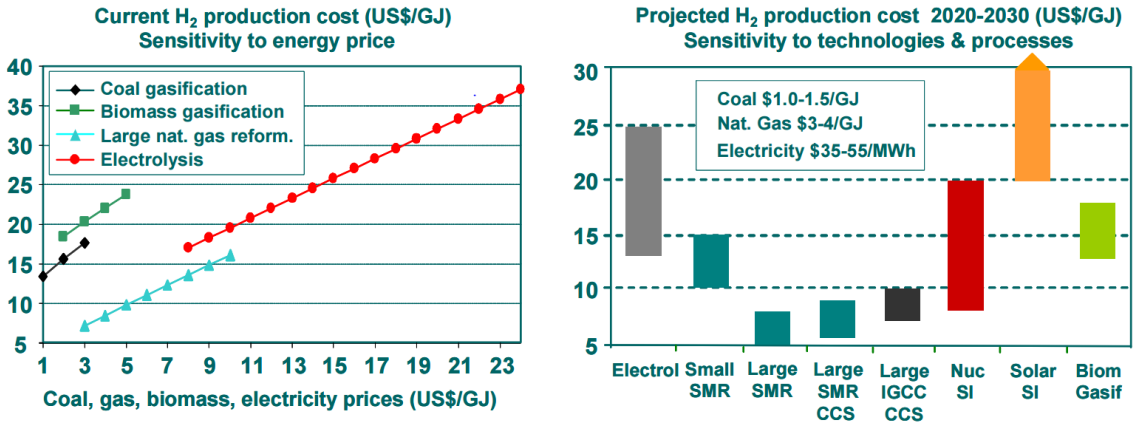

Figure 1.8: Current and predicted H_2 production cost (US$ GJ^{-1})[34]

SMR is a process that has been utilised for well over a century and is therefore at technical maturity; the process is now working close to the theoretical production limits in regards to syngas production[4,26]. As a result SMR is a more energy efficient means of producing hydrogen than many of the other contemporary methods with several comparison studies reporting large scale SMR to be substantially more efficient than any other industrially available technologies[17,22,34–36]. The financial and thermodynamic advantages large scale SMR offers combined with the favourable predictions for the cost of hydrogen production in the future seem to suggest that SMR will be the dominant hydrogen production method for years to come.

1.2.1.5 Feedstock Considerations

This conclusion is supported by the probable widespread availability of natural gas over the next few decades. The BP 2017 Statistical Review of World Energy indicates that there is little or no danger of a shortage of natural gas in the near future[37], Figure 1.9. The proven reserves of natural gas (i.e. natural gas that geological and engineering information indicates with reasonable certainty can be recovered in the future from known reservoirs under existing economic and operating conditions) outstrip the consumption of natural

gas by close to two orders of magnitude – if production were to carry on at the rate recorded over 2014, it would take 54.1 years to consume all of the proven reserves (as of 2014)[37]. Moreover, considering that proven reserves have increased unabated since 1990 and that the increase in the reserves year on year far outstrips that of the consumption, the argument that natural gas will become scarce in the near future becomes untenable.

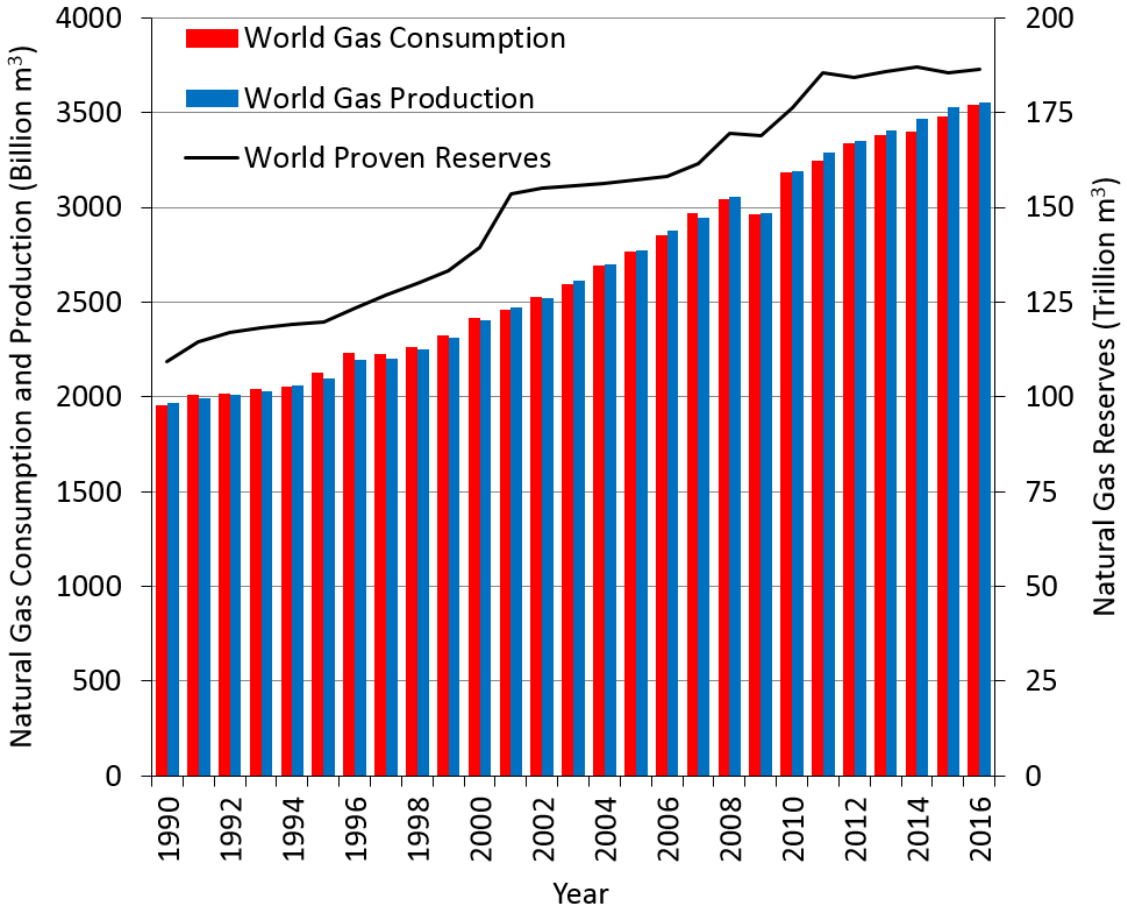

Figure 1.9: World natural gas consumption and production (billions of m^3) and proven reserves (trillions of m^3)[37]

Therefore, due to the superior hydrogen production efficiency and maturation of the SMR process and the almost certain increase in production of natural gas, SMR is likely to continue to be the most industrially relevant hydrogen production method well into the 21st century.

1.2.1.6 Issues Concerning Steam Methane Reforming

Despite its technical maturity and suitability to hydrogen production when compared to other methods, the SMR process still has several important issues that must be analysed if any improvements are to be made.

1.2.1.6.1 The Primary Reformer

Many of the issues presented by the SMR process revolve around the high reaction temperatures required as well as the manner in which that heat is provided to the endothermic SR reactions carried out in the primary reformer[25,31].

As stated earlier the equilibrium position of the SR reaction is limited by the provision of heat to the surface of the catalyst where the reaction stake place, however the limiting step is the maximum permissible heat flux through the walls of reactor tubes. The high stress process conditions (up to 1000 °C and 35 bar) experienced by the reformer tubes mean that even slight increases in the wall temperature of the reformer tubes can significantly increase the rate of tube deformation and rate of tube rupture (failure). Consequently all efforts must be made to provide an even heat flux across the reformer and avoid the formation of localised high temperature areas of the reformer tubes known as hotspots[25,31].

In an ideal system, the firing of the furnace ensures that heat flux is constant radially and ensures that the highest heat flux is provided at the entrance to the reformer where the majority of reactant conversion occurs[25]. In practice, factors internal to the reformer tubes such as the packing density and arrangement of the catalyst, uneven pressure drop through the reformer tubes, local concentrations of the reactant and product gases and carbon formation mean that the provision of even heat flux inside the reformer tubes is extremely difficult to achieve and hotspots are inevitably formed.

In addition, external firing of the reactor tubes on the furnace side can be difficult to control in such large furnaces. This creates radial and axial temperature gradients in the tube wall through the formation of hotspots. These hotspots cause localised areas of accelerated deformation of the reformer tubes, and increasing the rate of tube failure[25,31]. Moreover, radial temperature gradients within the tubes are created due to the conduction of heat through the catalyst bed; these gradients are created by insulation of the catalyst pellets close to the centre of the tube by pellets further from the centre, thereby increasing the chances of the formation of hotspots[5].

Hotspots not only cause accelerated rates of deformation and failure of the reformer tubes but also affect the formation of carbon in the reformer tubes. Carbon formation is promoted at high temperatures and reducing conditions and is predominantly caused by two processes which form carbon at different rates. The rapid formation of carbon occurs when concentrations of steam or H_2 product fall below certain limits; this can occur due to poor micro (individual catalytic sites) or macro (areas of the reformer tubes) distribution of these species[25,31]. A local lack of steam resulting from poor mixing or

accidental discontinuity of steam supply causes the slower thermal cracking (Equation 1.10), disproportionation (Equation 1.11) and CO reduction (Equation 1.12) reactions to occur on the nickel catalyst more easily than the faster SR or WGS reactions[25].

$CH_{4(g)} \rightarrow 2H_{2(g)} + C_{(s)}$ $\Delta H_{298K} = +74.6$ kJ mol^{-1} **Equation 1.10**

$2CO_{(g)} \leftrightarrows CO_{2(g)} + C_{(s)}$ $\Delta H_{298K} = -172.4$ kJ mol^{-1} **Equation 1.11**

$CO_{(g)} + H_{2(g)} \leftrightarrows H_2O_{(g)} + C_{(s)}$ $\Delta H_{298K} = -131.3$ kJ mol^{-1} **Equation 1.12**

Steady accumulation of carbon in the reformer also occurs when there is low catalyst activity in the inlet portion of the reformer tube. Low catalyst activity, induced via catalytic poisoning or sintering from prolonged use, causes lower H_2 yields thereby shifting the equilibrium of the thermal cracking reaction to produce more solid carbon[25].

The deposition of carbon deactivates the nickel catalyst and exacerbates the formation of hotspots, thereby reducing the efficiency of the reforming stage and increasing the rate of tube deformation and failure[25,31]. It can also induce increased pressure drop through the reformer tubes. If carbon formation causes sufficient damage to the performance of the reformer, it must either be removed from the catalyst by purging with a H_2/H_2O mixture or the catalyst replaced entirely; both of these options require plant down time and are therefore avoided if possible[25,31].

Pressure drop through the reformer tubes can also cause issues with uneven heat flux. Differences in inter-tube pressure drop can manifest due to carbon formation or differences in the packing density of the catalyst; this can cause preferential flow of reactants into the reformer tubes with less pressure drop, causing an uneven distribution of reactants into each tube. This results in uneven heat demand for the SR reactions and the formation of hotspots and their associated penalties to H_2 production efficiency and increased tube deformation.

In summary many of the issues associated with the reformer are a direct result of the heat limitation of the SR reaction, the external firing of the reformer tubes and the unequal heat flux across the reformer tube wall; this leads to reduction in efficiency, formation of carbon, poisoning of the catalyst and premature failure of reformer tubes.

1.2.1.6.2 Other Process Issues

There are certainly more issues with SMR than just the provision of heat to the reformer. The high stress conditions experienced by the reactor tubes mean that they are fabricated from high cost alloys such as HK40 (Cr 25 %, Ni 20 %, Co 4 %) and IN519 (Cr 24 %, Ni 24

%, Nb 1.5 %, Co 3 %); while conventional steel would fail rapidly in these conditions, HK40 or IN59 can withstand temperatures up to 1150 °C and tolerate up to 100,000 hours of operation[25,31]. These reformer tubes account for most of the capital cost of the reformer and in spite of the high cost alloys used often fail prematurely. Each time a tube fails, there is significant down time and tube replacement which can induce large maintenance costs[25,31].

Another issue is the size of the average SMR plant. Lyon and Cole state that hydrogen production is not economically feasible at hydrogen production scales smaller than 130,000 Nm^3 per day[5]. In fact a typical modern tubular reformer plant typically produces 300,000 Nm^3 using as many of 650 tubes each measuring between 7.5 - 12 m long[25]. When a reformer of this size is combined with the required and extensive desulphurisation stages, pre-reformer, WGS, purification processes and various heat integration and steam generation systems, SMR plants have a huge plant area, are capital intense and extremely complex[25,26].

Furthermore, the purification processes, such as PSA and amine scrubbing, have specific issues. MEA is an expensive process due to the steam regeneration of the solvent and the regular replacement of solvent due to degradation[26]. PSA units are required to remove many trace gases from the product including methane carbon dioxide and carbon monoxide. Not only does this require many separation stages (resulting in complex and expensive equipment that requires large plant areas) but also results in a loss of at least 10 % of the H_2 product as mentioned earlier; this is recycled to fuel the reformer furnace together with the unconverted methane and CO. Each of the SMR plant units described here have distinct optimum temperatures of operation, requiring complex heat integration measures to be implemented throughout the plant to attain high thermal efficiencies and adding to the capital and operational expenditures[26].

Another serious disadvantage of this process is the production of significant greenhouse gases (GHG) due to its heavy use of natural gas as both a feedstock for the process and as a fuel for the provision of heat. The emissions from SMR both in isolation and in comparison to other hydrogen production methods have been quantified by several studies[18,38,39]. Spath and Mann[38] conducted a life cycle assessment of SMR plant simulating an SMR plant with an output of 135,000 kg of hydrogen per day, 88 % efficiency based on higher heating values and with a plant layout similar to that in Figure 1.7. They found that per net kg of hydrogen produced, 8.89 kg of carbon dioxide were produced by the operation of the plant; this amounted to 74.78 % of the GHG emissions associated with

hydrogen production from the extraction and distribution of natural gas to the final hydrogen product[38]. This figure varies between 9 – 11 kg CO_2 kg^{-1} H_2, but when compared with other hydrogen production methods including electrolysis using renewable electricity and SMR with carbon capture and storage (via solvent based capture), it can be seen that they perform poorly in terms of CO_2 emissions[17,18,38,39], Figure 1.10.

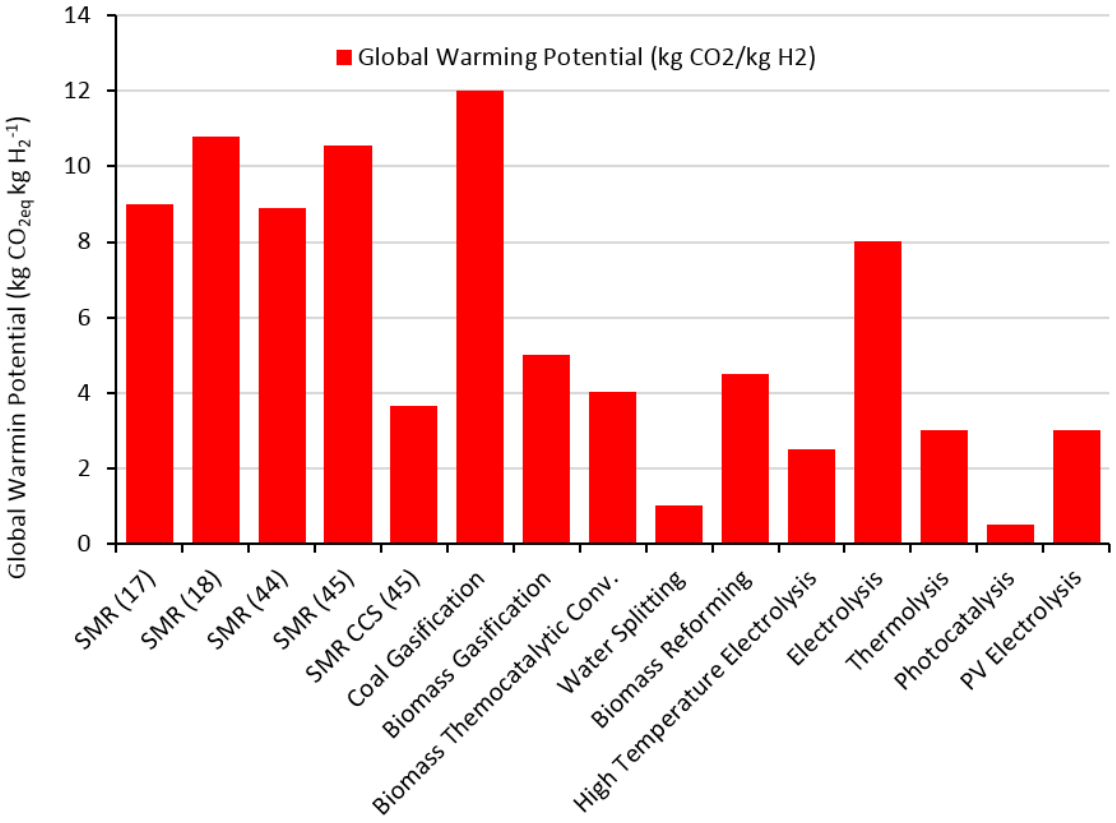

Figure 1.10: A comparison of the various emissions per net unit of hydrogen produced associated with SMR and various other hydrogen production methods[17,18,38,39]

Additionally due to its technical maturity, this process is now working close to the theoretical production limits in regards to syngas production and as such it is now incredibly difficult to improve the hydrogen production efficiency of the SMR process[4,26].

1.2.1.7 Conclusions

The advantages of widespread feedstock availability through natural gas expansion and the maturity of the hydrogen production efficiency of SMR process, it is clear that the production of hydrogen is likely to continue to use the reforming of natural gas as the primary hydrogen production technique for years to come.

However, SMR presents a range of issues including difficult heat provision, high levels of process complexity and heat integration, large plant area, high capital and maintenance costs, costs of transporting the natural gas and hydrogen to and from the plant over long

distances due to centralised production and large associated GHG gas emissions. It is therefore an obvious target for process intensification; process intensification was defined by Reau, Ramshaw and Harvey[40] as "any chemical engineering development that leads to a substantially smaller, cleaner, safer and more energy efficient technology". Intensification of the process would allow steam reforming to facilitate H_2 production on small and medium scales allowing the use of distributed variable feedstocks as well as extend the use of steam reforming to mobile applications.

1.2.2 Chemical Looping Reforming Processes

Process intensification of SMR can be achieved through the application of two chemical looping processes. Adanez et al.[23] defined chemical looping as a cycling process that utilises a solid material to carry oxygen between separate processes; the oxygen is first consumed and the material reduced to facilitate fuel conversion either for combustion or hydrogen production, and subsequently re-oxidised before the process can begin again. Chemical looping steam reforming (CLSR) mainly addresses the issues surrounding heat provision to the reformer tubes in SMR by using an oxygen carrier that provides a means of even heat supply without the need for methane combustion. Sorption enhanced chemical looping steam reforming (SECLSR) uses the advantages of the CLSR process and combines them with CO_2 adsorption (using solid sorbents) to benefit from synergistic intensification of the SMR process via equilibrium shifts and complementarity of reactive heat demands and releases.

1.2.2.1 Chemical Looping Steam Reforming

The CLSR process relies on the cyclical reduction and oxidation of a metal oxide, known as an Oxygen Carrier (OC), to produce hydrogen from the SR reactions without the need for external heating. The CLSR process consists of two stages, the endothermic steam reforming half cycle and the exothermic oxidation half cycle as represented by cycle *a* and *b*, Figure 1.11 (overleaf); NiO and CH_4 are used as examples of an OC and fuel respectively[23,32,41].

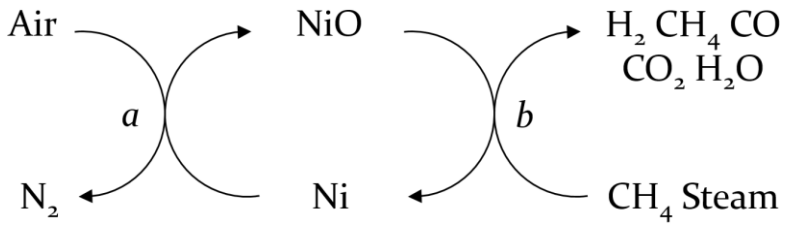

Figure 1.11: schematic of CLR where (*a*) is exothermic and (*b*) is endothermic[42]

If the OC is taken to be in its oxidised state (i.e. NiO in this case) it is first exposed to a feed stream of fuel (e.g. CH_4) and steam. This mixture reduces the OC to the catalytically active state (in this case Ni) and catalyses the SR reaction to produce a syngas of H_2, CO, CO_2 and any unconverted methane and steam. The main reactions involved in the reduction of the OC are shown below using nickel as an example. It can be seen that Equation 1.14 to Equation 1.16 combine linearly to give Equation 1.13.

$CH_{4(g)} + 4NiO_{(s)} \rightarrow 4Ni_{(s)} + CO_{2(g)} + 2H_2O_{(g)}$ $\Delta H_{1200K} = 135$ kJ mol^{-1} **Equation 1.13**

$CH_{4(g)} + NiO_{(s)} \rightarrow Ni_{(s)} + CO_{(g)} + 2H_{2(g)}$ $\Delta H_{1200K} = 213$ kJ mol^{-1} **Equation 1.14**

$CO_{(g)} + NiO_{(s)} \leftrightarrows Ni_{(s)} + CO_{2(g)}$ $\Delta H_{1200K} = -48$ kJ mol^{-1} **Equation 1.15**

$H_{2(g)} + NiO_{(s)} \leftrightarrows Ni_{(s)} + H_2O_{(g)}$ $\Delta H_{1200K} = -15$ kJ mol^{-1} **Equation 1.16**

Under the oxidation half cycle the OC is subjected to an air atmosphere, causing oxidation of the OC and of any carbon built up during the SR half cycle, Equation 1.17 and Equation 1.18. This oxidation half cycle also strips the oxygen in the air feed from N_2 producing an effluent that may at worst consist of an oxygen depleted, CO_2 contaminated, N_2 rich flow, and at best, (if no carbon had been deposited previously, and no excess air had been fed), a pure N_2 flow. This also results in the production of a syngas product devoid of N_2 under the following reduction/steam reforming half cycle.

$2Ni_{(s)} + O_{2(g)} \rightarrow 2NiO_{(s)}$ $\Delta H_{1200K} = -468$ kJ mol^{-1} **Equation 1.17**

$C_{(s)} + O_{2(g)} \rightarrow CO_{2(g)}$ $\Delta H_{1200K} = -393$ kJ mol^{-1} **Equation 1.18**

The advantage of the CLSR process lies in the looping of these two cycles; the exothermic oxidation reactions can in principle provide the requisite energy for the endothermic reduction and reforming reactions without the need for external heat provision. Moreover, the heat energy generated under oxidation is produced uniformly (radially) across the catalyst bed. This not only avoids many of the heat provision issues associated with the typically externally heated SMR process, but also eliminates the NO_x emissions generated by the combustion of methane in the furnace, thereby significantly reducing the environmental impact of SMR. Furthermore, careful control avoiding carbon deposits and adjusting air feed would permit easy capture of all the process CO_2 released under the air feed half cycle, thus curbing the GHG intensity of the SMR process[5,23,32,41].

The OC is cyclically exposed to the reducing fuel/steam atmosphere and the oxidizing air atmosphere in one of two ways: (1) by alternating the fuel/steam mix and air feeds to a single packed bed reactor (and using two reactors simultaneously to produce constant

products) or (2) by physically moving the OC between two fluidised beds reactors, each one fed with a continuous stream of fuel/steam or air[23,41,43].

The choice of OC is integral to the design of the CLSR process. An OC must present high reactivity for the reduction and oxidation reactions involved and maintain that reactivity over extended cycling. It must exhibit high oxygen transfer capacity and favourable thermodynamic properties. The OC should also be readily reduced by a number of fuel mixtures, and act as an effective catalyst for the SR reactions involved in the process. In addition to these 3 criteria the cost, toxicity, thermal stability and resistance to attrition (when used in fluidised beds) are all important factors to be considered[23,32,41,44–47].

Although pure metal oxides are adept at lattice oxygen storage, they typically cannot provide the reactivity required for their effective use over any more than a few cycles; therefore a ceramic support, such as Al_2O_3 or $MgAl_2O_4$, can be used to enhance redox stability and activity, increase the mechanical strength and reduce agglomeration of the OC. Nickel when supported on alumina (Ni/α-Al_2O_3 or Ni/γ-Al_2O_3) is by far the most widely researched OC for syngas and H_2 production. This is thanks to superior catalytic activity for the SR reactions (when compared to Fe, Cu and Mn), acceptable oxygen transfer capacity and high redox reaction rates at the temperatures encountered in CLSR [23,41,42,45,47–50].

1.2.2.2 Sorption Enhanced Chemical Looping Reforming

SE-CLSR is a technique that seeks to improve the CLSR process via the use of a solid CO_2 sorbent[26]. Under the steam reforming half cycle a solid sorbent allows the absorption of CO_2 produced during the reduction of OC and from the subsequent SR and WGS reactions thereby shifting the equilibrium of these reactions via le Chatelier's principle. Sorption enhancement of the steam reforming half cycle therefore enables SR and WGS at lower temperatures (750 °C), with less carbon formation and allows almost complete CH_4 conversion and a higher hydrogen yield and purity (between 95 – 98 % on a dry basis rather than 80 %). This not only makes the high temperature alloys used in SMR redundant but also greatly intensifies the process, removing the separate WGS reactor and largely eliminating the need for product purification (PSA or solvent scrubbing)[26,30,32,51]. CaO is currently the most widely studied solid CO_2 sorbent in SECLSR thanks to its low cost, widespread geographical availability and favourable chemistry:

$$CaO_{(s)} + CO_{2(g)} \leftrightarrows CaCO_{3(s)} \qquad \Delta H_{298K} = -178 \text{ kJ mol}^{-1} \qquad \textbf{Equation 1.19}$$

Combining the SR/WGS and sorption reactions, the overall reaction is slightly exothermic meaning that no additional heat need be supplied to the system to facilitate SR[26,30,51].

$$CH_{4(g)} + CaO_{(s)} + 2H_2O_{(g)} \leftrightarrows CaCO_{3(s)} + 4H_{2(g)} \quad \Delta H_{298K} = -13 \text{ kJ mol}^{-1} \qquad \textbf{Equation 1.20}$$

However, the sorbent is eventually exhausted in the above carbonation reaction and it must be regenerated via calcination at ~ 850 °C. This is achieved in the oxidation half cycle of SECLSR by utilising heat produced by the oxidation of the OC and of any carbon formed (Equation 1.17 and Equation 1.18) thereby thermally decomposing calcium carbonate[30,32,51]:

$$CaCO_{3(s)} \leftrightarrows CaO_{(s)} + CO_{2(g)} \qquad \Delta H_{298K} = 178 \text{ kJ mol}^{-1} \qquad \textbf{Equation 1.21}$$

Additionally, after oxidation of the OC and thermal decomposition of the $CaCO_3$ is complete, subjection of these materials to the feed of steam and fuel causes the reduction of the OC (Equation 1.13) to become sorption enhanced thereby achieving faster and more complete reduction[52].

SECLSR can be conducted with the use of a packed bed or fluidised bed reactor, however a key component in the intensification of the process is how the OC and the sorbent are mixed (e.g. to achieve direct heat coupling between the endothermic steam reforming and reduction reactions with the exothermic carbonation reaction). Much of the research published on the SECLSR process has used a solids inventory consisting of separate sorbent and OC particles mixed to obtain a certain ratio, however the use of bifunctional OC's or intimately mixed OC and sorbent that combine both the OC and sorbent into the same particle are developing rapidly[53–56].

Use of separate OC and sorbent particles not only means the synthesis procedures of the two materials can be optimised for their respective functions, but also that low cost sorbent and or OC materials (e.g. calcium oxide and haematite) can be used with few alterations[56]. However the rate of the adsorption reaction and the effectiveness of the sorption enhancement can be limited by the mass transfer of the CO_2 produced via the SR/WGS reactions from the OC to the sorbent[57]. The rates of mass transfer are also directly affected by the particle size of the OC and sorbent materials; an intricate balance therefore must be established between the particle sizes, flow rate of gaseous reactants and pressure drop through the bed to optimise the coupled process.

The use of bifunctional OC's produces a porous volume of solid containing both active sorbent and OC active sites thereby effectively removing inter and intraparticle diffusion and removing limitation via mass transfer between the OC and sorbent[57]. However much

of the research into bifunctional OC's using CaO have shown that the catalytic activity of these materials significantly decreases over relatively few (> 10) redox cycles[56,58,59]. Moreover, the design and synthesis of these materials is intrinsically a compromise between the two functions of the material preventing specialised synthesis procedures for OC and sorbent materials to be used. Furthermore the main advantage of bifunctional OC materials (i.e. lack of inter/intraparticle diffusion) becomes irrelevant when the SR/WGS and adsorption reactions are not mass transfer limited[57].

1.2.2.3 Conclusions

In summary the CLSR and SECLSR processes can mitigate many of the most problematic issues in SMR for hydrogen production thereby facilitating process intensification. CLSR is designed to be an autothermal process that supplies heat energy to the endothermic SR reaction in a uniform manner throughout the reactor; this avoids the external heating of the reaction vessel and the GHG emissions associated with powering the natural gas furnace as well as many of the heat provision issue found in SMR. It also eliminates the presence of the diluent nitrogen in the syngas product despite using air as the oxidant in the main reactions tasked with providing net heat. SECLSR takes the advantages of CLSR and uses a solid sorbent to significantly reduce the temperature of operation, the burden of product purification and increase the purity of the hydrogen produced when compared to SMR. Morover SECLSR can reduce the magnitude of thermal oscillations between half cycles and provide a facilitated route to CO_2 capture if required.

Both of these chemical looping processes greatly intensify SMR and could facilitate the development of future small and medium scale hydrogen production, catering to distributed sources of feedstocks such as unconventional gases (e.g. shale well gas and coal bed methane) and biomass derived products (e.g. agricultural wastes from large farms, anaerobic digestion plants, biorefinery waste streams).

1.3 Research Rationale

Feedstock availability, high H_2 production efficiency and low cost emphasise that the industrial production of hydrogen is likely to continue to be dominated by SMR for years to come. However due to technical maturity and issues with heat provision, plant size and complexity, GHG emissions and high capital and maintenance costs, alteration and intensification of this process is essential. CLSR and SECLSR processes can mitigate many of the most problematic issues in SMR for hydrogen production reducing emissions and

intensifying the process facilitating the development of future small and medium scale hydrogen production. The development of OC materials for use in these innovative processes is essential to the adoption of these hydrogen production technologies.

The properties of the catalyst used in SMR are dictated by the demands of the process. Heat limitation of the SR reaction forces the use of long thin reactors; this in turn dictates the use of catalysts with high density and mechanical strength to support the weight of catalyst in the tube and to provide a means for heat conduction through the catalyst bed. Moreover, a large particle size and shaped pellets are used to decrease pressure drop as much as possible.

The CLSR process facilitates a change in reactor geometry away from tall thin reactors as the process is not limited by heat transfer through the reactor walls to the catalyst bed. This removes many of the physical constrictions upon the catalysts and allows the consideration of radically different OC geometries. The use of structured OC's developed with fibrous support materials potentially offer further process intensification thanks to several advantages that dovetail well with the CLSR process.

OC's synthesised with fibrous support materials possess excellent mass transfer properties; they offer a means to decrease the particle size of the material used without a great increase in pressure drop by virtue of a higher void fraction compared to granulated or pelletised catalysts. A decrease in the particle size increases the surface area to volume ratio of the OC thereby increasing reactivity of the catalytically active OC and reduces the likelihood of mass transfer limitation of the reduction and oxidation reactions. Moreover, the high void fraction results in a less dense bed of malleable OC material with reduced pressure drop characteristics. The reduced thermal inertia and mass transfer resistance of such a bed of material allows fast and homogenous heat provision during oxidation for the endothermic SR reactions.

The use of fibrous materials could also result in additional benefits to the SECLSR process. As stated earlier, the use of separate sorbent and OC particles can be limited by mass transfer of the reactants and products between the two particles; the smaller effective particle sizes facilitated by fibrous supports mean that these limitations can be minimised. Moreover, intricate mixing methods could be facilitated utilising textile technology to create thin mats of alternated OC and sorbent supported material for easy separation, or, for materials of similar lifetimes, to weave knit or embroider fibrous OC's and sorbent into

a homogeneously mixed material, thereby allowing optimal synthesis procedures for the materials in addition to more effective mixing.

1.4 Research Scope and Objectives

The primary aim of this thesis is to synthesise Co doped Ni oxygen carriers supported by a structured aluminosilicate fibrous material known as Saffil® and to apply them to the CLSR process for the first time.

This thesis will detail the development of nine 18 wt% Ni loaded OC's utilising Saffil® fibres (Sf) as a support material and possessing various levels of Co doping (0, 0.6 and 1.8 wt% Co) produced using three methodologies; wet impregnation (WI), deposition precipitation (DP) and hydrothermal synthesis (HT). The Saffil® fibres consist of primarily of γ-Al_2O_3 (~ 95 %) and SiO_2 (~ 5 %) and present a median width of 3 - 4 μm and an assumed fibre length of ~ 5 mm (see Section 3.1). These OC's were tested in packed bed SR and CLSR processes using a reactor designed, built and developed by the author in house at the University of Leeds and be benchmarked against a conventional 18 wt% Ni/α-Al_2O_3 steam reforming catalyst using N_2 diluted CH_4/H_2O feedstock as a fuel. The conventional catalyst was supplied as raschig rings and was ground to produce granules sized between 150 – 250 μm prior to use in the SR and CLSR experiments.

Although these fibrous Sf OC's have been designed and tested for use in the CLSR process, it is envisioned they will be utilised in the full SECLSR process in future; development of calcium oxide-based sorbents using the Catalytic Grade (CG) Saffil® support is ongoing at the University of Leeds (Sergio Ramirez Solis's PhD Thesis) and use of both these materials in the SECLSR process is expected. However, development of these sorbent materials and optimisation of the SECLSR process with the Saffil® based OC's and sorbents is outside of the scope of this thesis.

This thesis can be split into five chapters that detail the novel application of fibrous structured OC's to CLSR:

Chapter 2: Reviews the literature in the areas of chemical looping processes, the development of OC's for use in those processes, heterogeneous catalysis and the use of fibrous catalysts in hydrogen production. This will establish the novelty of fibrous structured materials in chemical looping and explain the rationale behind their use.

Chapter 4: Details the synthesis and thorough characterisation of the novel fibrous OC's and assesses the effects of three different Ni/Co loading methodologies (wet impregnation, deposition precipitation and hydrothermal synthesis) and varying levels of cobalt doping upon the physical characteristics of the support and the fresh OC materials.

Chapter 5: (a) Tests the novel fibrous OC's in a packed bed reactor under SR conditions at bench scale and compares their catalytic performance against a conventional SR catalyst currently used in industry, **(b)** Assesses the effects of their use in bench scale SR experiments at on the physical characteristics of the materials via detailed post-process characterisation.

Chapter 6: (a) Achieves use of fibrous OC's in a packed bed reactor under CLSR conditions at bench scale for the first time and benchmarks the extent of reduction and subsequent catalytic performance of the materials against the conventional SR catalyst, **(b)** Assesses the effects of the bench scale CLSR experiments on the physical characteristics of the used materials.

Chapter 7: Selects and assigns an appropriate gas-solid kinetic model to the reduction of the novel fibrous OC materials and the conventional SR catalyst to characterise the reduction reaction and identify and analyse any differences in reactivity or kinetics between the conventional and fibrous materials.

2 Literature Review

The following chapter reviews the basic concepts and recent research progress in chemical looping processes and oxygen carrier development pertinent to the work carried out in this thesis. As such it discusses the origins, major variations in process and reactor design and possible fuels for several chemical looping reforming processes as well as the CLSR process as defined in Section 1.2.2.1. Recent developments in OC synthesis and development are summarised with particular attention paid to the development and synthesis of Ni/Al_2O_3 OC's. A review of solid-state kinetic theory and the prevalent solid-state kinetic models applied to the reduction of Ni/Al_2O_3 OC's is conducted. Finally, an overview of the use of fibrous geometries in catalytic processes is given along with an assessment of their use for hydrogen production technologies and the benefits of their application to CLSR.

2.1 Chemical Looping Processes

The development of hydrogen production using chemical looping can be traced back to the advent of the steam-iron process in the early 1900's and the development of the chemical looping combustion (CLC) process from the 1950's onwards. However much of the work on chemical looping reforming (CLR) processes, i.e. chemical looping processes designed for the production of hydrogen, started around the turn of the millennium, thanks to the important works by Lyon and Cole[5] and Ryden and Lyngfelt[60] and has gained momentum since. As such there are now a wide range of chemical looping processes for both power generation and the production of hydrogen.

CLC is a power generation technology from which many of the CLR concepts were developed and there are four major CLR processes that have been proposed to produce hydrogen using chemical looping technology; chemical looping water splitting (CLWS), steam methane reforming with chemical looping combustion (SMR-CLC), sorption enhanced chemical looping steam reforming (SECLSR) and chemical looping steam reforming (CLSR).

This section will briefly discuss the major chemical looping technologies developed thus far and further investigate the process studied in this work, CLSR. This discussion will include the major reactor options and the feedstock used in the process.

2.1.1 Chemical Looping Combustion

Chemical looping combustion (CLC) uses the reduction of an OC to provide oxygen for combustion of a fuel in absence of N_2. This means that the fuel and air never mix thereby producing a flue gas of CO_2 diluted only with H_2O which can be simply condensed to produce a product gas of almost pure CO_2. Under the oxidation cycle, oxygen depleted air or even pure N_2 is produced, Figure 2.1.

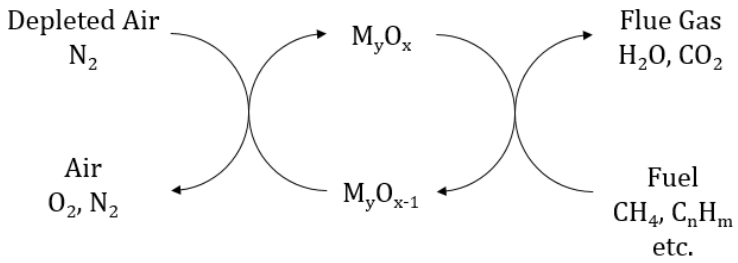

Figure 2.1: Schematic of a CLC system

The inherent CO_2 separation coupled with an overall process enthalpy equal to conventional combustion, greatly facilitates CO_2 capture, compression and storage (CCS) for power generation[23,61]. This gives CLC a great advantage over other energy intense power generation CCS technologies such as oxyfuel combustion using cryogenic air separation or post combustion carbon capture using MEA based solvents in that no extra energy is expended to capture the CO_2 from the process[61].

The concept of CLC was initially developed by Lewis and Gilliland[62] in 1954 however the term chemical looping combustion was not coined until the work by Ishida et al.[63] in 1987 and no practical research, beyond thermodynamic studies and OC screening, was conducted until the early 2000's[23]. Over the next decade several projects proved the concept of CLC using gaseous fuels in large reactors for hundreds of hours; this culminated in various works[64] cofounded by the EU project "Chemical Looping Combustion CO_2-Ready Gas Power" and the 2nd phase (2005 - 2009) of "The CO_2 Capture Project" which included showing the use of a 120 $kW_{thermal}$ CLC unit[65], long term operation (1000 hours) of a CLC process and scale up of OC material production[66,67]. Moreover the direct CLC of solid fuels was facilitated by the advent of the chemical looping oxygen uncoupling (CLOU) process[68]. This process avoids the slow rate of homogeneous reaction between an OC and solid fuels by using OC's (e.g. Cu, Co, and Mn) that release gas phase oxygen on reduction thus facilitating heterogeneous reaction; this allows great process intensification over processes that rely upon the gasification of the solid fuels prior to use

in CLC[61,68]. As a result a multitude of fuels have been used in CLC including CH_4[65–67], syngas from coal or biomass, solid coal and biomass, petroleum coke and bio-oil[23,61].

Typically CLC is conducted using two interconnecting fluidised bed reactors; this system has the advantages of not only enabling excellent contact between the fuel and OC but the facile movement of the OC between the reactors[41,69]. However at high temperatures and pressure recommended for high efficiency power generation, fluidised beds become difficult to operate due to problems in OC movement between the beds; packed beds (typically two in tandem to ensure constant production) perform better under these conditions and offer intrinsic separation of gas and particles but require feed switching increasing cost and complexity[23,41].

As in previous chemical looping processes, the selection of the OC is an important task. Although factors such as environmental cost, attrition agglomeration and effects of carbon deposition are important when choosing an OC for CLC, the choice of OC is often dictated by its thermodynamic behaviour and the effects this choice has upon the mass and energy balance of the reactors. Any OC selected will have a certain selectivity toward the desired combustion products; OC's based upon Cu, Co, Fe, Ni and Mn were found by Jerndal et al.[70] to practically completely combust CH_4, H_2 or CO feedstocks.

However, the thermodynamic properties of the OC must be balanced by its oxygen transfer capacity. This factor essentially represents the quantity of oxygen the OC can transport (i.e. Ni → NiO transports 1 mol of oxygen per mol of Ni), relative to the availability of the active transport component and dictates the rate of solids cycling; the higher the oxygen transfer capacity, the lower the rate of solids circulation must be to satisfy the oxygen demand from the combustion reactions[23]. The aforementioned OC's that perform well thermodynamically such as Mn_2O_3/Mn_3O_4 or Co_3O_4/CoO, often present much lower oxygen capacity than competing OC's highlighting the complexity of factors that influence the selection of OC's[23].

Furthermore, each OC can present a different enthalpy of reaction when undergoing reduction in the fuel reactor which can have a drastic effect on the operation on the CLC system. Typically syngas fuels (H_2 or CO) result in an overall exothermic reaction in the fuel reactor, however under a feed of CH_4 many widely used OC materials (excepting Cu and certain transitions of Co, Fe and Co) can produce an endothermic reaction; in this case heat must be supplied to the reaction via the movement of solids from the air reactor and therefore will affect the solids circulation rate[23].

Adanez et al.[23] cites the development of demonstration of the technology on a larger scale ($MW_{thermal}$) and operation with pressurised atmospheres as the main concerns in the further development of CLC, although they also state that the development of OC's must strike a balance between the efficacy of the OC as pertaining to specific fuels or reactor types and the economic and environmental cost of said OC. Unsurprisingly, there has been a vast amount of work conducted in the development of chemical looping combustion technologies and the OC used in the process. For further reading refer to the reviews of Moghtaderi[61] and in particular Adanez et al.[23].

2.1.2 Chemical Looping Water Splitting

Chemical looping water splitting (CLWS), also known as the steam-iron process, cyclically reduces an OC, typically iron oxide, with a reducing carbon containing gas and oxidises with steam to produce separate streams of pure H_2 and carbonaceous product. Initially this process was conducted as a two stage process (Figure 2.2a) and in its simplest form i.e. using CO as a reducing agent, carries out the WGS reaction overall[71,72].

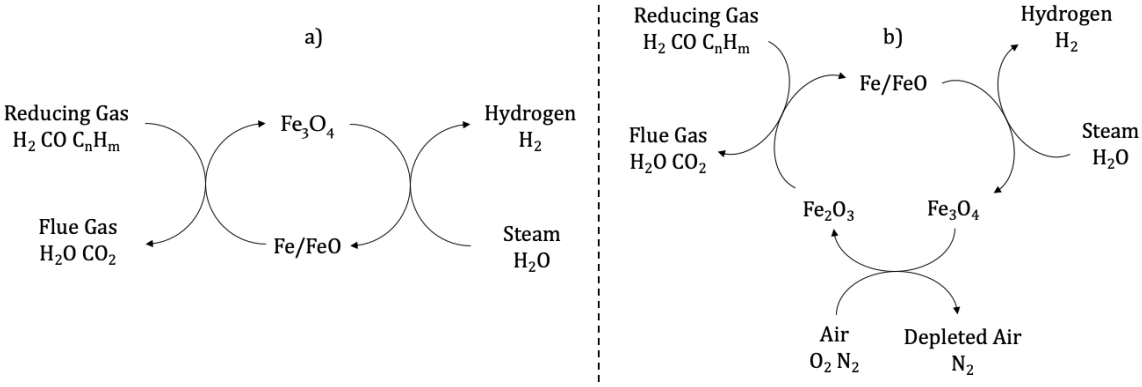

Figure 2.2: the 2-stage (a) and 3-stage (b) steam iron process using iron oxide as the OC and CO as the reducing gas

The process is ideally carried out between 850 - 900 °C under atmospheric pressure[72]. The use of iron oxide for this process can be attributed to the thermodynamic advantages this OC provides for the process; the transition of iron oxide through its oxidation states allow a high hydrogen mole fraction to be achieved during reduction, Table 2.1[72,73] (overleaf). Furthermore iron oxide is a cheap and plentiful resource and relatively harmless to both human health and the environment[71].

Table 2.1: Oxidation states of iron oxide when used in the steam-iron process[71]

Species	Chemical Formula	Oxidation States
Iron	Fe	0
Iron (II) oxide, wüstite	FeO	+2
Iron (II,III) oxide, magnetite[(a)]	Fe_3O_4	+2/+3
Iron (III) oxide, haematite	Fe_2O_3	+3

[(a)] Where magnetite consists of a mixture of wüstite and haematite

The steam-iron process was first implemented by Howard Lane in 1903 with the invention of the Lane hydrogen producer; this was the first process to use a hydrocarbon gas (town gas; essentially gasified coal) and water to cyclically reduce and oxidise iron oxide to produce pure products of CO_2 and H_2[74]. Over the next 70 years several patents detailing improvements to the process were made, thereby proving the concept in principle[71,73]. This process gradually developed into the CLWS process around the 2000's as interest in the hydrogen economy and the reduction of emissions from hydrogen production increased. However issues with the iron oxide OC and provision of heat to the reduction reactions when alternative feedstocks are used were never addressed[71]. As such, research into CLWS after the 1970's has centred on improvement of the OC materials and heat integration.

CO was originally considered as a feedstock in earlier works due to the simplicity of the reactions involved using this reductant, and the slightly exothermic nature of the overall WGS reaction. However, given that pure CO is not an ideal primary feedstock (it is usually separated from syngas), other reducing agents including methane, syngas (mix of H_2 and CO) from gasification of biomass or coal, solid coal, and low grade heavy oils are common[75–79].

However when many of these feedstocks (e.g. CH_4) are used to reduce the iron oxide in a simple two stage process (Figure 2.2a), the overall process can be highly endothermic and must be provided with extra heat to maintain high H_2 yield[75]. This can be achieved through use of a third stage which either combusts some of the feedstock or uses an air reactor to further oxidise the magnetite to haematite as shown in Figure 2.2b[80]. The heat produced by this highly exothermic reaction can be integrated in CLWS through the use of either packed bed reactors with high temperature feed switching or through movement of the OC between 3 CFB reactors[80,81].

The greatest barrier to the efficacy of this process has been the high agglomeration and thermal sintering of the iron oxide OC that causes rapid deactivation of the oxygen carrier thereby reducing its oxygen carrying capacity and reducing the yield of hydrogen produced[71,72,82]. As a result, the iron oxide OC must be replaced frequently. One of the main avenues of research into CLWS is improvements in iron based OC materials

including supported iron oxides and iron containing perovskites that can improve the stability of these materials[72,73,82,83]. An excellent summary of these studies is given in the review by Thursfield et al[72].

2.1.3 Steam Methane Reforming with Chemical Looping Combustion

Often cited as the first modern CLR technology, steam methane reforming integrated with chemical looping combustion (SMR-CLC), was first suggested by Ryden and Lyngfelt.[60] This process entailed the production of hydrogen through conventional catalytic steam reforming but used a CLC system with two fluidised beds to provide heat for the endothermic SR reactions, Figure 2.3.

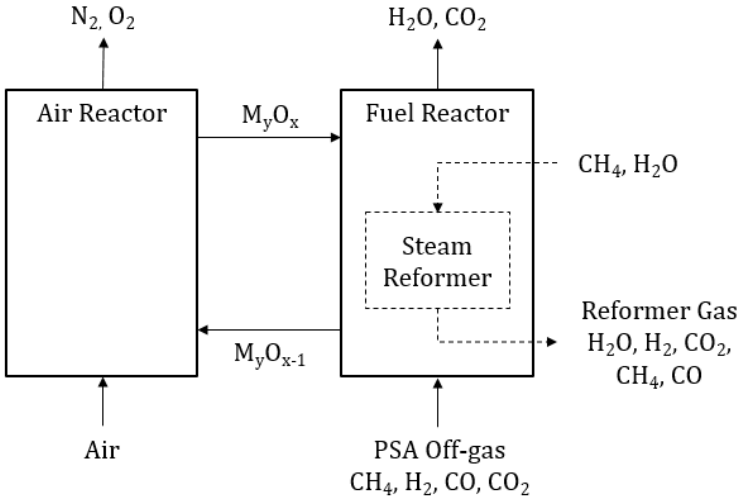

Figure 2.3: Schematic of an SMR-CLC system

In this process reformer tubes are situated in either the air reactor or fuel reactor and WGS and PSA carried out post reforming. Pans et al.[84] suggested the air reactor is more suitable location for the reformer tubes due to the direct heat available from the oxidation of the OC. SMR-CLC increases both the magnitude and homogeneity of the heat transfer through the reformer tubes to the SR reaction and allows both the pressurisation of the H_2 production and the capture nearly 100% of CO_2 emissions from the process (due to use of PSA-off gas as a CLC fuel)[60,84,85]. However the increase in process complexity from use of a CLC unit and the continued presence of the WGS and PSA process units in addition the erosion of reformer tubes due to high attrition and temperature in the fluidised bed are serious issues[43].

2.1.4 Chemical Looping Steam Reforming

Currently there are two schools of thought concerning the perceived objective of the CLSR process.

The first, known hereafter as chemical looping partial oxidation (CLPO), postulates that the partial oxidation of the methane, facilitated by the reduction of the OC and the release of undiluted oxygen, produces hydrogen from a hydrocarbon fuel in a slightly exothermic reaction without the need for external heat. The OC is then oxidised by air to regenerate the OC and allow further partial oxidation of the fuel feed[86].

$CH_{4(g)} + M_yO_{x(s)} \rightarrow M_yO_{x-1(s)} + CO_{(g)} + 2H_{2(g)}$ ΔH_{298K} = exothermic **Equation 2.1**

$M_yO_{x-1(s)} + 0.5O_2 \rightarrow M_yO_{x(s)}$ ΔH_{298K} = highly exothermic **Equation 2.2**

CLPO requires the use of a low oxygen to fuel ratio to prioritise partial oxidation and an appropriate OC; this OC should prioritise preferential selectivity toward the production of H_2 and CO rather than to H_2O and CO_2 and also must also prioritise a reduction reaction that allows the fuel reactor to operate in a either thermo-neutral or slightly exothermic manner. The first study to suggest CLPO was authored by Stobbe et al.[86] in 1999 and much of the early work conducted in CLR concerned the CLPO process and development of OC's (such as Mn, Fe, Ce, Cu, Ni and perovskites) and process schemes to facilitate partial oxidation of fuels[48,49,86–88]. In particular the groups led by Lyngfelt and Abad were active in the development of the concept using a range of transition metal OC's (Mn, Fe, Cu and particularly Ni) in two interconnecting fluidised beds[50,89–91].

The second, termed CLSR (described in Section 1.2.2.1.) and the chosen subject of this thesis, prioritises the reduction of the OC by a fuel/steam mixture to facilitate the catalysis of the SR and WGS reactions in an endothermic reaction. The exothermic oxidation of the OC by air provides the heat to power the endothermic reduction and SR/WGS in principle allowing autothermal operation of the process[92].

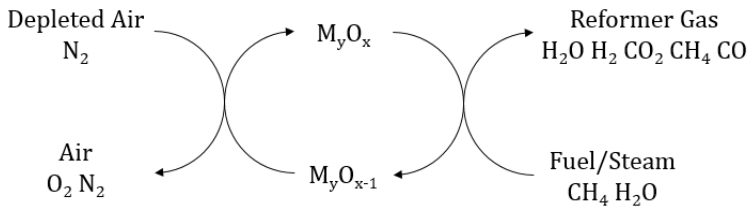

Figure 2.4: Schematic of a CLSR system

The CLSR process, Figure 2.4, prioritises an OC that is easily and rapidly reduced by the fuel/steam mixture through either partial or complete oxidation of methane, is

catalytically active for the steam reforming process and can maintain that catalytic activity and reduction reactivity over many cycles. The research by Lyon and Cole[5] and Dupont and co-workers[52,92–95] have been instrumental in the development of CLSR, both as a standalone concept and as part of the development of SECLSR. Much of this work concerned the use of Ni based OC's due to their high catalytic activity and reduction reactivity[5,52,92–95].

The CLSR process presents several advantages over the CLPO process for CLR; firstly and most importantly the process produces a higher H_2 yield and H_2/CO ratio thereby increasing the hydrogen production efficiency of the process; secondly it is conducted at lower temperatures, 700 °C[5,52,92] compared to 950 °C[50,89–91] in the CLPO process, thereby reducing energy demand and sintering and deactivation of the OC's; and thirdly the full use of the heat from fuel combustion (over the 2 feed cycles) is enabled due to the integration of the heat from the endothermic SR/reduction reactions and the oxidation reactions[5,52,92–95]. The main criticism of the CLSR and CLPO process is the need for an additional WGS and purification stages (either PSA or solvent scrubbing) to produce a pure hydrogen product, a problem that increases plant complexity and cost and reduces the overall efficiency of the process. This is largely solved by the implementation of SECLSR.

As the main scope of this thesis covers the development and use of OC's in the CLSR process, it is worthwhile to investigate this process in more detail covering the specific reactors used to carry out CLSR and some of the feedstocks used in the process.

2.1.4.1 CLSR Reactor Concepts

Operation of the CLSR process requires subjecting the OC to reducing and oxidising atmospheres cyclically. This can be achieved either using two interconnected fluidised beds where the OC is physically cycled between different atmospheres or using one fixed bed where the stationary OC is subjected to different atmospheres by high temperature feed switching, Figure 2.5 (overleaf).

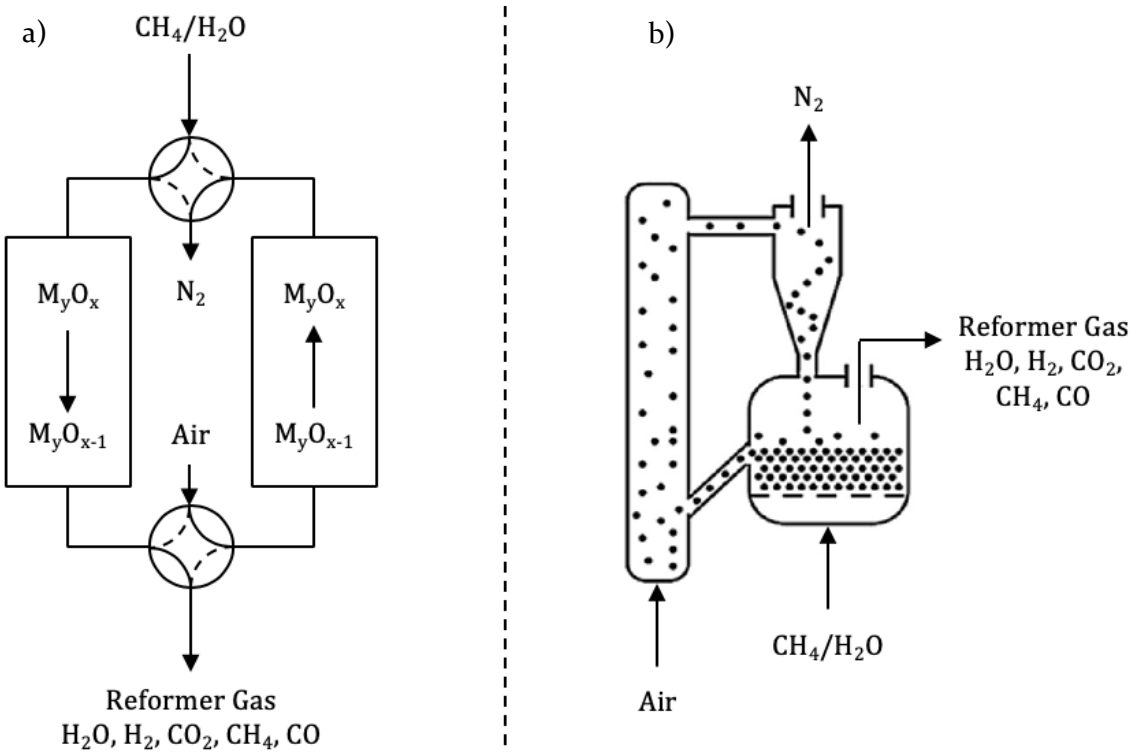

Figure 2.5: Concurrent use of two fixed bed reactors for continuous hydrogen production (a) and two interconnected fluidised bed reactors (b) for CLR

In the fluidised bed system two reactors known as the air and fuel reactors, fluidise the bed of OC material (and reforming catalyst if these aren't the same material) thereby transporting the particles to and from the reducing and oxidising atmospheres; this carries out the redox cycle and facilitates heat transfer between the endothermic fuel reactor and exothermic air reactor. The two reactors are separated by loop seals to prevent movement of gases between the reactors[89,91]. The fixed bed system relies on high temperature feed switching to expose the OC to the reducing fuel steam mixture and the oxidising air in two stages known as the steam reforming and oxidation half cycles. If two packed beds are used concurrently to carry out the steam reforming and oxidation half cycles then continuous production of the reformer gas can be achieved[42,45].

The primary advantage of fluidised beds is the almost complete absence of hotspots due to the homogenous temperature profile observed in these reactors. However, issues arise due to the transport and fluidisation of the OC particles; the high temperatures and pressures required for economical operation cause fluidisation and circulation of the OC to be difficult and is exacerbated with the onset of particle sintering and agglomeration. Furthermore, not only is particle separation from the gaseous products particularly difficult under these conditions but additional energy is required to transport the particles from one reactor to the other[41,45,69].

The main advantage of the fixed bed reactor is the inherent solid-gas separation coupled with the ease that pressurised atmospheres can be used; this is substantially more difficult with fluidised bed systems and increases the economic viability of the process[41,45]. Moreover, the fixed bed reactor provides a compact reactor design and ensures material costs are reduced. Optimised usage of the OC can also be achieved using a fixed bed reactor; a larger difference in the degree of oxidation between the reduced and oxidized forms of the oxygen carrier can be attained when compared to fluidised beds[42,45]. However, the need for high temperature high gas flow switching systems mean that fixed bed reactors can be technically quite difficult to operate. Moreover heat transfer and thermodynamic considerations in a fixed bed are far more important in a fixed bed reactor than the typically uniform thermal gradients found in fluidised beds[23,41,45]

2.1.4.2 CLSR Feedstocks

As explained earlier methane or natural gas is the most logical feedstock for use in CLSR given its continued availability at relatively low cost, the fast heterogeneous reactions and catalysis possible through its use and the experience gained from SMR; as such the vast majority of process and OC development for CLSR has used methane as a feedstock[23,43,71]. The suitability of methane to the CLSR process means there has been little interest in other gaseous fuels for the process however a number of studies have been published on the use of alternative liquid and solid fuels[43,96]. The use of these feedstocks largely fall outside the scope of this thesis and are therefore summarised briefly; further detail can be found in the reviews by Luo et al.[43] and Udomsirichakorn and Salam[96].

A range of solid and liquid fossil fuels have been used in the CLPO process. Continuous operation of a 300 $W_{thermal}$ CLPO system using a kerosene feedstock achieved a high fuel conversion (in excess of 99.9 %) using a NiO/MgO–ZrO_2 OC thereby showing similar performance to gaseous fuels[97]. Chemical looping gasification (CLG) of coal has been achieved by some studies; this process is very similar to CLPO in that the CLG requires an OC that is selective to the production of syngas through gasification of the solid fuel rather than complete combustion of the coal[43,96]. This has been achieved through the use of various Ca and Fe based OC's with $BaFe_2O_4$ and $CaFe_2O_4$ being particularly selective to gasification[98,99]. However, these processes offer little in the way of improvements or advantages in either hydrogen production efficiency or GHG emissions when compared to the use of methane as a feedstock.

The use of liquid or solid biomass derived fuels in CLSR though offers a means of achieving sustainable hydrogen production through CLSR. A number of studies were conducted by Dupont and co-workers on diverse liquid feedstocks such as sunflower[95], pine and palm empty fruit bunch (PEFB) oils[100], waste cooking oil (WCO)[52] and acetic acid[101]; of particular note was the performance of the pine and PEFB oils which offered high conversion of the feedstock, 97 % and 89 % respectively, and high H_2 yield efficiency of 60 % and 80 % at 600 °C[100].

Moreover the application of CLSR to glycerol and ethanol feedstocks has been demonstrated; both of these feedstocks can be produced sustainably with glycerol being a major by-product of biodiesel processing and ethanol produced through the fermentation of starch and sugar rich biomass[102,103]. Jiang et al.[103,104] studied CLSR using glycerol and ethanol as feedstocks in CLSR in combination with a range of OC's utilising Ni supported by Al_2O_3, $NiAl_2O_4$ and montmorillonite with and without Ce doping: glycerol conversion of up to 99 % was achieved and hydrogen product purity at 600 °C reached 90 % of the equilibrium value[104]; ethanol conversion reached 80 % and was maintained over 20 cycles with high H_2 selectivity (70 %) while using a montmorillonite supported Ni OC[103].

An interesting application for the CLPO process is the treatment of biomass derived syngas to remove and reform biomass tars; tars are readily condensable hydrocarbons (below 350 °C) that are produced as by-products from the gasification of biomass and are associated with a host of issues for downstream processes in solid biomass gasification. A number of studies have shown that partial oxidation and catalytic of reforming of the tars is possible with Ni, Cu, Mn, perovskites and ilmenite ($FeTiO_3$) OC's[105–108]; Ni/Al_2O_3 OC's produced the best catalytic performance, converting up 96 % of tars present in a biomass derived syngas at 880 °C[107].

2.1.5 Sorption Enhanced Chemical Looping Steam Reforming

In spite of much of the literature referencing SMR-CLC as the first modern chemical looping reforming technology, Lyon and Cole[5] developed a process known as unmixed combustion (UMC) in 2000; this process is analogous to the SECLSR process (as described in Section 1.2.2.1) and was conducted using a packed bed reactor coupled with feed switching. This packed bed process was further developed by Dupont et al.[92,95] and Pimenidou et al.[52,94] who renamed it unmixed steam reforming (USR) and studied the use of waste biomass feedstocks and sorbent screening. This process produces a pure hydrogen product without the need for additional WGS reactors or product purification. However,

the SECLSR process has an issue in that the CO_2 produced via calcination is diluted by N_2 therefore making carbon capture difficult. This issue can be remedied by using pure oxygen or using solvent based capture but these methods reduce efficiency and increase plant complexity[30,32,51].

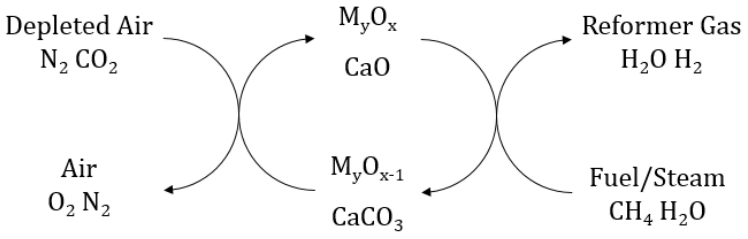

Figure 2.6: Schematic of an SECLSR system

Ryden and Ramos[32] and Fernandez et al.[30] extended the concept to fluidised bed reactors with a 3 reactor design, Figure 2.7.

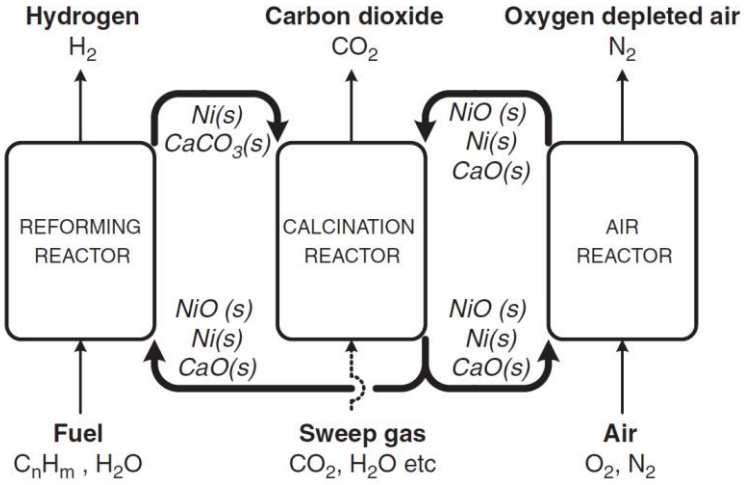

Figure 2.7: The SECLSR concept as proposed by Ryden and Ramos[32]

This concept proved via process modelling and thermodynamic calculations that the production of high purity H_2, CO_2 and N_2 streams could be produced by this process thereby enabling carbon capture with no intrinsic efficiency penalty[30,32]. This process is typically limited by the reactivity of the sorbent and its ability to be cycled without losing adsorption capacity; low cost calcium oxide based sorbents quickly lose their CO_2 capacity over continued cycling and must be replaced frequently[109].

2.1.6 Summary

Chemical looping technology has been used by several processes to facilitate CO_2 capture from power generation and intensify hydrogen production. Although chemical looping technology has existed since the early 1900's, much of the research into the technology has been conducted since the year 2000.

CLC allows intrinsic CO_2 separation for power generation by avoiding the combustion of fuel in air through use of an OC. CLWS was developed from the steam iron process and enables the production of high purity H_2 CO_2 and N_2 through the oxidation and reduction of iron-based OC's. SMR-CLC improves heat provision to the SMR process through the use a CLC reactor that increases the possible heat transfer coefficient through the reformer tubes and allows CO_2 capture from the combustion of the fuel used. CLSR enables the production of hydrogen without external provision of heat to the endothermic SR reactions; this is achieved by heat integration of the endothermic SR and OC reduction reactions with the OC oxidation reaction. SECLSR improves upon CLSR by implementation of solid CO_2 sorbents to perform in-situ purification of the H_2 product thereby improving H_2 yield and making WGS and PSA process units redundant.

As highlighted in Section 1.2.2 and above, CLSR and SECLSR solve many of the issues with the dominant form of hydrogen production, SMR, while using similar feedstocks and reactor technology (in the case of packed beds). The purpose of this thesis is to develop and test novel fibrous OC's for use in chemical looping processes; the use of CLSR using a methane feedstock as a means of testing these materials allows the assessment of the novel OC's efficacy in terms of reduction reactivity, catalytic activity for the SR and WGS reactions and reactivity over several redox cycles to be assessed. The performance of the OC's can be used as a basis to build knowledge for their eventual use in the SECLSR thereby facilitating the production of pure H_2 with CO_2 capture.

2.2 Oxygen Carriers for CLSR

Since the interest in chemical looping technologies was sparked in the early 2000's much of the work published on the CLSR process has concerned the development of oxygen carriers; over 700 OC's have been tested for use in chemical looping applications, with supported transition metals having seen the most research activity. Metal oxides of Ni, Fe, Mn, Cu and Co have all been used, supported on alumina, zirconia, silica, titania, or bentonite[23,43].

The following section highlights the desirable properties that OC's used in CLSR should possess and discusses the relative advantages and disadvantages of the most prevalent OC materials used in CLSR. Further details can be found on a range of OC's in the reviews by Luo et al.[43] and Protasova et al.[110].

2.2.1 Desirable Properties

Ryden et al.[32,111] state the following criteria for OC's used in CLPO processes:

(1) High reaction rates for both the reduction and oxidation of the OC with fuel and air respectively over repeated cycling

(2) Thermodynamically able to convert fuel into CO and H_2 with high selectivity during reduction and able to be readily oxidised under air at relevant conditions

(3) Sufficient oxygen ratio to enable sensible solids inventory

(4) Able to either inhibit carbon formation, or to be resistant to the effects of carbon formation

(5) Be cheap and preferably environmentally friendly

(6) Low tendency for fragmentation, attrition, and agglomeration when used in fluidised beds

In addition to these factors a further criterion should be added for OC's used specifically in CLSR:

(7) High catalytic activity for the SR (and to a lesser extent WGS) reaction when the OC is present in its reduced state.

A number of different OC's have been suggested that satisfy these criteria, chief among them being Ni, Fe, Ce and perovskites although many other materials have been used in CLR processes.

2.2.2 Nickel OC's

Nickel is an attractive candidate when selecting a suitable OC for the CLSR process due to the high catalytic activity of the reduced metal Ni, and the high reactivity of the metal to both reduction and oxidation reactions. It is therefore both the most widely researched OC material and the catalyst of choice in the SMR process.

Zafar et al.[48,49] compared the reactivity of OC's consisting of CuO, Mn_2O_3, NiO, and Fe_2O_3 supported by SiO_2 and $MgAl_2O_4$ under CH_4/H_2O and 5 % O_2 atmospheres. These

experiments utilised a fluidised bed CLPO process, and showed that the NiO based OC's, supported on either SiO_2 or $MgAl_2O_4$, showed the fastest rate of reduction, and closely matched the rate of oxidation of CuO (which showed the highest rate of oxidation). Moreover only the NiO based OC's were able to produce a product stream with high H_2 and CO selectivity when the conversion of the OC was high (i.e. the extent of reaction from M_xO_y to M_xO_{y-1})[48].

Zafar et al.[48] are quick to point out that NiO OC's represent an excellent candidate for CLPO process due to the high selectivity to H_2 and CO at higher OC conversions; however they fail to mention that this can likely be attributed to the catalytic effect of reduced Ni upon the SR reforming reaction rather than the effect of partial oxidation of methane facilitated by the OC. The catalytic properties of reduced Ni for the SR are well reported; a number of studies have found that Ni not only greatly outperforms Co, Fe and Cu in terms of catalytic activity for the SR of methane, but matches some noble metals (namely Pt, Pd, and Ir) typically famed for their catalytic activity[112–114]. This catalytic activity is vitally important for the CLSR process.

If the suitability of Ni as an OC is well established, the main research avenue for the application of Ni based OC's is in the supports used and the synthesis methods employed to anchor this effective active metal.

A series of supports have been largely discounted as supports by several studies. Antzara et al.[115] showed that TiO_2 and SiO_2 were considered poor support materials due to low reactivity during reduction and rapid deactivation of the OC's resulting in rapidly decreasing methane conversion during steam reforming. Moreover SiO_2 supported OC's were found by Zafar et al.[48] to undergo significant agglomeration and redox reactivity deactivation as the number or redox cycles increased. TiO_2 and MgO supported Ni OC's were found to produce very slow reaction rates and occasionally a lack of any redox reaction rate due to the formation of stable phases of $NiTiO_3$ or $Mg_{0.4}Ni_{0.6}O$[116,117].

Ni supported by alumina (Al_2O_3) has been identified as a suitable OTM due to its excellent reactivity toward methane and supression of carbon formation; several studies have been conducted on this material and found it to be a very appropriate support particularly in α-Al_2O_3 form[23,41]. De Diego et al.[50] found that α, γ, and θ-Al_2O_3 supports all provided very high oxidation reaction rates, while the α-Al_2O_3 provided the highest rates in reduction reactions and the γ-Al_2O_3 the lowest. This is known to be caused by the solid state reaction between the Al_2O_3 support and the deposited NiO that forms the hard to reduce $NiAl_2O_4$

spinel; a reaction that is stronger between NiO and γ-Al_2O_3 than NiO and α-Al_2O_3[118]. This discrepancy can be minimised by either pre coating the γ-Al_2O_3 with MgO, CaO or by heat treating the γ-Al_2O_3 to form α-Al_2O_3 prior to Ni loading[44]. Another support that has been widely investigated is $MgAl_2O_4$. This material has been shown to outperform other supports such as Al_2O_3 and SiO in terms of reaction rates in oxidation and reduction reactions[49]. It has been shown in a few large multi-cycle experiments that both $MgAl_2O_4$ and Al_2O_3 based Ni OTMs did show any significant changes in reactivity, surface structure and solid structure after many redox cycles and presented no fluidisation or agglomeration issues[89,91,119].

However, there are downsides to the use of Ni in OC's. The toxicity of Ni is an environmental concern, and this combined with the relatively high cost of Ni (compared to metals such as Fe Mn and Cu) form some arguments against its use[23,41,43]. Two widely recognised criticisms of Ni OC's are the poor selectivity for partial oxidation of fuel (typically CH_4) and the propensity for carbon formation. Both of these factors are important issues when Ni OC's are used in CLPO, however when used in CLSR, they become less problematic; the poor selectivity of the Ni OC to partial oxidation of the fuel (i.e. more likely to completely combust the fuel used under reduction) is less problematic in CLSR as the majority of the H_2 producing burden is placed on the reduced Ni catalysed SR reaction[120]; furthermore in spite of Ni sensitivity to carbon, the steam feed (typically S:C 3) used in CLSR greatly reduces carbon formation[89].

2.2.3 Iron OC's

Iron and iron oxide-based OC's are seen as an alternative to Ni based OC's due to their abundance, non-toxicity, low cost, high melting point (and therefore high resistance to agglomeration) and a reduced tendency for carbon formation. A high resistance to sulphur poisoning also means that they are particularly suited to the reforming of fuels with high sulphur content (e.g. coal)[43,110]. However if pure iron oxide is used in the CLSR process, the reduction and oxidation reactivity rapidly and severely reduces with continued cycling (> 10 cycles); this is caused by the reduction of the haematite (Fe_2O_3) to metallic Fe, which is inconvenient as this reduction reaction produces a much higher H_2 yield than that of Fe_3O_4 to FeO[121].

The addition of a ceramic support material such as Al_2O_3 can stabilise the performance of iron-based OC's allowing their long term use. Forutan et al.[122] found that when supported by Al_2O_3 (unspecified whether α, γ, or θ-Al_2O_3) the use of Fe produced OC's with the

highest stability over redox cycles, resistance to sintering and greatest oxygen capacity compared to similar Co, Cu and Mg OC's at high temperatures (700 – 1050 °C).

However the downsides to the use of Fe based OC's are numerous; lower redox reactivity, steam reforming activity and oxygen transport capacity than Ni based OC's means their use is uncommon in CLSR processes[43,110].

One solution is the use of Ce based promoters for use with Fe – Al_2O_3 OC's; Hafizi et al.[122] showed that the addition of 5 wt% Ce (or 5 % Ca) to a 15 wt% Fe – Al_2O_3 OC allowed for greater CH_4 conversion and H_2:CO molar ratio across 15 cycles with far greater resistance to decreasing activity than the undoped Fe OC. Furthermore, Zhu et al.[123] showed that the use of CeO_2 as a support for iron oxides can provide improved activity and stability for both methane conversion and hydrogen yield as long as the surface area of the OC remains high and the Ce:Fe molar ratio is close to unity.

2.2.4 Ceria OC's

Proof of concept for the use of CeO_2 in CLR processes has been achieved by Zhu et al.[124] who found that direct conversion of methane to CO and H_2 during reduction was possible resulting a syngas with a molar ratio of 2 H_2: 1 CO. However thermal cracking of methane resulting in carbon deposition and the rapid loss of reducibility of CeO_2 over the first 10 redox cycles means that significant research into mixed metal oxides using Ceria has been conducted[43,110].

Although Ce-based oxides such as Ce-Zr, Ce-Fe, and $CeAl_2O_3$ have seen interest, the addition of Rh and Pt to Ce-based oxides is particularly interesting[43]; these materials have produced accelerated H_2 and CO formation rates under reduction and decreased the activation energy of syngas production when compared to CeO_2 OC's. Fathi et al.[87] showed with a Pt and Rh doped CeO_2 OC supported by γ-Al_2O_3 the conversion of methane was drastically enhanced over 20 cycles and the minimum temperature for reduction was reduced.

2.2.5 Perovskites as OC's

Perovskite-type oxide materials are a series of mixed oxides with the general formula ABO_3 where A represents an alkali, rare earth or alkaline earth metal ion while B represents a transition metal ion[71]. Perovskites present an alternative means to both provide oxygen carrying properties and catalysis for partial oxidation and the SR reaction. They can

present good redox properties, thermal stability, and in partial oxidation, excellent selectivity to H_2 and CO[43,110].

Lanthanum Ferrites ($LaFeO_3$) have been identified as a promising material for CLR processes due to their catalytic effect on the methane conversion for synthesis gas as well as their reasonable oxygen capacity and high stability[43,110]. Dai et al.[125] showed that compared to other perovskites (A = Nd and Eu), $LaFeO_3$ was the most selective to H_2 and CO during reduction and proved the most catalytically active for the SR reactions and produced no carbon over repeated cycling. Moreover defect perovskite materials (where lower cation valences cause oxygen vacancies) such as $La_xSr_{1-x}FeO_{3-\delta}$ offer better OC reactivity, selectivity and stability as well as improved resistance to carbon than conventional perovskites[43,110,111].

However, in general the reduction and oxidation reactions in perovskites are slower than most competitors making process design difficult. Moreover the oxygen carrying capacity and hydrogen yield of these materials is often lacking thereby limiting their practical application in CLSR[43,110].

2.2.6 Other OC materials

In many ways Mn OC's share many traits with Fe based OC's; manganese is non-toxic, low cost and widely available material which offers a greater oxygen capacity than Fe based OC's. Despite these advantageous qualities, Mn OCs show low reactivity to the conversion of methane to syngas also tend to form stable irreversible phases when used in several redox cycles with a wide range of supports including SiO_2, TiO_2, Al_2O_3, ZrO_2 and $MgAl_2O_4$. Furthermore far higher wt.% of Mn must be deposited on the support used, which can cause issues in OC synthesis[43,45,110].

Copper OCs typically provide an excellent oxygen transfer capacity and excellent redox reactivity (especially at low temperatures) when compared to Ni based OCs. It is also far cheaper than Ni and Co and presents none of the toxicity of those metals [43,110]. However, thanks to copper's low melting point, agglomeration becomes a serious issue especially when temperatures exceed 750°C. When this factor is considered with copper OCs poor mechanical strength, high attrition rates low oxidation cycle efficiency, copper has seen little use in CLSR research[43,45,110].

Cobalt OCs can be considered an option due to their high oxygen transport capacity, and catalytic activity in the SR reaction. In spite of this, Cobalt OC's show low reactivity to, and fast deterioration of, the redox reactions necessary in the CLR concept[126]. This material

is also more expensive than the other options presented here, and presents environmental concerns due to its toxic nature[43,110]. Additionally cobalt tends to form strong interactions with Al_2O_3, TiO_2 and MgO supports and as Al_2O_3 is one of the most widely used supports in CLR, this presents a serious issue[126–128].

2.2.7 Summary

The short review of the main OC's used in CLR processes points toward the use of Ni supported by Al_2O_3 as an effective OC for use in CLSR; the sufficient oxygen transfer capacity it offers coupled with high oxidation and reduction reaction rates result in its use in the vast majority of CLR experiments for good reason. It is especially suited to use in the CLSR rather than the CLPO process due to its high catalytic activity for the SR reaction, which is responsible for the burden of H_2 production in the CLSR process. This means the poor selectivity to CO and H_2 during reduction of the OC often quoted as a disadvantage for CLPO processes is much less of an issue.

The use of Ni/Al_2O_3 OC's in a CLSR process is therefore well justified. However, development of Ni OC's based upon the use of the predominantly γ-Al_2O_3 Saffil® fibrous support material will require a more detailed examination of both the metal support interactions experienced in these materials and the reduction and oxidation processes encountered in CLSR.

2.3 Development of Ni/Al_2O_3 Oxygen Carriers for CLSR

Of crucial importance in the development of Ni/Al_2O_3 in CLR processes is the interaction between metallic nickel and the various crystalline phases of Al_2O_3. As alluded to in the review above (Section 2.2) the metal support interactions have a significant affect upon the efficacy of the OC both during reduction and oxidation as well as during SR by metallic Ni. Therefore, further review of these interactions and how they affect the CLR process is needed.

Consequently, the process of reduction and oxidation of Ni/Al_2O_3 OC's will be examined in detail; the theory of solid-gas (heterogeneous) reactions will be discussed with a review of the literature concerning the application of several kinetic models to the reduction and oxidation of Ni/Al_2O_3 OC's.

2.3.1 Synthesis of Ni/Al_2O_3 Oxygen Carriers

Ni/Al_2O_3 OC's are typically synthesised in a similar manner to Ni/Al_2O_3 catalysts utilised to great effect in SMR. There are two main methods by which these materials are typically synthesised: impregnation and precipitation. Sometimes the processes are combined to facilitate impregnation of a support material with a precipitation process in a method known as deposition precipitation.

2.3.1.1 Impregnation

Impregnation involves the deposition of active metal upon a preformed support structure. In this technique, the preformed alumina support is either dipped into a metal salt solution, typically nickel nitrate $Ni(NO_3)_2.6H_2O$, or the solution is introduced to the alumina in volume equal to the pore volume of the support in what is typically termed "incipient wetness" impregnation. Take up of the solution is a function of the solution concentration and support porosity but key to this method is the process of drying the solution to effect precipitation of the metal salt[129]. This process must ensure that the salt is deposited as uniformly as possible throughout the pore structure and surface of the support; in actuality this is difficult to achieve and typically this method results in a non-uniform deposition may be expected[130,131]. After this point calcination is carried out to decompose the metal salts to their corresponding oxides

The prime advantage of this method is the production of the support and the catalyst can be conducted in different processes. Other advantages of this method include its simplicity in terms of raw materials and the mechanical strength of the produced catalyst[25,129]. However due to the limitations of the drying process it is difficult to achieve high metal loadings without multiple impregnation and calcination cycles thereby increasing the economic and energy cost. Moreover, low crystallite sizes are difficult to obtain due to the difficult to control drying process and the lack of any great interaction with the support material.

2.3.1.2 Co-precipitation

Co-precipitation involves the formation of both the support and active metal in one synthesis step. In this process metal salts, typically nickel nitrate ($Ni(NO_3)_2.6H_2O$) and aluminium nitrate ($Al(NO_3)_3$) are mixed with a basic solution of any number of hydroxide or carbonate precipitants including but not limited to NaOH, KOH, Na_2CO_3, K_2CO_3 or NH_4OH (ammonia); the gradual addition of the basic precipitant to the acidic and low solubility metal salt precursor causes an increase in the pH of the solution and results in

supersaturation, nucleation and consequently precipitation of the desired metal in the form of metal hydroxides or carbonates.[129]

$NaOH \rightarrow Na^+ + OH^- \uparrow$ **Equation 2.3**

$Na_2CO_3 \rightarrow 2Na^+ + CO_3^{2-} \uparrow$ **Equation 2.4**

$NH_4OH \rightarrow NH_4^+ + OH^- \uparrow$ **Equation 2.5**

A rise in pH causing precipitation of a metal hydroxide can also be achieved through the slow decomposition of urea above 90 °C in aqueous media[41,46], Equation 2.6.

$CO(NH_2)_2 + 3H_2O \rightarrow 2OH^- + 2NH_4^+ + CO_2 \uparrow$ [130] **Equation 2.6**

Both co-precipitation and deposition precipitation (detailed below) can facilitate the production of hydrotalcite-like materials also known as layered double hydroxides (LDH). These precipitates can be described by the general formula $[M_{1-x}^{2+}M_x^{3+}(OH)_2]^{x+}[A_{x/n}]^{n-} \cdot mH_2O$ where M^{3+} = Al and M^{2+} = Ni. The presence of these structured materials prior to calcination have been known to decrease crystallite size and improve the homogeneity of dispersion of metal oxides thereby improving catalytic activity and increased hydrogen productivity and selectivity during SR[132,133]. Regardless of whether LDH's are formed the precipitates are typically non-stoichiometric and amorphous; they are then filtered, washed and calcined to decompose the hydroxides/carbonates to the corresponding oxides.

The co-precipitation method facilitates a high metal loading in one process step and uniform macro distribution of the metal loaded. Moreover the low solubility of the metal salts results in very high supersaturations that lead to small particle sizes as well as small crystallite sizes (5 - 15 nm) and high surface areas (50 – 200 $m^2\ g^{-1}$)[25,129] However intimate interaction between the support and loaded metal is guaranteed; this can be advantageous in catalysis, but is generally undesirable for OC's.

2.3.1.3 Deposition Precipitation

Deposition precipitation, is a combination of the two methods detailed above and has been used as an alternative to provide increased homogeneity of dispersion of active metals over supports[129]. If the precursor solution is homogeneously distributed throughout the porous support the precipitation of the non-soluble hydroxides can occur uniformly over the support. This process provides a more homogenous deposition of metal when compared to incipient wetness deposition[46,130].

Moreover, carrying out the ageing process hydrothermally (at elevated pressure as well as temperature) can lead to higher yields and greater crystallinity of the insoluble hydroxides formed[134]. Research conducted using hydrothermal synthesis for the production of OC's is rare and has not been investigated in comparison with other synthesis methods[135,136].

2.3.2 Metal Support Interactions

As stated earlier when Ni/Al_2O_3 OC's are fabricated and used in CLR processes, a solid state reaction occurs between the Al_2O_3 support and the impregnated NiO which results in the formation of nickel aluminate, $NiAl_2O_4$[50,118]. This metal support interaction should be avoided if possible; while NiO deposited on the support can be easily and rapidly reduced at low temperatures (< 400 °C), the reduction of bulk $NiAl_2O_4$ is slower and requires higher temperatures (> 800 °C)[137–140]. Therefore, the formation of bulk $NiAl_2O_4$ slows the production of catalytically active metallic Ni during reduction and thereby reduces the effectiveness of the OC material.

Metal support interactions and the formation of $NiAl_2O_4$ was investigated by Bolt et al.[118] for Ni as well as for Co, Cu and Fe and found the rate of the solid state reaction between the transition metal, be that Ni Co Cu or Fe, and the Al_2O_3 was affected by a number of factors.

Bolt et al.[118] found the rate of the solid state reaction between NiO and Al_2O_3 has been found to occur in two phases. The initial phase of the reaction is controlled by nucleation of $NiAl_2O_4$ and occurs while grain boundaries between the NiO and Al_2O_3 are still present and or the nucleation of the $NiAl_2O_4$ is slow due to relatively low temperatures (below 800 °C). At this point the movement of Ni^{2+} and Al^{3+} ions into the first few monolayers of the Al_2O_3 and NiO phases respectively is facilitated by the higher mobility of these ions along the surface of the individual grains when compared to the bulk. This results in the formation of an effectively two-dimensional "surface spinel" compound which is similar in composition to bulk $NiAl_2O_4$ spinel but generally lacks either sufficient crystallite size or long-range three-dimensional order to be detectable by XRD. The surface spinel compound may then grow out to form bulk $NiAl_2O_4$ with the reaction front progressing toward the centre of the grains both from the grain boundaries and from the original interface. At this point the reaction is controlled by the diffusion of Ni^{2+} and Al^{3+} through the bulk $NiAl_2O_4$ phase and follows the parabolic growth rate law i.e. the thickness of the $NiAl_2O_4$ layer increases with the square root of the time spent at elevated temperatures.

The rate of these reactions, and therefore the degree of metal support interaction, in Ni/Al_2O_3 OC's used in CLR processes was found to be influenced by the crystalline phase of Al_2O_3 used, the transition metal impregnated upon the Al_2O_3 support and the temperatures at which the materials are synthesised and used in process.

2.3.2.1 Effect of Alumina Phase

In the study mentioned above, Bolt et al.[118] found that the use of γ-Al_2O_3 rather than α-Al_2O_3 when synthesising Ni/Al_2O_3 materials, resulted in a faster solid-state reaction between the two reactants the metal and support thereby producing a greater proportion of $NiAl_2O_4$; they attributed this to the differences in crystal structure between the two alumina phases.

The differences in crystalline structure between the two phases result from the process used to produce alumina supports; alumina is typically produced through the calcination of source alumina hydroxide, typically gibbsite ($Al(OH)_3$) or boehmite (AlOOH), through various transition aluminas (including γ, η, δ, θ, κ, and $\varnothing$) with various meta-stable structures until the thermodynamically stable α-Al_2O_3 phase is achieved[141].

α-Al_2O_3 is only produced at very high temperatures and is the most thermodynamically stable of the alumina phases. Its consists of a trigonal structure (R-3c) with the O^{2-} anions in a hexagonally close-packed arrangement with the Al^{3+} cations occupying 0.6$\dot{6}$ of the octahedral interstitial sites due to the required cation to anion ratio[142], Figure 2.8.

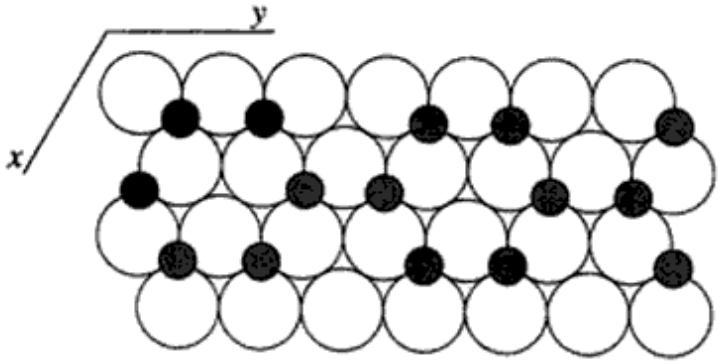

Figure 2.8: a) the HCP arrangement of O^{2-} anions (white circles) in α-Al_2O_3 with the Al^{3+} cations (black dots) occupying two thirds of the octahedral interstitial sites[143]

Conversely γ-Al_2O_3 is a meta-stable structure formed between 300 °C – 1000 °C and presents a "defect spinel" structure[144]. The conventional spinel structure, dictated by AB_2O_4 where A and B are cations (Ni^{2+} and Al^{3+} in $NiAl_2O_4$) and O is the oxygen anion, Figure 2.9. This structure consists of a cubic close packed (Fd-3m) array of oxygen atoms with the A and B cations occupying 0.125 of the tetrahedral sites and 0.5 of the octahedral

sites. The occupancy of these sites results in face centred cubic cell which is 2^3 times the size of the basic oxygen array resulting in a unit cell of $A_8B_{16}O_{32}$[118,143].

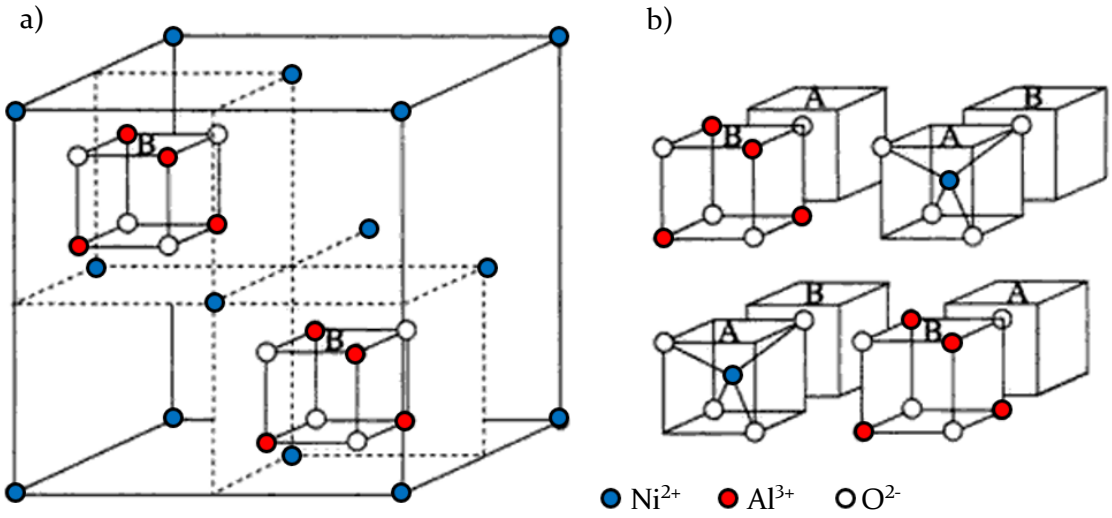

Figure 2.9: the spinel structure (AB_2O_4 using $NiAl_2O_4$) where the smaller cubes A and B show the AO_4 tetrahedra and B_4O_4 cubes where B are situated in the octahedral sites. Only B cubes are shown in the unit cell for clarity[143].

The structure of γ-Al_2O_3 deviates from that shown in Figure 2.9, due to the presence of only Al^{3+} cations in the tetrahedral and octahedral sites. As such the structure has been reported as tetragonally distorted however the ascribed Fd-3m space group is still common. To satisfy the stoichiometry of γ-Al_2O_3, 2.66̇ vacant cation positions per unit cell are formed, therefore producing a unit cell containing 32 oxygen atoms and 21.33̇ aluminum atoms[145]. The precise location of these vacancies is controversial[144].

Bolt et al.[118] attributed the faster reaction between NiO and γ-Al_2O_3 to three factors; (1) increased grain boundary density produced by the smaller crystallite sizes typically exhibited by γ-Al_2O_3 compared to α-Al_2O_3 means greater facilitation of Ni^{2+} and Al^{3+} ions along grain boundaries; (2) the similarity of the defect spinel structure of γ-Al_2O_3 to $NiAl_2O_4$ reduces the thermodynamic energy barrier for the reaction between γ-Al_2O_3 and NiO and facilitates the movement of Ni^{2+} into the vacant lattice sites of γ-Al_2O_3; (3) the thermodynamic metastability of γ-Al_2O_3 due to the method of synthesis.

The literature pertaining to the relative effectiveness of Ni based OC's supported by both γ-Al_2O_3 and α-Al_2O_3 supports the hypotheses suggested by Bolt et al.

De Diego et al.[50] used dry impregnation, with calcination at 550 °C and sintering at 950 °C, to load similar Ni mass upon both γ-Al_2O_3 and α-Al_2O_3. They found, using XRD, that that the OC using γ-Al_2O_3 produced only $NiAl_2O_4$, whereas those using α-Al_2O_3 produced

both NiO and $NiAl_2O_4$ phases. Reduction reactivity tests conducted between 800 °C – 950 °C using a reducing CH_4/ H_2O feed showed that the OC's was split into two phases whereby a fast, initial reaction rate was attributed to reduction of NiO and a slower secondary phase was attributed to the reduction of $NiAl_2O_4$. In the Ni/γ-Al_2O_3 OC the initial fast reduction of NiO was responsible for less of the overall conversion of the OC during reduction than the α-Al_2O_3 therefore showing the OC based on α-Al_2O_3 was more reactive. All OC's tested showed approximately equal reactivity under oxidation using air. Moreover, when tested in a batch CLPO process, similar H_2/CO ratios were produced at similar OC reduction conversion.

Dueso et al.[44] compared the reduction and oxidation reactivity of a Ni/γ-Al_2O_3 and a Ni/α-Al_2O_3 OC prepared by incipient wetness impregnation and used between 800 °C – 950 °C as part of an investigation into reduction and oxidation kinetics of these materials. XRD determined that $NiAl_2O_4$ was present in all samples. They found that the Ni/α-Al_2O_3 was more reactive (i.e. higher percentage conversion during fast reduction of NiO) during reduction by CH_4, H_2 and CO especially after 5 redox cycles. Reactivity under oxidation was much faster but followed suit with the Ni/α-Al_2O_3 found to be more reactive reaching full conversion noticeably quicker than Ni/γ-Al_2O_3; this was again attributed to a greater amount of $NiAl_2O_4$ in the Ni/γ-Al_2O_3 sample.

Another study by De Diego et al.[146] studied the use similar OC's in the study above this time in 900 W_{th} CFB reactor between 800 °C – 900 °C. XRD determined that $NiAl_2O_4$ was present in all samples. They again found that the Ni/α-Al_2O_3 was more reactive both initially and after 50 hours of operation than the Ni/γ-Al_2O_3 with little difference in the reactivity experienced over this period; this contrasts with the Ni/γ-Al_2O_3, which showed better reactivity after 50 hours of use. Although the use of the two OC's resulted in similar gas compositions, the higher reactivity of the Ni/α-Al_2O_3 meant that a lower solid cycling rate could be used.

2.3.2.2 Effect of Calcination and Process Temperature

Unsurprisingly, increasing calcination or process temperature employed in synthesis or CLR processes increases the rate at which $NiAl_2O_4$ forms. This is true of the initial nucleation controlled reaction responsible for the production of the "surface spinel" as well as for the diffusion controlled reaction that governs the formation of bulk $NiAl_2O_4$[118].

However the transition between the formation of the "surface spinel" and growth of detectable bulk $NiAl_2O_4$ is not realised until temperatures in excess of 600 °C are

reached[137]. This effect has been reviewed both in literature pertaining toward the use of Ni/Al_2O_3 materials as a catalyst for SMR and for its use in CLC and CLR process.

Lo Jacano et al.[147] used incipient wetness impregnation to produce $Ni/\gamma\text{-}Al_2O_3$ SMR catalysts that were consequently calcined at 600 °C for 24 hours. These materials were found to have no $NiAl_2O_4$ phase detectable by XRD after this particularly long calcination process. Lansink Rotgerink et al.[148] co-precipitated a range of Ni/Al_2O_3 SMR catalysts (the alumina phase produced was not stated) with calcination temperatures ranging from 350 °C – 600 °C (3 hours). In temperature programmed reduction (TPR) experiments using H_2 as a reducing agent, they showed that only when calcination temperatures exceeded 600 °C was evidence for the presence of $NiAl_2O_4$ present in the form of two reduction events. Richardson and Twigg[149,150] discovered in two investigations concerning the reduction of $Ni/\alpha\text{-}Al_2O_3$ SMR catalysts produced by incipient wetness impregnation (calcination 6 hours at 650 °C), that no evidence for spinel formation was found using TPR or XRD in the fresh catalysts.

Once the Ni/Al_2O_3 is subjected to temperatures higher than 600 °C the prevalence of the bulk phase becomes more prominent. This has widely been experienced in much of the literature pertaining to the use of Ni/Al_2O_3 OC's used in both CLC and CLPO due to the high temperatures (in excess of 800 °C) encountered in these processes.

Mattisson et al.[49] used dry impregnation to produce a $Ni/\gamma\text{-}Al_2O_3$ OC which was calcined at 550 °C 5 hours. No $NiAl_2O_4$ was detectable in the OC's before use in a series of reduction reactivity experiments using a mixture of 10 % CH_4, 10 % H_2O, 5 % CO_2 or after use at 750 °C; only after experiments conducted at 850 °C and 950 °C was $NiAl_2O_4$ detectable by XRD. In another work Mattisson et al.[117] found that when preparing a $NiAl_2O_4$ to be used as a support material for NiO impregnation, reaction of NiO and Al_2O_3 precursors to form $NiAl_2O_4$ was only achieved at sintering temperatures above 950 °C. Moreover a variety of works by the group led by Abad[46,131,151] used both Ni α and $\gamma\text{-}Al_2O_3$ OC's in a series of CLPO and CLC experiments with the materials usually prepared by impregnation used calcination at 550 °C (0.5 hours) and sintering at 950 °C (1 hour). As a result of this sintering process in combination with their use at temperatures in excess of 800 °C as dictated by CLPO and CLC, almost all their materials showed the presence of bulk Al_2O_4 detectable by XRD.

2.3.2.3 Effect of Promoters

Bolt et al.[118] identified that the rate of reaction between Co and Al_2O_3 was faster than that between Ni and Al_2O_3 due to an increased rate of diffusion of Co^{2+} through the anion sublattice of the spinel $CoAl_2O_4$ compared to that of Ni^{2+} though $NiAl_2O_4$. This increased rate of diffusion can be attributed to the difference in site energy preference for octahedral or tetrahedral sites between the two cations. As stated earlier a spinel structure has only 0.125 of the tetrahedral sites and 0.5 of the octahedral sites occupied by cations and these vacancies create a voidal diffusion path through the spinel structure; the lower a cations site energy preference (i.e. closest to zero), the more facile the diffusion through the vacancies of the spinel structure. While Ni^{2+} presents a strong octahedral site preference (~50 kJ mol^{-1}), Co^{2+} presents a less severe tetrahedral site preference (13 kJ mol^{-1}).

Hossain et al.[127,152] investigated the effect upon reactivity, stability and reduction and oxidation kinetics of doping small amounts of cobalt on a Ni α-Al_2O_3 OC for CLC. Using a 10:1 – 40:1 Ni/Co ratios and incipient wetness impregnation with calcination at 750 °C for 4 hours, they found that even in small amounts the Co promoters preferentially react to form surface and bulk $CoAl_2O_4$ thereby reducing the mass of $NiAl_2O_4$ produced and increasing the relative mass of NiO available for facile reduction and oxidation. They showed that when Ni/Co ratios were below 30:1, reactivity under reduction and oxidation as well as methane conversion in CLC and metal dispersion all increased while crystallite size decreased.

Hossain et al.[153,154] also used γ-Al_2O_3 doped with 5 % La as a support for a Ni OC and compared the reactivity stability and reduction and oxidation kinetics to conventional Ni γ-Al_2O_3 and a Ni α-Al_2O_3 OC's. The addition of the La promoter to the γ-Al_2O_3 support prior to Ni loading allowed a greater proportion of the reducible material on the Ni/La γ-Al_2O_3 OC was present as NiO leading to greater reduction conversion, reactivity and methane conversion in CLC compared to both Ni γ-Al_2O_3 and a Ni α-Al_2O_3 OC's. It was theorised that the La modified the surface of the γ-Al_2O_3 not only allowing the textural properties (i.e high porosity and surface area) of the γ-Al_2O_3 support to be maintained even after use at high temperature but inhibiting the formation of $NiAl_2O_4$.

2.3.2.4 Effect of Synthesis Method

Both Gayan et al.[46] and Li et al.[155] have compared the efficacy of Ni Al_2O_3 OC's in both CLC and SMR respectively, synthesised through both incipient wetness impregnation and deposition precipitation.

Gayan et al.[46] found that the use of incipient wetness impregnation in combination with a γ-Al_2O_3 support (with calcination at 950 °C) resulted in an OC with no NiO phase detectable in XRD. Conversely the use of deposition precipitation produced an OC with free NiO as detected by both XRD and TPR; this was attributed to the formation of hydrotalcite like insoluble Ni hydroxides known as layered double hydroxides (LDH) prior to calcination. The presence of NiO in the OC using DP and γ-Al_2O_3 resulted in higher reduction reactivity than the Ni γ-Al_2O_3 OC fabricated through wet impregnation. When tested in CLC it was found that the Ni γ-Al_2O_3 OC fabricated through deposition precipitation was more selective to H_2 and CO than the wet impregnated OC during reduction, thus highlighting the effectiveness of this method of synthesis for use in CLSR. In this work Gayan et al. also found that the method of synthesis had little effect upon the metal support interaction and thus efficacy of any Ni OC's fabricated with the use of α-Al_2O_3.

Li et al.[155] discovered that precipitation methods were able to produce smaller Ni crystallite sizes of 5 nm in a Ni γ-Al_2O_3 catalyst compared to 15 nm for the catalyst synthesized using impregnation; lower crystallite size is important in the production of effective catalysts (details in Section 2.4.4). Moreover, the impregnated catalyst showed evidence of bulk $NiAl_2O_4$ detectable via XRD whereas only evidence of surface spinel was found via TPR for the catalyst prepared by precipitation.

2.3.3 Reduction of Ni/Al_2O_3 OC's

Possibly the most important processes during any chemical looping process is the reduction of the OC in the fuel reactor or during the SR half cycle. The rate at which this reaction proceeds can influence many important factors such as the required solids cycling rate in fluidised bed applications, the frequency of feed switching in packed beds and the rate at which the OC becomes catalytically active. As a result, the kinetics and mechanism of reduction have been studied using a range of kinetic models and reductants.

The following section reviews the basics of heterogeneous reactions and the models used to define the kinetics of reduction for Ni/Al_2O_3.

2.3.3.1 Heterogeneous Reactions

The reduction and oxidation reactions of the OC's reactions investigated in this work are all examples of gas-solid reactions. It is generally accepted that there are 6 steps which can

control the rate at which reduction reactions involving gases and solids can occur[44,49,101,156,157], Figure 2.10:

(1) Gas moves from the bulk gas phase to (a) the surface of the OC and (b) through boundary layer around the particle

(2) Diffusion of the reactant to reach unreacted solid; this involves (a) diffusion of gas through the porous structure and/or (b) diffusion through layer of product formed during the reaction

(3) Adsorption of gaseous reactant to solid surface

(4) Chemical reaction between the reactant gas and solid, typically involving several steps

(5) Desorption of gaseous product from the solid surface

(6) Transport of the gaseous products through the reversal of steps 1 and 2.

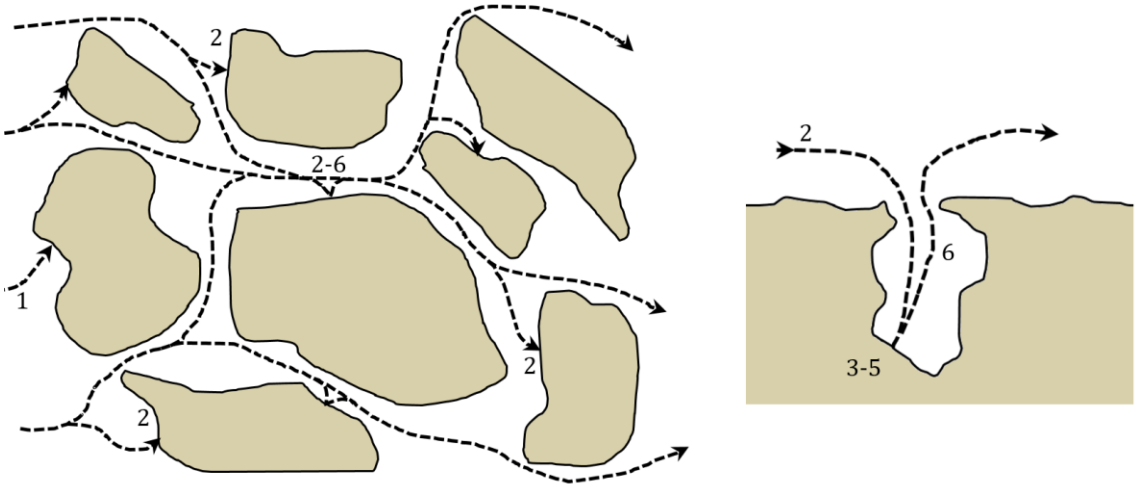

Figure 2.10: Diagram of the 6 stages of heterogeneous reaction

These stages simplify a very complex process in which all these steps have their own kinetics and resistances that can influence or limit the global rate of reduction; it is therefore important to understand that the rate-limiting step, i.e. the step with the highest resistance, will define the outcome of any analysis when attempting to quantify kinetics. Generally, the global rate of reaction is best reflected when the rate limiting step is not a transport phenomenon (steps 1 and 2 above). This will be explored in detail in Chapter 7.

The rate of many solid state reactions can be expressed with the following rate law[158,159]:

$$\frac{d\alpha}{dt} = Ae^{-\left(\frac{E_A}{RT}\right)} \times f(\alpha)$$ **Equation 2.7**

$$\frac{d\alpha}{dt} = k \times f(\alpha)$$ **Equation 2.8**

Where A is the pre-exponential factor, also termed the frequency factor, E_A is the activation energy of the reaction, T is absolute temperature, R is the universal gas constant, $f(\alpha)$ is the kinetic model, α the reactant conversion in time t and k the rate constant. In its integral form the rate law may therefore be expressed by[158,159]:

$$g(\alpha) = \int_0^{\alpha} \frac{d\alpha}{f(\alpha)} = k \times t$$ **Equation 2.9**

2.3.3.2 Kinetic Models of Heterogeneous Reactions

There are several kinetic models that can accuractely describe solid state reactions. These models typically fall into 4 main groups: nucleation, product layer diffusion, geometrical contraction and reaction order models, Table 2.2.

Table 2.2: Kinetic models of solid state reactions[158,159]

Model Type	Model	Differential Form $f(\alpha)=1/k\ d\alpha/dt$	Integral Form $g(\alpha)=kt$
Nucleation	Power Law (P2)	$2\alpha^{1/2}$	$\alpha^{1/2}$
	Power Law (P3)	$3\alpha^{2/3}$	$\alpha^{1/3}$
	Power Law (P4)	$4\alpha^{3/4}$	$\alpha^{1/4}$
	Avrami-Erofeyev (A2)	$2(1-\alpha)[-\ln(1-\alpha)]^{1/2}$	$[-\ln(1-\alpha)]^{1/2}$
	Avrami-Erofeyev (A3)	$3(1-\alpha)[-\ln(1-\alpha)]^{2/3}$	$[-\ln(1-\alpha)]^{1/3}$
	Avrami-Erofeyev (A4)	$4(1-\alpha)[-\ln(1-\alpha)]^{3/4}$	$[-\ln(1-\alpha)]^{1/4}$
Geometrical Contraction	Contracting Area (R2)	$2(1-\alpha)^{1/2}$	$1-(1-\alpha)^{1/2}$
	Contracting Area (R3)	$3(1-\alpha)^{2/3}$	$1-(1-\alpha)^{1/3}$
Diffusion	1-D (D1)	$1/(2\alpha)$	α^2
	2-D (D2)	$-[1/\ln(1-\alpha)]$	$((1-\alpha)\ln(1-\alpha))+\alpha$
	Jander 3-D (D3)	$[3(1-\alpha)^{2/3}]/[2(1-(1-\alpha)^{1/3})]$	$(1-(1-\alpha)^{1/3})^2$
	Ginstling-Brounshtein 3-D (D4)	$3/[2((1-\alpha)^{-1/3}-1)]$	$1-(^{2/3})\alpha-(1-\alpha)^{2/3}$
Reaction order	Zero-order (F0/R1)	1	α
	First-order (F1)	$(1-\alpha)$	$-\ln(1-\alpha)$
	Second-order (F1)	$(1-\alpha)^2$	$[1/(1-\alpha)]-1$
	Third-order (F1)	$(1-\alpha)^3$	$(1/2)[(1-\alpha)^{-2}-1]$

The kinetic model selected to describe reduction reactions of Ni based OC materials during chemical looping steam reforming varies between studies, however typically either the Avrami-Erofeyev (A2 or A3) or geometrical contraction (R2 or R3) models have been employed[44,101,127,156,160].

The geometric contraction models accounts for some of the structural properties of the solid particle including crystallite size and porosity. Essentially the geometrical contraction model (also known as shrinking core model) assumes that the nucleation and nuclei growth of the solid product is rapid enough that uniform layer of product is immediately formed, Figure 2.11.

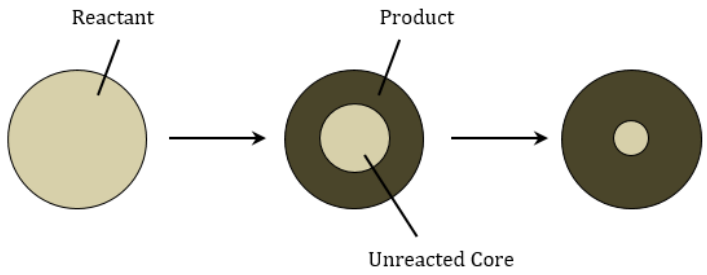

Figure 2.11: Diagram of the geometrical contraction model

The rate of reduction therefore is assumed to be controlled by either the chemical reaction at the boundary between the product and reactant or the diffusion of the reactant through the product layer. The R2 and R3 models account for the progress of the reaction through cylindrical (R2) or spherical (R3) solid particles[158], Table 2.2. They can be characterised by parabola-like shaped α vs t curve (Figure 2.12b) that is influenced by the shape of the solid particle in question.

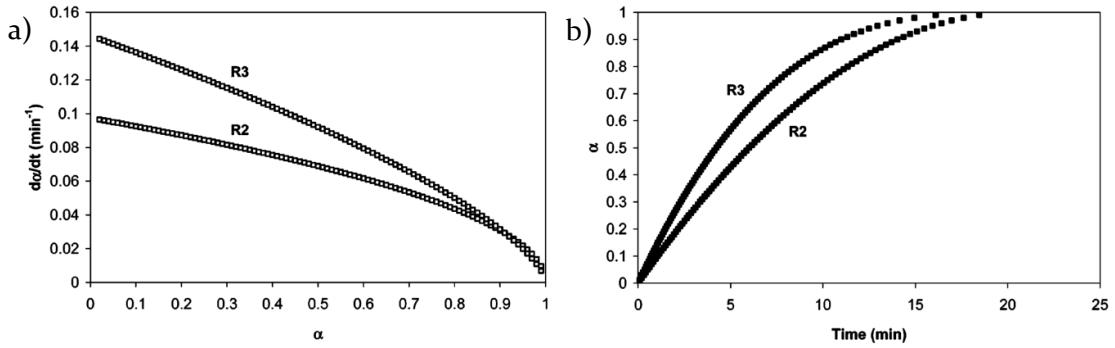

Figure 2.12: Isothermal $d\alpha/dt$ vs t (left) and α vs t plots (right) indicative of geometric contraction (a and b) models for solid-state reactions[158]

The Avrami-Erofeyev nucleation model assumes that the formation and growth of nuclei are the rate limiting step in the reaction. They can be characterised by the sinusoidal shape of the resultant α vs t curve (Figure 2.13b, overleaf).

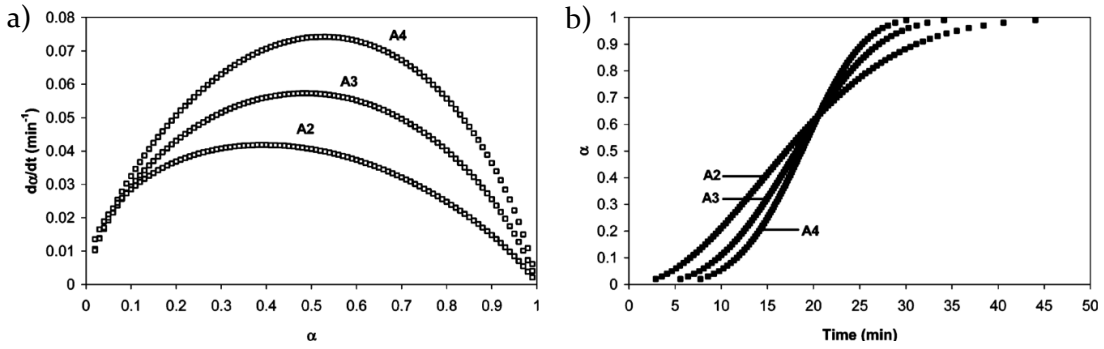

Figure 2.13: Isothermal $d\alpha/dt$ vs t (left) and α vs t plots (right) indicative of Avrami-Erofeyev (a and b) models for solid-state reactions[158]

The shape of this curve is a direct result of three phenomena that occur as the solid-state reaction takes place. A slow initial rate of conversion is assumed to be caused by the rate of nucleation of the new solid phase (Figure 2.14a); the time required for a significant number of nuclei of the new phase to be formed is relatively slow compared to the second phase which is characterised by a sharp increase in the rate of conversion[158,159]. This increase in conversion rate is assumed to be caused by both the rapid growth of the nuclei of the new phase into particles and the continued formation of new nuclei of the in the original phase (Figure 2.14b-d). Finally a decay of the rate of conversion is experienced as a result of the lack of available original phase available for nuclei formation or growth of particles[158,159].

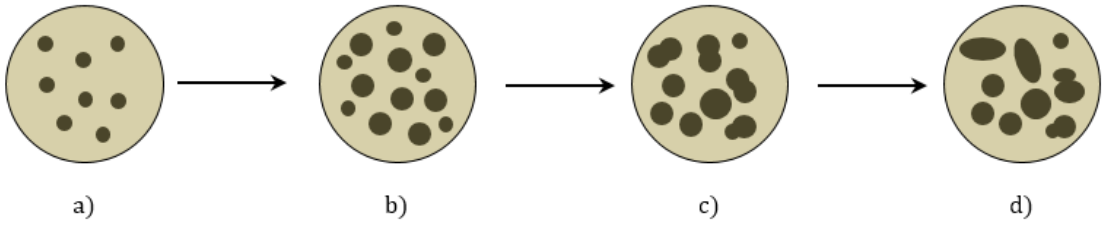

Figure 2.14: Diagram of the geometrical contraction model applicable to NiO crystallites

The specific Avrami-Erofeyev model (denoted by the Avrami index: A2, A3, A4) is known to be related to the type of nucleation (instant homogeneous, constant, increasing or decreasing rate) and geometry of nuclei growth (1D, 2D, 3D). However, it should not be assumed that each model is prescriptive of a single type of nucleation or dimension of growth; rather a combination of factors can influence the assignation of a specific model. For example Criado and Ortega[161] stated that the A3 model could refer to both instant homogenous nucleation followed by 3D growth as well as by constant rate of nuclei formation followed by 2D growth.

Table 2.3: Physical meaning of the Avrami Erofeyev models suggested by Criado and Ortega[161]

Nucleation	Growth Geometry	Model
Instant, Homogeneous	2D	A2
	3D	A3
Constant Rate	1D	A2
	2D	A3
	3D	A4

Despite this ambiguity, the Avrami index affects the relative prevalence of the rate of nuclei growth to the overall rate of conversion i.e. the α vs t curve becomes steeper in the

intermediate region with the relative time associated with nuclei formation and decay of growth reduced.

Zhou et al.[160] reviewed a wide range of kinetic studies, primarily concerning the reduction in H_2 of unsupported and supported Ni based OC's, although other reducing gases such as CO and CH_4 were reviewed. Their review highlights that many of these studies use the R3 geometric contraction model to describe the reduction of NiO whether supported or not. Additionally Zhou et al.[160] sourced data from a number of the reviewed studies and performed statistical analysis to prescribe kinetic models that provided the best fit and were statistically significant; when coupled with their own experimental work, Zhou et al.[160] showed that the Avrami-Erofeyev nucleation model was, in the vast majority of cases, a better fit. Hossain et al.[152,154] investigated the kinetics of reduction for both a Ni/Co and Ni/La γ-Al_2O_3 OC's under a CH_4 and H_2 atmosphere at non-isothermal conditions (from ambient to 950 °C). They found that with both materials that the Avrami-Erofeyev model (A1) was a better fit for the kinetic data (as judged by R^2 values and percentage deviation between the experimental and modelled data) than the R3 shrinking core model[152]. Cheng et al.[101] showed that the reduction of a Ni α-Al_2O_3 by CH_4 and various model biocompounds (ethanol, acetone, acetic acid and furfural) was found to be excellently modelled by the A2 Avrami-Erofeyev model with R^2 values ranging from 0.95 to 0.99.

2.3.4 Summary

The formation of both bulk and "surface spinel" of $NiAl_2O_4$ as a result of the solid-state reaction between NiO and Al_2O_3 causes a loss in reduction activity and thereby both slows the production of catalytically active metallic Ni. This reduces the effectiveness of the OC material in CLSR. If the complete avoidance of the production of any spinel phase is effectively impossible at the temperatures required for both the synthesis of OC's and their use in the CLSR process, then the minimization of these phases should be a priority for an effective OC. Avoidance of bulk $NiAl_2O_4$ can largely be avoided through the selection of appropriate selection of synthesis method, calcination temperature (< 800 °C), selection of alumina phase and use of promoters. Additionally, a brief summary of the kinetic models used to describe heterogeneous solid gas reactions and the literature concerning the use of these models in chemical looping processes has been conducted.

The information reviewed in this section allows the selection of synthesis procedures for novel Saffil® based Ni OC's for use in CLSR that should avoid the production of bulk $NiAl_2O_4$ and minimise the formation of surface spinel $NiAl_2O_4$. Moreover, appreciation of

typical kinetic models used to describe the reduction of these OC's in the CLSR process should allow effective study of the differences in reactivity between the conventional SR catalyst and the novel Saffil® OC's.

2.4 Heterogeneous Catalysis and Structured Catalysts for Steam Reforming

While the metal support interactions and study of the reduction kinetics is vital in the design of an effective Ni/Al_2O_3 for use in CLSR, the intricacies of the CLSR process and its reliance on the OC to be catalytically active in the SR reaction mean that the catalytic aspects of the OC design must be considered. Moreover, while the use of fibrous structured catalysts is to the author's knowledge novel in OC design and the CLSR process, they have been utilised to intensify SMR.

It is therefore beneficial to review the basic aspects of catalysis, the desired properties of catalysts for use in steam reforming and review the use of structured catalysts when applied to intensification of steam reforming.

2.4.1 Heterogeneous Catalysis

The typical definition of heterogeneous catalyst is a solid material that increases the chemical rate of reaction of a gas phase reaction without undergoing change themselves. This definition is problematic in that it understates several important factors of catalysis. Firstly, the solid catalyst almost always undergoes physical change and secondly it is directly involved in the reaction even if it does not represent a reactant or product of that reaction. Realistically there are several different essential features of heterogeneous catalysis[129]:

(1) The solid catalyst material increases the rate of a gas phase reaction via interaction of the solid material with gas phase species by means of the formation of reaction intermediates.

(2) The overall Gibbs free energy change of the reaction is unchanged i.e. only the speed at which the reaction occurs and not the quantity of equilibrium products of that reaction is affected by catalysis.

(3) The reaction steps that are catalysed typically take place between the topmost atomic layers of the solid catalyst and extend no more than one atomic diameter into the gas phase.

(4) The productivity of the catalyst must be high. On a micro scale this means that each catalysed step of the reaction must occur many times at any given reaction site before deactivation; on a macro scale this means that for each tonne of catalyst used, many more tonnes of the reaction product must be formed.

The step-wise progression of a heterogeneously catalysed gas phase reduction is similar to that of a heterogeneous reaction between solid and gaseous species (as described in Section 2.3.3.1). The main differences between the two systems arise due to the behaviour of the solid involved in the reaction; in heterogeneous reactions between gaseous and solid reactants, the formation of a solid product layer causes resistance to diffusion of the reactants and products through the solid particle. In heterogeneous catalysis, although there is no solid product layer, the availability of active catalytic sites (i.e. areas or crystallites where catalysis of the gaseous reaction may occur) dictates the processes of adsorption of gaseous reactants to the active sites of the solid catalyst, chemical reaction of the reactants involving the catalyst and desorption of the products[129].

2.4.2 Desired properties

To be considered an effective catalyst a material must typically balance three essential virtues namely activity, selectivity and longevity.

The activity of a catalyst describes the catalysts ability to lower the activation energy of a reaction. As per Equation 2.7, the rate of all chemical reactions is an exponential function of the activation energy of that reaction; therefore a lowering of activation energy for one or all important mechanistic steps during the desired reaction results in a great increase in the rate of reaction. The activity of the catalyst is typically measured by the reactant conversion, either as a percentage or by mass of reactant converted per mass of catalyst per hour, or via a turnover frequency (TOF). TOF describes the total number of moles of the desired product formed by one mole of active site per hour[129].

Selectivity of the catalyst is the ability of the catalyst to give the desired product out of all possible products. The degree to which a catalyst is selective is determined by its ability to lower the activation energy and greatly increase the rate of the desired reaction relative to the unwanted reaction that produces by-products. By-products are almost always the result of reactions with higher activation energies and therefore increasing temperature usually increases the formation of by-products more than the desired product. This attribute is typically measured by product yield; the fraction or percentage of reactant converted into the desired product[129].

The longevity of the catalyst refers to the time for which the catalyst can produce the required activity and/or selectivity for the given process[129].

The processes of adsorption is critically important to both the activity and selectivity of the catalyst to a specific reaction. On collision with a solid catalyst particle, a gas molecule may either rebound from the solid with no further effect or is retained either close to or on the surface of the catalyst. This retention of the gas molecule by the solid catalyst is known as adsorption and can occur via three different routes where interaction between the gas and solid varies[129], Figure 2.15.

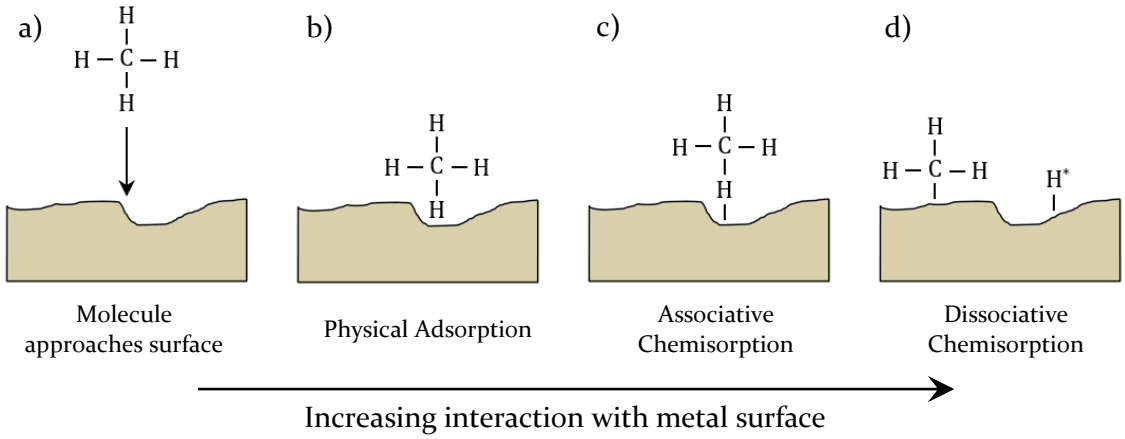

Figure 2.15: Schematic of adsorption and possible subsequent reaction of CH_4 over various surfaces (adapted from [129])

Physical adsorption (physisorption) is dependent on the boiling point of the gas and involves no change to the gas molecule resulting in an unselective process with a low energy of adsorption. This process is not dependent on the catalyst surface but often acts as a precursor to chemisorption. Associative chemisorption presents a higher energy of adsorption than physisorption and results in the adsorption of the entire gas molecule through weakening of the bonds in the gas species. Dissociative chemisorption involves adsorption of the gas molecule as two or more molecular fragments, typically as intermediates or radicals, through the breaking of gas species bonds on adsorption[129].

The type of adsorption that results through the interaction of the metal catalyst and the gaseous species present is specific to the catalyst used can dictate the activity and selectivity of the catalyst. To illustrate this, the adsorption of CO molecules onto α-Al_2O_3, a Cu catalyst and a Ni catalyst can be considered. The adsorption energy between α-Al_2O_3 and CO is low and no special bonding between the two species occurs; this results in simple physisorption and therefore no reaction is favoured. The presence of a Cu or Ni catalyst induces chemisorption via associative and dissociative chemisorption

respectively; the weakening of the C-O bond enabled by the associative adsorption of CO to a Cu catalyst facilitates the hydrogenation of CO to methanol whereas the dissociative adsorption of CO to a Ni catalyst facilitates the formation of CH_4 and H_2O[129].

$$CO + 2H_2 \leftrightarrows CH_3OH \qquad \textbf{Equation 2.10}$$

$$CO + 3H_2 \leftrightarrows CH_4 + H_2O \qquad \textbf{Equation 2.11}$$

Considering the dependence of chemisorption processes upon the catalyst used and the gaseous species present, appropriate catalyst selection must match the catalyst to the desired reaction to effect acceptable activity and selectivity.

2.4.3 Catalyst Shape and Size Effects

The shape and size of a catalyst particle is a compromise between the minimisation of pore diffusion effects, which favours small particles with high voidage, and the pressure drop across the reactor which favours larger particle sizes with low voidage[129].

When considering an appropriate size of catalyst particle to be used in any process the effectiveness factor of the catalyst should be considered. The effectiveness factor, η, of a porous catalyst refers to the relationship between the actual rate of reaction and the rate of reaction possible if the entire internal surface area of the catalyst were exposed to conditions present at the surface of the catalyst pellet[162]:

$$\eta = \frac{Actual\ overall\ rate\ of\ reaction}{Rate\ of\ reaction\ if\ whole\ particle\ exposed\ to\ surface\ conditions} \qquad \textbf{Equation 2.12}$$

This factor ranges from 0 to 1 and gives an indication of the relative importance of diffusion and reaction limitation of the reaction studied; a high effectiveness factor results in a reaction rate limited only by the chemical reaction at the surface of the catalyst, whereas a low effectiveness factor will be diffusion limited. It therefore follows that a catalyst possessing a higher effectiveness factor will result in faster rate of reaction producing a more active and likely selective catalyst[162].

The effectiveness factor can be increased by decreasing the size of the catalyst particle. Smaller particle sizes effectively increases the surface area to volume ratio and therefore: (1) increases the likelihood of catalytically active sites i.e. active metal at the topmost atomic layers of the solid catalyst, being present on the surface of the particle and (2) decreases the distance through the porous structure of the particle the gas phase reactants must diffuse to reach active sites within the pore structure[129,162,163].

However decreasing particle size also increases the pressure drop trough the catalyst bed; this pressure drop is directly related to the voidage, ε, of the catalyst material used[163,164]. Bed voidage is the proportion of the catalyst bed that does not consist of solid material and is dictated by the size and eccentricity of the catalyst particles. As particle size increases the voidage of the bed also increases due to a decrease in packing density. Furthermore the more eccentric the bed material (i.e. the deviation of the shape from spherical) the greater the voidage of the bed will be[165].

2.4.4 Steam Reforming Catalysts

Ridler[25] suggest that the key catalytic properties for a steam reforming catalyst are activity and longevity of the catalyst, although selectivity is still important to prevent the formation of carbon through the various carbon forming reactions. For this purpose, several studies have assessed the activity of various metals for the SR reaction including Rh, Ru, Ni, Pt and Ir. All these metals are able to catalyse the SR reaction due to their facilitation of dissociative chemisorption of CH_4, the widely acknowledged rate limiting step in a catalysed SR system not limited by transport effects. In many of these studies a general hierarchy in the activity, typically measured by TOF, was found with Ru and Rh exhibiting the highest activity, with Ni Ir Pt and Pd offering less activity[112,114]:

$$Ru \sim Rh > Ni \sim Ir \sim Pt \sim Pd >> Co \sim Fe$$

Although there is debate over the exact hierarchy, especially concerning the relative activity of Ni, Ir, Pt, and Pd, Ru and Rh always show the highest activity. However, these metals are also very expensive. As a result, Ni metal has been seen as an ideal catalyst for the SR reaction due to the excellent compromise it represents between the cost of the metal and its activity and selectivity to the SR reaction[25,114].

The surface area of Ni metal available for catalysis following reduction will dictate the activity of the catalyst in SMR; it is therefore imperative to maximise this surface area to maximise the TOF of the catalyst. The use of pure metallic Ni produced from the reduction of NiO could be used in theory however the surface area to volume ratio of available Ni metal would be very low and the cost of the catalyst would therefore be high. For this reason, a similarly to OC's used in CLR, the nickel metal is typically precipitated with or impregnated upon an Al_2O_3 refractory support material.

However, loading increasing amount of Ni onto the Al_2O_3 support will not always yield increasing activity. As stated earlier it is the surface area of the Ni metal available for

catalysis that will dictate the activity of the catalyst; this factor is mainly influenced by the crystallite size and dispersion of the Ni metal across the support, Figure 2.16.

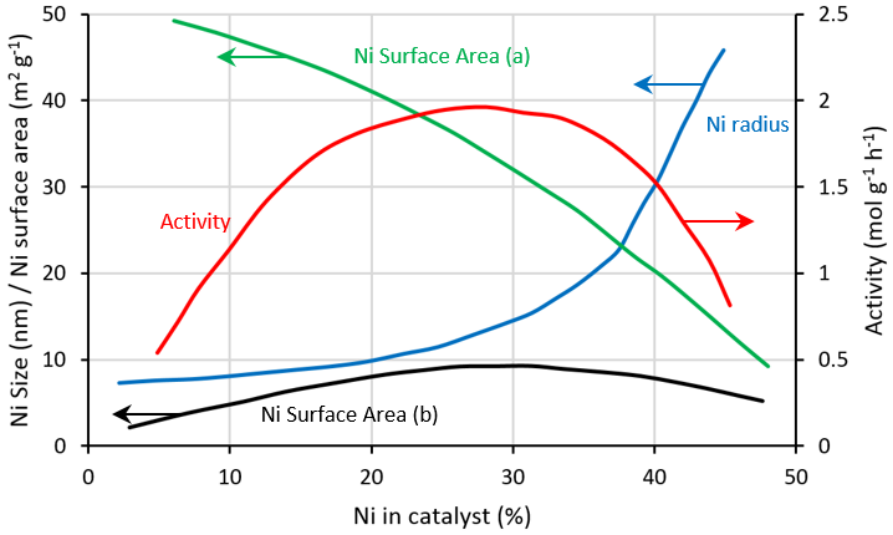

Figure 2.16: Relationship between Ni content, surface area, crystallite size and activity of a typical Ni/α-Al_2O_3 catalyst[25] (a) m^2 g^{-1} of Ni (b) m^2 g^{-1} of catalyst[25]

Increasing the dispersion of metal and decreasing the diameter of particles (i.e. increasing the surface area to volume ratio) generally improves the TOF of Ni catalysts in SR; Jones et al.[114] showed that at S:C 4 and 773 K the TOF of Ni catalysts supported by $MgAl_2O_4$ and α-Al_2O_3 there was linear relationship between dispersion and TOF. Moreover Bengaard et al. found smaller crystallite sizes generally improved the TOF of Ni/Al_2O_3. Smaller crystallites were found present more steps and kinks on their surface which were found to be significantly more reactive than less topographically diverse crystals.

Both Bengaard et al.[166] and Christensen et al.[167] also found that a reduction in crystallite size results in greater resistance to carbon formation; Christensen et al.[167] showed that the carbon threshold value, defined as the steam to carbon ratio that gives no observed carbon formation in SMR, was reduced from over S:C 2 to below 0.4 when crystallite size was reduced from 80 nm to 10 nm. Bengaard et al.[166] attributed this resistance to carbon presented by smaller crystallites to a critical nucleus of graphene that must be formed before stable graphite may form; when small crystallites are used the relatively large nuclei cannot form due to constriction from the steps and kinks in the smaller particle.

As a result, the wt% loading of Ni that strikes a good balance between activity dispersion and crystallite size for Ni Al_2O_3 is approximately 15 wt% for impregnated catalysts and around 20 wt% for precipitated catalysts with an impregnated 18 wt% NiO/α-Al_2O_3 a typical industrially employed catalyst.

Although the synthesis method largely dictates the crystallite size and dispersion of the Ni metal factors such as the initial reduction of the NiO and the environment of their use will alter the effectiveness of the catalyst.

Reduction of the NiO after synthesis but prior to use in SMR can be conducted with a number of atmospheres. As stated earlier there is a large amount of literature pertaining to the reduction of Ni Al_2O_3 OC's pertaining to their use in chemical looping processes. However when applied to SMR, the highest Ni surface area can be achieved by conducting reduction using pure H_2 (rather than with steam) at approximately 600 °C. Below this temperature, reduction is slow and typically will not reach completion while reduction above this temperature sintering of the crystallites can occur[25].

Sintering describes the growth of individual metal crystallites or agglomeration of crystallites into larger particles during the use of the catalyst. The conditions of steam reforming, namely high temperatures (~ 800 °C) and high steam to carbon ratios, encourages sintering of Ni crystallites during SR and is one of the main causes (along with carbon formation) of degradation of catalytic activity. Sintering of Ni crystallites has been proposed to occur via on of two suggested mechanisms at temperatures in the vicinity of 700 °C: (1) particle migration, proposes the movement of entire Ni crystallites over the surface of the support resulting in coalescence with other crystallites and **(2)** atom migration (Ostwald ripening)**,** which proposes the emission of atoms from crystallites that move over the surface of the support to be "captured" by other crystallites thereby resulting in sintering[168–170].

2.4.5 Structured Catalysts for Steam Reforming

As stated earlier, hydrogen production using steam reforming has reached technical maturity and to improve it requires some form of process intensification; CLSR is one way to achieve this through changing the process scheme and relying on chemical looping to provide even heat provision. However the use of structured catalysts can also aid in the intensification of steam reforming and as such has received increasing interest over the last 20 years[171–173]. Further information on the aspects of design and use of these structures catalysts can be found in the reviews of Baharudin and Watson[171], Tronconi et al.[164] and Riechelt et al[174].

There are three primary varieties of structures catalysts that have been shown to intensify the process of steam reforming: honeycomb monoliths, open-cell foams and fibre mats[164,171,174], Figure 2.17. The vast majority of these structured catalysts are manufactured

using preformed ceramic, metal or glass (in the case of fibrous catalysts) substrates onto which the catalytically active phase is introduced[171].

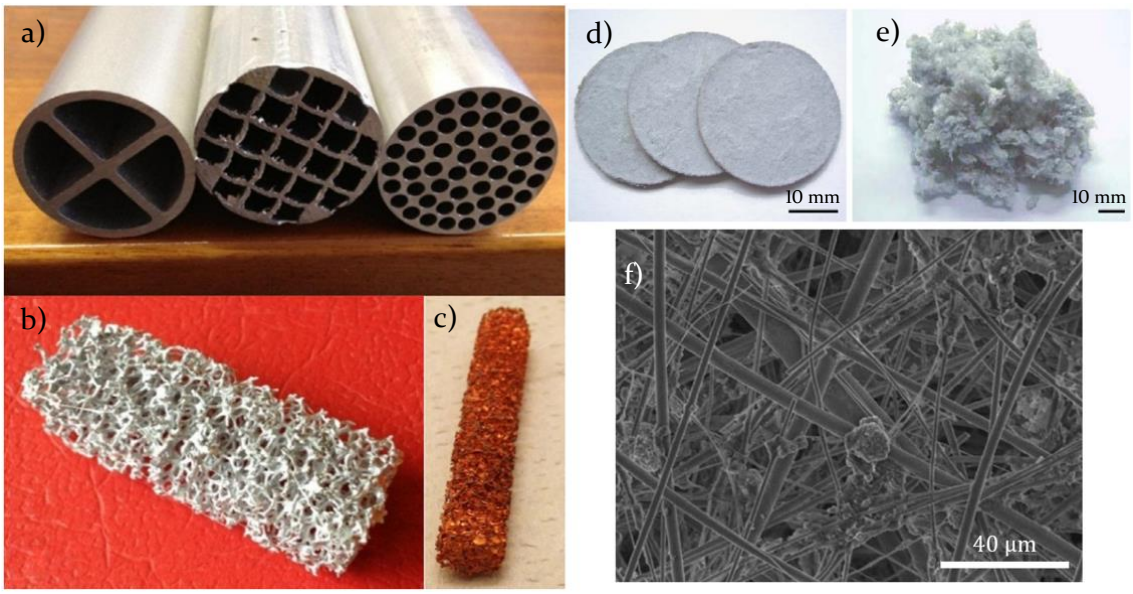

Figure 2.17: Various honeycomb monoliths, foams and fibre structures used in structured catalysis (a) metal honeycomb monolith substrate, (b) Al open-cell foam (c) Cu open-cell foam[164], (d) fibre filter Cu/ZnO catalyst made with paper making techniques (e) loose packed fibre Cu/ZnO catalyst (f) SEM micrograph of Cu/ZnO catalyst[175]

These structures attempt to solve two of the most pressing issues with SMR, namely the provision of heat to the endothermic SR reaction and the issues with mass transfer and the compromise between catalytic effectiveness and pressure drop.

As stated in Section 1.2.1.6., heat provision to the endothermic SR reaction in the reformer is problematic. In a conventional reformer tube using pelletised catalyst, considerable radial and axial thermal gradients of in excess of 100 °C are established between the interior of the reactor tube and the centre of the catalyst bed is typical as well as the top and bottom of the reactor[25,172]. Conductive heat transfer between the catalyst pellets is negligible as only point contact exists between the individual pellets and therefore convective heat transfer from the gas phase dominates. As such, increasing the flow velocity of the gas phase could increase radial and axial heat transfer at the expense of increased pressure drop. The use of structured catalysts of suitable material and geometry allows a significant increase in conductive heat transfer both radially and axially; this reduces the furnace temperatures required to give the desired operating temperature within the reactor bed thereby intensifying the process[164,171,172].

In industrial SMR optimum particle size and shape is determined by compromise between the effectiveness factor, activity and cost of the catalyst, the cost of the vessel and the cost

of pressure drop through the bed[163–165]. In industrial SMR, 18 wt% Ni/α-Al_2O_3 catalysts are used that are extruded into ring shapes with an approximate diameter of 17 mm and lengths between 6 and 17 mm; these catalysts exhibit low effectiveness factors in the order of 10^{-2} (resulting in 95 % the catalyst not being used) and their use therefore results in the SR reaction being strongly diffusion limited[176]. The effectiveness factor may be improved through decreasing the size of the particles used but this causes an increase in pressure drop. The structured catalysts described above attempt to improve the mass transfer characteristics of the catalyst bed used in steam reforming by simultaneously increasing the geometric area per volume of particle and the void fraction (ε) of the bed therefore increasing the effectiveness factor and reducing pressure drop[164,171,177].

The choice of substrate material primarily affects three factors: the conductive heat transfer capability of the catalyst, the ease of washcoating and quantity of catalyst able to be deposited and the mechanical strength of the catalyst. Metal substrates typically show better mechanical strength and more effective thermal conductivity. They also are generally able to be fabricated with thinner walls (honeycomb monoliths), struts (foams) or fibres when compared to ceramics, thereby offering lower pressure drop at equal geometric surface area. However, the washcoating of metal substrates is far more difficult; not only must the washcoat consist of a mixture of the catalytically active component as well as a high surface area inorganic oxide (typically alumina), but the adhesion of the washcoat is far more difficult on the non-porous metal surface. Conversely ceramic substrates may provide more facile washcoating, using only the active component, but typically are less conductive and mechanically strong[163,171].

Each of the above structures have their own advantages and disadvantages for their use in SR processes and these will be reviewed briefly below.

2.4.5.1 Honeycomb Monolith Catalysts

Honeycomb monoliths are unitary three-dimensional cellular structures consisting of many parallel channels through which the gaseous reactants flow (Figure 2.17). The straight fluid path offered by the substrate and larger bed void fractions of 0.7 – 0.8 when compared to the approximate 0.35 – 0.5 of typical pelletised SR catalysts results in a drastic reduction (up to two orders of magnitude) in pressure drop[163,174]. Simultaneously the effectiveness factor of catalyst is increased as the thin washcoated active catalyst phase results in a short diffusion distance for the reactants to reach active catalytic sites.

Moreover if suitable materials are chosen for the substrate material conductive heat transfer is facilitated[171].

Palma et al.[172] compared the performance of conventional SR pellet catalysts and Ni/Ce-Al_2O_3 washcoated ceramic substrate honeycomb monoliths (made from silicon carbide and cordierite) in SMR in terms of the CH_4 conversion, CO_2 yield and concentration of H_2. Their results showed that use of the honeycomb monolith catalysts increased CH_4 conversion by ~ 13 % over the conventional catalysts at the same bed temperature exhibiting increased catalytic activity due to improved heat transfer. Furthermore, the more thermally conductive SiC honeycomb monolith could achieve a bed temperature of 700 °C with a furnace temperature of 830 °C, while the traditional ceramic cordierite honeycomb monolith and the conventional SR catalyst could only achieve a bed temperature of 700 °C with a furnace temperature of 940 °C highlighting the advantages of thermally conductive honeycomb monoliths to the SR process.

However the use of honeycomb monolith structured catalysts has several shortfalls: the shape of the honeycomb monolith is difficult to manipulate (unlike foams or fibres) and therefore apply to unconventionally shaped packed bed reactors; the channels formed by the substrate prevent radial convective heat transfer as well as radial mixing of reactants resulting in non-uniform heat demand across the reactor. Moreover washcoating, even of ceramic substrates, can be difficult and the mass of active catalytic phase able to be deposited upon the walls of the substrate without a decrease in catalyst effectiveness is small compared with conventional pelletised catalysts[164,171,174].

2.4.5.2 Open-Cell Foam Catalysts

Open cell foam catalysts consist of interconnecting solid struts which surround void spaces, often known as cells, through which gaseous or liquid media is able to flow freely. These structures solve some of the issues associated with honeycomb monolith catalysts; open-cell foam catalysts can produce smaller strut diameters therefore providing a higher geometric surface areas per unit volume and allow for even higher void fractions than ranging from 0.75 to 0.95. The increase in surface area allows for higher surface area of the catalytic phase and thereby improves the effectiveness factor of these catalysts. Moreover radial mass and heat transfer is possible while maintaining the connected structure vital to conductive heat transfer while they are more easily shaped to fit a range of reactor types[163,164,174,176–178].

However, this increased functionality does come at a cost of increased pressure drop due the turbulence of the gas phase through the tortuous structure of the foam. Furthermore there is currently a lack of reliable engineering correlations for the prediction of global heat transfer rates in foams, validated at a representative scale[164].

Giani et al.[179] compared the mass transfer and pressure characteristics of conventional pellets, honeycomb monoliths and foam catalysts for the oxidation of CO, an adiabatic mass transfer limited process. They found with the use of a trade-off index that quantifies the trade-off between mass transfer and pressure drop that while foams significantly improve upon the behaviour of pelletised beds, they were bested by honeycomb monoliths. However, they also state that in diffusion limited processes, foams are more likely to allow equal conversion in a smaller reactor when compared with honeycomb monoliths.

2.4.5.3 Fibrous Catalysts

Fibrous catalysts typically consist of micron sized metal, glass or ceramic fibres which either consist of, or are impregnated/washcoated with the active catalyst phase. These fibres can be arranged into mats, where they are compressed to form a variety of shapes and void fractions or woven into meshes or cloths[174,177]. Unlike monolith honeycombs or foams, there is no intrinsic difference between the possible boundary layer mass transfer and pressure drop characteristics when compared to pelletised catalysts[180].

Reichelt and Jahn[180] found that when the sauter diameter was used as the characteristic length, mass transfer and pressure drop correlations originally developed for packed beds of spheres could be satisfactorily applied to fibre-based catalyst support materials. Use of the sauter diameter accounts for the different limiting values of the Sherwood number at low Reynold's numbers; $Re \rightarrow 0 = 2$ for a single sphere and $Re \rightarrow 0 = 0$ for a single cylinder in crossflow as if the cylinders are considered to possess at least one infinite dimension[180].

However, the great advantage of fibrous catalysts that they offer the possibility of using much smaller particle sizes while producing similar or reduced pressure drop through the catalyst bed. This allows fibrous catalysts to present much higher geometric surface areas per unit volume and much smaller effective diffusion lengths therefore greatly increasing the effectiveness factor of the catalyst compared not only to pellets but to both foams and honeycomb monoliths[174,177,180–182]. This makes them particularly appropriate for use in diffusion limited processes such as SMR[177]. This is made possible high eccentricity of the fibres which results in a bed voidage (between 0.7 and 0.9) on par with foams and

exceeding both monolith honeycombs and pellets. Furthermore fibre catalysts can offer a comparable performance to honeycomb reactors while exhibiting lower material and manufacturing costs and more facile washcoating/impregnation[174].

2.4.6 Summary

The use of Ni as the primary active catalyst phase for the novel fibrous OC's developed and tested in this project is based on the excellent activity, selectivity and longevity in the catalysis of SR. The catalytic effectiveness of Ni is derived from its ability to facilitate the dissociative chemisorption of CH_4; although metals such as Ru and Rh provide higher turnover frequencies, Ni strikes an excellent balance between activity and cost as evidenced by its use in industrial SMR in a pelletised form.

Key to the activity of the catalyst is the maximisation of the Ni surface area. This cannot be achieved simply by increasing the percentage loading of Ni upon a refractory support, rather the minimisation of Ni crystallite size and maximisation of the dispersion of Ni upon the support must be prioritised. While the method of Ni loading has a major impact upon the Ni crystallite size and dispersion, a loading of 18 wt% Ni strikes an excellent balance between these factors as evidenced by the use of this loading in industrial SMR catalysts. Consequently, this loading was adopted for use in the OC materials developed herein.

The size and shape of pelletised catalysts in industrial SMR is dictated by a compromise between the effectiveness factor, activity and cost of the catalyst, the cost of the vessel and the cost of pressure drop through the catalyst bed; these factors cause the SR catalysts to present poor effectiveness factors and are therefore strongly diffusion limited. However, the use of structured catalysts such as honeycomb monoliths, open-cell foams and fibres can achieve process intensification by improving heat transfer in the reformer and or improving the effectiveness factor of the catalyst without an increase in pressure drop. Of the structures reviewed, fibrous support materials are particularly interesting as they exhibit the greatest ability to increase the effectiveness factor for the typically diffusion limited SR reaction.

2.5 Fibrous Catalysts and Application to CLSR

To this author's knowledge the use of fibrous support materials for the production of OC's for use in chemical looping processes has not been investigated. It is therefore important to understand the development and application of other fibrous geometry materials in

catalysis and hydrogen production to provide proper context for their use in CLSR. Moreover, it is important to highlight the rationale of the use of ceramic CG Saffil® fibres for the development of Ni Al_2O_3 OC's for use in CLSR as conducted by this thesis.

2.5.1 Background

The use of fibrous catalysts dates back to the early 1900's where noble metal (Pt and later Pt-Rh alloys) gauzes were first employed in the catalytic oxidation of ammonia for the production of nitric acid[183]. Furthermore Ag gauzes have been used for a number of decades for the production of methanol to formaldehyde and ethanol to acetaldehyde[177].

However the first application to which fibrous catalysts were used to intensify chemical processes can be attributed to their use in catalytic combustion of methane and liquefied petroleum gas (LPG)[174,177]. Catalytic combustion using fibrous supports was first suggested in the 1970's by Trimm et al.[184,185] (ceramic fibres) and Radcliffe et al.[186] (glass fibres), and typically uses noble metals such as Pt Pd and Rh as the active phase. The noble metal catalysts increase the rate of oxidation of the fuel at low temperatures, however the oxidation reaction rapidly becomes mass transfer limited as temperature increases; the use of fibrous support materials greatly increase in the rate of reaction of the diffusion limited phase have been used due to their very high surface area to volume ratio and high effectiveness factors[181,187].

Fibrous catalysts have been produced in various forms and structures to provide varying levels of particles and void sizes. These forms range from loose fibre masses, through compacted fibre pads (often used in catalytic combustion) to wire meshes and gauzes[174,177]. Moreover complex techniques can produce sophisticated fibrous structures such as micro-encapsulated fibre catalysts (MFEC) [174,175,188]. These developments among others, have seen fibrous catalysts become increasingly flexible to meeting the demands of a range of processes including reduction of NO_x emissions in low temperature selective catalytic reduction, the steam reforming of methanol for hydrogen fuel cells and the removal of nitrates and nitrites from water[174,177].

2.5.2 Materials Selection

There are three major types of fibre that have been investigated for use as catalytic supports: metal fibres, ceramic fibres and glass fibres[174].

The use of bulk metal fibres, typically in the form of noble metal gauzes, offers a catalytic material with high mechanical strength and excellent thermal conductivity. However, the

low surface area of active metal and the resultant high cost of these structures mean that their use is restricted to very fast reactions such as those described above. Metal catalysts therefore must be coated in a thin layer of a high surface area material such as alumina or zeolites and subsequently impregnated with catalytic material to be considered for slower reactions[174,177].

Unfortunately, washcoating as used in honeycomb monolith production can struggle to provide appropriate adhesion and dispersion on fibres less than 50 μm in diameter[177]. In spite of this a number of techniques have been developed that allow adequate coating of smaller diameter (< 50 μm) metal fibres including spray coating[189], atomic layer deposition[190] and the thermal decomposition of CH_4 for the deposition of carbon nanotubes[191]. Unsurprisingly these coating procedures can be difficult and the subsequent impregnation steps add further complexity and as such these materials have seen little interest in recent research with wire meshes and gauzes far more prevalent[174].

Glass fibres can represent promising catalyst support materials due to their chemical inertness (preventing harmful metal support interactions) and the range of surface areas possible through various synthesis methods[174]. The most common alumina-silicate based materials initially present low surface areas however they are often subjected to leaching using hydrochloric acid. This increases the surface area of the fibre to between 50 and 100 $m^2\ g^{-1}$ by dissolving the non-silicate components of the fibre, thereby increasing porosity. Although this process greatly weakens the thermochemical and mechanical strength of the fibres, it allows direct deposition of the active catalytic phase via conventional methods such as impregnation, but also through chemical vapour deposition[174,177]. Glass fibres have been used as support materials for a range of processes. In particular they have seen use in exhaust gas cleaning in the reduction of NO[192] and oxidation of CO[193], SO_2[194] and remaining hydrocarbons[195] where the avoidance of diffusion limitation was key to their application.

In spite of their widespread use as conventional catalytic supports, ceramic materials are rarely applied as fibrous structured materials perhaps due to their comparatively poor heat transfer properties[174]. The use of ceramic fibre catalysts has typically been constrained to catalytic combustion after Trimm et al. first examined their use in catalytic combustion of methane for space heating using platinum group metals [184,185]. However the use of porous ceramic fibres such as γ-Al_2O_3 offers a support substrate the presents high surface area, ease of coating and high thermal stability[174].

2.5.3 Use in Hydrogen Production

Application of fibrous support materials and fibrous catalysts to the production of hydrogen is a subject that has gained momentum recently in form of microfibrous entrapped catalysts (MFEC's).

MFEC's are produced by mixing inorganic ceramic, glass or metal fibres with finely crushed (< 250 μm) ceramic powders and organic fibres (typically cellulose) into a slurry that is consequently casted via papermaking processes. Once appropriately dried and calcined the organic fibres are thermally decomposed leaving a matrix of inorganic fibres within which the catalyst particles are trapped. This production technique allows the voidage of the material to be adjusted for specific applications through the variation of the volume content of organic fibres. Moreover higher rates of radial and axial heat transfer can be achieved through conductive heat transfer though the fibre matrix, especially if metal fibres are used[174,175,188].

The group headed by Wariishi[175,196,197] at Kyushu University has been active in the application of Cu/ZnO catalysts suspended by ceramic fibres, initially a refractory ceramic fibre then SiC based fibres, in paper like structures for use in the intensification of methanol steam reforming.

Fukahori et al.[175] compared the performance of 100 mesh Cu/ZnO powders, commercial 3 mm x 3 mm Cu/ZnO pellets, and bulk fibres (i.e. same material but not in paper like sheets, Figure 2.17e), the paper like material (Figure 2.17d) in fixed bed methanol steam reforming experiments. They found that when compared on an equal volume basis, the paper materials were able to double (~ 40 % to ~ 80 %) the methanol conversion and hydrogen yield per g catalyst of the commercial pellets while exhibiting only a ~20 % increase in CO; this is important as CO is a major poison to the efficiency of proton-exchange membrane fuel cell (PEMFC). The paper like materials provided comparable performance, in terms of methanol conversion and hydrogen yield to the powdered catalyst but reduced the CO concentration from ~ 0.9 % to ~0.6 %. They theorised that the greater void fraction of the paper material inhibits the formation of localised equilibrium states that lead to the reverse water gas shift reaction and the production of CO. The use of these materials were tested in autothermal reforming of methanol by Koga et al.[196] where the results were similar, with the paper catalysts outperforming pellets and matching the powder in terms of methanol conversion and hydrogen yield while producing less CO.

When Fukahori et al.[197] added more thermally conductive SiC fibres to the paper like materials, they found that during methanol steam reforming the methanol conversion efficiency was increased while production of CO decreased. The presence of SiC fibres likely facilitated heat transfer through the catalyst bed resulting in the favouring of the SR reaction and suppression of the reverse water gas shift reaction.

Following on from this work, the group led by Tatarchuk at Auburn University have conducted several research papers on the benefits of the use of metallic fibres for use in MFEC's precisely for their improved heat transfer properties when compared to ceramic fibres[188,198,199].

The paper by Sheng et al.[188] showed that Cu, Ni and steel fibres entrapping 180 to 250 μm alumina particles all improved the radial thermal conductivity and inside wall heat transfer coefficient when compared to an packed be of similarly sized alumina spheres; this was due to the conductive heat transfer made possible by the sintered connections between fibres which was far more effective than that offered by point contact of the alumina spheres. It was found in a later paper that increasing the sintering times used when the metallic MFEC is synthesised, further increases thermal conductivity by maximising the contact area between fibres[198]. These conclusions were further validated by a CFD study that showed the poor heat transfer in flowing gases of the packed bed was due to the lack of effective axial heat transfer that is facilitated by metal fibres[199].

These findings were furthered by Tang et al. who used an MFEC consisting of 8 μm nickel microfibers entrapping a $ZnO/CaO/Al_2O_3$ catalyst for use in steam reforming of methanol; their experiments showed that the MFEC employed was able to produce a product gas of nearly identical composition to that of a conventional bed of $ZnO/CaO/Al_2O_3$ catalyst at similar throughput with half the mass catalyst dosage. They also showed that the pressure drop incurred by the MFEC material was significantly lower at all gas velocities tested than the traditional packed bed[200].

2.5.4 Application of Ni OC's using CG Saffil® Fibrous Supports to CLSR

The utilisation of fibrous structured Ni based OC/catalyst materials in the CLSR process facilitates the intensification of SMR through the combination of improved heat provision and improved catalytic effectiveness without a penalty to pressure drop.

The thesis concerns the application of the ceramic aluminosilicate microfibrous support known as CG Saffil® (Sf) to the production of Ni based OC's for use in CLSR. The fibres consist of γ-Al_2O_3 (95 %) and SiO_2 (5 %) exhibiting median fibre diameters of 3 – 4 μm and

an assumed fibre length of ~ 5 mm (see Section 3.1). The very small particle sizes offered by this material greatly decrease the likelihood of diffusion limitation effects upon both the reduction/oxidation of the produced OC materials as well as on the steam reforming reactions facilitated by the reduced Ni catalyst; this encourages maximisation of the rates of reaction for both these processes without the typical penalty to pressure drop exhibited when particle size is decreased. This is made possible due to the high eccentricity of the microfibers that results in a far higher void fraction (ε between 0.7 and 0.9) when compared to packed beds of conventional pelletised materials (ε = 0.35 – 0.5).

While the thermal conductivity of the predominantly γ-Al_2O_3 microfibres is not as high as some metal fibres (such as Cu and Al), point contact between the microfibers should nonetheless be increased allowing for improved conductive heat transfer compared to the limited point contact between particles in a conventional packed bed. The prevalence of γ-Al_2O_3 in the fibres means NiO precursors can be deposited straight onto the high specific surface area (~ 100 m^2 g^{-1}) fibre; this avoids the added complication in synthesis method and the adhesion issues encountered in the washcoating of metal fibres. Moreover, considering the wealth of knowledge on the fabrication of conventionally shaped Ni/Al_2O_3 OC's and SR catalysts, an optimal synthesis procedure can be adopted to produce the fibrous structured OC's proposed.

Further justification for the use of ceramic microfibers as an OC support material can be found in the heat transfer provided by the CLSR process. As stated earlier, the heat generated by the oxidation of the OC is produced at the surface of the OC particle throughout the reactor. This means that heat for the SR reaction is readily available at the surface of the particle as soon as oxidation has occurred and removes many of the heat transfer issues associated with conventional SMR. Furthermore, the less dense nature of the fibrous catalyst bed (due to higher void fraction), results in a lower thermal inertia and therefore more thermally responsive reactor, an important attribute for the feed switching that would be required in CLSR.

2.6 Summary

This review has shown that the application of microfibrous structured OC materials to the CLSR process would not only be novel work but could greatly intensify the production of hydrogen through the steam reforming of methane.

Application of microfibrous structured OC's to the CLSR process could result in a number of synergistic benefits over the use of conventional catalyst pellets including a reduction in particle size without a penalty to pressure drop, improved conductive heat transfer, a less dense catalyst bed resulting in reduced thermal inertia and increased thermal responsiveness, and the generation of heat at the surface of the OC, facilitating the provision of heat to the SR reaction. The selection of the predominantly γ-Al_2O_3 fibrous support material and NiO/Ni active OC/catalyst metal has been heavily influenced by the wealth of knowledge garnered through research into the synthesis and application of both OC's and SR catalysts for use in CLR processes and SMR respectively.

The review of the main OC's used in CLR processes points toward the use of Ni supported by Al_2O_3 as an effective OC for use in CLSR; the sufficient oxygen transfer capacity it offers coupled with high oxidation and reduction reaction rates result in its use in the vast majority of CLR experiments for good reason. It is especially suited to use in the CLSR rather than the CLPO process due to its high catalytic activity for the SR reaction, which is responsible for the burden of H_2 production in the CLSR process. This means the poor selectivity to CO and H_2 during reduction of the OC often quoted as a disadvantage for CLPO processes is much less of an issue. However, the formation of both bulk and surface spinel's of $NiAl_2O_4$ as a result of the solid-state reaction between NiO and Al_2O_3 causes a loss in reduction activity and thereby slows the production of catalytically active metallic Ni and reduces the effectiveness of the OC material in CLSR. Formation of bulk $NiAl_2O_4$ can largely be avoided through the selection of appropriate selection of synthesis method, calcination temperature (< 800 °C), selection of alumina phase and use of promoters (such as Co). The synthesis method can also have a pronounced effect upon the activity of the reduced Ni OC; maximisation of the Ni surface area should be prioritised by the minimisation of Ni crystallite size and maximisation the dispersion of Ni upon the support.

3 Methodology

This chapter details the various equipment, methods and materials used in this thesis. The materials and methods used to produce the fibrous Saffil® OC's are detailed along with a description of the conventional granulated steam reforming catalyst used for benchmarking. The solids characterisation techniques used and their associated equipment and methods are also discussed. Moreover, the configuration and operation of the bench top packed bed reactor used for the SR and CLSR experiments is explained along with the elemental balances used to interpret the experimental data. Finally, the sources of experimental error pertaining to the use of the packed bed reactor are considered.

3.1 Oxygen Carrier Synthesis

A range of nine 18 wt% Ni loaded OC's utilising Saffil® fibres (Sf) as a support material and possessing various levels of Co doping (0, 0.6 and 1.8 wt% Co) were produced using three methodologies; wet impregnation (WI), deposition precipitation (DP) and hydrothermal synthesis (HT). A summary of the desired OC's and the materials used during synthesis are shown in Table 3.1. These materials are referred to using the above factors e.g. 1.8Co 18Ni Sf-WI.

Table 3.1: Summary of the desired OC's and the materials used during synthesis

Sample	Desired Loading (wt%)			Support Used (g)	Source Compound Required (g)		Urea Used (g)
	Ni	Co	Ni:Co		$Ni(NO_3)_2.6H_2O$	$Co(NO_3)_2.6H_2O$	
18Ni Sf-WI	18	0	0	10.88	11.83	0.00	0.00
0.6Co 18Ni Sf-WI	18	0.6	30:1	10.46	11.38	0.31	0.00
1.8Co 18Ni Sf-WI	18	1.8	10:1	10.25	11.15	0.93	0.00
18Ni Sf-DP	18	0	0	10.05	10.93	0.00	3.75
0.6Co 18Ni Sf-DP	18	0.6	30:1	10.65	11.58	0.32	4.08
1.8Co 18Ni Sf-DP	18	1.8	10:1	10.37	11.27	0.94	4.19
18Ni Sf-HT	18	0	0	4.30	4.68	0.00	1.60
0.6Co 18Ni Sf-HT	18	0.6	30:1	4.15	4.52	0.12	1.59
1.8Co 18Ni Sf-HT	18	1.8	10:1	4.35	4.73	0.39	1.76

Catalytic Grade Saffil® (referred throughout as Saffil®, Sf) is produced by Unifrax Ltd and consists of aluminosilicate fibres (γ-Al_2O_3 ~ 95 % and SiO_2 ~ 5 %) with a median fibre diameter of 3 – 4 μm and an as received length between 100 – 750 mm; preparation of the Sf OC's involves cutting the as-received fibre mat into ~ 5 x 5 x 5 mm shreds. As a result, the fibre length of the Sf-OC's was assumed to be approximately 5 mm. It is suitable for high temperature applications up to 1600 °C and is highly porous (~100 $m^2\ g^{-1}$).

$Ni(NO_3)_2.6H_2O$ and $Co(NO_3)_2.6H_2O$ (purity 99.9 %, Fischer Scientific) were used as source compounds; the required mass of these compounds needed to produce the desired wt% loading of Ni and Co was calculated with the following equations:

$$m_{Ni(NO_3)_2.6H_2O} = \left(\frac{m_{Sf}\, x_{Ni,desired}}{100 - x_{Ni,desired}}\right)\left(\frac{\overline{W}_{Ni(NO_3)_2.6H_2O}}{MW_{Ni}}\right) \quad \textbf{Equation 3.1}$$

$$m_{Co(NO_3)_2.6H_2O} = \left(\frac{m_{Sf}\, x_{Co,desired}}{100 - x_{Co,desired}}\right)\left(\frac{\overline{W}_{Co(NO_3)_2.6H_2O}}{MW_{Co}}\right) \quad \textbf{Equation 3.2}$$

Where m_i is the mass of component i used, $x_{i,\ desired}$ is the mass fraction of component i loading desired, and $\overline{W}_i$ is the molecular weight of component i.

In the DP and HT methods urea ($(CO(NH_2)_2$, Fischer Scientific) was used as a precipitant. The mass of urea used was calculated via a molar ratio to the Ni and Co desired via the following equation:

$$m_{CO(NH_2)_2} = \in \left[m_{Ni(NO_3)_2.6H_2O}\left(\frac{MW_{Ni}}{MW_{Ni(NO_3)_2.6H_2O}}\right) + m_{Co(NO_3)_2.6H_2O}\left(\frac{MW_{Co}}{MW_{Co(NO_3)_2.6H_2O}}\right)\right] \quad \textbf{Equation 3.3}$$

Where $\in$ is the desired molar Ni/Co:urea ratio.

All materials were weighed accurate to 2 decimal places with the use of a 4 decimal place weighing balance.

3.1.1 Wet Impregnation (WI)

The required mass of the Ni and Co compounds (examples shown in Table 3.1) were dissolved in 250 ml of distilled water, into which 10 g Saffil® (cut into approximately 5 mm^3 shreds) was introduced. The mixture was placed in a drying oven for 6 hours under an air atmosphere at 100 °C evaporating any water and thereby impregnating the fibres with a Ni/Co nitrate salt. The resultant material was then calcined at 600 °C for 4 hours under an air atmosphere to decompose the Ni/Co nitrates to oxides.

3.1.2 Urea-Degradation Precipitation (DP)

The Ni and Co source compounds and 10 g of shredded Saffil® were added to 250 ml water into which urea was also added at a molar ratio of 1.7 Ni/Co:Urea (shown in Table 3.1). This mixture was placed in a beaker covered with a watch glass (to minimise evaporation of the precursor solution) and placed in a furnace heated at 10 °C min^{-1} to 95 °C for dwell

time of 24 hours under an air atmosphere. This allowed for the degradation of urea to raise pH and precipitate Ni/Co hydroxides as per Equation 2.6[130]:

$$CO(NH_2)_2 + 3H_2O \rightarrow 2OH^- + 2NH_4^+ + CO_2 \uparrow \quad \textbf{Equation 2.6}$$

The use of 1.7 Ni:Urea ratio and 24 hour aging time was used to maximise the Ni deposited; in the work of Zhao et al. this ratio and aging time was found to maximise the NiO deposited onto structured ceramic filters[130]. The mixture was then placed in drying oven for 6 hours under an air atmosphere at 100 °C evaporating any water. The resultant material was then calcined at 600 °C for 4 hours.

3.1.3 Hydrothermal Synthesis (HT)

The Ni and Co source compounds and 4 g of shredded Saffil® were added to 100 ml water into which urea ($CO(NH_2)_2$, Fischer Scientific) was also added at a molar ratio of 1.7 Ni/Co:Urea. Different support mass and thus mass of source compounds were used in HT due to the smaller size of the HT reaction vessel. The mixture was transferred to a 125 ml Teflon lined sealed autoclave and placed in a furnace heated at 10 °C min^{-1} to 95 °C for dwell time of 24 hours under an air atmosphere. The vapour pressure generated during this dwell time by the water in the precursor solution at 95 °C and the CO_2 produced by the decomposition of urea provides autogenous pressure of approximately 8 atm. After the dwell time at 95 °C, the mixture was then placed in drying oven for 6 hours under an air atmosphere at 100 °C evaporating any water. The resultant material was then calcined at 600 °C for 4 hours.

3.1.4 Conventional Catalyst (18NiO GR OC)

A conventional 18 wt% NiO/α-Al_2O_3 manufactured by Twigg Scientific & Technical Ltd (TST) was used for comparison in the CLSR experiments. Although this material is used industrially as a steam reforming catalyst, it is also indicative of a typical OC used in CLR processes and as such will be referred to from this point onwards as the 18NiO GR OC.

It was supplied as Raschig rings and was ground and sieved to between 150 – 250 μm (with an assumed average particle size of 200 μm) to attempt to avoid diffusion limitation of the OC reduction reactions; further details can be found in Section 7.2 and other works[201]. The 18NiO GR OC had a BET surface area of 3.2 $m^2 g^{-1}$ [100].

3.2 Characterisation

This section details the various characterisation methods used to analyse the Saffil® support and the produced fibrous Sf OC's prior to use in the packed bed reactor. Moreover, these techniques were also used to assess the effects upon the Sf OC's incurred by use in the SR and CLSR experiments.

3.2.1 Powder X-ray Diffraction

The crystallite size and phase composition of the raw support and Sf OC's was analysed using powder X-ray diffraction (XRD). The used OC's were also analysed by XRD after the SR and CLSR experiments

In powder XRD, X-rays (electromagnetic radiation with $\lambda < 1$ nm) are generated and fired at the powdered sample from a range of angles. If the X-ray photons from this incident beam are elastically diffracted on contact with the atoms in the sample (i.e. with a change in direction but not wavelength) these diffracted beams can be detected and measured by the XRD machine.[202] When the incident beam hits a crystal plane in an ordered crystalline material, the elastically diffracted beams constructively interfere with one another as they leave the sample resulting in a sharp increase in measured intensity of the diffracted beams detected by the equipment. This results in a measured diffraction peak[202]. Constructive interference only occurs at specific angles of incidence for specific crystal planes with equal interplanar distance in a crystalline material; these angles are defined by Bragg's Law[202], Equation 3.4.

$$2d \sin\theta = n\lambda \qquad \textbf{Equation 3.4}$$

Where, λ is the wavelength of X-ray (nm), θ is the Bragg angle (°), n is the order of the diffraction peak and d is the interplanar distance (nm), Figure 3.1.

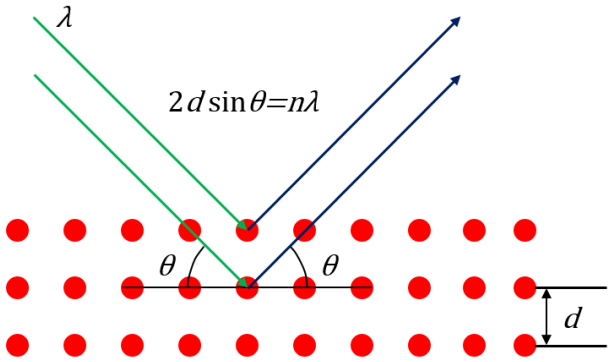

Figure 3.1: Diagram illustrating the application of Bragg's law[202]

Therefore, as the incident beam hits the sample at different angles, constructive interference occurs at specific Bragg angles indicative of the arrangement of atoms in different crystal planes. This allows the identification of the sample's crystal structure and therefore the composition of its crystalline phases. The random orientation of crystals in a powdered sample ensures an equal probability of the presence of each crystal plane at the surface of the sample. As a result, varying the angle of incidence can identify all possible diffraction directions without the depth of penetration of X-rays becoming an issue[202].

XRD analysis was carried out using a Bruker D8 X-ray diffractometer with a Cu X-ray tube with a wavelength of ~15.406 nm. A step size of 0.025 °, a scan speed of 2 s per step and a 2θ range of 10 - 75 ° were used. Background determination, peak identification and phase identification were conducted using analysis software XPert HighScore Plus. Phase identification was achieved through comparison of the experimentally derived XRD pattern and the best matching reference patterns in International Centre for Diffraction Data (ICDD) database. All samples were ground by pestle and mortar to form a fine powder prior to analysis.

3.2.1.1 Scherrer Analysis

Scherrer analysis was conducted to approximate the crystallite size of specific crystallite phases. This is achieved by analysing the broadening of diffraction peaks due small crystal or grain sizes. Very small crystals cause broadening of the diffraction peak as the incident X-rays are diffracted at angles close to but not at the exact Bragg angle. This effect increases as the size of the grain or crystal decreases toward a single plane of atoms or a singular atom itself. As this broadening effect is only pronounced at small crystallite sizes, this analysis is only valid for crystallite sizes up to 200 nm[202].

Individual peaks were chosen for the determination of the crystallite size of specific using the Scherrer equation[202]:

$$\tau = \frac{K\lambda}{(\beta - \beta_0)cos\theta}$$ **Equation 3.5**

Where: τ is the mean size of the ordered crystalline domains (nm); K is a dimensionless shape factor; λ is the X-ray wavelength (nm); β_0 is the instrumental line broadening at the full width half maximum (FWHM) of the peak (rad), β is the sample line broadening at FWHM (rad) and θ is the Bragg angle (°). For the following analysis K is taken to be 0.9

(widely considered to be a good approximation[202]), λ is the Cu $K\alpha_1$ wavelength of 15.406 nm and β_o is 0.09 rad.

3.2.1.2 Rietveld Refinement

Rietveld refinement is a curve fitting technique that uses the least square method to minimise the difference between an experimentally derived XRD pattern and one constructed by a mathematical model. The model is constructed using standard ICDD phase patterns which are then refined to match the experimental data as closely as possible using several model fitting parameters. The magnitude of the modelled peaks is refined using crystal structure parameters such as atom coordinates and unit cell dimensions, the shape of the peaks via parameters related to instrumental and microcrystalline broadening effects and the profile intensity by parameters related to various systematic effects such as adsorption and transmission of X-rays. If the refinement is sufficiently accurate, both macroscopic information such as phase mass fractions can be determined as well as crystal structure information such as lattice parameters[202,203].

The goodness of fit (GOF) of the modelled data to the experimental data can be assessed by taking the square of the ratio of the weighted residual value (R_{wp}) to the statistically expected residual value (R_{exp}); a GOF > 4 is typically considered satisfactory[101].

In this work Rietveld refinement was only used to approximate the mass fraction of reduced and oxidised Ni/Co phases after the OC's were used in CLSR. Due to the nature of the support causing excessive peak broadening and the lack of a suitably accurate ICDD standard, determination of the mass fractions of the Saffil® support in the OC's was prohibitively inaccurate. Furthermore, due to overlapping peak data from the Saffil® support only certain peaks were selected for Rietveld refinement to improve the accuracy of the model; as such the mass fractions of the Ni and NiO in the samples used in CLSR could only be estimated to ± 0.05.

3.2.2 Atomic Absorption Spectroscopy

Quantitative elemental analysis of the Ni and Co of the synthesized OC's was conducted with the use of atomic absorption spectroscopy (AAS). In this technique, the concentration of metallic elements in a given solution can be quantitatively assessed by aspirating the solution into a high temperature flame so that the solution is vaporised and gaseous metal atoms are formed. Although some of these atoms may be sufficiently excited to be raised to a higher energy level thereby emitting characteristic radiation which can be measured (this is the principle of flame emission spectroscopy), the vast majority of the

atoms of the metal element present will be in the form of unexcited or ground state atoms[204]. These ground state atoms are capable of absorbing radiant energy at a resonance wavelength specific to the gaseous metal; by shining a light source of this specific wavelength (known as a resonance line) through the flame and atomised material, a fraction of this light proportional to the number of ground state atoms present in the flame is absorbed. The analysis of calibration solutions of known concentrations is used to relate the measured absorption of the resonance line to the concentration of the solutions. By using this calibration when analysing the sample, the concentration of the metallic element in the solution can be revealed[204].

A Varian 240s Atomic Absorption Spectrophotometer was used to carry out this analysis. A nebuliser-burner system was used in conjunction with and air/acetylene flame at approximately 2400 K. Resonance lines for analysis of both Ni and Co were produced by hollow cathode lamps and a monochromator was used to isolate the resonance line from all non-absorbed emissions by a diffraction grating.

Prior to analysis the Sf OC's were digested into solution; in each analysis 0.1 g of each sample was digested in 10 ml of 1:1 HCl and heated under reflux for 30 min. The solution was then diluted to 200 ml with distilled water in a volumetric flask. This achieved a concentration of the analytes of approximately 90 ppm Ni and between 3 – 9 ppm Co. For Ni calibration, 6 solutions were prepared ranging in Ni concentration from 50 – 100 ppm using diluted 1000 ppm Ni solution (from $NiCl_2$, 99.99 % purity VVR International). For Co calibration, 6 solutions of standard were prepared ranging in Co concentration from 3 – 15 ppm using diluted 1000 ppm Co solution (from $CoCl_2$, 99.99 % purity VVR International).

Based on the sample concentrations, appropriate wavelengths of resonance line and diffraction grating width were chosen according to the manufacturers recommendation; for Ni, 352.4 nm resonance line wavelength, and diffraction grating slit width 0.2 nm were recommended , for Co these factors were set to 240.7 nm and 0.5 nm[205].

3.2.3 Physical Adsorption

Physical adsorption was used to characterise the textural properties of the OC's produced including the specific surface area, the specific porous volume, the shape of the pores and the pore distribution.

In physical adsorption a solid particle is typically exposed to gaseous N_2 in an enclosed vessel close to its condensation temperature. The pressure is increased in the vessel,

causing condensation of the gas and therefore adsorption of the gas in the pore volume of the solid. Once saturation of the pore volume is complete, the pressure of the system is then reduced vaporising the liquid and causing desorption. The volume of gas adsorbed or desorbed onto the solid is expressed as a function of the relative pressure (P_{eq} / P_0); the ratio of equilibrium pressure (P_{eq}) of the gas in contact with the liquid to the saturated vapour pressure of the gas (P_0) at the process temperature. This results in isotherm plots that represent the adsorption and desorption equilibria. Differences between the adsorption and desorption isotherms result in hysteresis loops, analysis of which can reveal both the size and shape of the pores in the solid. Depending on the size and shapes of the pores in the material analysed, mathematical models known as the Brauner-Emmett-Teller (BET) and Barrett-Joyner-Halenda (BJH) models can identify the specific surface area, the total pore volume and the average pore radius of the material[206,207].

A Quantachrome Instruments NOVA 2200e Surface Area and Pore Size analyser was used to analyse physical adsorption data producing pore data and SSA via the BJH and the BET methods. All samples were degassed at 200 °C for three hours in a vacuum to remove any moisture or contaminants from the OC's prior to analysis. All samples were analysed using N_2 as the adsorbate gas (BOC, purity 99.99 %) at a temperature in the region of 77 K and an equilibrium time of 60 s. A sample mass of 0.2 g was used in all cases, and filler rods and at least 5 BET points used for surface area measurement. These factors were used to minimise experimental error[208].

3.2.4 Electron Microscopy

Transmission, scanning and scanning transmission electron microscopy (TEM, SEM and STEM respectively) have been used in the following work to characterise both the fresh and used OC's. TEM allowed the examination of crystallite size and further examination of the crystallite structure through production of images and diffraction patterns, SEM was used to examine morphology and STEM was used to carry out localised semi-quantitative elemental analysis through EDX spectroscopy.

Electron microscopy relies on the bombardment of the sample with a high energy beam of electrons under high vacuum[209,210]. The diameter of this incident beam dictates the possible resolution achievable by the equipment and is affected by both the energy of the electrons in the beam, and the quality of the magnetic lenses used to focus it. In theory the higher the energy of the electrons, the smaller their wavelength according to the following formula[209]:

$$\lambda = \frac{1.22}{E^{0.5}}$$ **Equation 3.6**

Where λ is the wavelength of the electrons (nm) and E is the electron volts (keV) i.e. the energy imparted to the electrons by the emission source acceleration voltage. However no electron microscope is practically able to approach wavelength limit of resolution due to imperfections in the electron lenses[209,210].

In both SEM and TEM, electrons are emitted from a source and pass down through a series of electromagnetic condensing lenses and apertures which control the diameter and focus of the electron beam and on the sample. On contact with the material the electron may interact with the sample either elastically or inelastically[209–211].

Inelastic interactions of electrons result when energy is transferred from the incident beam to the atoms of the sample and results in the production of 3 types of radiation. Secondary electrons (SE) are generated when an incoming electron collides with a single periphery electron in the sample atom. Backscattered electrons (BSE) are generated when the electron interacts with the electronic cloud of the sample atom deflecting it at a high angle; this effect increases with the atomic number of the element. Thirdly X-rays are generated when the incoming electrons provide enough energy to excite an inner shell electron from the sample; if this electron is replaced by a higher shell election an X-ray emission with a wavelength characteristic of the atom will be generated[209–211], Figure 3.2.

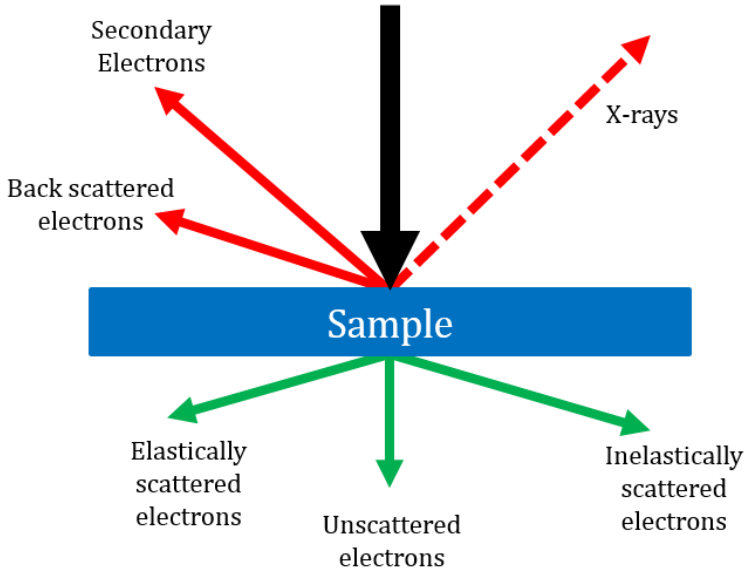

Figure 3.2: Diagram of elastic and inelastic interaction of electrons with the sample in electron microscopy[211]

Elastic interactions occur when the incident electrons transfer no energy to the sample atoms, either passing through the sample undeviated (direct beam electrons) or scattering

constructively (when hitting a crystal plane in a crystalline material) or destructively thereby creating diffracted electrons[209,210].

The difference between SEM and TEM depend on the electrons analysed to produce the image. TEM uses direct beam and diffracted beam electrons that are transmitted through the sample and as a result cannot analyse samples thicker than 100 – 200 nm; SEM detects and measures inelastically scattered electrons and can therefore be used to analyse the surface topological features of comparatively thick samples[209,210].

3.2.4.1 Scanning Electron Microscopy

SEM uses an electron beam with accelerating voltages ranging from 0.5 – 30 kV to scan the sample and produce highly magnified images through the detection of inelastically scattered electrons. These images can exhibit far higher resolutions than the human eye or light microscopy, while also maintaining depth of field i.e. the ability to image topological features[210].

An image is generated by scanning the sample and measuring the inelastically scattered electrons and X-rays generated. The intensity of this radiation is measured by several detectors and converted to an electric signal to represent a pixel; therefore, intensity of radiation is proportional to the contrast of the pixel in the image. Detection of secondary electrons can describe the sample's morphology and texture by providing topographical contrast, analysis of backscattered electrons detect the distribution of phases by showing atomic number contrast and analysis of X-rays, using a system known as energy dispersive X-ray (EDX) analysis can provide elemental analysis of the sample[210].

In this work a Hitachi SU8230 high performance cold field emission (CFE) scanning electron microscope (SEM) was used. The samples were affixed to 10 mm aluminium stubs via carbon tape and all samples were carbon coated (thickness 2 - 3 nm) prior to SEM analysis. The materials heavily charged under the electron beam; therefore, low voltage (1-2 kV) and current (0.9 μA) settings were used to reduce this. The software ImageJ was used to carry out size measurements in the SEM images.

3.2.4.2 Focussed Ion Beam milling (FIB) SEM

Focussed ion beam milling coupled with SEM is a technique used to create cross sections of, and simultaneously image the produced OC's to examine the deposited layer of metal oxide and to examine the interior of the Saffil® fibres.

FIB relies on the bombardment of solid materials with ions to induce sputtering; a process by which atoms are removed from the surface of the sample via elastic collision of heavy ions[212,213]. This is achieved when the sample atom receives kinetic energy from the ion greater than the sample atoms binding energy. Gallium is typically used as an ion source as its heavy atomic weight maximises momentum transfer of the ions to the sample, thus maximising sputtering[212,213]. Moreover, it presents a low melting point and vapour pressure and thereby ensures facile application. A reserve of solid gallium is heated to form a liquid which is flowed along the surface of a tungsten needle toward the tip. An electric field is applied to the tip which extracts Ga^+ ions from a point source of 2 - 5 nm in diameter. The ions are then accelerated in an electrical field of up to 30 keV and focused by a series of electromagnetic lenses under high vacuum in a similar manner to SEM[212,213].

Before sputtering is induced, the sample area is coated with a thin protective layer of platinum; this prevents sputtering of the surface of the sample outside the desired cross-section. The layer is produced by introducing Trimethyl-Platinum gas onto the sample where the gas is adsorbed and subsequently the organic molecules decomposed by the ion beam thus depositing the platinum in a predetermined area[212,213].

Although the ions themselves can be used for imaging, provision of an SEM column as well as a FIB column (dual beam FIB) allows accurate control and observation of the cross-sectioning process, while utilising a full range of analytical techniques (SE, BSE, EDX) without unwanted sputtering[212,213].

In this study a FEI Helios G4 CX DualBeam - High resolution monochromated FEGSEM with precise Focused Ion Beam (FIB) was used to conduct FIBSEM analysis. The samples were affixed to 10 mm aluminium stubs via carbon tape and all samples were carbon coated (thickness 2 - 3 nm) prior to FIBSEM analysis. A gallium ion source was used in conjunction with Trimethyl-Platinum was used as the source gas for the protective platinum layer. The software ImageJ was used to carry out crystallite size measurements in FIBSEM.

3.2.4.3 Transmission Electron Microscopy

TEM relies on the detection and analysis of direct beam and diffracted electrons from the incident beam transmitted through the sample. It uses an electron beam with far higher accelerating voltages (> 80 kV) than SEM, allowing a great increase of resolution at higher magnifications and analysis of materials down to the atomic level[209].

In TEM the transmitted electrons are focussed by the objective lens to produce the first intermediate image of the electron density distribution of the specimen. In doing so, the objective lens forms two planes due to the different electrons transmitted through the sample; direct beam electrons are focussed on the image plane and the diffracted electrons upon the back focal plane or diffraction plane. The intermediate lens then dictates whether the TEM produces an image or a diffraction pattern by focussing on either the image plane or the diffraction plane to produce the second intermediate image. The projection lens then magnifies the second intermediate image onto a fluorescent screen where the electrons can be converted to a signal which can be displayed on a coupled computer[209], Figure 3.3.

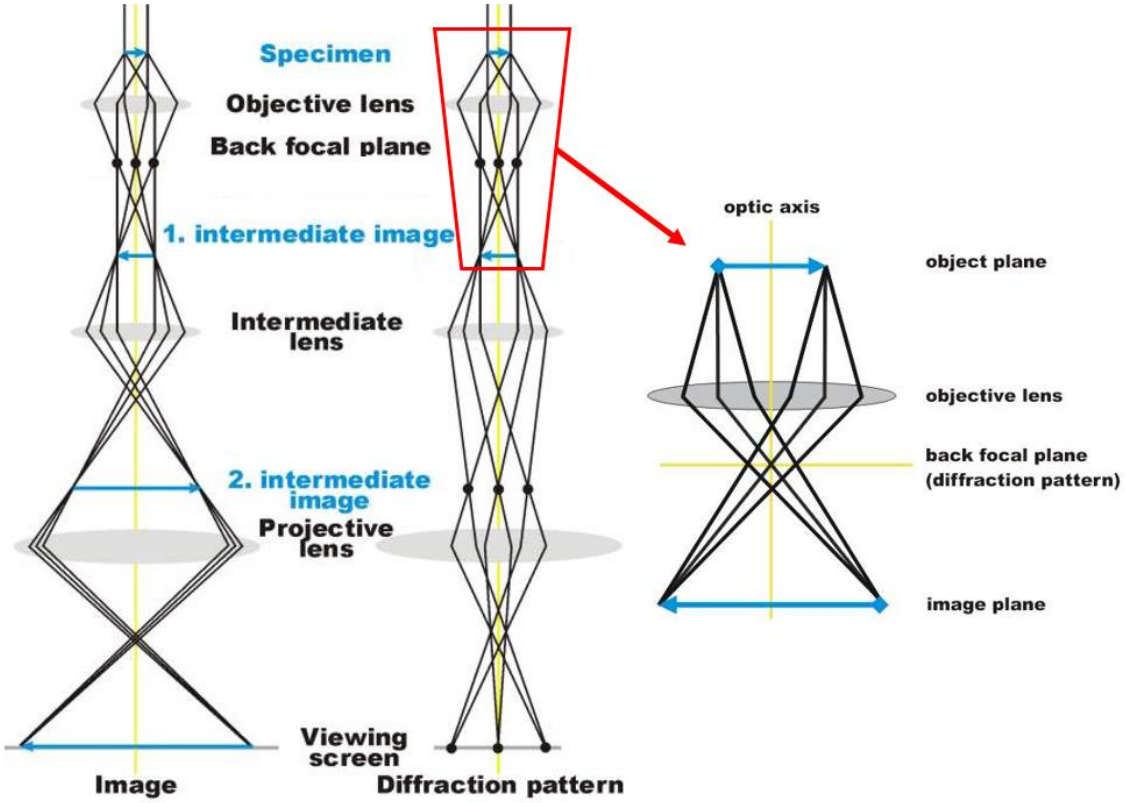

Figure 3.3: Ray diagram of a TEM in image and diffraction pattern modes and an inset diagram of the image plane and back focal plane[214,215]

3.2.4.3.1 Imaging

If all transmitted electrons in are used in the production of an image, very little contrast would be present. An aperture is therefore used to collect either the direct beam electrons thereby creating a bright-field image or the diffracted electrons creating dark-field image. In a bright-field image, areas where sample is present will appear dark compared to their surroundings due to the blocking of electrons by heavier atoms (mass contrast), the thickness of the specimen (thickness contrast) or by diffracted electrons being blocked by the aperture (Bragg contrast). Conversely, in a dark-field image, areas where no sample is present will appear dark as no diffraction of the electrons has occurred; therefore bright areas are produced when strongly diffracted electrons may reach the first intermediate image[209,210].

3.2.4.3.2 Selected Area Electron Diffraction

The selected area electron diffraction (SAED) patterns are created by the diffraction of the electrons as they pass through the sample; where electrons pass through the sample, contrast is produced. Undiffracted electrons form the bright spot at the centre of the pattern, while diffracted electrons form the spots and rings of contrast. The diffraction of the electrons through the sample are dictated by two diffraction angles: **(1)** the radial angle of diffraction (i.e. Bragg angle, 2θ) is determined by the interplanar spacing *d* of the crystal **(2)** the azimuthal angle of diffraction (ϕ) determined by the azimuthal angle orientation of the crystal planes to the incident beam.

Thus, if the electrons diffract through a single crystal, a series of bright spots of contrast are produced at a distance from the central spot corresponding to the interplanar distance of the atomic planes of that single crystal at that orientation. If the electrons are diffracted through a polycrystalline sample, the random orientation of those crystals result in many azimuthal diffraction angles causing many different spots at set interplanar distance thereby forming a concentric ring.

By measuring the diameter of the concentric rings formed and relating that to the reciprocity of an electron diffraction pattern, the d-spacing of the crystals in the TEM sample can be identified. The measurement of the diameter of the rings is however sensitive to the height of the specimen and to magnetic hysteresis of the TEM lenses and therefore d-spacings can only be measured within a tolerance of 10 %.

3.2.4.4 Scanning Transmission Electron Microscopy

As its name suggests STEM combines these two techniques by equipping a TEM with beam shift scan coils to move the electron beam over the sample to enable scanning and by adding detectors for inelastically scattered electrons and X-rays. STEM allows transmission electron imaging and EDX capabilities down to atomic resolutions. Furthermore the EDX using an STEM can provide increased spatial resolution and sensitivity capabilities over a regular SEM system[210].

In this work a STEM was used with a high angle annular dark field (HAADF) STEM detector; this equipment uses an annular detector at a high angle to avoid detection of Bragg diffracted beams thereby detecting only mass and thickness contrast. This allows greater atomic contrast in HAADF images and is particularly useful in catalyst characterisation to identify crystallites of a relatively higher atomic number on relatively lower atomic number supports[210].

In this work a FEI Titan^3 Themis: a Scanning Transmission Electron Microscope (STEM) operating at 300 kV and fitted with a high angle annular dark field (HAADF) STEM detector, an FEI Super-X 4-detector EDX system and a Gatan One-View CCD. EDX analysis was performed using Bruker Espirit software (version 1.9.4). All samples were ground in ethanol and pipetted onto 400 mesh holey carbon coated Cu TEM grids (Agar Scientific). The software ImageJ was used to carry out crystallite size measurements in TEM.

3.2.5 CHN Analysis

CHN elemental analysis can rapidly determine mass fractions of carbon, hydrogen and nitrogen in a wide variety of sample types including solid liquid volatile and viscous sample. It was used herein to determine the quantity of carbon deposited upon the OC sample after its use in SR.

In CHN analysis the sample is dropped into a furnace at high temperature (1000 - 1800 °C) in an oxygen rich atmosphere; any carbon, hydrogen and nitrogen is converted to CO_2, H_2O and N_2/NO_x respectively[204]. These combustion products and the excess oxygen are swept from the combustion chamber by a helium carrier gas. The oxygen and any unwanted contaminants are filtered out by several absorbents prior to separation of the combustion products by gas chromatography and subsequently measured via thermal conductivity detectors. High quality calibration standards are used to relate the thermal

conductivity of the gases to the samples of known C, H and N mass fractions; this allows quantitative assessment of each element in the sample[204].

In each experiment 15 mg of powdered sample was placed into a tin capsule which was compressed as much as possible to remove any air and placed in an auto-sampler prior to analysis. Use of two calibration standards (Sandy Soil (0.83 % C) and Soil (2.29 % C), Elemental Microanalysis) assured an accurate quantitative assessment of the elements. Oxygen (BOC, purity 99.99 %) and Helium (BOC, purity 99.99 %) were used as the oxidant and carrier gas respectively.

3.2.6 Thermogravimetric Analysis

A Mettler Toledo thermogravimetric analyser (TGA) was used for characterisation of the synthesised OC's through temperature programmed reduction (TPR) and reduction capacity determination cycles using a 5 % H_2 reductant.

TGA quantitatively analyses the mass change of a solid or liquid sample when subjected to a linear temperature change. TGA equipment typically consists of a precision balance, a furnace capable of programmable temperature increases and often a gas switching system. Thermogravimetric curves represent mass change as a function of either time or temperature depending on the specific methodology or information required[204].

All experiments used an analytical grade 80 µl α-alumina crucible loaded with 5 mg sample per experiment. Every effort was made to pack the material in as homogenous manner as possible. Blank runs of the equipment i.e. use of an empty crucible and using the same temperature heating rate, dwell times and gas flows were conducted, and the TG curves subtracted from the sample runs to avoid gas buoyancy effects. All gas flows were controlled by analogue rotameters.

3.2.6.1 Temperature Programmed Reduction

Temperature programmed reduction (TPR) was conducted to characterise the dominant form of Ni and possibly Co deposited during synthesis. All the synthesised OC's were heated to 100 °C at 10 °C min^{-1} under a 50 sccm flow of N_2 (BOC, purity 99.99 %). The samples were then held at this temperature for 1 hour to remove any adsorbed moisture or air. The flow was then switched to a flow of 5 vol % H_2 in 95 vol % N_2 (BOC, purity 99.99 %) and the sample heated to 950 °C at 5 °C min^{-1}.

3.2.6.2 Reduction Capacity Determination

Reduction capacity of the OC's were also analysed using the Mettler Toledo TGA equipment. These experiments subjected the OC's to 7 redox cycles at 700 °C using a reducing gas of 5 vol% H_2 in 95 vol% N_2 and an oxidising gas of pure bottled air. The ratio of the weight percent of oxygen lost during reduction in the TGA experiments ($m_{red,OC}$) and the total theoretical weight percent loss if all the NiO present was reduced ($m_{red,max,OC}$) was used as an indication of reduction extent (α_{red}) of the OC's:

$$\alpha_{red} = \frac{m_{red},OC}{m_{red,max},OC} \quad \textbf{Equation 3.7}$$

$$m_{red},OC = \frac{m_{t=0},OC - m_t,OC}{m_0,OC} \times 100 \quad \textbf{Equation 3.8}$$

Where $m_{t=0,OC}$ is the OC mass at the beginning of the reduction event, $m_{t,OC}$ is the OC mass at time t and $m_{0,OC}$ is the OC mass measured before the TGA experiment.

$$m_{red,max},OC = \frac{\bar{W}_O \left(\frac{m_0,OC\ x_{Ni}}{\bar{W}_{Ni}} + \frac{m_0,OC\ x_{Co}}{\bar{W}_{Co}}\right)}{m_0,OC} \times 100 \quad \textbf{Equation 3.9}$$

Where $\bar{W}_i$ is the molar mass of element i, x_i is the mass fraction of element i in the OC.

The methodology used in all reduction capacity determination experiments was as follows: All the OC's were heated to 700 °C at 10 °C min^{-1} under a 50 sccm flow of N_2 (BOC, purity 99.99 %). The samples were then held at this temperature for 1 hour to remove any adsorbed moisture or air. The OC's were then subjected to 50 sccm flow of 5 vol% H_2 in 95 vol% N_2 (BOC, purity 99.99 %) for 20 min, followed by a purge of N_2 for 5 mins. The samples were then oxidised using a 50 sccm flow of pure bottled air (BOC) for 20 min, followed by a purge of N_2 for 5 mins. This process was repeated for 7 reduction/oxidation cycles.

3.3 Packed Bed Reactor Configuration and Operation

Use of a packed bed reactor system allowed three different sets of experiments to assess the performance of the Sf OC's in comparison to the 18NiO GR OC. The SR experiments (Chapter 5) assessed the OC's ability to provide consistent outputs under SR conditions when pre-reduced by a N_2 diluted H_2 feed. The CLSR experiments (Chapter 6) cyclically reduced and oxidised the OC's to assess the ease and extent of reduction and oxidation and also to assess the SR performance of the OC's during cycling. The reduction kinetics

experiments (Chapter 7) were carried out to quantify the reduction kinetics of the Sf OC's and the 18NiO GR OC.

3.3.1 Equipment

The packed bed reactor system shown in Figure 3.4 was used in all experiments:

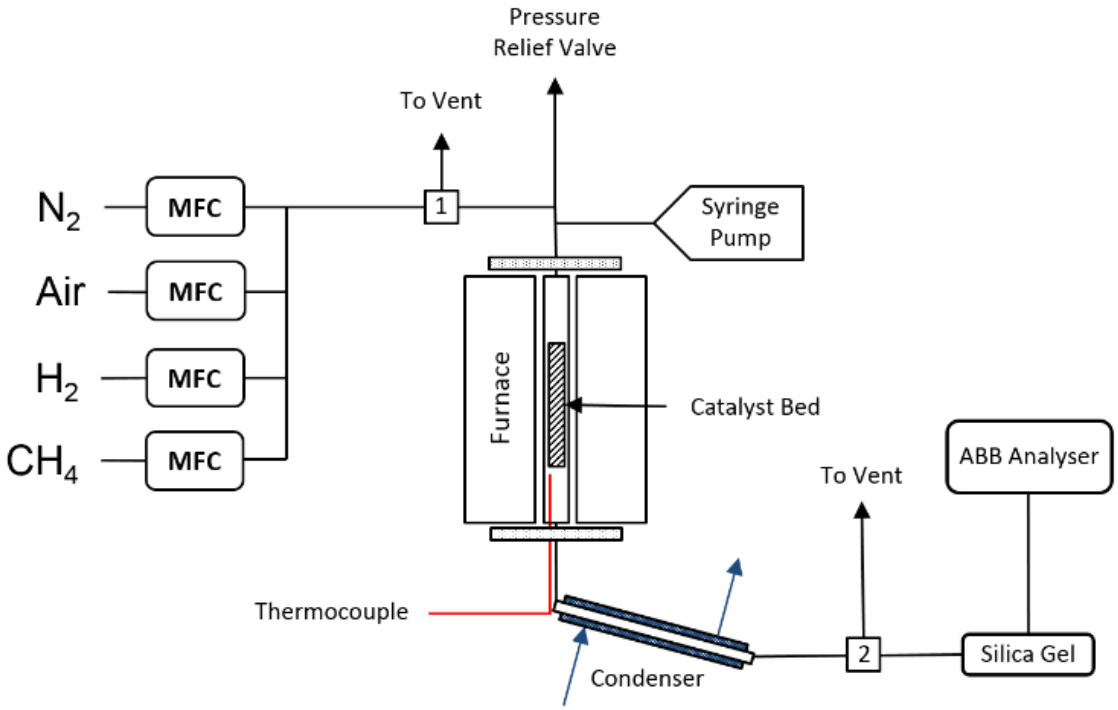

Figure 3.4: Reactor set-up for the SR, CLSR and the reduction kinetics experiments

CH_4, H_2 and N_2 (BOC, purity 99.995 %) and site compressed air were used as reactant gases. Mass flow controllers (0.1 – 200 sccm, Bronkhorst EL-FLOW) set the flow rate of CH_4 and H_2 whereas N_2 and Air, which required higher flow rates, were controlled by electric rotameters (Bronkhorst MASS-VIEW 0 – 2000 sccm). A programmable syringe pump was used to introduce distilled water into the heated zone of the reactor to satisfy the S:C required for each experiment.

The 316 stainless steel (SS) reactor had an inside diameter of 13.2 mm and a length of 750 mm of which the bottom 500 mm was heated using a vertical tube furnace (Elite Thermal systems TSVH12/30/450) controlled by a temperature controller (Eurotherm 3216). Additionally, a second K-type thermocouple was placed adjacent to the bottom basket and was used to monitor temperature in the catalyst bed to ensure the desired temperature was reached in each experiment. The OC's in each experiment were held in the reactor by several cylindrical mesh baskets (volume 1.25 cm^3) resting on a small steel bar welded across the tube. The bed length was limited to approximately 200 mm to ensure that

sufficient distance was maintained from the ends of the furnace so as to maintain constant temperature throughout the catalyst bed. The limit on catalyst bed length meant that a maximum of 10 baskets could be used in the reactor during each experiment providing a maximum bed volume of 12.5 cm^3.

As the analysers used in the apparatus were highly sensitive to water, a condenser (jacketed heat exchanger using a cooling fluid consisting of 1:1 mix of water and ethylene glycol chilled to 2 °C) and a moisture trap (silica gel) were used to remove water prior to gas analysis. The outlet composition of the remaining gases was recorded in vol% every 5 s by an ABB Advanced Optima analyser using three modules; Uras 14 (CO, CO_2 and CH_4 measured by infrared absorption) Caldos 15 (H_2 via thermal conductivity) and Magnos 106 (O_2 via paramagnetic analysis).

3.3.2 Experimental Variables for Isothermal SR and CLSR Experiments

This section details the determination of appropriate experimental conditions for the isothermal SR and CLSR experiments. This was achieved using chemical equilibrium calculations, preliminary experiments and interpretation of experimental results.

3.3.2.1 Temperature and S:C Ratio

Appropriate temperature and S:C ratio conditions for the isothermal SR and CLSR experiments were chosen by calculating chemical equilibrium compositions at a range of assigned temperatures at atmospheric pressure using the computer program CEA (Chemical Equilibrium with Application) developed by NASA Lewis Research Centre (see Section 3.5). A temperature of 700 °C and a molar steam to carbon ratio (S:C) of 3 were found to maximize the equilibrium methane conversion and provide high hydrogen yield efficiency and purity while minimizing solid carbon deposition and steam input (see Section 5.1.1 for more details).

3.3.2.2 Mass of OC and OC Bed Volume

The volume and mass of the OC bed materials used in the packed bed reactor was chosen to provide a valid comparison between the 18NiO GR OC and the Sf OC's in the isothermal SR and CLSR experiments. To achieve this, two sets of experimental conditions were used and are defined overleaf.

Equal Mass conditions compared the performance of the two types of OC on an equal mass basis. The very low bulk density of the Sf OC's (ρ_{bulk} ~ 0.16 g cm^{-3}, ε = 0.94) meant that 2 g of these materials would fill the bed volume of 12.5 cm^3 (10 SS baskets). In contrast

the high bulk density of the 18NiO GR OC (ρ_{bulk} ~ 0.8 g cm^{-3}, ε = 0.78; this is far higher than conventional pelletised OC's (ε ~ 0.35 - 0.5) due to granulation of the 18NiO GR OC to 200 μm) would result in a bed volume of just 2.5 cm^3; therefore, the 18NiO GR OC material was diluted with silica sand granules of equal size. This provided an equal bed volume resulting in an approximately equivalent residence time through the catalyst bed and thereby comparable results.

Equal Volume conditions compared the performance of the two types of OC on an equal volume basis. The catalyst bed volume was set at 2.5 cm^3 (2 SS baskets) and filled with the different materials. This resulted in 0.4 g of each fibrous Sf OC material was used in each SR experiment and was compared to 2 g of the 18NiO GR OC; there was therefore 80 % less OC mass used when testing the Sf OC's compared to the 18NiO GR OC.

3.3.2.3 Reactant Flow Rates

The fuel feedstock consisted of 10 vol% (dry, STP) CH_4 diluted by a N_2 carrier gas in all experiments. The water feed rate was then set to provide the desired S:C 3 for the fuel mixture. Similarly, the pre-reduction mixture consisted of 5 vol% H_2 diluted by an N_2 carrier gas. These mixtures were produced by setting the desired flow rate of pure reactant gases using the MFC and rotameters. The base flow rate of N_2 carrier gas is used to indicate the flow rate of reactants through the bed in the preliminary experiments; in all cases the CH_4 was adjusted to provide 10 vol% at STP and the water set to satisfy a molar S:C 3.

Table 3.2: Experimental conditions for the isothermal SR and CLSR experiments

Conditions	m_{OC} (g)		V_{bed} (cm^3)		$\dot{V}_{i,in}$ (sccm)			T (°C)	S:C
	Sf OC	GR OC	Sf OC	GR OC	N_2	CH_4	H_2O		
Equal Mass (EM)	2.0	2.0	12.5	12.5	1000	111.0	0.25	700	3
Equal Volume (EV)	0.4	2.0	2.5	2.5	800	88.8	0.20	700	3

The flow rates of the reactive gases used in the EM and EV conditions defined in Table 3.2 were determined through trial and error experimentation. Base N_2 carrier gas flow rates of 200 – 1000 sccm (in 200 sccm intervals) were tested for the EV conditions and 200 – 1600 sccm for the EM conditions in preliminary SR experiments and the results compared to the equilibrium methane conversion as calculated by CEA. This showed that the EM and EV regimes were both working away from equilibrium allowing valid comparison of the two materials without exclusion of any possible improvements that the Sf OC's could provide (see Section 5.1).

The EM CLSR experiments showed that water provision to the packed bed was problematic and this made the rate of reduction and consequently the extent of reduction of the OC's unreliable (see Section 6.1.1.2). This also meant that it was difficult to assess whether the reduction of the OC's was limited by mass or diffusion transfer. As a result, the EM CLSR conditions could only be used to assess the SR performance of the OC's following auto-reduction and was not used to analyse the rate or extent of reduction of the OC's.

The EV CLSR experiments were specifically designed to avoid the issues encountered in the EM CLSR experiments while offering another basis of comparison between the Sf OC's and the 18NiO GR OC's. The reduction in bed volume solved the issues with erratic water provision and further modifications were made to the experimental procedure to improve the accuracy of measurement of the rate of reduction of the OC's in a series of preliminary experiments. These conditions were shown to avoid external mass transfer limitations for the reduction of both the Sf OC's and 18NiO GR OC (see Section 7.2.1) and combined with increased accuracy from the modifications above allowed a far more valid comparison between the Sf OC's and the 18NiO GR OC's in terms of rate and extent of reduction.

3.3.3 Steam Reforming Methodology

The SR experiments assessed the ability of the OC materials to act as a catalyst for the SR reaction. These isothermal SR experiments involved reduction of the OC materials to their catalytically active Ni metal phase by a N_2 diluted 5% H_2 feedstock followed by SR of a N_2 diluted CH_4/H_2O feedstock (S:C 3) at 700 °C.

The SR experiments were conducted under the EM and EV conditions (Table 3.3) resulting in two sets of experiments, the results of which are detailed in Chapter 5.

Table 3.3: Experimental conditions for the SR experiments

SR Conditions	m_{OC} (g)		V_{bed} (cm^3)		$\dot{V}_{i,in}$ (sccm)			T (°C)	S:C
	Sf OC	GR OC	Sf OC	GR OC	N_2	CH_4	H_2O		
Equal Mass (EM)	2.0	2.0	12.5	12.5	1000	111.0	0.25	700	3
Equal Volume (EV)	0.4	2.0	2.5	2.5	800	88.8	0.20	700	3

The operation procedure for the EM and EV SR experiments was similar with only the flow rates of the reactants, mass of OC and bed volume changed between the two conditions.

3.3.3.1 Steam Reforming Procedure

(1) The reactor was loaded with OC material and diluted as necessary as per the EM or EV conditions.

(2) The reactor was heated at 10 °C min^{-1} to a bed temperature of 700 °C under a flow of 200 sccm N_2.

(3) Once the desired bed temperature was reached, a mixture of 5 vol% H_2 in N_2 was flowed through the catalyst bed at 1000 sccm until the OC was fully reduced (i.e. the outlet concentration of H_2 reached 5 vol%). This ensured that the OC was in the catalytically reduced metal form rather than the non-catalytically active oxide phase.

(4) The reactor was purged with 1000 sccm N_2 (EM) or 800 sccm N_2 (EV) until H_2 was no longer present in the outlet.

(5) The water feed was switched on and pumped water into the reactor at the intended molar steam to carbon (S/C) ratio as per EM or EV conditions. When water contacted the reduced bed materials as steam, H_2 was formed via oxidation of the bed materials through water splitting; as soon as this was detected by the analysers, the requisite flow of CH_4 was added to the N_2 flow to commence SR, resulting a total flow of reactant gas at 10 vol% CH_4. The CH_4 and water feeds were maintained for 1 hour.

(6) After 1 hour of SR the CH_4/H_2O feeds and furnace were switched off and a purge of N_2 (200 sccm) was commenced; this N_2 flow was maintained until the furnace reached ambient temperature.

3.3.4 Chemical Looping Steam Reforming Experiments

The EM and EV CLSR experiments used slightly different methodologies; the EM CLSR experiments involved 6 SR half-cycles and 6 oxidation half-cycles carried out at 700°C, while the EV CLSR experiments conducted 7 cycles at the same temperature. The ability of the OC's to be auto-reduced by a N_2 diluted CH_4/H_2O feedstock (S:C 3) at 700 °C, the extent of that reduction (α_{red}) and their subsequent catalytic activity and selectivity for the SR and WGS reactions were examined under the steam reforming half cycle. Under the oxidation half cycle the ability of the OC materials to be oxidised and the extent of that oxidation (α_{ox}) was determined.

The CLSR experiments were conducted under the EM and EV regimes (Table 3.4) resulting in two sets of experiments the results of which are detailed in Chapter 6.

Table 3.4: Experimental conditions for the CLSR experiments

CLSR Conditions	m_{OC} (g)		V_{bed} (cm^3)		$\dot{V}_{i,in}$ (sccm)			T (°C)	S:C	Redox Cycles
	Sf OC	GR OC	Sf OC	GR OC	N_2	CH_4	H_2O			
Equal Mass (EM)	2.0	2.0	12.5	12.5	1000	111.0	0.25	700	3	6
Equal Volume (EV)	0.4	2.0	2.5	2.5	800	88.8	0.20	700	3	7

3.3.4.1 EM Chemical Looping Steam Reforming Procedure

Prior to the commencement of the EM CLSR experiments, the OC's were pre-treated (as per similar investigations[52,93,216,217]) by an initial reduction of the OC material by the N_2 diluted 5 vol% H_2 feed followed by 20 minutes of steam reforming following the procedure described in steps 1 to 5 (Section 3.3.3.1). This was to ensure that all OC's used had experienced similar conditions prior to use in the EM CLSR experiments. The OC's were then oxidised in air. These initial SR and oxidation half cycles are referred to as the 0^{th} steam reforming and oxidation half cycles respectively.

The EM CLSR methodology followed the same course as the SR methodology, up to step 5. The following steps were then taken:

(6) After 20 minutes of SR (0^{th} SR half cycle), the CH_4 and water flows were switched off and the reactor was purged with N_2 (1000 sccm) for 5 mins.

(7) The N_2 flow was switched off and the air flow set to 1000 sccm for 5 mins (0^{th} oxidation half cycle); this was to ensure that any reduced material in the OC bed was oxidised.

(8) The reactor was then purged for 5 mins under N_2 (1000 sccm).

(9) The CH_4/H_2O flows were switched on simultaneously facilitating auto-reduction of the OC and carrying out SR (1^{st} SR half cycle). The CH_4/H_2O feeds were maintained for 20 minutes in each steam reforming half cycle.

(10) The CH_4/H_2O flows were switched off and the reactor was purged with N_2 (1000 sccm) for 5 mins.

(11) The N_2 flow was switched off and the air flow set to 1000 sccm for 5 mins (1^{st} oxidation half cycle).

(12) Steps 6 - 11 were repeated until the OC had been reduced and oxidized 6 times.

(13) After the 6^{th} and final oxidation cycle was complete, the air feed and furnace were switched off and a purge of N_2 (200 sccm) was commenced; this N_2 flow was maintained until the furnace reached ambient temperature.

3.3.4.2 EV Chemical Looping Steam Reforming Procedure

As stated earlier, EV CLSR experiments developed on the EM CLSR experiments to improve the reliability of the reduction data produced. When designing the EV CLSR experiments it was found that if the H_2O feed was switched on more than 30 s before the CH_4 feed, neither auto-reduction of the OC nor SR would commence. By then pausing the H_2O feed in increasing 5 second intervals, auto reduction of the OC could be induced; this allowed far more accuracy in determining the rate of reduction of the OC's (Section 6.1.2).

The EV CLSR methodology followed the same course as the SR methodology, up to step 5 for the purposes of OC pre-treatment. The following steps were then taken:

(6) After 1 hour of SR (0^{th} SR half cycle), the CH_4 and water flows were switched off and the reactor was purged with N_2 (800 sccm) for 5 mins.

(7) The N_2 flow was switched off and the air flow set to 1000 sccm for 10 mins (0^{th} oxidation half cycle); this was to ensure that any reduced material in the OC bed was fully oxidised.

(8) The reactor was then purged for 5 mins under N_2 (800 sccm).

(9) The H_2O feed was switched on and allowed to flow for 1 min after which the CH_4 feed was also switched on; this caused the auto-reduction of the OC to be inhibited and accordingly the CH_4 concentration in the outlet increased to feed conditions (10 vol%).

(10) The H_2O flow was paused for 5 s to initiate auto-reduction of the OC by the CH_4 reactant; if auto-reduction was not detected (as evidenced by a drop in CH_4 concentration) within 1 min this pause was increased to 10 s and so on in 5s intervals until auto-reduction was achieved. The CH_4/H_2O feeds were then maintained for 20 minutes in each steam reforming half cycle.

(11) The CH_4/H_2O flows were switched off and the reactor was purged with N_2 (800 sccm) for 5 mins.

(12) The N_2 flow was switched off and the air flow set to 1000 sccm for 5 mins (1^{th} oxidation half cycle).

(13) Steps 6 - 11 were repeated until the OC had been auto-reduced by the CH_4 seven times.

(14) After the 7^{th} and final steam reforming half cycle was complete, the CH_4/H_2O feed and furnace were switched off and a purge of N_2 (200 sccm) was commenced; this N_2 flow was maintained until the furnace reached ambient temperature.

Stopping the experiment after the final SR half cycle allowed the characterisation of the partially reduced OC's to be achieved; this allowed comparison of the extent of reduction during the EV CLSR experiments as determined by XRD (Reitveld refinement) and the packed bed reactor.

3.3.5 Determination of Reduction Kinetics

These experiments were used to analyse the kinetics of auto-reduction of the OC's by the N_2 diluted CH_4/H_2O feedstock (S:C 3) at temperatures ranging between 450 - 700 °C in 50 °C intervals. Different conditions (Table 3.5) were used in these experiments so that equal mass of catalyst was maintained between the Sf OC's and the 18NiO GR OC.

Table 3.5: Experimental conditions for the determination of reduction kinetics

CLSR conditions	m_{OC} (g)		V_{bed} (cm^3)		$\dot{V}_{i,in}$ (sccm)			T (°C)	S:C
	Sf OC	GR OC	Sf OC	GR OC	N_2	CH_4	H_2O		
Reduction Kinetics (RK)	0.4	0.4	2.5	0.4	800	88.8	0.20	450 - 700	3

The reduction kinetics CLSR conditions or 'RK CLSR' conditions are those used to define reduction kinetics also avoid external mass transfer limitation and were used to ensure that equal mass of solid reactant (M_{oc}) was present without any dilution via silica sand (see Section 7.2).

3.3.5.1 Procedure for Determination of Reduction Kinetics

The procedure of the kinetic determination experiments was similar to the EV CLSR methodology and there maximised the accuracy of the rate of reduction of the OC and therefore the extent of reduction.

The procedure used for the determination of kinetics followed the same course as the SR methodology, up to step 5. The following steps were then taken:

(6) After 1 hour of SR (0^{th} SR half cycle), the CH_4 and water flows were switched off and the reactor was purged with N_2 (1000 sccm) for 5 mins.

(7) The N_2 flow was switched off and the air flow set to 1000 sccm for 10 mins (0^{th} oxidation half cycle); this was to ensure that any reduced material in the OC bed was fully oxidised.

(8) The reactor was then purged using a flow of 800 sccm N_2, and the reactor temperature set to reach a bed temperature of 450 °C.

(9) The H_2O feed was switched on and allowed to flow for 1 min after which the CH_4 feed was also switched on; this caused the auto-reduction of the OC to be inhibited and CH_4 concentration in the outlet increased to feed conditions.

(10) The H_2O flow was paused for 5 s to attempt to initiate auto-reduction of the OC by the CH_4 reactant; if auto-reduction was not detected (as evidenced by a drop in CH_4 concentration) this pause was increased to 10 s and so on in 5s intervals until auto reduction was achieved. The CH_4/H_2O feeds were then maintained for 20 minutes.

(11) After the 20 min steam reforming half cycle at 450 °C, steps 6 - 10 were repeated, with the bed temperature increased by 50 °C under a flow of 800 sccm N_2 after each oxidation half cycle. This was repeated until one steam reforming half cycle had been achieved at each temperature between 450 - 700 °C.

(12) After the final oxidation cycle was complete, the air feed and furnace were switched off and a purge of N_2 (200 sccm) was commenced; this N_2 flow was maintained until the furnace reached ambient temperature.

Due to time constraints and a lack of evidence for an effect of Co doping upon the reduction behaviour of the OC's, only the 18Ni Sf-WI, Sf-DP and Sf-HT materials and the 18NiO GR OC's were tested.

3.4 Elemental Balances and Process Outputs

Elemental balances were conducted to gain useful data from the packed bed reactor experiments. These balances combined with reasonable assumptions allowed the comparison of the performance of the various OCs tested in the rig system. Before the balances were conducted, the data available and the data required from the experiments were quantified.

Data measured directly in the experiments or set by the design of the experiment directly available from the results:

(1) The molar fraction of CO_2, CO, CH_4, O_2 and H_2 in the dry outlet gas measured by ABB gas analysers,

(2) The volume flow rate of reactants H_2O, CH_4 and Air and the carrier gas N_2 fed into the reactor,

(3) The mass of the OC used in each experiment and the wt% of NiO in said OC.

Process outputs included:

(1) The yields of product molar gases

(2) The percentage conversion of H_2O and CH_4

(3) The reduction rate (r_{red},OC) of the OC from $MOx_{(s)}$ to $M_{(s)}$, and oxidation rate (r_{ox},OC) of $M_{(s)}$ to $MOx_{(s)}$

(4) The extent of reduction (α_{red}) and oxidation (α_{ox}) of the OC (also termed the solids conversion)

(5) The carbon balance

(6) The H_2 yield efficiency and purity

From these outputs several measures of OC effectiveness can be calculated allowing comparisons.

3.4.1 Experimental Data

The following terms were either defined by the design of the SR, CLSR or kinetic experiments or directly measured in each experiment:

$\dot{V}_{CH_4,in}$ $\dot{V}_{N_2,in}$ $\dot{V}_{Air,in}$	Volumetric flow rate (STP) of gas feeds into the reactor (sccm)
$\dot{V}_{H_2O,in}$	Volumetric flow rate (STP) of liquid water into the reactor (sccm)
$\bar{W}_{H_2O}$	Molar mass of water (18 g mol^{-1})
$\bar{W}_{CH_4}$	Molar mass of methane (12 + 4 x 1 = 16 g mol^{-1})
m_{OC}	Mass of OC (g)
V_{bed}	Volume of catalyst bed (cm^3)
$\bar{W}_{Ni}$, $\bar{W}_{Co}$	Molar mass of Ni (58.69 g mol^{-1}) and Co (58.93 g mol^{-1})
m_{Ni}, m_{Co}	mass fraction of Ni/Co in the OC
$y_{i,out}$	Dry molar fraction of species *i* in the outlet (H_2 CH_4 CO CO_2 O_2)

The volume flow rates (at 20 °C and 101325 Pa) of CH_4, N_2 and Air were set to satisfy the desired flows of gaseous reactants in the feed stream. The volume flow rate of water pumped via the syringe pump was calculated to satisfy a 3:1 molar ratio of H_2O to CH_4.

Assuming ideal gases, the molar flow rate of CH_4:

$$\dot{n}_{CH_4,in} = \frac{P\,\dot{V}_{CH_4,in}}{R\,T} \qquad \textbf{Equation 3.10}$$

The molar flow rates of the other gaseous reactants in the feed were calculated similarly:

$$\dot{n}_{N_2,in} = \frac{P\,\dot{V}_{N_2,in}}{R\,T} \qquad \textbf{Equation 3.11}$$

$$\dot{n}_{O_2,in} = \frac{P\,\dot{V}_{Air,in}(y_{O_2}\,in\ air)}{R\,T} \qquad \textbf{Equation 3.12}$$

Volumetric flow rate of H_2O was calculated by use of density and relative molecular mass (101325 Pa and 20 °C).

$$\dot{V}_{H_2O,in} = 3\,\dot{n}_{CH_4,in}\,\rho_{H_2O}\,\bar{W}_{H_2O} \qquad \textbf{Equation 3.13}$$

It was assumed that the water pumped into the reactor was completely vaporised and entered the catalyst bed in the vapour phase.

The dry molar fraction (assuming ideal gases and therefore vol% is equal to mol%) of N_2 was calculated by difference.

$$y_{N_2,out} = 1 - \sum (y_{H_2}, y_{O_2}, y_{CH_4}, y_{CO_2}, y_{CO})_{out,dry} \qquad \textbf{Equation 3.14}$$

3.4.2 Nitrogen Balance

A nitrogen balance was conducted to calculate the total and component dry molar flows in the outlet.

$$\dot{n}_{dry,out} = \frac{\dot{n}_{N_2,in}}{y_{N_2,out}} \qquad \textbf{Equation 3.15}$$

$$\dot{n}_{i,out} = y_{i,out}\ \dot{n}_{dry,out} \qquad \textbf{Equation 3.16}$$

3.4.3 Carbon Balance

A carbon balance was conducted and the results used to estimate experimental error associated with the packed bed reactor. More information can be found in Section 3.6.4.

3.4.4 Hydrogen Balance

A hydrogen balance was conducted to approximate the molar flow rate of water from the reactor before removal prior to gas analysis.

$$\dot{n}_{H_2O,out} = \frac{4\dot{n}_{CH_4,in} + 2\dot{n}_{H_2O,in} - 4\dot{n}_{CH_4,out} - 2\dot{n}_{H_2,out}}{2} \quad \textbf{Equation 3.17}$$

3.4.5 Oxygen Balance

An oxygen balance was carried out in order to approximate both the reduction under methane–steam feed and oxidation rates under air feed of the various OCs used:

$$r_{red}, OC = \frac{\dot{n}_{dry,out}\left(y_{CO,out} + 2y_{CO_2,out} + 2y_{O_2,out}\right) - \dot{n}_{H_2O,in} \times X_{H_2O}}{\frac{m_{OC}\, m_{Ni}}{\bar{W}_{Ni}} \times \frac{m_{OC}\, m_{Co}}{\bar{W}_{Co}}} \quad \textbf{Equation 3.18}$$

$$r_{ox}, OC = \frac{2\dot{n}_{O_2,out} - \left(y_{CO,out} + 2y_{CO_2,out} + 2y_{O_2,out}\right)\dot{n}_{dry,out}}{\left(\frac{m_{OC}\, m_{Ni}}{\bar{W}_{Ni}} \times \frac{m_{OC}\, m_{Co}}{\bar{W}_{Co}}\right)} \quad \textbf{Equation 3.19}$$

These formulae yield the rate of reduction per mol of Ni/NiO available in the OC, and are therefore present units of s^{-1}. The rates in mol s^{-1} (as used in Section 7.2.2) can be obtained by removing the denominator of the above equations.

Note the possible evolution of CO and CO_2 during the oxidation under air feed in Equation 3.19 would have resulted from incomplete and complete burn out respectively of coke that had accumulated on the OC during previous methane and steam feeds.

The extent of reduction/oxidation was determined by time integration of the rates of reduction/oxidation (in s^{-1}):

$$\alpha_{red} = \int_0^t r_{red}, OC\, dt \quad \textbf{Equation 3.20}$$

$$\alpha_{ox} = \int_0^t r_{ox}, OC\, dt \quad \textbf{Equation 3.21}$$

3.4.6 Process Outputs

From the elemental balances several equations were used to compare the performance of the OCs tested in the packed bed experiments. H_2 yield efficiency was calculated as the molar ratio of H_2 produced per mol of carbon in the feed to the maximum theoretical H_2 yield produced via the SR and WGS reactions, not taking into account thermodynamic equilibrium limitations. The theoretical maximum yield for a CH_4 feedstock is 4 mol H_2 per mol of carbon in the feed.

$$H_2\ Yield\ Efficiency = \left[\frac{\left(\frac{\dot{n}_{H_2,out}}{\dot{n}_{CH_4 in}}\right)}{4}\right] \times 100\% \qquad \textbf{Equation 3.22}$$

$$H_2\ Purity = \left(\frac{y_{H_2,out}}{y_{CO,out} + y_{CO_2,out} + y_{CH_4,out} + y_{H_2,out}}\right) \text{x } 100\% \qquad \textbf{Equation 3.23}$$

CH_4 and H_2O conversion were calculated using the following formulas:

$$CH_4\ Conversion = \left(\frac{\dot{n}_{CH_4,in} - \dot{n}_{CH_4,out}}{\dot{n}_{CH_4,in}}\right) \text{x } 100\% \qquad \textbf{Equation 3.24}$$

$$H_2O\ Conversion = \left(\frac{\dot{n}_{H_2O,in} - \dot{n}_{H_2O,out}}{\dot{n}_{H_2O,in}}\right) \text{x } 100\% \qquad \textbf{Equation 3.25}$$

3.5 Thermodynamic Equilibrium Calculations

Thermodynamic equilibrium calculations were used to assess the theoretical ideal performance of the packed bed system and to identify when said system is equilibrium limited. The computer program CEA (Chemical Equilibrium with Application) developed by NASA Lewis Research Centre was used to facilitate this.[218,219]

CEA is a calculator program that uses the minimisation of the Gibbs free energy to compute chemical equilibria for a given system. The Gibbs free energy of the system (G) can be defined as the driving force for that system to reach equilibrium; this energy is derived from the enthalpy (H) and entropy (S) of reaction in the system at a given temperature and pressure[218,219]:

$$G(p,T) = H - TS \qquad \textbf{Equation 3.26}$$

Any initial chemical system with a defined composition of reactants at a given temperature and pressure will have an initial Gibbs free energy. If the system is both isobaric and

isothermal, this system will undergo chemical change (i.e. chemical reactions) to minimise the Gibbs free energy of the system. These reactions will continue to such a point that the Gibbs free energy of the mixture of remaining reactants and products is minimised. At this point, reactions will cease and the system is considered at equilibrium[218,219].

By calculating this minimal value of Gibbs free energy, the CEA software can evaluate the chemical reactions that will take place within a defined system and thereby the chemical composition of that system once it has reached equilibrium. This method of equilibrium evaluation makes no assumptions about the kinetics, reaction pathways or the species involved in the defined system[218,219] but requires a system of species to be considered as potential products to be known.

The CEA software requires the input of temperature and pressure and the moles of reactant species. Once the system is defined, the calculation is performed and outputs provided as molar compositions of species present at equilibrium. A series of calculations were conducted using a range of temperatures from 200 – 1000 °C and using a feed molar S:C of 1 to 5 (i.e. inputting 1 mol of $CH_{4(g)}$ and varying the $H_2O_{(g)}$ from 1 mol to 5mol). The molar outputs were then used to calculate the H_2 purity and yield efficiency and the CH_4 and H_2O conversions under each condition (Equation 3.22 - Equation 3.25).

3.6 Experimental Error

The nature of the experimental work conducted throughout this thesis results in the use of several techniques, measurements and equipment that have intrinsic inaccuracies. These inaccuracies can combine to affect the results reported; as such this section will discuss the inaccuracies associated with the experimental equipment used, the methods by which these errors were mitigated (if possible), and the possible effects these errors may have on the results.

3.6.1 Mass Flow Controllers

Bronkhorst EL-FLOW MFC's are used in the packed bed reactor to control the volume flow of CH_4 and H_2. The MFC's had a range of 0.1 - 200 sccm and an associated error of 0.5 % of the indicated value (i.e the set point of the MFC) plus 0.1 % of the full scale of the MFC. Given below are the typical set points used in each experiment and the associated possible error in volume flow, Table 3.6

Table 3.6: Experimental error associated with Bronkhorst EL-FLOW MFC's

Flow Conditions	$\dot{V}_{i,in}$ (sccm)	Error (sccm)	Error (% set point)	Error (vol%)
Equal Mass (EM)	111	± 0.76	± 0.68	± 0.07
Equal Volume (EV)	88.8	± 0.64	± 0.72	± 0.07
Reduction Kinetics (RK)	88.8	± 0.64	± 0.72	± 0.07

The error in in the above flow rates was mitigated as far as possible by weekly calibration of the MFC's with an Agilent technologies ADM1000 flow meter (accurate to ±0.005 sccm). As the MFC's used were brand new this calibration was rarely needed as the flows were within ±1 sccm in most cases. Moreover, when the error is calculated as vol% of the desired mixture (i.e. taking the ratio of the error in sccm of desired gas flow by the total flow used in the experiment) the error in the desired vol% supplied to the experiment is negligible in both the experiments conducted.

Bronkhorst Mass view electric rotameters are used in the packed bed reactor to control the volume flow of N_2 and Air. These rotameters had a range of 1 - 1000 sccm and an associated error of 1% of the indicated value plus 0.5% of the full scale. Given below is the error associated with these devices, Table 3.7.

Table 3.7: Experimental error associated with Bronkhorst Mass View rotameters

Flow Conditions	$\dot{V}_{i,in}$ (sccm)	Error (sccm)	Error (% set point)	Error (vol%)
Equal Mass (EM)	1000	± 15	± 1.63	± 1.35
Equal Volume (EV)	800	± 13	± 1.5	± 1.46
Reduction Kinetics (RK)	800	± 13	± 1.5	± 1.46

Again, the error in in the above flow rates was mitigated as far as possible by regular (weekly) calibration of the MFC's with a Agilent technologies ADM1000 flow meter (accurate to ±0.005 sccm).

Any errors in the volume flow of the reactants into the system, whether due to gradual drift of the MFC/rotameters from their set-point or by second to second fluctuations, will have knock on effects on for the mass balance and derived data associated with the packed bed reactor system. In practice these effects are difficult to quantify let alone identify during an experiment. However, with accurate calibration of the analysers, MFC's and rotameters used in the reactor system the accuracy of the experiments can be maximised.

3.6.2 Analysers

The ABB Advanced Optima analysers used to measure the outlet composition of the product gases consisted of three modules each of which had an error associated with the measurement of the gas.

Table 3.8: Experimental error associated with ABB gas analysers

Analyser	Species	Error (% span[a])	Span[a] (vol%)	Error (vol%)	Zero Drift[b] (vol%)	Sensitivity Drift[b,c] (vol%)
Uras 14	CO	≤ 1.0	10	≤ 0.10	≤ 0.10	≤ 0.10
	CH_4	≤ 1.0	20	≤ 0.20	≤ 0.20	≤ 0.20
	CO_2	≤ 1.0	15	≤ 0.15	≤ 0.15	≤ 0.15
Caldos 15	H_2	≤ 2.0	40	≤ 0.80	≤ 0.40	≤ 0.40
Magnos 106	O_2	≤ 0.5	20.96	≤ 0.10	≤ 0.03	≤ 0.1

[a] Span gas is the vol% of gas used for calibration [b] Drift is movement of the value per week [c] Sensitivity drift refers to drift of the measured value

The errors are detailed in Table 3.8, show that the error in measurement is insignificant when compared to the variance during the various SR and CLSR experiments. Despite this, efforts were made to improve the accuracy of the analysers.

3.6.2.1 Caldos 15 Thermal Conductivity Correction

As stated earlier the Caldos 15 analysers uses a thermal conductivity detector. This detector uses a Wheatstone bridge with a calibrated hot wire to measure the quantity of H_2 in N_2 in the product gas. When gases other than H_2 or N_2 are present in the product stream, e.g. CO, CO_2 CH_4 or O_2, the inherent thermal conductivities of these gases can affect the H_2 concentration reported by the analyser. To compensate for this effect a correction factor based on the thermal conductivities of the gases present relative to N_2 was used.

$$y_{H_2,out} = \sum \left(\frac{\lambda_i}{\lambda_{H_2}} y_i \right) + y_{H_2} \qquad \textbf{Equation 3.27}$$

Where λ_i is the thermal conductivity of the species i (at STP, 20 °C, 101325 Pa), and y_{H_2} is the H_2 concentration detected by the analyser. Importantly if $\lambda_i > \lambda_{N_2}$, then λ_i must be multiplied by -1 as per the equation below:

$$y_{H_2,out} = \left(\frac{\lambda_{CO}}{\lambda_{H_2}} y_{CO} + \frac{\lambda_{CO_2}}{\lambda_{H_2}} y_{CO_2} - \frac{\lambda_{CH_4}}{\lambda_{H_2}} y_{CH_4} - \frac{\lambda_{O_2}}{\lambda_{H_2}} y_{O_2} \right) + y_{H_2} \qquad \textbf{Equation 3.28}$$

To test the efficacy of this correction, factor several concentrations of CH_4 and CO_2 were flowed into the analyser and the as read and H_2 concentration recorded. As shown in Figure 3.5 (overleaf), the accuracy of the H_2 measurement was far improved when corrected when compared to the as-read values.

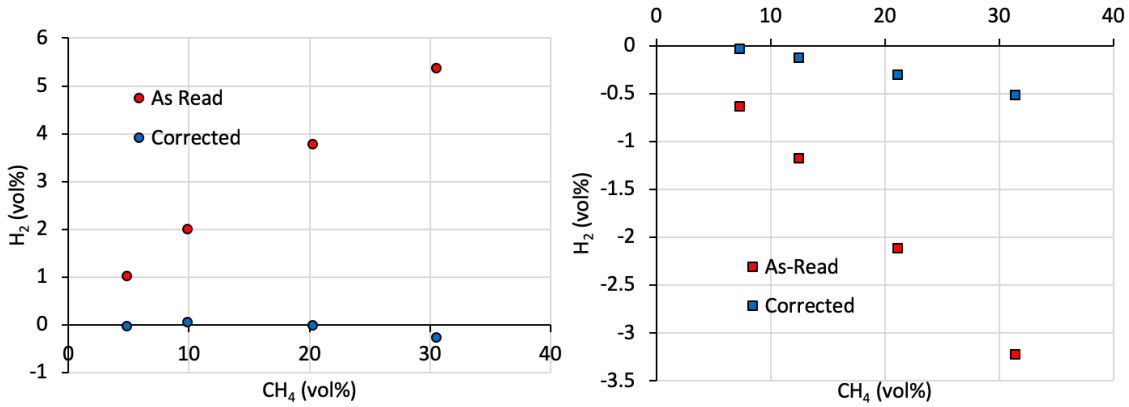

Figure 3.5: Vol% H_2 as-read by the Caldos 15 analyser and after correction detailed in Equation 3.28 using CH_4 (left) and CO_2 (right)

3.6.2.2 Calibration

Over time the zero point and measured value of the analysers can drift from their set point causing errors proportional to the time between calibrations. This drift was corrected for by calibrating the instruments every two weeks; this was deemed appropriate as the drift values in Table 3.8 were minimal (half that of the measurement error) and due to the time taken to run a full calibration of the analysers. The concentrations of the analysed gases used for calibration are shown in Table 3.8 stated as span gases. The calibration gas concentrations used were roughly twice the process concentrations as per the recommendation of the manufacturer and run at similar flow rates to the process conditions to maximise accuracy of the calibration.

After calibration, a bottled gas (BOC) containing a mixture of H_2, CH_4, CO_2 and CO was used to assess the efficacy of each calibration. The calibration gas consisted of 30 vol% H_2; 2 vol % CH_4; 15 vol % CO_2; 8 vol % CO and balance N_2.

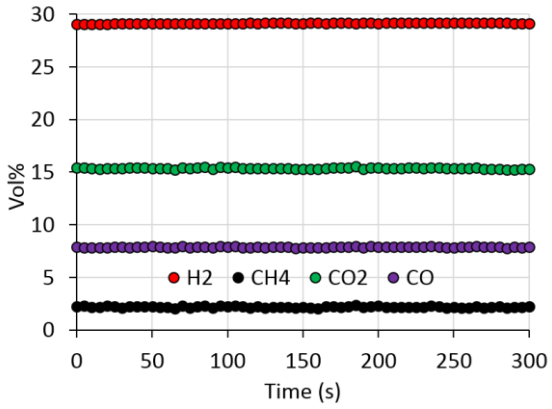

Figure 3.6: Vol% of the calibration gas as determined by the ABB analysers post calibration with the Caldos 15 correction factor applied

Figure 3.6 shows excellent agreement between the calibration gas and the vol% as determined by the ABB analysers post calibration with the Caldos 15 correction factor applied.

3.6.3 Gas leaks

Gas leaks can form at the various connection points between the tube fittings used to construct the packed bed reactor. Gas leaks prior to entry into the reactor can affect the number of moles of each species into the reactor and leaks after the reactor affect the nitrogen balance thereby creating knock on effects into the other elemental balances. As such a calibration flow meter (Agilent technologies ADM1000) was used to assess whether the volume flow of gases at the input was matched by the volume flow at the outlet with an air flow. Any large discrepancies in the flows would indicate a leak. A leak detection test was also conducted on any fitting that had been tightened or loosened in the setting up each experiment. Furthermore, all tube connections on the rig were tested monthly with leak detector (e.g. Snoop).

3.6.4 Carbon Balance

As stated earlier it is difficult to assess the effect of the inaccuracies involved with the provision of the reactant gases and detection of the product gases upon the results of the SR and CLSR experiments. In this work, carbon balances were conducted for each SR and CLSR experiment to assess the discrepancy between the molar flows of carbon into the equipment compared to the molar carbon flows detected in the dry outlet. This allows an approximation of the sum of all the equipment errors as both the reactant flows and product flows are used in this calculation.

$$\dot{n}_{C,out} = \sum (\dot{n}_{CO}, \dot{n}_{CH_4}, \dot{n}_{CO_2})_{out,dry} \qquad \textbf{Equation 3.29}$$

$$\%\ Error = \left(\frac{\dot{n}_{C,out}}{\dot{n}_{C,in}}\right) \text{x } 100\% \qquad \textbf{Equation 3.30}$$

The result of the calculation described by Equation 3.30 can inform the likely cause of errors in the experimental system. If the result of Equation 3.30 was greater than 100%, the molar flow of carbon out of the reactor was greater than the molar flow in; this could suggest a relative lack of N_2 of CH_4 in the reactant flows caused by MFC error. If less than 100%, the carbon flows in were larger than out and this could suggest either carbon accumulation in the reactor or a leak in the reactor system.

4 Characterisation of OC Materials

Characterisation of the as-received CG Saffil® support was carried out prior to loading of Ni/Co oxides. This allowed the effects of synthesis upon the support to be accurately examined and to systematically characterise the support material.

Characterisation of the Sf OC's was carried out to confirm the loading of the Ni/Co oxides upon the Saffil® support and to assess any physical changes to the support material implemented by the differing synthesis methodologies. The data gathered in this section was instrumental in explaining the performance of the OC's in the SR and CLSR experiments.

4.1 Phase Composition Determination and Crystallite Analysis

XRD was used to assess the phase composition of the support material and the produced OC's as well as to estimate the average crystallite size via application of the Scherrer equation.

The XRD pattern for the as-received Saffil® fibres shows several broad, low intensity peaks at 2θ of characteristic of gamma alumina, γ-Al_2O_4 (ICDD 00-010-0425) and SiO_2 (ICDD 01-080-6157), Figure 4.1. The peaks at 37.5°, 45.6°, 60.5° and 66.5° 2θ all matched the reference data γ-Al_2O_3.

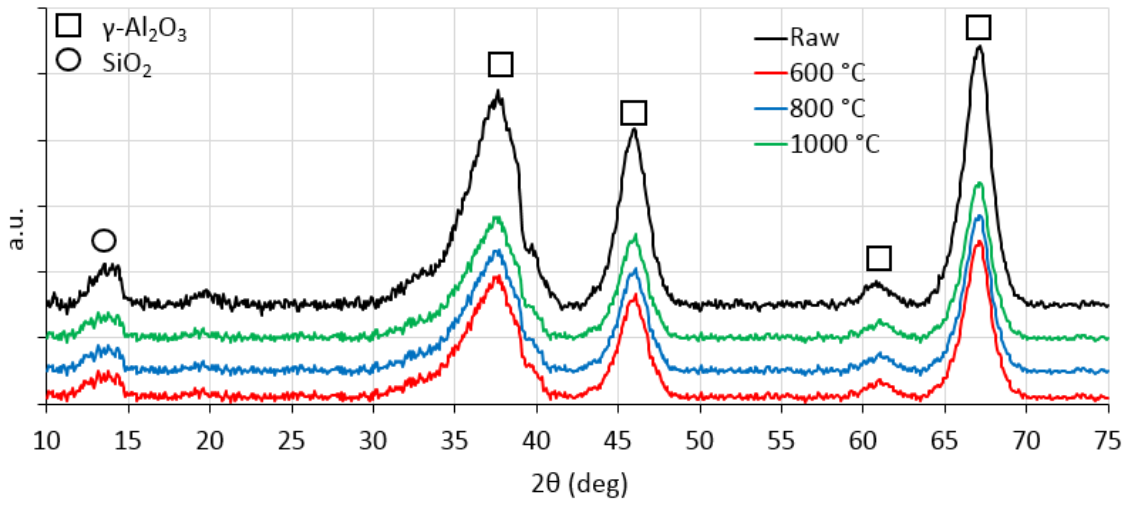

Figure 4.1: XRD pattern of the as-received Saffil® support and calcined at 600, 800 and 1000 °C

Application of the Scherrer equation (Equation 3.5) suggests the average crystallite size of the γ-Al_2O_3 in the Saffil® fibres was found to be 4 nm (Table 4.1). This explains the peak broadening experienced in Figure 4.1. As a result of these broad peaks, XRD could not be used to quantitatively assess γ-Al_2O_3 or SiO_2 phase compositions (via Reitveld refinement) in the support and synthesised OC's. The other XRD patterns in Figure 4.1 were produced by calcining the as-received Saffil® fibres for 4 hours in an oxygen atmosphere at 600, 800 and 1000 °C. These patterns show that no changes to the crystallite structure of the Saffil® were experienced when used in conditions similar to those during calcination and the SR and CLSR processes.

Table 4.1: Mean crystallite size calculated with Scherrer's equation

Sample	2θ (deg)	Crystallite Size[(a)] (nm)
Saffil®	13.7, 37.5, 46.0, 61.0, 67.0	4
18Ni Sf-WI	37.2, 43.3, 62.9	16
0.6Co 18Ni Sf-WI	37.2, 43.3, 62.9	35
1.8Co 18Ni Sf-WI	37.2, 43.3, 62.9	31
Mean WI	37.2, 43.3, 62.9	28
18Ni Sf-DP	37.2, 43.3, 62.9	7
0.6Co 18Ni Sf-DP	37.2, 43.3, 62.9	6
1.8Co 18Ni Sf-DP	37.2, 43.3, 62.9	6
Mean DP	37.2, 43.3, 62.9	6
18Ni Sf-HT	37.2, 43.3, 62.9	14
0.6Co 18Ni Sf-HT	37.2, 43.3, 62.9	8
1.8Co 18Ni Sf-HT	37.2, 43.3, 62.9	8
Mean HT	37.2, 43.3, 62.9	10
18NiO GR OC	37.2, 43.3, 62.9	55

[(a)] Where crystallite size refers to the mean size of crystallites of the phase analysed.

XRD was also used to identify the predominant crystal phase in which the Ni and Co oxides were deposited. Figure 4.2 shows (overleaf) that all OCs produced peaks at 2θ of 37.3°, 43.3° and 62.9°; these peaks are characteristic of NiO (ICDD 04-013-0888) suggesting that the dominant phase of nickel formed is NiO during all three of the synthesis methodologies used.

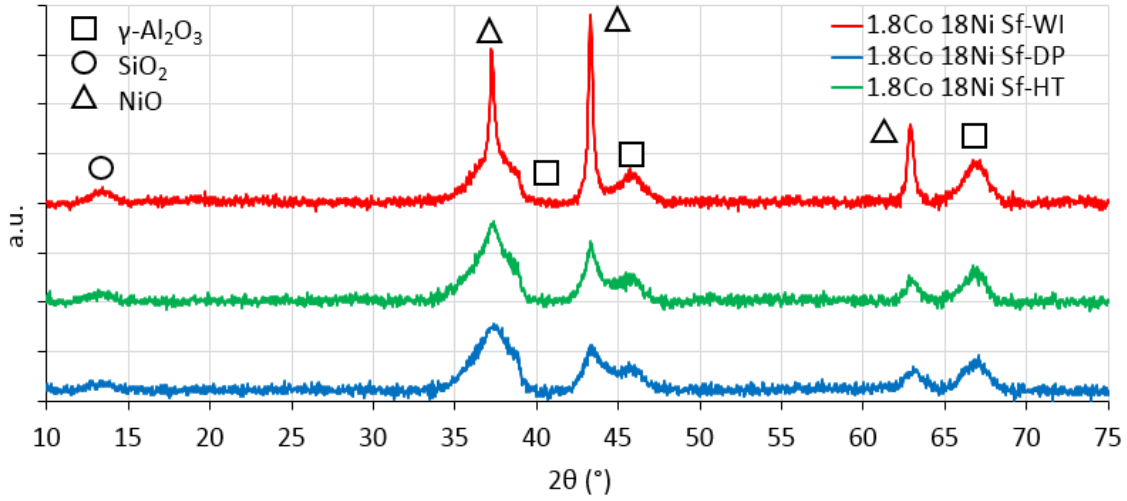

Figure 4.2: XRD pattern of the fresh 1.8Co 18Ni Sf-WI, 1.8Co 18Ni Sf-DP and 1.8Co 18Ni Sf-HT OC's

Important in the context of OC performance, there was no peak at that 59.9° present in any of the samples tested that would be characteristic of the undesired bulk $NiAl_2O_4$. However the concentration of any $NiAl_2O_4$ formed may be below XRD detection limits (> 5%) and the broad γ-Al_2O_3 peaks present from the Saffil® support could make identification of smaller peaks difficult[202]. Despite this, the avoidance of bulk $NiAl_2O_4$ detectable by XRD suggests that the synthesis techniques used are appropriate for the production of Ni Sf-OC's.

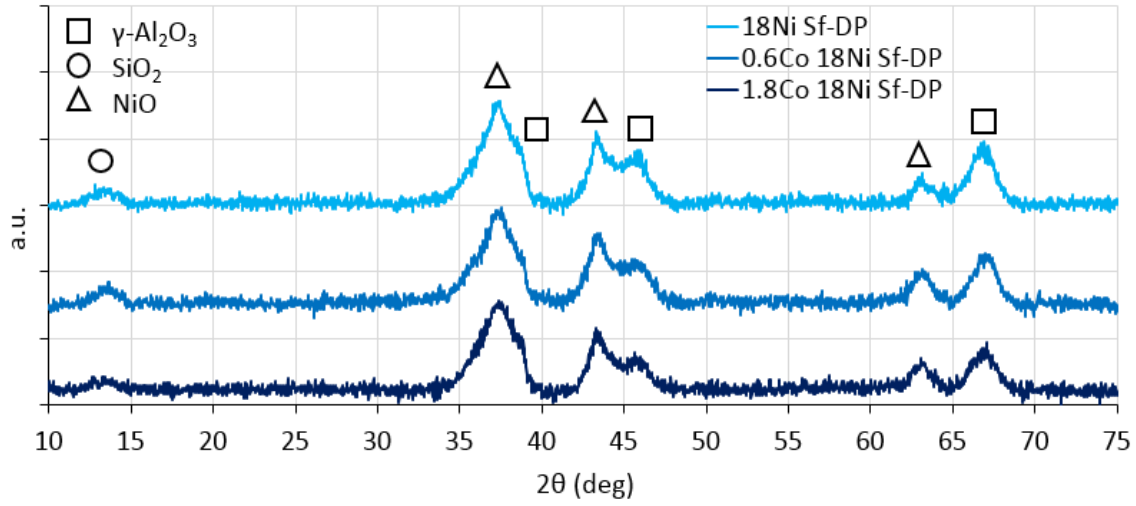

Figure 4.3: XRD pattern of the fresh 18Ni Sf-DP, 0.6Co 18Ni Sf-DP and 1.8Co 18Ni Sf-DP OC's

Figure 4.3 compares the XRD patterns of all the Sf-DP OC's. These patterns show no peak associated with cobalt oxide phases (CoO, Co_3O_4 or $CoAl_2O_4$) in the 0.6 and 1.8Co doped samples. The lack of cobalt phases in the XRD patterns was attributed to the small amount of cobalt deposited (as confirmed by AAS) again likely falling below XRD detection limits.

Additionally, the broad γ-Al_2O_3 peaks present from the Saffil® support could make identification of smaller peaks difficult.

The XRD pattern corresponding to the fresh 18NiO GR OC, Figure 4.4, shows evidence of only α-Al_2O_3 (ICCD 04-015-8993) and NiO (ICDD 04-013-0888). There was no $NiAl_2O_4$ phase detected.

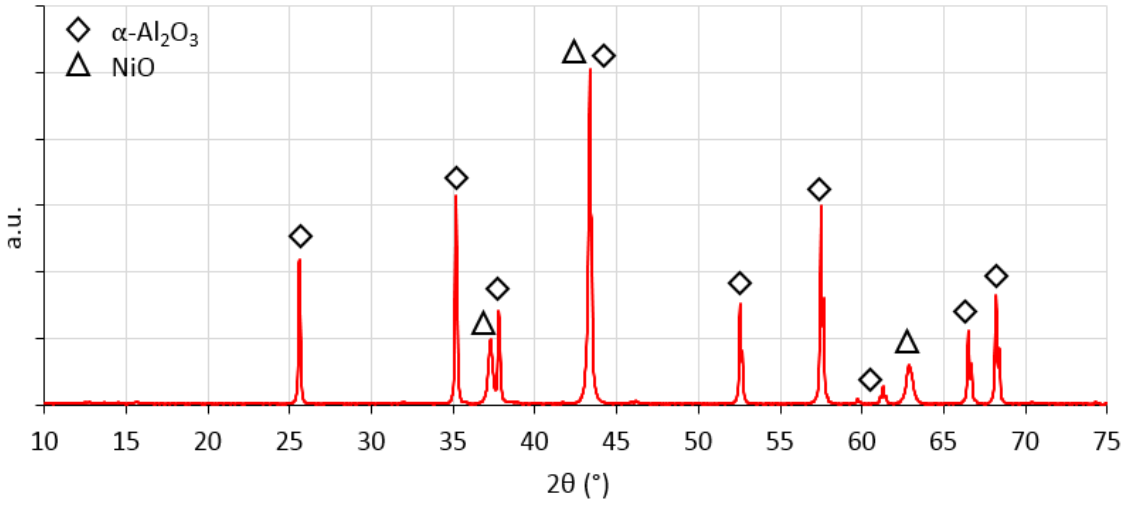

Figure 4.4: XRD pattern of the fresh 18NiO GR OC

The breadth of the NiO peaks in Figure 4.2 are reflected in the Scherrer analysis of the XRD patterns, Table 4.1. The average crystallite size of the NiO for the OCs produced via the WI methodology is 28 nm, whereas the DP and HT methodologies provided far lower NiO crystalline domains of 6 nm and 10 nm respectively. These results largely agree with TEM analysis of the crystallite sizes shown in Section 4.4. Moreover, all the Sf OC's could produce smaller NiO crystallites than those exhibited by the 18NiO GR OC (55 nm). Scherrer analysis also showed that the crystallite size of the α-Al_2O_3 was likely larger than 200 nm and therefore could not be accurately quantified by this method.

Doping cobalt reduced the average crystallite size of the NiO as determined by Scherrer analysis by 16 % in the Sf-DP sample and 40 % in the Sf-HT sample. The NiO crystallites in the Sf-WI OC approximately doubled in size with the addition of Co. However, when the results of the TEM analysis are consulted and the relatively small absolute change in the crystallite size of the Sf-DP and Sf-HT OC's are considered, it would suggest that doping of cobalt may not be responsible for the increase in size.

4.2 Quantitative Elemental Analysis

The peak broadening exhibited by the Saffil® support in Figure 4.1 caused quantitative phase analysis for the γ-Al_2O_3 or SiO_2 phases in the synthesised OCs using Rietveld refinement to be prohibitively inaccurate. As such, Atomic Adsorption Spectrophotometry (AAS) was used to quantitatively assess the deposition of the Ni and Co onto the support.

Table 4.2: Quantitative element analysis of the synthesized OC's

Catalyst	Desired Loading (wt%)			Metal Loaded (wt%)		
	Ni	Co	Ni:Co	Ni	Co	Ni:Co
18Ni Sf-WI	18	0	0	17.66	0.00	-
0.6Co 18Ni Sf-WI	18	0.6	30	15.97	0.48	33.35
1.8Co 18Ni Sf-WI	18	1.8	10	19.29	1.57	12.33
18Ni Sf-DP	18	0	0	17.31	0.00	-
0.6Co 18Ni Sf-DP	18	0.6	30	18.09	0.51	35.61
1.8Co 18Ni Sf-DP	18	1.8	10	17.20	1.36	12.65
18Ni Sf-HT	18	0	0	19.76	0.00	-
0.6Co 18Ni Sf-HT	18	0.6	30	18.08	0.50	35.83
1.8Co 18Ni Sf-WI	18	1.8	10	17.88	1.46	12.27

As shown in Table 4.2, Ni/Co loading was effective with all the synthesis methodologies used able to provide equal to or in excess of the desired loading for Ni. While the cobalt loading was slightly more erratic, the desired Ni:Co ratios were largely achieved.

4.3 Morphology and Topography

Scanning electron microscopy (SEM) was used to characterise the morphology of the as-received CG Saffil® fibres and to assess the morphology of the Ni/Co oxide coatings produced during synthesis.

SEM images in Figure 4.5a and b (overleaf) show the Saffil® fibres are smooth and cylindrical. The widths of these fibres ranged from 2 - 5 μm, close to the median values of 3 - 4 μm stated by the manufacturer.

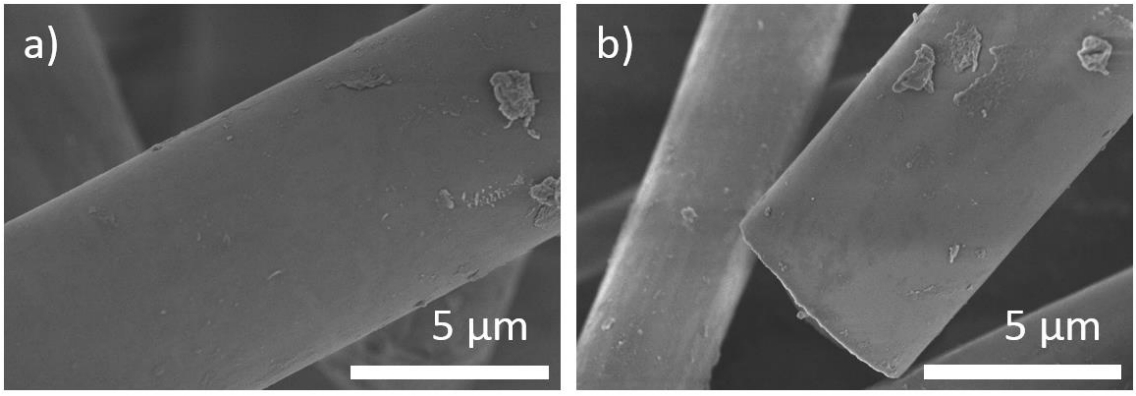

Figure 4.5: SEM images of the raw Saffil® fibres (a and b)

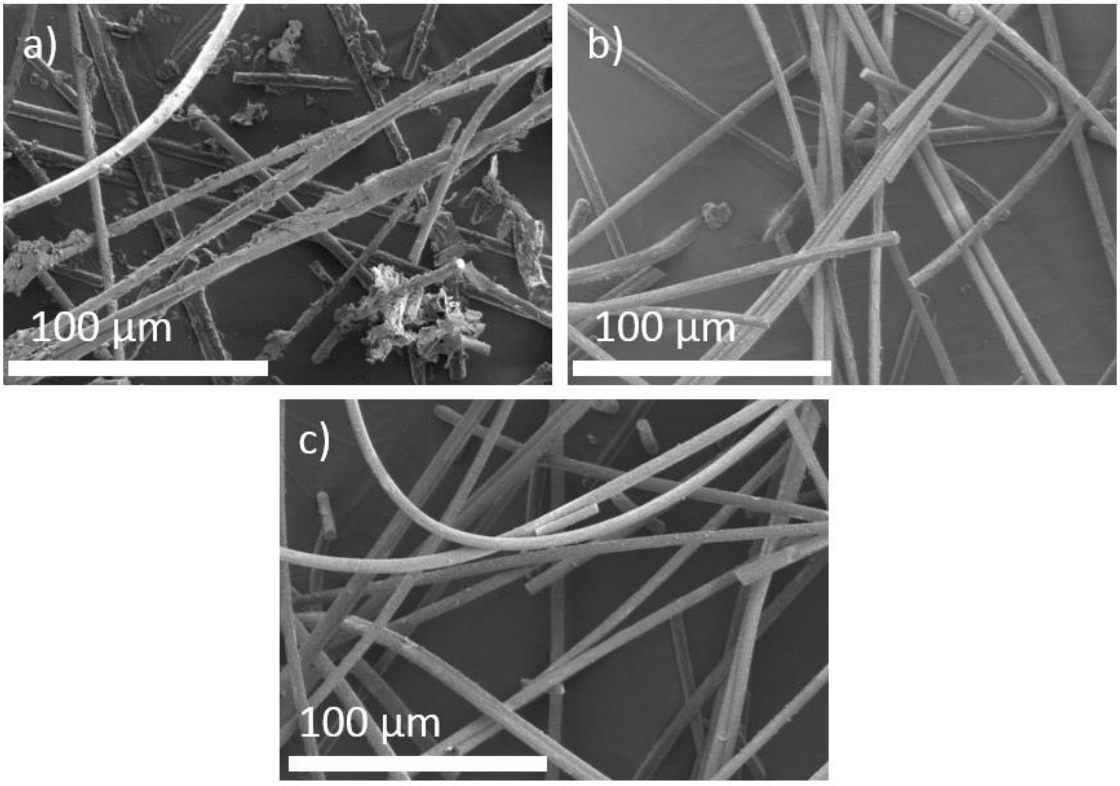

Figure 4.6: SEM images of 18Ni Sf-WI (a), 18Ni Sf-DP (b), and 18Ni Sf-HT (c) showing macro-distribution of deposited phases

All Sf-WI OCs exhibited erratic deposition of metal oxides both locally on each fibre and globally between different fibres (Figure 4.6a). Some fibres were completely covered in a thick layer of metal oxides forming micron sized clusters of particles that protruded from the surface coating. Other fibres in the same sample showed very little deposited material with the Sf fibre still clearly visible. This is evident when comparing Figure 4.7a - c to Figure 4.7d – f (overleaf).

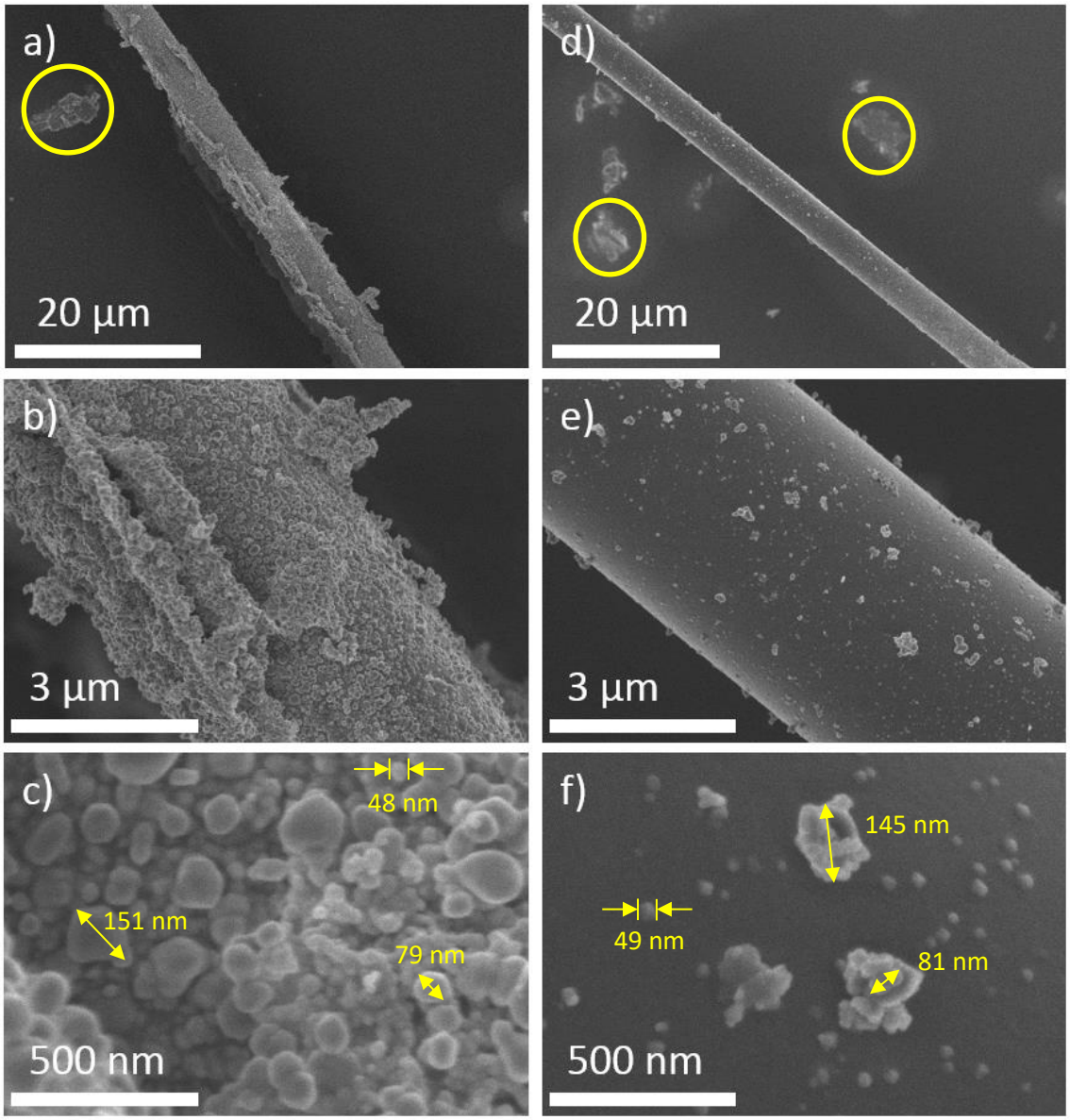

Figure 4.7: SEM images of 18Ni Sf-WI with a heavy coating (a, b and c) and light coating (d, e and f)

Additionally, there were far more cases of large unsupported aggregates of the deposited metal oxides present in the Sf-WI samples (as highlighted in Figure 4.7a and b) when compared to the Sf-DP or Sf-HT samples. The morphology of the deposited material across all the Sf-WI OCs was predominantly round nodular particles; these particles may consist of individual crystals or several crystals compacted together.

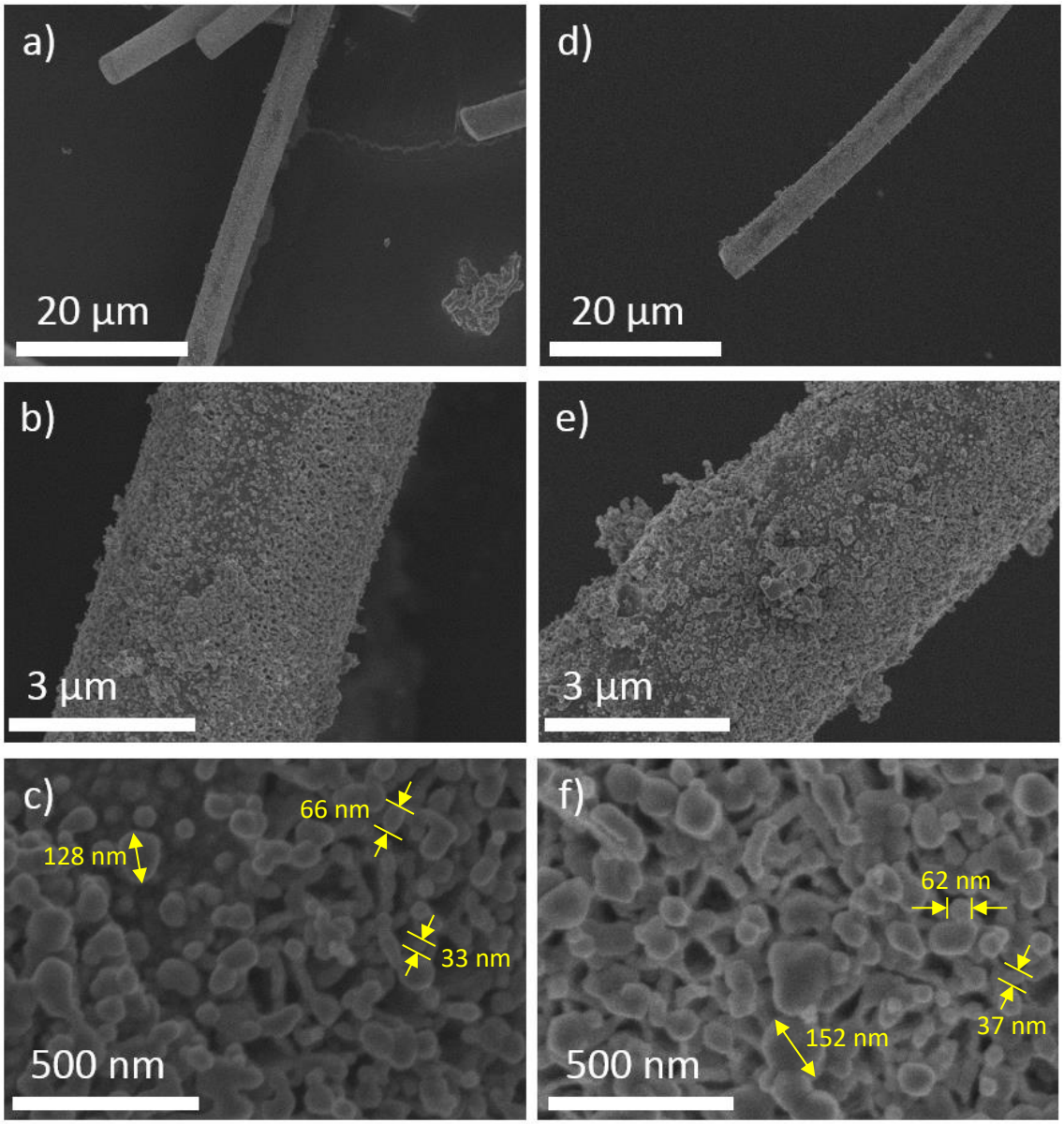

Figure 4.8: SEM images of 0.6Co 18Ni Sf-WI (a, b and c) and 1.8Co 18Ni Sf-WI (d, e and f)

Comparing Figure 4.7 and Figure 4.8, there appeared to be some differences in the particle size of the deposited coating when comparing the 18Ni Sf-WI samples to those doped with Co. To test this hypothesis, 100 measurements were of the maximum diameter particle diameters identified in Figure 4.7 and Figure 4.8 and the results shown in Table 4.3. From this data, there is a slight reduction in the mean particle size when the 18Ni Sf-WI and Co doped samples are compared. However, this data presents a large standard deviation presenting further evidence of erratic distribution and particle size and possibly crystallite size of the deposited layer in the Sf-WI samples.

Table 4.3: Comparison of particle size (a) in the Sf-WI OC's and void size(c) in the Sf-DP and Sf-HT OC's measured in SEM

	Particle Size[a,b] (nm)			Void Size[b,c] (nm)					
	18Ni Sf-WI	0.6Co 18Ni Sf-WI	1.8Co 18Ni Sf-WI	18Ni Sf-DP	0.6Co 18Ni Sf-DP	1.8Co 18Ni Sf-DP	18Ni Sf-HT	0.6Co 18Ni Sf-HT	1.8Co 18Ni Sf-HT
Mean	80	60	60	196	183	167	175	180	125
SD	29	19	23	47	85	60	51	46	32
Max	169	141	146	437	410	323	334	290	272
Min	38	32	22	100	62	45	85	92	62

[a] Where particle size refers to the maximum diameter of particles identified in SEM images. [b]Based on 100 measurements via ImageJ. [c] Where void size refers to the maximum diameter of inter-ridge voids identified in SEM images.

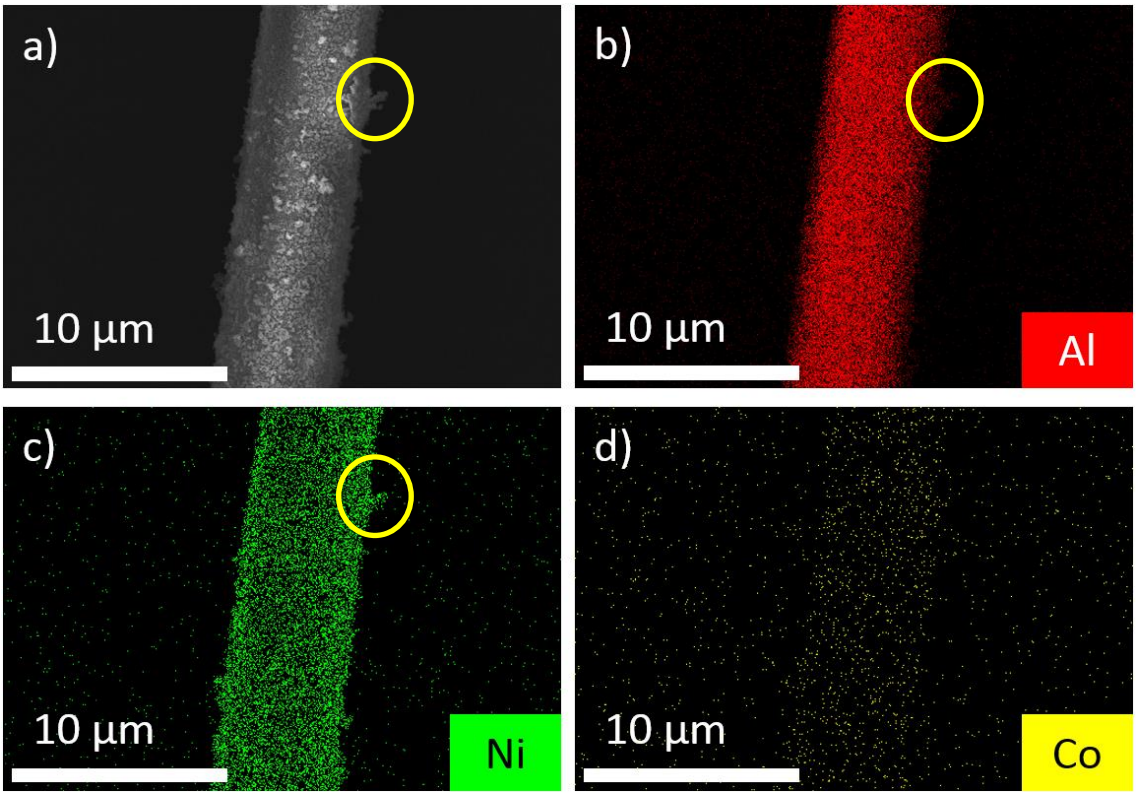

Figure 4.9: SEM images of 1.8Co 18Ni Sf-WI (a) and accompanying EDX maps showing Al (b) Ni (c) and Co (d)

Figure 4.9 shows that the coating of nodular particles deposited upon the fibres in the 1.8Co 18Ni Sf-WI sample consist of both Ni and Co oxides; this, coupled with XRD data, confirms that the deposited layer of nodular crystals identified in Figure 4.7 was NiO and those identified in Figure 4.8 consist of and NiO and likely CoO/Co_3O_4. The protrusions of large clusters of particles from the surface of the fibre identified in Figure 4.7a-c (circled) were also seen in Figure 4.9a. These protrusions were also seen in the Ni and Al EDX maps shown in Figure 4.9c and Figure 4.9b indicating that Al was present in the deposited metal oxide layer. This could suggest dissolution of Al into the deposited layer and therefore was

investigated further using TEM/EDX where higher resolution analysis could be conducted (Section 4.4).

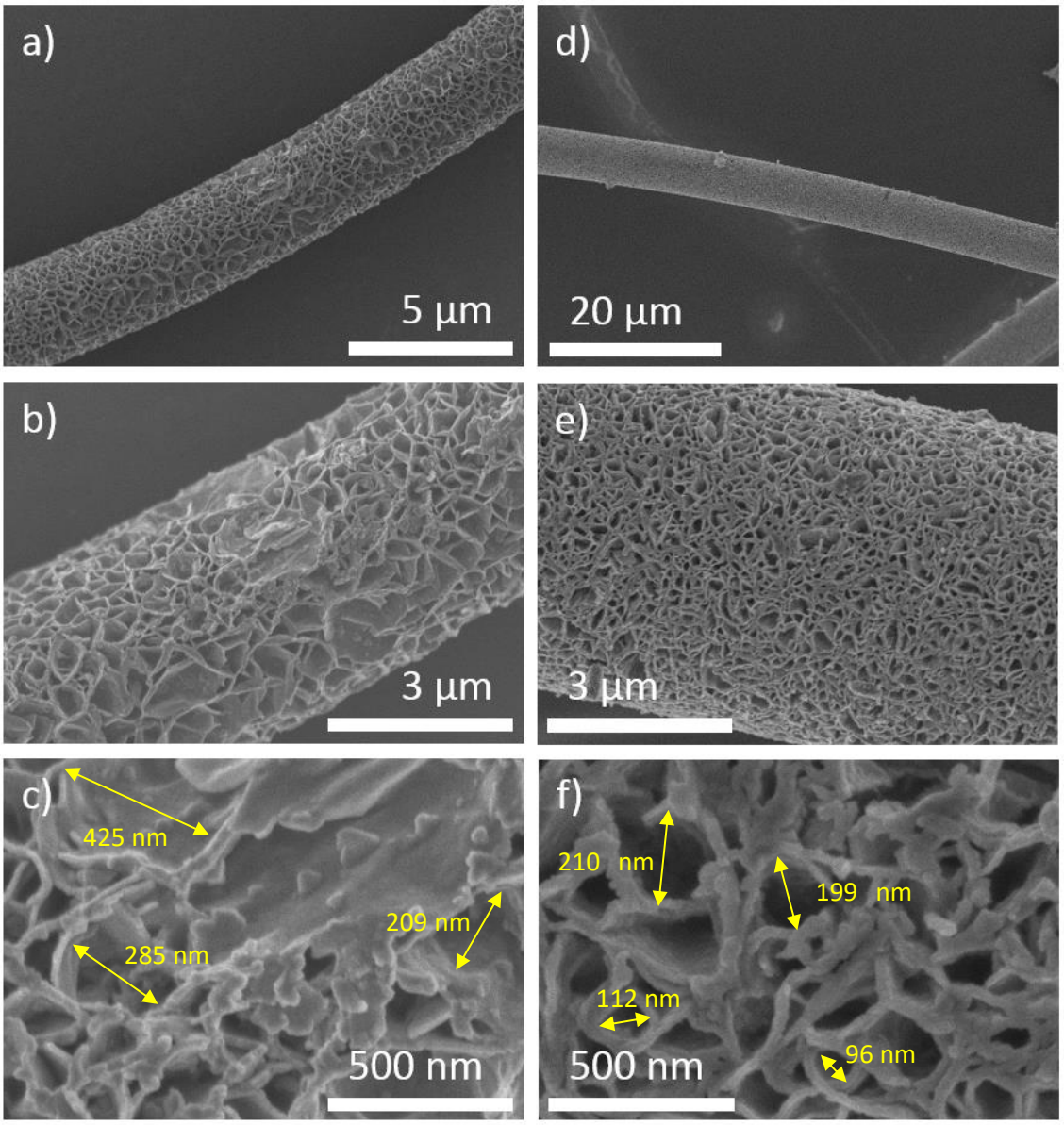

Figure 4.10: SEM images of 18Ni Sf-DP (a, b and c) and 0.6Co 18Ni Sf-DP (d, e and f)

The Sf-DP OCs exhibit a very different morphology of deposited metal oxide. The metal oxide coating was formed from a series of folded layers, possibly representing a series of interconnected platelet crystallites, with edges normal to the surface of the fibres. Thus, a network of folded 'ridges' with solid walls framing void spaces was formed. The ridges present appear to be thin laterally, < 100 nm in thickness, and were assembled in a coiled manner to create a porous structure with ≤ 500 nm lateral void dimensions as shown in Figure 4.10 a-f and Figure 4.11a-c. Another distinct difference is the distribution of the metal oxide over the Sf fibres. In all the Sf-DP OC's the deposition was largely homogeneous with little or no evidence of uncoated fibres, Figure 4.6b.

Co doping in the Sf-DP samples again had a slight effect upon the morphology of the deposited material. Co doping caused the ridges of deposited material to become closer knit thereby reducing the void size of the deposited layer. This effect is noticeable when comparing the images of the 0.6Co 18Ni Sf-DP and 1.8Co 18Ni Sf-DP OCs (Figure 4.10d-f and Figure 4.11a-c) and the 18Ni Sf-DP OC (Figure 4.10a-c). To further examine this effect, 100 measurements of the void sizes of each sample were conducted (Table 4.3). Despite a large standard deviation in the void size data, this shows that Co doping slightly reduced the average void size of the deposited metal oxide.

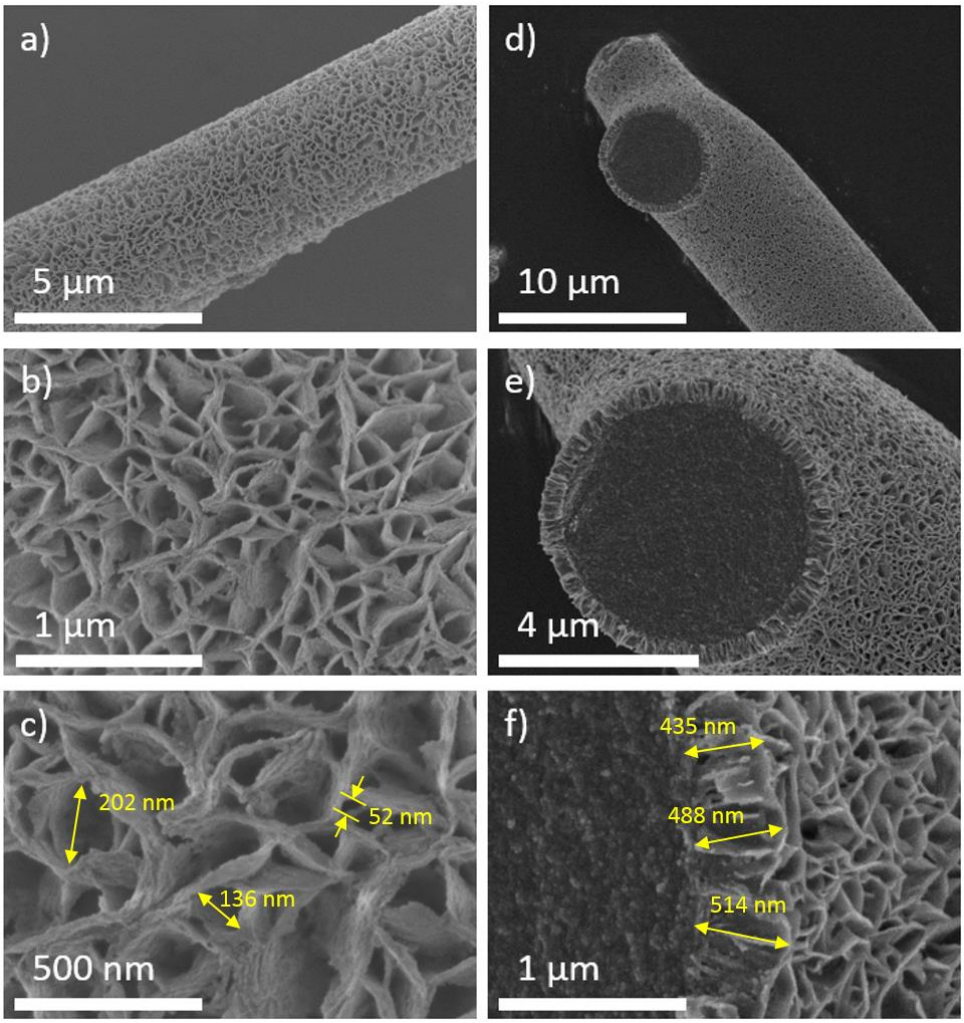

Figure 4.11: SEM images of 1.8Co 18Ni Sf-DP (a, b and c) and a cross section of 1.8Co 18Ni Sf-DP (d, e and f)

Figure 4.11d-f shows an SEM cross section of a 1.8Co 18Ni Sf-DP fibre in which the metal oxide layer varies between ~ 300 nm and 600 nm in thickness with a mean of ~ 400 nm (based on 100 measurements). The ridge structure extends from the outer surface to the fibre-coating interface indicating a progressive growth of the metal oxide layer perpendicular to the fibre surface. The EDX maps shown in Figure 4.12 (below) show this

best in that the deposited predominantly Ni layer and the exposed predominantly Sf fibres are clearly visible in the EDX maps.

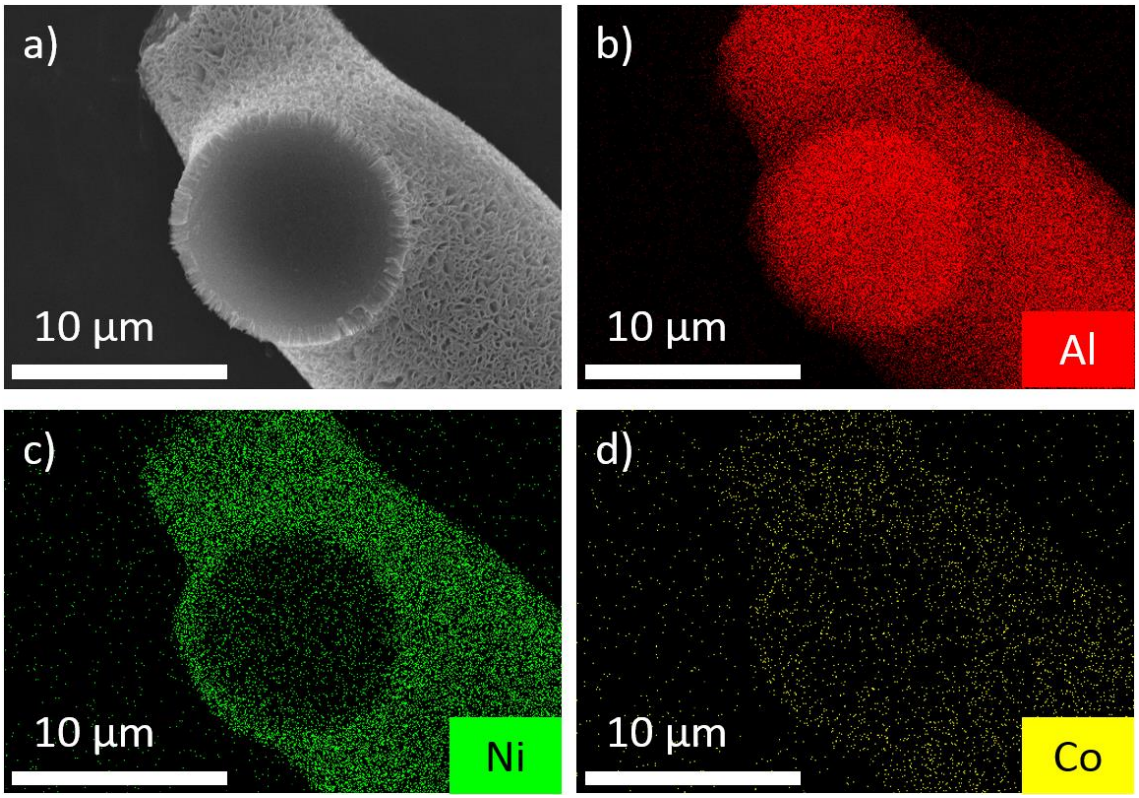

Figure 4.12: SEM images of 1.8Co 18Ni Sf-DP (a) and accompanying EDX maps showing Al (b) Ni (c) and Co (d)

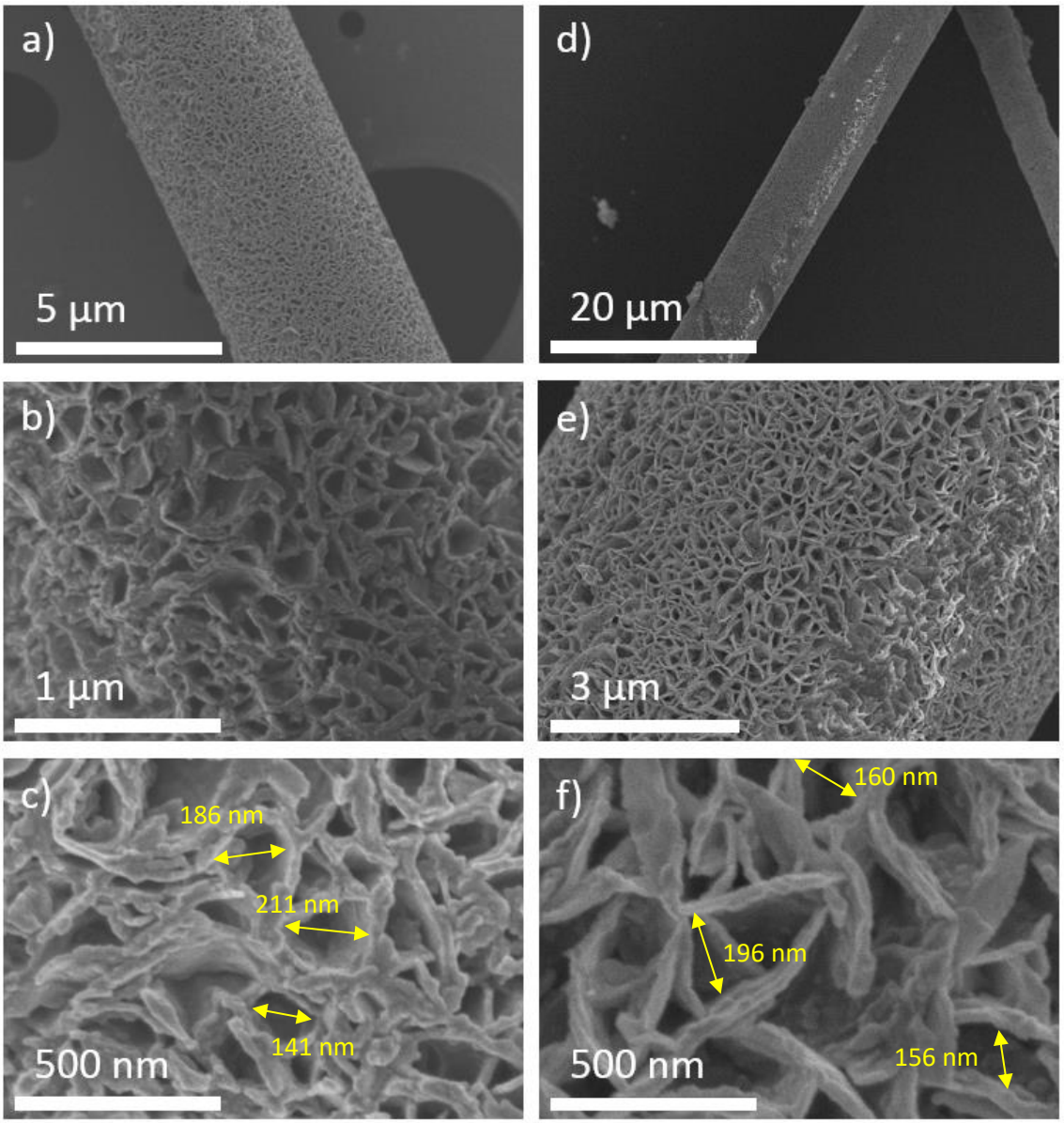

Figure 4.13: SEM images of 18Ni Sf-HT (a, b and c) and a cross section of 0.6Co 18Ni Sf-HT (d, e and f)

The morphology of the Sf-HT OCs is similar to the Sf-DP OC's with the deposited material arrayed in a layered honeycomb structure of ridges and voids. The Sf-HT OC's did not produce OCs with substantially different void diameters when compared to the Sf-DP OC's. Again, Co doping was found to slightly reduce the void volume (Table 4.3). The Sf-HT OC's also provided the most homogeneous distribution of the active metal upon the fibres (Figure 4.6c). This was true even on inspection of the different samples by the naked eye; the deposition of the green nickel oxide phase upon the white fibre was more uniform in the Sf-HT sample when compared to the Sf-DP and Sf-WI samples.

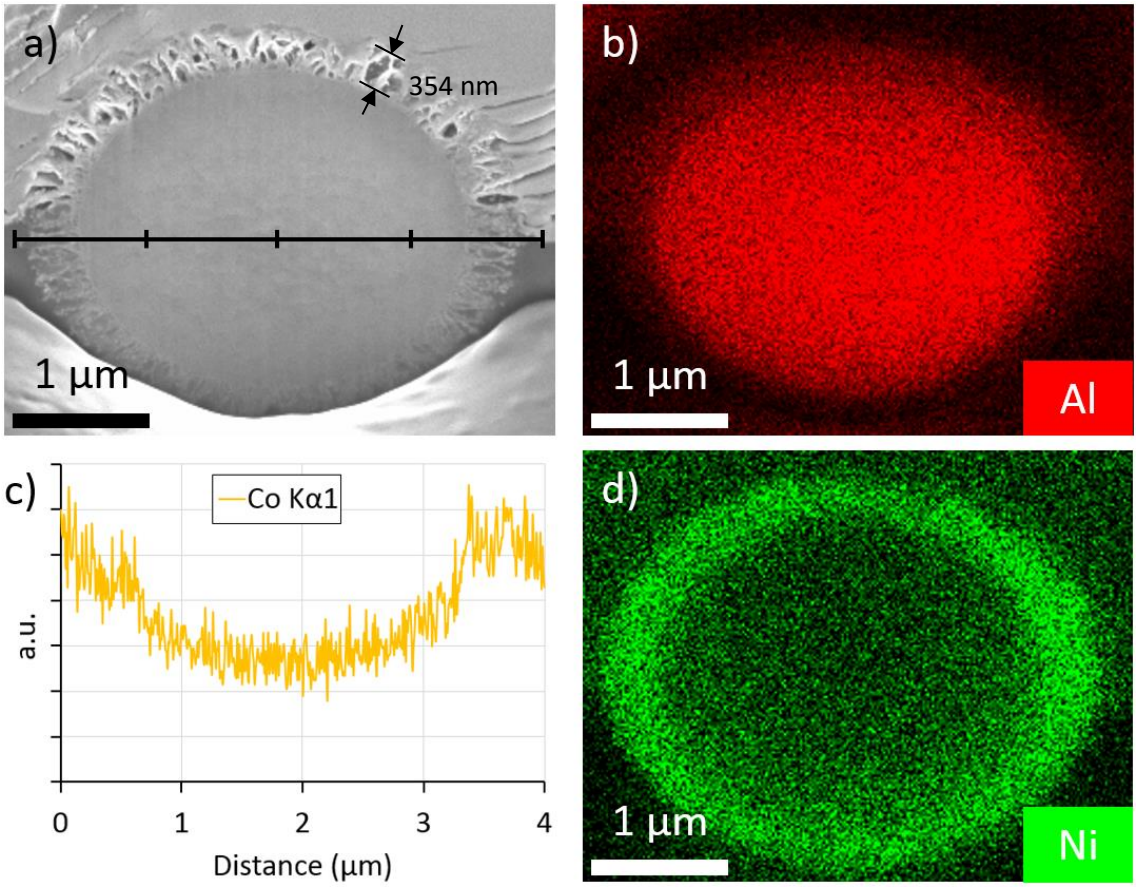

Figure 4.14: SEM images of 1.8Co 18Ni Sf-HT with line scan shown (a) and accompanying EDX maps showing Al (b) Ni (d) and Co spectra corresponding to the line scan (c)

Figure 4.14a shows a 1.8Co 18Ni Sf-HT sample cross section prepared using FIB/SEM; the depth of the deposited layer shown in this cross section measured on average ~ 350 nm (based on 100 measurements). The Al and Ni EDX maps shown in Figure 4.14b and d again show a high concentration of Ni in the deposited layer however the concentration of Al around the edge of the fibre is far less defined; this again shows evidence of Al permeation of the deposited layer. Additionally the EDX spectra (Figure 4.14c) from the line scan shown in Figure 4.14a shows that the concentration of cobalt noticeably increases in the deposited layer in spite of the low Co loading producing a noisy spectra.

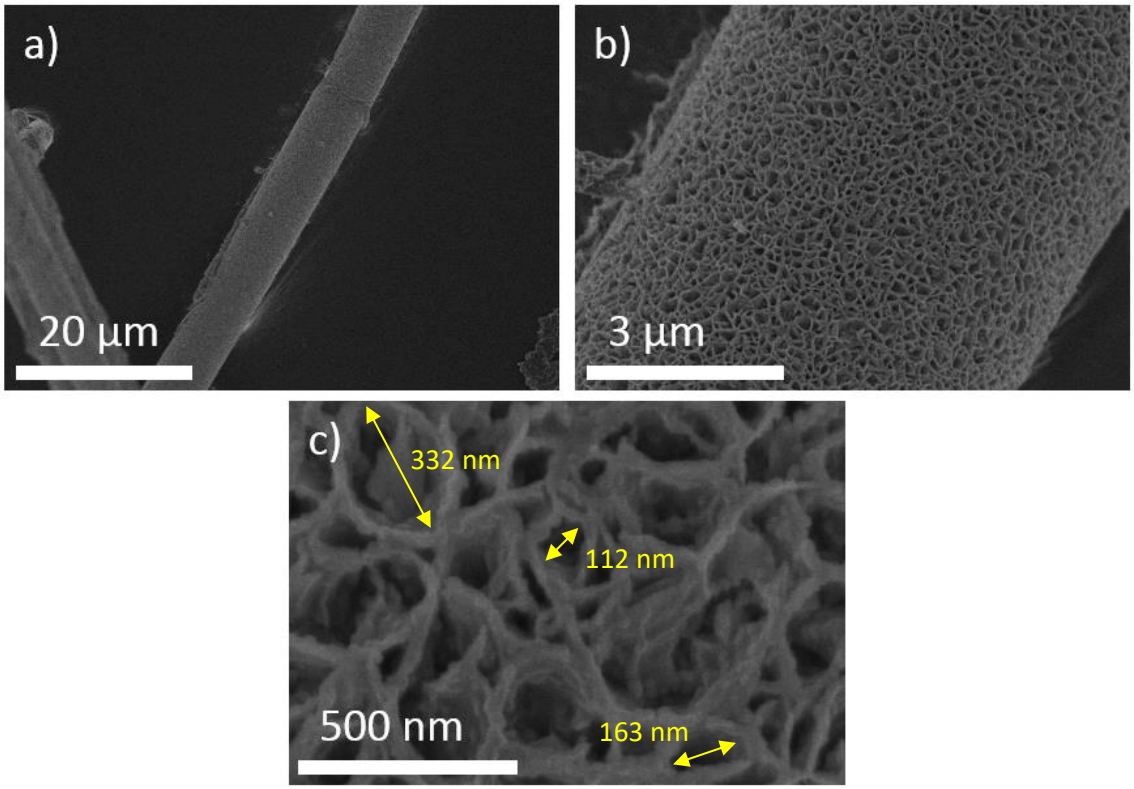

Figure 4.15: SEM images of 1.8Co 18Ni Sf-HT (a, b and c)

Images of the fresh 18NiO GR OC are shown in Figure A.1.1a (Appendix A.1), and exhibit granule sizes of approximately 200 µm, well within the intended range. Figure A.1.2b shows that the granules consist of interconnected clusters measuring between 500 – 2000 nm; these clusters form a close-knit porosity in the granules. Figure A.1.2c shows clear evidence of smaller isolated particles (50 - 150 nm) deposited upon these large clusters. SEM/EDX (as shown in Figure A.1.4) confirmed that the larger clusters contain high concentrations of Al while the smaller particles contain a high concentration of Ni; this suggests that the larger clusters consist of α-Al_2O_3 while the smaller isolated particles consist of NiO. This suggests that the Ni content of the 18NiO GR OC is distributed upon the clusters of α-Al_2O_3 throughout the porous structure of the large (~ 200 µm) granule; this contrasts sharply to the Sf-OC's where the vast majority of the Ni content of the Sf-OC's is deposited in a deposited layer less than 500 nm deep.

4.4 Crystal Size, Phase and Elemental Analysis

Transmission electron microscopy (TEM) was used to analyse the size of the crystals in the CG Saffil® support and the deposited Ni/Co oxide layer identified in the Sf-OC's via SEM, confirm the crystalline phases identified in XRD, and to confirm the presence of Ni and Co in the deposited layer.

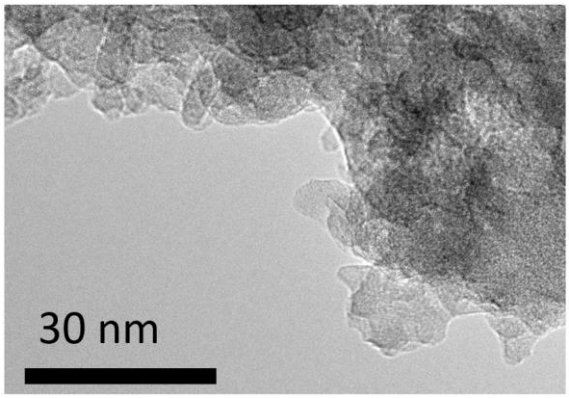

Figure 4.16: TEM image of the raw Saffil® fibres

TEM imaging in Figure 4.16 shows the crystal sizes of the support are approximately 4-6 nm in diameter. This evidence agrees with the crystallite size found via Scherrer analysis, Table 4.1.

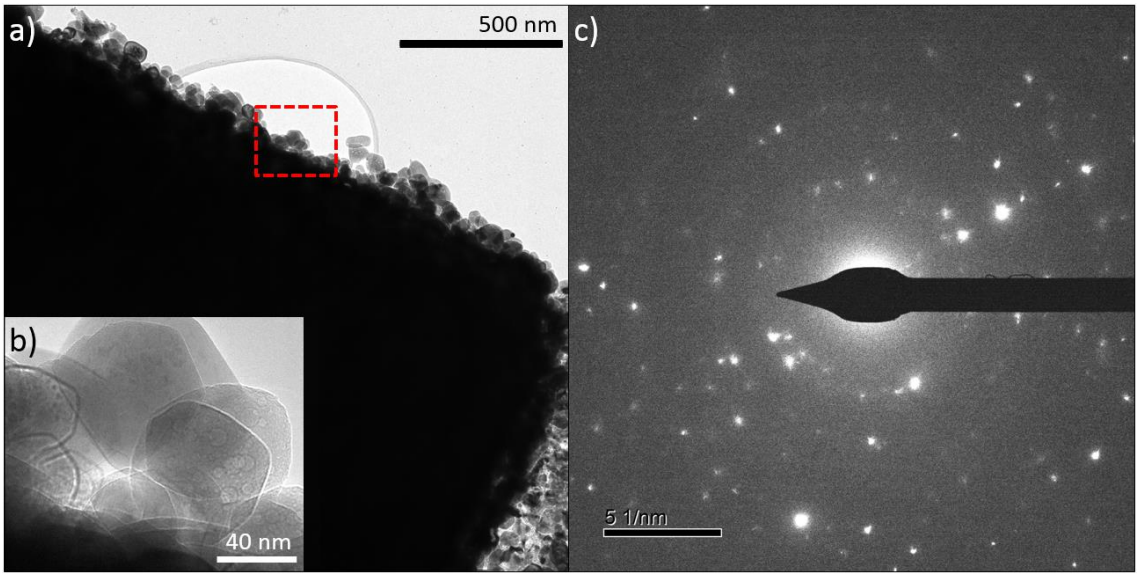

Figure 4.17: TEM images (a and b), and selected area electron diffraction (SAED) pattern (c) of the 18Ni Sf-WI sample

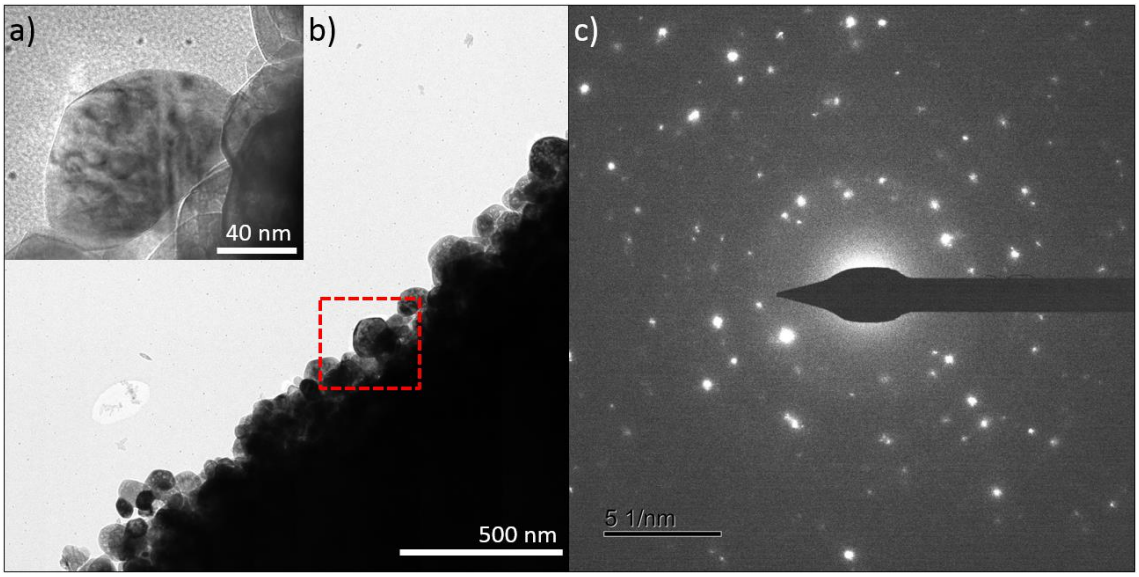

Figure 4.18: TEM images (a and b), and SAED pattern (c) of the 1.8Co 18Ni Sf-WI sample

The 18Ni Sf-WI sample shown in Figure 4.17a and b exhibits round, nodular crystals similar in size and shape to the forms observed in SEM images (Figure 4.7 and Figure 4.8). The TEM image and the almost total lack of rings present in the selected area electron diffraction (SAED) pattern in Figure 4.17b suggests that the particles seen in the SEM images are predominantly single crystallites. This morphology of crystal and evidence for the prevalence of single crystallite particles was replicated in the 1.8Co 18Ni Sf-WI sample shown in Figure 4.18a and b.

Table 4.4: Comparison of crystallite size[(a)] as measured in TEM

Crystallite Size[(a,b)] (nm)	18Ni Sf-WI	1.8Co 18Ni Sf-WI	18Ni Sf-DP	0.6Co 18Ni Sf-HT	1.8Co 18Ni Sf-HT
Mean	40.2	58.0	5.0	9.1	9.9
SD	14.6	29.8	1.6	2.5	2.7
Min	13.1	14.9	2.1	5.0	5.6
Max	93.3	141.7	10.0	15.9	26.1

[(a)] Where crystal size refers to the maximum diameter identified in TEM images. [(b)]Based on 100 measurements via ImageJ

Table 4.4 shows that the crystallite size as determined by TEM analysis (and Scherrer analysis of XRD, Table 4.1) for the 18Ni Sf-WI sample is slightly smaller than the average particle size as determined by SEM analysis. This suggests that although most of the particles exhibited in the SEM images likely consist of single crystallites, there are likely some polycrystalline particles present; this is corroborated by the very faint rings present in the SAED pattern in Figure 4.17b.

The crystallite size of the 1.8Co 18Ni Sf-WI sample as identified by TEM, has excellent agreement with the SEM data for the 0.6Co and 1.8Co WI samples implying that for the regions analysed, the nodules present likely consist of single crystallites. This is corroborated by the lack of rings in the SAED pattern shown in Figure 4.18. However, the disagreement in crystallite sizes between the Scherrer analysis (bulk) and TEM (localised) combined with high standard deviations of the TEM crystallite sizes could suggest further evidence of inconsistent distribution of the deposited layer.

The variability in coating integrity, crystallite sizes and formation of unsupported aggregates of Ni/Co oxide is typical of a wet impregnation synthesis method. WI relies upon the evaporation of a solvent (H_2O) to cause a series of precipitation steps thereby depositing a metal salt ($Ni/Co(NO_3)_2$) upon the support. During evaporation the volume of solution gradually reduces thereby forming individual droplets of solution. As this evaporation can occur quickly relative to diffusion of the dissolved salt through the solvent, each droplet may possess different solute concentrations. If these droplets form upon the surface of the fibre, a coating of the salt will be deposited upon the fibre the thickness of which is dependent on the concentration of the salt in these droplets; this leads to the differences in the macrodistribution of the deposited Ni/Co oxides exhibited in Figure 4.7, Figure 4.8 and Figure 4.9. Furthermore, if these droplets are not formed on the surface of the fibre, unsupported aggregates can be formed.

Precipitation through evaporation also influences the microdistribution (i.e. distribution over each fibre) of the deposited Ni/Co salts. The precipitation process can be mass transfer limited by the size of the pores on the support; precipitation can occur at different rates not only between the pores and the surface of the support but also between pores of differing sizes. These factors combine to result in non-uniform distributions of the metal oxides locally over each fibre[220].

The TEM images of the Sf-DP sample (Figure 4.19a and b, overleaf) indicated a ridged coating as evidenced by the SEM images of the same sample (Figure 4.10a, b and c). The same ridged coating was shown in the TEM images of the Sf-HT OC's shown in Figure 4.20a and b and Figure 4.21a and b. Table 4.4 shows component primary crystallite sizes are in agreement with the XRD peak broadening analysis with a smaller standard deviation than in the Sf-WI samples. This agreement between the crystallite size as measured in TEM (Table 4.4) and XRD (Table 4.2) is also shown in the 0.6Co 18Ni Sf-HT and 1.8Co 18Ni Sf-HT samples. Furthermore, the SAED patterns for the Sf-DP and Sf-HT show very clear rings indicating that the ridges consist of a polycrystalline material.

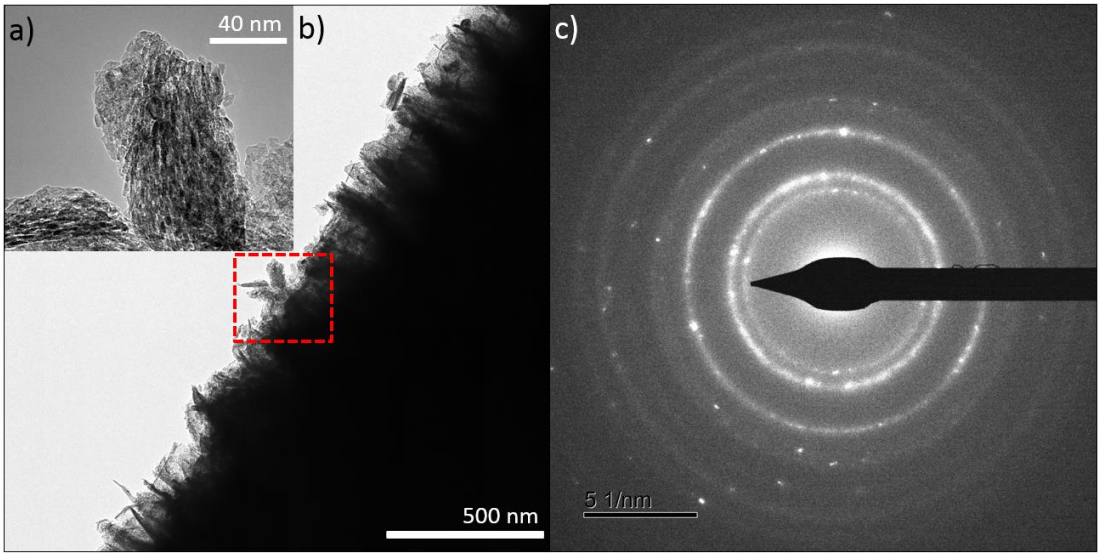

Figure 4.19: TEM images (a and b), and SAED pattern (c) of the 18Ni Sf-DP sample

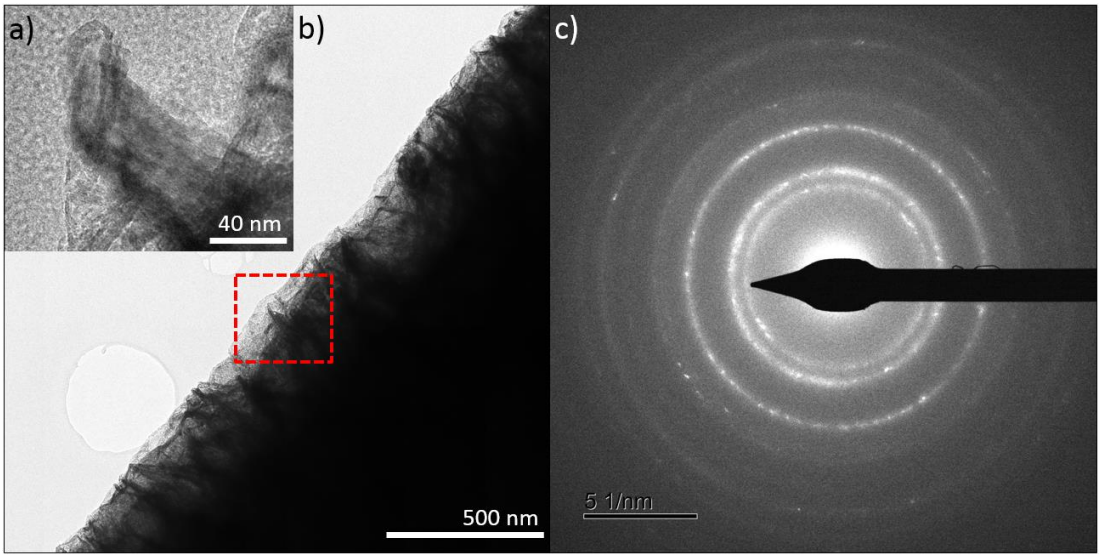

Figure 4.20: TEM images (a and b), and SAED pattern (c) of the 0.6Co 18Ni Sf-HT sample

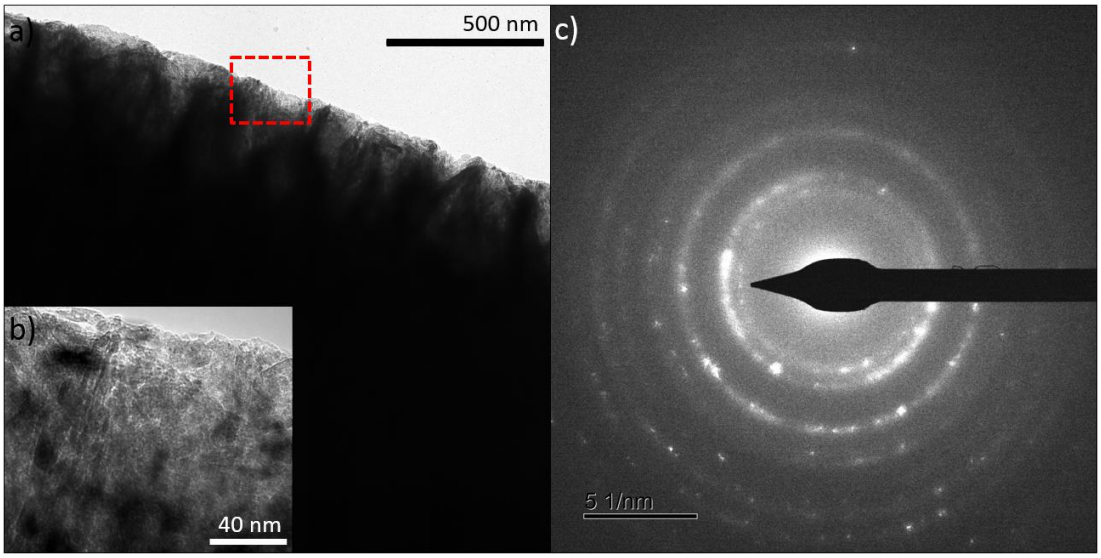

Figure 4.21: TEM images (a and b), and SAED pattern (c) of the 1.8Co 18Ni Sf-HT sample

SAED patterns shown in Figure 4.17 to Figure 4.21 analyse the crystal phases present in the smaller areas analysed by TEM in order to compare them to the bulk phase data as analysed by XRD. Further SAED ring data can be found in Table A.2.1 (Appendix A.2).

Table 4.5: D-spacing (nm) of the SAED rings identified in TEM

Rings	SAED d-spacing (nm)					XRD phase d-spacing (nm)				
	18Ni Sf-WI	1.8Co 18Ni Sf-WI	18Ni Sf-DP	0.6Co 18Ni Sf-HT	1.8Co 18Ni Sf-HT	α-Al_2O_3	γ-Al_2O_3	NiO	$NiAl_2O_4$	Co_3O_4
1	0.253	0.250	0.248	0.251	0.251	0.255	-	0.241	0.243	0.244
2	0.218	0.213	0.215	0.213	0.217	0.217	0.228	0.209	-	0.233
3	0.153	0.153	0.151	0.151	0.152	0.152	0.152	-	0.155	0.156
4	0.142	0.130	0.127	-	0.140	0.134	-	0.126	-	0.128
5	0.128	0.125	0.124	0.125	0.126	0.123	-	0.126	-	0.123
6	0.104	0.107	-	-	0.107	0.110	-		-	0.108
7	0.097	0.096	0.097	0.095	0.097	-	-	0.096	-	0.099
8	0.089	0.088	0.087	-	0.089	-	0.088		-	0.089

Measurement of the concentric rings identified in TEM allows the d-spacings of the phases present in the sample to be evaluated, Table 4.5; however the diameter of the rings is sensitive to the height of the specimen and to magnetic hysteresis of the TEM lenses and as such each ring measured in SAED was compared to d-spacings of phases identified in XRD with a 10% tolerance[209,210]. Table 4.5 shows that almost all the d-spacings found via SAED can be matched to those present in the XRD phase references found during XRD analysis. This suggests that there is very little difference between the bulk material analysed by XRD and the localised areas analysed by electron diffraction. Importantly there was no clear evidence for the presence of $NiAl_2O_4$ in SAED, but future analysis of the interface would be required to establish if any localised interfacial reactions occur.

The corresponding HAADF STEM images (Figure 4.22a - Figure 4.26a) and EDX maps (Figure 4.22 b, c and d - Figure 4.26b, c and d) for the TEM images confirm a surface layer containing Ni and or cobalt in all samples (overleaf). EDX also allowed the location of the fibre to be approximated (white and black arrows inset); from this the depth of Ni/Co oxide coating could be approximated. The 18Ni Sf-WI and 1.8Co 18Ni Sf-WI samples indicated a deposited layer of < 200 nm. The Sf-DP and Sf-HT samples indicated a coating depth of 270 nm and 350 nm respectively; this agreed with the evidence presented in SEM and FIB/SEM analysis shown in Figure 4.11d, e and f and Figure 4.14.

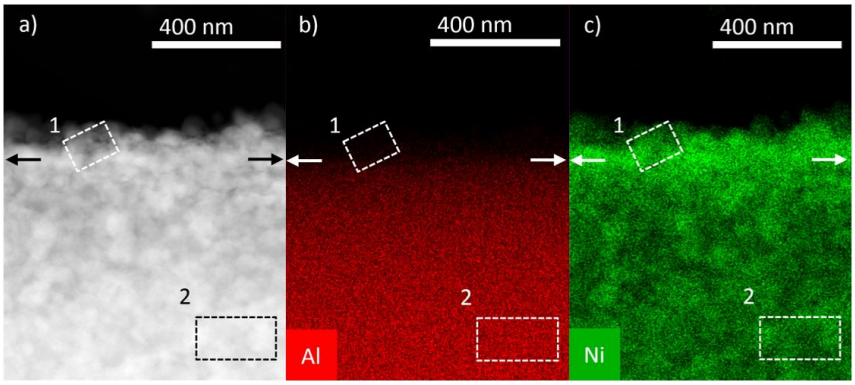

Figure 4.22: HAADF image (a) and EDX mapping of Al (b) and Ni (c) of the 18Ni Sf-WI sample with highlighted areas showing the location of semi-quantitative analysis

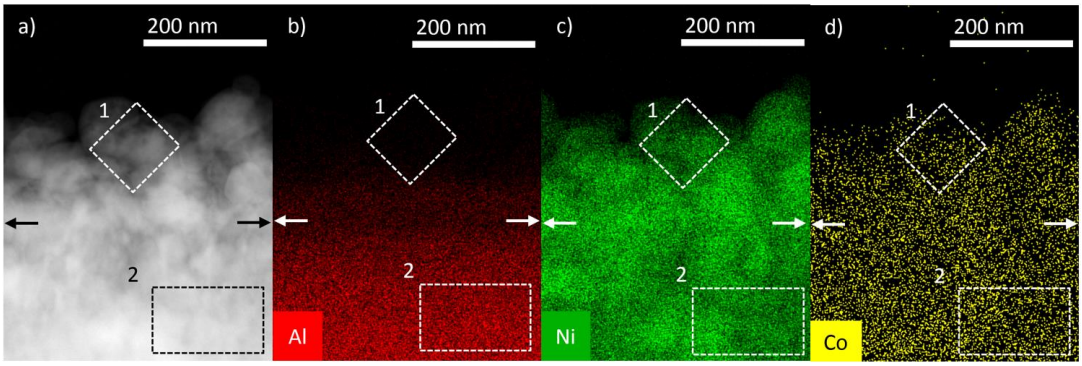

Figure 4.23: HAADF image (a) and EDX mapping of Al (b) Ni (c) and Co (d) of the 1.8Co 18Ni Sf-WI sample

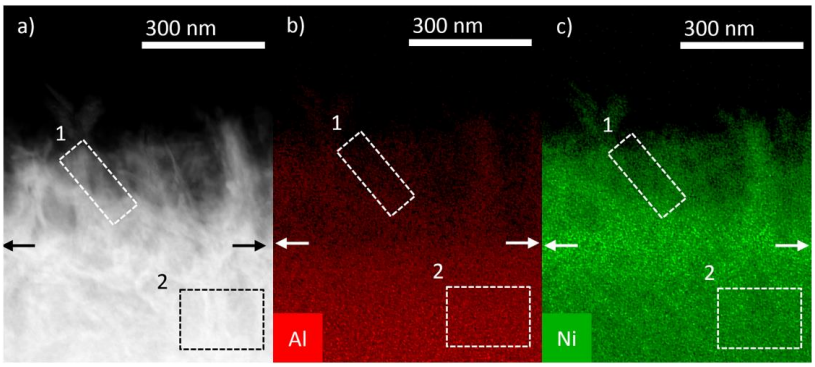

Figure 4.24: HAADF image (a) and EDX mapping of Al (b) and Ni (c) of the 18Ni Sf-DP sample

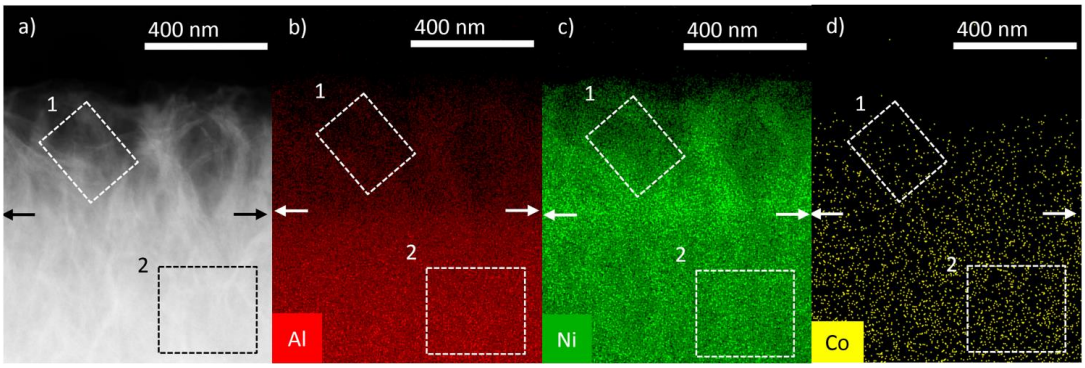

Figure 4.25: HAADF image (a) and EDX mapping of Al (b) Ni (c) and Co (d) of the 0.6Co 18Ni Sf-HT sample

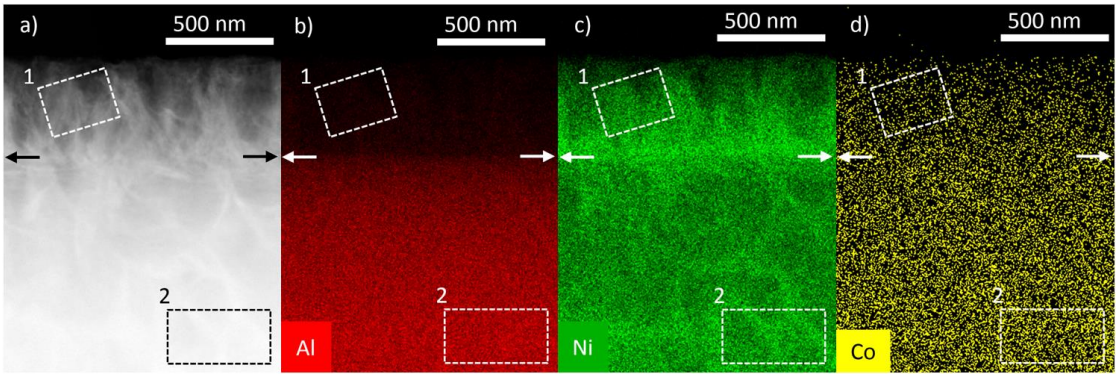

Figure 4.26: HAADF image (a) and EDX mapping of Al (b) Ni (c) and Co (d) of the 1.8Co 18Ni Sf-HT sample

The EDX maps also show that there is aluminium in the deposited layer of all the samples and indicate that there is a greater proportion of aluminium in this layer in the Sf-DP and Sf-HT samples when compared to the Sf-WI sample.

Table 4.6: Semi-quantitative elemental analysis of EDX maps

Sample	Area 1[(a)]			Area 2[(a)]		
	Al (wt%)	Co (wt%)	Ni (wt%)	Al (wt%)	Co (wt%)	Ni (wt%)
18Ni Sf-WI	15	-	85	72	-	28
1.8Co 18Ni Sf-WI	6	1	93	58	1	41
18Ni Sf-DP	28	-	72	69	-	31
0.6Co 18Ni Sf-HT	35	0	65	72	0	28
1.8Co 18Ni Sf-HT	33	1	66	76	1	23

[(a)] Where Area 1 and 2 refer to the highlighted areas in

Table 4.6, shows the semi-quantitative analysis of Areas 1 and 2 in shown Figure 4.23 to Figure 4.26 (For the corresponding EDX spectra see Appendix A.3). The quantity of Al in the deposited layer (Area 1) increases from Sf-WI to Sf-DP and from Sf-DP to Sf-HT. The presence of Al in the deposited layer of the Sf OC's suggests some form interaction between the Ni/Co oxide layer and the Saffil® support.

As discussed in Section 2.3.2, any metal support interactions observed in Ni/Al_2O_3 OC's are typically attributed to the solid state interaction between NiO and Al_2O_3 as initially proposed by Bolt et al.[118] They suggested that the movement of Ni^{2+} and Al^{3+} ions into the first few monolayers of the Al_2O_3 and NiO phases respectively at high temperatures (in excess of 600 °C[148]) results in the formation of an effectively two-dimensional "surface spinel"; this compound, which is reportedly similar in composition to bulk $NiAl_2O_4$ but lacks sufficient crystallite size or long range three-dimensional order to be detectable by XRD, may then grow out to create bulk $NiAl_2O_4$ at temperatures above 800 °C[118].

As formation of bulk $NiAl_2O_4$ has been ruled out via XRD, formation of "surface spinel" might explain the presence of Al in the deposited NiO layer, but does not explain the

distance of the Al from the surface of the support (tens of nanometres compared to 0.1 - 0.4 nm in the work of Lo Jacano et al.[147]) nor the differences in concentration of the Al in the Sf-WI, Sf-DP and Sf-HT samples. The study of Bolt et al.[118] used vacuum vapour deposition to deposit a layer of Ni directly to γ-Al_2O_3 and α-Al_2O_3 supports which were then calcined to produce NiO; their study therefore neglects the possibility of liquid phase interactions occurring during the typical OC synthesis methodologies such as Sf-WI or Sf-DP.

The presence of varying levels of Al in the deposited layer of the Sf OC's could be explained by possible dissolution of alumina during synthesis. Espinose et al.[221] reported that addition of nickel and cobalt nitrate to water can increase the dissolution of a pure powdered γ-Al_2O_3 support by three orders of magnitude when compared to water at neutral pH. This is thought to be caused by three phenomena occurring simultaneously at the support/solution interface. The adsorption of Ni^{2+} and Co^{2+} ions first occurs on to the alumina support as per traditional site binding models. This promotes the kinetically limited dissolution of Al^{3+} ions from the alumina support, which in turn causes coprecipitation of the Ni^{2+} or Co^{2+} ions with the dissolved Al^{3+} ions.[221] Similarly, dissolution of γ-Al_2O_3 to form Al^{3+} ions in Ni precursor solutions was found in the work of Mieth and Schwarz[222]. The Sf fibres were only in contact with the precursor solution for a limited amount of time in the WI method (i.e. until the precursor solution has evaporated) at atmospheric pressure, thereby severely limiting this dissolution effect. Contrast this with the DP and HT synthesis methods where the Sf fibres were in contact with the more basic precursor solution for far longer, dissolution would be significantly increased. Furthermore, the elevated pressures utilised in the HT method would further increase this dissolution effect thereby increasing the proportion of Al in the deposited layer.

The involvement of an increased number of Al^{3+} ions in the precipitation process may promote layered double hydroxide (LDH) intermediates of the type $[M_{1-x}^{2+}M_x^{3+}(OH)_2]^{x+}[A_{x/n}]^{n-}\cdot mH_2O$ where M^{3+} = Al and M^{2+} = Ni/ Co which lead to the distinctive folded layer morphology of the transition metal coatings of DP and HT oxygen carriers. The formation of these intermediates has been proposed to follow the below procedure[223]:

1) The hydrolysis of urea at elevated temperatures causes a rise in pH as per Equation 2.6.

2) The basic nature of the precursor solution causes a kinetically limited dissolution of Al^{3+} ions in the form of $[Al(OH)_4]^-$ from the alumina support. This reaction occurs simultaneously with the formation and nucleation of the of $Ni(OH)_2$ upon the Sf fibre

$$Al_2O_3 + 3H_2O + 2OH^- \rightarrow 2[Al(OH)_4]^-$$ **Equation 4.1**

$$Ni^{2+} + 2OH^- \rightarrow Ni(OH)_2$$ **Equation 4.2**

3) With the aid of carbonate ions formed from the CO_2 evolved in the urea hydrolysis, nuclei of Ni/Co-Al LDH's are formed upon the support through the structural transformation of both the $Ni(OH)_2$ and $Al(OH)_4^-$ complexes.

$$CO_2 + H_2O \rightarrow CO_3^{2-} + 2H^+$$ **Equation 4.3**

$$(1\text{-}x)Ni(OH)_2 + xAl(OH)_4^- + x/2CO_3^{2-} \rightarrow [Ni_{1-x}Al^{3+}_x(OH)_2]^{x+}(CO_3^{-2})_{x/2} + 2xOH^-$$ **Equation 4.4**

4) From these nuclei the nascent LDH's grow rapidly in the direction parallel to the cation/anion layers in the material. This high lateral growth rate of the anisotropic LDH crystals tends to occur perpendicular to the support as this maximises their growth and avoids collisions between growing crystallites.

The above process has produced hexagonal platelets of LDH materials perpendicular to the support in several other conventionally structured Ni γ-Al_2O_3 catalysts[167,223–225]. These morphologies were maintained during the 4 stages of dehydration (Equation 4.5), dihydroxylation (Equation 4.6), decomposition of anions (Equation 4.7) and oxide segregation (Equation 4.8) that occur during drying and calcination to produce NiO[167,223–226]. Although these platelets resemble the ridges shown in Figure 4.10 - Figure 4.15, they have not been shown to produce networks of platelets as evidenced in the above figures, a property that may increase stability of the deposited metal oxide layer over many redox cycles.

$$[Ni_{1-x}Al^{3+}_x(OH)_2]^{x+}(CO_3^{-2})_{x/2} + 2xOH^- \rightarrow [Ni_{1-x}Al^{3+}_x(OH)_2]^{x+}(CO_3^{-2})_{x/2}$$ **Equation 4.5**

$$[Ni_{1-x}Al^{3+}_x(OH)_2]^{x+}(CO_3^{-2})_{x/2} \rightarrow [Ni_{1-x}Al^{3+}_xO]^{x+}(CO_3^{-2})_{x/2}$$ **Equation 4.6**

$$[Ni_{1-x}Al^{3+}_xO]^{x+}(CO_3^{-2})_{x/2} \rightarrow Ni_{1-x}Al^{3+}_xO_{1+x/2}(CO_2)$$ **Equation 4.7**

$$Ni_{1-x}Al^{3+}_xO_{1+x/2}(CO_2) \rightarrow NiO + NiAl_2O_4 + CO_2$$ **Equation 4.8**

Equation 4.8 suggests that if LDH's are formed prior to calcination, then $NiAl_2O_4$ spinel phase will be formed in a 1:1 ratio to NiO. In this system, given the lack of a detectable bulk $NiAl_2O_4$ phase in either XRD or SAED, the production of NiO and $NiAl_2O_4$ in a 1:1 ratio seems unlikely. With NiO being the dominant phase produced (as per XRD) there is likely to be gradual precipitation of other non-soluble phases of nickel and cobalt hydroxide in

addition to LDH formation, especially considering the formation of LDH's will be somewhat limited by the dissolution of the alumina fibres and the provision of Al^{3+} ions.

In any case the formation of amorphous non-soluble nickel and cobalt hydroxides via the decomposition of urea in aqueous solution allows the precursor solution to more completely infiltrate the pore volume of the support and avoid the mass transfer limitations associated with evaporation[46,130]. This allows the avoidance of inconsistent microdistribution of the deposited phase experienced during WI. Moreover, reliance of LDH nucleation and growth upon the dissolution of the alumina fibres increases the probability that the LDH precursor is only formed on the fibre at a more consistent rate across the sample, largely avoiding formation of unsupported aggregates or erratic macrodistribution of the deposited phase. These factors combine to produce a more homogenous distribution of the metal oxide layer onto the Sf fibres after drying and calcination compared to the WI OC's.

4.5 Thermogravimetric Phase Identification

Temperature programmed reduction (TPR) was used to further investigate the degree of interaction between NiO and γ-Al_2O_3 as a result of the synthesis methods used to produce the Sf OC's. There are two clear reduction events, represented by mass loss and a peak in the rate of mass loss (Figure 4.27a and b, overleaf), shown in the TPR of the 18Ni Sf-WI, Sf-DP and Sf-HT samples analysed. The first event occurs at 400 - 415 °C and the second at 680 - 720 °C and as such, neither of these events can be attributed to reduction of bulk NiO (reduction below 300 °C) or $NiAl_2O_4$ (reduction above 800 °C)[138–140].

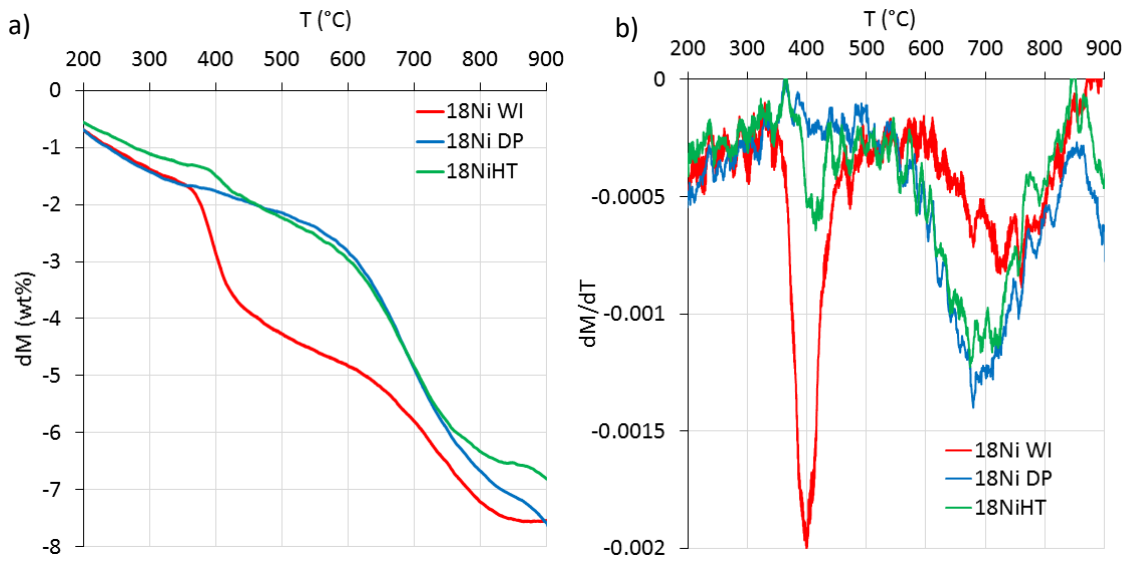

Figure 4.27: TPR profile showing weight loss as a percentage of the original sample mass (a) and the differential of the mass loss with temperature (b)

The reduction event at ~ 400°C is responsible for most of the mass lost during reduction in the Sf-WI OC. This event is attributed to a "weak" interaction between the NiO and γ-Al_2O_3 during synthesis that causes the reduction of the NiO to become less facile, thus increasing the temperature at which it occurs.

In the literature, this "weak" interaction is typically attributed to the formation of an amorphous "surface spinel" of $NiAl_2O_4$, the depth of which is limited by the diffusion of ions possible during calcination[118,138]. The literature on this subject tends to adopt the term "surface spinel" for any solid state interaction between NiO and Al_2O_3 not evidenced by a bulk detectable $NiAl_2O_4$ phase via XRD; the identification of this spinel phase is rarely evidenced with anything other than TPR analysis similar to that shown in Figure 4.27. Considering the lack of any evidence for the formation of a specific surface or bulk $NiAl_2O_4$ phase in this work, the "weak" solid state interaction that dominates the reduction of the Sf-WI OC is attributed simply to a solid-state chemical interaction between the NiO and Al_2O_3 phases.

The reduction event at ~ 700 °C is responsible for most of the mass lost during reduction in the Sf-DP and Sf-HT OC's; this event is attributed to a "strong" interaction between the NiO and γ-Al_2O_3 during synthesis that further increases the temperature at which reduction of the NiO occurs. This stronger interaction is caused by chemical interdiffusion of the dissolved Ni^{2+}/Co^{2+} and Al^{3+} ions facilitated by the dissolution of Al in the precursor solution and subsequent calcination during synthesis, as explained in Section 4.4.

These results show that the DP and HT methods increase the interaction between the NiO and γ-Al_2O_3 over the WI method as per TEM/EDX and that most of the Ni present on the OC's ia able to be reduced at 700 °C.

4.6 Specific Surface Area and Porosity

Physical adsorption of the Saffil® fibres and the Sf-OC's all yield type IV isotherms coupled with type H2 hysteresis loops suggesting the material exhibits non-uniform pores sized between 2 and 100 nm in diameter[227,228] (See Appendix A.4 and A.5). These isotherms were analysed with the BET and BJH adsorption methods. The 18NiO GR OC had a BET surface area of 3.2 g m^{-2} [100].

The specific surface area (SSA) of both the Saffil® fibre and the synthesised OCs are shown in Table 4.7. Clearly the use of the WI synthesis methodology reduces the SSA of the Sf-WI OC material compared to its naked support. When the two other synthesis methodologies are examined, only the 18Ni Sf-DP OC showed an SSA lower than that of the Saffil® fibres; the other five OC's generated by HT and DP routes exhibit a higher SSA than that of the naked Saffil® fibres. The OCs produced via the hydrothermal synthesis route produced the most consistent results with all three OCs showing an SSA more than 115 m^2 g^{-1} of material and varying in SSA by only 5 m^2 g^{-1}. There was no consistent effect from cobalt doping upon the SSA of the OCs.

Table 4.7: BET specific surface area and pore volume and diameter determined by BJH analysis of the desorption and adsorption isotherms

Sample	Multi point BET	BJH Desorption		BJH Adsorption	
	SSA (m^2 g^{-1})	Pore Volume[(a)] (cm^3 g^{-1})	Pore Diameter (nm)	Pore Volume[(a)] (cm^3 g^{-1})	Pore Diameter (nm)
Saffil®	106	0.19	3.4	0.18	4.8
18Ni Sf-WI	75	0.12	3.5	0.12	4.7
0.6Co 18Ni Sf-WI	61	0.11	3.3	0.11	4.4
1.8Co 18Ni Sf-WI	65	0.11	3.4	0.11	4.6
Mean WI	67	0.11	3.4	0.12	4.6
18Ni Sf-DP	102	0.17	3.5	0.16	4.5
0.6Co 18Ni Sf-DP	120	0.19	3.6	0.18	4.5
1.8Co 18Ni Sf-DP	118	0.18	3.6	0.17	4.5
Mean DP	113	0.18	3.5	0.17	4.5
18Ni Sf-HT	117	0.20	3.6	0.20	4.7
0.6Co 18Ni Sf-HT	118	0.20	3.4	0.19	4.5
1.8Co 18Ni Sf-HT	115	0.19	3.7	0.19	4.6
Mean HT	117	0.20	3.6	0.19	4.6

[(a)] Where the cumulative pore volume applies to pores between 1.7 – 300 nm in diameter

The increase in SSA brought about by the Sf-DP and Sf-HT methods may be explained when cross referencing the BET data with the SEM images in Figure 4.11 to Figure 4.15. The ridges and voids formed by the impregnated material could be instrumental in increasing the SSA of the DP and HT produced OCs, certainly the greater coverage of the fibres with this morphology compared to the Sf-WI OC's are believed to have some role in the increased surface area. Moreover the smaller crystallite size of the deposited material in the Sf-DP and Sf-HT OC's as exhibited by Figure 4.19, Figure 4.20 and Figure 4.21 could present a reason for the increased surface area.

Analysis of pore volume and size via BJH determined pore size distributions can be problematic due to systematic errors encountered in the process. Reported inaccuracies involved in the BJH method including adsorbate phase transitions, tensile strength effects and monolayer formation in meso/microporous materials mean BJH analysis should be relied upon to provide qualitative rather than quantitative information[208,229,230].

In spite of this, the most suitable isotherm for BJH analysis must be selected before the data can be evaluated. When desorption isotherms are used to calculate pore sizes and volumes in mesoporous materials with ink bottle shaped pores (type IV and H2), tensile strength effects (TSE) in pores can skew the pore size distribution toward a pore size of ~3.8 nm due to a forced closing of the hysteresis loop at P/P_0 of 0.44 - 0.48[229]. Analysis of the isotherms (Appendix A.5) from the Saffil® and Sf OC's shows that the hysteresis loop closes within this pressure range. This is evident when the BJH adsorption and desorption average pore sizes are analysed; the decrease of more than 1 nm (an approximate increase of 25%) in the average pore diameter toward the critical pore size of 3.8 nm when comparing the BJH desorption and adsorption data suggests that TSE was observed in the samples. As such the BJH adsorption data will be used.

The data presented in Table 4.7 suggests that there is effectively no change in the average pore diameter of the materials characterised. However, the pore volume (encompassing pores between 1.7 nm and 300 nm) likely decreases when the WI method is used to load the Ni/Co on to the Saffil® fibre; this contrasts with the DP and HT methods where the pore volume of the support is largely unchanged. This suggests that the WI method could cause blocking of pores thereby reducing the overall quantity of adsorbent able to be adsorbed during the process; this could explain the loss in surface area as identified by the BET analysis. Additionally the proposed perpendicular growth of the Ni/Co oxides platelets identified in the DP and HT OC's (Figure 4.11 to Figure 4.15), could prevent this

blocking of pores by virtue of the void spaces and honeycomb structure presented, presenting areas where the pore structure of the support is preserved.

4.7 Summary

Characterisation of the raw Saffil® support and the fibrous Sf OC's was conducted. XRD patterns of the Saffil® support showed broad low intensity peaks characteristic of small grain γ-Al_2O_3 (> 10 nm) up to 1000 °C in an air atmosphere; this small crystallite size was corroborated by TEM. XRD of all the Sf OC's showed NiO was the dominant form of metal oxide deposited upon the support with no evidence of bulk nickel aluminate spinel ($NiAl_2O_4$). This agreed with SAED and TPR analysis. AAS confirmed loading of the Ni and Co intended by the three synthesis procedures was sufficiently accurate. TPR of the Sf OC's ruled out the formation of bulk $NiAl_2O_4$, but implied that interactions had occurred between the NiO deposited and the γ-Al_2O_3 in the support that increased the temperature of reduction; this interaction was stronger in the Sf-DP and Sf-HT OC's than in the Sf-WI OC's.

SEM and TEM showed the Ni/Co oxide deposited upon the Sf OC's formed a distinct layer (measuring between 200 and 500 nm) upon the Sf fibres. Sf-WI OC's exhibited a morphology of round nodular crystals with evidence of erratic macro and microdistribution of the deposited metal oxide layer. This inconsistent distribution was attributed to the reliance on precipitation through evaporation utilised in the WI method. The Sf-WI OC's also presented lower SSA and pore volume than the Saffil® support suggesting blocking of pores on the support. SEM also showed that the Ni content of the 18NiO GR OC is distributed in small particles (50 - 150 nm) upon larger clusters of α-Al_2O_3 (500 – 2000 nm) throughout the porous structure of the granules.

SEM, FIB/SEM and TEM showed the Sf-DP and Sf-HT OC's exhibited far more uniform distributions of NiO both upon each fibre and throughout the sample. The morphologies observed consisted a network of ridges formed perpendicular to the support framing void spaces to create a honeycomb structure. NiO crystallite sizes of the Sf-DP and Sf-HT OC's were found to be much smaller compared to the Sf-WI OC's exhibiting crystallite sizes ~ 6 nm and ~10 nm respectively. Using TEM/EDX, FIB/SEM and a fortuitous cross-section, the depth of the deposited layer was shown to be consistent across the two synthesis methods at ~ 300 and 400 nm respectively. The Sf-DP and Sf-HT OC's presented improved SSA over the Saffil® support by virtue of the smaller crystallite sizes and the

morphology of the deposited layer. The morphologies, greater homogeneity and increased surface area of the Sf-DP and Sf-HT OC's were attributed to the greater interaction between the support and the NiO deposited during synthesis possibly through formation of LDH precursors.

5 Isothermal Performance of Fibrous Oxygen Carriers during Steam Reforming of Methane

This chapter details the use of the Sf OC's in steam reforming (SR) experiments to assess their performance in relation to the 18NiO GR OC. The methodology for these experiments was developed using both equilibrium calculations and initial experiments to create a robust testing regime. These experiments assess the performance of the tested materials in relation to their ability to act at catalysts for the SR and WGS reactions when pre-reduced by a N_2 diluted H_2 feed. The OC's materials were then characterised to assess the effect of the SR experiments upon their physical properties.

5.1 Methodology Determination

An equilibrium model and a series of preliminary flow rate investigations and blank experiments were used to identify appropriate temperature and S:C conditions, avoid equilibrium limitation and discover the effects of the reactor and Saffil® support upon the SR experiments respectively. The results of these investigations dictated the methodology set out in Section 3.3.3, and ensured the performance of oxygen carrier materials in SR (Section 5.2) were optimised.

5.1.1 Equilibrium Model Investigations

CEA software (developed by NASA Lewis Research Centre) was used in conjunction with the elemental balances and process outputs (Section 3.4) to carry out several thermodynamic equilibrium calculations at atmospheric pressure and identify the theoretical maximum H_2 yield efficiency, H_2 purity and CH_4 and H_2O conversions of the SR thermodynamic system at equilibrium over a range of temperatures and S:C ratios. This not only allowed for the identification of the ideal theoretical conditions of temperature and S:C ratio for use in the SR and CLSR methodologies but also the point at which those experiments were equilibrium limited (Section 5.1.2).

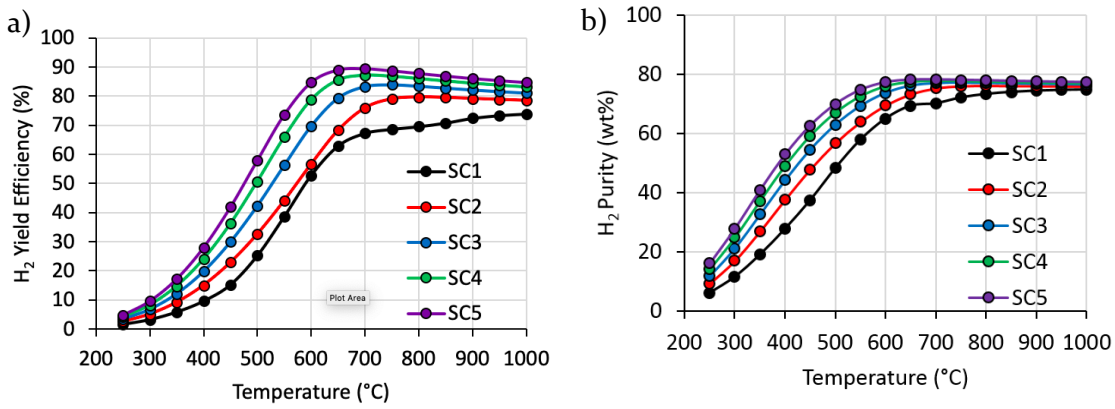

Figure 5.1: Equilibrium H_2 yield efficiency (a) and H_2 purity (b) at S:C 1-5

Figure 5.1a shows that H_2 yield efficiency generally increases with temperature up to a peak, and with S:C ratio. Increasing temperatures improves the H_2 yield by favouring the endothermic SR reaction over the mildly exothermic WGS reaction. Increasing the S:C ratio shifts the SR reaction to the product side via Le Chatelier's principle thereby increasing H_2 yield. An increase in the CO yield in the SR reaction as well as higher S:C ratio in turn shift the WGS reaction to the product side, compounding the increase in the H_2 yield.

At S:C ratios above stoichiometric (S:C > 1), the maximum yield H_2 efficiency is achieved between 700 and 800 °C, with S:C > 3 achieving their maximum value at 700 °C. At temperatures higher than 700 °C the reverse WGS reaction begins to reduce the H_2 yield. At stoichiometric S:C 1, the maximum H_2 yield efficiency is achieved at the highest temperature tested and there is a noticeable difference in the shape of the S:C 1 line between 450 and 800 °C. These differences can be attributed to the formation of solid carbon via thermal cracking of the CH_4 (Equation 1.10) promoted by a lack of steam available for the SR and WGS reactions.

The H_2 purity (Figure 5.1b) again increases with temperature and S:C ratio with purity maximised at 700 °C at S:C ratios above 3. This is again largely due to the prevalence of the SR reaction at higher temperatures and S:C ratios.

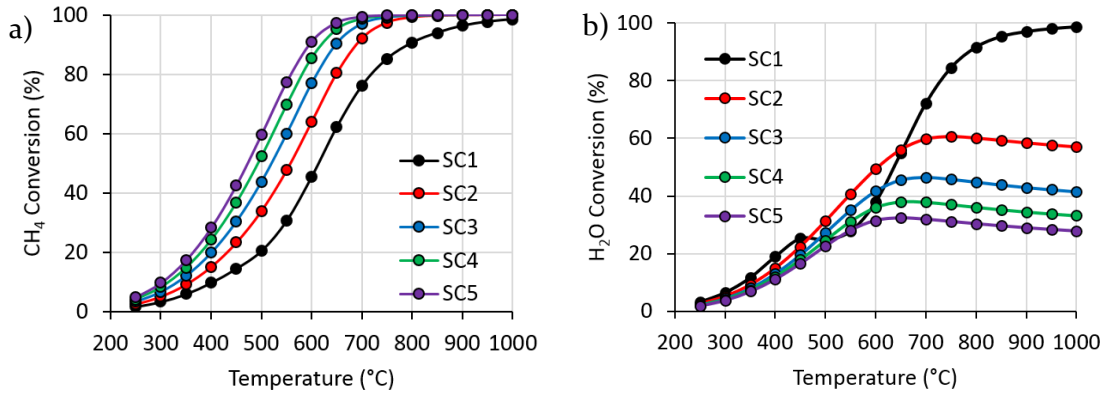

Figure 5.2: Equilibrium CH_4 conversion (left) and H_2O conversion (right) at S:C 1-5

Figure 5.2 shows CH_4 and H_2O conversion at atmospheric pressure increased with temperature, with CH_4 conversion reaching 100% in all cases above a stoichiometric S:C ratio at 800 °C. The H_2O conversion is clearly greatly affected by the S:C ratio; this is expected as excess water in S:C ratios above stoichiometric (S:C 2) will decrease the water conversion. At S:C 1, the decrease in water conversion between 400 and 600 °C is caused by a prevalence of methane cracking between 450 and 800 °C effectively reducing the water concentration by competing with the SR and WGS reactions.

For the SR and CLSR experiments conditions of 700 °C and a S:C ratio of 3 were used. An excess of steam in the system not only increases the H_2 yield efficiency and purity and the CH_4 conversion at all temperatures, it also avoids carbon deposition by shifting the SR and WGS reactions toward the products. Specifically a S:C ratio of 3 was chosen as it represents an excellent trade-off, providing excellent carbon suppression and product yield while also minimising energy demand for important process factors such as for steam generation and condenser load; it is not a coincidence that this S:C ratio is currently used in most industrial SMR processes[25]. 700 °C was used as an operation temperature as it provides close to 100% CH_4 conversion at 101325 Pa and avoids the onset of the reverse WGS reaction (T > 700 °C) thereby maximising the H_2 yield efficiency and purity and H_2O conversion.

5.1.2 Reactant Flow Rate Investigations

Appropriate reactant flow rates for the EM (equal mass) and EV (equal volume) conditions defined in Section 3.3.2 and used in the SR and CLSR experiments were determined by several preliminary experiments. These experiments used 2 g of 18Ni Sf-WI OC (V_{bed} = 12.5 cm^3) for the EM conditions and 0.4 g of 18Ni Sf-WI OC (V_{bed} = 2.5 cm^3) for the EV conditions and varied the flow rate of the reactant gases through the catalyst bed. The aim

was to determine flow rates that would ensure the SR and CLSR experiments in both EV and EM conditions were not equilibrium limited; this would allow meaningful comparison of outputs between the Sf OC's and 18NiO GR OC. Moreover, avoiding equilibrium limitations ensures that the reactions occurring during the experiments are either internally or externally mass transfer limited or kinetically limited.

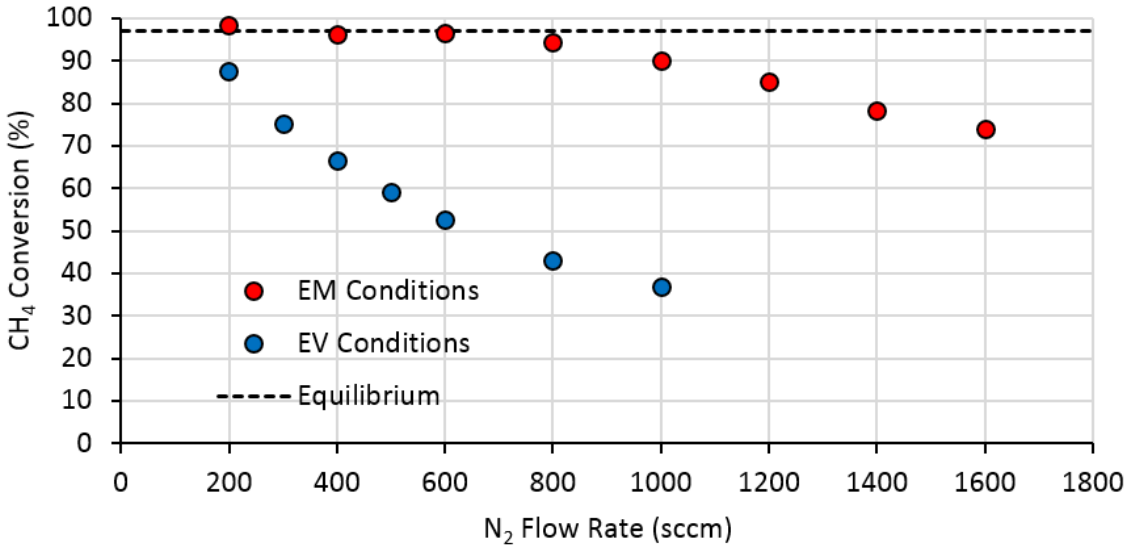

Figure 5.3: Average CH_4 conversion during SR for several reactant flowrates under both EV (equal volume) and EM (equal mass) conditions; 10% CH_4 in N_2 and S:C 3 was used in all experiments with the flow rate of the carrier gas used as reference

Figure 5.3 shows that for EM conditions, all flowrates above 800 sccm avoided equilibrium limitation when applied to CH_4 conversion, however as the carbon balance can vary in these experiments from ~ 95 % to ~ 105 %, 1000 sccm was chosen to ensure that the experiment were sufficiently distanced from equilibrium conditions. EV conditions avoided equilibrium limitation at all flow rates tested, but to avoid mass transfer limitations to the reduction reaction (see Section 7.2.1) a base carrier gas flow rate of 800 sccm was used.

5.1.3 Blank Experiments

Two "blank" experiments were undertaken to assess the effects of the reactor equipment and the support materials upon the process outcomes. Both experiments utilised the EM CLSR methodology so that the effect upon SR can be assessed during the first SR cycle and the effects upon redox cycling on the consequent cycles. In the first experiment (shown overleaf in Figure 5.4) there was no material loaded into the stainless steel (SS) baskets of the reactor.

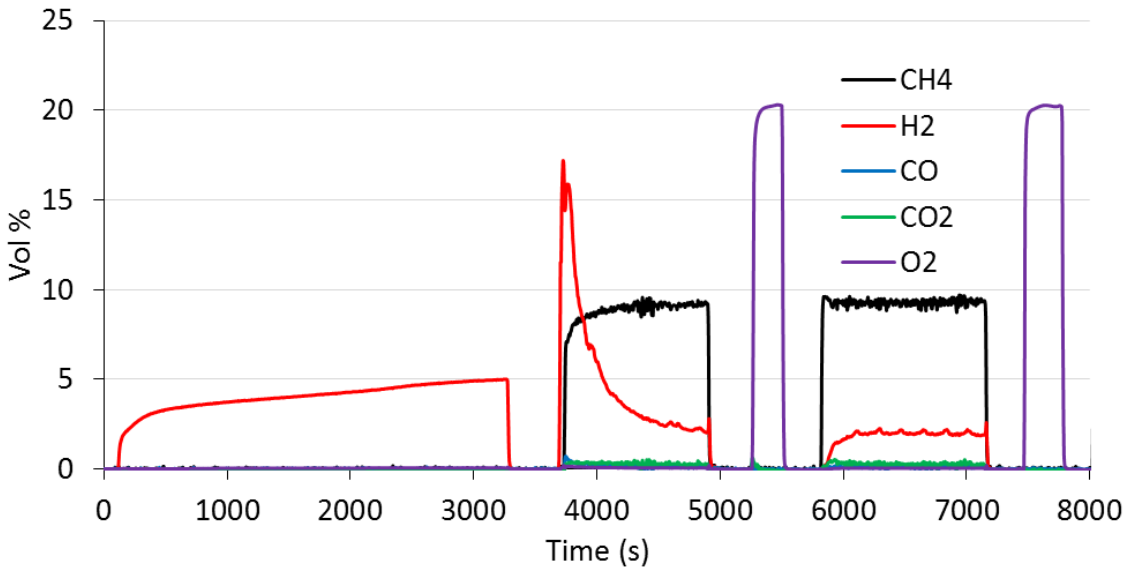

Figure 5.4: Dry outlet composition during initial reduction and 0th SR half cycle for the blank EM CLSR experiment at 700 °C and S:C 3

Figure 5.4 shows a gradual consumption of H_2 over the course of approximately an hour after the first 100 seconds of the blank experiment. This implies that the stainless steel (SS) baskets used to hold the various catalysts and the SS reactor tube was able to be reduced by the flow of 5 vol% H_2/N_2 mixture. This is unfortunate as it creates some ambiguity over whether the reduced SS contributes to the performance of the OC materials under the 0th SR half cycle; however this step is essential in ensuring all the OC is reduced prior to the beginning of a SR experiment, especially as there is no way of knowing whether the catalyst has reduced to its maximum until the outlet H_2 concentration returns to 5% (reduction feed stream is 5% H_2/N_2).

The 0th SR half cycle (shown in Figure 5.4) clearly shows an initial peak in H_2 concentration in the outlet followed by a gradual reduction throughout the SR cycle. This peak is expected to be produced by water splitting on the reduced metallic materials within the reactor system as per the reaction below:

$$M_yO_{x-1(s)} + H_2O_{(g)} \leftrightarrows M_yO_x + H_{2(g)} \qquad \textbf{Equation 5.1}$$

This phenomenon of water splitting was encountered due to the design of the reactor system. The aim of the reactor at the onset of an experiment for both the CH_4 and steam to reach the catalyst bed simultaneously. This is difficult to achieve as the water is fed into the reactor as a liquid and relies upon the furnace to vaporise the feed and thus takes longer to reach the catalyst bed than the CH_4. As a result, if the H_2O and CH_4 feeds are switched on simultaneously, the CH_4 will reach the catalyst bed before the steam, thus encouraging thermal cracking. This causes the production of solid carbon thereby

subsequently hindering the performance of the catalyst material used, until either the end of the SR experiment, or until the first oxidation stage during CLSR, and should therefore be avoided. Consequently, the water feed was always switched on first, with the CH_4 feed switched on when H_2 was first detected in the outlet gas. This may result in a decrease in the available reduced OC material to catalyse the reactions, which can affect the performance of the materials used, however, as will be shown in the CLSR experiments, the CH_4/H_2O mixture is able to re-reduce the OC material oxidised by the initial water splitting. Accordingly, the degree to which the water splitting peak in H_2 outlet concentration is detectable will depend on the effectiveness of the onset of the feeds into the system. The gradual decline in H_2 concentration at the outlet is attributed to the gradual decrease in activity of the water splitting reaction as the reactor materials oxidise.

Minor steady state activity of the SR and especially WGS reactions for the blank runs is evident in Figure 5.5 from the concentrations of CO (~ 0.03 vol%) CO_2 (~ 0.5 vol%) and H_2 (~ 2 vol%) present and indeed the low H_2O and CH_4 conversions (both ~4 %); this activity for the SR and WGS was shown in all SR half cycles.

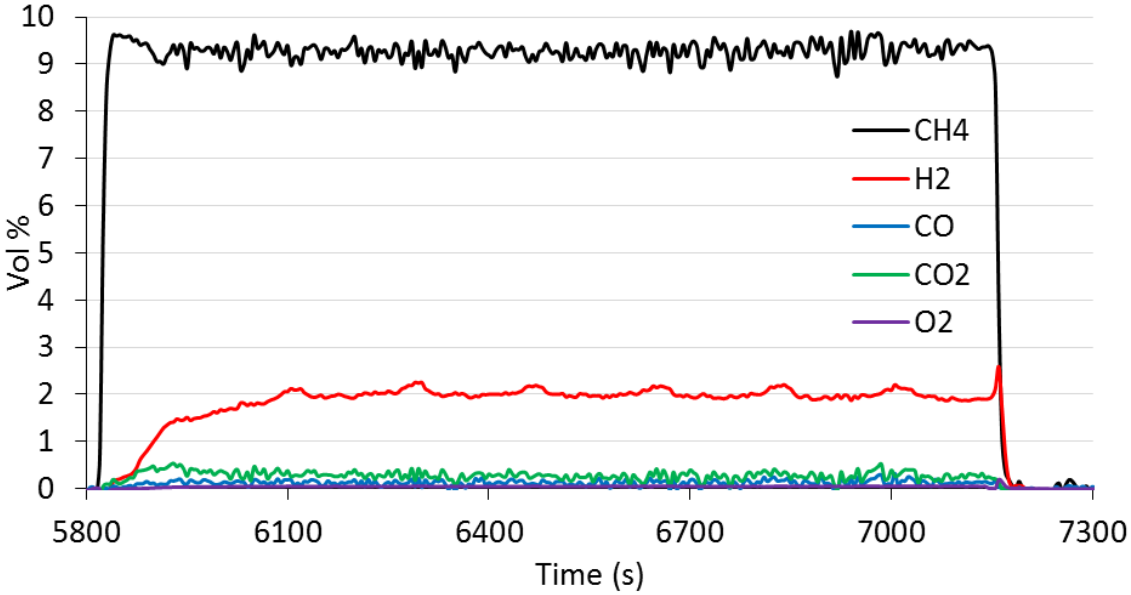

Figure 5.5: Dry outlet composition during the 1st SR half cycle of the blank EM CLSR experiment at 700 °C and S:C 3 (same experiment as Figure 5.4)

This activity suring the CLSR experiments could arise from Ni or Co in the reactor from previous experiments (despite thorough cleaning between experiments) or caused by homogenous gas phase SR and WGS, but a more likely explanation would be reduction of the 316 SS reactor tube; 316 SS contains up to 14 wt% Ni and could cause heterogeneous catalysis of the SR and WGS reactions when reduced. This hypothesis would explain the

gradual increase in production of H_2, CO and CO_2 over the first 300 s of SR half cycle, and resultant steady state production of these gases after this point. When the rate of reduction during these blank SR half cycles was determined (Appendix A.9), the effect of the reduction of the reactor materials in absence of OC material upon the rate and extent of reduction of the OC materials was deemed to be negligible (for more information see Section 6.1.1.2)

This experiment was then repeated using as-received (unloaded) Saffil® material in the reactor. The results were not significantly different from the blank experiment, suggesting the unloaded support has no catalytic effect upon the SR, WGS or water splitting processes.

Subtraction of these blank experiments from the outputs of the SR and CLSR experiments could not be facilitated due to the manual operation of the rig and the resultant differences in output with time. Despite this, the effects of water splitting and SR/WGS activity of the rig equipment was likely consistent across experiments and thus comparison between the 18NiO GR OC and the Sf OC's is still valid. Future work must include the comparison of the SS reactor tube with a more inert material such as alumina or quartz despite the issues this may cause with effective sealing of the reactor.

5.2 Performance of Oxygen Carrier Materials in SR of Methane

These experiments were used to assess the catalytic activity and selectivity of the Sf OC's and the 18NiO GR OC for the SR and WGS reactions. The OC materials were pre-reduced by a N_2 diluted H_2 feed and then subjected to a mixture consisting of a N_2 diluted H_2O and CH_4 at a 3:1 molar ratio near atmospheric pressure under which steam reforming was carried out.

5.2.1 Equal Mass (EM) Conditions

The experiments used two flow regimes that varied the flow rate of the reactants and the volume and mass of the OC materials used. Under EM conditions, both the mass of OC (M_{OC}, 2g) used and the volume of the bed (V_{bed}, 12.5 cm^3) were equal, Table 3.3 (reproduced below). This was achieved through the dilution of the denser 18 NiO GR OC with silica sand of equal particle size.

Table 3.3: Experimental conditions for the SR experiments

SR Conditions	m_{OC} (g)		V_{bed} (cm^{-3})		$\dot{V}_{i,in}$ (sccm)			T (°C)	S:C
	Sf OC	GR OC	Sf OC	GR OC	N_2	CH_4	H_2O		
Equal Mass (EM)	2.0	2.0	12.5	12.5	1000	111.0	0.25	700	3
Equal Volume (EV)	0.4	2.0	2.5	2.5	800	88.8	0.20	700	3

5.2.1.1 EM SR Outlet Concentrations

Figure 5.6 shows the dry outlet composition during the first 3000 seconds of a typical EM SR experiment where the conventional 18NiO GR OC was used. The primary product from the experiment was H_2 with by-products of both CO and CO_2; these outputs were expected and showed the immediate onset of both the SR and WGS reactions catalysed by the pre-reduced OC's. Unreacted CH_4 was also detected in the outlet of the experiments. This was again expected as the preliminary flow experiments showed that CH_4 conversion would not be complete at these reactant flow rates.

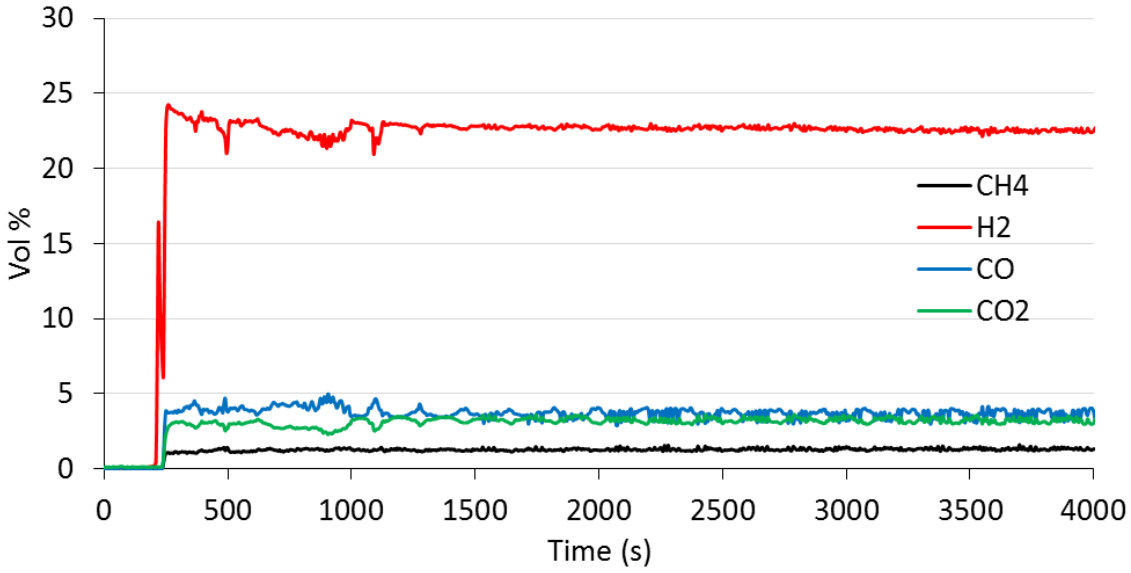

Figure 5.6: Dry outlet composition during the first 4000 seconds of EM SR using the 18NiO GR OC diluted with silica sand at 700 °C and S:C 3 as representative of a typical EM SR experiment

Initially, a H_2 peak is seen in Figure 5.6 that does not correspond with the presence of any carbon gases. This initial peak is attributed to water splitting due to H_2O reaching the OC bed before CH_4. The first peak is then followed quickly by a higher peak in H_2 which does correspond to increases in the carbon gases and can be attributed to the onset of steam reforming on arrival of the CH_4 into the OC bed. The slight drop in H_2 concentration between 250 and 1000 s is also ascribed to the declining effects of water splitting.

Observation of the relative steady state molar fractions of product gases and unconverted CH_4 in the dry outlet gas can yield further information on the reactive system. Section 5.3.1 shows that carbon formation during steady state steam reforming was negligible and therefore any H_2 present in the outlet was likely generated by the SR and or WGS reactions (Equation 1.4 and Equation 1.5). For each mol of CH_4 consumed by the SR reaction, the molar product ratio of H_2:CO will be 3:1. However CO may go on to participate in the WGS reaction; this results in a molar product ratio of H_2:CO_2 of 4:1 for each mol of CH_4 consumed. Therefore, considering both CO and CO_2 are present in the outlet, the expected mol fraction (i.e. vol% divided by 100) of H_2 in the outlet for a given conversion of CH_4 can be found:

$$y_{H_2,exp} = 3y_{CO,out} + 4y_{CO_2,out} \qquad \textbf{Equation 5.2}$$

Using the data point at 2280 s in Figure 5.6, the CO and CO_2 detected in the outlet were measured at 3.05 vol% and 3.30 vol% respectively while H_2 detected in the outlet was measured as 22.55 vol%; the expected H_2 production based on the H_2:CO and H_2:CO_2 ratios was 22.36 vol%. The excellent agreement between these figures combined with an average carbon balance of 106.1 % (see Section 5.2.1.2) shows that the system was working close to the theoretical limits and therefore a high confidence in the result was assured.

When Figure 5.6 is compared to the dry outlet composition using the 1.8Co HT Sf OC shown in Figure 5.7, it is clear that the 18NiO GR OC and the Sf OC's produced very similar outputs in both composition and ratio of products. This shows that the Sf OC's can effectively catalyse both SR and WGS reactions and are likely similar in performance to 18NiO GR OC. Steady state conditions are achieved with both the Sf OC's and the 18NiO GR OC by 1000 s.

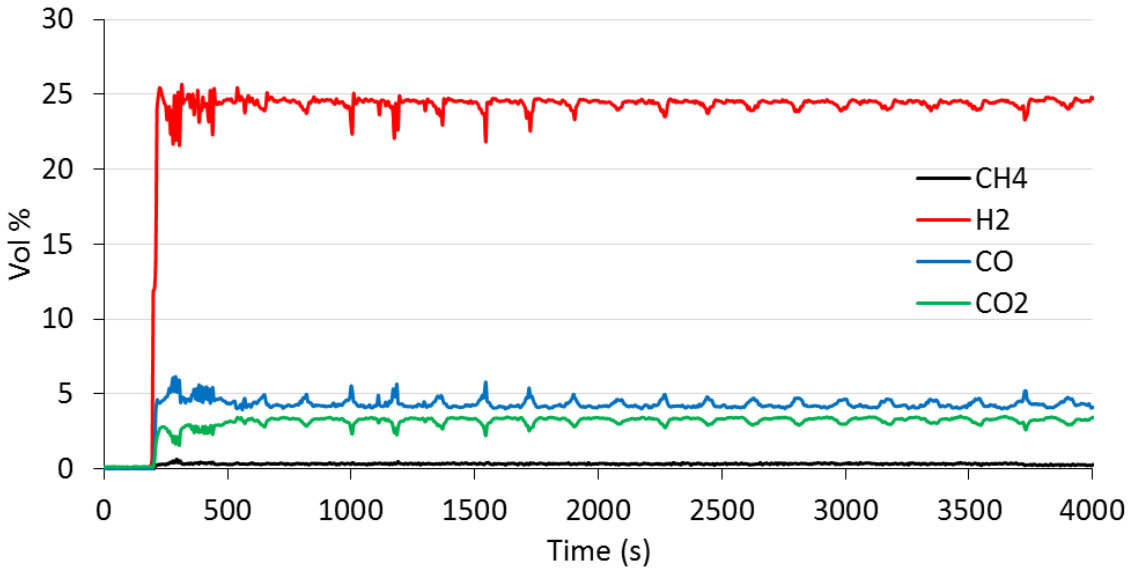

Figure 5.7: Dry outlet composition during the first 4000 seconds of EM SR using the 1.8Co 18Ni Sf-HT OC at 700 °C and S:C 3 as representative of a typical EM SR experiment using Sf OCs

Figure 5.7 shows no evidence of H_2O splitting either in an initial peak in H_2 production or any decrease in H_2 production during the first 1000 s of the experiment; this may be caused by a predominance of SR over water splitting when the CH_4/H_2O feeds arrive in the bed simultaneously. Figure 5.7 is representative of the Sf OC materials tested under EV SR conditions.

Using the data point at 2470 s in Figure 5.7, the H_2 detected in the outlet was measured as 24.55 vol% while the expected H_2 production based on the H_2:CO and H_2:CO_2 ratios was 25.20 vol%. The average carbon balance was also 105.1 % indicating a high degree of confidence in the results.

None of the samples tested under EM conditions showed any appreciable deactivation during the SR experiments; longer experiments may be useful is assessing the effects of long-term use on both the performance of the OC's and their physical characteristics.

5.2.1.2 EM SR Process Outputs

Analysis of the outlet concentrations from the SR experiments can only yield so much information about the performance of the OC materials and their catalytic activity in the SR process. As such, the process outputs listed in Section 3.4.6, H_2 purity, H_2 yield efficiency and CH_4 conversion, were used to provide a more in-depth comparison between the materials tested.

Figure 5.8 shows the average CH_4 conversion and H_2 yield effcicency and purity during the EM SR experiments (once steady state conditions had been reached) for all nine Sf OC's and conventional 18NiO GR when diluted with sand (s) and their equilibrium values.

Experimental error in the SR experiments was estimated using the carbon balance, Figure 5.8. In all SR experiments the carbon balance was more than 100% ranging from 101.9 – 106.1 % suggesting the error in the system was likely created by slight over provision input feeds in the mass flow controller (MFC) regulation. Despite this, the carbon balances closely clustered near 100% suggests a high degree of accuracy in the measurements and elemental balance analysis.

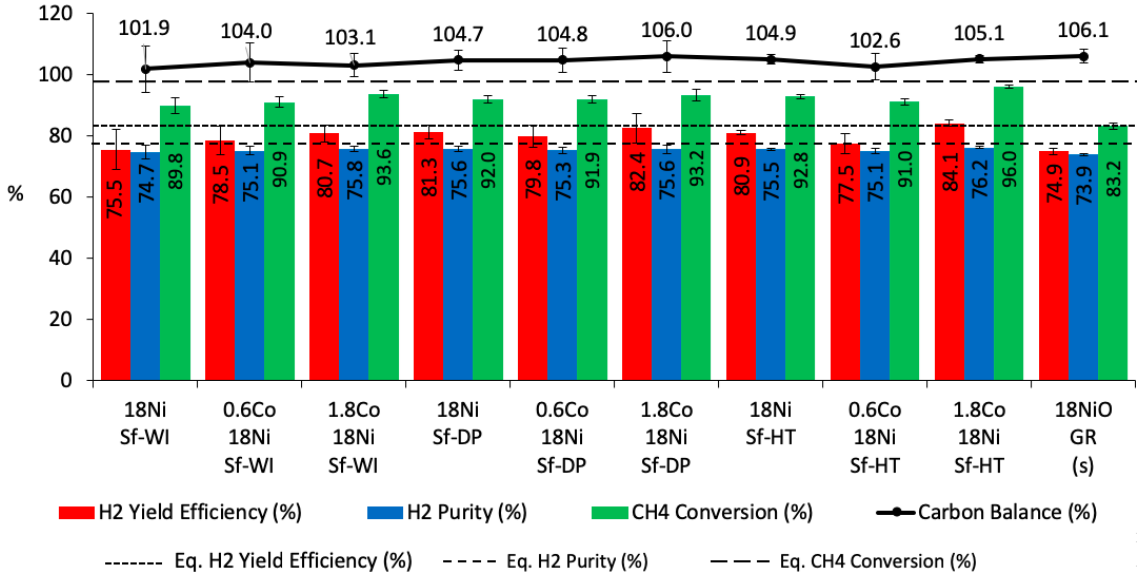

Figure 5.8: Average H_2 yield efficiency and purity and CH_4 conversion over the EM SR experiments compared with equilibrium values at 700 °C and S:C 3. Error bars represent the standard deviation across the experiment

While some experiments showed large standard deviation in the mean CH_4 conversion, H_2 yield and purity (e.g. 18Ni Sf-WI) as measured across the EM SR experiments, but generally these factors were small and thus effective comparison between the 18NiO GR OC can be made.

Comparison of the 18NiO GR OC with the Sf OC's (Figure 5.8), shows the Sf OC's present a significant increase in CH_4 conversion over the 18NiO GR OC with the increase ranging from 6.6 to 12.8 percentage points (pp). The synthesis method had a small effect upon CH_4 conversion with the Sf-WI OC's showing an average CH_4 conversion of 91.6 % compared to Sf-DP OC's at 92.4 % and Sf-HT OC's at 93.4 %. There was however more variability in the H_2 yield efficiency presented by the Sf OC's; improvements over the 18NiO GR OC

ranged from 0.6 pp to 9.2 pp with the Sf-WI OC's showing the poorest average H_2 yield efficiency at 78.2 % with the Sf-DP and Sf-HT OC's presenting 81.2 % and 80.8 % respectively. H_2 purity was also improved in the Sf OC's with the increase ranging from 0.8 pp to 2.3 pp but synthesis route did not have a significant effect. Cobalt doping did not influence the CH_4 conversion or H_2 purity or yield of the Sf OC's. The best performing Sf OC was found to be the 1.8Co 18Ni Sf-HT OC which showed percentage point increases in CH_4 conversion, H_2 yield and H_2 purity of 12.8 pp, 9.2 pp and 2.3 pp; the standard deviation associated with the results from the 1.8Co 18Ni Sf-HT OC and 18NiO GR OC indicate a high degree of statistical confidence in this result.

5.2.2 Equal Volume (EV) Conditions

Under EV conditions V_{bed} was fixed at 2.5 cm^3 and so the mass of the Sf OC's was limited to 0.4 g, compared to 2g of the 18NiO GR OC without sand dilution, Table 3.3 (reproduced below). This represents an 80% reduction in catalyst mass between the Sf OC's and the 18NiO GR OC.

Table 3.3: Experimental conditions for the SR experiments

SR Conditions	m_{OC} (g)		V_{bed} (cm^{-3})		$\dot{V}_{i,in}$ (sccm)			T (°C)	S:C
	Sf OC	GR OC	Sf OC	GR OC	N_2	CH_4	H_2O		
Equal Mass (EM)	2.0	2.0	12.5	12.5	1000	111.0	0.25	700	3
Equal Volume (EV)	0.4	1.0	2.5	2.5	800	88.8	0.20	700	3

5.2.2.1 EV SR Outlet Concentrations

Comparing the dry outlet compositions for the EM (Figure 5.6) and EV (Figure 5.9) conditions for the 18NiO GR OC, Figure 5.9 (overleaf) shows that there is an increase in unreacted CH_4 (~ 2 vol%) and a decrease in H_2 (~ 3 vol%), CO (~ 2%) while CO_2 remained largely unchanged. This suggests that with a decrease in residence time through the catalyst bed the efficacy of the SR reaction was reduced, unsurprising as the reactants have less time to react with the reduced Ni catalyst present.

Using the data point at 2000 s in Figure 5.9 (overleaf), the H_2 detected in the outlet was measured as 19.64 vol% while the expected H_2 production based on the H_2:CO and H_2:CO_2 ratios was 19.65 vol%; this indicates that the system is working close to theoretical limits and idicating a high degree of confidence in the results.

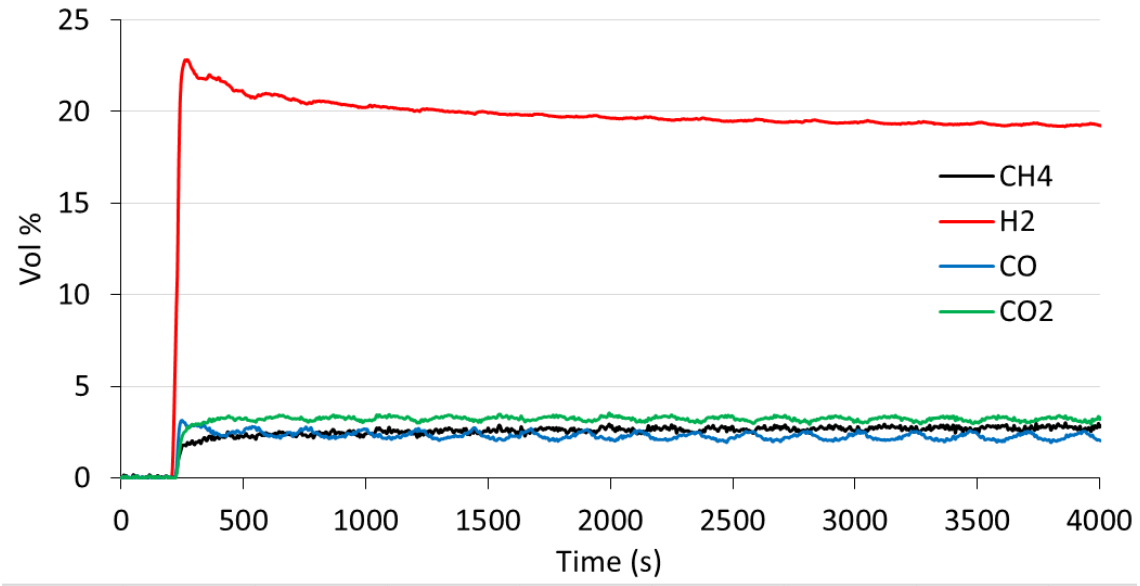

Figure 5.9: Dry outlet composition during the first 4000 seconds of EV SR using the 18NiO GR OC at 700 °C and S:C 3 as representative of a typical EV SR experiment

Figure 5.9 also shows a pronounced peak in H_2 production at the start of the SR cycle that gradually subsides over the first 2000 s of the experiment. This was attributed to the gradual oxidation of the SS reactor materials via water splitting during the SR half cycle. This effect was considered negligible after 2000 s of the SR experiments. After water splitting had subsided, none of the samples tested under EV conditions showed any appreciable deactivation during the SR experiments. The effect of water splitting upon the H_2 production under EV conditions is more pronounced than in the EM conditions due to the lower overall H_2 production as a result of decreased SR activity.

When used in EV SR conditions, the 0.6Co 18Ni Sf-DP OC also shows an increase in CH_4 concentration (~ 3.5 vol%) and a decrease in H_2 (~ 9 vol%), CO (~ 2 vol%) and CO_2 (~ 1 vol%) compared to EM SR conditions, Figure 5.10 (overleaf). These changes in the dry outlet conditions between the EV and EM SR conditions are more pronounced than the 18NiO GR OC; this is likely due to the changes in the OC bed. When using the 18NiO GR OC without sand dilution, only the bed volume is reduced when the EV conditions are used. For the Sf OC's the mass of the OC is reduced by 80% in addition to the reduction in bed volume; this results in both less residence time in the OC bed and less active catalytic phase (Ni) to react with, thereby compounding the reduction in effectiveness of the SR reaction. Using the data point at 2010 s in Figure 5.10 (overleaf), the H_2 detected in the outlet was measured as 16.29 vol% while the expected H_2 production based on the H_2:CO and H_2:CO_2 ratios was 16.11 vol%; this excellent agreement suggests that the results are valid and working close to theoretical limits.

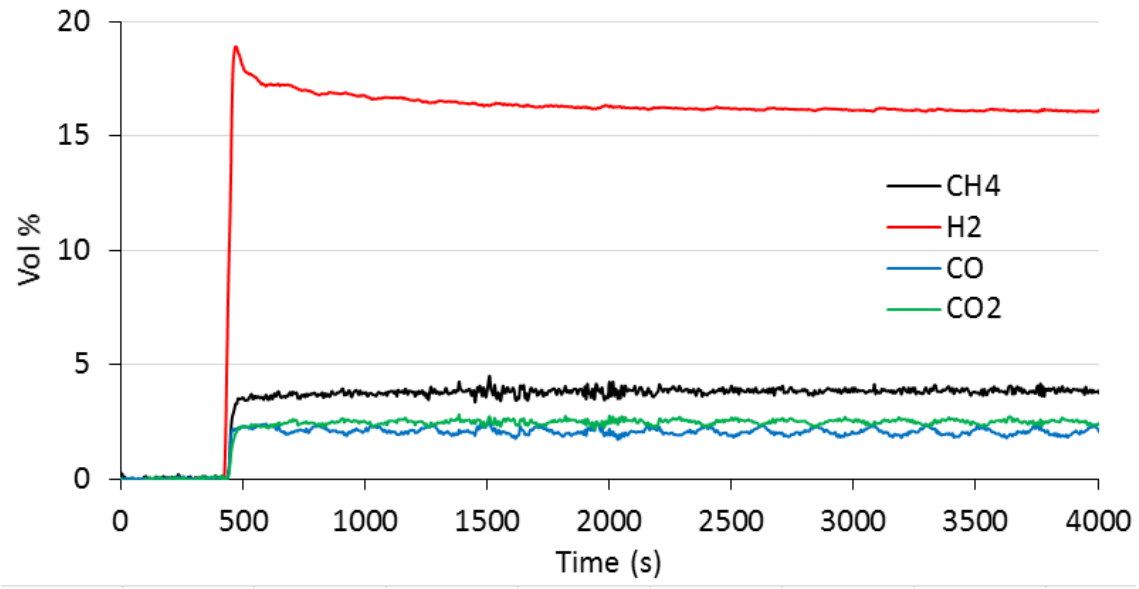

Figure 5.10: Dry outlet composition during the first 3000 seconds of EV SR using the 0.6Co 18Ni Sf-DP OC at 700 °C and S:C 3 as representative of a typical EV SR experiment using Sf OCs

On comparison with the 18NiO GR OC under EV SR conditions, the dry outlet concentrations produced by the 0.6Co 18Ni Sf-DP OC again show reductions in H_2 (~ 3 vol%) and CO_2 (~ 0.5 vol%) and an increase in unreacted CH_4 (~ 1 vol%); this suggests that under EV SR conditions, the 18NiO GR OC may be slightly more effective. Figure 5.10 can be considered to be representative of the Sf OC materials tested under EV SR conditions.

5.2.2.2 EV SR Process Outputs

Figure 5.11 (overleaf) shows the average CH_4 conversion and H_2 yield efficiency and purity during the EV SR experiments for all nine Sf OC's and 18NiO GR OC and their equilibrium values. Averages were taken between 2000 s and the end of the experiment to account for the influence of water splitting. Experimental error estimated using the carbon balance was again very close to 100% suggesting a high degree of accuracy in the measurements and elemental balance analysis.

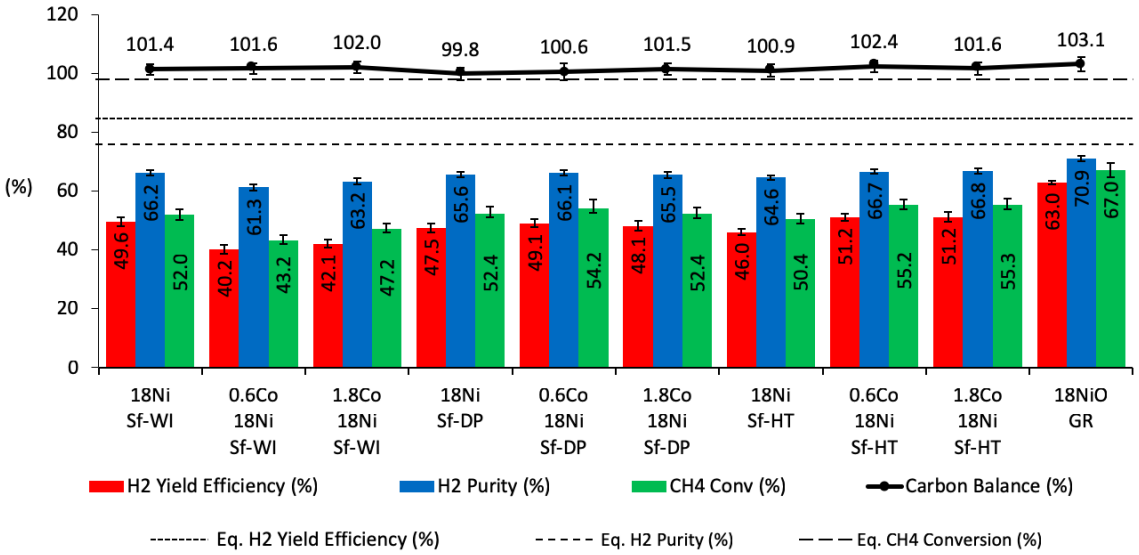

Figure 5.11: Average H_2 yield efficiency and purity and CH_4 conversion over the EV SR experiments compared with equilibrium values at 700 °C and S:C 3. Error bars represent the standard deviation across the experiments

Comparison of the 18NiO GR OC and the best performing Sf OC, 1.8Co Sf-HT (Figure 5.11), yields a decrease in CH_4 conversion of 11.5 pp (66.8 % to 55.3 %), H_2 yield efficiency of 11.8 pp (63.0 % to 51.2 %) and H_2 purity 4.1 pp (70.9 % to 66.8 %). This shows that the Sf OC's are less effective in SR than the 18NiO GR OC under EV conditions. However, this deficit is relatively small when the lower OC mass used for the Sf OC's under EV SR conditions is considered (80% less than the 18NiO GR OC); these results show that fibrous OC's can be competitive in SR performance to a granulated commercial catalyst while offering a great reduction in the required mass of OC. The standard deviation across all samples implies a high level of statistical confidence in these results.

The performance of the Sf OC's tested was significantly reduced under EV conditions compared to EM SR conditions, with the decrease in CH_4 conversion ranging from 35.8 pp to 47.6 pp, the decrease in H_2 yield efficiency between 25.9 pp and 38.6 pp and the decrease in H_2 purity between 8.5 pp and 13.8 pp. These reductions were far less pronounced when comparing the performance of the 18NiO GR OC under EV and EM conditions. The reduction in SR performance of both the Sf OC's and the 18NiO GR OC under EV conditions was attributed to the reduction in bed volume in the EV method which would cause a reduction in residence time and therefore a decrease in reactant conversion and production of the H_2, CO and CO_2 by-products.

The performance of the Sf OC's under EV SR conditions exhibited an unexpected result in that cobalt doping negatively affected the performance of the Sf-WI OC's. CH_4 and H_2 yield efficiency and purity when using the 0.6Co 18Ni Sf-OC were reduced by 8.8 pp, 9.4

pp and 4.7 pp respectively when compared to the 18Ni Sf-WI OC, with the 1.8Co 18Ni Sf-WI showing decreases in these factors of 4.6 pp, 7.5 pp and 3.8 pp. Conversely there was a smaller net positive effect from cobalt doping on the Sf-DP and Sf-HT OC's, with the Co-doped materials showing an increase in the aforementioned factors of up to 4.9 pp, 5.2 pp and 2.1 pp respectively. This variability in the effect of cobalt in the Sf-WI OC's was not seen in such stark contrast under EM SR conditions, or under EV CLSR conditions (Section 6.1.1.4), suggesting that this shortfall in the cobalt doped Sf-WI OCs may be variability in the experimental conditions rather than an effect of the synthesis method.

When discounting the cobalt doped Sf-OC's and comparing the 18Ni Sf-WI, the Sf-DP and Sf-HT OC's, there was little difference between the efficacies of the OC's. CH_4 conversion varied by only 2.0 pp, H_2 yield efficiency by 3.6 pp and H_2 purity by 1.6 pp with the Sf-WI OC performing best. This would imply the synthesis method has less effect upon the measured factors under EV SR conditions than in EM conditions.

5.2.3 Discussion

When evaluated on an equal mass (EM) basis, the fibrous Sf OC's were able to improve the CH_4 conversion, H_2 yield efficiency and H_2 purity from the SR of CH_4 by up to 12.8 pp, 9.2 pp and 2.3 pp (1.8Co 18Ni Sf-HT) respectively when compared to the 18NiO GR OC. Moreover, when compared on an equal volume (EV) basis, the fibrous Sf OC's produced only a slight penalty to performance (as measured by the factors above) to the 18NiO GR OC despite operating with 80% less mass of catalytic material (0.4 g of Sf OC vs. 2 g of 18NiO GR OC).

The improvement in SR performance offered under EM conditions and the small penalty to performance despite an 80% reduction in OC mass under EV conditions shows that the properties of the structured fibrous Sf OC's are beneficial to their performance in SR.

These improvements in catalytic performance stem from both the differences in effective particle size exhibited by the OC's as well as the manner in which the Ni is distributed upon or throughout the two types of OC material. The increased void fraction in the OC bed combined with the far smaller effective particle diameter of the Sf OC's (~ 200 μm to < 10 μm) exhibited by the Sf OC's, will facilitate the movement of the bulk CH_4/H_2O gas throughout the OC bed as well as reduce the effective diffusion length of the CH_4 reactant through the boundary layer around the OC particle. This also increases the surface area to volume ratio of the OC material, thereby increasing the likelihood of catalytically active sites being present on the surface of the particle[129,162,163]. Furthermore, the CH_4 reactant

must diffuse throughout the 200 μm internal porous structure of the 18NiO GR OC to reach all of the Ni content of this OC, while the vast majority of the Ni content of the Sf-OC's is deposited in an outer layer less than 500 nm deep; this greatly reduces the effective diffusion length necessary for the CH_4 reactant to reach a greater number of active catalytic sites. These factors will also reduce the effective diffusion length for the reaction products to move from the catalytic sites back into the bulk gas phase, further benefitting facile mass transfer. These factors combine to likely increase the effectiveness factor of the Sf OC's when compared the 18NiO GR OC thereby decreasing any diffusion limitation of the SR reaction and improving catalytic activity.

Further indication of beneficial mass transfer properties of the Sf OC's can be found in the results of models for internal and external mass transfer during reduction of the OC's in Section 7.3.1.

Additionally, the porosity of the Sf OC's and the deposition of Ni internally within the Sf fibres may also have an influence on the performance of the two materials; the CG Saffil® fibres are highly porous (mesopores) as a result of the temperature sintering process used in their manufacture that ensures a material consisting of predominantly γ-Al_2O_3. This porosity means that the Sf OC's present surface areas of appoximately 100 $m^2 g^{-1}$ while the 18NiO GR OC presents a surface area of just 3.2 $m^2 g^{-1}$. Figure 4.12 and Figure 4.14 indicate that there are likely two forms of Ni present on the fibrous OC's; "external Ni" that is present in the deposited layer of the OC and constitutes the majority of the Ni deposited and "internal Ni" present throughout the porous Sf fibre. The added internal surface area of the Sf OC's could play a role in improving the catalytic performance; any Ni particles deposited within the pore structure as "internal Ni" are likely to be much smaller than present in the "external Ni" structure thereby presenting a greater surface area to volume ratio and as a result could also be responsible for improving the activity of the Sf OC's. The relative influence of this "internal" and "external" Ni in catalysis of SR is difficult to estimate; although H_2/CO/N_2O chemisorption can be used to analyse Ni surface area, there is no simple means of estimating the internal and external surface area of the support materials.

The Sf OC's produced via decomposition of urea (Sf-DP and Sf-HT) rather than by simple wet impregnation (Sf-WI) were shown to have a slightly positive effect upon CH_4 conversion and H_2 yield efficiency and purity under EM SR conditions. The improvements in the H_2 yield efficiency and CH_4 conversion could be explained by the lower Ni crystallite size (Section 5.3.2), improved coating uniformity and more open texture of the reduced

Sf-DP and Sf-HT materials (Section 5.3.4). These factors are known to be important in conventional non-fibrous Ni/γ-Al_2O_3 catalysts and likely increase the surface area of Ni available for catalysis thus increasing the activity of the Sf OC's[82,132,133,167,224,225,231]. Moreover, the void-like structure presented by these materials will facilitate the entry and egress of reactant and products to the surface of the support fibre and subsequently into the porous structure of the Sf OC's.

Cobalt doping did not appear to have any great effect upon the performance of the Sf OC's under the two conditions.

These results show that use of microfibrous catalysts in fixed bed SR processes can achieve an impressive degree of process intensification; under two different conditions fibrous OC's were shown to provide competitive performance with a conventional granulated SR catalyst currently used in industrial SMR. Moreover, the possibility to greatly reduce the mass of catalytic material needed for effective SMR through use of a fibrous OC is an incredibly promising result particularly for mobile or transportable H_2 generation applications.

Further work on the specific mass of Sf OC's required to match the conventional granulated catalysts on an equal volume basis without dilution would yield more evidence to prove the competitiveness of these new support geometries. Additionally, experiments investigating the compressibility of the Sf OC's the possible effects upon void fraction, performance, mass and heat transfer and pressure drop seem particularly interesting (see Chapter 9).

5.3 Post SR Characterisation of OC Materials

The OC's used in the EM SR experiments were subjected to characterisation via a number of techniques to assess the effect of the EM SR experiments upon the structure and physical characteristics of the materials: CHN analysis was used to analyse the mass of solid carbon produced over the course of the experiment; SEM was used to assess the morphological changes; XRD to identify any changes in the crystallite structure and BET used to assess the textural changes of the materials.

5.3.1 Elemental Analysis of Carbon Deposition

CHN was used to assess the carbon deposition upon the Sf OC's and the 18NiO GR OC during the EM SR reforming experiments. Table 5.1 shows the carbon content of two

reference compounds were found to agree (to 2 decimal places) with their certified values ensuring accuracy of the results.

Table 5.1: CHN analysis of the OC's used in the EM SR experiments

Sample	$x_{C_{(s)}}$ (wt %)	$n_{C_{(s)}}$ (mol)	$C_{(s)}$ Yield (mol/mol C Feed)
Sandy Soil (Ref)	0.83	-	-
Soil (Ref)	2.29	-	-
18Ni Sf-WI	0.09	1.56×10^{-4}	4.82×10^{-4}
0.6Co 18Ni Sf-WI	0.11	1.84×10^{-4}	5.69×10^{-4}
1.8Co 18Ni Sf-WI	0.09	1.50×10^{-4}	2.12×10^{-4}
18Ni Sf-DP	0.11	1.83×10^{-4}	4.76×10^{-4}
0.6Co 18Ni Sf-DP	0.13	2.13×10^{-4}	3.96×10^{-4}
1.8Co 18Ni Sf-DP	0.12	2.05×10^{-4}	4.93×10^{-4}
18Ni Sf-HT	0.07	1.15×10^{-4}	2.99×10^{-4}
0.6Co 18Ni Sf-HT	0.10	1.75×10^{-4}	3.50×10^{-4}
1.8Co 18Ni Sf-WI	0.10	1.66×10^{-4}	2.05×10^{-4}
18NiO GR	0.07	1.20×10^{-4}	1.64×10^{-4}

The moles of solid carbon and the yield of solid carbon for each material tested (Table 5.1) was calculated with the use of Equation 5.3 and Equation 5.4, where t_{exp} is the time on stream of the experiment:

$$n_{C_{(s)}} = \frac{m_{OC}\, x_{C_{(s)}}}{\bar{W}_C} \qquad \textbf{Equation 5.3}$$

$$C_{(s)}Yield = \frac{n_{C_{(s)}}}{\dot{n}_{CH_4,in}\, t_{exp}} \qquad \textbf{Equation 5.4}$$

Table 5.1 clearly shows that very little carbon is deposited onto any of the OC's used in the EM SR experiments. This shows that under the conditions tested all materials used offered high selectivity to the SR and WGS while showing little or even negligible activity to the solid carbon forming thermal cracking of CH_4, disproportionation or CO reduction reactions. Suppression of carbon formation is an essential requirement of any catalyst used in SR as carbon formation causes a reduction in hydrogen yield by virtue of its use as a reactant in thermal cracking and by use of the hydrogen product in CO reduction. Moreover, carbon formation is one of the main causes of catalyst deactivation in SR and poses crucial challenge in industrial SR processes. Table 5.1 shows the Sf OC's resisted carbon formation to approximately the same extent as the 18NiO GR OC, an excellent indication of their suitability for the SR process and again shows that the Sf OC's can match a conventional granulated SR catalyst in an extremely important process factor.

5.3.2 Phase Composition Determination and Crystallite Analysis

XRD was used to assess the effects of the EM SR experiments upon the crystalline structure the materials used.

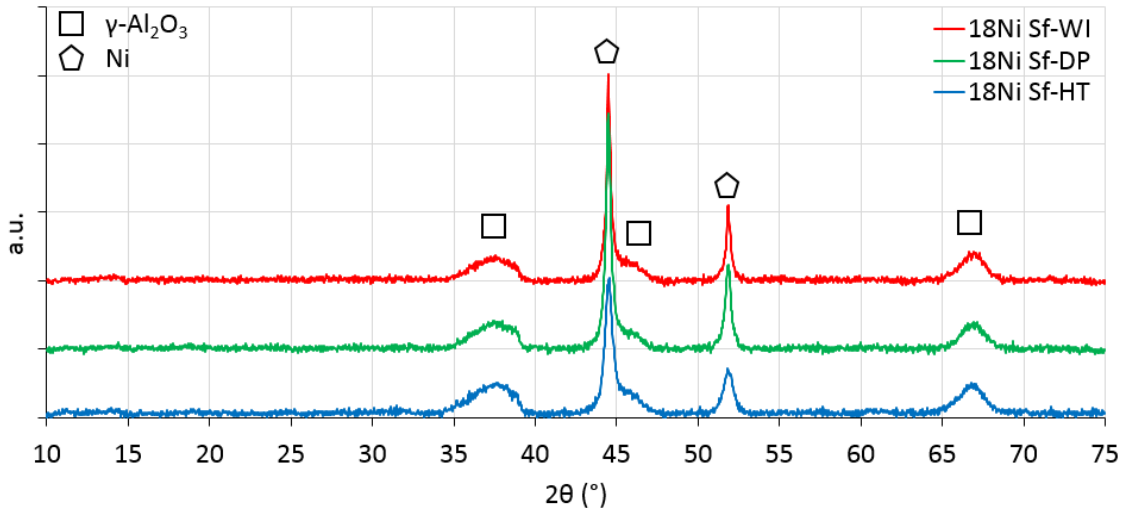

Figure 5.12: XRD pattern of the 18Ni Sf-WI, 18Ni Sf-DP and 18Ni Sf-HT OC's used in the EM SR experiments

Figure 5.12 shows that the characteristic peaks of NiO (ICDD 04-013-0888) at 2θ of 37.3°, 43.3° and 62.9° have disappeared and been replaced with peaks at 2θ of 44.5° and 51.8° characteristic of Ni (ICDD 04-010-6148); this indicates that the SR experiment completely reduced the all the Sf OC's whether in the initial reduction by 5% H_2 or by the CH_4 steam feed. No evidence was found of reduced Co phases as shown in Figure 5.13 (overleaf). A SiO_2 peak was present in the 0.6Co 18Ni DP OC at 26.6°; this was not seen in any other XRD pattern and was caused by the SiO_2 (quartz) sample holder used during XRD. Complete reduction of the 18NiO GR OC's is shown similarly in Figure 5.14 (overleaf).

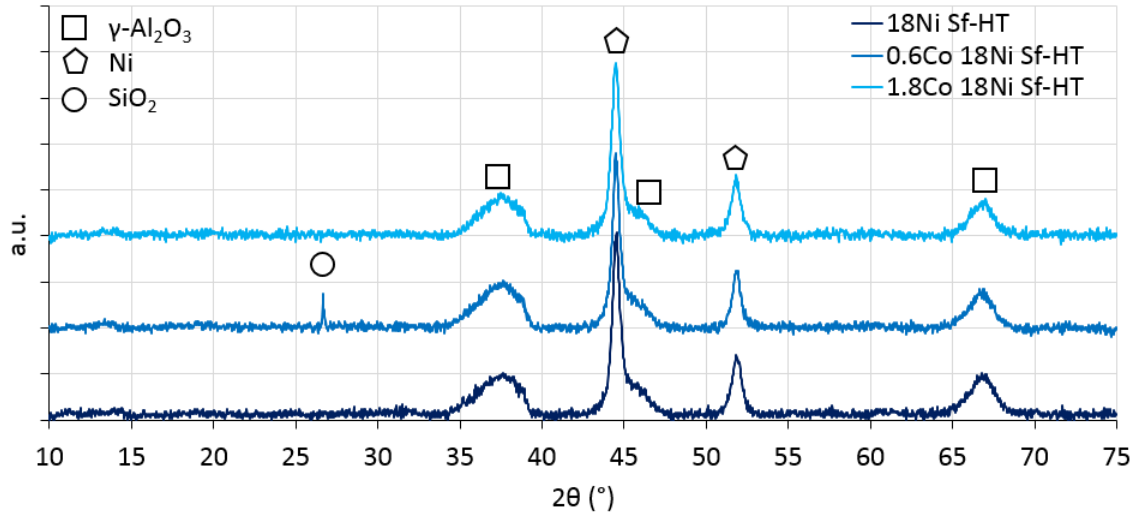

Figure 5.13: XRD pattern of the 18Ni Sf-HT, 0.6Co 18Ni Sf-HT and 1.8Co 18Ni Sf-HT OC's used in the EM SR experiments

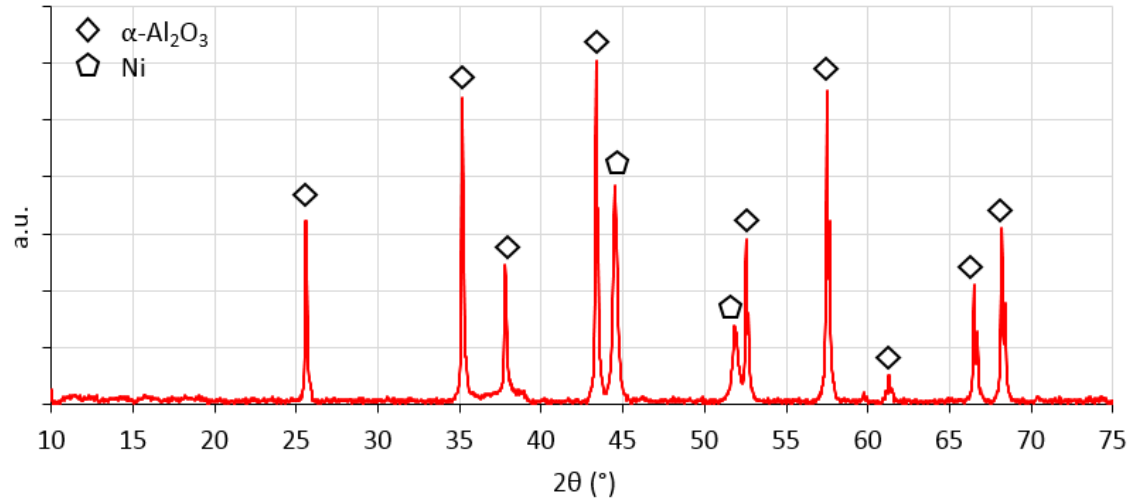

Figure 5.14: XRD pattern of the 18NiO GR OC used in the EM SR experiments

Scherrer analysis was performed on the XRD patterns produced and the results presented in Table 5.2 (overleaf). The used Sf-DP (23 nm) and Sf-HT (17 nm) OC's still present average Ni crystallite sizes far smaller than the Sf-WI OC's (60 nm) when compared with the fresh sample; an important factor in SR activity. Only the Sf-WI OC's showed higher Ni crystallite size when compared to the 18NiO GR OC (48 nm). All the OC's tested showed an increase in crystallite size on reduction from NiO to Ni and after use in the SR experiments.

Table 5.2: Mean size of the ordered crystalline domains in the fresh OC's and those used in the EM SR experiments calculated with Scherrer's equation

Sample	Fresh OC's		Post EM SR OC's	
	2θ (deg)	NiO Crystallite Size[(a)] (nm)	2θ (deg)	Ni Crystallite Size[(b)] (nm)
18Ni Sf-WI	37.2, 43.3, 62.9	16	44.5, 51.8	57
0.6Co 18Ni Sf-WI	37.2, 43.3, 62.9	36	44.5, 51.8	70
1.8Co 18Ni Sf-WI	37.2, 43.3, 62.9	32	44.5, 51.8	54
Mean WI	37.2, 43.3, 62.9	28	44.5, 51.89	60
18Ni Sf-DP	37.2, 43.3, 62.9	7	44.5, 51.89	38
0.6Co 18Ni Sf-DP	37.2, 43.3, 62.9	6	44.5, 51.8	14
1.8Co 18Ni Sf-DP	37.2, 43.3, 62.9	6	44.5, 51.8	16
Mean DP	37.2, 43.3, 62.9	7	44.5, 51.8	23
18Ni Sf-HT	37.2, 43.3, 62.9	14	44.5, 51.89	17
0.6Co 18Ni Sf-HT	37.2, 43.3, 62.9	8	44.5, 51.8	19
1.8Co 18Ni Sf-HT	37.2, 43.3, 62.9	8	44.5, 51.8	16
Mean HT	37.2, 43.3, 62.9	10	44.5, 51.8	17
18NiO GR	37.2, 43.3, 62.9	55	44.5, 51.8	48

[(a)] Where crystallite size refers to the average size of the NiO ordered crystalline domains
[(b)] Where crystallite size refers to the average size of the Ni ordered crystalline domains

Increases in crystallite size when comparing the fresh NiO crystallites and the Ni crystallites in the OC's used in the SR experiments can be attributed to high temperature (700 °C) reduction of the OC's by H_2 prior to SR and to the high temperatures and S:C ratios experienced under the CH_4/H_2O feed during SR. Sintering of Ni crystallites supported by Al_2O_3 under SR conditions is widely reported and can be exacerbated by high temperatures and high S:C ratios; it is therefore unsurprising that sintering has occurred under the SR conditions outlined here[166–170].

The 18NiO GR OC crystallite size reduced slightly during the SR experiments. Richardson et al.[150,156] have shown via XRD studies that on reduction of $NiO/\alpha\text{-}Al_2O_3$ SR catalysts at temperatures below 500 °C, the newly formed Ni crystallites tend to be smaller (up to 50%) than the original NiO crystallites. However, when subjected to high temperatures in an inert atmosphere, sintering produced Ni crystallites of similar size to the original NiO crystallites. Given that reduction using H_2 was carried at 700 °C, for approximately an hour and SR was conducted for a further hour, growth of Ni crystallites was to be expected, and thus the Ni size is only slightly lower than the NiO size.

Compared to the Sf-WI OC's, the Sf-DP and Sf-HT OC's appeared to be more resistant to increases in the crystallite size. Following use in the EM SR experiments, the crystallite size of the Sf-WI OC's increased by an average of 32 nm compared to the Sf-DP and Sf-HT OC's, where increases of only 7 nm and 16 nm respectively were experienced. This resistance to sintering may stem from suppression of particle migration; the network of

ridges formed by the honeycomb structure and the increased interaction between the support and the deposited Ni/Co in the Sf-DP and Sf-HT OC's could increase the stability of the Ni crystallites thereby reducing migration and therefore coalescence.

Increases in size of up to 50% when comparing fresh NiO and reduced Ni (conducted at 700°C with H_2) in NiO/γ-Al_2O_3 SR catalysts has been reported[232]; given that the Sf-OC's were then used in SR for a further hour, the large increase in the Ni crystallite size of the Sf-WI OC's was not exceptional.

5.3.3 Specific Surface Area and Porosity

BET and BJH analysis of the adsorption isotherms was conducted to assess the effects of the EM SR experiments upon the OC's. Figures A.5.4 to A.5.6. (Appendix A.5) show no evidence that the isotherm or hysteresis loop type has changed, implying little change to the pore structure of the OC's as a result of the SR experiments.

Table 5.3: BET specific surface area of the fresh OC's and those used in the EM SR experiments

Sample	Multi point BET	
	Fresh OC's	EM SR OC's
	SSA (m^2 g^{-1})	SSA (m^2 g^{-1})
Saffil®	106	N/A
18Ni Sf-WI	75	91
0.6Co 18Ni Sf-WI	61	92
1.8Co 18Ni Sf-WI	65	91
Mean WI	67	91
18Ni Sf-DP	102	100
0.6Co 18Ni Sf-DP	120	96
1.8Co 18Ni Sf-DP	118	95
Mean DP	113	97
18Ni Sf-HT	117	92
0.6Co 18Ni Sf-HT	118	86
1.8Co 18Ni Sf-WI	115	91
Mean HT	117	90

The average SSA of the Sf-HT and Sf-DP OC's both reduced when used in the EM SR experiments, Table 5.3. The Sf-HT OC's were found to reduce in average SSA by 27 m^2 g^{-1}, with the loss in SSA consistent across the three samples. The 0.6Co 18Ni Sf-DP and 1.8Co 18Ni Sf-DP samples also reduced by a similar amount, reducing in SSA by 24 m^2 g^{-1} and 27 m^2 g^{-1} respectively, while the 18Ni DP sample reduced by only 2 m^2 g^{-1} from 102 m^2 g^{-1} to 100 m^2 g^{-1}. Both the Sf-DP and Sf-HT OC's still offered a higher surface area than the fresh WI OC's a fact attributed to the morphology of the deposited layer in these OC's. The reduction in SSA could be due to sintering of the Ni crystallites during the EM SR

experiments, a hypothesis corroborated by the increase in crystallite size from Scherrer analysis from XRD. Additionally, a breakdown in the ridged honeycomb structure seen in SEM images in Section 5.3.4, that was in part held responsible for the increase in SSA over the WI and Saffil® support, may offer some explanation as to the reduction in SSA.

In a surprising result, the SSA of the Sf-WI OC's increased after use in the EM SR experiments by between 15 and 30 $m^2 g^{-1}$ with an average increase of 24 $m^2 g^{-1}$. This was unexpected and therefore repeat measurements were made of the fresh and used Sf-WI OC's, with both measurements returning values within 1 $m^2 g^{-1}$. An explanation for this can be found in the increase in pore volume of the Sf-WI OC's to approximately the same pore volume as shown by the as-received Saffil® fibres. Sintering of the nodular crystallites could cause a contraction of the Ni layer thereby reducing the likelihood of blocked pores and so increasing internal surface area.

Table A.5.1 (Appendix A.5) shows the pore volume of the Sf-DP and Sf-HT OC's was not significantly changed after the EM SR experiments and while the pore diameter of the Sf-WI, Sf-DP and Sf-HT OC's increased slightly after SR, this rise was not seen as a significant result.

Zin et al[100] showed that the SSA of the 18NiO GR OC was not significantly altered after during 2 hours SR of pine oil and PEFB steam reforming reducing from 3.2 g m^{-2} to 2.7 g m^{-2}; this combined with evidence from Scherrer analysis above and SEM (Section 5.3.4) suggests very little sintering of the 18NiO GR OC occurred.

5.3.4 Morphology and Topography

SEM was used to assess the effects of the EM SR experiments upon the morphology of the Ni/Co coating and the Saffil® fibres. EDX analysis of the used OC's was proposed to evaluate the distribution of the carbon formed upon the OC's after use in the SR experiment. However, in practice this was difficult achieve. The carbon tape used to affix the sample to the SEM stub and the carbon coating used to reduce charging of the sample and improve imaging in all other SEM images would make identification of deposited carbon impossible. As such, a copper-based tape and an iridium coating was used. Despite this, results were poor, with identification of carbon deposits proving impracticable likely due to the very small mass of carbon deposited causing a high signal to noise ratio.

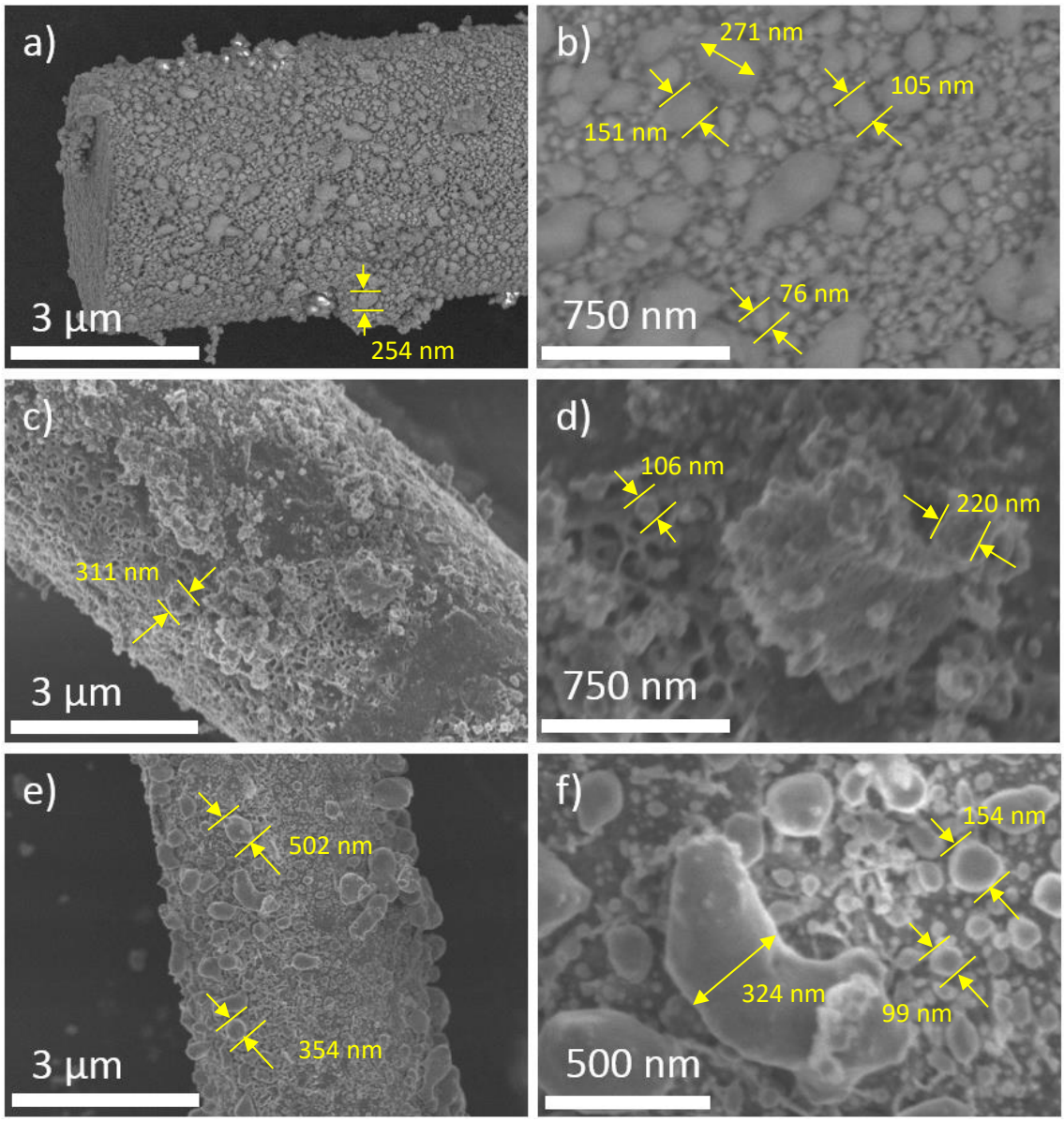

Figure 5.15: SEM images of 18Ni Sf-WI (a and b), 0.6Co 18Ni Sf-WI (c and d) and 1.8Co 18Ni Sf-WI (e and f) after use in the EM SR experiments

Figure 5.15a, c and e clearly show that the size of the nodular NiO particles seen in the fresh Sf-WI OC's (Figure 4.7 and Figure 4.8) has increased during reduction to Ni and subsequent use in the EM SR experiments. This is likely due to sintering of the Ni/Co layer due to high temperatures and S:C ratios experienced during the EM SR experiments. This effect was quantified by taking a size distribution of the above images, Table 5.4 (overleaf).

Table 5.4: Comparison of particle size[(a)] in the Sf-WI OC's and void size[(c)] in the Sf-DP and Sf-HT OC's used in the EM SR experiments measured in SEM

	Particle Size[(a,b)] (nm)			Void Size[(b,c)] (nm)					
	18Ni WI	0.6Co 18Ni WI	1.8Co 18Ni WI	18Ni DP	0.6Co 18Ni DP	1.8Co 18Ni DP	18Ni HT	0.6Co 18Ni HT	1.8Co 18Ni HT
Mean	111	160	200	251	279	251	234	245	190
SD	45	65	121	68	59	63	40	52	43
Max	266	321	570	459	519	480	328	409	433
Min	50	62	54	141	173	137	149	146	110

[(a)] Where particle size refers to the maximum diameter of particles identified in SEM images. [(b)]Based on 100 measurements via ImageJ. [(c)]Where void size refers to the maximum diameter of inter-ridge voids identified in the non-sintered SEM images.

Table 5.4 shows that the average particle size as determined by SEM shows an increase over the fresh samples of ~ 30 nm in the 18Ni Sf-WI OC, ~ 100 nm in the 0.6Co 18Ni Sf-WI OC and ~ 140 nm in the 1.8Co 18Ni Sf-WI OC (Table 4.3). This increase in particle size mirrors the increase in crystallite size shown by Scherrer analysis, however it is clear from the above images that the magnitude of that increase is far larger in the particles shown in the SEM measurements. This suggests that not only are the individual crystallites of Ni increasing in size through coalescence of separate crystallites but also that many separate crystallites have sintered into larger agglomerations composed of multiple crystallites.

It is difficult to assess whether the cobalt may have decreased the resistance to sintering of the deposited layer due mainly to the large standard deviation associated with the measurements. In any case, the sintering of the crystallites seemed to have little effect over the hour of the SR experiments with no appreciable drop off in the performance of the OC's experiments.

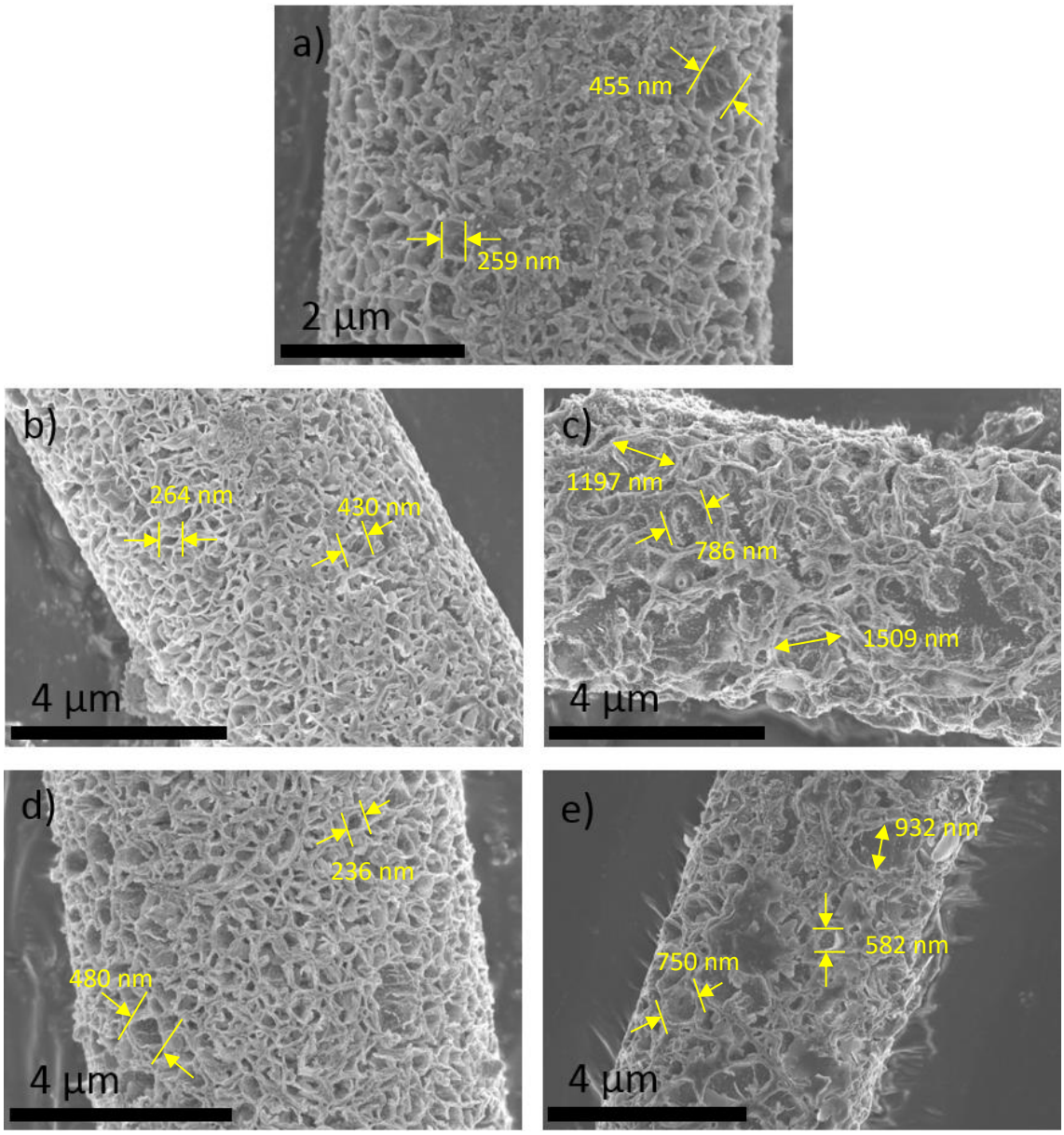

Figure 5.16: SEM images of 18Ni Sf-DP (a), 0.6Co 18Ni Sf-DP (b and c) and 1.8Co 18Ni Sf-WI (d and e) after use in the EM SR experiments. Images a, b and d show intact ridged morphology and c and e show evidence of sintering

Figure 5.16a, b and d shows that the folded ridged morphology of the NiO seen in the fresh Sf-DP OC's (Figure 4.10 and Figure 4.11a, b and c) has been maintained throughout the reduction to Ni and the subsequent EM SR experiments in all cases. There is some evidence in Figure 5.16c and e of a breakdown in these structures both in formation of nodular crystallites as in the fresh Sf-WI OC's (shown in Figure 5.16a) and in a widening and partial breakdown of the ridged structure resulting in much larger voids. It must be stated at this point that examples of this severe alteration were rare in the SEM images taken and the majority of images showed the intact honeycomb structure. However, inspection of Table 5.4 shows that the void sizes of the samples with intact structures has

increased to approximately 250nm in all the Sf-DP OC's as a result of their use in the EM SR experiments. Both the breakdown in the honeycomb structure and the more general increase in void size could be explained by sintering of the Ni crystals in the Sf-DP OC's (as evidenced by Scherrer analysis) either during reduction or during the SR experiments.

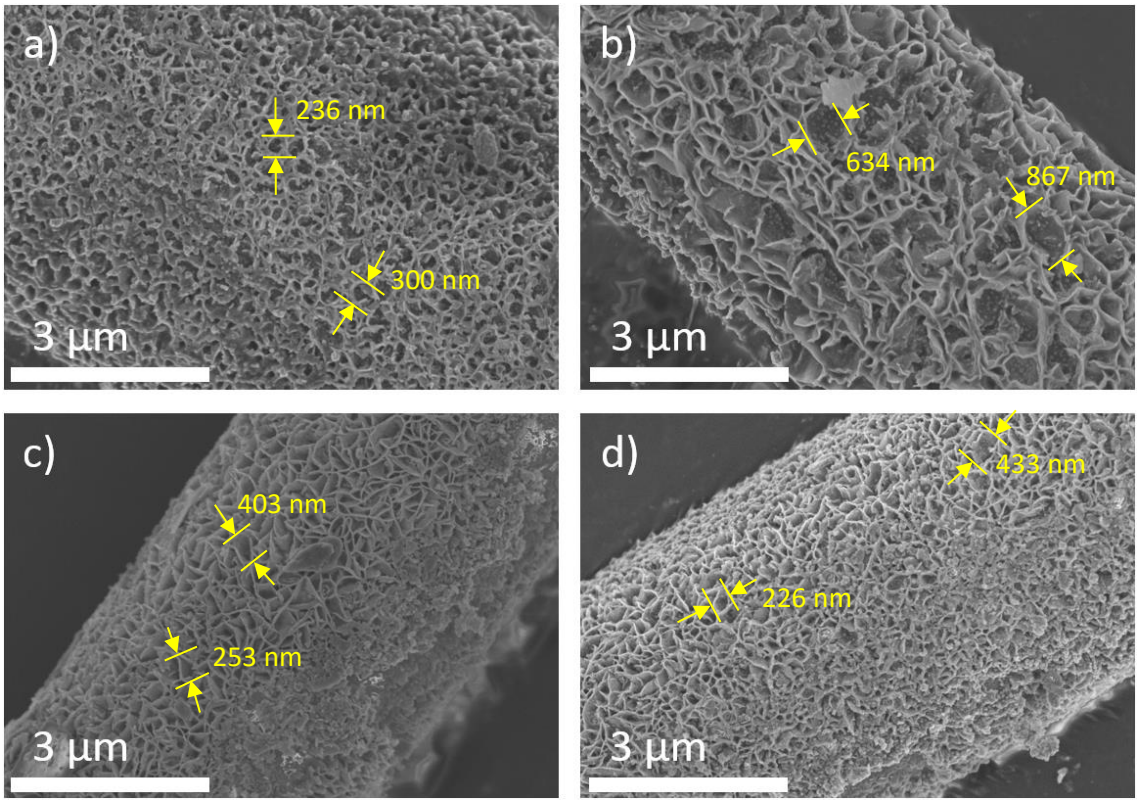

Figure 5.17: SEM images of 18Ni Sf-HT (a and b), 0.6Co 18Ni Sf-HT (c) and 1.8Co 18Ni Sf-HT (d) after use in the EM SR experiments

In a similar manner to the Sf-DP OC's, the ridged morphology of the NiO layer present in the fresh HT samples was maintained throughout reduction to Ni and the subsequent EM SR experiments, Figure 5.17. The increase in void size across the Sf-HT OC's was approximately 60 nm. The 18Ni Sf-OC and 0.6Co 18Ni Sf-OC presented very similar void and crystallite sizes (as determined by Scherrer analysis) to the Sf-DP OC's; this provides more evidence to suggest the void sizes and crystallite sizes of the Sf-DP and Sf-HT OC's are linked. Evidence of sintering was also present but not widespread in the Sf-HT OC's, with sporadic evidence for a break down structure into larger voids, Figure 5.17c. Small nodular crystallites were also shown in Figure 5.17c providing further evidence for sintering of the deposited layer.

Comparison of Figures A.1.2 a, b and c and A.1.3 a, b and c show that there was little or no change to the morphology of the 18NiO GR OC during the SR experiments; this agreed with the very small decrease in Ni crystallite size determined via Scherrer analysis.

5.4 Summary

SR experiments were conducted upon the Sf OC's and their performance compared with that of the 18NiO GR OC both on an Equal Mass (EM) and Equal Volume (EV) basis (Table 3.3 – reproduced below). After these experiments the effects on the physical characteristics of the OC materials used were determined via solids characterisation.

Table 3.3: Experimental conditions for the SR experiments

SR Conditions	m_{OC} (g)		V_{bed} (cm^{-3})		$V_{i,in}$ (sccm)			T (°C)	S:C
	Sf OC	GR OC	Sf OC	GR OC	N_2	CH_4	H_2O		
Equal Mass (EM)	2.0	2.0	12.5	12.5	1000	111.0	0.25	700	3
Equal Volume (EV)	0.4	2.0	2.5	2.5	800	88.8	0.20	700	3

Through a series of equilibrium calculations and preliminary flow experiments the optimum conditions for EM and EV runs were established and equilibrium limitation were avoided. Blank experiments showed water splitting of reduced metallic reactor materials in the 0^{th} SR half cycle. Moreover, SR activity was present during all SR half cycles; this was likely caused by reduction of the reactor materials by the CH_4/H_2O feeds. Given that all OC's are tested using the same equipment these effects were assumed to be constant throughout the experiments and as such comparison of the between the Sf OC's and 18NiO GR OC is still valid.

The EM and EV SR experiments showed that stable outputs of the primary products of H_2, CO and CO_2 were achieved in all cases with no appreciable evidence of catalyst deactivation during of SR of methane. Comparison of the Sf OC's and 18NiO GR OC under EM SR conditions indicated that the Sf OC's were able to outperform the 18NiO GR OC in terms of CH_4 conversion, H_2 yield efficiency and H_2 purity by up to 12.8, 9.2 and 2.3 percentage points (pp) respectively (1.8Co 18Ni Sf-HT). Under EV conditions, the Sf OC's were able to produce a comparable performance to a conventional catalyst (albeit slightly lower) despite operating with 80% less mass of OC (0.4 g of Sf OC to 2 g of 18NiO GR OC). These improvements in catalytic performance shown by the Sf OC's are likely caused by a reduction in the effective diffusion length required for CH_4 to transfer from the bulk gas to active Ni catalytic sites and for reactions products to diffuse away from those sites into the bulk gas phase. This is facilitated by the decrease in effective particle size (~ 200 μm to > 10 μm) and the defined layer of Ni/NiO coating exhibited by the Sf OC's; these factors combine to lower diffusion barriers for the SR reaction. These results show that process intensification of fixed bed SR processes can be achieved with the use of microfibrous Co

doped Ni OC's using Saffil® as a support. Additionally, the Sf-DP and Sf-HT OC's were marginally more effective than the Sf-WI OC's (under EM conditions) which was attributed to lower crystallite size, improved coating uniformity and more open texture of the deposited active phase.

Post EM SR experiment characterisation showed that: according to CHN analysis of the used materials, all materials used exhibited little or even negligible activity to the formation of solid carbon; all materials were fully reduced from NiO to Ni and the average crystallite size increased in all samples after use in SR (as shown by XRD); all samples showed evidence of some sintering in the reduced Ni/Co layer with the Sf-WI OC's evidencing particular susceptibility to this effect. Resistance to sintering in the Sf-DP and Sf-HT OC's was attributed to the ridged morphology seen in the SEM images throughout these samples; specific surface area (SSA) in the Sf-WI OC's determined by the BET method increased by 25 - 30 m^2 g^{-1} due to pore unblocking induced by sintering of the Ni/Co layer. SSA in the Sf-DP and Sf-HT OC's reduced after use in the SR experiments, but still exhibited higher SSA than both the fresh and used Sf-WI OC's (BET).

6 Isothermal Performance of Fibrous Oxygen Carriers during Chemical Looping Steam Reforming of Methane

This chapter details the novel application of fibrous structured OC's to a chemical looping reforming process. The performance of the Sf OC's in CLSR experiments benchmarked against the 18NiO GR OC over several redox cycles. The OC materials were then characterised to assess the effect of the CLSR experiments upon their physical properties.

6.1 Performance of Oxygen Carrier Materials in CLSR

These experiments analyse several characteristics of the OC's tested. Under the steam reforming half cycle the OC materials were examined for their ability to be reduced by a N_2 diluted H_2O and CH_4 feedstock at a 3:1 molar ratio and consequently their catalytic activity and selectivity for the SR and WGS reactions. Furthermore, the extent of the reduction (α_{red}) was also determined. Under the oxidation half cycle the ability of the OC materials to be re-oxidised and the extent of that re-oxidation (α_{ox}) was determined.

6.1.1 Equal Mass (EM) Conditions

The experiments used two conditions that varied the flow rate of the reactants and the volume and mass of the OC materials used. Under EM conditions, both the mass of OC (m_{OC}, 2g) used and the volume of the bed (V_{bed}, 12.5 cm^3) were equal, Table 3.4 (reproduced below). This was achieved through the dilution of the denser 18NiO GR OC with silica sand granules of equal size.

Table 3.4: Experimental conditions for the CLSR experiments

CLSR Conditions	m_{OC} (g)		V_{bed} (cm^3)		$\dot{V}_{i,in}$ (sccm)			T (°C)	S:C	Redox Cycles
	Sf OC	GR OC	Sf OC	GR OC	N_2	CH_4	H_2O			
Equal Mass (EM)	2.0	2.0	12.5	12.5	1000	111.0	0.25	700	3	6
Equal Volume (EV)	0.4	2.0	2.5	2.5	800	88.8	0.20	700	3	7

6.1.1.1 Single Cycle EM CLSR Outlet Concentrations

Figure 6.1 (overleaf) shows the dry outlet composition for the 2nd EM CLSR cycle during the SR and oxidation half cycles using the 0.6Co 18Ni Sf-DP OC as representative of all the Sf OC's tested.

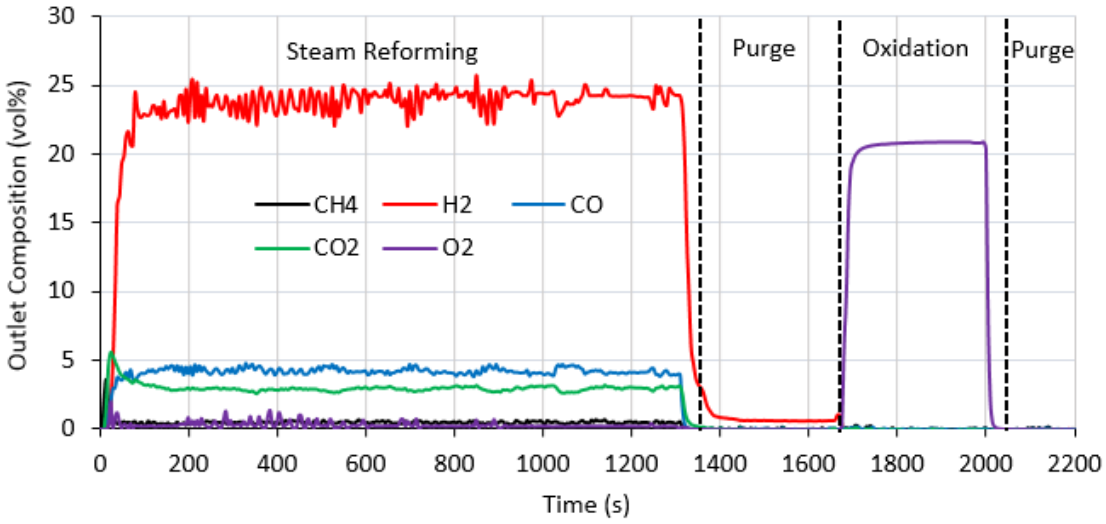

Figure 6.1: Dry outlet composition during the 2nd cycle of EM CLSR using 0.6Co 18Ni Sf-DP OC at 700°C and S:C 3 as representative of a typical EM CLSR experiment using Sf OCs

Figure 6.1 above shows that during a typical SR half-cycle, the dry outlet was composed of a primary product of H_2 with by-products of both CO and CO_2 and a small amount of unreacted CH_4 detected. This shows that the OC's were able to effectively catalyse the SR and WGS reactions implying that a fraction of the Ni/Co oxides present on the OC materials were auto-reduced to their catalytically active phase by the CH_4/H_2O feedstock.

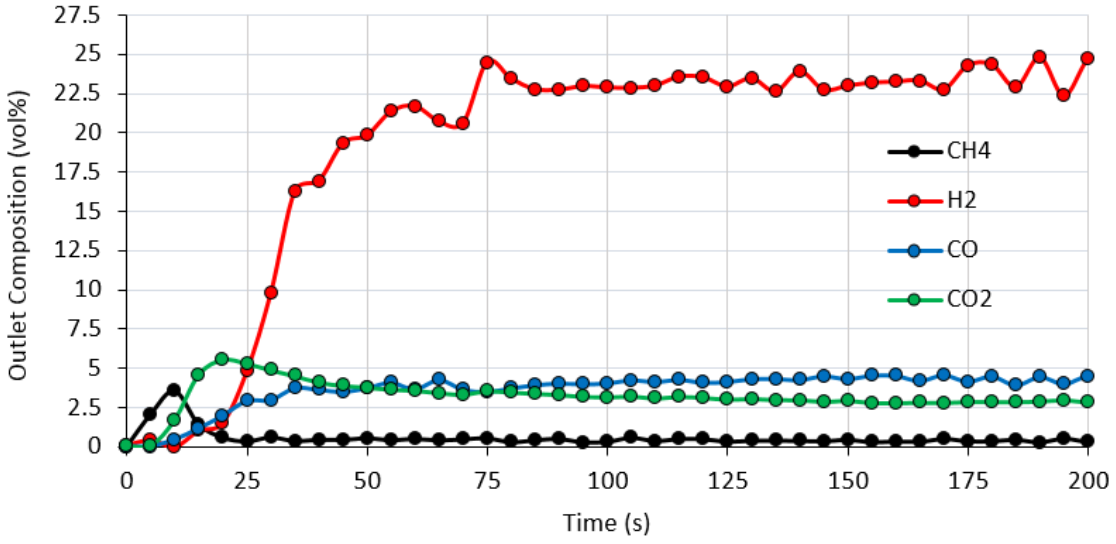

Figure 6.2: Dry outlet composition during the first 200 s of the 2nd EM SR half-cycle using 0.6Co 18Ni Sf-DP OC at 700°C and S:C 3

Further evidence of auto-reduction can be observed in the 2nd EM steam reforming half-cycle of the 0.6Co 18Ni Sf-SP OC shown in Figure 6.2. After an initial rise in CH_4 in the outlet, CO and especially CO_2 concentrations increased, coinciding with a decrease in CH_4. This was evidence of reduction of the NiO present to Ni. The prevalence of CO_2 in the

product stream early in the auto-reduction process implies that complete oxidation of CH_4 (Equation 1.14) dominated the reduction of the OC when the extent of the reduction was low (i.e. more NiO than Ni). This may be through direct reduction of the OC via complete oxidation, or through partial oxidation of CH_4 (Equation 1.14) quickly followed by secondary reduction reactions (Equation 1.15 and Equation 1.16) consuming CO and H_2 thereby increasing the CO_2 (and the undetectable H_2O) concentration in the outlet. This agrees with the CLPO and CLC literature concerning Ni based OC's in that they have higher selectivity to OC reduction via complete combustion of CH_4 (Equation 1.13) during the early stages of reduction than to partial oxidation of CH_4 (Equation 1.14)[48,127]. The relevant equations are reproduced below:

$CH_{4(g)} + 4NiO_{(s)} \rightarrow 4Ni_{(s)} + CO_{2(g)} + 2H_2O_{(g)}$ $\Delta H_{1200K} = 135$ kJ mol^{-1} **Equation 1.13**

$CH_{4(g)} + NiO_{(s)} \rightarrow Ni_{(s)} + CO_{(g)} + 2H_{2(g)}$ $\Delta H_{1200K} = 213$ kJ mol^{-1} **Equation 1.14**

$CO_{(g)} + NiO_{(s)} \leftrightarrows Ni_{(s)} + CO_{2(g)}$ $\Delta H_{1200K} = -48$ kJ mol^{-1} **Equation 1.15**

$H_{2(g)} + NiO_{(s)} \leftrightarrows Ni_{(s)} + H_2O_{(g)}$ $\Delta H_{1200K} = -15$ kJ mol^{-1} **Equation 1.16**

Peak CO_2 concentration corresponded with a large rise in H_2 concentration; as the extent of reduction increased, more Ni was produced and thus more Ni was available to catalyse the SR and WGS reactions. As the reduction neared completion, CO_2 concentration began to reach steady state between 50 - 75 s, the SR and WGS reactions dominate and the reduction is completed. The expected (based on H_2:CO and H_2:CO_2) and detected H_2 vol% were similar (24.27 % and 24.21 % respectively at 1200 s Figure 6.1) showing high accuracy.

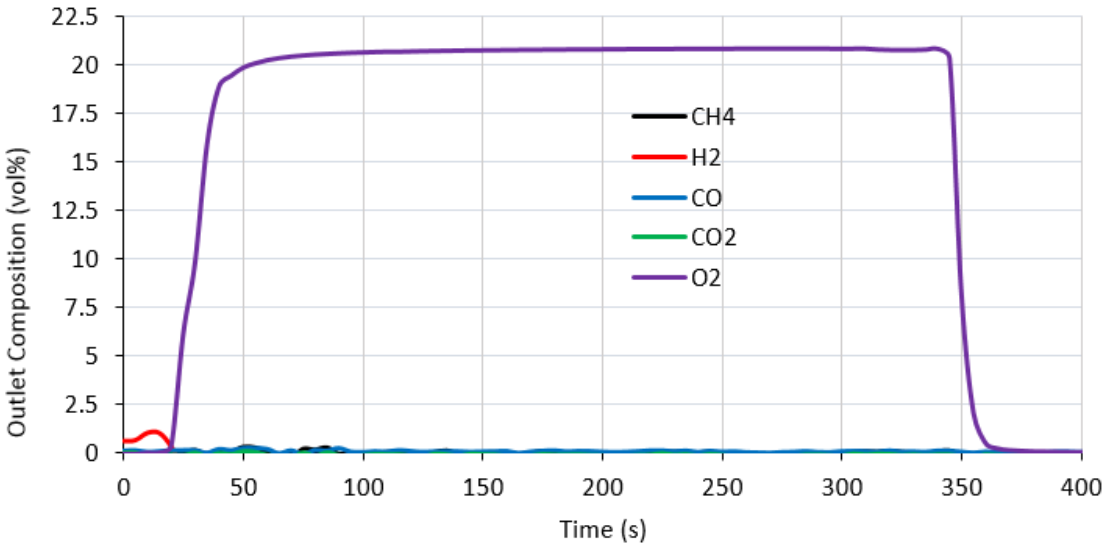

Figure 6.3: Dry outlet composition during the 2nd EM oxidation half-cycle using 0.6Co 18Ni Sf-DP OC at 700°C and S:C 3

Figure 6.1 and Figure 6.3 show no CO_2 peak during the oxidation half cycle to suggest combustion of solid carbon (Equation 1.17). This implies a lack of carbon deposition during reduction and steam reforming. Therefore, oxidation of the OC is favoured (Equation 1.18). No CO_2 peak was observed in any of the samples tested under EM conditions.

$C_{(s)} + O_{2(g)} \rightarrow CO_{2(g)}$ $\Delta H_{1200K} = -393$ kJ mol^{-1} **Equation 1.17**

$2Ni_{(s)} + O_{2(g)} \rightarrow NiO_{(s)}$ $\Delta H_{1200K} = -468$ kJ mol^{-1} **Equation 1.18**

Moreover, the outlet concentration of O_2 reached approximately 21% in all case by the end of the 300 s under an air feed. This suggests the oxidation reaction had finished by 300s (see Section 6.1.1.3 for more details).

The process outlet concentrations (as shown by Figure 6.1, Figure 6.2 and Figure 6.3) were very similar to those exhibited by the 18NiO GR OC (see Figure A.6.1, Figure A.6.2 and Figure A.6.5, Appendix A.6). The 18NiO GR OC showed a greater proportion of CO_2 in the dry outlet during auto-reduction than the example above, which could suggest a greater prevalence of the reduction via complete combustion of CH_4. Higher selectivity to CO_2 during reduction of a NiO/α-Al_2O_3 OC when compared to a NiO/γ-Al_2O_3 OC has been reported elsewhere[46,119]. Generally, the Sf OC's produced slightly more H_2 and slightly less unconverted CH_4 during SR. No CO_2 peak was found indicative of $C_{(s)}$ oxidation.

6.1.1.2 Single Cycle Reduction of OC's during EM CLSR

Detailed analysis of the reduction and oxidation of the OC's was achieved using the rates of reduction and oxidation (r_{red},OC and r_{ox},OC) and extent of reduction and oxidation (α_{red} and α_{ox}) as defined in Section 3.4.5 and the process outputs listed in Section 3.4.6 (H_2 purity, H_2 yield efficiency and CH_4 conversion).

Figure 6.4a and b (overleaf) shows the first 200 s of the 1st EM steam reforming half-cycle using 18Ni Sf-WI OC. The onset of OC reduction is clearly shown at t=0 in both Figure 6.4a and b. Before this point only N_2 is flowing through the reactor and therefore no products are detected in the outlet. CH_4 and H_2O conversion as well as r_{red},OC up to this point are also constant at approximately 100%, -67% and 1.6×10^{-4} mol s^{-1} respectively as determined by elemental balance calculations. Negative H_2O conversion after t=0 signifies a production of H_2O in excess of the feed rate[52,93,101], this coupled with an increase in CH_4 conversion implies that reduction of the OC through complete combustion (Equation 1.13) was achieved. After 15 s, an abundance of the reduced OC caused the initiation of the SR and WGS reactions thereby consuming H_2O and thus increasing the H_2O conversion.

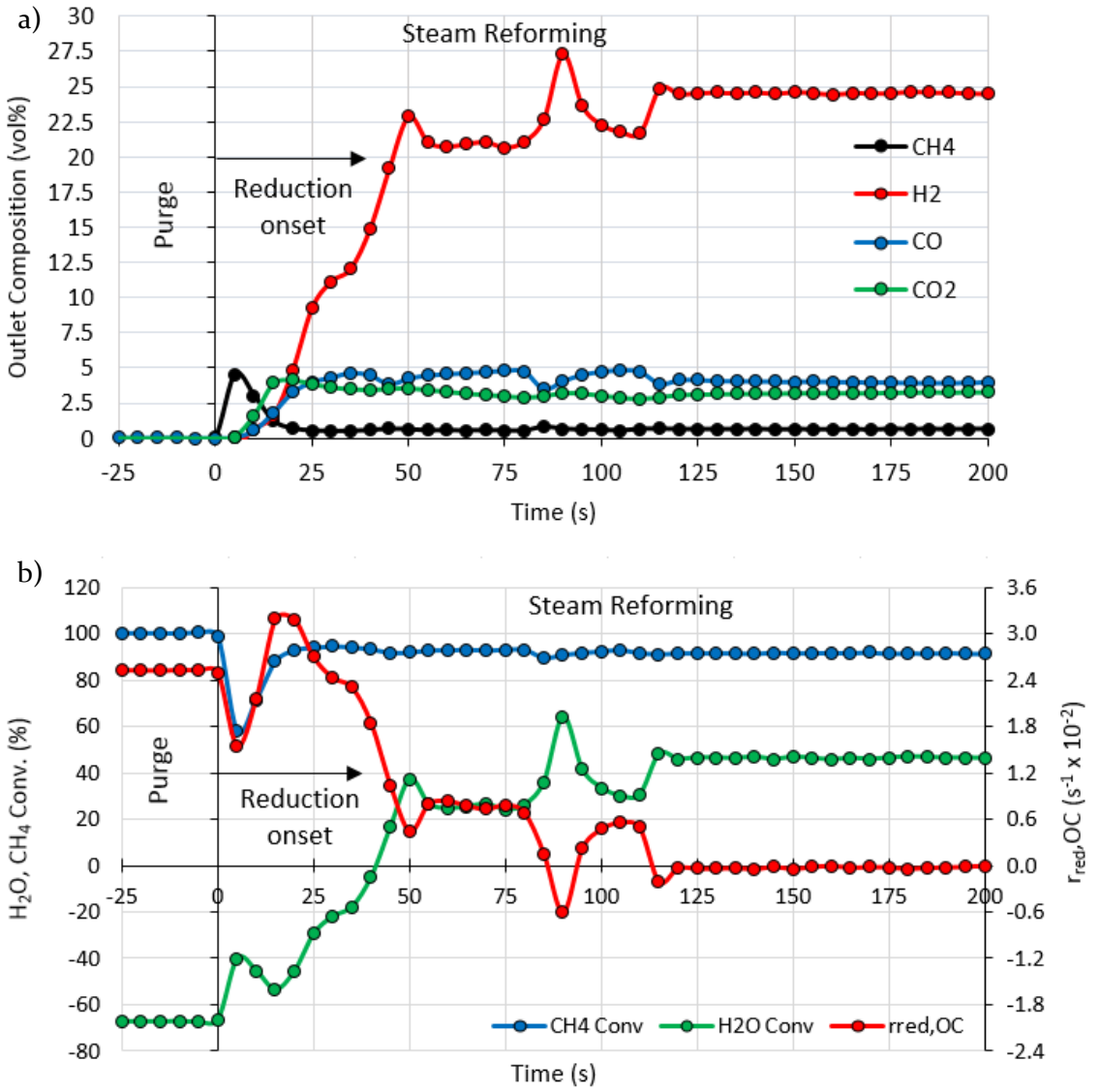

Figure 6.4: Dry outlet composition (a) CH_4 and H_2O conversion vs rate of reduction of the OC (r_{red},OC) (b) during the first 200 s of the 1st EM steam reforming half-cycle using 18Ni Sf-WI OC at 700°C and S:C 3

If r_{red},OC, CH_4 and H_2O conversion are assumed to be zero at t=0, as indicated by the lack of outlet concentrations and constant r_{red},OC, CH_4 and H_2O conversion at t=0 shown above, integration of r_{red},OC from t=0 can yield the extent of reduction (α_{red}) of the OC at any given time on stream.

Figure 6.5b plots the reduction extent (α_{red}) through integration of the rate of reduction (r_{red},OC) over time. Integration of r_{red},OC should be limited to the defined reduction peak and thereby stopped when steady state conditions are reached. This limits any cumulative error that could be accrued owing to very minor elemental imbalances that could be amplified over long integration periods.

This graphs shows that under EM conditions, r_{red},OC shows a reduction profile up to 50 s corresponding to α_{red} = 1 (100%). After 50s, a spike in H_2 concentration and matching decreases in carbon gases caused unexpected rises in r_{red},OC until 120 s. This erratic output was experienced throughout the EM experiments, including those using the 18NiO GR OC (Figure A.6.3 and A.6.4, Appendix A.6), and was the cause for the extent of reduction exceeding unity in all cases. This erratic rate of reduction was not seen any of the EV CLSR experiments, or in similar works[101].

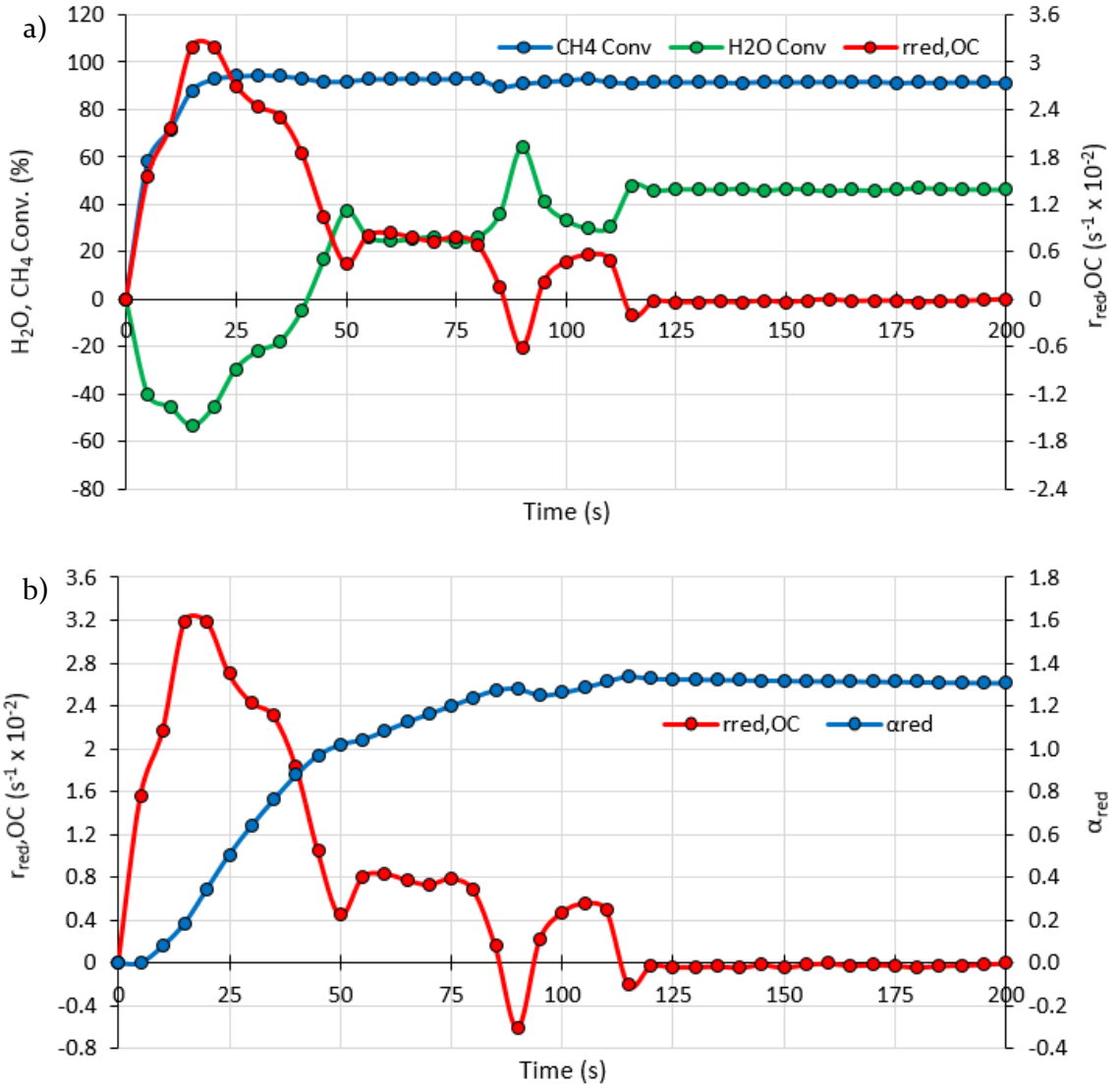

Figure 6.5: CH_4 and H_2O conversion vs r_{red},OC (a) and r_{red},OC and reduction extent (α_{red}) of the 18Ni Sf-WI OC during the first 200 s of the 1st EM steam reforming half-cycle 700°C and S:C 3

The erratic nature of the r_{red},OC was attributed to irregular provision of water into the reactor as the H_2O conversion shown in Figure 6.5 is roughly the inverse of r_{red},OC (Equation 3.18). In spite of the plausible α_{red} up to 50 s shown in the above example, these deviances from steady state conditions mean that even the data during the first 50 s could

be affected by erratic water provision thereby making the r_{red},OC and α_{red} derived from EM conditions potentially unreliable. This meant that data generated on the extent of reduction under EM conditions was not used for further analysis. The causes of the erratic water provision are detailed in Section 6.1.2.1.

Consultation of Figure A.9.1 (Appendix A.9.) shows that during the SR half cycle of the blank experiment (see Section 5.1.3) there was no discernable effect upon the CH_4, CO or CO_2 concentration immeadiately following the onset of the CH_4/H_2O feed. Moreover, the rate of reduction prior to SR activity being detected (as evidenced by H_2 CO and CO_2 production) was negligible, especially when compared to that of the reduction events of the OC's seen during the EV and EM CLSR experiments (Figure A.9.2). This suggests that any reduction of the reactor materials will likely have a negligible effect on the r_{red},OC or α_{red} during the reduction of the OC.

6.1.1.3 Single Cycle Oxidation of NiO OC's during EM CLSR

Figure 6.6 shows the 1st oxidation half cycle conducted with the 18Ni Sf-WI OC. Similarly to the reduction reaction, oxidation of the OC as indicated by a change in r_{ox},OC, and rapidly increasing O_2 concentration in the outlet after t=0. If $r_{ox,}$OC, is assumed to be zero at t=0, as indicated by the lack of O_2 outlet concentration and constant $r_{ox,}$OC, at t=0 shown above, integration of $r_{ox,}$OC from t=0 yields the extent of reduction (α_{ox}) of the OC at any given time on stream.

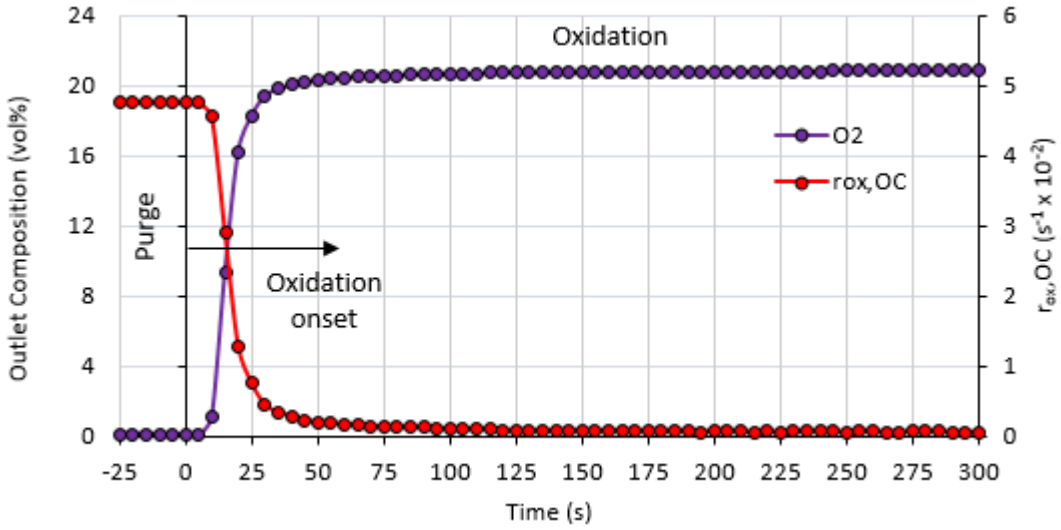

Figure 6.6: Outlet O_2 concentration and $r_{ox,}$OC (during the first 300 s of the 1st EM oxidation half-cycle at 700°C and S:C 3

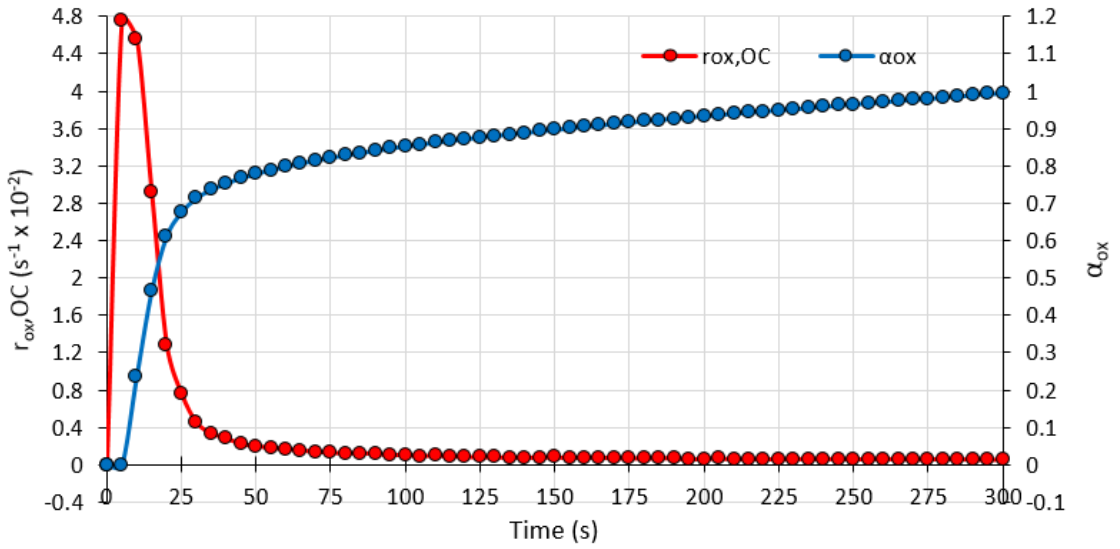

Figure 6.7: r_{ox},OC and oxidation extent (α_{ox}) of the 18Ni Sf-WI OC during the first 300 s of the 1st EM oxidation half-cycle at 700°C and S:C 3

The extent of oxidation reached 100% in Figure 6.7b; this was achieved in all the EM CLSR experiments with both the Sf OC's and the 18NiO GR OC (Figure A.6.6, Appendix A.6). However, the lack of data points between the start of oxidation and peak r_{ox},OC, the high rates of reaction experienced in the oxidation half cycle (a property widely acknowledged in the literature[23,44,131,160]) as well as the reliance on integration of steady state data means that there are some reservations about the reliability of this data. To corroborate re-oxidation of the OC materials, XRD was conducted after the last EM oxidation cycle (Section 6.2.1.2). This analysis showed that complete re-oxidation of the Sf-DP, Sf-HT and 18NiO GR OC was achieved within the 5 minutes oxidation half cycle, with these samples showing no evidence of the reduced Ni phase; however, the Sf-WI OC's were shown to still contain small amounts of the reduced Ni phase after the final oxidation half cycle. This will be discussed further in Section 6.1.2.4.

Due to the disagreement between these methods of analysis, and the inaccuracies described above, the oxidation of the OC's using r_{ox},OC or α_{ox} was not studied further; as such no assumptions are made on the oxidation extent for the 18Ni Sf-WI OC's during EM CLSR.

6.1.1.4 Average SR Performance over 6 EM CLSR cycles

More in-depth analysis of the catalytic activity of the OC's after auto-reduction in the SR half cycle was facilitated using the process outputs listed in Section 3.4.6 (H_2 purity, H_2 yield efficiency and CH_4 conversion).

The average H_2 purity and yield and CH_4 conversion averaged over 6 EM CLSR cycles for all nine Sf OC's are compared to those of the 18NiO GR OC and equilibrium values in Figure 6.8. The carbon balance shows an average error of > 5 % between the molar flows of carbon in and out of the reactor across all experiments, indicating acceptable accuracy in the measurements and elemental balance analysis.

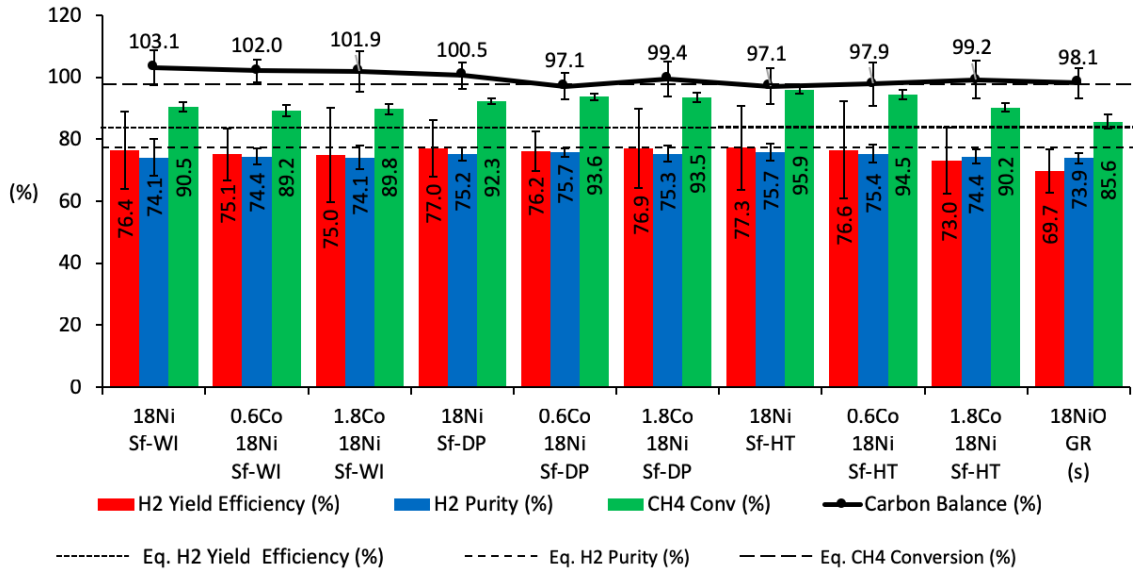

Figure 6.8: Average H_2 purity and yield efficiency and CH_4 conversion over 6 EM CLSR cycles compared with equilibrium values at 700°C and S:C 3. Error bars represent the standard deviation of the mean CH_4 conversion, H_2 purity and yield efficiency over 6 SR half cycles.

When equal mass (2g) of OC material is used, all the Sf OC's presented an improvement in terms of average CH_4 conversion over the conventional 18NiO GR OC, Figure 6.8. The increase in CH_4 conversion ranged from 3.6 to 10.3 percentage points (pp) and when compared to the error bars, these increases were statistically significant. When the changes in H_2 yield efficiency and purity are observed, the standard deviation of these factors is too high for any changes to be considered statistically significant. This high variance in the measurement of the H_2 yield efficiency and purity can again be attributed to the erratic water provision to the reactor. The 18Ni Sf-HT OC was the most effective OC tested, returning a 10.3 pp improvement in CH_4 conversion (86 % to 96 %). The Sf-DP and Sf-HT OC's improved the CH_4 conversion by approximately 3 pp over the Sf-WI OC's in a statistically significant result. Cobalt doping did not influence the CH_4 conversion or H_2 purity or yield efficiency of the Sf OC's.

6.1.1.5 SR Performance per EM CLSR cycle

The CH_4 conversion per cycle over the 6 EM CLSR test cycles is shown in Figure 6.9 and indicates that the performance of the Sf OC's was consistently superior to that of

conventional 18NiO GR OC, with the Sf-HT OC's having optimum performance. The increase in CH_4 conversion after cycle 4 in the 18NiO GR OC was unexpected, but still shows that increases shown by the Sf OC's across the 6 cycles tested are significant.

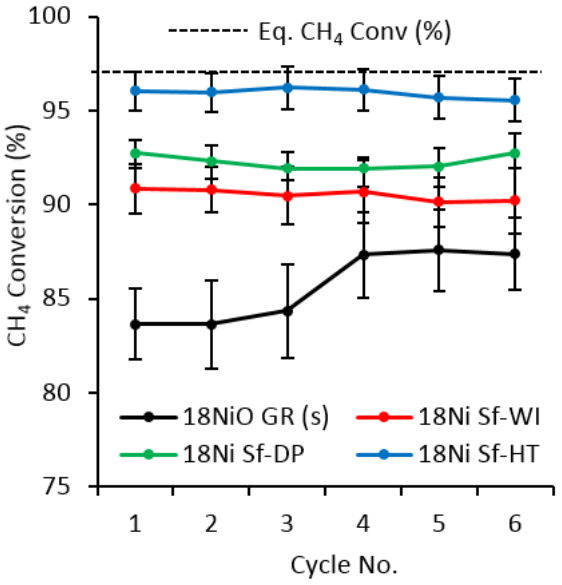

Figure 6.9: CH_4 conversion over 6 EM CLSR cycles compared with equilibrium values at 700°C and S:C 3. Error bars represent the standard deviation of the mean CH_4 conversion, in each SR half cycle.

6.1.2 Equal Volume (EV) Conditions

Under EV conditions V_{bed} was fixed at 2.5 cm^3 and so the mass of the Sf OC's was limited to 0.4 g compared to 2g of the 18NiO GR OC, Table 3.4 (reproduced below). This represents an 80% reduction in catalyst mass between the Sf OC's and 18NiO GR OC.

Table 3.4: Experimental regimes for the CLSR experiments

CLSR Conditions	m_{OC} (g)		V_{bed} (cm^3)		$\dot{V}_{i,in}$ (sccm)			T (°C)	S:C	Redox Cycles
	Sf OC	GR OC	Sf OC	GR OC	N_2	CH_4	H_2O			
Equal Mass (EM)	2.0	2.0	12.5	12.5	1000	111.0	0.25	700	3	6
Equal Volume (EV)	0.4	2.0	2.5	2.5	800	88.8	0.20	700	3	7

6.1.2.1 Single Cycle EV CLSR Outlet Concentrations

Comparison of Figure 6.10 (overleaf) and Figure 6.1 show that the outlet concentration profiles with time on stream of the species measured during the SR half cycle in EV conditions are noticeably smoother than in EM conditions. This was attributed to the provision of water to the reactor; the erratic outputs shown in Figure 6.1 (vol%) and Figure 6.5 (r_{red},OC) were thought to have been produced by the formation of droplets from the water feed tube. This was noticeable under EM conditions due to the proximity of the

catalyst bed to the water feed tube as on vaporisation, there would be little time for the steam to disperse through the feed mixture thereby producing fluctuations in water provision rather than a constant feed of water vapour. This was thought to be absent from the EV experiments as any vaporised droplets formed have more time to disperse evenly in the feed gases, reducing the effect.

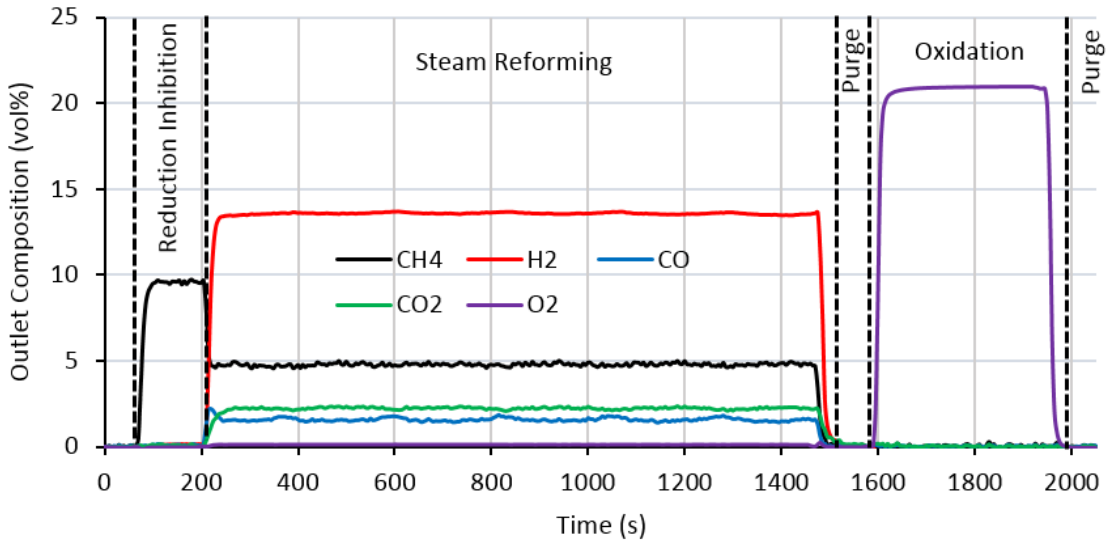

Figure 6.10: Dry outlet composition during the 2nd cycle of EV CLSR using 18Ni Sf-DP OC at 700°C and S:C 3 as representative of a typical EV CLSR experiment using Sf OC's

As stated in Section 3.3.4.2, it was found during the design of the EV CLSR experiments that if the H_2O feed was switched on more than 30 s before the CH_4 feed, auto-reduction of the OC would not occur. This is shown before 200 s in Figure 6.10 as evidenced by the CH_4 concentration remaining constant at ~ 10 %. Reduction inhibition may be caused by an abundance of adsorbed water upon the surface of the NiO crystals; adsorbed water in the form of hydrogen-bonded molecules or hydroxyl groups has been found to inhibit the nucleation of Ni atoms during reduction of NiO α-Al_2O_3 catalysts by H_2[150,156]. As a result, saturation of the NiO by pre-feeding H_2O could possibly inhibit the OC reduction reaction completely. By pausing the feed of H_2O, desorption of these species is likely promoted through the high carrier gas flow rates used in these experiments (compared to those used in Richarson et al.[150,156]), thereby allowing CH_4 to adsorb onto the surface of the NiO to facilitate reduction. This process allowed more accurate measurement of r_{red},OC (see Section 6.1.2.2).

Figure 6.11 shows a simultaneous increase in H_2, CO and CO_2 and decrease in CH_4 concentration in the outlet After 200 s, clear evidence of commencement of the reduction of the OC.

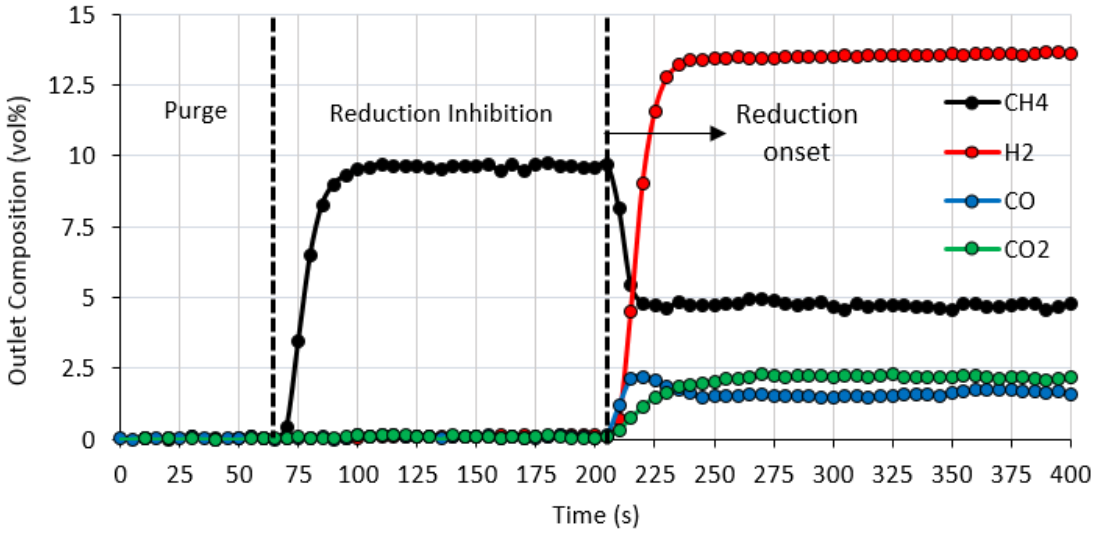

Figure 6.11: Dry outlet composition during the first 200 s of the 2nd EV steam reforming half cycle using 18Ni Sf-DP OC at 700°C and S:C 3

In contrast to the EM conditions, the concentration of CO was higher than that of CO_2 during the early stages of reduction, and the large rise in H_2 concentration (as a result of catalysed SR) occurred almost simultaneously with production of CO and CO_2. This suggests the lower mass of the Sf OC's used and resulting decreased residence time through the bed experienced in the EV CLSR experiments may have hindered the secondary reduction reactions (Equation 1.15 and Equation 1.16), therefore favouring direct reduction of the OC by partial oxidation of CH_4 (Equation 1.13).

As in EM CLSR conditions, the 18NiO GR OC (Figure A.8.1, Appendix A.8) shows a greater proportion of CO_2 in the dry outlet during auto-reduction than the 18Ni Sf-DP OC above. Higher selectivity to CO_2 during reduction of a NiO/α-Al_2O_3 OC when compared to a NiO/γ-Al_2O_3 OC has been reported elsewhere[46,119].

The 1st SR half cycle of the EV CLSR experiment where the 18Ni Sf-HT OC was used was conducted using simultaneous flow of H_2O and CH_4 into the reactor, as per the EM CLSR methodology. This SR half cycle (Figure A.7.1, Appendix A.7) confirmed that there was no change to the reduction behaviour of the OC's as a result of the pre-saturation of the OC bed with water after reduction had been initiated.

Once the system reached steady state, the expected (based on H_2:CO and H_2:CO_2) and detected H_2 vol% were similar (13.60 % and 13.61 % respectively at 1110 s in Figure 6.10) showing high accuracy.

Comparison of the dry outlet concentrations during SR after OC reduction under EM (Figure 6.1) and EV (Figure 6.10) conditions shows a reduction in H_2 (~ 9 vol%) and CO (~

2.5 vol%) concentration and an increase in unconverted CH_4 (~ 4 vol%) using Sf OC's. This was attributed to the lower residence time through the OC bed and the large decrease in the mass of OC used in EV conditions. Similar changes (increase in H_2 and CO, decrease in CH_4) were shown when comparing the 18NiO GR OC between EM (Figure A.6.1) and EV CLSR (Figure A.8.1) experiments and between the 18NiO GR OC (Figure A.8.1) and Sf OC's (Figure 6.10) during EV CLSR. This was again attributed to the lower residence time when comparing the 18NiO GR OC in EM and EV CLSR conditions and the lesser OC mass when comparing the 18NiO GR OC and Sf OC's in EV CLSR.

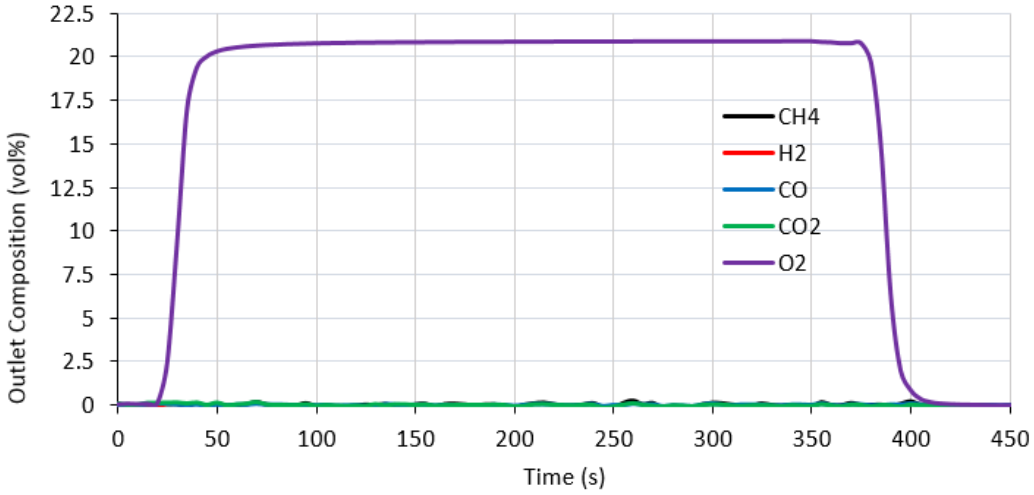

Figure 6.12: Dry outlet composition during the first 200 s of the 2nd EV oxidation half-cycle using 18Ni Sf-DP OC at 700°C and S:C 3

Figure 6.12 clearly shows no peak in CO or CO_2 during the oxidation half cycle, thus discounting the formation of $C_{(s)}$ in any of the EV CLSR experiments. Addionally, outlet concentration reached ~ 21 vol% O_2 in all case by 300 s, suggesting the oxidation reaction had finished.

6.1.2.2 Single Cycle Reduction of NiO OC's during EV CLSR

Detailed analysis of the reduction the OC's was achieved using the rates of reduction and oxidation ($r_{red,OC}$) and extent of reduction (α_{red}) as defined in Section 3.4.5 and the process outputs listed in Section 3.4.6 (H_2 purity, H_2 yield efficiency and CH_4 conversion).

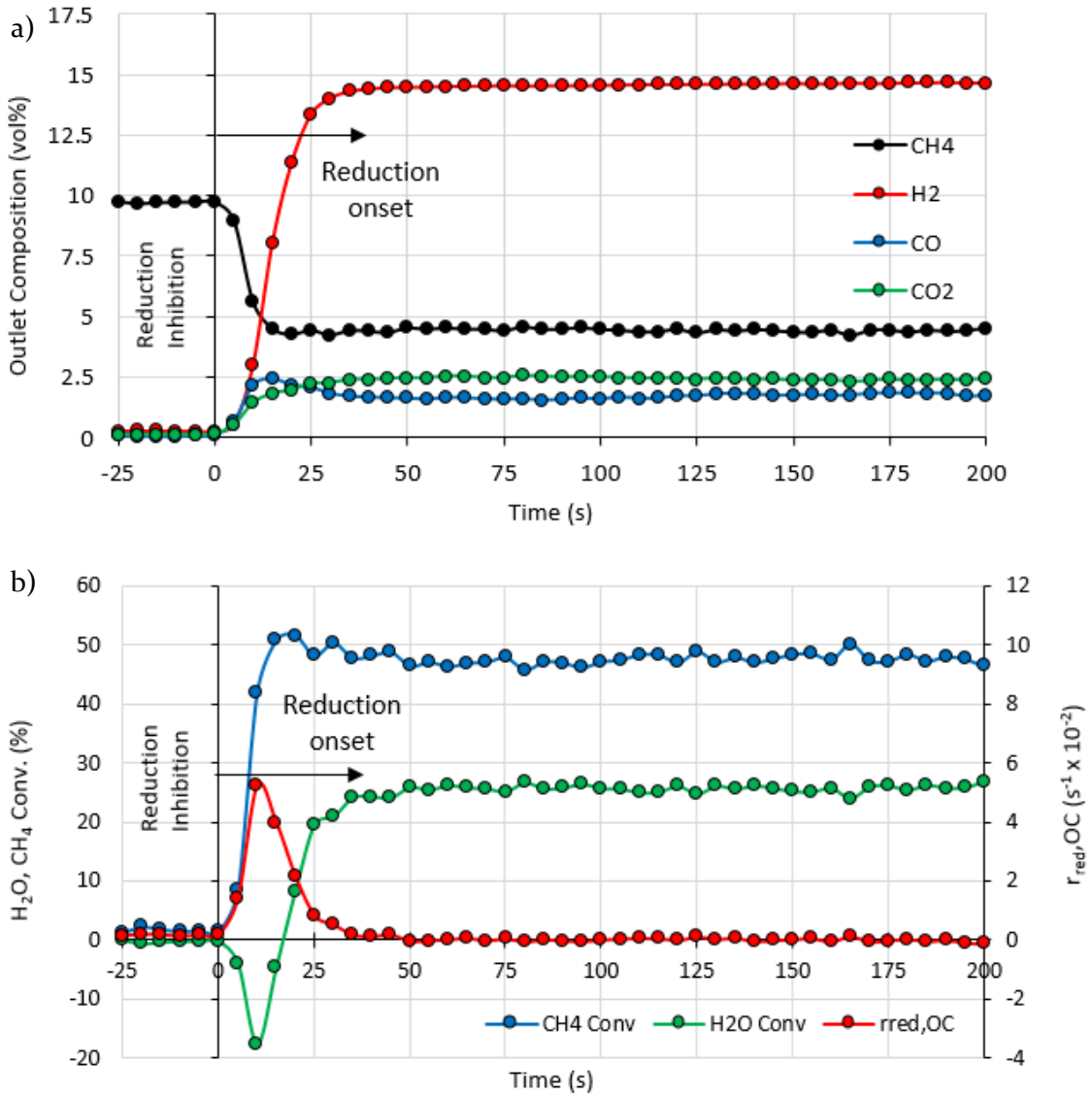

Figure 6.13: Dry outlet composition (a) CH_4 and H_2O conversion vs rate of reduction of the OC (r_{red},OC) (b) during the first 200 s of the 4th EM steam reforming half-cycle using 18Ni Sf-HT OC at 700°C and S:C 3

Figure 6.13b shows that the increase r_{red},OC occurs simultaneously with negative H_2O conversion and an increase in CH_4 conversion, suggesting reduction of the OC through the partial oxidation of CH_4 (Equation 1.14). This is also shown in Figure A.8.1 (Appendix A.8) for the 18NiO GR OC, which suggests a prevalence of reduction through complete combustion of CH_4. The system reaches steady state conditions by 50 s after reduction; as a result, integration of r_{red},OC was conducted up to this point for Sf-OC's. Integration of r_{red},OC should be limited to the defined reduction peak to limit any cumulative error that could be accrued.

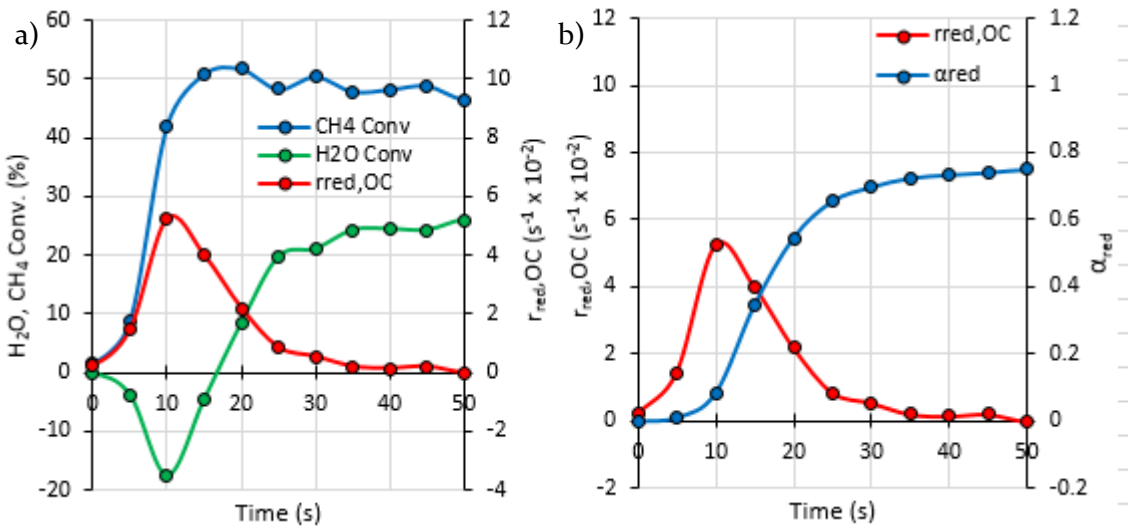

Figure 6.14: CH_4 and H_2O conversion vs r_{red},OC (a) and r_{red},OC and reduction extent (α_{red}) of the 18Ni Sf-HT OC and during the first 50 s of the 4th EM steam reforming half-cycle at 700°C and S:C 3

It is noticeable in Figure 6.14a and b that r_{red},OC is far less erratic in the EV experiments than in the EM experiments, with none of the unexpected rises and falls with time on stream that characterised the EM experiments. This was attributed to steadier provision of water to the OC bed during the EV experiments and meant that the calculated conversion of NiO to Ni (α_{red}) was far more reliable. The r_{red},OC profile shown for the 1st SR half cycle of the EV CLSR experiment carried out with simultaneous CH_4/H_2O flow (Figure A.7.1 and A.7.2, Appendix A.7), shows that the beginning of the reduction reaction is difficult to identify and on time integration results in a α_{red} far above unity. This shows that initial inhibition of the auto-reduction of the OC via water saturation of the OC bed results in more accurate measurement of r_{red},OC and α_{red}.

Figure 6.14b shows that the reduction reaction reached its final extent of 0.75 by 50 s; this coincided with steady state conditions in Figure 6.13a, and stable CH_4 and H_2O conversions in Figure 6.14a, further showing that the reduction reaction was complete. The r_{red},OC of the 18NiO GR OC was slower to reach and decline from a lower peak r_{red},OC when compared to the Sf OC's (Figure A.8.3, Appendix A.8), suggesting slower kinetics of reduction for the 18 NiO GR OC. Due to this lower rate of reduction, the integration of the rate was conducted up to 100 s in when using the 18NiO GR OC. The r_{red},OC and reduction kinetics of the fibrous and granulated materials will be compared at equal mass without sand dilution in Chapter 7.

6.1.2.3 Comparison of Reduction Extent during EV CLSR

The increased accuracy of measurement for r_{red},OC meant that the α_{red} of the different OC materials under EV conditions could be compared. Furthermore two additional methods were used to assess and cross-examine the reduction capacity of the OC's used in this work: reduction capacity determination via TGA is detailed in Appendix A.10 and Rietveld refinement of XRD data from the EV CLSR experiments is detailed in Section 6.2.1.1.

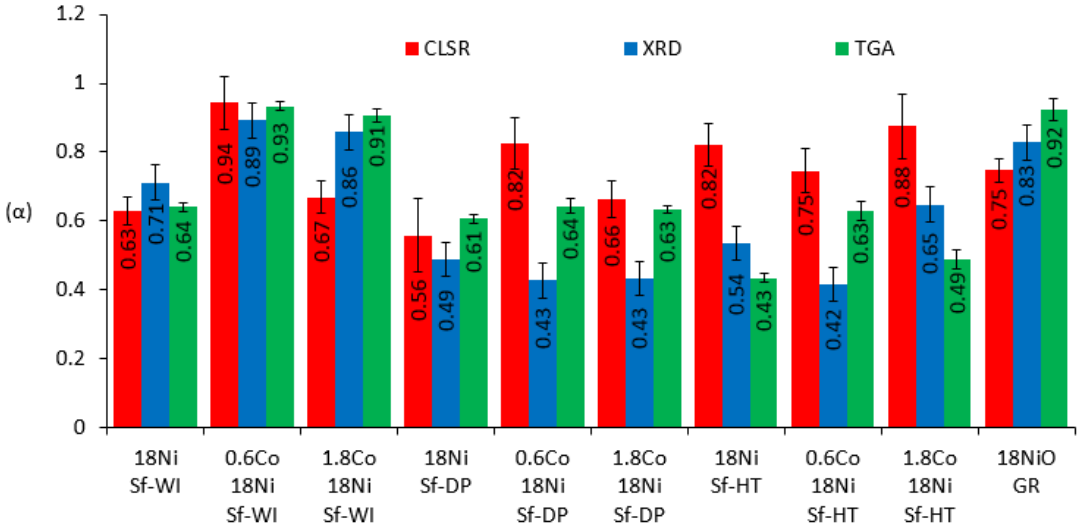

Figure 6.15: Average reduction capacity (α_{red}) of the OC's determined via EV CLSR experiments (7 redox cycles, CH_4/H_2O, air), TGA (7 redox cycles, H_2, air) and Rietveld refinement of the OC's used in EV CLSR (7th cycle, CH_4/H_2O, air). Error bars for the TGA and EV CLSR data is the standard deviation of α_{red} across 7 reduction cycles and for the Rietveld refinement was set at ± 0.05.

In spite of efforts to ensure that r_{red},OC and α_{red} were as reliable as possible, the large standard deviation in the extent of reduction over 7 cycles shown in the Sf OC's (Figure 6.14) suggests there may be limitations to this analysis. The high standard deviation in the extent of the Sf OC's as determined by the EV CLSR experiments is believed to be caused by a combination of a very fast reduction rate coupled with the relatively slow sampling rate (5 s^{-1}) of the ABB analysers. This would explain the smaller standard deviation shown by the 18 NiO GR OC in the above experiments; the slower rate of reaction in these OC's could mean that more data is gathered during reduction thereby resulting in more consistent measurement of the rate and extent of reduction. Unfortunately, if the volume flow rates of reactants into the bed were decreased or the m_{OC} increased in an effort to increase the number of data points available, the system would either become externally mass transfer limited (detailed in Chapter 7) or encounter further issues with erratic water provision, thereby making derivation of accurate reduction data under these conditions impractical. Measuring the reduction extent over many cycles (> 100) however may help

to increase statistical confidence in these results and would be useful in identifying the longevity of this factor over and industrially relevant number of cycles (see Chapter 9).

Moreover certain caveats concerning the analyses employed must be noted: (1) the reduction capacity data determined via EV CLSR experiments was considered to be the most representative of real process conditions; (2) the TGA results (Appendix A.10) though consistent, represent reduction by a different reducing agent (H_2 rather than CH_4/H_2O) in different experimental conditions (5 mg of mass and 50 sccm flows) (3) Rietveld refinement for the determination of mass fraction of Ni and NiO in the sample was only carried out on selected peak data and not the whole XRD pattern due to accuracy issues (see Section 4.1) and could only be estimated for the final reduction event (after the 7th SR half cycle).

Table 6.1: Reduction extent (α_{red}) per redox cycle determined via EV CLSR experiments (7 redox cycles, CH_4/H_2O, air)

Cycle No.	Sample									
	18Ni Sf-WI	0.6Co 18Ni Sf-WI	1.8Co 18Ni Sf-WI	18Ni Sf-DP	0.6Co 18Ni Sf-DP	1.8Co 18Ni Sf-DP	18Ni Sf-HT	0.6Co 18Ni Sf-HT	1.8Co 18Ni Sf-HT	18NiO GR
1	0.61	1.03	0.60	0.78	0.83	0.63	N/A[(a)]	0.84	0.96	0.74
2	0.64	0.98	0.72	0.50	0.88	0.66	0.86	0.81	0.80	0.82
3	0.70	0.92	0.67	0.50	0.72	0.67	0.76	0.73	0.97	0.73
4	0.57	1.03	0.67	0.49	0.80	0.76	0.74	0.69	0.83	0.75
5	0.61	0.94	0.71	0.51	0.82	0.68	0.83	0.67	0.88	0.76
6	0.65	0.87	0.60	0.51	0.78	0.59	0.82	0.73	0.73	0.72
7	0.64	0.83	0.71	0.61	0.95	0.67	0.91	0.76	0.96	0.72
Mean	0.63	0.94	0.67	0.56	0.82	0.66	0.82	0.75	0.88	0.75
	0.75			0.68			0.81			0.75
StDev	0.042	0.077	0.047	0.105	0.075	0.053	0.062	0.062	0.093	0.034

[(a)] Extent not determined due to use of simultaneous CH_4/H_2O feed

Nontheless, the extent of reduction as determined by TGA and to a lesser extent XRD analysis, shows that in general the magnitude of reduction extent followed the order 18NiO GR OC > Sf-WI > Sf-DP > Sf-HT. This was also true in terms of average reduction extent of the materials determined by EV CLSR with the 18NiO GR OC and Sf-WI OC's showing similar reduction extent while extent of reduction in the Sf-DP OC's decreased. This would agree with the literature in this area and reflect the increasing degree of metal support interactions that are likely to have occurred during synthesis and use in the EV CLSR experiments; greater interaction between these phases has been known to negatively affect the reactivity and reduction extent of conventional Ni/Al_2O_3 OC's[46,131,233].

The least interaction would be experienced between the NiO and the α-Al_2O_3 in the 18NiO GR OC due to the higher thermodynamic stability α-Al_2O_3 support; this limits the "weak" solid state interaction between the NiO and Al_2O_3 phases encountered at high temperatures ensuring the facile reduction.

Increased metal support interactions are likely to be experienced in the 18Ni Sf-WI OC due to the use of the predominantly γ-Al_2O_3 Sf fibres which encourages the interchange of Ni^{2+} and Al^{3+} ions at high temperatures thereby exacerbating interactions. However, it was found in all three methods that cobalt doping in the WI OC's seemed to increase the reduction extent in these materials; the 0.6Co 18Ni Sf-WI OC offered the highest average reduction capacity (0.94), while the 1.8Co 18Ni Sf-WI OC was found to improve the reduction extent over the 18Ni WI OC. This effect was not replicated in the Sf-DP or Sf-HT samples. This implies that any promoter effect of Co (i.e. preferential interaction between the CoO/Co_2O_3 and γ-Al_2O_3) only applies to the solid-state reaction responsible for the "weak" interactions found in the Sf-WI OC.

The Sf-HT and Sf-DP OC's were shown to have a stronger interaction with the Saffil® fibres due to chemical interdiffusion of the dissolved Ni^{2+}/Co^{2+} and Al^{3+} ions facilitated by the dissolution of Al in the precursor solution and subsequent calcination during synthesis. This is likely responsible for the decreases in reduction exhibited by these materials as determined by TGA and XRD analysis.

The Sf-HT OC's showed the least agreement between the methods and the greatest variability in the extent determined, ranging from 0.88 to 0.42.

It is clear therefore that further work is required to accurately define and compare the reduction extent of the OC materials tested. As stated earlier, an increased number of cycles in the EV CLSR experiments perhaps coupled with a decrease in reactant flow rate (in spite of any implications this may have on the kinetics of reduction) would allow more accurate measurement of the reduction extent and increase statistical confidence in any results generated through the CLSR experiments.

6.1.2.4 Single Cycle Oxidation of NiO OC's during EV CLSR

As stated in Section 6.1.1.3, extent of oxidation as determined by EM CLSR experiments reached 100% in all cases but was subject to several limitations and therefore the rate and extent of oxidation in the EV CLSR experiments will not be discussed here. Nonetheless, the full re-oxidation of the Sf-DP, Sf-HT and 18 NiO GR OC materials was corroborated by XRD conducted after the last EM oxidation cycle (Section 6.2.1.2). This shows that when

using the maximum mass of OC material (2g) the 5 mins of oxidation half cycle (air at 1000 sccm) was sufficient to fully re-oxidise these materials. Considering the equal air flow rates used in both the EV and EM CLSR experiments and the 80 % reduction in mass of the Sf-OC materials between EM and EV experiments, it can be assumed that full re-oxidation of the Sf-DP, Sf-HT and 18 NiO GR OC's is achieved in the EV CLSR experiments.

However, the full re-oxidation of the Sf-WI OC's during EM CLSR was not confirmed by XRD with the patterns showing small quantities of the reduced Ni phase remaining in these samples (Section 6.2.1.2). The 80% lower mass of Sf-WI OC used and equal flow rates of air used under the EV compared to EM CLSR experiments suggests the full re-oxidation of the Sf-WI OC's materials under EV CLSR was likely achieved. However, without confirmation of this via XRD and considering issues with relying on the rates of reduction and oxidation determined by the EV CLSR experiments, no reliable conculsions can be made about the extent of oxidation in the Sf-WI OC's.

6.1.2.5 Average SR Performance over 7 EV CLSR cycles

More in-depth analysis of the catalytic activity of the OC's after reduction in the SR half cycle was facilitated using the process outputs listed in Section 3.4.6. The average H_2 purity and yield efficiency and CH_4 conversion over 7 EV CLSR cycles for all nine Sf-OC's is compared to the 18NiO GR OC and equilibrium values in Figure 6.16.

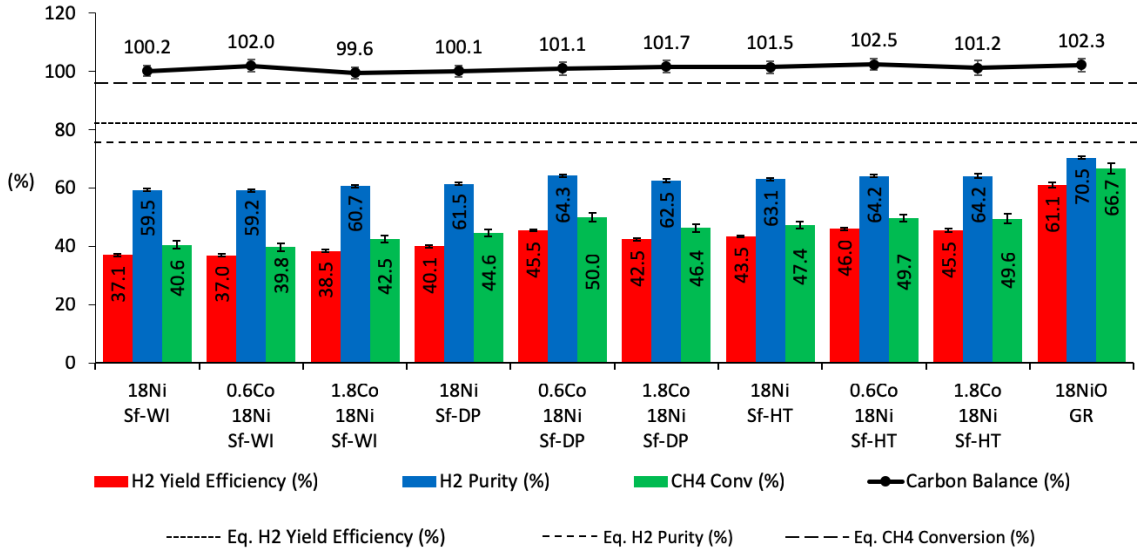

Figure 6.16: Average H_2 purity and yield efficiency and CH_4 conversion over 7 EV CLSR cycles compared with equilibrium values at 700°C and S:C 3. Error bars represent the standard deviation of the mean CH_4 conversion, H_2 purity and yield efficiency over 7 SR half cycles.

The carbon balance shows an error < 2.5 % across all experiments, indicating more accuracy in the EV CLSR conditions compared to the EM CLSR experiments. Moreover,

the standard deviation across all factors was low, indicating statistical significance in the results.

The performance of the Sf OC's under EV CLSR conditions (i.e. an 80% lower mass) was most affected by the synthesis method used, as shown in Figure 6.16. The Sf-WI OC's exhibited the poorest average CH_4 conversion (41.0 %), H_2 yield efficiency (37.5 %) and H_2 purity (59.8 %). The Sf-DP OC's improved these factors by 6.0, 5.2 and 3.0 percentage points (pp), and Sf-HT improved them by 7.9 pp, 7.5 pp and 4.1 pp respectively.

Cross referencing the reduction extent of the Sf OC's with their CH_4 conversion (as an indicator of catalytic activity for SR) over 7 EV CLSR cycles, there seems to be little correlation between two factors. Theory would suggest the greater the proportion of catalytically active Ni present in the OC material, the greater the catalytic activity of said material; however, the Sf-DP OC's, which showed the lowest average reduction extent, did not produce the worst methane conversion under EV CLSR experiments, nor did the Sf-WI OC's produce the best. These results suggest that the differences in physical characteristics (crystallite size and homogeneity and morphology of the NiO/Ni) between the Sf-WI and Sf-DP/Sf-HT OC's and specifically the folded ridged morphology of the Ni/Co layer present in the Sf-DP/Sf-HT OC's, may have a beneficial effect upon the CLSR process and therefore the performance of these materials as oxygen carrier catalysts.

Cobalt doping had a minor (if not negligible) positive effect on the performance of the Sf OC's, increasing the CH_4 conversion by ~2% and H_2 yield efficiency by ~ 2% and H_2 purity by ~1%.

Mirroring results in the EV SR experiments, the 18NiO GR OC outperformed the best Sf OC, 0.6Co 18Ni Sf-DP, offering improvements of 16.7 pp for CH_4 conversion, 15.6 pp for H_2 yield and 6.2 pp and for H_2 purity, Figure 6.16. Again, the large discrepancy in catalytic material used for the Sf OC's under EV CLSR conditions (80% less) is assumed to be largely responsible for this. These results show evidence that fibrous OC's can offer only a slight penalty to catalytic activity with greatly diminished catalyst inventory.

The performance of all the OC's was significantly lower under EV conditions compared to EM CLSR conditions. The decrease in performance was more pronounced in the Sf OC's compared to the 18NiO GR OC but in both cases was attributed to the reduction in bed volume causing a reduction in residence time and therefore a decrease in reactant conversion and production of the H_2, CO and CO_2 by-products.

6.1.2.6 SR Performance per EV CLSR cycle

All the Sf OC's tested experienced a slight reduction in CH_4 conversion, H_2 yield and H_2 purity over the 7 EV CLSR cycles (Figure 6.17)

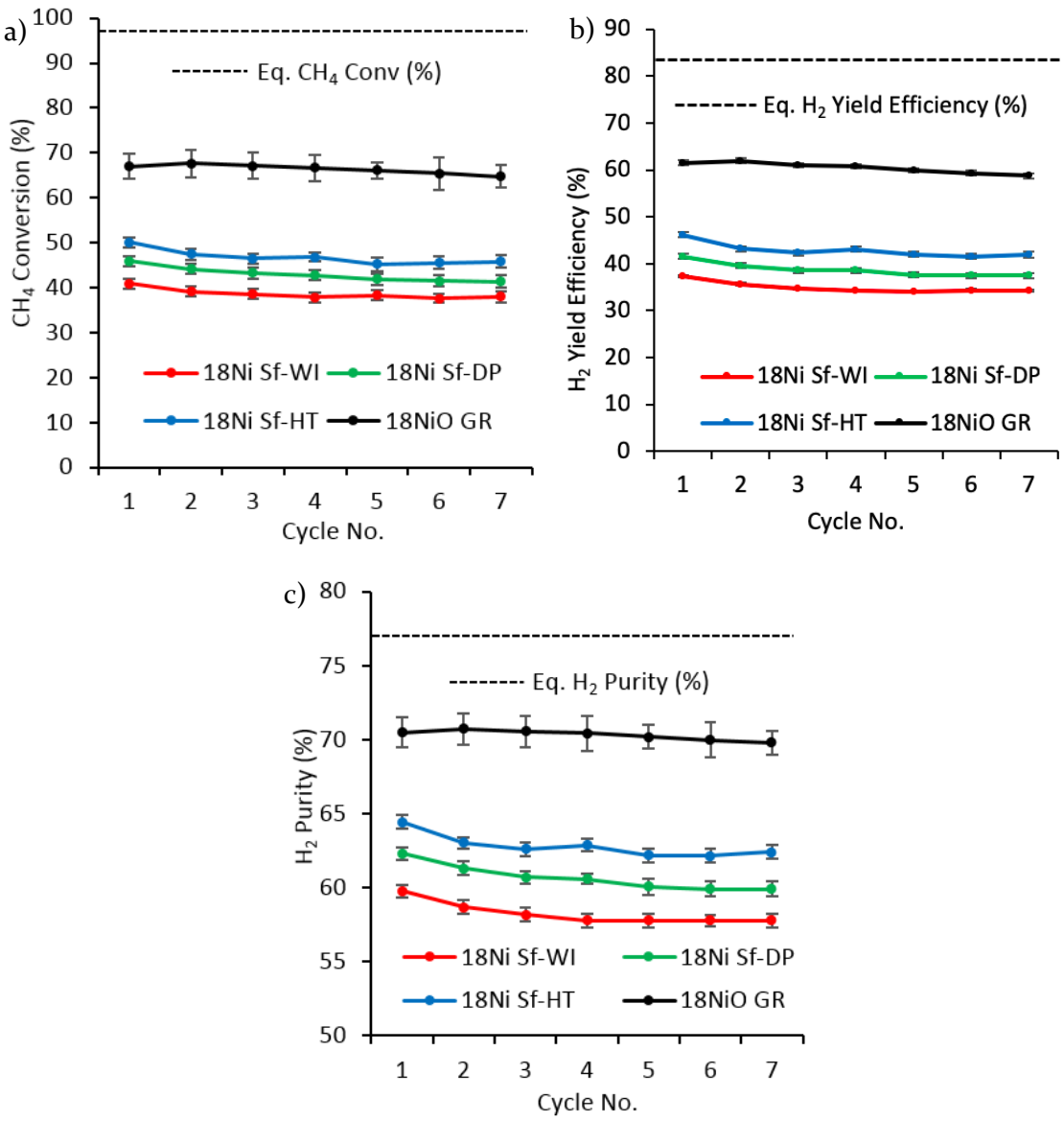

Figure 6.17: CH_4 conversion (a) and H_2 yield efficiency (b) and H_2 purity (c) over 7 EV CLSR cycles compared with equilibrium values at 700°C and S:C 3.

The deterioration in performance of the Sf-OC's between the 1st and 7th cycle varied by process output; CH_4 conversion dropped by an average of 4.0 pp, H_2 yield efficiency by 3.75 pp and H_2 purity by 2.2 pp. However much of the loss in performance was experienced in the first 3 cycles, and by the 5th cycle almost no decrease in performance was experienced. In contrast, the decrease in performance between the 1st and 7th for the 18NiO GR OC was smaller, with CH_4 conversion falling by 3.0 pp and H_2 yield efficiency and purity declining by 3.2 pp and 0.7 pp respectively. However, this deterioration was more

linear with cycles and was still evident in the later ones tested. The deterioration in performance was attributed to sintering of the Ni/NiO crystallites in the OC materials, a phenomenon that is often encountered in CLSR processes. Evidence of sintering across all the OC's tested is exhibited in Sections 6.2.

Testing the materials over many redox cycles (> 100) is still required however and will allow the effects of repeated cycling on both the extent of reduction and their subsequent catalytic activity in CLSR to be assessed over an industrially relevant number of cycles (Chapter 9).

6.1.3 Discussion

All the OC's tested were able to be reduced by the feed mixture of CH_4/H_2O and subsequently catalyse the SR and WGS for H_2 production from CLSR. The average reduction extent (α_{red}) of the OC's determined by EV CLSR was inconsistent but when combined with evidence from XRD and TGA investigations, these results suggested that reduction extent was influenced by the degree of metal support interactions between the NiO and Al_2O_3 phases in the OC's. As a result, the Sf-WI OC's likely showed a higher reduction extent than the Sf-DP and Sf-HT OC's. Furthermore, cobalt doping was found to increase the extent of reduction in the Sf-WI samples but had little effect on the Sf-DP and Sf-HT OC's.

Methods used to determine final extent of reduction such as TGA and Rietveld refinement of XRD spectra, both used to cross-reference the results obtained by elemental balances, were either rudimentary (Rietveld refinement) or not representative of process conditions (TGA) and must be refined further to achieve effective comparison. Further experiments to test the long term (>100 cycles) reduction extent of these materials could aid in confirming these results.

The catalytic performance of the OC's tested in the EV and EM CLSR experiments appeared to mirror the results shown in the SR experiments. The EM CLSR experiments showed that the Sf OC's could outperform 18NiO GR OC in terms of CH_4 conversion, however erratic water provision made variance in the measurement of H_2 yield efficiency and H_2 purity prohibitively inaccurate. The increase in CH_4 conversion shown by the best performing Sf-OC, 18Ni Sf-HT OC was significant at approximately 10 pp. The EV experiments illustrated the Sf OC's could compete with the performance of the 18NiO GR OC while using a much lower mass of the OC (80% less). These results show proof of concept for the use of fibrous OC's in fixed bed CLSR processes for the first time.

The Sf-DP and Sf-HT OC's showed improved performance over the Sf-WI OC's in both the EV and EM CLSR conditions; this increase in performance from the DP OC's was achieved despite those materials likely exhibiting lower reduction extent than the Sf-WI OC's.

It is hypothesised that the morphology of "external Ni" ridges framing void spaces present in the Sf-DP/Sf-HT OC's allow for several advantages that enhance their performance over the Sf-WI OC's. Access and egress of the reactants and products to the fibre surface and internal porous structure during both reduction of the OC and catalysis of the SR and WGS reactions is theorised to be facilitated by the open ridged structure. The small lateral dimension (< 30 nm) of the ridges present offer a larger surface area to volume ratio compared to the large particles (> 100 nm) of Ni/NiO seen in the Sf-WI OC's. Moreover any interaction between the Ni and Al in the Sf-DP and Sf-HT OC's is likely to occur closer to the centre of the ridge, therefore creating a core of material that is more difficult to reduce; these factors combine with the open ridge morphology to result in the majority of any reduced Ni on the Sf-DP/Sf-HT OC's to be present at the surface of the material thereby allowing a greater proportion of the Ni to be easily accessible by the reactants. In contrast, a greater proportion of the Ni in the Sf-WI OC's is likely to be located at a greater depth in the larger particles. Additionally, the Ni present on the ridged structures in the Sf-DP and Sf-HT OC's consists of smaller crystallites (as confirmed by XRD) thereby aiding the production of a greater variety and number of catalytically active sites. Moreover, as stated earlier, "internal Ni" is expected to play some part in improving catalysis; given the void structure may allow better access and egress to the porous structure of the DP and HT Sf OC's thereby improving the catalytic activity of these materials.

This implies that the advantages in terms of physical characteristics (i.e. Ni crystallite size, surface area and morphology of Ni layer, availability of Ni close to the surface of the fibre) of the Sf-DP and Sf-HT OC's contribute more to the catalytic activity of the OC's than increased mass percent of Ni present in the OC material.

Performance as evidenced by CH_4 conversion, H_2 yield efficiency and H_2 purity was relatively stable over 7 reduction/oxidation cycles; a slight decrease in SR efficacy was experienced in all the OC's tested. This decrease in performance over the cycles was seemingly not influenced by the synthesis methodology or by cobalt doping. Further experiments are required to test the long term (> 100 cycles) performance of the materials.

The unreliability of the rate and extent of oxidation as seen in the EM and EV CLSR experiments could be improved by reducing flow rates of air to more accurately measure

the onset of oxidation. This would allow accurate examination of the oxidation reactions but would greatly increase the length of the oxidation cycle required to fully oxidise the OC's in preparation for the next reduction event, thereby making study of both factors difficult over extended cycling. Conversely, either increasing the air flow rate or the oxidation cycle length can guarantee full oxidation of all the OC materials and furthermore improve the reliability of the reduction extent data over many cycles.

6.2 Post CLSR Characterisation of OC Materials

The OC's used in the CLSR experiments were subjected to characterisation via several techniques to assess the effect of CLSR upon the structure and physical characteristics of the materials: XRD to identify any changes in the crystallite structure, SEM was used to assess the morphological changes and BET used to assess the textural changes of the materials.

6.2.1 Phase Composition Determination and Crystallite Analysis

XRD was used to assess the effects of the CLSR experiments upon the crystalline structure the materials used. XRD was conducted on the Sf OC's and 18 NiO GR OC after the EV CLSR steam reforming half cycle (Section 6.2.1.1) and after the EM CLSR oxidation half cycle (Section 6.2.1.2) to assess the crystalline form of the Ni and NiO after these respective stages of the CLSR process.

6.2.1.1 Post EV CLSR steam reforming half-cycle

Figure 6.18 (overleaf) shows that after the EV SR half cycle was completed, the characteristic peaks of both NiO (ICDD 04-013-0888) and Ni (ICDD 04-010-6148) are present in the Sf OC's; this indicates that the Sf OC's were able to be reduced by the CH_4/H_2O mixture but were not completely reduced during the CLSR experiments. No evidence was found of reduced Co phases as shown in Figure 6.18 (overleaf). Similar evidence for partial reduction of the 18NiO GR OC is given in Figure A.11.1 (Appendix A.11).

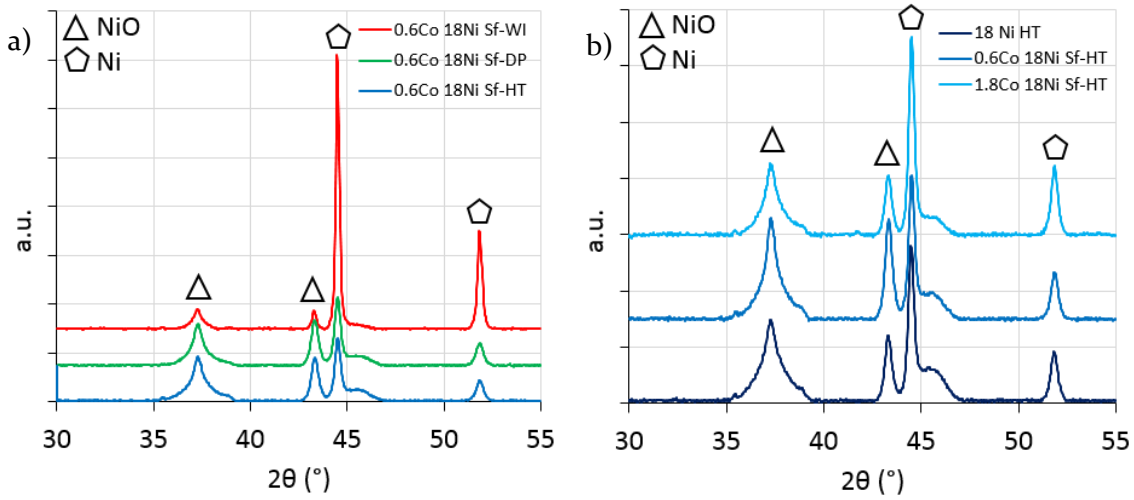

Figure 6.18: XRD pattern of the 0.6Co 18Ni Sf-WI, 0.6Co 18Ni Sf-DP and 0.6Co 18Ni Sf-HT OC's (a) and of the 18Ni Sf-HT, 0.6Co 18Ni Sf-HT and 1.8Co 18Ni Sf-HT OC's (b) used in EV CLSR showing partial reduction

Due to the pronounced nature of the Ni and NiO peaks shown in Figure 6.18, and the standards present in the ICDD database, rudimentary Rietveld refinement was conducted to approximate the relative mass fraction of Ni and NiO present in the OC's. Only the peaks at 2θ of 51.8° for Ni and 43.3° for NiO were selected for Rietveld refinement as they overlapped least with the broad peaks indicative of the Saffil® support.

Table 6.2: Mass fraction of Ni and NiO present in the OC's as determined by Rietveld refinement of the OC's used in the EV CLSR experiments

Sample	Peak Ranges (2θ)		Ni (x_i)	NiO (x_i)	GOF[(a)]
	Ni	NiO			
18Ni Sf-WI	42.6	51.0	0.71	0.29	1.77
	43.9	52.8			
0.6Co 18Ni Sf-WI	42.6	51.0	0.89	0.11	4.39
	43.9	52.8			
1.8Co 18Ni Sf-WI	42.6	51.0	0.86	0.14	4.66
	43.9	52.8			
18Ni Sf-DP	42.6	51.0	0.49	0.51	1.47
	43.9	52.8			
0.6Co 18Ni Sf-DP	42.6	51.0	0.42	0.57	1.81
	43.9	52.8			
1.8Co 18Ni Sf-DP	42.6	51.0	0.43	0.57	1.53
	43.9	52.8			
18Ni Sf-HT	42.6	51.0	0.54	0.46	1.61
	43.9	52.8			
0.6Co 18Ni Sf-HT	42.6	51.0	0.42	0.58	1.55
	43.9	52.8			
1.8Co 18Ni Sf-HT	42.6	51.0	0.65	0.35	1.59
	43.9	52.8			
18NiO GR	35.0	55.0	0.83	0.17	13.85

[(a)] Where GOF is goodness of fit and GOF ≤ 4 is typically considered satisfactory[101].

Although a GOF of approximately 4 is achieved for every Sf OC, the inherent limitation of selecting peaks rather than processing the whole XRD pattern reduces the accuracy of the mass fraction of the Ni and NiO present in the samples. Moreover, only a GOF of ~ 14 could be achieved for the 18NiO GR OC due to a strongly overlapping peak between NiO and α-Al_2O_3 at 43.3°. As such the mass fractions derived were assumed accurate to ±0.05. The results of this analysis are discussed in Section 6.1.2.2.

6.2.1.2 Post EM CLSR steam reforming half-cycle

Figure 6.19 and Figure 6.20 (overleaf) show that the NiO peaks (ICDD 04-013-0888) at 2θ of 37.3°, 43.3° and 62.9° have replaced those characteristic of Ni (ICDD 04-010-6148) at 2θ of 44.5° and 51.8° in all the Sf-DP and Sf-HT OC's. Evidence of full re-oxidation of the 18NiO GR OC is shown in Figure A.11.2 (Appendix A.11). The same flow rate of air was used in both the EM and EV CLSR experiments and given the higher mass of OC used in the EM experiments, full re-oxidation of the Sf-DP and Sf-HT and 18NiO GR OC's during the EV CLSR experiments is likely achieved.

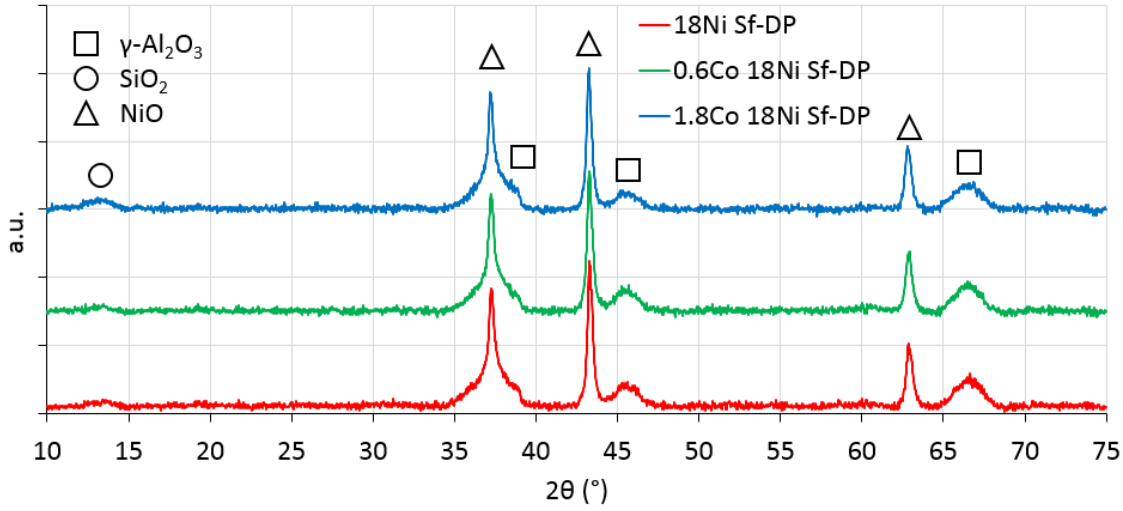

Figure 6.19: XRD pattern of the 18Ni Sf-DP, 0.6Co 18Ni Sf-DP and 1.8Co 18Ni Sf-DP OC's used in EM CLSR showing full re-oxidation

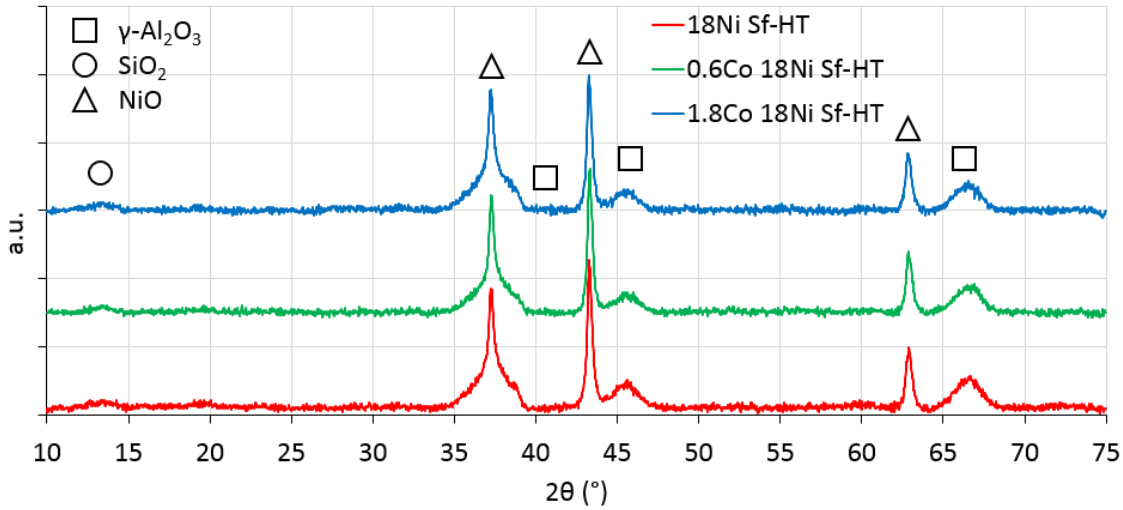

Figure 6.20: XRD pattern of the 18Ni Sf-HT, 0.6Co 18Ni Sf-HT and 1.8Co 18Ni Sf-HT OC's used in EM CLSR showing full re-oxidation

Figure 6.21 shows that peaks corresponding to Ni (44.5° and 51.8°) are still present in all the Sf-WI OC's showing that full oxidation was likely not achieved during the EM CLSR experiments. Considering the lack of reliable information on the oxidation extent in gained from the EM CLSR experiments, and the suggestion of partial oxidation in Figure 6.21 no reliable conclusions can be made about the extent of oxidation in the Sf-WI OC's.

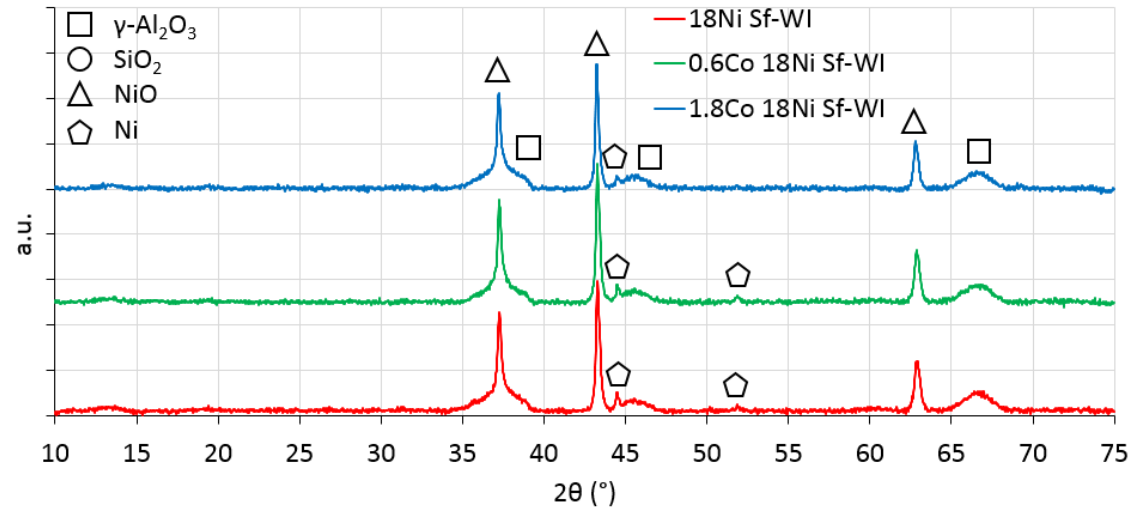

Figure 6.21: XRD pattern of the 18Ni Sf-WI, 0.6Co 18Ni Sf-WI and 1.8Co 18Ni Sf-WI OC's used in EM CLSR showing partial oxidation

6.2.1.3 Scherrer Analysis of Crystallite Size

The Ni and NiO crystallite sizes of the OC's after their use in the EM and EV CLSR experiments are compared with those found in the EM SR experiments and the fresh OC's, Table 6.3 (overleaf).

Table 6.3: Mean size of the ordered crystalline domains of the fresh OC's and those used in EM SR and EV and EM CLSR experiments as calculated with Scherrer's equation

Sample	Crystallite Size[a] (nm)				
	Fresh OC's (NiO)	Post EM SR[b] (Ni)	Post EV SRHC[c] (Ni)	Post EV SRHC[c] (NiO)	Post EM OHC[d] (NiO)
18Ni Sf-WI	16	57	83	15	60
0.6Co 18 Ni Sf-WI	36	71	109	36	65
1.8Co 18 Ni Sf-WI	31	54	99	43	75
Mean WI	28	61	97	31	67
18Ni Sf-DP	7	38	41	15	34
0.6Co 18 Ni Sf-DP	6	14	32	20	27
1.8Co 18 Ni Sf-DP	6	16	28	19	27
Mean DP	6	23	33	18	29
18Ni Sf-HT	14	17	34	18	29
0.6Co 18 Ni Sf-HT	8	19	34	20	48
1.8Co 18 Ni Sf-HT	8	16	36	19	29
Mean HT	10	17	35	19	35
18NiO GR	55	48	36	100	55

[a] Where crystallite size refers to the mean size of crystallites of the phase analysed, [b] refers to OC's used in the EM SR experiments and [c] refers to OC's used in the EV CLSR experiments analysed after the final steam reforming half cycle (SRHC) and [d] after the final EM CLSR oxidation half cycle (OHC)

All the OC's analysed after the EM CLSR oxidation half cycle (OHC) showed increased NiO crystallite size when compared to the fresh OC's. This was expected as the high temperatures and S:C ratios present in the CH_4/H_2O feedstock coupled with an experiment time of nearly 7 hours (including reactor heat up, reduction SR and CLSR cycling) are known to promote sintering through particle migration or Ostwald ripening[168–170]. Additionally, the oxidation of the Ni crystallites causes temporary increases in the temperature of the OC's thereby increasing thermal stress and promoting sintering. The Sf-DP (29 nm) and Sf-HT (35 nm) OC's exhibited average NiO crystallites approximately half the size of the Sf-WI OC's (67 nm) showing further evidence of their increased resistance to sintering through their ridged structure as seen in the SR experiments. As mentioned in Section 6.1.3, this smaller crystallite size of the Sf-DP and Sf-HT OC's is important in the context of the catalytic performance of these materials under CLSR conditions.

The OC's that were analysed by XRD after the EV CLSR steam reforming half cycle (SRHC) exhibited higher Ni crystallite sizes than the fully reduced OC's used in the EM SR experiments. This was again attributed to increased sintering as a result of the high temperatures, high S:C ratio in the CH_4/H_2O feedstock and increased duration and severity of the EM CLSR experiments. The increased size of the Ni crystallites compared the NiO crystallites of the fully oxidised OC's used in the EM CLSR experiments post OHC

may suggest that Ni is more prone to sintering either during reduction or operation under CLSR conditions.

The NiO sizes presented by the partially reduced OC's after the SRHC of the EV CLSR experiments were lower than the NiO present after the oxidation half cycle (OHC). This was unexpected given the only difference between the OC's at these two points in the experiment is the final oxidation cycle. Moreover, the partially reduced 18NiO GR OC behaved differently to the Sf OC's, showing decreased Ni crystallite size when compared to the fully reduced OC, while NiO size was halved between the partially reduced and the fully oxidised OC's. These unexpected results are difficult to understand without further investigation; in-situ TEM imaging of the reduction of the NiO crystallites in the Sf-OC's and 18NiO GR OC could shed more light on these results (see Chapter 9).

6.2.2 Specific Surface Area and Porosity

BET and BJH analysis of the adsorption isotherms was conducted to assess the effects of the CLSR experiments upon the Sf-OC's. Figures A.5.7 to A.5.9 (Appendix A.5) show no evidence to suggest significant change to the pore structure of the OC's as a result of the SR experiments.

Table 6.4: BET specific surface area of the fresh OC's and those used in the EM SR and EM CLSR experiments

Sample	Multi point BET		
	Fresh OC's	EM SR OC's	EM CLSR OC's
	SSA ($m^2\ g^{-1}$)	SSA ($m^2\ g^{-1}$)	SSA ($m^2\ g^{-1}$)
Saffil®	106	N/A	N/A
18Ni Sf-WI	75	91	84
0.6Co 18 Ni Sf-WI	61	92	89
1.8Co 18 Ni Sf-WI	65	91	60
Mean WI	67	91	78
18Ni Sf-DP	102	100	91
0.6Co 18 Ni Sf-DP	120	96	86
1.8Co 18 Ni Sf-DP	118	95	90
Mean DP	113	97	89
18Ni Sf-HT	117	92	72
0.6Co 18 Ni Sf-HT	118	86	77
1.8Co 18 Ni Sf-HT	115	91	72
Mean HT	117	90	73

The SSA of the Sf-WI OC's used in the EM CLSR experiments was reduced when compared those used in the EM SR experiments. The decrease in the 18Ni Sf-WI and 0.6Co 18Ni Sf-WI OC's was slight at 6 and 3 $m^2\ g^{-1}$ while a larger decrease was shown in the 1.8Co 18Ni Sf-WI OC. This larger drop (31 $m^2 g^{-1}$) in SSA was accompanied by a drop in the pore volume

of the 1.8Co 18Ni WI OC of approximately 33%. Sintering of the Ni/Co oxide layer experienced during CLSR conditions likely reduces the surface area of Ni/Co oxide layer on the Saffil® fibre, thereby reducing the SSA of the material from levels shown by the SR sample.

Further sintering of the Ni/Co oxide crystallites, as evidenced by Scherrer analysis, can also account for the reduction in SSA of the Sf-DP OC's used in CLSR from the fresh Sf-OC's (16 $m^2 g^{-1}$) and those used in the SR experiments (8 $m^2 g^{-1}$). However, the Sf-HT OC's show greater loss in SSA of 27 $m^2 g^{-1}$ compared to the fresh OC's and 17 $m^2 g^{-1}$ compared to the OC's used in the SR experiments perhaps showing an increased rate of sintering over the similar Sf-DP OC's. Table A.2.1 shows the pore volume of OC's was not significantly changed after the SR experiments and while the pore diameter of the Sf-WI, Sf-DP and Sf-HT OC's increased slightly after CLSR, this rise was not seen as a significant result.

6.2.3 Morphology and Topography

SEM was used to assess the effects of the EM CLSR process upon the morphology of the Sf-OC's.

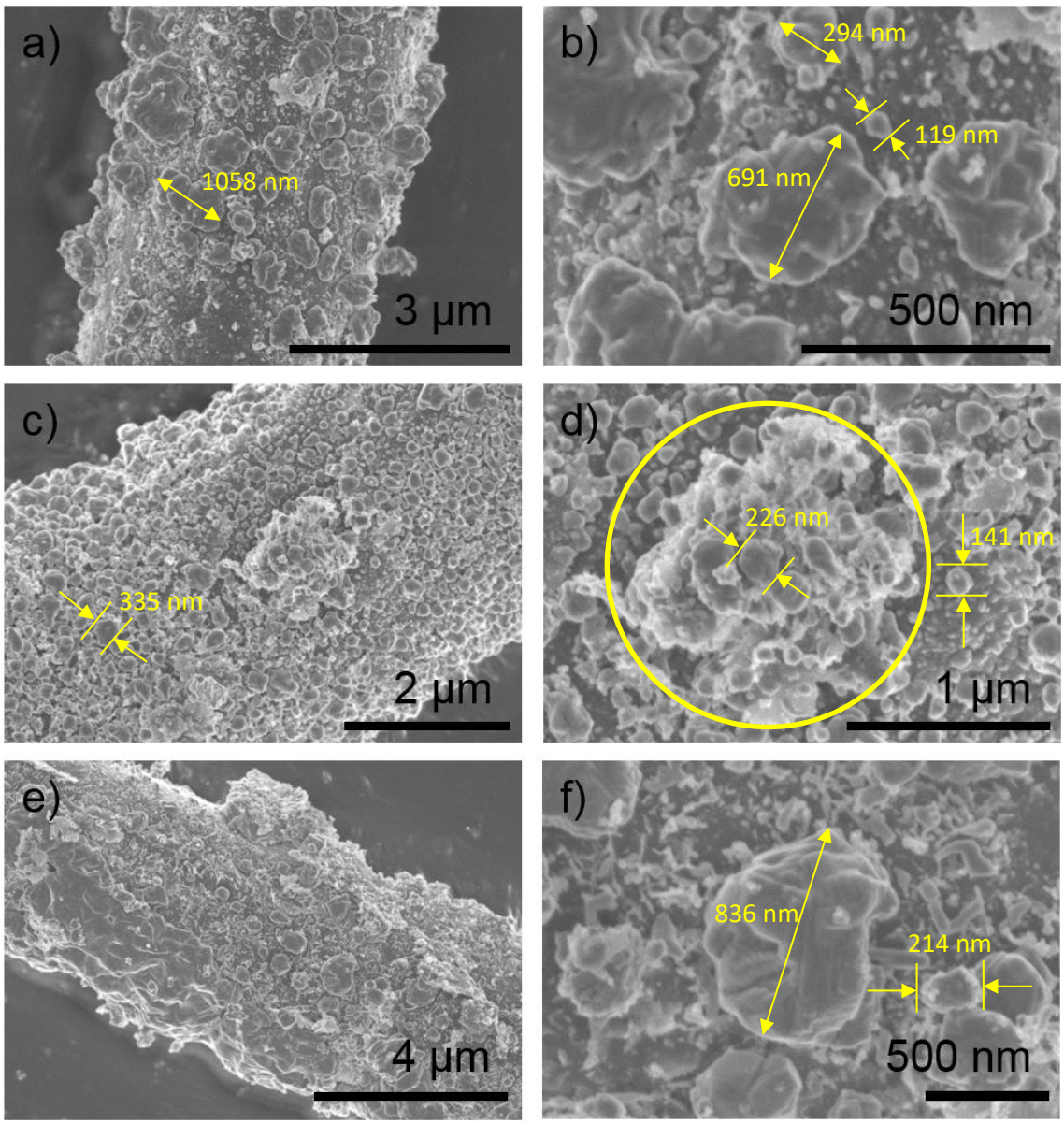

Figure 6.22: SEM images of 18Ni Sf-WI (a and b), 0.6Co 18Ni Sf-WI (c and d) and 1.8Co 18Ni Sf-WI (e and f) after use in the EM CLSR experiments

When compared to the fresh OC's, the size of the particles that constitute the Ni/Co oxide layer has clearly increased, Figure 6.22 and Table 6.5. The samples used in CLSR have also seen increased particle sizes over the samples used in the SR experiments; this varied from 15 nm in the 1.8Co 18Ni Sf-WI sample to over 130 nm in the 18Ni Sf-WI sample, Table 5.4. This growth in particle size can be attributed to enhanced sintering of the deposited layer as a result of the greater duration and severity of the CLSR experiments when compared to the SR experiments. Cross referencing the SEM data with the data from Scherrer

analysis, again suggests not only sintering through coalescence of different crystallites but also the formation of particles from the agglomeration of smaller crystallites. This is clearly shown in the large agglomeration of smaller particles shown centrally in Figure 6.22d.

The large standard deviation of the measurements taken and presented in Table 6.5 mean assessing the influence of cobalt is difficult and could not be relied upon.

Table 6.5: Comparison of particle size[(a)] in the Sf-WI OC's and void size[(c)] in the Sf-DP and Sf-HT samples used in the EM CLSR experiments measured in SEM

	Particle Size[(a,b)] (nm)			Void Size[(b,c)] (nm)					
	18Ni WI	0.6Co 18Ni WI	1.8Co 18Ni WI	18Ni DP	0.6Co 18Ni DP	1.8Co 18Ni DP	18Ni HT	0.6Co 18Ni HT	1.8Co 18Ni HT
Mean	246	190	215	232	236	289	328	341	205
SD	201	44	119	47	63	106	136	155	71
Max	1059	336	836	422	496	706	1105	814	372
Min	60	116	69	129	112	136	155	127	85

[(a)] Where particle size refers to the maximum diameter of particles identified in SEM images. [(b)]Based on 100 measurements via ImageJ. [(c)]Where void size refers to the maximum diameter of inter-ridge voids identified in the non-sintered SEM images.

Despite the increased thermal stress and duration of the CLSR experiments the ridged morphology exhibited by the fresh Sf-OC's has been maintained in all of the Sf-DP OC's, Figure 6.23 (overleaf). Again, there is some evidence presented for a partial degeneration of the tight-knit ridged oxide structure (as evidenced in Figure 6.23b and d), and presence of nodular particles as seen in the Sf-WI OC's. However, the average void size of the Sf-DP OC's was largely unchanged when compared to those exhibited by the Sf-DP OC's used in the SR experiments, therefore indicating that the increased duration and severity of the CLSR process did not have a dramatic effect on the void size. The NiO crystallite sizes as determined by Scherrer analysis noticeably increased when compared to those shown by the Sf OC's use in the EM SR experiments; however, this seemed to have little effect upon the ridged structures shown in the Sf-DP OC's.

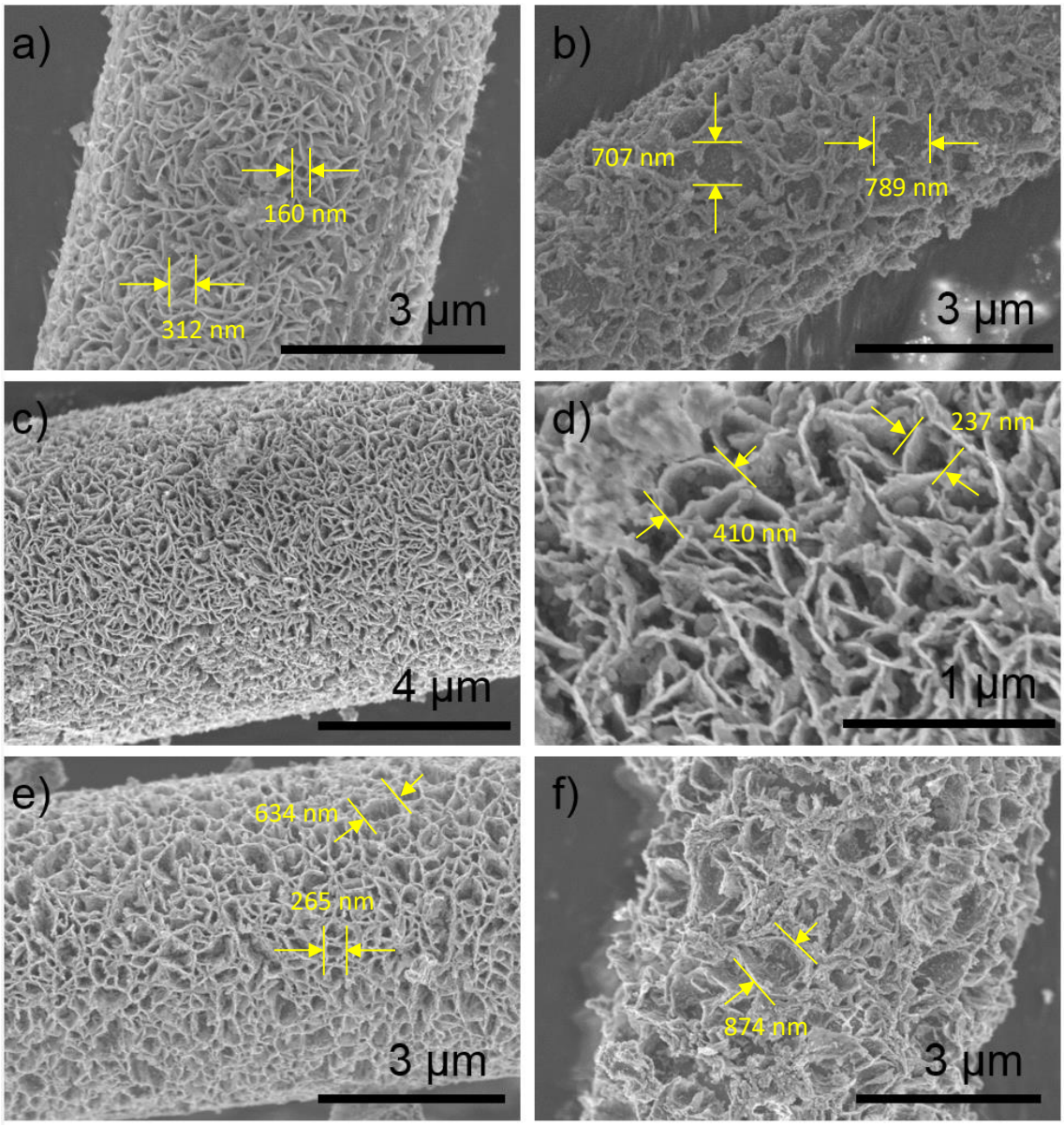

Figure 6.23: SEM images of 18Ni Sf-DP (a and b), 0.6Co 18Ni Sf-DP (c and d) and 1.8Co 18Ni Sf-WI (e and f) after use in the EM CLSR experiments. Images a, c, d and e show intact ridged morphology and b and f show evidence of sintering

Again, the Sf-HT OC's maintained the ridged morphology exhibited by all urea synthesised OC's, however evidence of increases in void size and partial degradation of that oxide structure were more widespread than in the Sf-DP OC's, Figure 6.24 (overleaf).

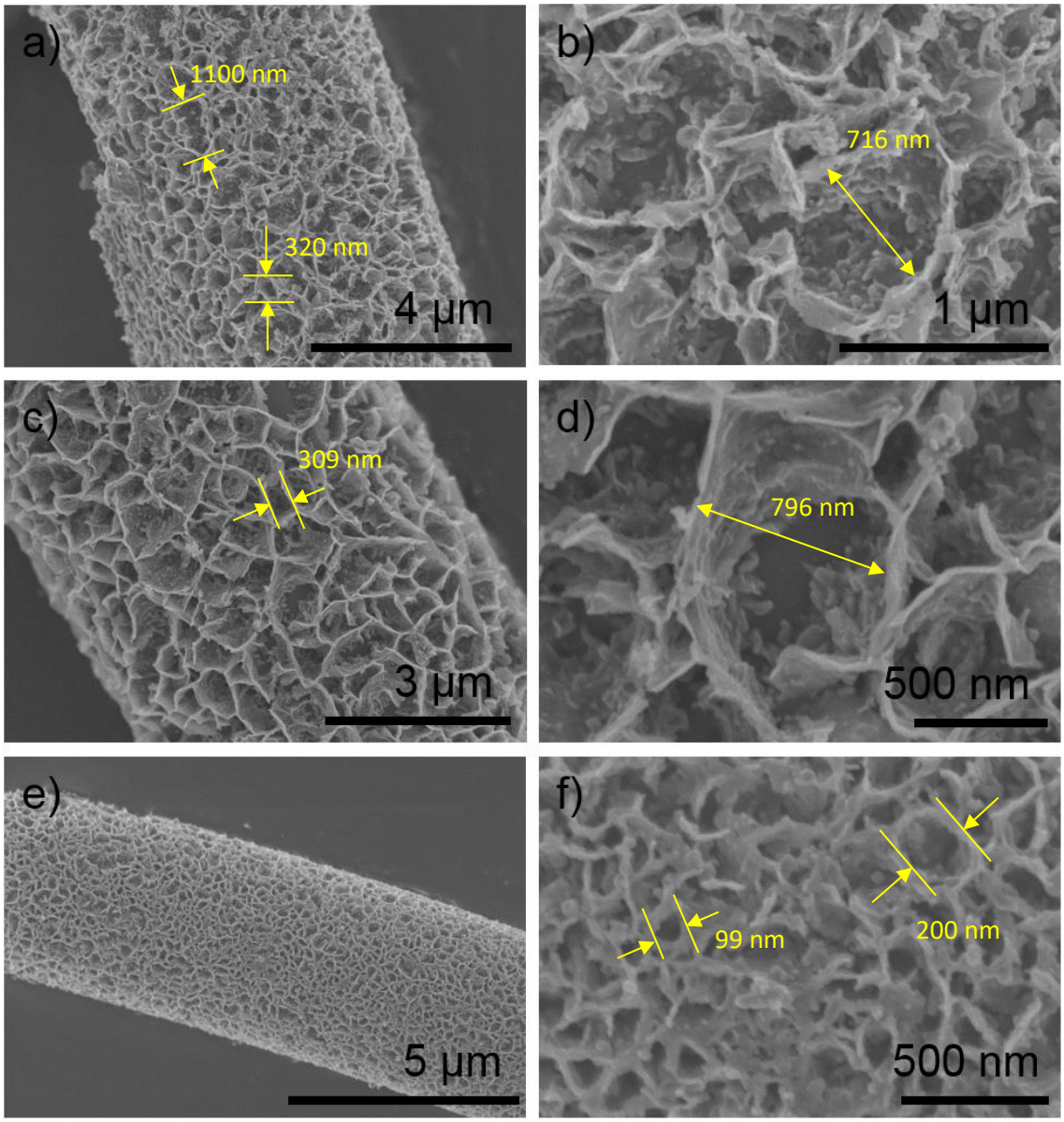

Figure 6.24: SEM images of 18Ni Sf-HT (a and b), 0.6Co 18Ni Sf-HT (c) and 1.8Co 18Ni Sf-HT (d) after use in the EM CLSR experiments

The change in void size between use in EM SR and EM CLSR conditions for the Sf-HT OC's is far more erratic than in the Sf-DP OC's with increases of approximately 100 nm in the 18Ni Sf-HT and 0.6Co 18Ni Sf-HT OC's while the 1.8Co 18Ni HT OC was largely unchanged, Table 6.5. An increase in void size in two of the three Sf-HT samples coinciding with the increased crystallite size across the Sf-HT OC's was here evidenced by a prevalence of the partial breakdown of the ridged morphology in the sample analysed. This therefore would suggest that an increase in crystallite size through sintering of the constituent NiO crystallites is instrumental in increasing the size of the voids shown. This may imply that the samples observed in the DP samples were not representative of the sample and any

partial degradation of the honeycomb structure may be more widespread than indicated in Figure 6.23.

The sintering seen in the Sf-WI, Sf-DP and Sf-HT samples above could present an explanation for the slight drop in the performance of the OC's over the 7 CLSR cycles conducted in the EM and EV CLSR experiments; sintering of Ni has been widely reported to reduce catalyst activity through reduction in the surface area of available Ni and therefore the restriction of the number of active catalytic sites.

Again, the 18NiO GR OC showed very little evidence of sintering either by SEM (Figure A.1.3d, e and f, Appendix A.1) or by Scherrer analysis of XRD, showing excellent resistance to increases in Ni/NiO size during the CLSR experiments.

6.3 Summary

CLSR experiments were conducted upon the Sf OC's and their performance compared with that of 18NiO GR OC both on an Equal Mass (EM) and Equal Volume (EV) basis. After these experiments the effects on the physical characteristics of the OC materials used were determined via solids characterisation.

Table 3.4: Experimental conditions for the CLSR experiments

CLSR Conditions	m_{OC} (g)		V_{bed} (cm^3)		$\dot{V}_{i,in}$ (sccm)			T (°C)	S:C	Redox Cycles
	Sf OC	GR OC	Sf OC	GR OC	N_2	CH_4	H_2O			
Equal Mass (EM)	2.0	2.0	12.5	12.5	1000	111.0	0.25	700	3	6
Equal Volume (EV)	0.4	2.0	2.5	2.5	800	88.8	0.20	700	3	7

The CLSR experiments showed that all the OC's tested in both the EM and EV CLSR experiments were able to be reduced by the feed mixture of CH_4/H_2O and subsequently catalyse the SR and WGS for H_2 production from CLSR.

The EV CLSR experiments showed that the average reduction extent (α_{red}) of the OC's determined by EV CLSR was inconsistent but when combined with evidence from XRD and TGA investigations, these results suggested that reduction extent was influenced by the degree of metal support interactions between the NiO and Al_2O_3 phases in the OC's. As a result, the Sf-WI OC's likely showed a higher reduction extent than the Sf-DP and Sf-HT OC's. Furthermore, Co doping was found to increase the extent of reduction in the Sf-WI samples but had little effect on the Sf-DP and Sf-HT OC's.

The EM CLSR experiments showed that once reduced, the Sf OC's could outperform the 18NiO GR OC in terms of CH_4 conversion during SR. The 18Ni Sf-HT OC was the most effective OC tested, returning a ~ 10 percentage point (pp) improvement in CH_4 conversion. Furthermore, the EV experiments showed that the Sf OC's could offer only a slight penalty to catalytic performance compared to the 18NiO GR OC despite operating with 80% less mass of catalytic material (0.4 g of Sf OC to 2 g of 18NiO GR OC). These results show proof of concept for the use of fibrous OC's in fixed bed CLSR processes for the first time. The Sf-DP and Sf-HT OC's showed improved performance over the Sf-WI OC's in both the EV and EM CLSR conditions despite exhibiting lower reduction extent (as determined in EV CLSR). This implies that the advantages in terms of physical characteristics (i.e. Ni crystallite size, surface area and morphology of Ni layer, availability of Ni close to the surface of the fibre) of the Sf-DP and Sf-HT OC's contribute more to the catalytic activity of the OC's than increased mass percent of Ni present in the bulk OC material.

Performance as evidenced by CH_4 conversion, H_2 yield efficiency and H_2 purity was relatively stable over 7 reduction/oxidation cycles although a slight decrease in efficacy was experienced in all the OC's tested. Further experiments are required to test the long term (> 100 cycles) performance of the materials over an industrially relevant number of cycles.

The rate and extent of oxidation were deemed to be unreliable due to the the lack of data points between the start of oxidation and peak $r_{ox,OC}$, the high rates of reaction experienced in the oxidation half cycle as well as the reliance on integration of steady state data. However, XRD analysis showed that full oxidation of the Sf-DP, Sf-HT and 18NiO GR OC's was achieved under EM CLSR conditions and therefore was likely achieved in the EV CLSR conditions. No conclusions could be made concerning the extent of oxidation in the 18Ni WI OC's.

Scherrer analysis demonstrated that all samples showed evidence of some sintering in the deposited Ni/Co layer, with the Sf-DP and Sf-HT OC's showing greater resistance to this effect. A reduction in SSA of the OC's was again experienced as a result of sintering of the Ni/Co layer during the CLSR process and suggested that the Sf-HT samples had experienced this effect to a greater extent. SEM illustrated that the ridged morphology in the Sf-DP and Sf-HT materials had endured the CLSR process, but sintering was observed and evidenced by void size increase in both the samples. SEM and Scherrer analysis

showed that sintering of the Sf-WI OC's occurred both within individual crystallites and through agglomeration of NiO particles.

7 Reduction Kinetics of Fibrous Oxygen Carriers during Chemical Looping Steam Methane Reforming

This chapter details the determination of kinetics for the reduction of the Sf OC's and 18NiO GR OC in the CLSR process using a packed bed reactor. The rate controlling step is determined and a nucleation and nuclei growth (Avrami–Erofeyev) solid state reaction model is used to approximate the kinetics of the reduction reaction facilitating the estimation of the associated rate constant, activation energy and pre-exponential factor.

7.1 Differential and Integral Reactors

When experimentally deriving the kinetics of a heterogeneous reaction using a packed bed reactor, two configurations are available; the differential (flow) reactor and the integral (plug flow) reactor[256]. These reactor configurations make different assumptions about the effects of reactant concentration upon the rate of reaction studied and therefore the difference between these assumptions must be explored.

7.1.1 Reactor Concepts

In a differential reactor the rate of the studied heterogeneous reaction is assumed to be equal at all points within the packed bed of the reactor. Given that rates of reaction are typically dependent upon the concentration of the reactants, this assumption is only valid when the conversion of the gaseous reactant is very low (X_i > 10%); this can be achieved through use of a small reactor (i.e. low fixed bed height) or very high flow rates of gaseous reactant[256]. The plug flow performance equation is therefore:

$$\frac{m_{OC}}{\dot{n}_{CH_4,in}} = \int_{X_{CH_4,in}}^{X_{CH_4,out}} \frac{dX_{CH_4}}{-r'_{CH_4}} \qquad \textbf{Equation 7.1}$$

$$\frac{m_{OC}}{\dot{n}_{CH_4,in}} = \left[\frac{X_{CH_4,out} - X_{CH_4,in}}{-r'_{CH_4}}\right] \qquad \textbf{Equation 7.2}$$

Therefore, given the conversion of the gaseous reactant is low enough, the rate of reaction is directly related to the conversion through the reactor and as a result, this reactor configuration is typically employed for the derivation of reaction kinetics[256].

An integral reactor assumes that due to a greater height of bed and therefore larger gaseous reactant conversions, the concentration of the gaseous reactant varies significantly throughout the bed; as a result these variations in reactant concentration are considered when the rate of reduction is calculated via an integration with respect to conversion across the reactor[256]. The performance equation is therefore:

$$\frac{m_{OC}}{\dot{n}_{CH_4,in}} = \int_0^{X_{CH_4}} \frac{dX_{CH_4}}{-r'_{CH_4}} \qquad \textbf{Equation 7.3}$$

This reactor configuration is more industrially relevant as it provides high specific product efficiencies. These reactors show variations in temperature and gas composition through the reactor bed that can affect rate measurement. Integral reactors are most useful for modelling of larger packed bed units where heat/mass transfer effects are considered and the input and product composition vary. They can be used to produce simple kinetic forms but become awkward and impractical for complicated reactions[256].

7.1.2 Application of an Integral Reactor for Derivation of Reduction Kinetics during CLSR

When applied to the derivation of kinetics for the reduction of fibrous and conventional granulated Ni OC's by a N_2 diluted CH_4/H_2O as carried out herein, two major issues in the use of the above performance equations arise. As stated earlier, CH_4 is a reactant both in the reduction of the OC and in the SR reaction and therefore the source of any conversion of the CH_4 reactant is difficult to ascertain. This can make derivation of accurate kinetic data difficult. Moreover, these performance equations neglect the solid as a reactant and assume that the solid/gas system consists of a solid catalyst, that does not take part in the reaction, and a gaseous reactant; as a result, these equations use only the change in concentration (i.e. conversion) of the gaseous reactant through the reactor.

As a result, the method for measuring reduction kinetics using an oxygen balance as shown in Section 3.4.5 was formulated. This allowed the measurement of reduction kinetics without relying on the conversion or concentration of the CH_4 reactant, thereby alleviating the above issues.

Typically, a differential reactor is utilised to derive reaction kinetics using several feed concentrations to simulate longditudinal sections of a reactor thereby providing direct kinetic rates without having to account for changes in reactant concentration; however, the very low conversions of gaseous reactants required to operate a differential reactor necessitates extremely accurate analysers with a frequent sampling rate. These

requirements were likely not met by the analysers used in the packed bed reactor and thus a differential reactor was not used.

The issue concerning the use of an integral reactor in these experiments is associated with the rate of OC reduction (r_{red},OC) and the extent of reduction (α_{red}) derived from the equipment. The rate of OC reduction is effectively averaged across the whole reactor and therefore neglect the effects of changing CH_4 concentration and temperature through out the bed; this cannot be easily remedied due to a lack of means to measure these properties accurately and with enough resolution at several different points. Despite this reservation, integral reactors are suitable for simple kinetic derivation and model fitting; with the kinetic models applied later in this chapter no assumptions are made on the dependence of the reduction reaction upon the concentration of CH_4.

7.2 Rate Controlling Step of Solid-Gas Reactions

As stated in Section 2.3.3, the reduction and oxidation reactions of the OC's reactions investigated in this work are all examples of gas-solid reactions. It is generally accepted that there are 6 steps which can control the rate at which reduction reactions involving gases and solids can occur[44,49,101,156,157]:

1. Gas moves from the bulk gas phase to (a) the surface of the OC and (b) through boundary layer around the particle
2. Diffusion of the reactant to reach unreacted solid; this involves (a) diffusion of gas through the porous structure and/or (b) diffusion through layer of product formed during the reaction
3. Adsorption of gaseous reactant to solid surface
4. Chemical reaction between the reactant gas and solid, typically involving several steps
5. Desorption of gaseous product from the solid surface
6. Transport of the gaseous products through the reversal of steps 1 and 2.

For the kinetic data derived from the experiments to accurately reflect the global reduction kinetics, the global rate of reaction must not be limited by transport effects. This means that mass transfer of the reactants or products throughout the bed and, the diffusion of the reactants or products from the bulk gas to the surface of the particle (external mass

transfer, step 1a and 1b) nor the pores within the particle (internal mass transfer, 2a/b) must be found to be rate limiting[101,128,234].

7.2.1 Mass Transfer Limitation Experiments

To reduce external and internal mass transfer limitations to negligible levels, high gas flows ($V_{i,in}$), low solids mass (m_{oc}) and low particle sizes (d_p) must be used[44,49]. The particle size of the Sf OC's could not be changed and the 18NiO GR OC was ground to the minimum diameter possible without causing issues with back pressure in the packed bed reactor or a loss of OC material from the baskets used to hold the OC; this meant that internal mass transfer limitation was minimised for the system and experiments investigating these factors were not undertaken.

External mass transfer limitations are absent from a kinetic system if the rate of reaction is no longer affected by increases in the flow rates of the reactants; as such experiments were designed to assess the effect of the volume flow rates of the reactant upon the rate of reduction of the OC and therefore determine if the system was externally mass transfer limited. These experiments utilised the EV CLSR conditions to compare the external mass transfer behaviour of the Sf and 18NiO GR OC's, Table 3.4 (reproduced below).

Table 3.4: Experimental conditions for the CLSR experiments

CLSR Conditions	m_{OC} (g)		V_{bed} (cm^3)		$\dot{V}_{i,in}$ (sccm)			T (°C)	S:C	Redox Cycles
	Sf OC	GR OC	Sf OC	GR OC	N_2	CH_4	H_2O			
Equal Mass (EM)	2.0	2.0	12.5	12.5	1000	111.0	0.25	700	3	6
Equal Volume (EV)	0.4	2.0	2.5	2.5	800	88.8	0.20	700	3	7

Figure 7.1 (overleaf) show that for flow rates of the N_2 diluted CH_4/H_2O feed below 800 sccm (based on the N_2 carrier gas flow rate) both the Sf-OC's and the 18NiO GR OC are externally mass transfer limited; the reduction extent over time increases with increasing flow rate. Above 800 sccm, the extent of reduction with time is effectively the same thereby proving that external mass limitation can be ruled out for both materials under these conditions

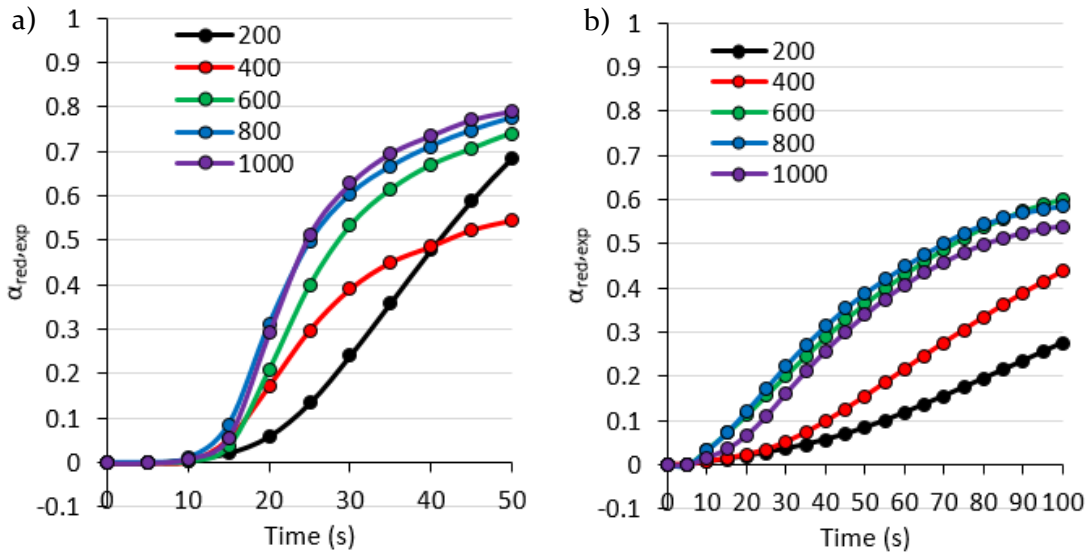

Figure 7.1: Reduction extent (α_{red}) over time of the 18Ni Sf-WI OC (a) and 18NiO GR OC (b) during the SR half cycle of CLSR at varying reactant flow rates (based on the flow rate of N_2 in sccm) under EV conditions

However, the comparison of reduction rate and subsequent description of reaction kinetics is facilitated with use of an equal mass of solid reactant without dilution via silica sand; given the results shown in Figure 7.1, a reduction in M_{OC} of the 18NiO GR OC will still result in the absence of mass transfer limitations. As such, for the results shown in this chapter, a different flow regime was used, Table 3.5 (reproduced below).

Table 3.5: Experimental conditions for the determination of reduction kinetics

CLSR Conditions	m_{OC} (g)		V_{bed} (cm^3)		$\dot{V}_{i,in}$ (sccm)			T (°C)	S:C
	Sf OC	GR OC	Sf OC	GR OC	N_2	CH_4	H_2O		
Reduction Kinetics (RK)	0.4	0.4	2.5	0.4	800	88.8	0.20	450 - 700	3

Consequently, the RK (reduction kinetics) CLSR conditions were used for further analysis of the reduction of the OC materials in terms of reduction rate profiles, extent of reduction and kinetic determination.

7.2.2 Models for External and Internal Mass Transfer Limitation

The above experiments show that the reduction reactions encountered in RK CLSR conditions are not limited by mass transfer of the reactant through the bulk of the catalyst bed or the boundary layer around the solid particles; however modelling of the external and internal mass transfer phenomena i.e. the diffusion of the reactant from the bulk fluid to the surface of the each individual particle and diffusion of the reactant through the porous particle itself must also be discounted before the reactions can be considered to be

kinetically controlled. To facilitate this, several theoretical calculations were conducted to model external and internal mass diffusion effects to discount limitation by these effects. All calculations were carried out using RK CLSR feed conditions.

7.2.2.1 External Mass Transfer Theory

When attempting to model external mass transfer of the gaseous reactant to the surface of the solid particle, it is convenient to consider a single particle past which the bulk fluid flows. The fluid velocity surrounding the immediate vicinity of the particle will vary, thereby forming a boundary layer, Figure 7.2.

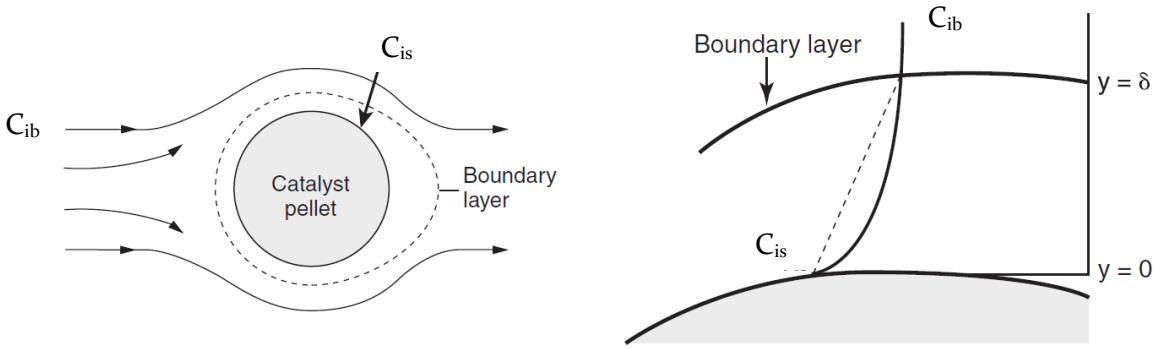

Figure 7.2: Illustration of the boundary layer around a spherical particle [234]

If this layer is assumed to be stagnant and the concentration and temperature of the fluid at the outer edge of the film are identical to those of the bulk fluid, the diffusional resistance to mass transfer of the reactant from the bulk to the surface of the particle will be found in this layer[234].

As per Fogler[234], the average molar flux of the reactant *i* from the bulk fluid to the surface of the particle is given by:

$$W_i = \frac{D'_i}{\sigma}(C_{ib} - C_{is})$$ **Equation 7.4**

Where C_{ib} and C_{is} are the concentration of the reactant *i* in the bulk fluid and at the surface of the particle respectively, D'_i is the effective diffusivity of the reactant *i* in the bulk phase and σ is the mean boundary layer thickness. The ratio of the latter two factors gives the mass transfer coefficient, k_c, of the system:

$$k_c = \frac{D'_i}{\sigma}$$ **Equation 7.5**

Thereby giving:

$$W_i = k_c(C_{ib} - C_{is}) \quad \textbf{Equation 7.6}$$

Limitation of the kinetics of a chemical reaction via external mass diffusion can be ruled out when the average molar flux (W_i) of the reactant from the bulk gas to the surface of the particle is much greater than the maximum chemical rate of reduction per unit of external area of particle (r_i) [101,234]:

$$r_i = \frac{r_{red,max}}{SA_{p,ext} \times \emptyset} \quad \textbf{Equation 7.7}$$

Where $r_{red,max}$ is the maximum rate of reaction (mol s^{-1}) , $SA_{p,ext}$ is the external surface area of the particle and $\emptyset$ refers to the stoichiometric moles of the solid reactant reduced by 1 mol of reactant according to the prevalent reaction.

Therefore if the ratio of $W_i : r_i$ is much greater than 1, external mass transfer limitation of the chemical reaction kinetics can be discounted.

7.2.2.2 Resolving Mass Transfer Coefficient

Estimation of the average molar flux requires the resolution of the mass transfer coefficient. This can be achieved through the use of the Frossling Correlation that states the mass transfer around a particle can be considered analogous to heat transfer around a particle of similar geometry [234,235]. As such the average molar flux of the reactant from the bulk fluid to the surface of the particle (Equation 7.4) can be considered analogous to the heat flux from the bulk fluid temperature to the temperature at the solid surface:

$$q = h(T_0 - T_s) \quad \textbf{Equation 7.8}$$

The heat transfer coefficient for spherical particles is typically described in terms of the dimensionless Nusselt, Prandtl and Reynold's numbers[234]:

$$Nu = \frac{h\, d_p}{\lambda_i} \quad \textbf{Equation 7.9}$$

$$Re = \frac{U_s \rho\, d_p}{\mu} \quad \textbf{Equation 7.10}$$

$$Pr = \frac{\mu C_p}{\lambda_i} \quad \textbf{Equation 7.11}$$

Where d_p is the diameter of a spherical particle, λ_i thermal conductivity, U_s is the superficial velocity, ρ the density, μ the viscosity and C_p the specific heat capacity of the fluid.

Through these three dimensionless numbers, heat transfer correlations can be used to relate these factors and calculate the heat transfer coefficient. **Equation 7.12** is applicable to flow around a spherical particle, as relevant to the conventional 18NiO GR OC material[234]:

$$Nu = 2 + 0.6\, Re^{\frac{1}{2}}\, Pr^{\frac{1}{3}}$$ **Equation 7.12**

The Frossling correlation allows the use of these heat transfer correlations to estimate the mass transfer coefficient for a particle of similar shape by substitution of the Nusselt and Prandtl with the dimensionless Sherwood and Schmidt numbers respectively [234,235]:

$$Nu = \frac{h\, d_p}{\lambda_i} \quad \rightarrow \quad Sh = \frac{k_c\, d_p}{D'_A}$$ **Equation 7.13**

$$Pr = \frac{\mu}{\rho}\left(\frac{\rho C_p}{\lambda_i}\right) = \frac{\nu}{\alpha_t} \quad \rightarrow \quad Sc = \frac{\nu}{D'_A}$$ **Equation 7.14**

Where ν is the kinematic viscosity or momentum diffusivity and is equivalent to the ratio of the viscosity to the density of the fluid ($\nu = \mu/\rho$) and α_t is defined at the thermal diffusivity and is equivalent to the ratio of the thermal conductivity to the product of the heat capacity and density ($\alpha_t = \lambda_i/\rho C_p$).

As such the following mass transfer correlation was used for estimation of the mass transfer coefficient for the 18NiO GR OC:

$$Sh = 2 + 0.6\, Re^{\frac{1}{2}}\, Sc^{\frac{1}{3}}$$ **Equation 7.15**

In the case of fibre-based catalysis, issues arise when mass or adapted heat transfer correlations are used to calculate the mass transfer coefficient and resolve the mass diffusivity flux around a cylinder. These issues are centred on the assumed use of spherical particles for both the diameter of the particle in the Sherwood and Reynold numbers and the overall mass transfer correlation used to relate the Reynold, Sherwood and Schmidt numbers [174,178,180,236–240]. As such there has been some consideration of these factors in recent literature, with several studies calculating equivalent diameters and empirically deriving mass transfer correlations when non-conventional support and or catalyst geometries are used. These geometries include foams, honeycombs, wire meshes and most importantly for this study fibre filters [174,178,180,236–240].

The first step in achieving accurate modelling of mass diffusion around fibrous solids is to define a characteristic length of the particles studied that can be used in place of the

diameter of the spherical particle [174,180]. In this work the Sauter diameter (d_s) as defined Riechelt and Jahn[180] was used:

$$d_s = \frac{6}{4} d_f \qquad \textbf{Equation 7.16}$$

This equivalent diameter was adapted by Lacroix et al.[241] who used a unit cubic cell model to calculate the equivalent diameter of struts surrounding a void formed in a SiC foam. They achieved this by relating the external specific surface area per unit cell volume ($S_{v,cell}$) to the external specific surface area per unit bed volume of spherical particles ($S_{v,bed}$) of equivalent void fraction:

$$If \quad S_{v,cell} = \frac{4}{d_p}(1-\varepsilon) \quad and \quad S_{v,bed} = \frac{6}{d_{str}}(1-\varepsilon) \quad then \quad d_p = \frac{6}{4} d_{str}$$

Where ε is the void fraction of the solid material, d_p is the diameter of the spherical particle and d_{str} is the calculated foam strut diameter. Riechelt and Jahn[180] showed that when d_{str} and d_p were considered analogous to d_f and d_s, the sauter diameter could be used to produce accurate mass transfer correlations for pellet and fibre packed beds.

Selecting an appropriate mass transfer correlation for fibre-based materials is highly dependent upon the Re number of the system being modelled. When considering mass transfer correlations for flow around a single sphere and around a single cylinder, Nu and Sh numbers are similar at a range of Re > 10; however at Re < 10, the Nu and Sh numbers start to diverge due to the theoretical limiting values of mass transfer at low Re number [180]. As shown in Equation 7.15, the limiting value for the Sh number of a single sphere in crossflow as Re $\rightarrow 0 = 2$, whereas the limiting value for the Sh number of a single cylinder in crossflow as Re $\rightarrow 0 = 0$ if the cylinders are considered to possess at least one infinite dimension [180]. The low Re numbers experienced in this work (shown later) dictated that mass transfer correlations for spherical particles were not used.

As such several mass transfer correlations developed for use with pellets, wire mesh and fibre-like materials were selected from the literature to model the mass diffusion around the Sf OC's detailed in Equations 7.14 to 7.20. These correlations represent a summary of the few appropriate correlations for fibre packed beds and should allow for accurate modelling of the mass transfer coefficient for Sf OC's.

Equation 7.17 and Equation 7.18 detail the mass transfer correlations developed by Reichelt and Jahn[174] and Dwivedi and Upadhyay[236] for use with conventional catalyst pellets (with sauter equivalent diameters to adjust for the use of fibres) in packed beds.

$$Sh_s = Sh_{s,Re_s=0} + 1.26\left[\frac{1-(1-\varepsilon)^{\frac{5}{3}}}{2-3(1-\varepsilon)^{\frac{1}{3}}+3(1-\varepsilon)^{\frac{5}{3}}-2(1-\varepsilon)^2}\right]^{\frac{1}{3}} \times\left[0.0991 {Pe_S}^{\frac{1}{3}}+\frac{0.037 {Re_S}^{0.8} Sc}{1+2.44 {Re_S}^{-0.1}\left(Sc^{\frac{2}{3}}-1\right)}\right] \quad \textbf{Equation 7.17}$$

Where Re_S, and Sh_S, are the Reynolds and Sherwood numbers calculated with the use of the sauter diameter; Pe_S is defined as the ratio of the products of the superficial velocity and the sauter diameter to the diffusion coefficient of the fluid ($Pe_S = ud_s/D'_i$).

$$Sh_s = 0.4548\frac{{Re_S}^{0.5931}}{\varepsilon}Sc^{\frac{1}{3}} \quad \textbf{Equation 7.18}$$

Equation 7.19 details the mass transfer correlation developed by Groppi et al.[178] for use with metallic and ceramic foams.

$$Sh = 0.91\left(\frac{Re}{\left(1-\frac{2}{\sqrt{3\pi}}(1-\varepsilon)\right)^2}\right)^{0.43} Sc^{\frac{1}{3}} \quad \textbf{Equation 7.19}$$

Equation 7.20, Equation 7.21 and Equation 7.22 detail mass transfer correlations developed by Satterfield and Cortez[240], Ahlstrom-Silversand and Odenbrand[238] and Sun et al.[239] respectively for woven wire mesh catalysts.

$$Sh = 0.94\left(\frac{Re}{\varepsilon}\right)^{0.283} Sc^{\frac{1}{3}} \quad \textbf{Equation 7.20}$$

$$Sh = 0.78\left(\frac{Re}{\varepsilon}\right)^{0.45} Sc^{\frac{1}{3}} \quad \textbf{Equation 7.21}$$

$$Sh = 1.08\left(\frac{Re}{\varepsilon}\right)^{0.5} Sc^{\frac{1}{3}} \quad \textbf{Equation 7.22}$$

Equation 7.23 details a mass transfer correlation developed for fibre filter catalysts (compressed fibre materials) by de Greef et al. (overleaf)[237]

$$Sh = 0.47\frac{Re^{0.5}}{\varepsilon}Sc^{\frac{1}{3}}$$ **Equation 7.23**

7.2.2.3 Model for External Mass Diffusion

The density, heat capacity, viscosity and thermal conductivity of the individual components of the reactant feed stream i.e. CH_4 H_2O and N_2 were estimated at 700 °C. Density was estimated for the CH_4 and N_2 using the ideal gas law and the density of steam using the National Institute of Standards and Technology (NIST) steam tables[242]. Heat capacity of all components was estimated by the Shomate equation using data from the NIST gas phase thermochemistry database[242]:

$$C_p^{\circ} = A + Bt_m + Ct_m^2 + Ct_m^3 + \frac{E}{t_m^2}$$ **Equation 7.24**

Where t_m is the temperature in Kelvin by 1000

Viscosity of all components was estimated with the Yoon-Thodos Method[243]:

$$\mu = \frac{46.1T_r^{0.618} - 20.4exp(-0.449T_r) + 19.4exp(-4.058T_r) + 1}{2.173424e10^{11}(T_c)^{\frac{1}{6}}\left(\overline{W}_i\right)^{-\frac{1}{2}}(P_c)^{-\frac{2}{3}}}$$ **Equation 7.25**

Where T_c and P_c are the critical temperature and the critical pressure (data from NIST) of the component, T_r is defined as the ratio of the temperature of the component to the critical temperature ($T_r = T/T_c$).

Thermal conductivity of CH_4 and N_2 was estimated using the Stiel-Thodos for linear and non-linear molecules respectively[243]. For linear molecules:

$$\frac{\lambda_i \overline{W}_i}{\mu\, C_v} = 1.30 + \left(\frac{R}{C_v}\right)\left(1.7614\frac{0.3523}{T_r}\right) \quad where \quad C_v = C_p - R$$ **Equation 7.26**

For non-linear molecules:

$$\frac{\lambda_i \overline{W}_i}{\mu\, C_v} = 1.15 + 2.033\left(\frac{R}{C_v}\right)$$ **Equation 7.27**

Thermal conductivity of H_2O was estimated using the Chung-Lee-Starling method[243]:

$$\frac{\lambda_i \overline{W}_i}{\mu\, C_v} = 3.75\psi\left(\frac{R}{C_v}\right)$$ **Equation 7.28**

Where:

$$\psi = 1 + \alpha\left(\frac{0.215 + 0.28288\alpha - 1.061\beta + 0.26665\gamma}{0.6366 + \beta\gamma + 1.061\alpha\beta}\right) \quad \textbf{Equation 7.29}$$

$$\alpha = \frac{C_v}{R} - 1.5 \quad \textbf{Equation 7.30}$$

$$\beta = 0.7862 - 0.7109\omega + 1.3168\omega^2 \quad \textbf{Equation 7.31}$$

$$\gamma = 2.0 + 10.5T_r^2 \quad \textbf{Equation 7.32}$$

And ω is the acentric factor and is 0.344 for H_2O[243]

The various volume flow rates of the CH_4, N_2 and H_2O at 700 °C were calculated using the ideal gas law for CH_4 and N_2 and using the density of steam (NIST steam table data[242]) to convert the mass flow of liquid water into the reactor into volume flow of steam. The estimated density, heat capacity viscosity and thermal conductivity of the individual components and their mass flows are given in Table 7.1.

Table 7.1: Summary of the estimations of density, thermal conductivity, viscosity and heat capacity of individual species in the RK feed mixture and for the combined RK feed mixture

Species	T (°C)	T (K)	ρ (kg m^{-3})	Cp (J kg^{-1} K^{-1})	μ (kg m^{-1} s^{-1})	k_t (J m^{-1} s^{-1} K^{-1})	Q (m^3 s^{-1})
N_2	700	973	0.351	1161	4.02×10^{-5}	0.066	4.43×10^{-5}
CH_4	700	973	0.201	4408	7.94×10^{-5}	0.439	4.92×10^{-6}
H_2O	700	973	0.223	2272	2.65×10^{-5}	0.084	1.49×10^{-5}
Feed	700	973	0.309	1669	4.00×10^{-5}	0.099	6.41×10^{-5}

The total volume flow rate of the reactants was calculated through the sum of the individual volume flow rates of the components. The concentration of each component in the feed stream was calculated by taking the ratio of the individual volume flow rates by the total feed volume flow rate. Accordingly, the concentrations are detailed in Table 7.2.

Table 7.2: Concentrations of individual species in the RK feed mixture at 700 °C

Species	T (°C)	T (K)	y_i (vol%)	C_i (mol m^{-3})
N_2	700	973	69.05	8.647
CH_4	700	973	7.66	0.960
H_2O	700	973	23.29	2.917

Estimation of the density, thermal conductivity, viscosity and heat capacity for the reactant feed stream as a whole, Table 7.1, was achieved using the following formula (applied to density as an example):

$$\rho_{mix} = (\rho_{CH_4} \times y_{CH_4}) + (\rho_{N_2} \times y_{N_2}) + (\rho_{H_2O} \times y_{H_2O}) \quad \textbf{Equation 7.33}$$

The superficial velocity (U_s) of the reactant stream was calculated by talking the ratio of the total mass flow rate of reactants to the cross-sectional area of the reactor (13.2 mm).

The Reynolds number was then calculated with use of sauter diameter for the Sf OC's (d_f = 3.5 µm, d_s = 5.25 × 10^{-6} m) and assumed average particle diameter (d_p = 200 µm = 2 × 10^{-4} m) of the 18NiO GR OC.

$$Re_S = \frac{U_s \rho \, d_s}{\mu} \; for \; fibres$$ **Equation 7.34**

$$Re = \frac{U_s \rho \, d_p}{\mu} \; for \; particles$$ **Equation 7.35**

The Schmidt number was then calculated via the following formula:

$$Sc = \frac{\mu}{\rho \, D'_{CH_4}}$$ **Equation 7.36**

The effective diffusivity of CH_4 in N_2 and H_2O the bulk gas was calculated with the Fuller-Schetter-Gittings method[244] for calculation of the diffusivity of a binary gas system.

$$D_{CH_4,N_2} = \frac{1.00 \times 10^{-8} T^{1.75} \left(\frac{1}{\bar{W}_{CH_4}} + \frac{1}{\bar{W}_{N_2}} \right)^{\frac{1}{2}}}{P \left[\left(\Sigma_{CH_4} \nu_{C,4H} \right)^{\frac{1}{3}} + \left(\Sigma_{N_2} \nu_{N_2} \right)^{\frac{1}{3}} \right]^2}$$ **Equation 7.37**

$$D_{CH_4,H_2O} = \frac{1.00 \times 10^{-8} T^{1.75} \left(\frac{1}{\bar{W}_{CH_4}} + \frac{1}{\bar{W}_{H_2O}} \right)^{\frac{1}{2}}}{P \left[\left(\Sigma_{CH_4} \nu_{C,4H} \right)^{\frac{1}{3}} + \left(\Sigma_{H_2O} \nu_{H_2O} \right)^{\frac{1}{3}} \right]^2}$$ **Equation 7.38**

This allowed the calculation of the diffusivity of CH_4 in the bulk gas (D'_{CH4}) was adapted to a multicomponent mixture by use of the Wilke equation[245]:

$$D'_{CH_4} = \frac{1 - y_{CH_4}}{\frac{y_{N_2}}{D_{CH_4,N_2}} + \frac{y_{H_2O}}{D_{CH_4,H_2O}}}$$ **Equation 7.39**

Where v_i is the special atomic diffusion volume of the component. The following values were taken from Fuller et al.[244] N_2 - 17.9, CH_4 - 24.42 and H_2O - 12.7. The results of these estimations are shown in Table 7.3.

Table 7.3: Summary of the estimations of velocity Reynolds, Schmidt and Péclet number and estimation of binary and multicomponent diffusion coefficients for the RK feed mixture at 700 °C

Oxygen Carrier	U_s (m s^{-1})	Re_s	Re	Sc	Pe	$D_{CH4,N2}$ (m^2 s^{-1})	$D_{CH4,H2O}$ (m^2 s^{-1})	D'_{CH4} (m^2 s^{-1})
18NiO GR	0.469	N/A	1.27×10^{-2}	7.074	N/A	2.12×10^{-5}	2.09×10^{-5}	1.83×10^{-5}
Sf	0.469	0.019	4.48×10^{-4}	7.074	0.135	2.12×10^{-5}	2.09×10^{-5}	1.83×10^{-5}

The Sherwood number was then calculated allowing the derivation of the mass transfer coefficient (k_c). The estimated molar flux of CH_4 (W_{CH4}) from the bulk to the surface was determined using an estimated concentration of CH_4 at the surface of the particle ($C_{CH4,s}$) and in the bulk gas ($C_{CH4,g}$); these concentrations were resolved using the ideal gas law, with $C_{CH4,g}$ the feed value and $C_{CH4,s}$ estimated using a representative maximum CH_4 conversion of $\alpha = 0.5$.

Table 7.4: Summary of the estimations of the mass transfer coefficient, average molar flux of CH_4 concentration of CH_4 in the bulk gas and at the surface of the particle, max rate of reduction per unit surface area and the flux to rate ratio for RK CLSR conditions

Mass Transfer Correlation		Sh	k_c (m s^{-1})	W_{CH4} (mol m^{-2} s^{-1})	$C_{CH4,s}$ (mol m^{-3})	$C_{CH4,g}$ (mol m^{-3})	$r_{red,max}$ (mol s^{-1})	r_{CH4} (mol m^{-2} s^{-1})	W:r
18NiO GR OC	Eq 7.12	3.030	0.184	0.089	0.480	0.960	3.58×10^{-5}	3.67×10^{-3}	24
Sf OC's	Eq 7.14	0.226	0.784	0.377	0.480	0.960	6.27×10^{-5}	6.03×10^{-3}	62
	Eq 7.15	0.087	0.304	0.146	0.480	0.960	6.27×10^{-5}	6.03×10^{-3}	24
	Eq 7.16	0.407	1.415	0.679	0.480	0.960	6.27×10^{-5}	6.03×10^{-3}	112
	Eq 7.17	0.797	2.773	1.331	0.480	0.960	6.27×10^{-5}	6.03×10^{-3}	220
	Eq 7.18	0.322	1.119	0.537	0.480	0.960	6.27×10^{-5}	6.03×10^{-3}	89
	Eq 7.19	0.358	1.248	0.599	0.480	0.960	6.27×10^{-5}	6.03×10^{-3}	99
	Eq 7.20	0.160	0.556	0.267	0.480	0.960	6.27×10^{-5}	6.03×10^{-3}	44

For both the pellets and fibre calculations, the highest maximum rate of reduction exhibited by the OC's under RK CLSR conditions was selected for use in these calculations.

As shown in Sections 6.1.1.1, the prevalent global reduction reaction was Equation 1.13, as such ∅ was taken to be 4 i.e. 4 mols of NiO reduced per mol of CH_4. The maximum rate of

reduction of the NiO OC materials per unit of external surface of particle was calculated with the Equation 7.40 for fibres and Equation 7.41 for spherical particles.

$$r_{CH_4,f} = \frac{r_{red,max}}{SA_{f,ext} \times nb_f} = \frac{r_{red,max}}{\left[\pi d_f L_f \times 2\pi \left(\frac{d_f}{2}\right)^2\right]\left[\frac{\rho_{bulk}}{\left(\pi \left(\frac{d_f}{2}\right)^2 L_f\right)\rho_f} V_{bed}\right] \times \emptyset}$$ **Equation 7.40**

$$r_{CH_4,p} = \frac{r_{red,max}}{SA_{p,ext} \times nb_p} = \frac{r_{red,max}}{4\pi \left(\frac{d_p}{2}\right)^2 \times \left[\frac{\rho_{bulk}}{\left(\frac{4}{3}\pi \left(\frac{d_p}{2}\right)^3\right)\rho_p} V_{bed}\right] \times \emptyset}$$ **Equation 7.41**

From the results in Table 7.4, it can be seen that the average molar flux of CH_4 from the bulk gas to the surface of the particle for the 18NiO GR OC is 24 times higher than the rate of reduction per unit of external area. This indicates that external mass transfer limitation was negligible for this geometry of particle.

Comparison of the various mass transfer correlations used for the fibre OC's show that the lowest W:r ratio was found to be 24, with all other correlations resulting in a W:r ratio above 44. This would imply that the reduction of the fibre OC's is not limited by external mass transfer, corroborating the experimental results described in Section 7.2.1.

Regardless of the above, it is useful to discuss selection of the most appropriate mass transfer correlation. Reichelt and Jahn[180] compared the accuracy of these mass transfer correlations over a number of different Reynolds numbers using a normalised route-mean square deviation (NRMSD) approach; they found that in the Reynolds number region of 0.009 - 1, Equation 7.19 was most accurate for fibre geometries. Moreover, the mass transfer correlation derived from a material most similar to the Sf OC's in physical characteristics was described by Equation 7.22. These correlations result in a W:r ratio of 112 and 99 respectively showing that fibre geometries are more suited to avoiding external mass transfer limitation of the reduction reactions than conventional geometries; another indication of their beneficial properties for CLSR processes.

Additionally, external mass transfer limitation was ruled out for the 2g of 18NiO GR OC used under EV CLSR conditions via the same calculations (Table A.12.1. Appendix A.12)

7.2.2.4 Internal Mass Transfer Theory

Internal mass transfer describes the process by which the reactant diffuses from the surface of the particle into and through the porous structure of the particle when a gradient of the reactant concentration is present between the pore and the particle surface; through this process the reactant is brought into contact with the particle to facilitate a heterogeneous reaction between the gas and solid. To rule out limitation of chemical reaction kinetics though internal diffusion, the effective rate of reaction must be shown to be faster than this diffusion process.

Determination of whether internal mass diffusion limits reaction kinetics can be achieved through use of the Weisz-Prater criterion (Equation 7.42). The Weisz-Prater criterion presents a ratio of the actual rate of reaction to the diffusion rate of the reactant through the porous structure of the particle. In general reactions that are diffusion limited are characterised by a $C_{WP} > 6$, while the complete absence of internal mass transfer limitation is absent when $C_{WP} < 0.3$; typically $C_{WP} < 1$ is used as the threshold value to effectively rule out internal mass transfer limitation[246].

$$C_{WP} = \frac{-r'_{red}(obs)\rho_p\left(\frac{d_p}{2}\right)^2}{D_e C_{A,s}} = \frac{Observed\ (actual)\ reaction\ rate}{Rate\ of\ Diffusion\ of\ A} \qquad \textbf{Equation 7.42}$$

Where $-r'_{red}(obs)$ is the maximum measured reaction rate per unit mass of catalyst and D_e is the effective diffusivity and is given by the equation below:

$$D_e = \frac{D'_A \phi_p \sigma_p}{\tilde{\tau}} \qquad \textbf{Equation 7.43}$$

Where ϕ_p is the porosity of pellet, σ_p the constriction factor τ is the tortuosity.

The likelihood of all pores within the particle being straight and cylindrical is in effect zero. As such, the effect of the porosity, tortuosity and degree of constriction for the pores throughout the particle upon the diffusivity of the reactant must be accounted for; the effective diffusivity D_e achieves this through the use of three factors:

$$\tilde{\tau} = tortuosity = \frac{Actual\ distance\ a\ molcule\ travels\ between\ two\ points}{Shortest\ distance\ between\ those\ two\ points} \qquad \textbf{Equation 7.44}$$

$$\phi_p = particle\ porosity = \frac{volume\ of\ void\ space}{total\ volume\ of\ voids\ and\ solids} \qquad \textbf{Equation 7.45}$$

$$\sigma_p = contriction\ factor = \frac{Maximum\ pore\ cross\ sectional\ area}{Minimum\ pore\ cross\ sectional\ area} \qquad \textbf{Equation 7.46}$$

7.2.2.5 Evaluation of the Weisz-Prater criterion

The following values for the porosity and tortuosity and constriction factors were used for the 18NiO GR OC:

$\phi_p = 0.59$ $\sigma_p = 0.8$ $\tau = 3.54$

The porosity and tortuosity were taken from a similar α-Al_2O_3 steam reforming NiO catalyst[101,247] and the constriction factor assumed a typical value[234].

For the Sf OC's the porosity was taken from a similar Saffil® product[248] and the tortuosity and constriction factor were assumed to be typical values[234]:

$\phi_p = 0.2$ $\sigma_p = 0.8$ $\tau = 3$

The effective diffusivity was then calculated and is shown in Table 7.5 along with the results of the Weisz-Prater criterion. The particle diameter (d_p) was taken to be the mean fibre diameter (3.5 μm) for the Sf materials and the average particle size (200 μm) for the conventional catalyst. The particle density (ρ_p) was taken to be the mean fibre density (3500 kg m^{-3}) for the Sf materials and the particle density (3946 kg m^{-3}) for the conventional catalyst. The observed reaction rate and concentration of CH_4 at the surface of the particle was taken to be $r_{red,max}$ and $C_{CH4,s}$ as shown in Table 7.4.

Table 7.5: Summary of the calculation of the Weisz-Prater criterion

Material	$r_{red,max}$ (mol s^{-1})	$-r'_{red}$(obs) (mol kg^{-1} s^{-1})	ρ_p (kg m^{-3})	dp (m)	D_e (m^2 s^{-1})	C_{WP}
18NiO GR OC	3.58×10^{-5}	0.089	3946	2.00×10^{-4}	2.44×10^{-6}	3.02
Sf OC's	6.27×10^{-5}	0.157	3500	3.50×10^{-6}	9.74×10^{-7}	3.59×10^{-3}

Table 7.5 shows that the $C_{WP} << 0.3$ in RK CLSR conditions for the Sf OC's indicating internal diffusion limitations were deemed completely absent from the conditions for which the kinetic model and rate constants parameters were derived.

However, the reduction reactions of the 18NiO GR OC presented a $6 > C_{WP} < 0.3$ and were therefore found to at least partially limited by internal mass transfer through the particle under both RK (Table 7.5) and EV CLSR (Table A.12.2. Appendix A.12) conditions.

7.2.3 Conclusions

A range of experiments were conducted using the packed bed reactor that showed that the peak rate of reduction was not affected by the flow rate of the gaseous reactants above a carrier gas flow rate of 800 sccm under EV CLSR conditions and therefore RK CLSR

conditions. These experiments were shown to rule out limitation of the reduction of the OC's through external mass transfer mass transfer of the reactant gas to the solid.

Limitation of the reduction reactions through mass diffusion of the reactant through the gas film surrounding the solid particle was ruled out by use of a model for the external mass diffusion in the RK CLSR experiments. The average molar flux of the reactants from the bulk gas to the surface of the particle was found to be significantly greater than the maximum rate of reduction experienced in the RK CLSR experiments regardless of the mass transfer correlation used or the material tested. Noticeably the ratio of molar flux to rate of reduction was higher in the Sf OC's than the 18NiO GR OC. This shows that the beneficial mass transfer properties of fibrous OC's (smaller particle diameter and larger void fraction) can be exploited to reduce the thickness of the boundary layer around OC particles, thereby reducing the effective diffusion length for reactants to reach, and products to leave, the particle surface.

Calculation of the Weisz-Prater criterion determined that the rate of reduction of the Sf OC's was not limited by the internal mass transfer of the reactant and product gases throughout the porous solid. Conversely it was found that the rate of reduction of the 18NiO GR OC was partially limited by internal mass transfer. This suggests that under the conditions used the Sf OC's can offer a higher effectiveness factor for the reduction reaction and therefore produce higher rate of reduction in similar conditions. This shows further proof of the valuable mass transfer properties of the structured fibrous OC's even when compared to a conventional OC that has been much more finely granulated than would be used in a scaled-up process.

7.3 Kinetics Modelling of CLSR Reduction Reaction

Although it was the aim of this chapter to define the kinetics of reduction of both materials without internal and external mass transfer limitations, assignation of an appropriate solid-state model can still yield interesting information on the reduction behaviour of the OC's tested. In the following section, the selection and application of an appropriate model for the reduction of the Sf OC's and the 18NiO GR OC in RK CLSR is carried out. The implications of the assignation of these models are thoroughly discussed with particular attention paid to the differences in the applied models for the Sf OC and 18NiO GR OC.

7.3.1 Kinetic Models of Solid-State Reactions

There are several kinetic models applicable to solid state reactions that can be used to accurately model any solid-state reaction. These models typically fall into 4 main groups: nucleation, product layer diffusion, geometrical contraction and reaction order models as shown in Table 2.2.

Table 2.3: Kinetic models of solid state reactions[158,159]

Model Type	Model	Differential Form $f(\alpha)=1/k\ d\alpha/dt$	Integral Form $g(\alpha)=kt$
Nucleation	Power Law (P2)	$2\alpha^{1/2}$	$\alpha^{1/2}$
	Power Law (P3)	$3\alpha^{2/3}$	$\alpha^{1/3}$
	Power Law (P4)	$4\alpha^{3/4}$	$\alpha^{1/4}$
	Avrami-Erofeyev (A2)	$2(1-\alpha)[-\ln(1-\alpha)]^{1/2}$	$[-\ln(1-\alpha)]^{1/2}$
	Avrami-Erofeyev (A3)	$3(1-\alpha)[-\ln(1-\alpha)]^{2/3}$	$[-\ln(1-\alpha)]^{1/3}$
	Avrami-Erofeyev (A4)	$4(1-\alpha)[-\ln(1-\alpha)]^{3/4}$	$[-\ln(1-\alpha)]^{1/4}$
Geometrical Contraction	Contracting Area (R2)	$2(1-\alpha)^{1/2}$	$1-(1-\alpha)^{1/2}$
	Contracting Area (R3)	$3(1-\alpha)^{2/3}$	$1-(1-\alpha)^{1/3}$
Diffusion	1-D (D1)	$1/(2\alpha)$	α^2
	2-D (D2)	$-[1/\ln(1-\alpha)]$	$((1-\alpha)\ln(1-\alpha))+\alpha$
	Jander 3-D (D3)	$[3(1-\alpha)^{2/3}]/[2(1-(1-\alpha)^{1/3})]$	$(1-(1-\alpha)^{1/3})^2$
	Ginstling-Brounshtein 3-D (D4)	$3/[2((1-\alpha)^{-1/3}-1)]$	$1-(^{2/3})\alpha-(1-\alpha)^{2/3}$
Reaction order	Zero-order (F0/R1)	1	α
	First-order (F1)	$(1-\alpha)$	$-\ln(1-\alpha)$
	Second-order (F1)	$(1-\alpha)^2$	$[1/(1-\alpha)]-1$
	Third-order (F1)	$(1-\alpha)^3$	$(1/2)[(1-\alpha)^{-2}-1]$

The kinetic model selected to describe reduction reactions of Ni based OC materials during chemical looping steam reforming varies between studies, however typically either the Avrami-Erofeyev (A2 or A3) or geometrical contraction (R2 or R3) models have been employed [23,44,101,127,156,160].

7.3.2 Model Selection Methodology

Khawam and Flanagan[158] and Hancock and Sharp[159] have both developed convenient methods for model selection for solid state reactions. Both methods allow the selection of an appropriate solid-state kinetic model based on nucleation, geometrical contraction, product layer diffusion or reaction order mechanisms. The method suggested by Khawam and Flanagan[158] uses an isothermal plot of $d\alpha/dt$ vs t and α vs t and compares the shape of the resultant curves to assign a kinetic model. Examples of the curves for the Avrami Erofeyev and geometrical contraction models are shown in Figure 7.3 overleaf (other models are shown in Figure A.13.1 and A.13.2, appendix A13).

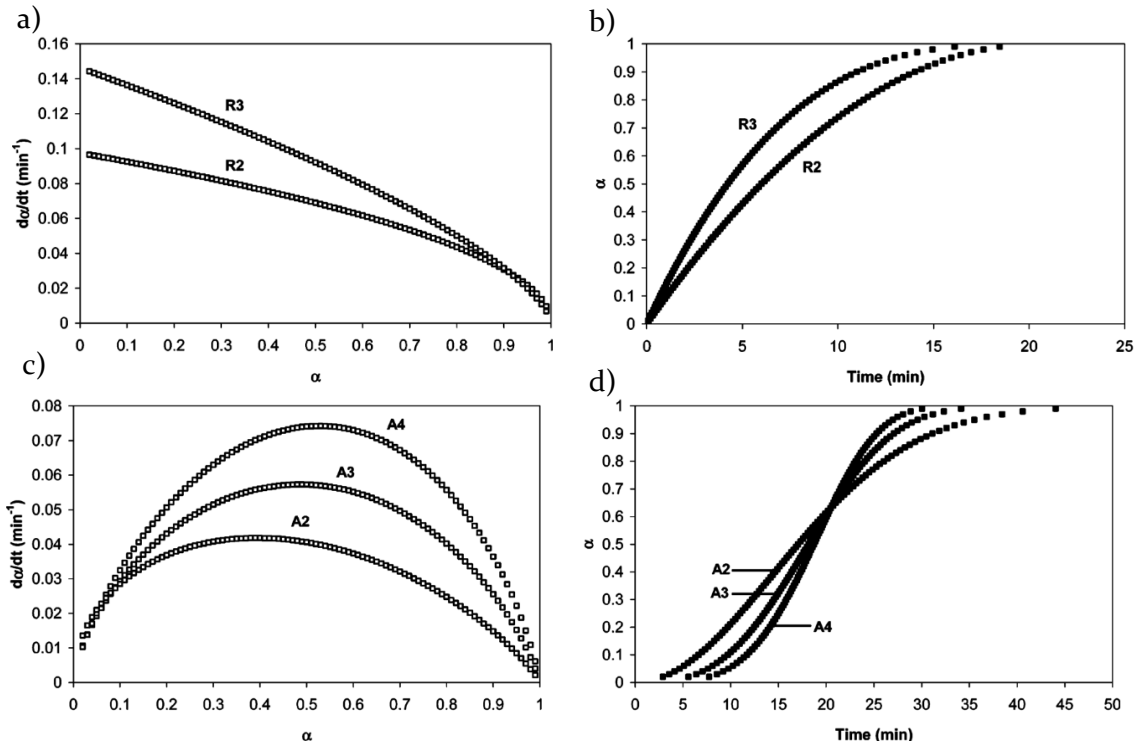

Figure 7.3: Isothermal $d\alpha/dt$ vs t (left) and α vs t plots (right) indicative of geometric contraction (a and b) and Avrami-Erofeyev (c and d) models for solid-state reactions[158]

The method suggested by Hancock et al[159] also uses a graphical transformation to assign a kinetic model to conversion data. This method makes use of an equation that in its basic form can be considered "almost universal" for the comparison of kinetic data for solid state reactions:

$$-\ln[\ln(1-\alpha_{red})] = \ln B + m \ln t \qquad \textbf{Equation 7.47}$$

Where B and m are constants that depend on the nucleation frequency and linear rate of grain growth and the geometry of the system respectively

Hancock et al[159] state that if $ln[-ln(1-\alpha_{red})]$ is plotted against $ln\ t$ while the range of conversion is limited to between 0.15 and 0.5, the resultant graph will provide a linear plot for which the gradient is equal to m. The value of m can then be used to identify a suitable kinetic model for the data.

In this work the method suggested by Khawam et al[158] was used to assign the appropriate model for the reduction of the OC materials. This was due to the ease of use of the Khawam method and the nature of the conversion data derived from the RK CLSR experiments. As shown in Figure 7.4a and Figure 7.5a, in the experiments conducted below 600°C the conversion of the OC's does not reach 0.5, and at temperatures above 650°C there were less than 3 data points between 0.15 and 0.5 therefore making the derivation of *m* prohibitively inaccurate.

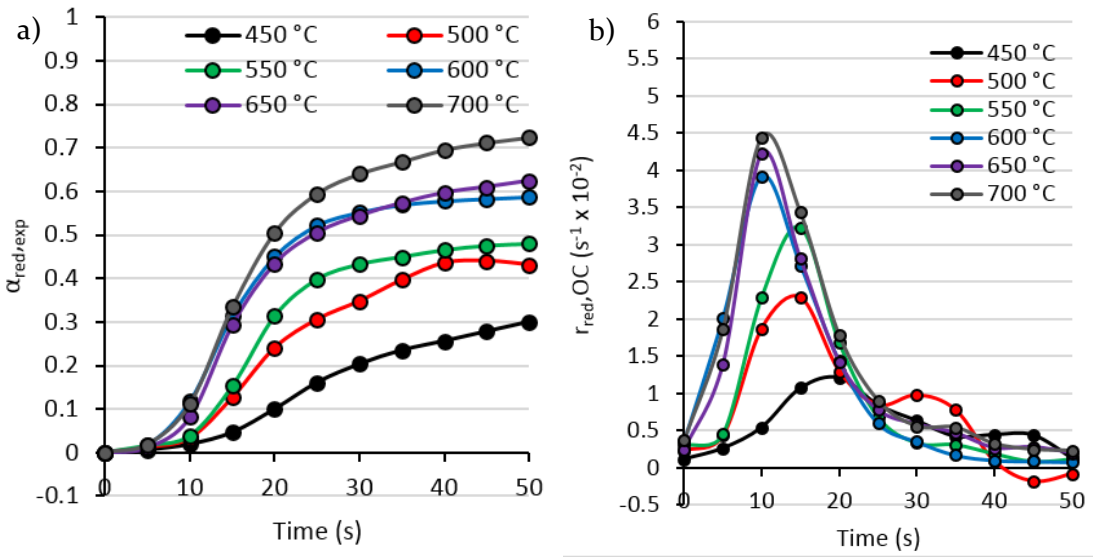

Figure 7.4: $\alpha_{red,exp}$ vs *t* (a) and r_{red},OC vs t (b) for the 18Ni Sf-WI OC under RK CLSR at 450 – 700 °C S:C 3 as representative of the kinetic data for the Sf OC's

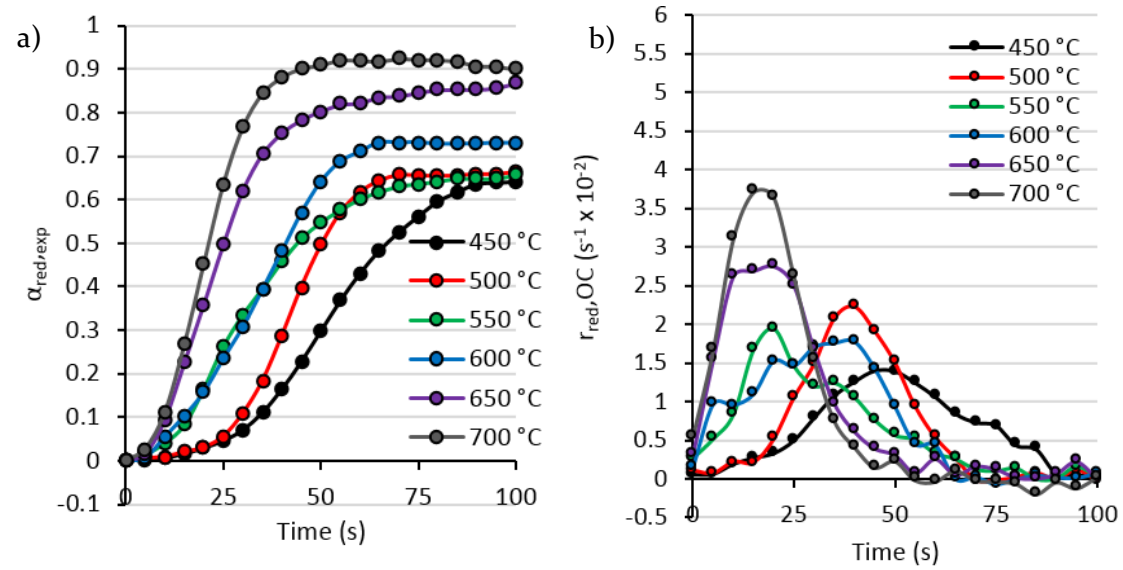

Figure 7.5: $\alpha_{red,exp}$ vs *t* (a) and r_{red},OC vs t (b) for the 18NiO GR OC under RK CLSR at 450 – 700 °C S:C 3

7.3.3 Model Fitting and Calculation of Rate Constant

Prior to model fitting the extent of reduction data was normalised between 0 to 50 s for the Sf OC's and 0 to 100 s for the 18NiO GR OC such that the maximum value in this range was equal to α = 1. This allowed for more accurate model fitting, as all the models (aside from the reaction order models) assume complete conversion. The ranges of 0-50 s and 0-100 s were chosen as the integration beyond the end of the reduction event (as seen in Figure 7.4b and Figure 7.5b) can result in accumulation of error.

The shape of the $d\alpha_{red,exp}/dt$ vs t curves shown in Figure 7.6 and the sinusoidal α vs t curves shown in Figure 7.7 indicated that the Avrami Erofeyev model would be the most suitable for all the OC's tested. Furthermore the difference in the maximum point of the $d\alpha/dt$ vs t curves indicates that the reduction Sf OC's and the 18NiO GR OC would use different Avrami Erofeyev models, with the conventional catalyst best fitted by the A2 model (a result found in similar studies[101]) and the Sf catalyst best fit by the A3 model.

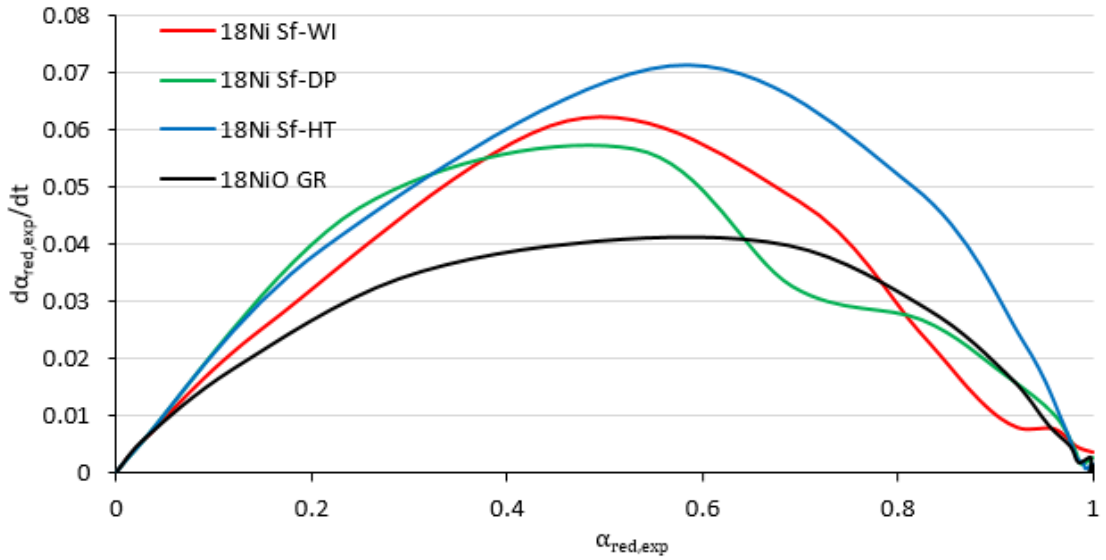

Figure 7.6: $d\alpha_{red,exp}/dt$ vs $\alpha_{red,exp}$ for the Sf OC's and 18NiO GR OC under EV CLSR at 700 °C and S:C 3

Derivation of the rate constant was achieved by minimising the deviation between experimentally derived α vs t data and modelled α vs t data produced via rearrangement of the A2 and A3 Avrami Erofeyev models:

$$\alpha_{sim} = 1 - e^{-kt^n} \qquad \textbf{Equation 7.48}$$

Where n is the Avrami index.

The percentage deviation between the experimental and modelled data in the range of 0 – 50 s (Sf OC's) and 0 – 100 s (18NiO GR OC) was expressed using the following formula[249,250]:

$$\% \, deviation = \frac{\sqrt{\frac{\sum_{\alpha=1,N}\left(\alpha_{exp} - \alpha_{sim}\right)^2}{N}}}{\alpha_{exp,max}} \times 100$$

Equation 7.49

The results of the models are shown in Figure 7.7 and Table 7.6 and show good agreement between the modelled and experimental data. Noticeably there is better agreement between the 18NiO GR OC data when compared to the data derived from the Sf OC's.

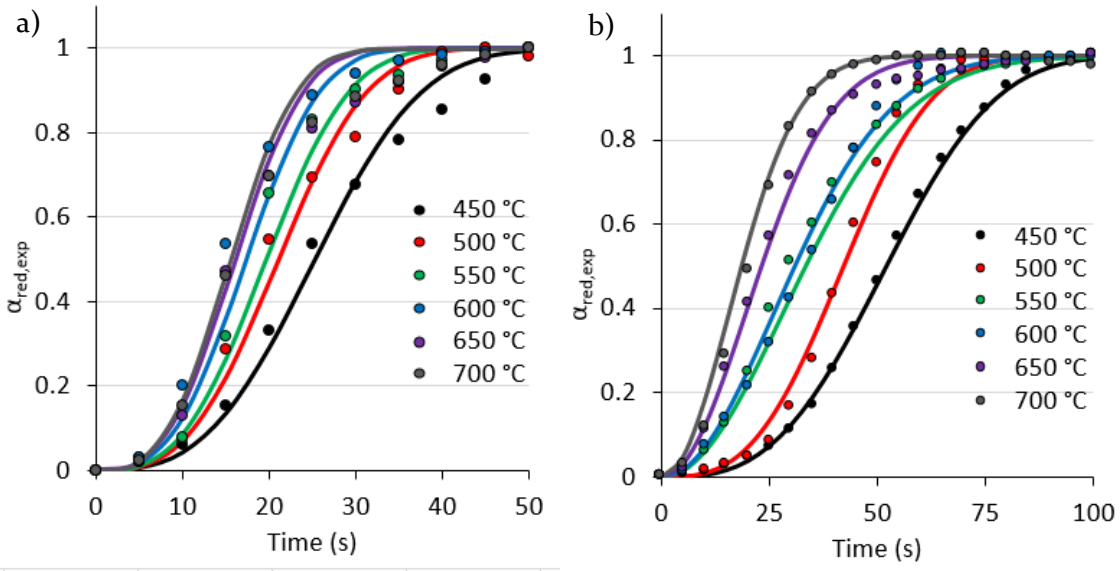

Figure 7.7: Normalised $\alpha_{red,exp}$ vs t (dots) $\alpha_{red,sim}$ vs t (lines) of the 18Ni Sf-DP OC (a) and 18NiO GR OC (b) under RK CLSR at 450 – 700 °C and S:C 3

This can be attributed to the much higher rate of reaction exhibited by the Sf OC's experienced during the first 25 s of the experiments, Figure 7.4; the higher rates of reaction of the Sf OC's when compared to the 18NiO GR OC and relatively low sampling rate of the ABB analysers (5 s^{-1}) meant that there were fewer data points on which to model the early part of the reaction. Unfortunately, the sampling rate could not be altered, nor could the rate of reduction without producing conditions that were not mass transfer limited.

7.3.4 Activation Energy and Pre-exponential Factor

Through minimising the deviation of the modelled and experimental data an approximation of the rate constant k could be made at 450 – 700 °C. As per the Arrhenius equation below, Equation 7.50, a plot of the natural logarithm of the rate constant against the inverse of the product of the gas constant and absolute temperature (Arrhenius plot)

will yield a line whose y-intercept corresponds to *ln A* and whose slope corresponds to the apparent activation energy E_A of the reaction.

$$k = Ae^{-\left(\frac{E_A}{RT}\right)} \qquad \textbf{Equation 7.50}$$

$$ln\ k = \ln A - \frac{E_A}{RT} \qquad \textbf{Equation 7.51}$$

The application of the Arrhenius equation to solid state kinetics has been critiqued due to the assumptions upon which the equation is based. The Arrhenius equation assumes that the energy distribution between gaseous molecules that participate in homogeneous reactions are well represented by Maxwell-Boltzmann equation; an assumption that cannot be satisfied when a solid molecule is considered[251,252]. In spite of this, and in absence of a more suitable method, application of the Arrhenius equation is the most widely applied and accepted kinetic concept for the description of the temperature dependence and reactivity of reaction rate in solid state kinetics[252].

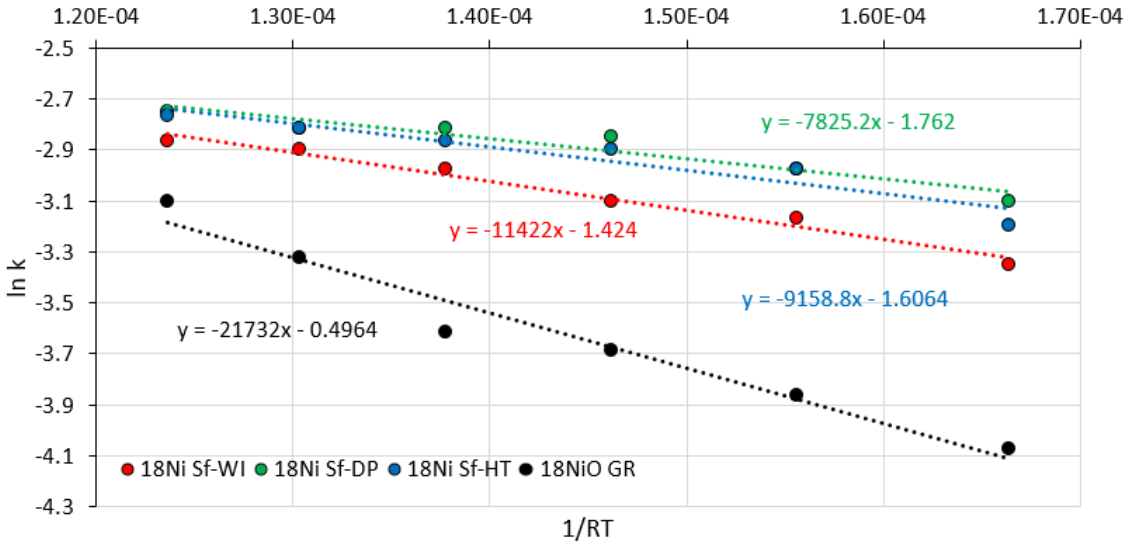

Figure 7.8: Arrhenius plots for the OC's tested under RK CLSR at 450 – 700 °C and S:C 3

The Arrhenius plots for the 18Ni Sf-WI, Sf-DP and Sf-HT OC's and the 18NiO GR OC are shown in Figure 7.8 and the derived values of the activation energy, E_A and the pre-exponential factor *A* are given in Table 7.6. The standard deviation of the slope (E_A) of the Arrhenius plot is used to estimate error the calculations.

Table 7.6: Model used and % deviation of the modelled data from the experimental data

Sample	Model Used	Deviation [a] (%)						E_A (kJ mol^{-1})	A (s^{-1})
		450 °C	500 °C	550 °C	600 °C	650 °C	700 °C		
18Ni WI	A3	4.1	4.7	5.2	6.8	6.0	6.1	11 ± 1	0.24
18Ni DP	A3	7.7	5.8	6.9	5.5	5.6	8.2	8 ± 1	0.17
18Ni HT	A3	11.1	13.0	4.2	5.3	4.4	4.8	9 ± 1	0.20
18 NiO GR	A2	1.1	3.6	3.6	2.3	2.9	2.9	22 ± 2	0.61

[a]As determined by Equation 7.49, in the range t = 0 – 50 s (Sf OC's) and t = 0 – 100 s

The E_A of a reaction can be described in terms of homogeneous kinetics as the energy barrier to be overcome to facilitate the conversion of reactants to products through the alteration of chemical bonds. In a similar manner, A describes the frequency with which the requisite reaction conditions occur[251,253]. Much of the published work concerning the application of the Arrhenius equation to solid state reactions seems to assume these definitions apply to the reactions between solids and gases by virtue of their adequate description of the kinetic data. To the author's knowledge, there is no accepted physical definition of what these factors entail when applied to heterogeneous reactions where solid and gas reactants are involved[253]. As such, the activation energies analysed in this work make no assumptions about the changes in reaction mechanism and are assumed to only characterise the temperature dependence of the reaction studied.

7.3.5 Discussion of Model Results

Application of the A2 and A3 Avarami-Erofeyev model to the reduction of the 18NiO GR OC and the Sf OC's respectively was achieved with good agreement and allowed the determination of the rate constant of the reduction reaction at a range of temperatures between 450 – 700 °C. Application of the Arrhenius equation to the kinetic data allowed the temperature dependency of the reduction reaction to be analysed. The discussion of these results is detailed below.

7.3.5.1 Rate of OC Reduction

The peak rate of reduction is noticeably increased in the Sf OC's when compared to the 18NiO GR OC at all temperatures above 500 °C (Figure 7.4b and Figure 7.5b). At 550 °C the peak rate of reduction in the 18Ni Sf-WI OC (3.22×10^{-2} s^{-1}) is nearly twice that of the 18NiO GR OC (1.94×10^{-2} s^{-1}), while at 600 °C and 650 °C the difference is even greater; the 18Ni Sf-WI OC exhibits a rate of reduction of 3.91×10^{-2} s^{-1} and 4.21×10^{-2} s^{-1} respectively at 600 °C and 650 °C while in the 18NiO GR OC, the rates are only 1.77×10^{-2} s^{-1}, 2.47×10^{-2} s^{-1} repectively. Even at 700 °C, the increase in peak rate of reaction is improved by 0.73×10^{-2} s^{-1}. Furthermore, while the peak rate of reduction for the Sf OC's is seen during

the first 10 s of the experiment, this peak rate is experienced later at temperatures below 650 °C for the 18NiO GR OC. This increase in the rate of reaction and decrease in onset of peak reduction of the Sf OC's is further evidence of the internal diffusion limitation of the reduction reactions in the 18NiO GR OC and the beneficial mass transfer properties of the fibrous OC's.

The assignation of the A2 and A3 models, Figure 7.6, to the Sf OC's and the 18NiO GR OC respectively, may suggest that diffusion limitation of the OC reduction reactions in the 18NiO GR OC may affect the behaviour of the nucleation of the nascent Ni particles and their consequent growth; a lack of sufficient reactant throughout the OC particle could limit the relative rate of nuclei formation and or the rate or dimensionality of nuclei growth. The A2 and A3 models are empirical models that describe many nucleation factors and determination of the changes to the nucleation process between the Sf OC's and the 18NiO GR OC require the use methods such as in-situ TEM or XRD to be confirmed.

7.3.5.2 Extent of OC Reduction

Figure 7.4 and Figure 7.5 shows that for both materials, as temperature increases, so does the rate of reduction and therefore the extent of reduction by the end of the observed event. There are distinct differences in the behaviour of the reduction events exhibited by the Sf OC's and 18NiO GR OC.

The reduction events of both materials are characterised by two stages of reduction. The Sf OC's generally reach a higher peak rate of reduction more quickly, typically between 10 – 15 s, afterwhich the rate of reduction quickly decreases. The 18NiO GR OC however presents a longer reduction event that reaches a lower peak rate between 20 - 35 s but extends to nearly 100s. This results in a higher extent of reduction by the end of the observed reduction event in the 18NiO GR OC when compared to the Sf OC's. This effect is seen at all temperatures tested.

Two stages in the reduction of NiO in conventional Ni α/γ-Al_2O_3 OC materials are widely reported when the solid-state kinetics for this reaction are determined in CLC and CLPO. These studies often attribute this initially fast rate to the reduction of free NiO followed by a slower rate to the reduction of bulk $NiAl_2O_4$ formed due to interaction between the Ni and the support during synthesis and use in CLC or CLPO; the greater the proportion of free NiO available on the OC, the greater the conversion over the initial period[44,46,47,117,119,131]. As stated in Section 2.3.2, many of these studies use high calcination and process temperatures (> 800 °C) and as a result bulk phase $NiAl_2O_4$ is often produced;

in this work due to the lower temperatures used, no bulk $NiAl_2O_4$ phase was detected in any of the OC's used however the effect of metal support interactions between NiO and the Al_2O_3 supports can explain this behaviour.

It is proposed that the increased reduction extent in the 18NiO GR OC is due to limited metal support interactions between the NiO and Al_2O_3 due to the use of the more thermodynamically stable α-Al_2O_3 support; this increases the ease of reduction of the NiO phase during the initial stage, and while the peak rate of reduction is lower than seen in the Sf OC's due to internal mass transfer limitation, more of the NiO is able to be reduced. The metal support interactions in the Sf OC's are promoted using the predominantly γ-Al_2O_3 Sf material resulting in less facile reduction of the NiO available in the OC. This means that despite the beneficial mass transfer properties of the structured Sf OC's producing a higher peak rate of reduction, the overall conversion of NiO to Ni is lower than the 18NiO GR OC.

7.3.5.3 Temperature Dependence of OC Reduction

The reduction of the Sf OC's presented a lower dependence on temperature than the 18NiO GR OC. This is clearly shown in Figure 7.7, by the lesser differences in both the $\alpha_{red,exp}$ vs t and the $\alpha_{red,sim}$ vs t curves and by the smaller apparent activation energies for these materials as shown in both Figure 7.8 and Table 7.6; the Sf OC's showed an average E_A of 9 kJ mol^{-1}, a reduction of ~ 40 % when compared to the 18NiO GR OC, 21 kJ mol^{-1}.

A survey of the literature shows that reported activation energies for the reduction of supported NiO OC's by CH_4 varies significantly between studies. Cheng et al.[101] derived an E_A of 38 kJ mol^{-1} using a similar Ni/α-Al_2O_3 SR catalyst to the material used in this study, whereas Moghtaderi and Song[254] indicated E_A of 55 kJ mol^{-1} for the reduction of a Ni/γ-Al_2O_3 OC. A study by Dueso et al.[44] used a two model approach, finding the reduction of NiO on a Ni/γ-Al_2O_3 to be as low as 5 kJ mol^{-1} while the $NiAl_2O_4$ present was shown to produce an activation energy of 375 kJ mol^{-1}. Moreover the works of Zafar et al.[255] and Hossain et al.[154] found activation energies of 114 kJ mol^{-1} (Ni/$MgAl_2O_4$) and 104 kJ mol^{-1} (Ni/γ-Al_2O_3) respectively.

It is generally known that the kinetics of both internally mass transfer limited reactions and those controlled by surface reaction rate both show an exponential temperature dependency; however, this temperature dependency is generally stronger in reactions controlled by the surface reaction rate than the diffusion limited reactions. Levenspiel[256] states that a reaction controlled by internal mass transfer will exhibit an activation energy

approximately half that of the same reaction when controlled by the surface reaction rate. When applied to the internally mass transfer limited I8NiO GR OC (E_A = 21 kJ mol^{-1}), this approximation results in a activation energy of approximately ~ 40 - 45 kJ mol^{-1} which compares favourably with similar works such as those by Cheng et al.[101] (38 kJ mol^{-1}) and Moghtaderi and Song[254] (55 kJ mol^{-1}).

The activation energy of the Sf OC's is lower than that of the I8NiO GR OC, however mass transfer limitation of this reaction was conclusively ruled out by the model results presented in Section 7.2.2. Moreover the work by Dueso et al.[44] showed that in conditions free from mass transfer limitations, the reduction of NiO was found to present an activation energy of just 5 kJ mol^{-1}. It is therefore reasonable that the Sf OC's offer a rate of reduction that is sufficiently rapid to decrease the temperature dependency of the reaction.

Despite a certain degree of agreement between the activation energies determined herein and selected studies in the literature, there is significant variability in the reported values of the reduction of supported NiO. This variability in derived values of E_A can be attributed to differences in methodology of OC preparation and equipment used to derive kinetics but also to the methodology of the analyses used to evaluate the resultant kinetic data.

In the studies shown above there were many differences in methodology that meant variability in the values reported is to be expected, including but not limited to: the nickel loading (wt%), support used, concentration of gaseous reactants, particle size, presence of steam or degree of air humidity, equipment used (TGA, in-situ XRD or SEM/TEM or gas analysis), and flow condition of the reactant gases. To the author's knowledge, no review of derived activation energies for methane reduction of supported Ni OC materials has been conducted and no studies exist that attempt to correlate reported E_A values with physical or chemical characteristics of the reactants involved. This makes for further difficulties in the comparison of E_A values from different studies.

However, of possibly more interest but more difficult to identify, are the differences in the data analyses used to determine heterogeneous reaction kinetics and their effect on the variability of reported E_A values. Under the International Confederation for Thermal Analysis and Calorimetry (ICTAC) kinetics project, several groups of volunteers derived values of E_A using the same source kinetic data and the mathematical methods they deemed appropriate; the differences in the resulting E_A values were significant, exceeding the uncertainties reported in each analyses[257]. Galwey[253] attributed these differences to

"unrecognized, but important and significant, inconsistencies" to the mathematical analysis methodologies employed in the derivation of the E_A values.

As a result of the differences in both experimental and mathematical methodologies, the values of E_A determined in this work are used (as suggested by Galwey and Brown[251]) only to provide a convenient and practical method of comparison between the reactivity and temperature dependence of the reduction reactions involved when using the Sf OC's and 18NiO GR OC in the RK CLSR experiments. The lower dependency on temperature of the Sf OC's combined with faster peak rate of reduction across a range of temperatures shows that the Sf OC's are more reactive under CLSR of methane than the highly idealised (i.e. much more finely ground OC granules than would be use in a CLSR process) conventional OC. This improvement in reactivity is attributed to a combination of the small effective particle sizes facilitated by the beneficial mass transfer properties of the Sf OC's and the contiguous NiO layer deposited upon the Sf fibres.

7.4 Summary

Practical experiments and theoretical calculations proved that the reduction of both the Sf OC's and the 18NiO GR OC was not limited by mass transfer of the reactant gas from the bulk gas phase to the surface of the OC particle through the boundary layer. Moreover, it was shown that the beneficial mass transfer properties of the fibrous OC's were able to increase the ratio of molar flux to rate of reduction, thereby reducing the effective diffusion length for reactants to reach, and products to leave, the particle surface.

Furthermore, calculation of the Weisz-Prater criterion (C_{WP}) showed that under the EV and RK CLSR conditions the reduction of the 18NiO GR OC was limited by the mass transfer of the reactant and product gases thoughout the porous structure of the 200 μm granules. Conversely the Sf OC's avoided this limitation. The ability to avoid internal mass transfer limitations under conditions where a highly idealised conventional OC could not, shows that the use of Sf fibrous OC's can offer a higher effectiveness factor for the reduction reaction in CLSR of methane and therefore produce higher rate of reduction in similar conditions.

The reduction behaviours of both the Sf OC's and the 18NiO GR OC were best described by the Avrami-Erofeyev nucleation and nuclei growth model. However, the two different materials were found to be best described by different variants of the Avrami-Erofeyev model with the reduction of the 18NiO GR OC best fit by the A2 model while the Sf OC's

were best fit by the A3 model. This difference in the Avrami index may suggest that internal mass transfer limitation may decrease the rate of Ni nuclei formation and growth.

The Sf OC's exhibited greater reactivity, with a higher peak rate of reduction (doubling that of the 18NiO GR OC between 550 °C and 650 °C) achieved earlier in the SR half cycle than the 18NiO GR OC. However, the 18NiO GR OC showed a greater extent of reduction of NiO available in the OC material across all temperatures.

The apparent activation energy as derived using the Arrhenius equation showed that the Sf OC's exhibited a decrease in E_A of reduction of 40% that of the 18NiO GR OC. This shows that the reduction of the Sf OC's is less temperature dependent and that the Sf OC's represent a more reactive OC than the 18NiO GR OC for the reduction reaction in CLSR of methane.

8 Conclusions

This thesis details the synthesis of Co doped Ni oxygen carriers (OC's) supported by a structured aluminosilicate fibrous material known as Saffil® and their novel application to the chemical looping steam reforming process.

A range of nine 18 wt% Ni loaded OC's utilising Saffil® fibres (Sf) as a support material and possessing various levels of Co doping (0, 0.6 and 1.8 wt% Co) were produced using three methodologies; wet impregnation (WI), deposition precipitation (DP) and hydrothermal synthesis (HT). The Saffil® fibres consist of primarily of γ-Al_2O_3 (~ 95 %) and SiO_2 (~ 5 %) and present a median width of 3 - 4 μm with an assumed fibre length ~ 5 mm. These materials are referred to using the above factors e.g. 1.8Co 18Ni Sf-WI.

The three methodologies were all able to produce OC's with the desired Ni and Co loadings, deposited in a defined outer layer consisting primarily of NiO with no evidence of the unwanted bulk nickel aluminate spinel ($NiAl_2O_4$). These materials were thoroughly characterised and compared to a conventional 18 wt% NiO/α-Al_2O_3 steam reforming catalyst in steam reforming (SR) and chemical looping steam reforming (CLSR) experiments using a benchtop packed bed reactor.

The conventional 18 wt% NiO/α-Al_2O_3 steam reforming catalyst (referred to as 18NiO GR) was supplied as raschig rings and was ground to produce granules sized between 150 – 250 μm prior to use in the SR and CLSR experiments.

8.1 Isothermal Steam Reforming Experiments

The SR experiments assessed the ability of the OC materials to effectively act as a catalyst for the SR reaction. These isothermal SR experiments involved reduction of the OC materials to their catalytically active Ni metal phase by a N_2 diluted 5% H_2 feedstock followed by 1 hour of SR of a CH_4/H_2O feedstock (S:C 3) at 700 °C. The SR experiments showed that stable outputs of the primary products of H_2, CO and CO_2 were achieved in all cases with negligible carbon deposition and no appreciable evidence of deactivation during of SR of methane.

When evaluated on an equal mass (EM) basis, the fibrous Sf OC materials were able to improve the CH_4 conversion, H_2 yield efficiency and H_2 purity from the SR of CH_4 by up to 12.8, 9.2 and 2.3 percentage points (pp) respectively (as exhibited by the 1.8Co 18Ni Sf-

HT OC) when compared to the 18NiO GR OC. Moreover, when compared on an equal volume (EV) basis, the fibrous Sf OC's produced only a small penalty to performance (as measured by the factors above) to the 18NiO GR OC despite operating with 80% less mass of OC (0.4 g of Sf OC to 2 g of 18NiO GR OC). These improvements in catalytic performance shown by the Sf OC's likely stem from a reduction in the effective diffusion length required for CH_4 to transfer from the bulk gas to active Ni catalytic sites and for reaction products to diffuse away from those sites into the bulk gas phase. This is facilitated by the decrease in effective particle size (~ 200 μm to > 10 μm) and the defined layer of Ni/NiO coating exhibited by the Sf OC's; these factors combine to lower any diffusion barriers of the SR reaction (see Section 5.2.3).

The SR experiments also showed that the Sf-DP/HT OC's were found to increase the CH_4 conversion by up to 2.0 pp when compared to the Sf-WI OC's under EM conditions. This was attributed to the differences in the physical characteristics of the deposited metal oxide layer imparted by the methodology of synthesis. The WI methodology produced a poorly distributed NiO coating consisting of round nodular particles that after use in the SR experiments produced an average Ni crystallite size of ~ 60 nm, with Ni agglomerates of up to 500 nm. The DP and HT methodologies however produced a contiguous NiO layer consisting of a network of ridges formed perpendicular to the support framing void spaces to create a honeycomb structure. Production of these structures can be attributed to a strong interaction between the NiO coating and the γ-Al_2O_3 support during synthesis (as confirmed by TPR). This was likely caused by the dissolution of Al^{3+} ions from the support and their interaction with Ni^{2+}/Co^{2+} ions in the precursor solution during precipitation (possibly through formation of LDH precursors). These structures were maintained after the SR experiments, provided an average Ni crystallite size of ~ 20 nm and were far more homogenous in their deposition; these factors likely increased the Ni surface area available for SR catalysis thus increasing catalytic activity.

8.2 Isothermal Chemical Looping Steam Reforming Experiments

The isothermal CLSR experiments were carried out at 700°C and consisted of 6 SR and oxidation half-cycles under EM conditions and 7 SR and oxidation half-cycles under EV conditions. The ability of the OC's to be reduced by a CH_4/H_2O feedstock (S:C 3) at 700 °C, the extent of that reduction (α_{red}) and their subsequent catalytic activity and selectivity

for the SR and WGS reactions were examined under the steam reforming half cycle. Under the oxidation half cycle the ability of the OC materials to be oxidised and the extent of that oxidation (α_{ox}) was determined.

The CLSR experiments showed that all the OC's tested in both the EM and EV CLSR conditions were able to be reduced by a CH_4/H_2O feedstock (S:C 3) at 700 °C and subsequently catalyse the SR and WGS for H_2 production from CLSR with a notable absence of carbon deposition.

The EV CLSR experiments showed that the average reduction extent (α_{red}) of the OC's determined by EV CLSR was inconsistent but when combined with evidence from XRD and TGA investigations, the results suggested that reduction extent was influenced by the degree of metal support interactions between the NiO and Al_2O_3 phases in the OC's. As a result, the magnitude of reduction extent followed the order 18NiO GR OC > Sf-WI > Sf-DP ~ Sf-HT. Co doping was found to improve the extent of reduction of the Sf-WI OC's but had little effect on the Sf-DP and Sf-HT OC's. Testing the extent of reduction over many cycles is still required to analyse any long-term deactivation of this factor.

Once reduced by the CH_4/H_2O feedstock, the fibrous Sf OC's could outperform the 18NiO GR OC in terms catalytic activity, increasing CH_4 conversion under EM conditions by up to ~ 10 pp (as exhibited by the 18Ni HT OC). Moreover, the fibrous Sf OC's showed only a slight deficiency in SR performance compared to the 18NiO GR OC despite operating with 80% less mass (0.4 g of Sf OC to 2 g of 18NiO GR OC). The Sf-DP and Sf-HT OC's showed improved performance in the steam reforming half cycle over the Sf-WI OC's in both the EV and EM CLSR conditions.

Performance as evidenced by CH_4 conversion, H_2 yield efficiency and H_2 purity was relatively stable over 7 reduction/oxidation cycles although a slight decrease in efficacy was experienced in all the OC's tested. Further experiments are required to test the long term (> 100 cycles) performance of the materials. Sintering of the Ni/NiO crystallites in all the Sf OC's was responsible for these slight decreases in activity over 7 cycles; this sintering effect, as evidenced from slight changes in morphology observed by SEM and Scherrer analysis of XRD, was more pronounced in the Sf-WI OC's than in the Sf-DP and Sf-HT OC's.

The full re-oxidation of the reduced Sf-DP, Sf-HT and 18NiO GR OC's was confirmed under EM CLSR conditions using XRD. Given the reduction in mass of OC used in EV CLSR

oxidation was also assumed complete under these conditions. Complete oxidation of the 18Ni Sf-WI was not achieved under EM CLSR with evidence of Ni peaks present in the XRD pattern; therefore, no reliable conclusions can be made about the extent of oxidation in the Sf-WI OC's.

8.3 Kinetic Modelling Experiments

Practical experiments and theoretical calculations proved that the beneficial mass transfer properties of fibrous OC's could increase the ratio of molar flux to rate of OC reduction, thereby reducing the effective diffusion length for reactants to reach, and products to leave, the particle surface. Moreover, The Sf OC's were able to avoid internal mass transfer limitations under conditions where a highly idealised conventional OC could not; this shows that the use of Sf fibrous OC's can offer a higher effectiveness factor for the reduction reaction and therefore produce higher rate of reduction in similar conditions.

In the temperature range of 450 – 700 °C the reduction reactions of the fibrous Sf OC's and the 18NiO GR OC were found to be best described by the Avrami-Erofeyev nucleation and nuclei growth model. The Sf OC's exhibited greater reactivity, with a higher peak rate of reduction (doubling that of the 18NiO GR OC between 550 °C and 650 °C) achieved earlier in the SR half cycle than the 18NiO GR OC. However, the 18NiO GR OC showed a greater extent of reduction of NiO available in the OC material across all temperatures.

The activation energy as derived using the Arrhenius equation showed that the Sf OC's exhibited a decrease in the activation energy of reduction of 40% when compared to the 18NiO GR OC. This shows that the reduction of the Sf OC's is less temperature dependent and that the Sf OC's represent a more reactive material than the 18NiO GR OC.

8.4 Summary

This thesis details the successful application of novel fibrous structured OC's to packed bed chemical looping steam reforming for the first time. The use of Co doped Ni OC's utilising microfibrous Saffil® supports in packed bed CLSR can offer several benefits when compared to a conventional steam reforming catalyst in granulated form. The fibrous structured OC's developed in this work can offer higher reduction reactivity when exposed to an N_2 diluted CH_4/H_2O feedstock. This was achieved while also improving catalytic activity for the subsequent steam reforming reaction, as evidenced by CH_4 conversion, H_2

purity and H_2 yield, when compared with an equal mass of granulated OC. When compared with an equal volume of solid bed material, representing an 80% reduction in the mass of fibrous OC used, only a slight penalty to the above factors was experienced.

9 Further Work

The opportunity for further development of the work presented in this thesis mainly revolves around four concepts: (1) further characterisation of the OC's produced and their metal support interactions; (2) Development of the packed bed reactor and increased cycling for the testing of the fibrous OC's; (3) investigation of the mass and heat transfer and pressure drop characteristics of the fibrous OC's; (4) the application of CO_2 sorbents (CaO) developed with Saffil® fibres in combination with the SF OC's developed here to investigate their use in SECLSR.

9.1 Characterisation

Further characterisation of the Sf OC's could yield more information on the causes of the results found in this work. $H_2/CO/N_2O$ chemisorption could be employed to analyse the Ni crystallite surface area and consequently the specific activity (as measured by TOF) of the fibrous OC's produced. This would also allow the effects of synthesis method, use in SR and CLSR experiments upon the catalytic activity of the OC's to be analysed; this could help to clarify why the Sf-DP OC's were more catalytically active than the Sf-WI OC's in the CLSR experiments despite showing decreased reduction extent. In-situ TEM imaging of the reduction of the NiO crystallites in the Sf-OC's and 18NiO GR OC could facilitate further information on any differences in nucleation behaviour of these materials and confirm whether the contiguous NiO/Ni layer found on the Sf fibres is responsible for their increased reactivity. Moreover, it may also elucidate the changes in Ni/NiO size during CLSR redox cycling. Further characterisation of the interactions between the support and the deposited layer could be facilitated using a combination of ion beam milling, TEM/EDX and X-ray photon spectroscopy (XPS) to attempt to definitively examine the interactions between NiO and Al_2O_3 and definitively confirm or deny the formation "surface spinel" $NiAl_2O_4$ in the deposited layer.

9.2 Development of the Packed Bed Reactor

Several developments should be made to the packed bed reactor and the CLSR experimental methodologies to improve several aspects of the equipment and testing regimes. Firstly, the use of an inert material for both the working tube of the reactor and the method of containing both the fibrous and conventional OC's should be implemented.

Options include alumina or quartz for the reactor material, in spite of issues that may be encountered in effectively sealing the equipment, although effective methods of containing and compressing fibrous OC's in an inert material may be more difficult to implement. This will limit any water splitting or SR activity from the reactor materials ensuring minimal effects upon the measured outcomes from the CLSR experiments. Improvement in water provision must be achieved if a range of OC masses, pellet sizes and fibrous forms are to be tested reliably. This could be implemented using pre-heating and vaporisation of the water feed; solutions could include using an off the shelf steam generator, or in-house built vaporiser using heating tape or bar heaters. Refinement of the CLSR methodology could be implemented to more closely examine the extent of reaction and oxidation in the OC's tested. If kinetics measurements are not desired, and the water provision into the reactor is made reliable, the mass of OC can be increased and reactant flows decreased to better analyse the reduction and oxidation reactions. Moreover, the use of a differential reactor, facilitated by a more accurate gas analysis method (e.g. mass spectrometry), should be investigated to improve the quality of data derived from the kinetic experiments. Testing the extent of reduction and subsequent catalytic activity of the fibrous OC's over hundreds of CLSR reduction/oxidation cycles is essential in proving their long-term activity and would allow their efficacy in CLSR to be assessed over an industrially relevant number of cycles. This could be achieved through automation of the benchtop packed bed reactor using a gas switching system equipped with solenoid valves and software such as LabView.

9.3 Mass and Heat Transfer in CLSR using Fibrous OC's

Key to the development of Sf OC's and their use in the CLSR process at lab scale and beyond is confirmation and quantification of any beneficial mass and heat transfer and pressure drop characteristics that the microfibrous Sf OC's present when compared to conventional granulated or pelletised OC's.

Investigation of pressure drop effects can be facilitated by the fitment of pressure sensors above and below the bed of solid material in the benchtop packed reactor used in this work. Moreover, changes in heat transfer radially and axially through the bed of OC could be monitored using several thermocouples throughout the OC bed. Through these modifications, the packed bed reactor developed in this work could identify any beneficial heat/mass transfer properties and or pressure drop characteristics that the Sf OC's (as tested herein) may possess when compared to conventionally structured OC's.

The void fraction of the Sf OC's will be key to these factors; the Sf-OC's developed in this work were compressed slightly to give a bulk density of 0.16 g cm^{-3} and a void fraction 0.94, however these factors can easily be changed. The Sf OC's are physically malleable and can therefore easily be compressed into a variety of forms and shapes thereby allowing the void fraction of these materials to be manipulated. Therefore, quantification of the effects of varying void fractions in the Sf OC's upon (1) the reduction reactivity, reduction extent and subsequent catalytic performance of the Sf OC materials; (2) the pressure drop through the OC bed; and (3) the heat transfer both radially and axially can be identified.

Moreover, comparison of the above factors between the Sf OC's (possessing various void fractions and or forms) and a range of conventionally structured OC's exhibiting a range of particle sizes and pellet shapes could aid in optimisation of the Sf OC's and allow a thorough assessment any further benefits of their use in the packed bed CLSR process.

9.4 Sorption Enhanced CLSR using Fibrous Support Materials

CaO based sorbents developed with the CG Saffil® material are currently being developed by Sergio Ramirez Solis at the University of Leeds; application of the Saffil® based OC materials developed in this work in combination with these sorbent materials can open interesting and novel research pathways for the packed bed SECLSR process.

The benefits of the sorption enhancement to both the reduction of the OC's and the subsequent SR/WGS reactions are well known (described in Section 1.2.2.2), however the combined use of microfibrous OC's and CO_2 sorbents could add further advantages. When separate OC and CO_2 sorbent materials are used, the rate of CO_2 adsorption from the OC reduction reaction and the subsequent SR/WGS reactions (and therefore the degree of sorption enhancement) is typically limited by the mass diffusion and transfer of the products and reactants between the two materials. The smaller effective particle sizes facilitated by fibrous OC's and sorbents mean that these limitations can be minimised with no great penalty to pressure drop due to the large void fraction of these materials. Moreover, intricate mixing between the sorbent and OC materials could be facilitated utilising textile technology (weaving, knitting or embroidering) to create a homogeneously mixed OC-sorbent material with adjustable void fractions. If sorbent and OC materials of differing effective life-times are used, easy separation and replacement of the sorbent and OC's could be facilitated by the production of thin fibre mats placed in alternating layers.

Several experiments investigating these factors could be designed using the packed bed reactor used in this work (assuming the suggested modifications above are made). Firstly, quantification of the sorption enhancement of the OC reduction reactions and subsequent SR and WGS reactions during the steam reforming half cycle, followed by proof of effective decarbonation of the sorbent materials in the oxidation half cycle must be established. This will likely be achieved using initially rudimentary mixing of the OC and sorbent material, however the effects of mixing methodology and void fraction of the combined OC and sorbent bed upon SECLSR outputs should also be undertaken. This should facilitate a series of comparison experiments to benchmark the fibrous OC's and sorbent's performance in the SECLSR process compared to conventionally structured alternatives (granules and or pellets). These experiments should be able to identify and maximise any improvement to the SECLSR process achieved using microfibrous structured materials thereby achieving further process intensification.

9.5 Development of CLSR and Fibrous OC's at Larger Scale

There are several gaps in the current knowledge base that must be filled before the CLSR process can be scaled up toward industrial implementation. First and foremost, the autothermal operation of the CLSR process, outside of start up, must be demonstrated. This will involve carrying out an energy (heat) balance across both the reduction/SR and oxidation cycles; key to this heat balance, and the factor that will dictate the ease of reaching autothermal conditions, is the Ni:CH_4 ratio and the cycling rate i.e. the frequency of atmosphere switching and the length of those cycles. Firstly, equilibrium modelling can be utilised to investigate this to similar to the work of Ortiz et al[120] for the CLPO process; in their study conducted at thermodynamic equilibrium, they found that autothermal operation could be achieved with a molar ratio of oxygen in the oxygen carrier (O_{NiO}) to CH_4 of ~1.2. Factoring in the enegetic demand involved in the vapourisation and preheating of the H_2O and CH_4 feeds using this approach can also be realised.

Equilibrium modelling as described above can then be used to provide an estimation for initial first experimental conditions for testing the autothermal CLSR process at bench and larger scales. In addition to development of the packed bed reactor as above, this will involve producing an automated larger lab or even pilot scale integral reactor system utilising from 500g to 10 kg of OC, operating over 100's of redox cycles. This system would likely operate using counter current flow to increase efficiency of H_2 production and cycling efficiency[42,45]. Using this equipment, the fibrous and conventional OC materials as

optimised in form factor by the benchscale reactor developed as above, could be implemented to scale up the results produced within this thesis to further show the possible benefits of using fibrous materials and to develop the system towards autothermal operation on a larger scale. With these increases in scale, the synthesis method used to impregnate the Sf fibres (which can easily and rapidly produced at large scale) with the active metal (Ni and or Co) must be refined. The current methods (i.e. wet impregnation and deposition precipitation) have only been used in this work to produce ~10 g of OC material; these methods could be further developed to produce larger quantities (> 500 g) of OC material, or alternative methods such as spray coating could be employed.

Concurrently the development of sophisticated process modelling (using programs such as Aspen Plus™ or PSE gPROMS™) shoud allow the development of the CLSR process on a larger scale by conducting more detailed energy balances and factoring in the influences of heat exchanger networks, steam generation and fluid mover demand. These models can be aided in their accuracy by utilising the kinetic and process data generated from this work, or further work using differential bench scale reactor or the larger scale reactor. Moreover, the work on assessing pressure drop effects in both the fibrous and conventional OC's can also be integrated into these models to assess any positive effects of increased bed voidage facilitated by fibrous OC's on fluid mover demand. The high detail of these models should also allow techno-economic assessments to be made on the process and thereby compare its efficiay to other CLR and hydrogen generation technologies.

References

1 T. Lipman, *An Overview of Hydrogen Production and Storage Systems with Renewable Hydrogen Case Studies*, 2011.

2 K. Mazloomi and C. Gomes, Hydrogen as an energy carrier: Prospects and challenges, *Renew. Sustain. Energy Rev.*, 2012, **16**, 3024–3033.

3 USEIA, *The Impact of Increased Use of Hydrogen on Petroleum Consumption and Carbon Dioxide Emissions*, 2008.

4 L. Barelli, G. Bidini, F. Gallorini and S. Servili, Hydrogen production through sorption-enhanced steam methane reforming and membrane technology: A review, *Energy*, 2008, **33**, 554–570.

5 R. K. Lyon and G. A. Cole, Unmixed Combustion: An Alternative to Fire, *Combust. Flame*, 2000, **121**, 249–261.

6 R. Ramachandran and R. K. Menon, An overview of Industrial uses of hydrogen, *Int. J. Hydrogen Energy*, 1998, **23**, 593–598.

7 P. Haussinger, R. Lohmuller and A. M. Watson, *Ullmann's Encycl. Ind. Chem.*, 2012, 353–392.

8 IEA, *Technology Roadmap*, 2015.

9 A. Vojvodic, A. J. Medford, F. Studt, F. Abild-Pedersen, T. S. Khan, T. Bligaard and J. K. Nørskov, Exploring the limits: A low-pressure, low-temperature Haber–Bosch process, *Chem. Phys. Lett.*, 2014, **598**, 108–112.

10 C. J. Dawson and J. Hilton, Fertiliser availability in a resource-limited world: Production and recycling of nitrogen and phosphorus, *Food Policy*, 2011, **36**, S14–S22.

11 J. W. Erisman, M. A. Sutton, J. Galloway, Z. Klimont and W. Winiwarter, How a century of ammonia synthesis changed the world, *Nat. Geosci.*, 2008, **1**, 636–639.

12 D. Fraile, J.-C. Lanoix, P. Maio, A. Rangel and A. Torres, *Overview of the market segmentation for hydrogen across potential customer groups based on key application areas*, Brussels, 2015.

13 J. Melorose, R. Perroy and S. Careas, World Population Prospects: The 2015 Revision, Key Findings and Advance Tables. Working Paper No. ESA/P/WP.241.,

United Nations, Dep. Econ. Soc. Aff. Popul. Div., 2015, **1**, 1–59.

14 Y. Jiao, H. Su and W. Hou, Improved optimization methods for refinery hydrogen network and their applications, *Control Eng. Pract.*, 2012, **20**, 1075–1093.

15 M. Ball and M. Weeda, The hydrogen economy – Vision or reality?, *Int. J. Hydrogen Energy*, 2015, **40**, 7903–7919.

16 R. Bhandari, C. A. Trudewind and P. Zapp, Life cycle assessment of hydrogen production via electrolysis – a review, *J. Clean. Prod.*, 2014, **85**, 151–163.

17 I. Dincer and C. Acar, Review and evaluation of hydrogen production methods for better sustainability, *Int. J. Hydrogen Energy*, 2014, **40**, 11094–11111.

18 C. Koroneos, Life cycle assessment of hydrogen fuel production processes, *Int. J. Hydrogen Energy*, 2004, **29**, 1443–1450.

19 J. Larminie, A. Dicks, J. Larminie and A. Dicks, in *Fuel Cell Systems Explained*, John Wiley & Sons, Ltd,., 2013, pp. 1–24.

20 D. K. Ross, Hydrogen storage: The major technological barrier to the development of hydrogen fuel cell cars, *Vacuum*, 2006, **80**, 1084–1089.

21 IEA, Renewables Trends, 2016, 12.

22 C. Acar and I. Dincer, Comparative assessment of hydrogen production methods from renewable and non-renewable sources, *Int. J. Hydrogen Energy*, 2014, **39**, 1–12.

23 J. Adanez, A. Abad, F. Garcia-Labiano, P. Gayan and L. F. de Diego, Progress in Chemical-Looping Combustion and Reforming technologies, *Prog. Energy Combust. Sci.*, 2012, **38**, 215–282.

24 IEA, *Energy Technology Perspectives 2015*, 2015.

25 D. E. Ridler and M. V. Twigg, in *Catalyst Handbook*, ed. M. V. Twigg, Wolfe Publishing Ltd, London, 2nd edn., 1989, pp. 225–283.

26 D. P. Harrison, Sorption-Enhanced Hydrogen Production: A Review, *Ind. Eng. Chem. Res.*, 2008, **47**, 6486–6501.

27 P. Haussinger, R. Lohmuller and A. M. Watson, *Ullmann's Encycl. Ind. Chem.*, 2012, 251–304.

28 K. Aasberg-Petersen, T. S. Christensen, C. Stub Nielsen and I. Dybkjær, Recent developments in autothermal reforming and pre-reforming for synthesis gas

production in GTL applications, *Fuel Process. Technol.*, 2003, **83**, 253–261.

29 G. G. Dimopoulos, I. C. Stefanatos and N. M. P. Kakalis, Exergy analysis and optimisation of a steam methane pre-reforming system, *Energy*, 2013, **58**, 17–27.

30 J. R. Fernández, J. C. Abanades, R. Murillo and G. Grasa, Conceptual design of a hydrogen production process from natural gas with CO_2 capture using a Ca-Cu chemical loop, *Int. J. Greenh. Gas Control*, 2012, **6**, 126–141.

31 A. M. Adris, B. B. Pruden, C. J. Lim and J. R. Grace, On the reported attempts to radically improve the performance of the steam methane reforming reactor, *Can. J. Chem. Eng.*, 1996, **74**, 177–186.

32 M. Rydén and P. Ramos, H_2 production with CO_2 capture by sorption enhanced chemical-looping reforming using NiO as oxygen carrier and CaO as CO_2 sorbent, *Fuel Process. Technol.*, 2012, **96**, 27–36.

33 J. Stocker, M. Whysall and G. Q. Miller, *50 years of PSA technology for hydrogen purification*, London, 2015.

34 IEA, *Hydrogen Production & Distribution*, 2007.

35 M. A. Rosen and D. S. Scott, Comparative efficiency assessments for a range of hydrogen production processes, *Int. J. Hydrogen Energy*, 1998, **23**, 653–659.

36 M. A. Rosen, Thermodynamic Comparison of hydrogen production processes, *Int. J. Hydrogen Energy*, 1996, **21**, 349–365.

37 BP, *BP Statistical Review of World Energy June 2017*, 2017.

38 P. L. Spath and M. K. Mann, Life Cycle Assessment of Hydrogen Production via Natural Gas Steam Reforming, *Energy*, 2001, NREL/TP-570-27637.

39 J. Dufour, D. Serrano, J. Galvez, J. Moreno and C. Garcia, Life cycle assessment of processes for hydrogen production: Environmental feasibility and reduction of greenhouse gases emissions, *Int. J. Hydrogen Energy*, 2009, **34**, 1370–1376.

40 D. Reay, C. Ramshaw and A. Harvey, *Process Intensification: Engineering for Efficiency, Sustainability and Flexibility*, Elsevier Science, 2013.

41 M. Tang, L. Xu and M. Fan, Progress in oxygen carrier development of methane-based chemical-looping reforming: A review, *Appl. Energy*, 2015, **151**, 143–156.

42 S. Noorman, M. van Sint Annaland and J. A. M. Kuipers, Experimental validation of

packed bed chemical-looping combustion, *Chem. Eng. Sci.*, 2010, **65**, 92–97.

43 M. Luo, Y. Yi, S. Wang, Z. Wang, M. Du, J. Pan and Q. Wang, Review of hydrogen production using chemical-looping technology, *Renew. Sustain. Energy Rev.*, 2018, **81**, 3186–3214.

44 C. Dueso, M. Ortiz, A. Abad, F. García-Labiano, L. F. De Diego, P. Gayán and J. Adánez, Reduction and oxidation kinetics of nickel-based oxygen-carriers for chemical-looping combustion and chemical-looping reforming, *Chem. Eng. J.*, 2012, **188**, 142–154.

45 S. Noorman, M. van Sint Annaland and Kuipers, Packed Bed Reactor Technology for Chemical-Looping Combustion, *Ind. Eng. Chem. Res.*, 2007, **46**, 4212–4220.

46 P. Gayán, C. Dueso, A. Abad, J. Adanez, L. F. de Diego and F. García-Labiano, NiO/Al_2O_3 oxygen carriers for chemical-looping combustion prepared by impregnation and deposition-precipitation methods, *Fuel*, 2009, **88**, 1016–1023.

47 M. R. Quddus, M. M. Hossain and H. I. De Lasa, Ni based oxygen carrier over gama-Al_2O_3 for chemical looping combustion: Effect of preparation method on metal support interaction, *Catal. Today*, 2013, **210**, 124–134.

48 Q. Zafar, T. Mattisson and B. Gevert, Integrated hydrogen and power production with CO_2 capture using chemical-looping reforming-redox reactivity of particles of CuO, Mn_2O_3, NiO, and Fe_2O_3 using SiO_2 as a support, *Ind. Eng. Chem. Res.*, 2005, **44**, 3485–3496.

49 Q. Zafar, T. Mattisson and B. Gevert, Redox investigation of some oxides of transition-state metals Ni, Cu, Fe, and supported on SiO_2 and $MgAl_2O_4$, *Energy and Fuels*, 2006, **20**, 34–44.

50 L. F. de Diego, M. Ortiz, J. Adánez, F. García-Labiano, A. Abad and P. Gayán, Synthesis gas generation by chemical-looping reforming in a batch fluidized bed reactor using Ni-based oxygen carriers, *Chem. Eng. J.*, 2008, **144**, 289–298.

51 A. Antzara, E. Heracleous, D. B. Bukur and A. A. Lemonidou, Thermodynamic analysis of hydrogen production via chemical looping steam methane reforming coupled with in situ CO_2 capture, *Int. J. Greenh. Gas Control*, 2015, **32**, 115–128.

52 P. Pimenidou, G. Rickett, V. Dupont and M. V Twigg, Chemical looping reforming of waste cooking oil in packed bed reactor, *Bioresour Technol*, 2010, **101**, 6389–6397.

53 K. R. Rout and H. A. Jakobsen, A numerical study of pellets having both catalytic- and capture properties for SE-SMR process: Kinetic- and product layer diffusion controlled regimes, *Fuel Process. Technol.*, 2013, **106**, 231–246.

54 H. R. Radfarnia and M. C. Iliuta, Development of Al-stabilized CaO-nickel hybrid sorbent-catalyst for sorption-enhanced steam methane reforming, *Chem. Eng. Sci.*, 2014, **109**, 212–219.

55 J. Solsvik and H. A. Jakobsen, A two property catalyst/sorbent pellet design for the sorption-enhanced steam-methane reforming process: Mathematical modeling and numerical analysis, *Energy Procedia*, 2012, **26**, 31–40.

56 P. Xu, Z. Zhou, C. Zhao and Z. Cheng, Catalytic performance of Ni/CaO-Ca5Al6O14 bifunctional catalyst extrudate in sorption-enhanced steam methane reforming, *Catal. Today*, 2016, **259**, 347–353.

57 W. Dietrich, P. S. Lawrence, M. Grünewald and D. W. Agar, Theoretical studies on multifunctional catalysts with integrated adsorption sites, *Chem. Eng. J.*, 2005, **107**, 103–111.

58 K. O. Albrecht, J. A. Satrio, B. H. Shanks and T. D. Wheelock, Application of a combined catalyst and sorbent for steam reforming of methane, *Ind. Eng. Chem. Res.*, 2010, **49**, 4091–4098.

59 J. A. Satrio, B. H. Shanks and T. D. Wheelock, Development of a novel combined catalyst and sorbent for hydrocarbon reforming, *Ind. Eng. Chem. Res.*, 2005, **44**, 3901–3911.

60 M. Rydén and A. Lyngfelt, Using steam reforming to produce hydrogen with carbon dioxide capture by chemical-looping combustion, *Int. J. Hydrogen Energy*, 2006, **31**, 1271–1283.

61 B. Moghtaderi, Review of the recent chemical looping process developments for novel energy and fuel applications, *Energy and Fuels*, 2012, **26**, 15–40.

62 US Patent No. 2665972, 1954.

63 M. Ishida, D. Zheng and T. Akehata, Evaluation of a chemical-looping-combustion power-generation system by graphic exergy analysis, *Energy*, 1987, **12**, 147–154.

64 L. I. Eide, in *Carbon Dioxide Capture for Storage in Deep Geologic Formations – Results from the CO_2 Capture Project - Volume 3*, ed. Lars Ingolf Eide, CPL Press,

Newbury, UK, 1st edn., 2009.

65 H. H. T. Pröll, P. Kolbitsch, J. Bolhàr-Nordenkampf, in *Carbon Dioxide Capture for Storage in Deep Geologic Formations – Results from the CO_2 Capture Project - Volume 3*, ed. L. I. Eide, CPL Press, Newbury, UK, 1st edn., 2009, pp. 75–85.

66 J. Adánez, F. García-Labiano, A. Abad, L. F. de Diego, P. Gayán and C. Dueso, in *Carbon Dioxide Capture for Storage in Deep Geologic Formations – Results from the CO2 Capture Project - Volume 3*, ed. L. I. Eide, CPL Press, Newbury, UK, 1st edn., 2009, pp. 85–95.

67 C. Linderholm, A. Lyngfelt, C. Béal, A. Trikkel, R. Kuusik, E. Jerndal and T. Mattisson, in *Carbon Dioxide Capture for Storage in Deep Geologic Formations – Results from the CO_2 Capture Project - Volume 3*, ed. L. I. Eide, CPL Press, Newbury, UK, 1st edn., 2009, pp. 67–75.

68 T. Mattisson, A. Lyngfelt and H. Leion, Chemical-looping with oxygen uncoupling for combustion of solid fuels, *Int. J. Greenh. Gas Control*, 2009, **3**, 11–19.

69 A. Lyngfelt, B. Leckner and T. Mattisson, A fluidized-bed combustion process with inherent CO_2 separation; Application of chemical-looping combustion, *Chem. Eng. Sci.*, 2001, **56**, 3101–3113.

70 E. Jerndal, T. Mattisson and A. Lyngfelt, Thermal Analysis of Chemical-Looping Combustion, *Chem. Eng. Res. Des.*, 2006, **84**, 795–806.

71 A. Thursfield, A. Murugan, R. Franca and I. S. Metcalfe, Chemical looping and oxygen permeable ceramic membranes for hydrogen production – a review, *Energy Environ. Sci.*, 2012, **5**, 7421.

72 A. Murugan, A. Thursfield and I. S. Metcalfe, A chemical looping process for hydrogen production using iron-containing perovskites, *Energy Environ. Sci.*, 2011, **4**, 4639.

73 C. D. Bohn, C. R. Müller, J. P. Cleeton, A. N. Hayhurst, J. F. Davidson, S. A. Scott and J. S. Dennis, Production of Very Pure Hydrogen with Simultaneous Capture of Carbon Dioxide using the Redox Reactions of Iron Oxides in Packed Beds, *Ind. Eng. Chem. Res.*, 2008, **47**, 7623–7630.

74 H. Lane, The Lane Hydrogen Producer, *Flight*, 1909, **1**, 524.

75 K. S. Go, S. R. Son, S. D. Kim, K. S. Kang and C. S. Park, Hydrogen production from

two-step steam methane reforming in a fluidized bed reactor, *Int. J. Hydrogen Energy*, 2009, **34**, 1301–1309.

76 N. Kobayashi and L. S. Fan, Biomass direct chemical looping process: A perspective, *Biomass and Bioenergy*, 2011, **35**, 1252–1262.

77 J. P. E. Cleeton, C. D. Bohn, C. R. Müller, J. S. Dennis and S. A. Scott, Clean hydrogen production and electricity from coal via chemical looping: Identifying a suitable operating regime, *Int. J. Hydrogen Energy*, 2009, **34**, 1–12.

78 J. Yang, N. Cai and Z. Li, Hydrogen Production from the Steam–Iron Process with Direct Reduction of Iron Oxide by Chemical Looping Combustion of Coal Char, *Energy & Fuels*, 2008, **22**, 2570–2579.

79 S. Fukase and T. Suzuka, Residual oil cracking with generation of hydrogen: deactivation of iron oxide catalyst in the steam-iron reaction, *Appl. Catal. A, Gen.*, 1993, **100**, 1–17.

80 P. Chiesa, G. Lozza, A. Malandrino, M. Romano and V. Piccolo, Three-reactors chemical looping process for hydrogen production, *Int. J. Hydrogen Energy*, 2008, **33**, 2233–2245.

81 P. Heidebrecht and K. Sundmacher, Thermodynamic analysis of a cyclic water gas-shift reactor (CWGSR) for hydrogen production, *Chem. Eng. Sci.*, 2009, **64**, 5057–5065.

82 Q. Song, W. Liu, C. D. Bohn, R. N. Harper, E. Sivaniah, S. A. Scott and J. S. Dennis, A high performance oxygen storage material for chemical looping processes with CO_2 capture, *Energy Environ. Sci.*, 2013, **6**, 288–298.

83 C. Dueso, C. Thompson and I. Metcalfe, High-stability, high-capacity oxygen carriers: Iron oxide-perovskite composite materials for hydrogen production by chemical looping, *Appl. Energy*, 2015, **157**, 382–390.

84 M. A. Pans, A. Abad, L. F. De Diego, F. García-Labiano, P. Gayán and J. Adánez, Optimization of H_2 production with CO_2 capture by steam reforming of methane integrated with a chemical-looping combustion system, *Int. J. Hydrogen Energy*, 2013, **38**, 11878–11892.

85 M. R. Rahimpour, M. Hesami, M. Saidi, A. Jahanmiri, M. Farniaei and M. Abbasi, Methane steam reforming thermally coupled with fuel combustion: Application of chemical looping concept as a novel technology, *Energy and Fuels*, 2013, **27**, 2351–

2362.

86 E. R. Stobbe, B. A. de Boer and J. W. Geus, The reduction and oxidation behaviour of manganese oxides, *Catal. Today*, 1999, **47**, 161–167.

87 M. Fathi, E. Bjorgum, T. Viig and O. A. Rokstad, Partial oxidation of methane to synthesis gas: Elimination of gas phase oxygen, *Catal. Today*, 2000, **63**, 489–497.

88 Y. Zeng, S. Tamhankar, N. Ramprasad, F. Fitch, D. Acharya and R. Wolf, A novel cyclic process for synthesis gas production, *Chem. Eng. Sci.*, 2003, **58**, 577–582.

89 M. Rydén, A. Lyngfelt and T. Mattisson, Synthesis gas generation by chemical-looping reforming in a continuously operating laboratory reactor, *Fuel*, 2006, **85**, 1631–1641.

90 M. Johansson, T. Mattisson, A. Lyngfelt and A. Abad, Using continuous and pulse experiments to compare two promising nickel-based oxygen carriers for use in chemical-looping technologies, *Fuel*, 2008, **87**, 988–1001.

91 M. Rydén, A. Lyngfelt and T. Mattisson, Chemical-looping combustion and chemical-looping reforming in a circulating fluidized-bed reactor using Ni- based oxygen carriers, *Energy & Fuels*, 2008, **22**, 2585–2597.

92 V. Dupont, A. B. Ross, E. Knight, I. Hanley and M. V Twigg, Production of hydrogen by unmixed steam reforming of methane, *Chem. Eng. Sci.*, 2008, **63**, 2966–2979.

93 N. Giannakeas, A. Lea-Langton, V. Dupont and M. V. Twigg, Hydrogen from scrap tyre oil via steam reforming and chemical looping in a packed bed reactor, *Appl. Catal. B Environ.*, 2012, **126**, 249–257.

94 P. Pimenidou, G. Rickett, V. Dupont and M. V Twigg, High purity H_2 by sorption-enhanced chemical looping reforming of waste cooking oil in a packed bed reactor, *Bioresour Technol*, 2010, **101**, 9279–9286.

95 V. Dupont, A. Ross, I. Hanley and M. Twigg, Unmixed steam reforming of methane and sunflower oil: A single-reactor process for H_2-rich gas, *Int. J. Hydrogen Energy*, 2007, **32**, 67–79.

96 J. Udomsirichakorn and P. A. Salam, Review of hydrogen-enriched gas production from steam gasification of biomass: The prospect of CaO-based chemical looping gasification, *Renew. Sustain. Energy Rev.*, 2014, **30**, 565–579.

97 P. Moldenhauer, M. Rydén, T. Mattisson and A. Lyngfelt, Chemical-looping

combustion and chemical-looping reforming of kerosene in a circulating fluidized-bed 300W laboratory reactor, *Int. J. Greenh. Gas Control*, 2012, **9**, 1–9.

98 Y. Liu and Q. Guo, Investigation into syngas generation from solid fuel using $CaSO_4$-based chemical looping gasification process, *Chinese J. Chem. Eng.*, 2013, **21**, 127–134.

99 R. Siriwardane, J. Riley, H. Tian and G. Richards, Chemical looping coal gasification with calcium ferrite and barium ferrite via solid-solid reactions, *Appl. Energy*, 2016, **165**, 952–966.

100 R. M. Zin, A. Lea-Langton, V. Dupont and M. V. Twigg, High hydrogen yield and purity from palm empty fruit bunch and pine pyrolysis oils, *Int. J. Hydrogen Energy*, 2012, **37**, 10627–10638.

101 F. Cheng, V. Dupont and M. V. Twigg, Direct reduction of nickel catalyst with model bio-compounds, *Appl. Catal. B Environ.*, 2017, **200**, 121–132.

102 B. Dou, V. Dupont, G. Rickett, N. Blakeman, P. T. Williams, H. Chen, Y. Ding and M. Ghadiri, Hydrogen production by sorption-enhanced steam reforming of glycerol, *Bioresour. Technol.*, 2009, **100**, 3540–3547.

103 B. Jiang, B. Dou, K. Wang, C. Zhang, Y. Song, H. Chen and Y. Xu, Hydrogen production by chemical looping steam reforming of ethanol using NiO/montmorillonite oxygen carriers in a fixed-bed reactor, *Chem. Eng. J.*, 2016, **298**, 96–106.

104 B. Jiang, B. Dou, Y. Song, C. Zhang, B. Du, H. Chen, C. Wang and Y. Xu, Hydrogen production from chemical looping steam reforming of glycerol by Ni-based oxygen carrier in a fixed-bed reactor, *Chem. Eng. J.*, 2015, **280**, 459–467.

105 F. Lind, M. Seemann and H. Thunman, Continuous catalytic tar reforming of biomass derived raw gas with simultaneous catalyst regeneration, *Ind. Eng. Chem. Res.*, 2011, **50**, 11553–11562.

106 F. Lind, M. Israelsson, M. Seemann and H. Thunman, Manganese oxide as catalyst for tar cleaning of biomass-derived gas, *Biomass Convers. Biorefinery*, 2012, **2**, 133–140.

107 N. Berguerand, F. Lind, M. Israelsson, M. Seemann, S. Biollaz and H. Thunman, Use of nickel oxide as a catalyst for tar elimination in a chemical-looping reforming reactor operated with biomass producer gas, *Ind. Eng. Chem. Res.*, 2012, **51**, 16610–16616.

108 K. Martin, L. Henrik and M. Tobias, Use of $CuO/MgAl_2O_4$ and $La_{0.8}Sr_{0.2}FeO_3/\gamma$-$Al_2O_3$ in chemical looping reforming system for tar removal from gasification gas, *AIChE J.*, **62**, 38–45.

109 A. Hafizi, M. R. Rahimpour and S. Hassanajili, High purity hydrogen production via sorption enhanced chemical looping reforming: Application of $22Fe_2O_3/MgAl_2O_4$and $22Fe_2O_3/Al_2O_3$ as oxygen carriers and cerium promote, *Appl. Energy*, 2016, **169**, 629–641.

110 L. Protasova and F. Snijkers, Recent developments in oxygen carrier materials for hydrogen production via chemical looping processes, *Fuel*, 2016, **181**, 75–93.

111 M. Rydén, A. Lyngfelt, T. Mattisson, D. Chen, A. Holmen and E. Bjorgum, Novel oxygen-carrier materials for chemical-looping combustion; $La_xSr_{1-x}Fe_yCo_{y-1}O_{3-s}$ perovskites and mixed-metal oxides of NiO, Fe_2O_3 and Mn_3O_4, *Int. J. Greenh. Gas Control*, 2008, **2**, 21–36.

112 E. Kikuchi, S. Tanaka, Y. Yamazaki and Y. Morita, Steam Reforming of Hydrocarbons on Noble Metal Catalysts (Part 1), *Bull. Japan Pet. Inst.*, 1974, **16**, 95–98.

113 J. R. Rostrup-Nielsen, Activity of nickel catalysts for steam reforming of hydrocarbons, *J. Catal.*, 1973, **31**, 173–199.

114 G. Jones, J. G. Jakobsen, S. S. Shim, J. Kleis, M. P. Andersson, J. Rossmeisl, F. Abild-Pedersen, T. Bligaard, S. Helveg, B. Hinnemann, J. R. Rostrup-Nielsen, I. Chorkendorff, J. Sehested and J. K. Nørskov, First principles calculations and experimental insight into methane steam reforming over transition metal catalysts, *J. Catal.*, 2008, **259**, 147–160.

115 A. Antzara, E. Heracleous, L. Silvester, D. B. Bukur and A. A. Lemonidou, Activity study of NiO-based oxygen carriers in chemical looping steam methane reforming, *Catal. Today*, 2016, **272**, 32–41.

116 B. M. Corbella, L. F. De Diego, F. García-Labiano, J. Adánez and J. M. Palacios, Performance in a fixed-bed reactor of titania-supported nickel oxide as oxygen carriers for the chemical-looping combustion of methane in multicycle tests, *Ind. Eng. Chem. Res.*, 2006, **45**, 157–165.

117 T. Mattisson, M. Johansson and A. Lyngfelt, The use of NiO as an oxygen carrier in chemical-looping combustion, *Fuel*, 2006, **85**, 736–747.

118 P. H. Bolt, F. H. P. M. Habraken and J. W. Geus, Formation of Nickel, Cobalt, Copper, and Iron Aluminates from α- and γ-Alumina Supported Oxides: A Comparative Study, *J. Solid State Chem.*, 1998, **135**, 59–69.

119 P. Gayán, L. F. de Diego, F. García-Labiano, J. Adánez, A. Abad and C. Dueso, Effect of support on reactivity and selectivity of Ni-based oxygen carriers for chemical-looping combustion, *Fuel*, 2008, **87**, 2641–2650.

120 M. Ortiz, L. F. De Diego, A. Abad, F. García-Labiano, P. Gayán and J. Adánez, Catalytic activity of ni-based oxygen-carriers for steam methane reforming in chemical-looping processes, *Energy and Fuels*, 2012, **26**, 791–800.

121 W. Liu, M. Ismail, M. T. Dunstan, W. Hu, Z. Zhang, P. S. Fennell, S. A. Scott and J. S. Dennis, Inhibiting the interaction between FeO and Al_2O_3 during chemical looping production of hydrogen, *RSC Adv.*, 2015, **5**, 1759–1771.

122 H. R. Forutan, E. Karimi, A. Hafizi, M. R. Rahimpour and P. Keshavarz, Expert representation chemical looping reforming: A comparative study of Fe, Mn, Co and Cu as oxygen carriers supported on Al_2O_3, *J. Ind. Eng. Chem.*, 2015, **21**, 900–911.

123 X. Zhu, Y. Wei, H. Wang and K. Li, Ce-Fe oxygen carriers for chemical-looping steam methane reforming, *Int. J. Hydrogen Energy*, 2013, **38**, 4492–4501.

124 X. Zhu, H. Wang, Y. Wei, K. Li and X. Cheng, Hydrogen and syngas production from two-step steam reforming of methane using CeO_2 as an oxygen carrier, *J. Nat. Gas Chem.*, 2011, **20**, 281–286.

125 X. P. Dai, R. J. Li, C. C. Yu and Z. P. Hao, Unsteady-state direct partial oxidation of methane to synthesis gas in a fixed-bed reactor using $AFeO_3$ (A = La, Nd, Eu) perovskite-type oxides as oxygen storage, *J. Phys. Chem. B*, 2006, **110**, 22525–22531.

126 H. Jin, T. Okamoto and M. Ishida, Development of a Novel Chemical-Looping Combustion: Synthesis of a Looping Material with a Double Metal Oxide of CoO-NiO, *Energy and Fuels*, 1998, **12**, 1272–1277.

127 M. M. Hossain and H. I. de Lasa, Reactivity and stability of Co-Ni/Al_2O_3 oxygen carrier in multicycle CLC, *AIChE J.*, 2007, **53**, 1817–1829.

128 M. M. Hossain, K. E. Sedor and H. I. de Lasa, Oxygen carrier for fluidized bed chemical-looping combustion: Desorption kinetics and metal–support interaction, *Chem. Eng. Sci.*, 2007, **62**, 5464–5472.

129 M. S. Spencer, in *Catalyst Handbook*, ed. M. V. Twigg, Wolfe Publishing Ltd, London, 2nd edn., 1989, pp. 17–82.

130 H. Zhao, D. J. Draelants and G. V Baron, Preparation and characterisation of nickel-modified ceramic filters, *Catal. Today*, 2000, **56**, 229–237.

131 C. Dueso, A. Abad, F. García-Labiano, L. F. De Diego, P. Gayán, J. Adánez and A. Lyngfelt, Reactivity of a NiO/Al_2O_3 oxygen carrier prepared by impregnation for chemical-looping combustion, *Fuel*, 2010, **89**, 3399–3409.

132 J. Ashok, M. Subrahmanyam and A. Venugopal, Hydrotalcite structure derived Ni-Cu-Al catalysts for the production of H_2 by CH_4 decomposition, *Int. J. Hydrogen Energy*, 2008, **33**, 2704–2713.

133 A. F. Lucrédio and E. M. Assaf, Cobalt catalysts prepared from hydrotalcite precursors and tested in methane steam reforming, *J. Power Sources*, 2006, **159**, 667–672.

134 P. S. Braterman, Z. P. Xu and F. Yarberry, *Layered Double Hydroxides (LDHs)*, 2005, vol. 36.

135 M. Dixit, G. N. Subbanna and P. V. Kamath, Homogeneous precipitation from solution by urea hydrolysis: a novel chemical route to the α-hydroxides of nickel and cobalt, *J. Mater. Chem.*, 1996, **6**, 1429–1432.

136 A. Lambert, C. Delquié, I. Clémeneçon, E. Comte, V. Lefebvre, J. Rousseau and B. Durand, Synthesis and characterization of bimetallic Fe/Mn oxides for chemical looping combustion, *Energy Procedia*, 2009, **1**, 375–381.

137 Z. Cheng, Q. Wu, J. Li and Q. Zhu, Effects of promoters and preparation procedures on reforming of methane with carbon dioxide over Ni/Al_2O_3 catalyst, *Catal. Today*, 1996, **30**, 147–155.

138 C. Li and Y. W. Chen, Temperature-programmed-reduction studies of nickel oxide/alumina catalysts: effects of the preparation method, *Thermochim. Acta*, 1995, **256**, 457–465.

139 L. Zhang, X. Wang, X. Shang, M. Tan, W. Ding and X. Lu, Carbon dioxide reforming of methane over mesoporous nickel aluminate/Γ-alumina composites, *J. Energy Chem.*, 2017, **26**, 93–100.

140 J. Horiguchi, Y. Kobayashi, S. Kobayashi, Y. Yamazaki, K. Omata, D. Nagao, M.

Konno and M. Yamada, Mesoporous NiO-Al_2O_3 catalyst for high pressure partial oxidation of methane to syngas, *Appl. Catal. A Gen.*, 2011, **392**, 86–92.

141 G. Paglia, C. E. Buckley, A. L. Rohl, R. D. Hart, K. Winter, A. J. Studer, B. A. Hunter and J. V. Hanna, Boehmite Derived γ-Alumina System. 1. Structural Evolution with Temperature, with the Identification and Structural Determination of a New Transition Phase, γ'-Alumina, *Chem. Mater.*, 2004, **16**, 220–236.

142 T. Shirai, H. Watanabe, M. Fuji and M. Takahashi, Structural Properties and Surface Characteristics on Aluminum Oxide Powders, *Annu. Rep. Adv. Ceram. Res. Cent. Nagoya Inst. Technol.*, 2009, **9**, 23–31.

143 A. Putnis, *An Introduction to Mineral Sciences*, Cambridge University Press, 1992.

144 M. Trueba and S. P. Trasatti, γ-alumina as a support for catalysts: A review of fundamental aspects, *Eur. J. Inorg. Chem.*, 2005, 3393–3403.

145 A. Ionescu, A. Allouche, J. P. Aycard, M. Rajzmann and F. Hutschka, Study of γ-alumina surface reactivity: Adsorption of water and hydrogen sulfide on octahedral aluminum sites, *J. Phys. Chem. B*, 2002, **106**, 9359–9366.

146 L. F. de Diego, M. Ortiz, F. García-Labiano, J. Adánez, A. Abad and P. Gayán, Hydrogen production by chemical-looping reforming in a circulating fluidized bed reactor using Ni-based oxygen carriers, *J. Power Sources*, 2009, **192**, 27–34.

147 A. Cimino, M. Lo Jacono and M. Schiavello, Structural, magnetic, and optical properties of nickel oxide supported on eta- and.gamma-aluminas, *J. Phys. Chem.*, 1971, **75**, 1044–1050.

148 H. G. J. L. Rotgerink, H. Bosch, J. G. Van Ommen and J. R. H. Ross, The effect of Ni-Al ratio on the properties of coprecipitated nickel-alumina catalysts with high nickel contents, *Appl. Catal.*, 1986, **27**, 41–53.

149 J. T. Richardson and M. V. Twigg, Reduction of impregnated NiO/α-Al_2O_3 Association of Al^{3+} ions with NiO, *Appl. Catal. A Gen.*, 1998, **167**, 57–64.

150 J. T. Richardson, M. Lei, B. Turk, K. Forster and M. V. Twigg, Reduction of model steam reforming catalysts: NiO/α-Al_2O_3, *Appl. Catal. A Gen.*, 1994, **110**, 217–237.

151 J. Adánez, C. Dueso, L. F. D. Diego, F. García-Labiano, P. Gayán and A. Abad, Methane combustion in a 500 W_{th} chemical-looping combustion system using an impregnated Ni-based oxygen carrier, *Energy and Fuels*, 2009, **23**, 130–142.

152 M. M. Hossain and H. I. de Lasa, Reduction and oxidation kinetics of Co-Ni/Al_2O_3 oxygen carrier involved in a chemical-looping combustion cycles, *Chem. Eng. Sci.*, 2010, **65**, 98–106.

153 M. M. Hossain, D. Lopez, J. Herrera and H. I. de Lasa, Nickel on lanthanum-modified γ-Al_2O_3 oxygen carrier for CLC: Reactivity and stability, *Catal. Today*, 2009, **143**, 179–186.

154 M. M. Hossain, M. R. Quddus and H. I. de Lasa, Reduction Kinetics of La Modified NiO/La-γAl_2O_3 Oxygen Carrier for Chemical-Looping Combustion, *Ind. Eng. Chem. Res.*, 2010, **49**, 11009–11017.

155 G. Li, L. Hu and J. M. Hill, Comparison of reducibility and stability of alumina-supported Ni catalysts prepared by impregnation and co-precipitation, *Appl. Catal. A Gen.*, 2006, **301**, 16–24.

156 J. T. Richardson, R. M. Scates and M. V. Twigg, X-ray diffraction study of the hydrogen reduction of NiO/α-Al_2O_3 steam reforming catalysts, *Appl. Catal. A Gen.*, 2004, **267**, 35–46.

157 H.-J. Ryu, D.-H. Bae, K.-H. Han, S.-Y. Lee, G.-T. Jin and J.-H. Choi, Oxidation and reduction characteristics of oxygen carrier particles and reaction kinetics by unreacted core model, *Korean J. Chem. Eng.*, 2001, **18**, 831–837.

158 A. Khawam and R. D. Flanagan, Solid-State kinetic Models: Basic and Mathematical Fundamentals, *J.Phys.Chem.B*, 2006, **110**, 17315–17328.

159 J. D. Hancock and J. H. Sharp, Method of Comparing Solid-State Kinetic Data and Its Application to the Decomposition of Kaolinite, Brucite, and $BaCO_3$, *J. Am. Ceram. Soc.*, 1972, **55**, 74–77.

160 Z. Zhou, L. Han and G. M. Bollas, Kinetics of NiO reduction by H_2 and Ni oxidation at conditions relevant to chemical-looping combustion and reforming, *Int. J. Hydrogen Energy*, 2014, **39**, 8535–8556.

161 J. M. Criado and A. Ortega, Non-isothermal crystallization kinetics of metal glasses: Simultaneous determination of both the activation energy and the exponent *n* of the JMA kinetic law, 1987, **35**, 1715–1721.

162 H. S. Fogler, *Elements of Chemical Reaction Engineering*, Prentice Hall, Upper Saddle River, NJ, 4th edn., 2006.

163 C. G. Visconti, Alumina: A key-component of structured catalysts for process intensification, *Trans. Indian Ceram. Soc.*, 2012, **71**, 123–136.

164 E. Tronconi, G. Groppi and C. G. Visconti, Structured catalysts for non-adiabatic applications, *Curr. Opin. Chem. Eng.*, 2014, **5**, 55–67.

165 W. J. Lywood, in *Catalyst Handbook*, ed. M. V. Twigg, Wolfe Publishing Ltd, London, 2nd edn., 1989, pp. 85–138.

166 H. S. Bengaard, J. K. Nørskov, J. Sehested, B. S. Clausen, L. P. Nielsen, A. M. Molenbroek and J. R. Rostrup-Nielsen, Steam reforming and graphite formation on Ni catalysts, *J. Catal.*, 2002, **209**, 365–384.

167 K. O. Christensen, D. Chen, R. Lødeng and A. Holmen, Effect of supports and Ni crystal size on carbon formation and sintering during steam methane reforming, *Appl. Catal. A Gen.*, 2006, **314**, 9–22.

168 J. Sehested, Four challenges for nickel steam-reforming catalysts, *Catal. Today*, 2006, **111**, 103–110.

169 J. Sehested, J. A. P. Gelten, I. N. Remediakis, H. Bengaard and J. K. Nørskov, Sintering of nickel steam-reforming catalysts: Effects of temperature and steam and hydrogen pressures, *J. Catal.*, 2004, **223**, 432–443.

170 J. R. Rostrup-Nielsen, K. Pedersen and J. Sehested, High temperature methanation. Sintering and structure sensitivity, *Appl. Catal. A Gen.*, 2007, **330**, 134–138.

171 L. Baharudin and M. J. Watson, Monolithic substrate support catalyst design considerations for steam methane reforming operation, *Rev. Chem. Eng.*, 2018, **34**, 481–501.

172 V. Palma, A. Ricca, M. Martino and E. Meloni, Innovative structured catalytic systems for methane steam reforming intensification, *Chem. Eng. Process. Process Intensif.*, 2017, **120**, 207–215.

173 V. Palma, M. Martino, E. Meloni and A. Ricca, Novel structured catalysts configuration for intensification of steam reforming of methane, *Int. J. Hydrogen Energy*, 2017, **42**, 1629–1638.

174 E. Reichelt, M. P. Heddrich, M. Jahn and A. Michaelis, Fiber based structured materials for catalytic applications, *Appl. Catal. A Gen.*, 2014, **476**, 78–90.

175 S. Fukahori, T. Kitaoka, A. Tomoda, R. Suzuki and H. Wariishi, Methanol steam

reforming over paper-like composites of Cu/ZnO catalyst and ceramic fiber, *Appl. Catal. A Gen.*, 2006, **300**, 155–161.

176 A. Zamaniyan, A. A. Khodadadi, Y. Mortazavi and H. Manafi, Comparative model analysis of the performance of tube fitted bulk monolithic catalyst with conventional pellet shapes for natural gas reforming, *J. Ind. Eng. Chem.*, 2011, **17**, 767–776.

177 Y. Matatov-Meytal and M. Sheintuch, Catalytic fibers and cloths, *Appl. Catal. A Gen.*, 2002, **231**, 1–16.

178 G. Groppi, L. Giani and E. Tronconi, Generalized Correlation for Gas/Solid Mass-Transfer Coefficients in Metallic and Ceramic Foams, *Ind. Eng. Chem. Res.*, 2007, **46**, 3955–3958.

179 L. Giani, G. Groppi and E. Tronconi, Mass-transfer characterization of metallic foams as supports for structured catalysts, *Ind. Eng. Chem. Res.*, 2005, **44**, 4993–5002.

180 E. Reichelt and M. Jahn, Generalized correlations for mass transfer and pressure drop in fiber-based catalyst supports, *Chem. Eng. J.*, 2017, **325**, 655–664.

181 H. Sadamori, Application Concepts and Evaluation of Small-Scale Catalytic Combustors for Natural Gas, *Catal. Today*, 1999, **47**, 325–338.

182 W. Zhou, Q. Wang, J. Li, Y. Tang, Z. Huang, J. Zhang and Q. Lu, Hydrogen production from methanol steam reforming using porous copper fiber sintered felt with gradient porosity, *Int. J. Hydrogen Energy*, 2015, **40**, 244–255.

183 UK Patent 20325, 1910.

184 D. L. Trimm and C. W. Lam, The combustion of methane on platinum-alumina fibre catalysts I: Kinetics and mechanism, *Chem. Eng. Sci.*, 1980, **35**, 1405–1413.

185 D. L. Trimm and C. W. Lam, The combustion of methane on platinum-alumina fibre catalyst II: Design and testing of a convective-diffusive type catalytic combustor, *Chem. Eng. Sci.*, 1980, **35**, 1731–1739.

186 S. W. Radcliffe and R. G. Hickman, Diffusive catalytic combustors, *J. Inst. Fuels*, 1975, **48**, 208–214.

187 J. H. Lee and D. L. Trimm, Catalytic combustion of methane, *Fuel Process. Technol.*, 1995, **42**, 339–359.

188 M. Sheng, H. Yang, D. R. Cahela and B. J. Tatarchuk, Novel catalyst structures with enhanced heat transfer characteristics, *J. Catal.*, 2011, **281**, 254–262.

189 V. Meille, S. Pallier, G. V. Santa Cruz Bustamante, M. Roumanie and J. P. Reymond, Deposition of γ-Al_2O_3 layers on structured supports for the design of new catalytic reactors, *Appl. Catal. A Gen.*, 2005, **286**, 232–238.

190 M. Kemell, M. Ritala, M. Leskelä, R. Groenen and S. Lindfors, Coating of highly porous fiber matrices by atomic layer deposition, *Chem. Vap. Depos.*, 2008, **14**, 347–352.

191 V. Martínez-Hansen, N. Latorre, C. Royo, E. Romeo, E. García-Bordejé and A. Monzón, Development of aligned carbon nanotubes layers over stainless steel mesh monoliths, *Catal. Today*, 2009, **147**, 71–75.

192 A. Suknev, A. C. van Veen, A. Toktarev, E. Sadovskaya, B. Bal'zhinimaev and C. Mirodatos, NO decomposition over a new type of low metal content fiberglass catalysts studied by the TAP technique, *Catal. Commun.*, 2004, **5**, 691–695.

193 L. Kiwi-Minsker, I. Yuranov, B. Siebenhaar and A. Renken, Glass fiber catalysts for total oxidation of CO and hydrocarbons in waste gases, *Catal. Today*, 1999, **54**, 39–46.

194 A. N. Zagoruiko, S. V. Vanag, B. S. Balzhinimaev, E. A. Paukshtis, L. G. Simonova, A. M. Zykov, S. N. Anichkov and N. D. Hutson, Catalytic flue gas conditioning in electrostatic precipitators of coal-fired power plants, *Chem. Eng. J.*, 2009, **154**, 325–332.

195 B. S. Balzhinimaev, E. A. Paukshtis, S. V. Vanag, A. P. Suknev and A. N. Zagoruiko, Glass-fiber catalysts: Novel oxidation catalysts, catalytic technologies for environmental protection, *Catal. Today*, 2010, **151**, 195–199.

196 H. Koga, S. Fukahori, T. Kitaoka, A. Tomoda, R. Suzuki and H. Wariishi, Autothermal reforming of methanol using paper-like Cu/ZnO catalyst composites prepared by a papermaking technique, *Appl. Catal. A Gen.*, 2006, **309**, 263–269.

197 S. Fukahori, H. Koga, T. Kitaoka, A. Tomoda, R. Suzuki and H. Wariishi, Hydrogen production from methanol using a SiC fiber-containing paper composite impregnated with Cu/ZnO catalyst, *Appl. Catal. A Gen.*, 2006, **310**, 138–144.

198 M. Sheng, D. R. Cahela, H. Yang, C. F. Gonzalez, W. R. Yantz, D. K. Harris and B. J. Tatarchuk, Effective thermal conductivity and junction factor for sintered

microfibrous materials, *Int. J. Heat Mass Transf.*, 2013, **56**, 10–19.

199 M. Sheng, C. F. Gonzalez, W. R. Yantz, D. R. Cahela, H. Yang, D. R. Harris and B. J. Tatarchuk, Micro scale heat transfer comparison between packed beds and microfibrous entrapped catalysts, *Eng. Appl. Comput. Fluid Mech.*, 2013, **7**, 471–485.

200 Y. Tang, L. Chen, M. Wang, J. Li and Y. Lu, Microfibrous entrapped ZnO-CaO/Al_2O_3 for high efficiency hydrogen production via methanol steam reforming, *Particuology*, 2010, **8**, 225–230.

201 S. Z. Abbas, V. Dupont and T. Mahmud, Kinetics study and modelling of steam methane reforming process over a NiO/Al_2O_3 catalyst in an adiabatic packed bed reactor, *Int. J. Hydrogen Energy*, 2017, **42**, 2889–2903.

202 B. D. Cullity and S. R. Stock, *Elements of X-Ray Diffraction*, Pearson, 3rd edn., 2001.

203 L. B. Mccusker, R. B. Von Dreele, D. E. Cox, D. Louër and P. Scardi, Rietveld refinement guidelines, *J. Appl. Crystallogr.*, 1999, **32**, 36–50.

204 A. I. Vogel and J. Mendham, *Vogel's textbook of quantitative chemical analysis*, Prentice Hall, 2000.

205 Varian, *Flame Atomic Adsorption Spectrometry: Analytical Methods*, Mulgrave, Victoria, 1989.

206 S. Brunauer, P. H. Emmett and E. Teller, Adsorption of Gases in Multimolecular Layers, *J. Am. Chem. Soc.*, 1938, **60**, 309–319.

207 E. P. Barrett, L. G. Joyner and P. P. Halenda, The Determination of Pore Volume and Area Distributions in Porous Substances. I. Computations from Nitrogen Isotherms, *J. Am. Chem. Soc.*, 1951, **73**, 373–380.

208 M. F. De Lange, T. J. H. Vlugt, J. Gascon and F. Kapteijn, Adsorptive characterization of porous solids: Error analysis guides the way, *Microporous Mesoporous Mater.*, 2014, **200**, 199–215.

209 D. B. Williams and C. B. Carter, *Transmission Electron Microscopy: A Textbook for Materials Science*, Springer, 2009.

210 R. F. Egerton, *Physical Principles of Electron Microscopy: An Introduction to TEM, SEM, and AEM*, Springer US, 2006.

211 F. Krumeich, ETH Zurich: Interactions of Electrons with Matter, http://www.microscopy.ethz.ch/interactions.htm, (accessed 8 January 2018).

212 R. Wirth, Focused Ion Beam (FIB) combined with SEM and TEM: Advanced analytical tools for studies of chemical composition, microstructure and crystal structure in geomaterials on a nanometre scale, *Chem. Geol.*, 2009, **261**, 217–229.

213 P. R. Munroe, The application of focused ion beam microscopy in the material sciences, *Mater. Charact.*, 2009, **60**, 2–13.

214 F. Krumeich, ETH Zurich: Image Modes in TEM - Principles of Image Formation, http://www.microscopy.ethz.ch/TEM_imaging.htm, (accessed 8 January 2018).

215 F. Krumeich, ETH Zurich: Imaging and Diffraction in the TEM (schematic), http://www.microscopy.ethz.ch/TEMED.htm, (accessed 8 January 2018).

216 A. Lea-Langton, R. M. Zin, V. Dupont and M. V. Twigg, Biomass pyrolysis oils for hydrogen production using chemical looping reforming, *Int. J. Hydrogen Energy*, 2012, **37**, 2037–2043.

217 O. A. Omoniyi and V. Dupont, Chemical looping steam reforming of acetic acid in a packed bed reactor, *Appl. Catal. B Environ.*, 2018, **226**, 258–268.

218 S. Gordon and B. J. McBride, *NASA Ref. Publ. 1311*, 1996, 184.

219 B. J. McBride and S. Gordon, *NASA Ref. Publ. 1311*, 1994, 184.

220 A. V. Neimark, L. I. Kheifez and V. B. Fenelonov, Theory of preparation of supported catalysts, *Ind. Eng. Chem. Prod. Res. Dev.*, 1981, **20**, 439–450.

221 J. Espinose, D. Caillerie, M. Kermarec and O. Clause, Impregnation of y-Alumina with Ni (II) or Co (II) Ions at Neutral pH: Hydrotalcite-Type Coprecipitate Formation and Characterization, *J. Am. Chem. Soc.*, 1995, **117**, 11471–11481.

222 J. A. Mieth and J. A. Schwarz, Effects of alumina dissolution and metal ion buffering on the dispersion of alumina supported nickel and ruthenium catalysts, *Appl. Catal.*, 1989, **55**, 137–149.

223 M. Li, G. Fan, H. Qin and F. Li, Investigation of the Structure and Catalytic Performance of Highly Dispersed Ni-Based Catalysts for the Growth of Carbon Nanostructures, *Ind. Eng. Chem. Res.*, 2012, **51**, 11892–11900.

224 J. T. Feng, Y. J. Lin, D. G. Evans, X. Duan and D. Q. Li, Enhanced metal dispersion and hydrodechlorination properties of a Ni/Al_2O_3 catalyst derived from layered double hydroxides, *J. Catal.*, 2009, **266**, 351–358.

225 Z. Xu, N. Wang, W. Chu, J. Deng and S. Luo, In situ controllable assembly of

layered-double-hydroxide-based nickel nanocatalysts for carbon dioxide reforming of methane, *Catal. Sci. Technol.*, 2015, **5**, 1588–1597.

226 Z. P. Xu, J. Zhang, M. O. Adebajo, H. Zhang and C. Zhou, Catalytic applications of layered double hydroxides and derivatives, *Appl. Clay Sci.*, 2011, **53**, 139–150.

227 D. Uzio, in *Physico-Chemical Analysis of Industrial Catalysts: A Practical Guide to Characterisation*, ed. J. Lynch, Editions Technip, Paris, France, 2003.

228 J. R. Anderson and K. C. Pratt, *Introduction to Characterisation and Testing of Catalysts, Academic Press*, Academic Press, Melbourne Australia, 1985.

229 J. C. Groen, L. A. A. Peffer and J. Pérez-Ramírez, Pore size determination in modified micro- and mesoporous materials. Pitfalls and limitations in gas adsorption data analysis, *Microporous Mesoporous Mater.*, 2003, **60**, 1–17.

230 M. Thommes, Physical adsorption characterization of nanoporous materials, *Chemie-Ingenieur-Technik*, 2010, **82**, 1059–1073.

231 T. Li, G. H. Li, L. H. Li, L. Liu, Y. Xu, H. Y. Ding and T. Zhang, Large-Scale Self-Assembly of 3D Flower-like Hierarchical Ni/Co-LDHs Microspheres for High-Performance Flexible Asymmetric Supercapacitors, *ACS Appl. Mater. Interfaces*, 2016, **8**, 2562–2572.

232 A. Zhao, W. Ying, H. Zhang, H. Ma and D. Fang, Ni-Al_2O_3 catalysts prepared by solution combustion method for syngas methanation, *Catal. Commun.*, 2012, **17**, 34–38.

233 X. You, X. Wang, Y. Ma, J. Liu, W. Liu, X. Xu, H. Peng, C. Li, W. Zhou, P. Yuan and X. Chen, Ni-Co/Al_2O_3 Bimetallic Catalysts for CH_4 Steam Reforming: Elucidating the Role of Co for Improving Coke Resistance, *ChemCatChem*, 2014, n/a-n/a.

234 H. S. Fogler, *Elements of Chemical Reaction Engineering*, Prentice Hall, Upper Saddle River, NJ, 4th edn., 2006.

235 N. M. Frössling, The Evaporation of Falling Drops, *Gerlands Beitr. Geophys.*, 1938, **52**, 170–216.

236 P. N. Dwivedi and S. N. Upadhyay, Particle-Fluid Mass Transfer in Fixed and Fluidized Beds, *Ind. Eng. Chem. Process Des. Dev.*, 1977, **16**, 157–165.

237 J. De Greef, G. Desmet and G. V Baron, Micro-fiber elements as perfusive catalysts or in catalytic mixers: Flow, mixing and mass transfer, *Catal. Today*, 2005, **105**, 331–

336.

238 A. Fredrik Ahlström-Silversand and C. Ulf Ingemar Odenbrand, Modelling catalytic combustion of carbon monoxide and hydrocarbons over catalytically active wire meshes, *Chem. Eng. J.*, 1999, **73**, 205–216.

239 H. Sun, Y. Shu, X. Quan, S. Chen, B. Pang and Z. Liu, Experimental and modeling study of selective catalytic reduction of NOx with NH3 over wire mesh honeycomb catalysts, *Chem. Eng. J.*, 2010, **165**, 769–775.

240 C. N. Satterfield and D. H. Cortez, Mass Transfer Characteristics of Woven-Wire Screen Catalysts, *Ind. Eng. Chem. Fundam.*, 1970, **9**, 613–620.

241 M. Lacroix, P. Nguyen, D. Schweich, C. Pham Huu, S. Savin-Poncet and D. Edouard, Pressure drop measurements and modeling on SiC foams, *Chem. Eng. Sci.*, 2007, **62**, 3259–3267.

242 E. W. Lemmon, M. O. McLinden and D. G. Friend, in *NIST Chemistry WebBook, NIST Standard Reference Database Number 69*, eds. P. J. Linstrom and W. G. Mallard, Gaithersburg MD, 2018.

243 B. E. Polling, G. H. Thompson, D. G. Friend, R. L. Rowley and W. V. Wilding, in *Perry's Chemical Engineer's Handbook*, eds. D. W. Green and R. H. Perry, McGraw-Hill, New York, 8th edn., 2008.

244 J. C. Fuller, Edward N.; Schettler, Paul D.; Giddings, A New Method for Prediction of Binary Gas - Phase Diffusion, *Ind. Eng. Chem*, 1966, **58**, 19–27.

245 C. R. Wilke, Diffusional properties of multicomponent gases., *Chem. Eng. Prog.*, 1950, **46**, 95–104.

246 C. Sievers, S. L. Scott, Y. Noda, L. Qi, E. M. Albuquerque and R. M. Rioux, Phenomena affecting catalytic reactions at solid–Liquid interfaces, *ACS Catal.*, , DOI:10.1021/acscatal.6b02532.

247 J. G. Xu and G. F. Froment, Methane Steam Reforming .2. Diffusional Limitations and Reactor Simulation, *Aiche J.*, 1989, **35**, 97–103.

248 J. H. T. E. R. Haar and J. Duszczyk, The influence of Saffil-alumina fibre reinforcement on gas entrapment and evolution in P/M AI-20Si-3Cu-1Mg-xAl_2O_3 composite, *J. Mater. Sci.*, 1993, **28**, 3103–3115.

249 G. Varhegyi, M. A. Jr, T. Szekely and P. Szabo, Kinetics of the thermal

decomposition of cellulose, hemicellulose, and sugarcane bagasse, *Energy & Fuels*, 1989, 329–335.

250 C. Branca and C. Di Blasi, Global Kinetics of Wood Char Devolatilization and Combustion, *Energy and Fuels*, 2003, **17**, 1609–1615.

251 A. K. Galwey and M. E. Brown, Application of the arrhenius equation to solid state kinetics: Can this be justified?, *Thermochim. Acta*, 2002, **386**, 91–98.

252 K. J. Warren and J. R. Scheffe, Kinetic insights into the reduction of ceria facilitated via the partial oxidation of methane, *Mater. Today Energy*, 2018, **9**, 39–48.

253 A. K. Galwey, Solid state reaction kinetics, mechanisms and catalysis: a retrospective rational review, *React. Kinet. Mech. Catal.*, 2015, **114**, 1–29.

254 B. Moghtaderi and H. Song, Reduction properties of physically mixed metallic oxide oxygen carriers in chemical looping combustion, *Energy and Fuels*, 2010, **24**, 5359–5368.

255 Q. Zafar, A. Abad, T. Mattisson and B. Gevert, Reaction kinetics of freeze-granulated $NiO/MgAl_2O_4$ oxygen carrier particles for chemical-looping combustion, *Energy and Fuels*, 2007, **21**, 610–618.

256 O. Levenspiel, *Chemical Reaction Engineering*, John Wiley & Sons, New York, 3rd edn., 1999.

257 M. E. Brown, M. Maciejewski, S. Vyazovkin, R. Nomen, J. Sempere, A. Burnham, J. Opfermann, R. Strey, H. L. Anderson, A. Kemmler, R. Keuleers, J. Janssens, H. O. Desseyn, C. R. Li, T. B. Tang, B. Roduit, J. Malek and T. Mitsuhashi, Computational aspects of kinetic analysis Part A: The ICTAC Kinetics Project-data, methods and results, *Thermochim. Acta*, 2000, **355**, 125–143.

258 J. R. Anderson and K. C. Pratt, *Introduction to characterization and testing of catalysts*, Academic Press, 1985.

Appendices

A.1 SEM and SEM/EDX of the 18NiO OC

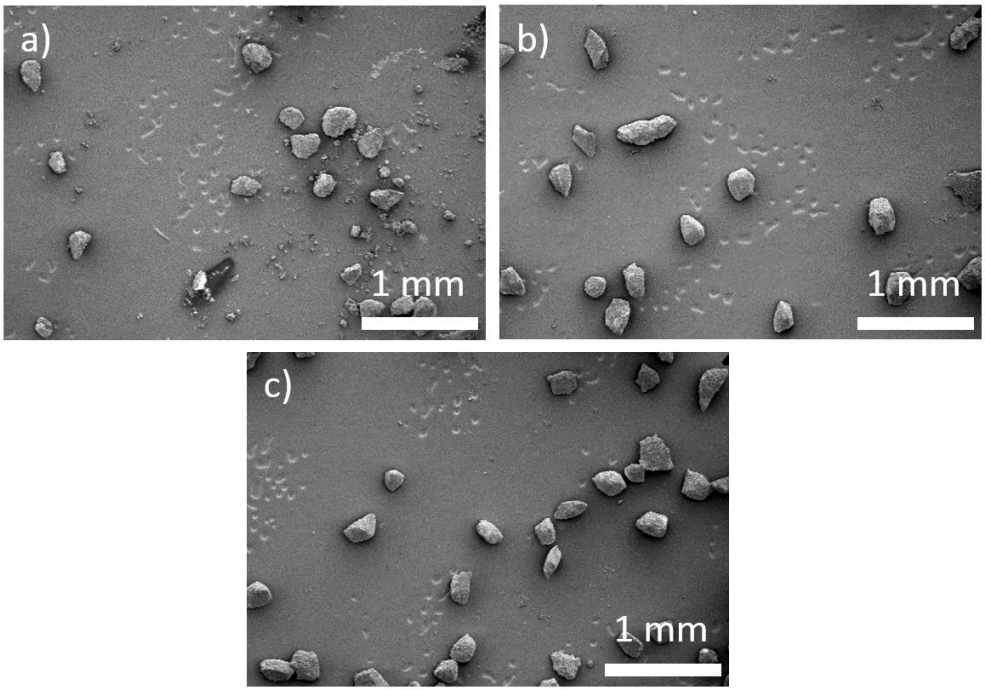

Figure A.1.1: SEM images of the fresh 18NiO GR OC (a), and those used the EM SR (b) and EM CLSR (c) experiments showing granule size of ~ 200 µm

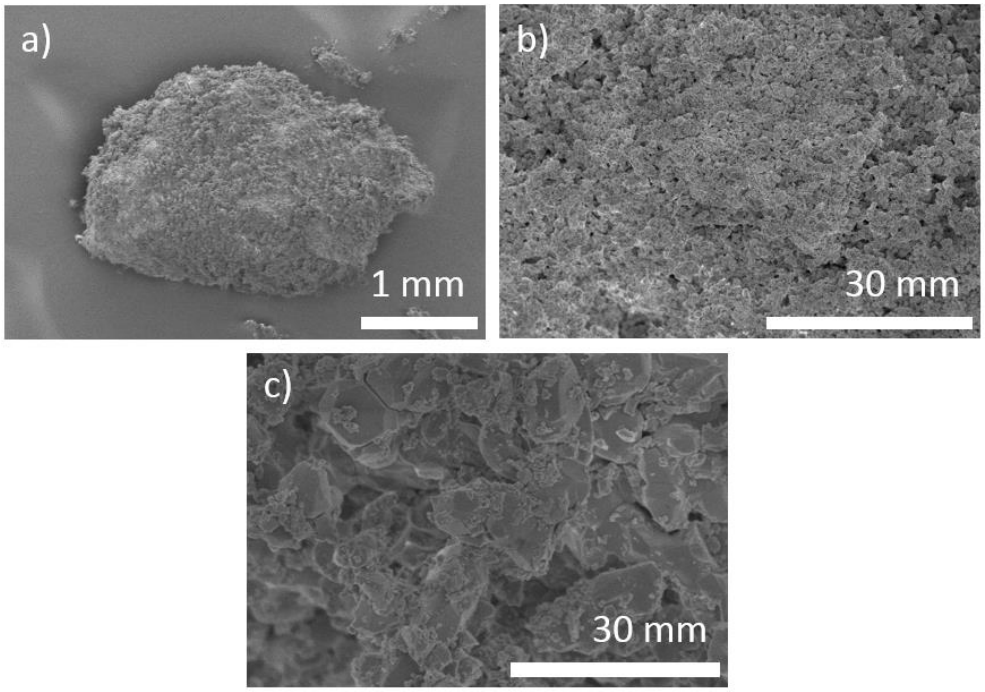

Figure A.1.2: SEM images (a,b and c) of the fresh 18NiO GR OC showing porosity of granule

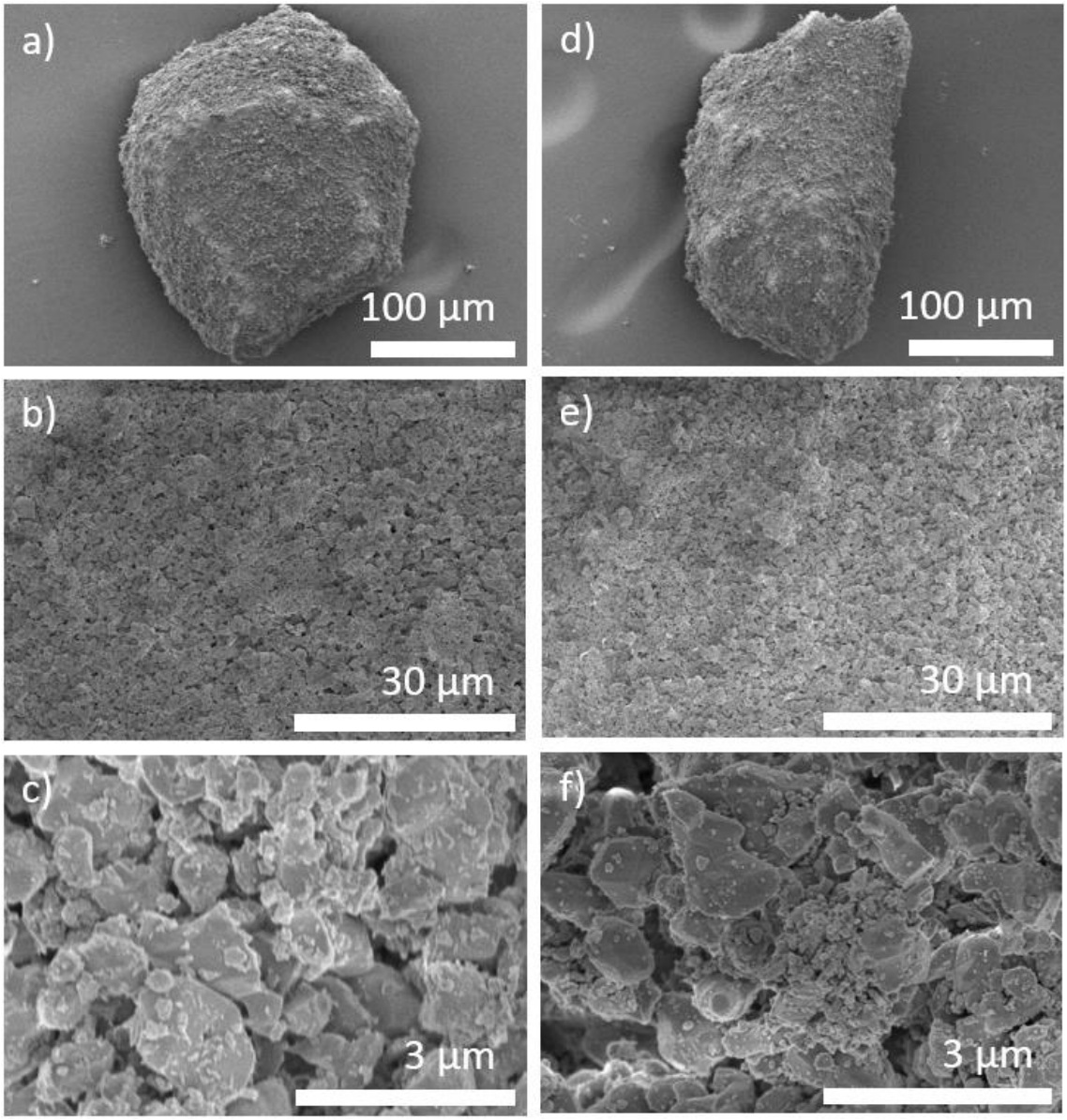

Figure A.1.3: SEM images (a,b and c) of the 18NiO GR OC used in the EM SR experiments (reduced) and (c, d and e) of the 18NiO GR used in the EM CLSR experiments (oxidised)

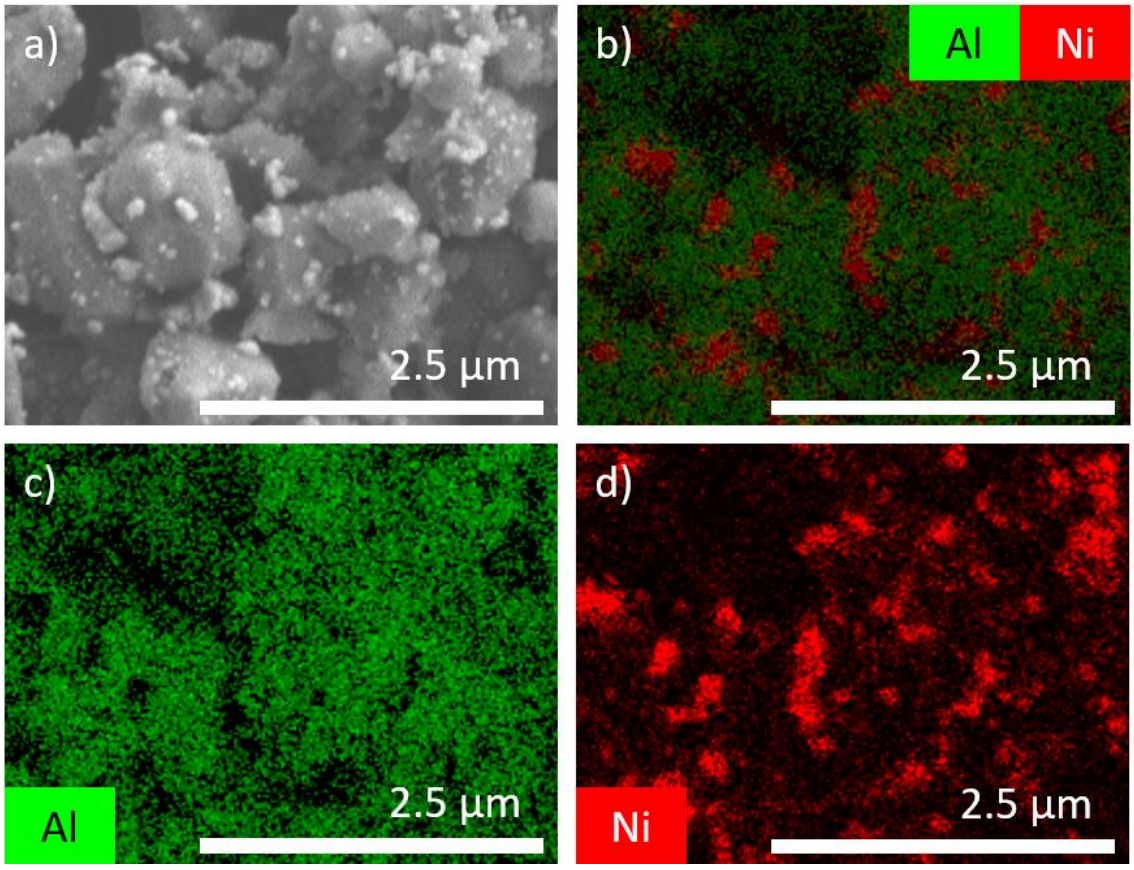

Figure A.1.4: SEM image (a) and EDX maps (b, c and d) of the fresh 18NiO GR OC used in the showing smaller Ni crystallites deposited upon larger α-Al_2O_3 clusters

A.2 Selected Area Electron Diffraction

Table A.2.1: Comparison of the d-spacings from the rings identified in Figure 4.17 to Figure 4.21 and d-spacings from phases identified during XRD analysis

Ring No.	Phase	h	k	l	d [A]	2Theta [deg]	I [%]
1	α-Al_2O_3	1	0	4	2.551	35.154	100
	Co_3O_4	3	1	1	2.437	36.856	100
	$NiAl_2O_4$	3	1	1	2.430	36.963	75
	NiO	1	0	1	2.410	37.279	55
	NiO	0	0	3	2.410	37.279	55
2	Co_3O_4	2	2	2	2.333	38.559	9
	γ-Al_2O_3	2	2	2	2.280	39.492	50
	α-Al_2O_3	0	0	6	2.165	41.677	2
	NiO	0	1	2	2.087	43.330	100
	α-Al_2O_3	1	1	3	2.085	43.357	66
3	Co_3O_4	5	1	1	1.555	59.371	29
	$NiAl_2O_4$	5	1	1	1.550	59.599	13
	α-Al_2O_3	2	1	1	1.547	59.739	1
	γ-Al_2O_3	5	1	1	1.520	60.899	30
	α-Al_2O_3	1	2	2	1.515	61.117	2
	α-Al_2O_3	0	1	8	1.511	61.300	14
4	α-Al_2O_3	1	2	5	1.336	70.420	1
	Co_3O_4	6	2	0	1.278	74.139	2
	α-Al_2O_3	2	0	8	1.276	74.296	2
	NiO	1	1	3	1.258	75.494	13
	NiO	0	1	5	1.258	75.494	13
5	NiO	1	1	3	1.258	75.494	13
	NiO	0	1	5	1.258	75.494	13
	α-Al_2O_3	1	0	10	1.239	76.868	29
	α-Al_2O_3	1	1	9	1.234	77.229	12
	Co_3O_4	5	3	3	1.233	77.363	6
6	α-Al_2O_3	0	2	10	1.099	89.000	9
	Co_3O_4	6	4	2	1.080	90.998	3
	Co_3O_4	7	3	1	1.052	94.123	8
7	Co_3O_4	7	3	3	0.987	102.545	0
	Co_3O_4	6	4	4	0.980	103.615	0
	NiO	2	0	5	0.958	107.074	3
	NiO	2	1	1	0.958	107.074	3
	NiO	1	0	7	0.957	107.268	2
	Co_3O_4	8	2	2	0.953	107.941	1
8	Co_3O_4	9	1	1	0.887	120.531	0
	γ-Al_2O_3	8	4	0	0.884	121.239	10
	Co_3O_4	8	4	2	0.882	121.749	0
	Co_3O_4	6	6	4	0.862	126.796	0

A.3 TEM/EDX Spectra

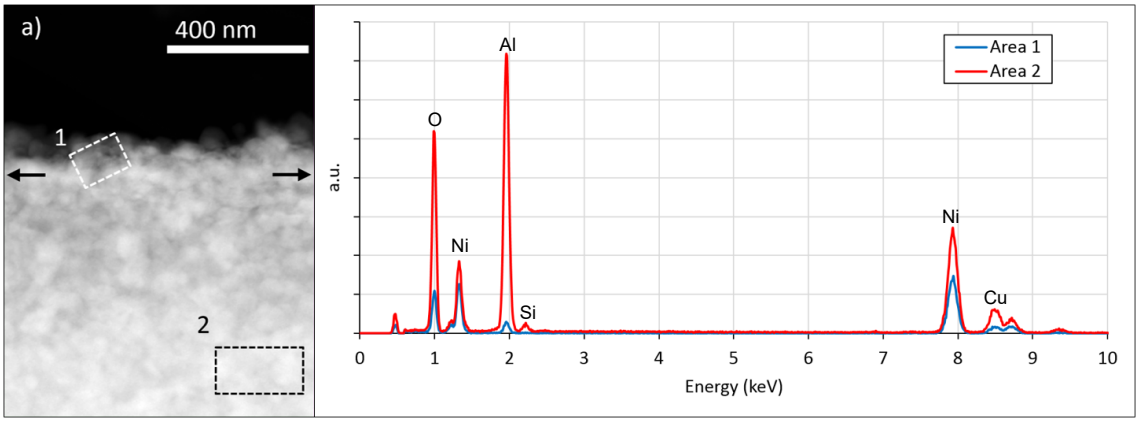

Figure A.3.1: HAADF image and EDX spectra from areas 1 and 2 in the fresh 18Ni Sf-WI OC

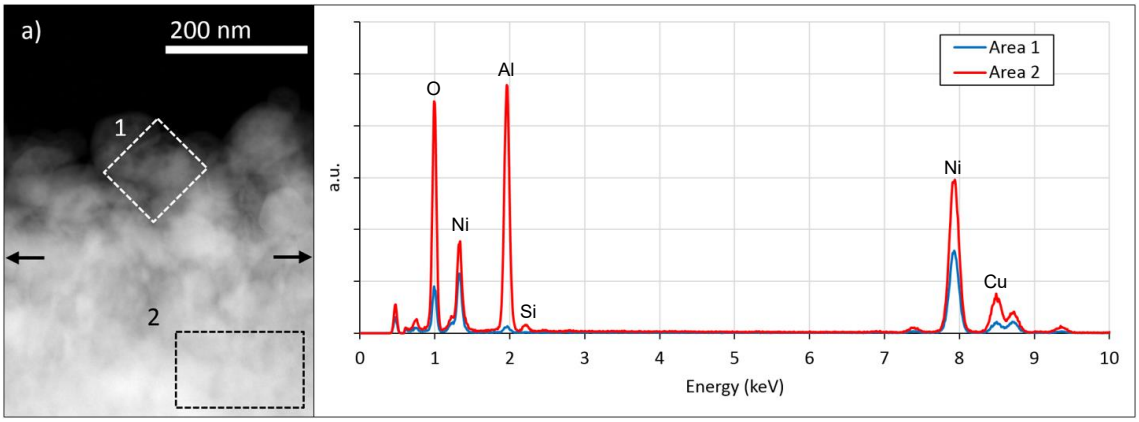

Figure A.3.2: HAADF image and EDX spectra from areas 1 and 2 in the fresh 1.8Co 18Ni Sf-WI OC

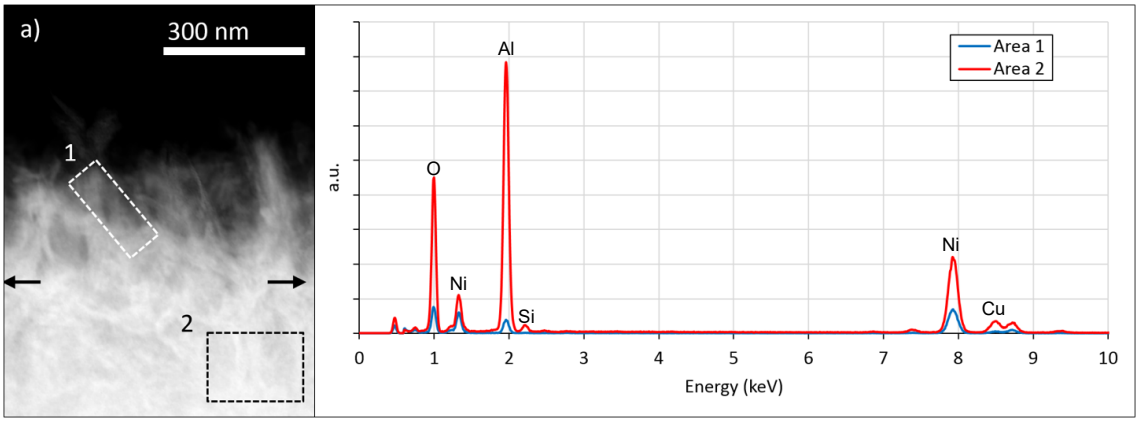

Figure A.3.3: HAADF image and EDX spectra from areas 1 and 2 in the fresh 18Ni Sf-DP OC

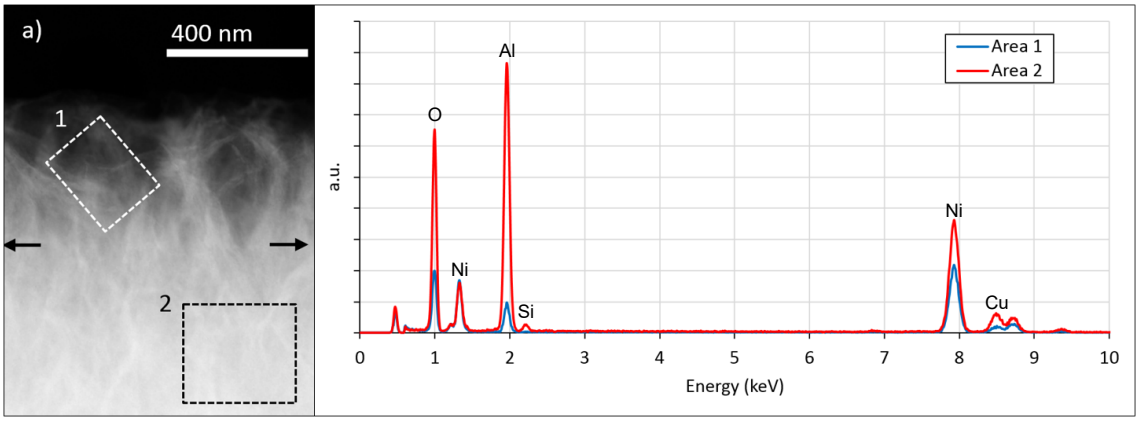

Figure A.3.4: HAADF image and EDX spectra from areas 1 and 2 in the fresh 0.6Co 18Ni Sf-HT OC

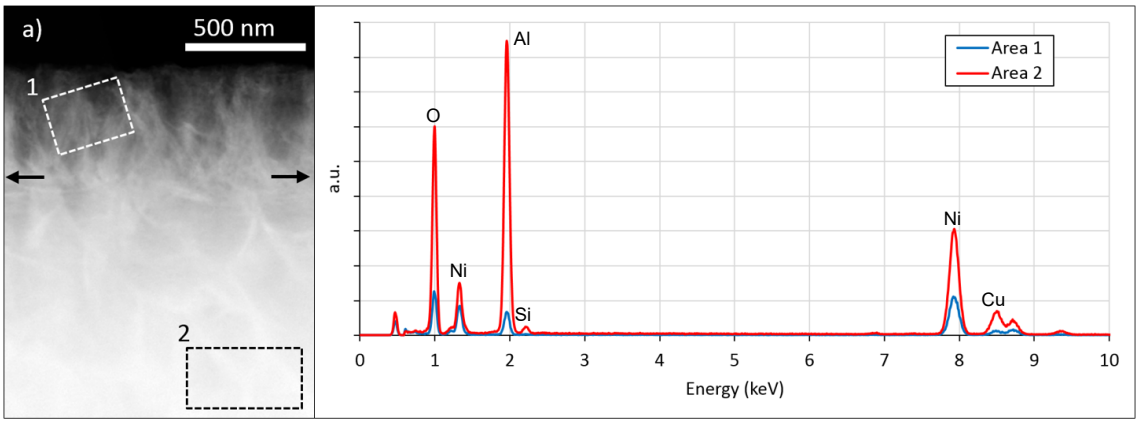

Figure A.3.5: HAADF image and EDX spectra from areas 1 and 2 in the fresh 1.8Co 18Ni Sf-HT OC

A.4 IUPAC Isotherm and Hysteresis Loop Classifications

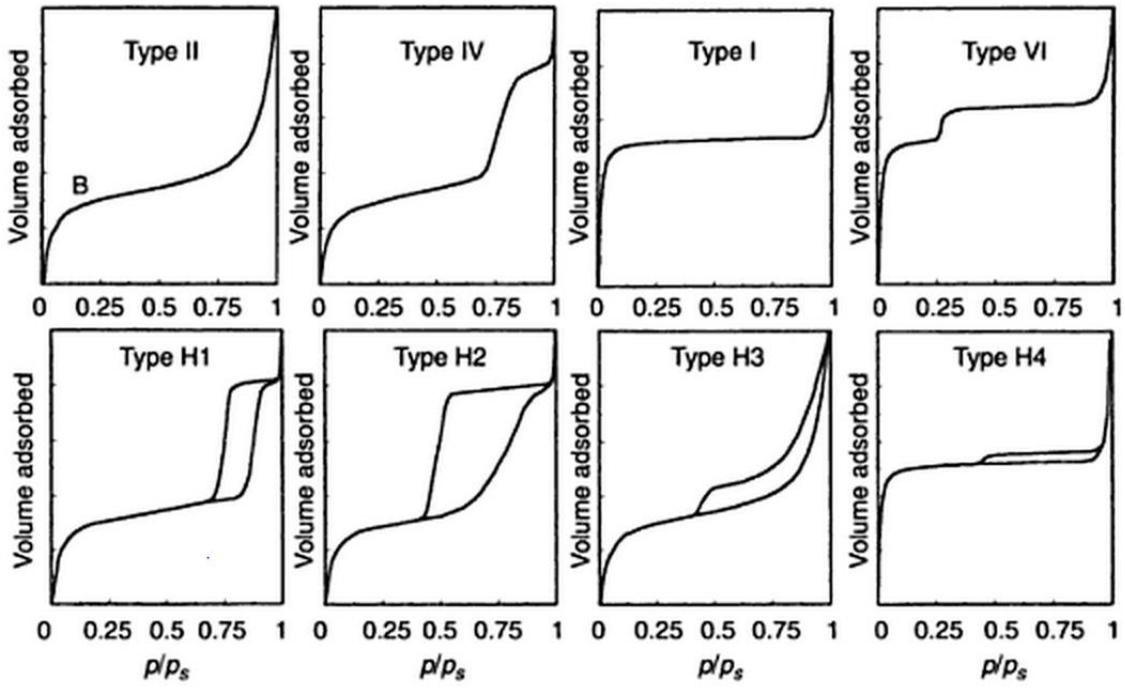

Figure A.4.1: IUPAC hysteresis loop and isotherm classifications

The IUPAC classifications of isotherms (Figure A.1.1) allow a sample's pore size to be assessed; Type I isotherms indicate pore diameters of 4 nm or smaller; these are also known as micropores. Type II isotherms indicate a pore diameter in excess of 50 nm. Type IV is characteristic of a mesoporous solid which contains pores of radius 2 – 100 nm. Type VI indicates groups of adsorption sites that are homogeneous in regards to energy[227,258].

In mesoporous samples, the hysteresis loop can provide information of the geometry of the pores in that sample. The IUPAC classifications of hysteresis loops (Figure A.1.1) allow a samples pore geometry to be assessed; Type H1 suggest tubular pores at both ends with various cross sections and slightly widened regions; termed ink bottle and trough shaped pores. Type H2 also suggest ink bottle shaped pores but can also propose voids between close packed particles. Type H3 and H4 suggest slit pores and tapered slit pores respectively[227,258].

A.5 Physical Adsorption Isotherms

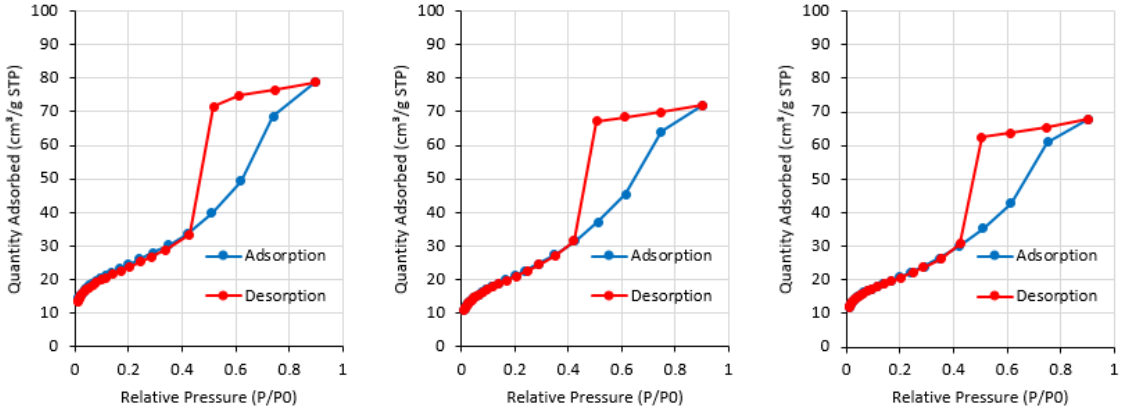

Figure A.5.1: Physical adsorption isotherms for fresh 18Ni Sf-WI, 0.6Co 18Ni Sf-WI and 1.8Co 18Ni Sf-WI OC's from left to right

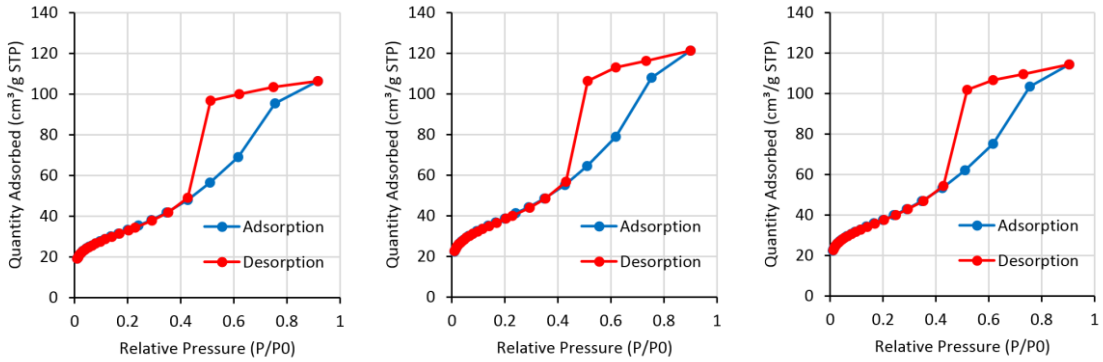

Figure A.5.2: Physical adsorption isotherms for fresh 18Ni Sf-DP, 0.6Co 18Ni Sf-DP and 1.8Co 18Ni Sf-DP OC's from left to right

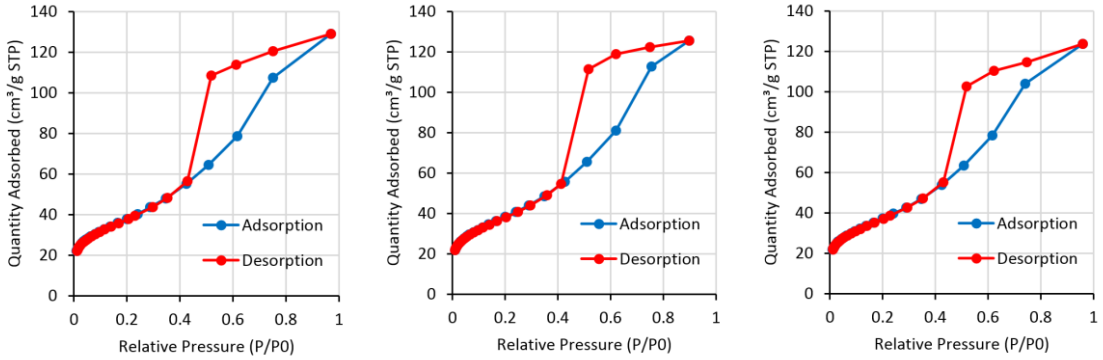

Figure A.5.3: Physical adsorption isotherms for fresh 18Ni Sf-HT, 0.6Co 18Ni Sf-HT and 1.8Co 18Ni Sf-HT OC's from left to right

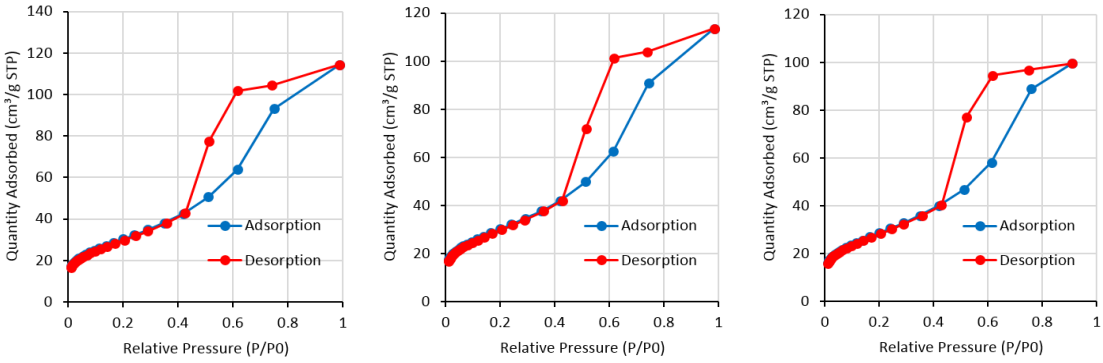

Figure A.5.4: Physical adsorption isotherms for 18Ni Sf-WI, 0.6Co 18Ni Sf-WI and 1.8Co 18Ni Sf-WI OC's after use in the EM SR experiments from left to right

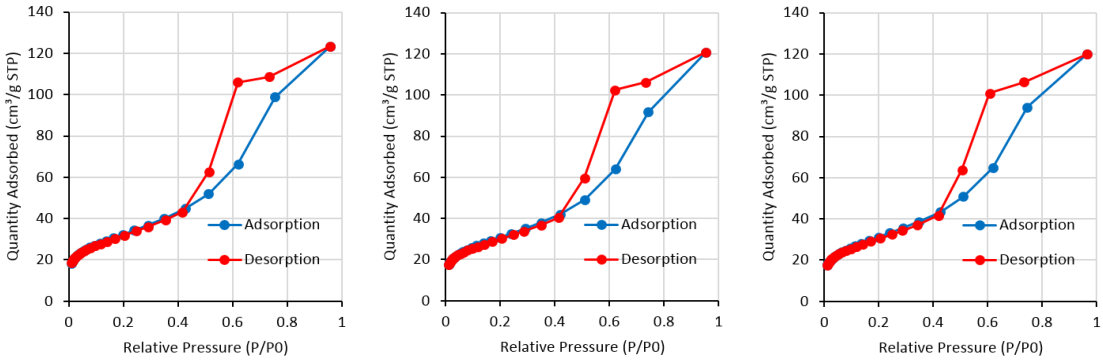

Figure A.5.5: Physical adsorption isotherms for 18Ni Sf-DP, 0.6Co 18Ni Sf-DP and 1.8Co 18Ni Sf-DP OC's after use in the EM SR experiments from left to right

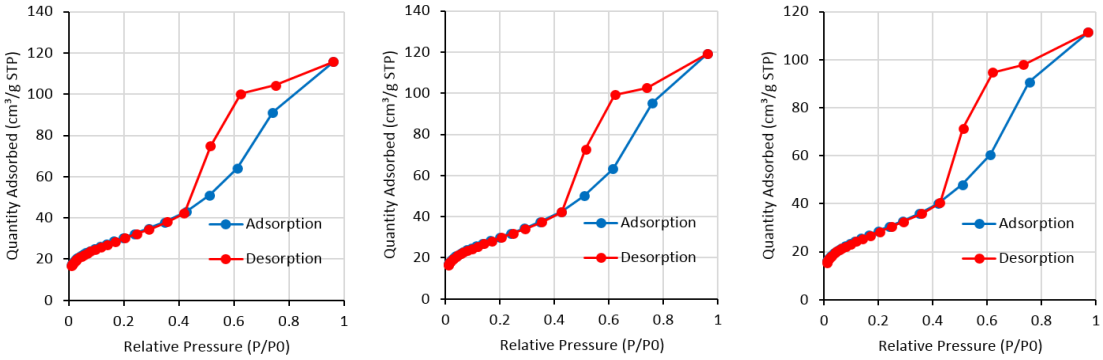

Figure A.5.6: Physical adsorption isotherms for 18Ni Sf-HT, 0.6Co 18Ni Sf-HT and 1.8Co 18Ni Sf-HT OC's after use in the EM SR experiments from left to right

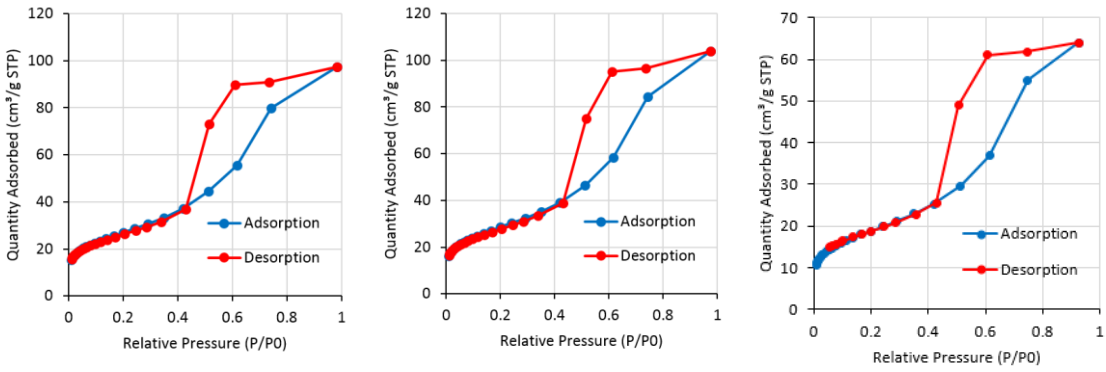

Figure A.5.7: Physical adsorption isotherms for 18Ni Sf-WI, 0.6Co 18Ni Sf-WI and 1.8Co 18Ni Sf-WI OC's after use in the EM CLSR experiments from left to right

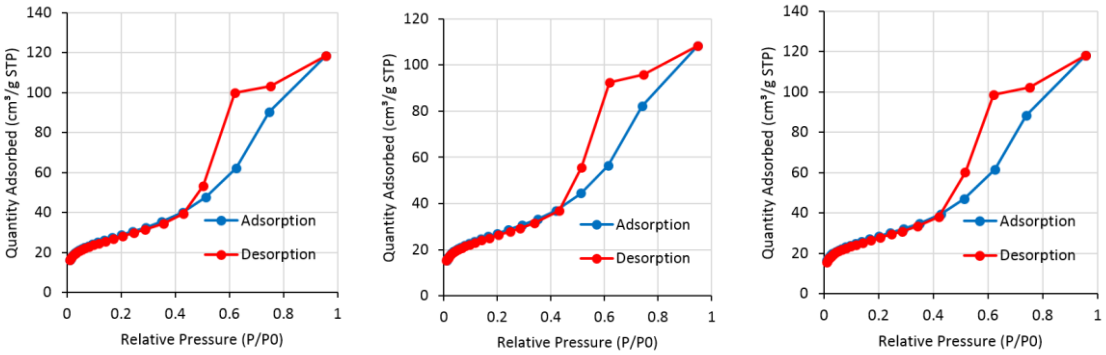

Figure A.5.8: Physical adsorption isotherms for 18Ni Sf-DP, 0.6Co 18Ni Sf-DP and 1.8Co 18Ni Sf-DP OC's after use in the EM CLSR experiments from left to right

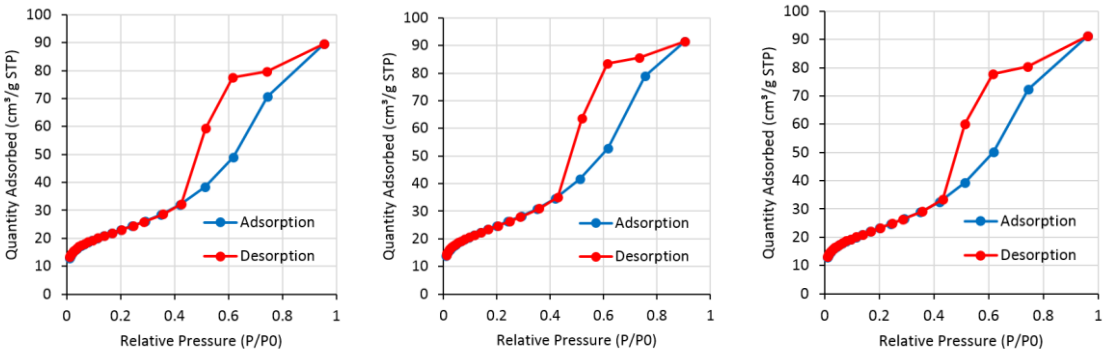

Figure A.5.9: Physical adsorption isotherms for 18Ni Sf-HT, 0.6Co 18Ni Sf-HT and 1.8Co 18Ni Sf-HT OC's after use in the EM CLSR experiments from left to right

Table A.5.1: Pore volume and diameter of the OC's used in EM SR and EM CLSR determined by BJH analysis of the adsorption isotherms

Sample	BJH Adsorption					
	Fresh OC's		EM SR OC's		EM CLSR OC's	
	Pore Volume$^{(s)}$ (cc g^{-1})	Pore Diameter (nm)	Pore Volume$^{(s)}$ (cc g^{-1})	Pore Diameter (nm)	Pore Volume$^{(a)}$ (cc g^{-1})	Pore Diameter (nm)
Saffil®	0.18	4.8	N/A	N/A	N/A	N/A
18Ni Sf-WI	0.12	4.7	0.17	5.0	0.15	5.1
0.6Co 18Ni Sf-WI	0.11	4.4	0.17	5.1	0.16	5.1
1.8Co 18Ni Sf-WI	0.11	4.6	0.15	4.8	0.11	5.0
Mean WI	0.12	4.6	0.17	5.0	0.15	5.1
18Ni Sf-DP	0.16	4.5	0.19	5.3	0.18	5.5
0.6Co 18Ni Sf-DP	0.18	4.5	0.18	5.4	0.16	5.5
1.8Co 18Ni Sf-DP	0.17	4.5	0.18	5.3	0.18	5.6
Mean DP	0.17	4.5	0.18	5.3	0.18	5.5
18Ni Sf-HT	0.20	4.7	0.18	5.1	0.17	5.3
0.6Co 18Ni Sf-HT	0.19	4.5	0.18	5.3	0.16	5.0
1.8Co 18Ni Sf-HT	0.19	4.6	0.17	5.1	0.17	5.2
Mean HT	0.19	4.6	0.18	5.2	0.17	5.1

A.6 EM CLSR using 18NiO GR OC

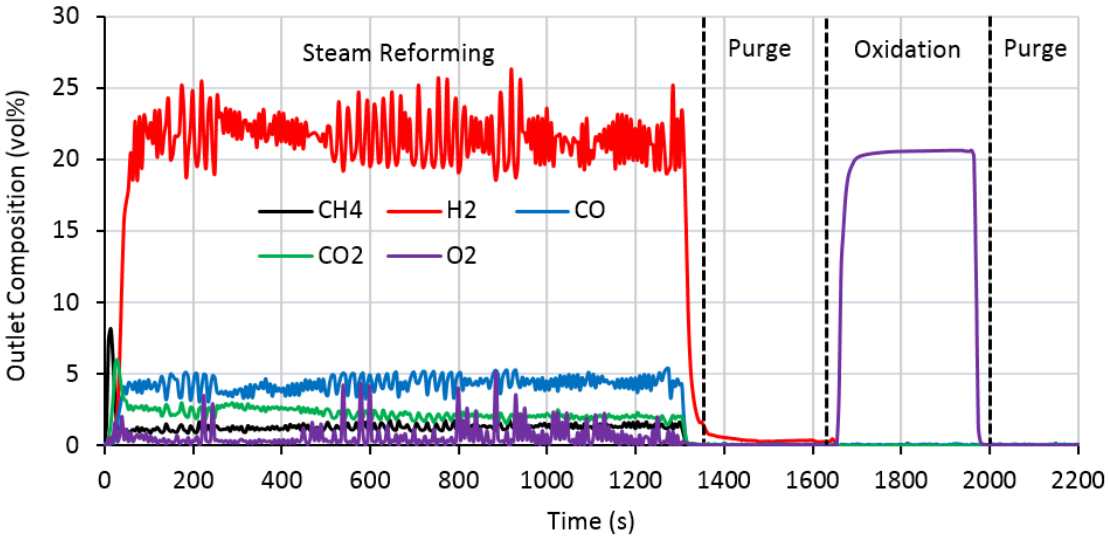

Figure A.6.1 Dry outlet composition during the 4th cycle of EM CLSR using the 18NiO GR OC at 700°C and S:C 3

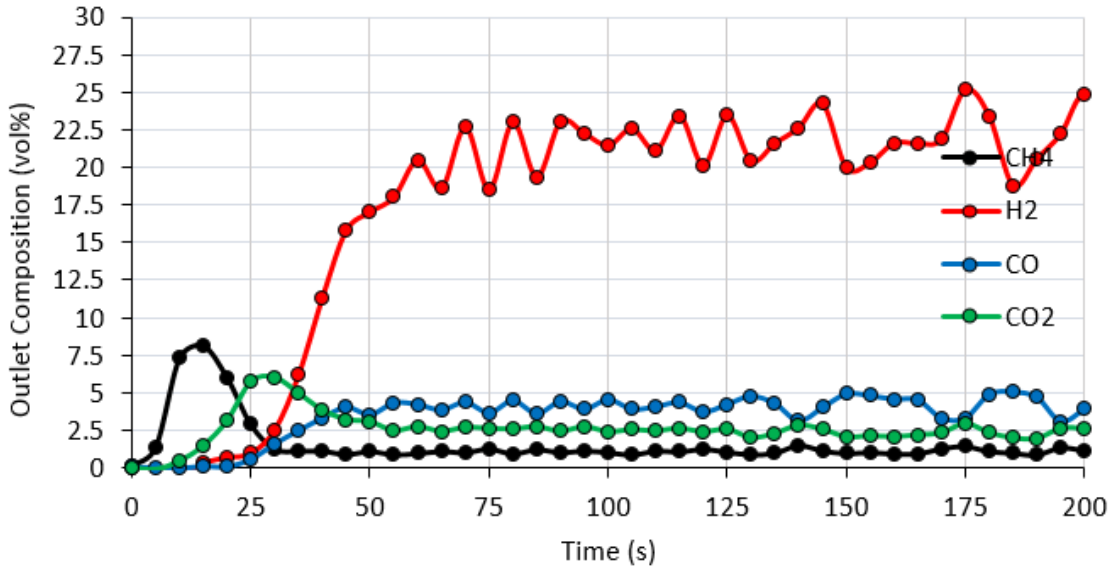

Figure A.6.2: Dry outlet composition during the first 200 s of the 4th EM steam reforming half-cycle using the 18NiO GR OC at 700°C and S:C 3

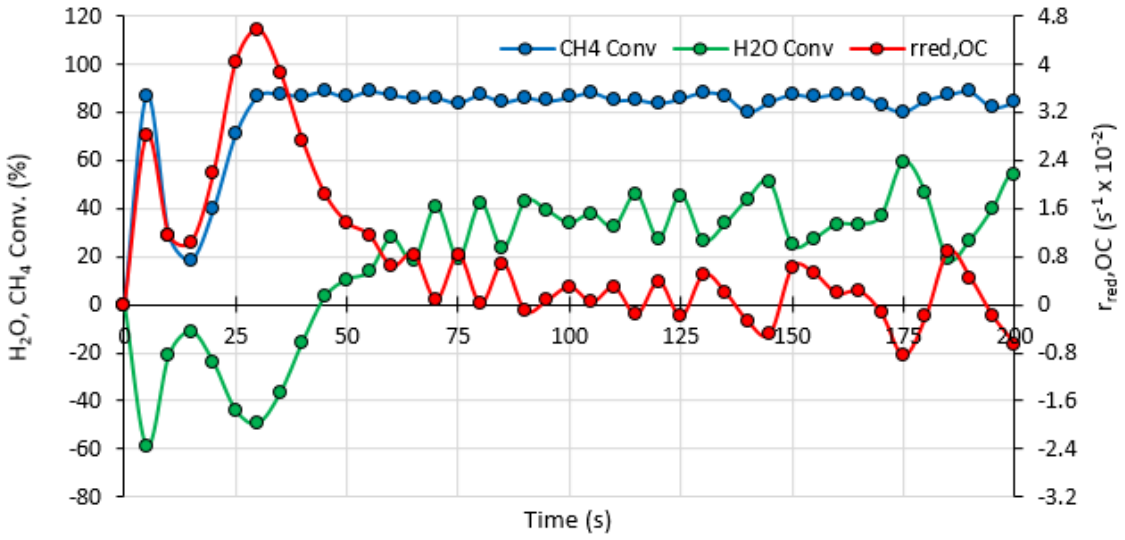

Figure A.6.3: CH_4 and H_2O conversion vs rate of reduction of the oxygen carrier ($r_{red,OC}$) during the first 200 s of the 5th EM steam reforming half-cycle using the 18NiO GR OC at 700°C and S:C 3

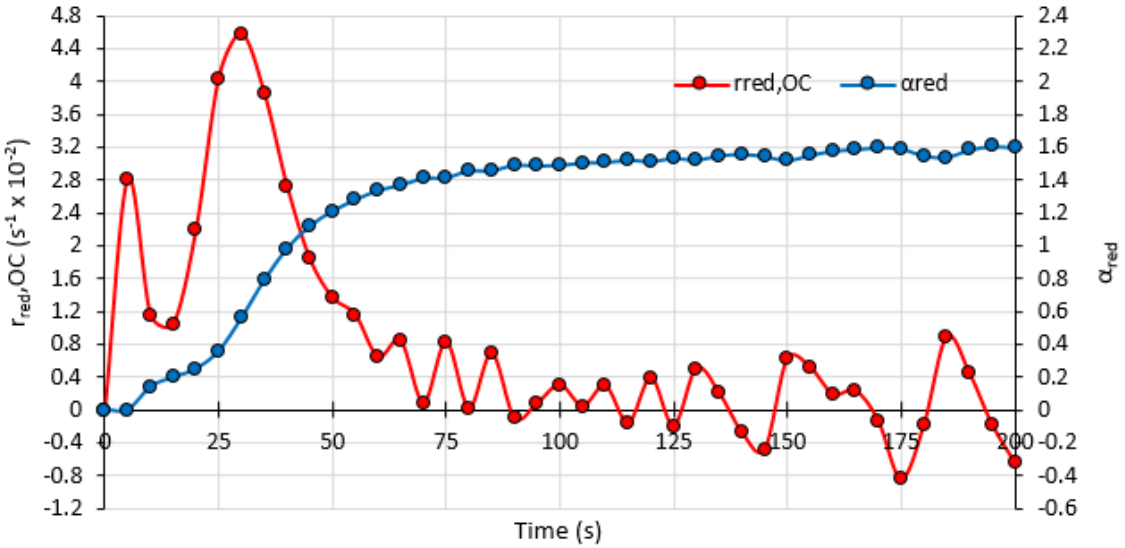

Figure A.6.4: Rate of reduction and solids conversion (α_{red}) of the 18NiO GR OC during the first 200 s of the 5th EM steam reforming half-cycle at 700°C and S:C 3

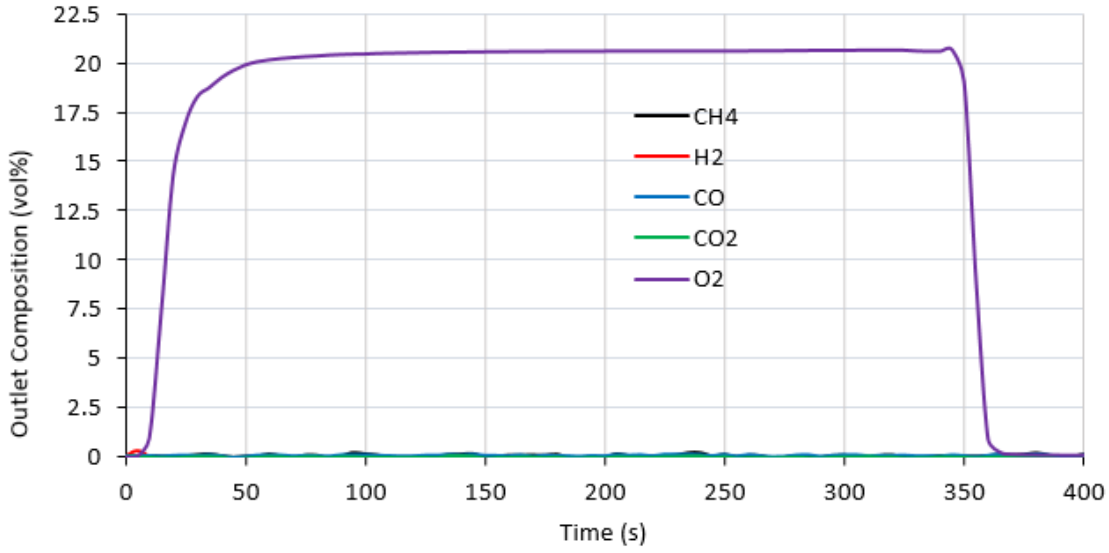

Figure A.6.5: Dry outlet composition during the 4th EM oxidation half-cycle using the I8NiO GR OC at 700°C and S:C 3

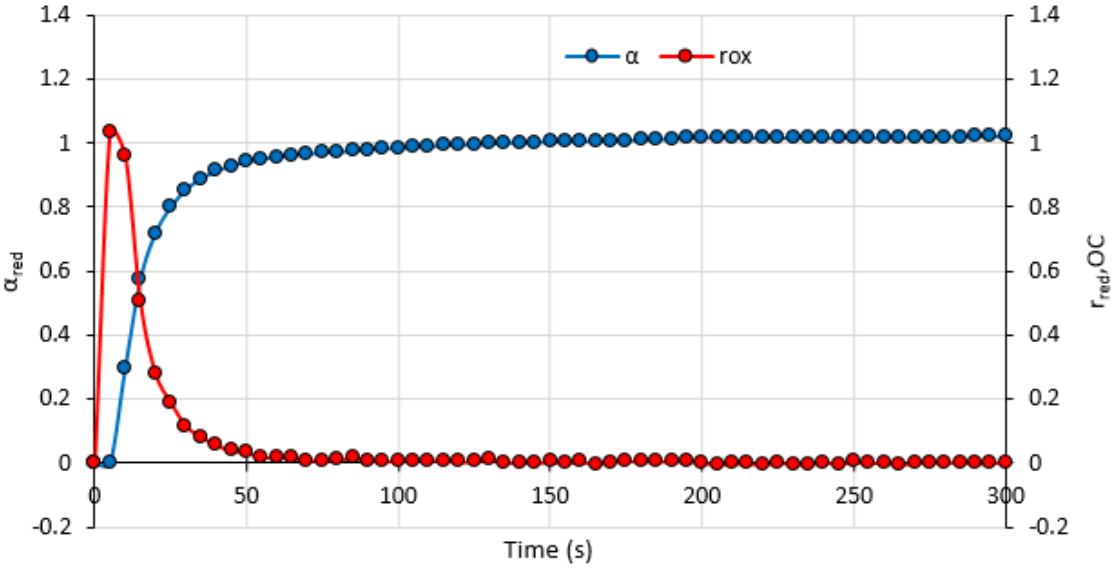

Figure A.6.6 Rate of oxidation and solids conversion (α_{ox}) of the I8NiO GR OC during the first 200 s of the 2nd EM oxidation half-cycle at 700°C and S:C 3

A.7 EV CLSR using simultaneous feed of CH_4 and H_2O and 18Ni HT OC

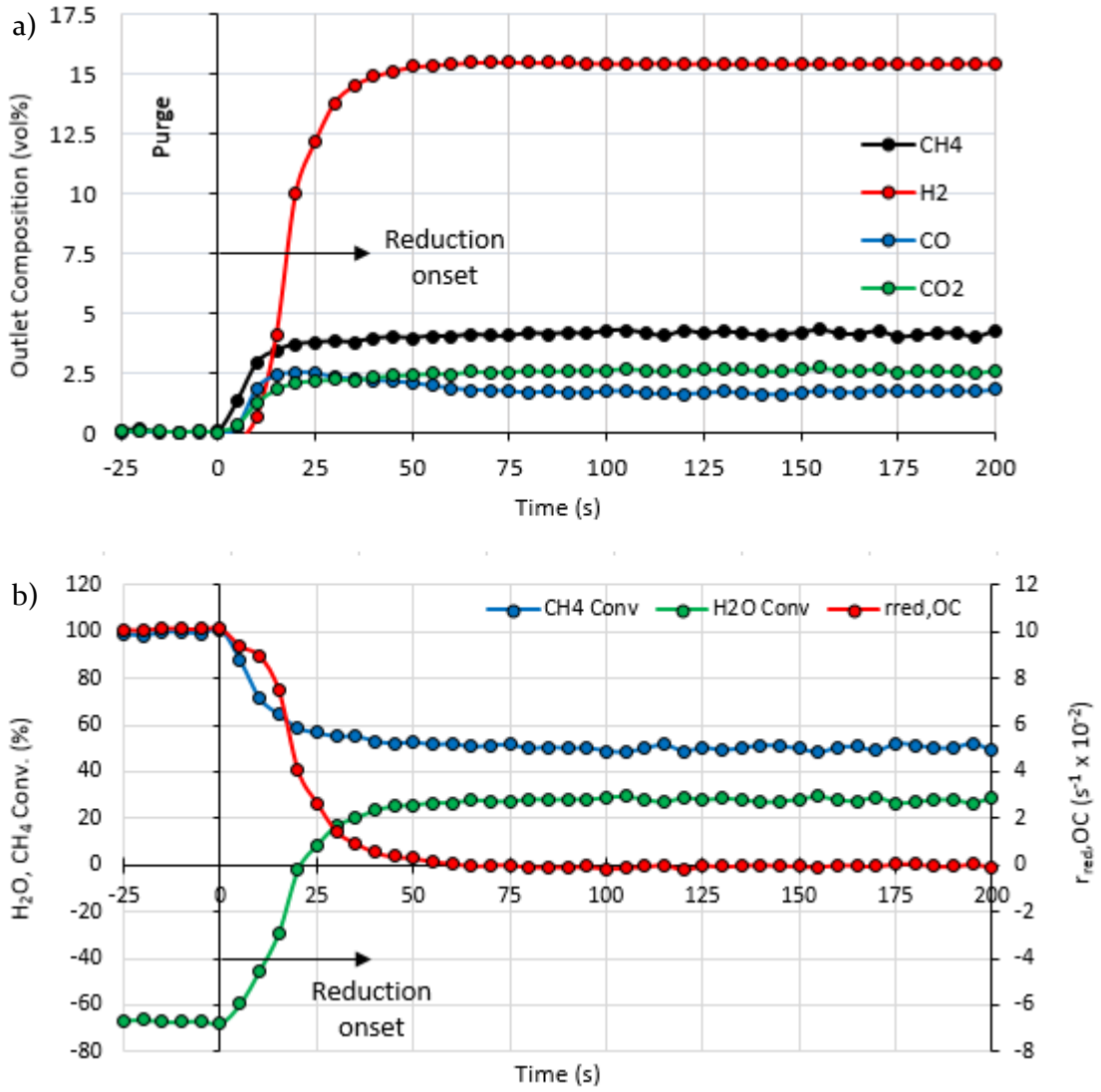

Figure A.7.1: Dry outlet composition (a) and CH_4 and H_2O conversion vs r_{red},OC (b) during the first 200 s of the 1st EV steam reforming half-cycle using the 18Ni Sf-HT OC at 700°C and S:C 3 in a preliminary experiment with simultaneous feed of CH_4 and H_2O

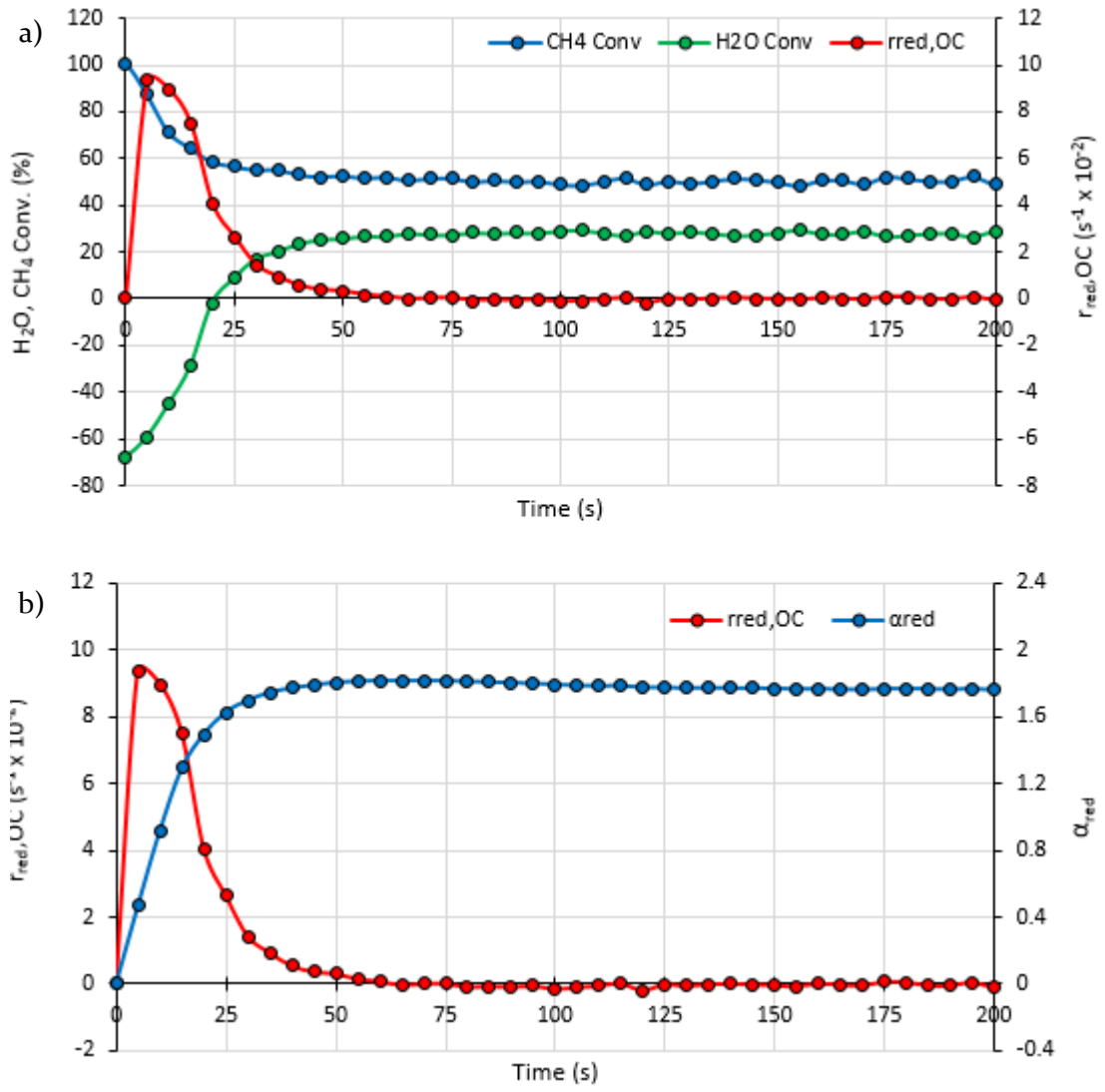

Figure A.7.2: CH_4 and H_2O conversion vs r_{red},OC (a) and r_{red},OC and reduction extent (α_{red}) of the 18Ni Sf-HT OC during the first 200 s of the 1st EM steam reforming half-cycle 700°C and S:C 3 in a preliminary experiment with simultaneous feed of CH_4 and H_2O

A.8 EV CLSR using 18NiO GR OC

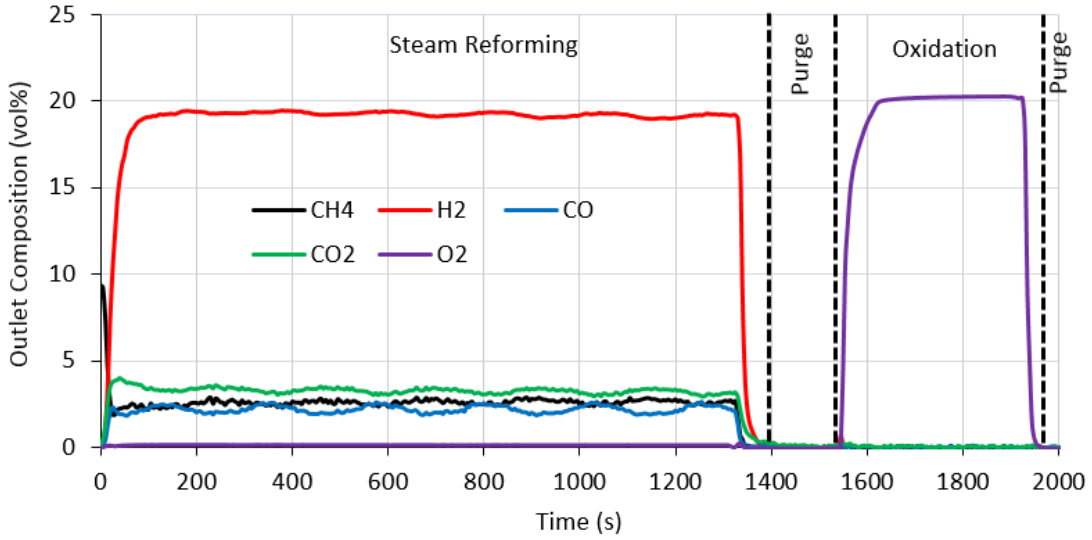

Figure A.8.1 Dry outlet composition during the 4th cycle of EV CLSR using the 18NiO GR OC at 700°C and S:C 3

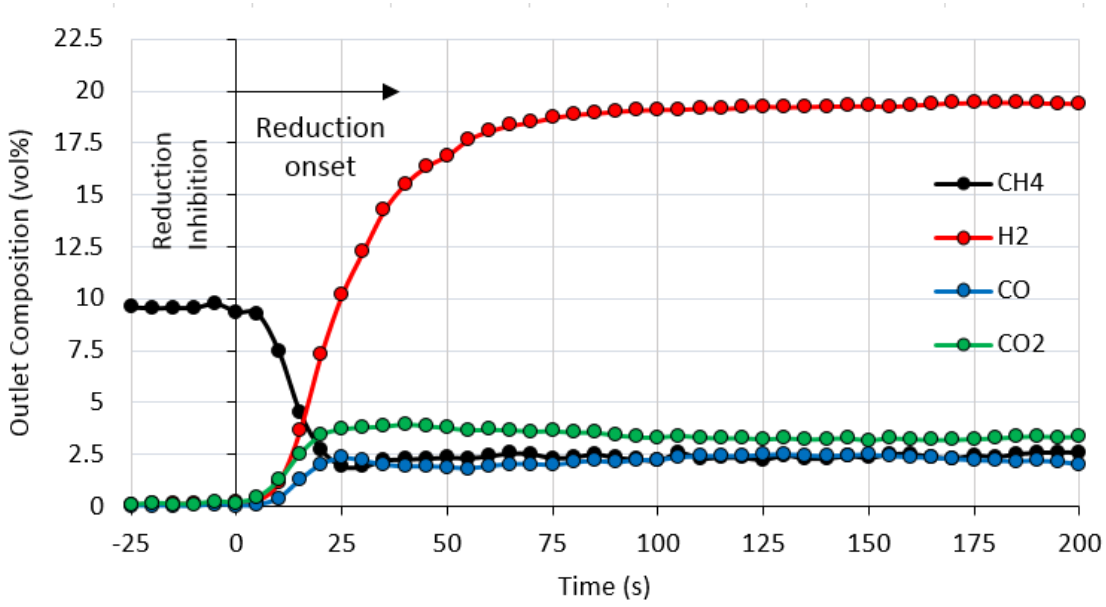

Figure A.8.2: Dry outlet composition during the first 200 s of the 4th EV steam reforming half-cycle using the 18NiO GR OC at 700°C and S:C 3

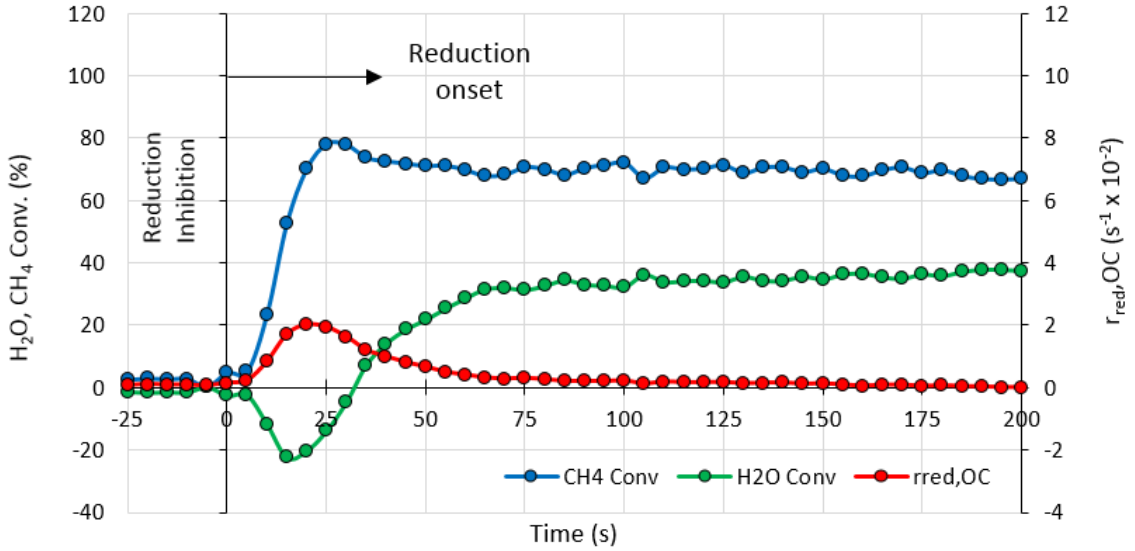

Figure A.8.3: CH_4 and H_2O conversion vs rate of reduction of the oxygen carrier (r_{red},OC) during the first 200 s of the 4th EV steam reforming half-cycle using the 18NiO GR OC at 700°C and S:C 3

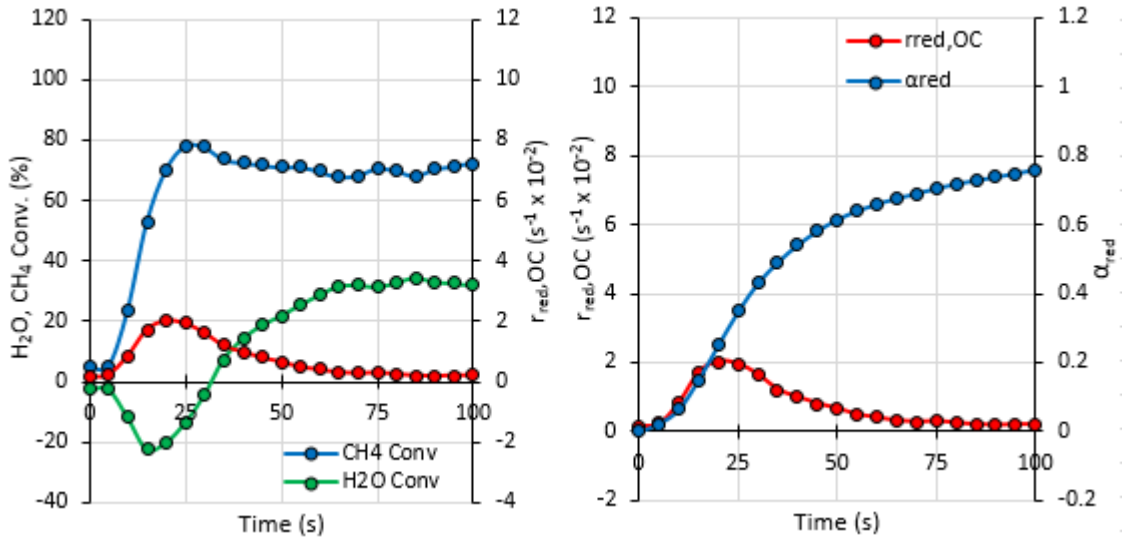

Figure A.8.4: CH_4 and H_2O conversion vs r_{red},OC (a) and r_{red},OC and reduction extent (α_{red}) of the 18NiO GR OC and during the first 200 s of the 4th EM steam reforming half-cycle at 700°C and S:C 3

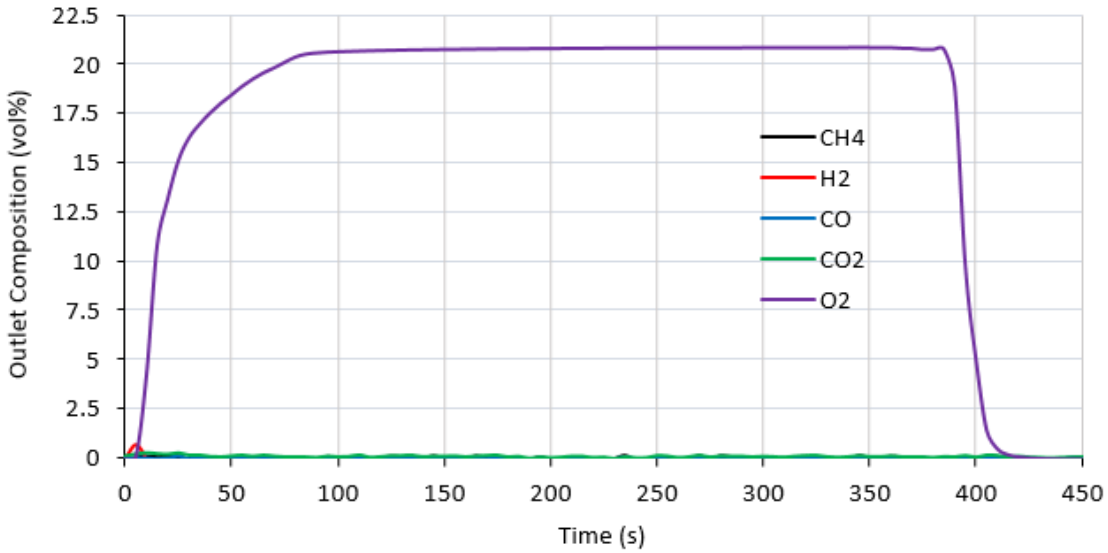

Figure A.8.5: Dry outlet composition during the first 200 s of the 4th EV oxidation half-cycle using the 18NiO GR OC at 700°C and S:C 3

A.9 Effect of Reactor Materials upon Rate of Reduction

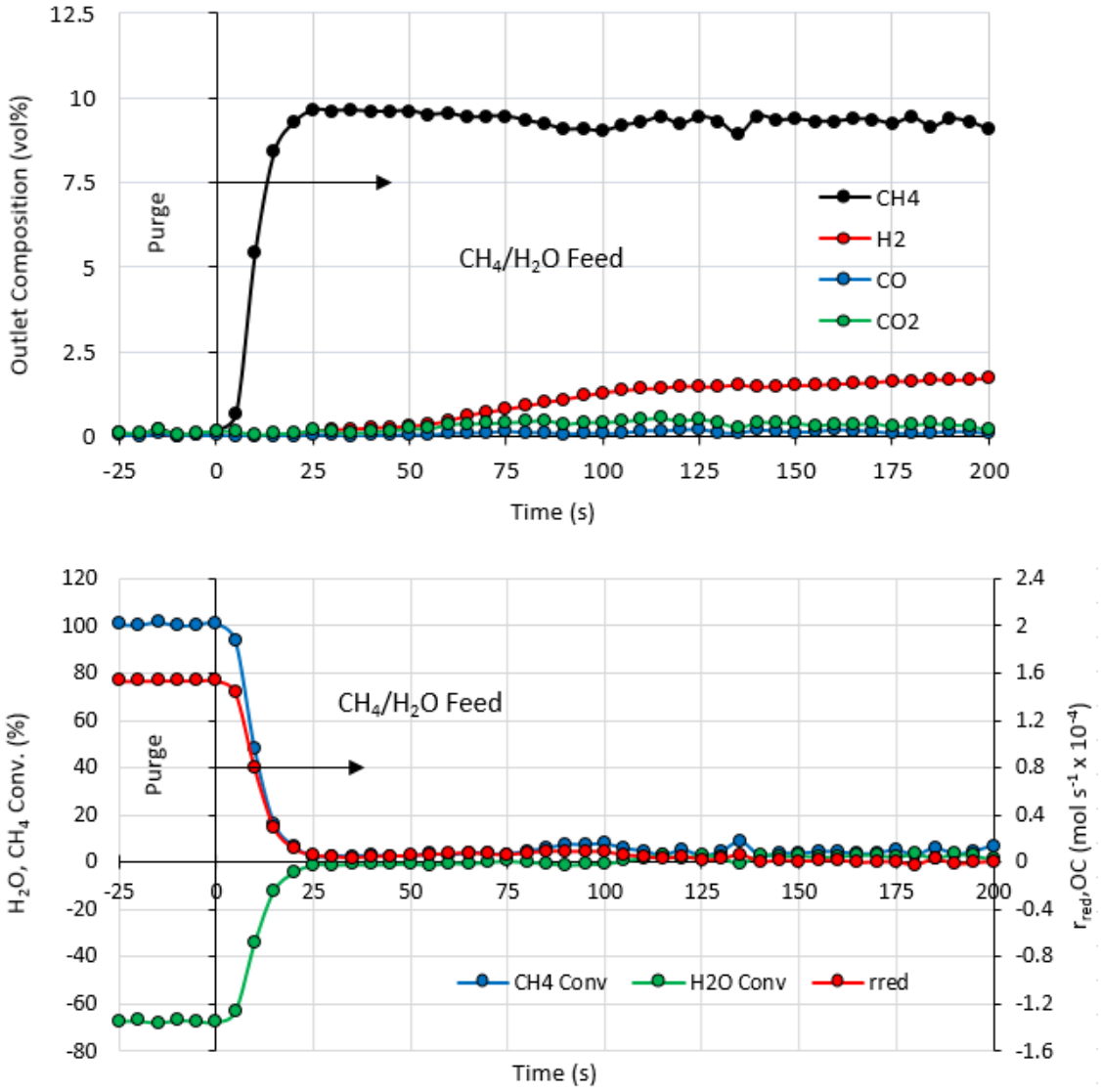

Figure A.9.1: Dry outlet composition (a) CH_4 and H_2O conversion vs rate of reduction (r_{red}) (b) during the first 200 s of the 1st EM steam reforming half-cycle of the blank experiment at 700°C and S:C 3

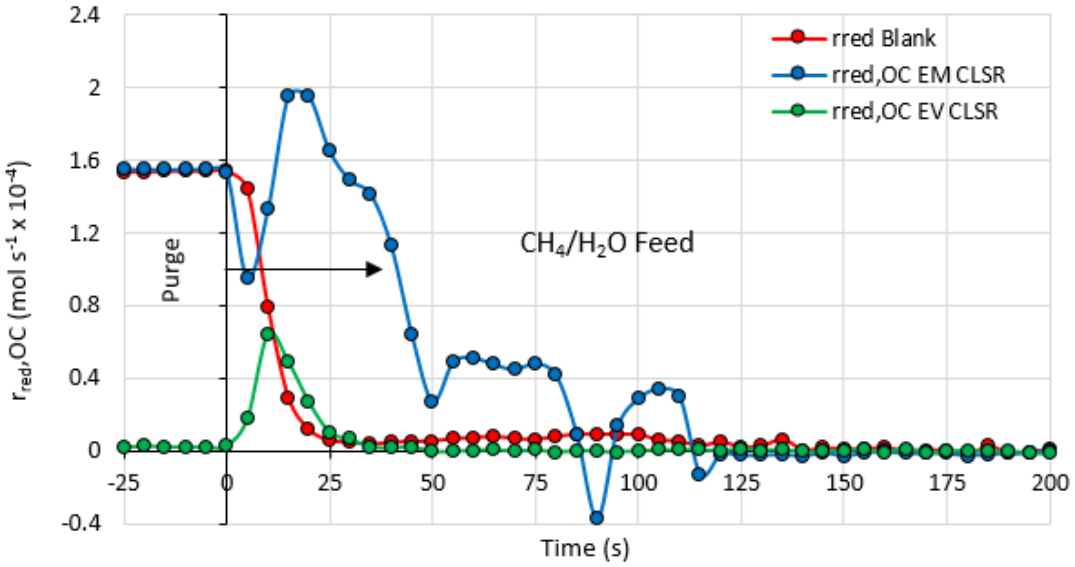

Figure A.9.2: Comparison of r_{red} and $r_{red,OC}$ (mol s^{-1}) during the first 200 s of a SR half cycle in the the blank and EV/EM CLSR experiments using 18Ni Sf-WI OC 700°C and S:C 3

A.10 TGA Reduction Capacity Determination

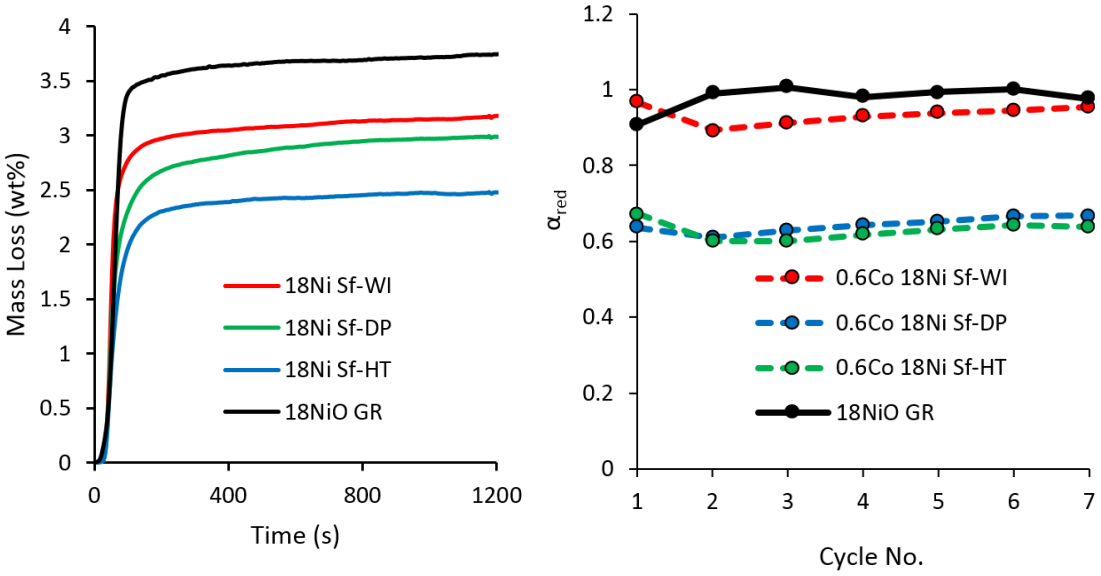

Figure A.10.1: 7th redox cycle mass loss of 18Ni Sf-WI, Sf-DP and Sf-HT OC's compared with the 18NiO GR OC (a) and the reduction capacity (α_{red}) of the 0.6Co 18Ni Sf-WI, Sf-DP and Sf-HT OC's compared with the 18NiO GR OC (b)

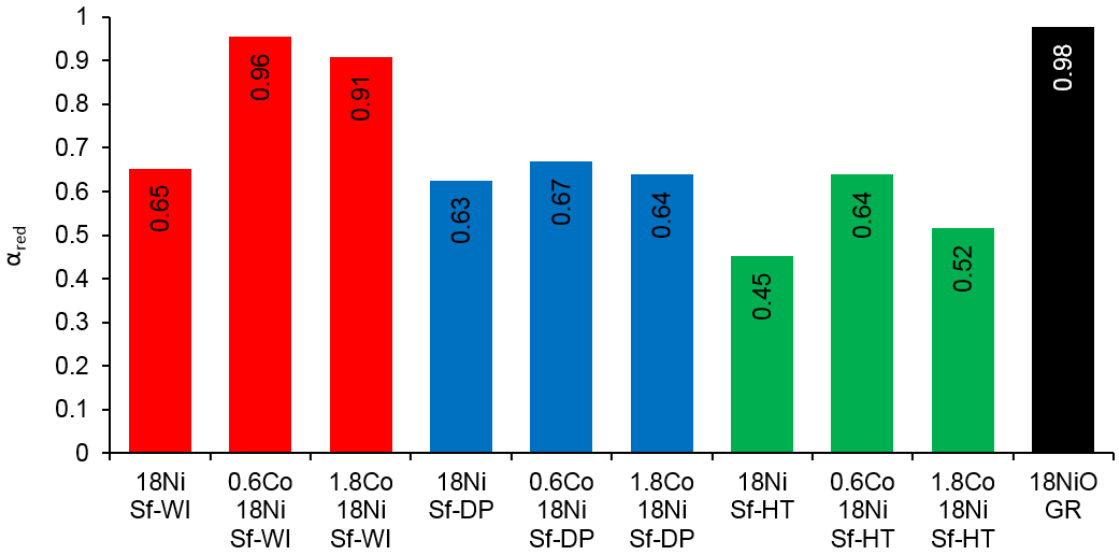

Figure A.10.2: 7th redox cycle mass loss of the OC's determined by TGA (7 redox cycles, H_2, air)

Table A.10.1 the reduction capacity (α_{red}) determined by TGA (7 redox cycles, H_2, air) of the Sf and conventional OC's

Cycle No.	Sample									
	18Ni Sf-WI	0.6Co 18Ni Sf-WI	1.8Co 18Ni Sf-WI	18Ni Sf-DP	0.6Co 18Ni Sf-DP	1.8Co 18Ni Sf-DP	18Ni Sf-HT	0.6Co 18Ni Sf-HT	1.8Co 18Ni Sf-HT	18NiO GR
1	0.65	0.97	0.94	0.61	0.64	0.62	0.43	0.67	0.45	0.85
2	0.63	0.89	0.88	0.60	0.61	0.62	0.42	0.60	0.45	0.93
3	0.62	0.91	0.88	0.59	0.63	0.63	0.42	0.60	0.48	0.95
4	0.64	0.93	0.90	0.60	0.64	0.65	0.43	0.62	0.51	0.92
5	0.64	0.94	0.91	0.61	0.65	0.64	0.44	0.63	0.49	0.94
6	0.65	0.94	0.92	0.61	0.67	0.64	0.44	0.64	0.51	0.94
7	0.65	0.96	0.91	0.63	0.67	0.64	0.45	0.64	0.52	0.92
Mean	0.64	0.93	0.91	0.61	0.64	0.63	0.43	0.63	0.49	0.92
StDev	0.012	0.025	0.019	0.011	0.021	0.012	0.013	0.026	0.027	0.032

A.11 XRD Patterns for the 18NiO GR OC used in CLSR

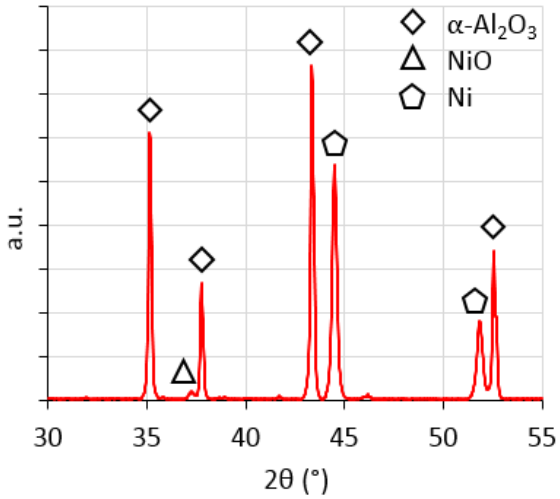

Figure A.11.1: XRD pattern of the 18NiO GR OC used in the EV CLSR experiments

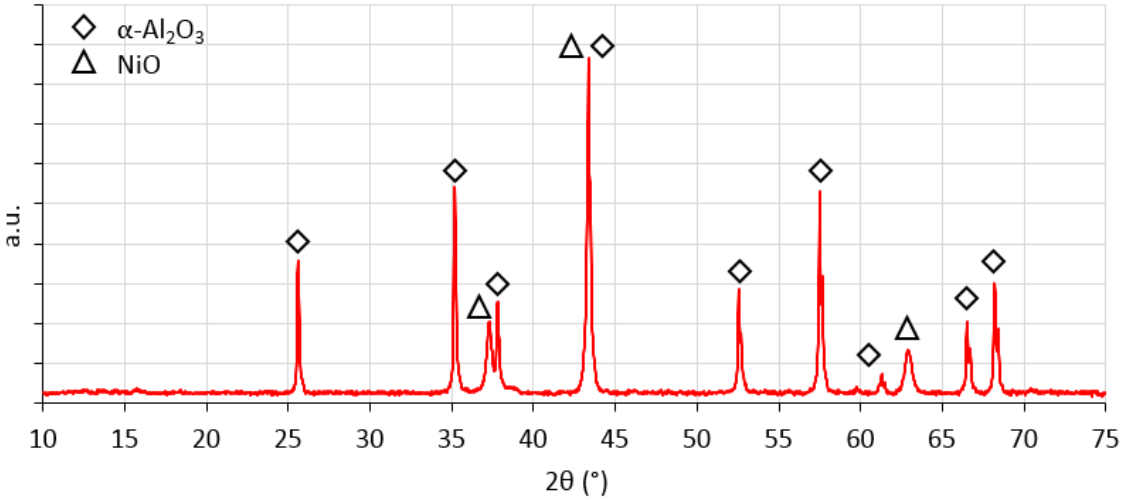

Figure A.11.2: XRD pattern of the 18NiO GR OC used in the EM CLSR experiments

A.12 Model for External Diffusion and Evaluation of Weisz-Prater Criterion for EV CLSR

Table A.12.1: Summary of the estimations of the mass transfer coefficient, average molar flux of CH_4 concentration of CH_4 in the bulk gas and at the surface of the particle, max rate of reduction per unit surface area and the flux to rate ratio for the 18NiO GR OC under EV CLSR conditions

Mass Transfer Correlation		Sh	k_c (m s^{-1})	W_{CH4} (mol m^{-2} s^{-1})	$C_{CH4,s}$ (mol m^{-3})	$C_{CH4,g}$ (mol m^{-3})	Max r_{red} (mol s^{-1})	r_{CH4} (mol m^{-2} s^{-1})	W:r
18NiO GR OC	Eq 7.12	3.030	0.184	0.0885	0.479	0.960	1.03×10^{-4}	1.69×10^{-3}	52

Table A.12.2: Summary of the calculation of the Weisz-Prater criterion for the 18NiO GR OC catalyst under EV CLSR conditions

Material	Max rred (mol s^{-1})	$-r'_A$(obs) (mol kg^{-1} s^{-1})	ρ_p (kg m^{-3})	dp (m)	De (m^2 s^{-1})	$C_{CH4,s}$ (mol m^{-3})	C_{WP}
18wt% NiO Pellet	1.03×10^{-4}	0.052	3946	2.00×10^{-4}	2.44×10^{-6}	0.479	1.73

A.13 Solid State Reaction Models

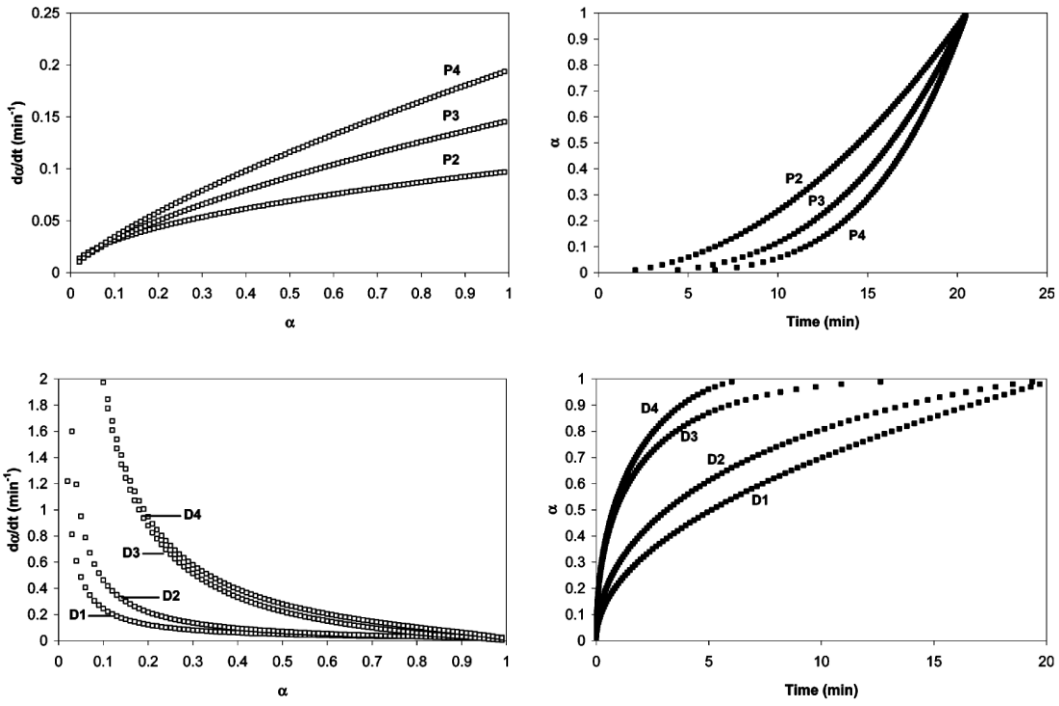

Figure A.13.1: Isothermal $d\alpha/dt$ vs t (left) and α vs t plots (right) indicative of power law (top) and diffusion (bottom), models for solid-state reactions[158]

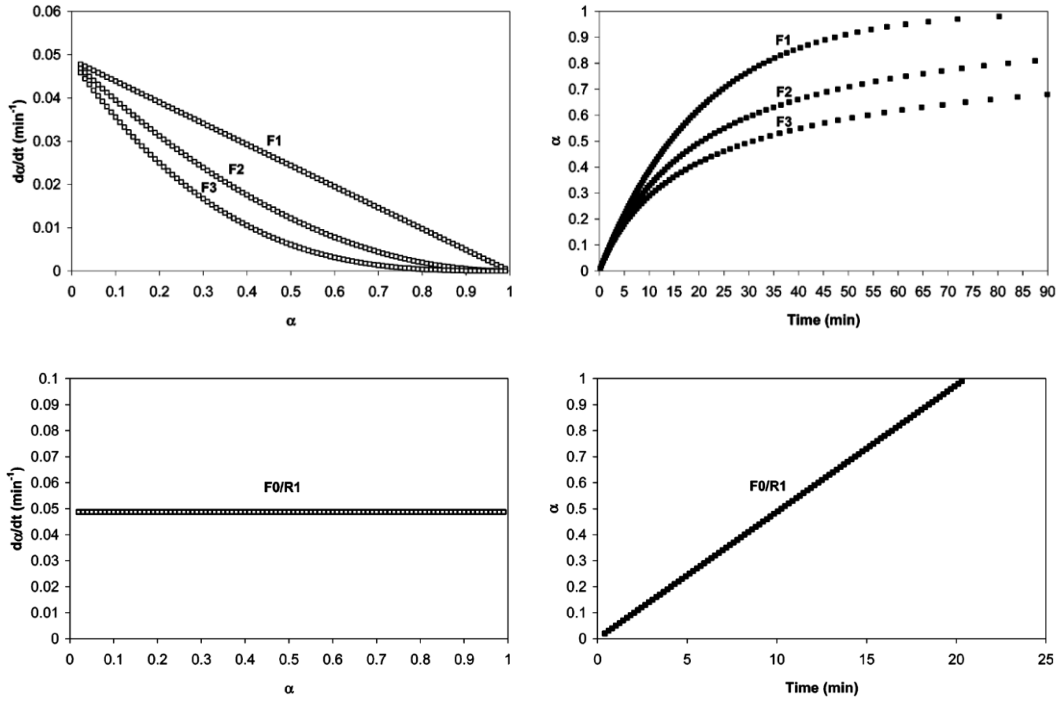

Figure A.13.2: Isothermal $d\alpha/dt$ vs t (left) and α vs t plots (right) indicative of reaction order (top) and zero order (bottom) models for solid-state reactions[158]